applied sciences

Special Issue Reprint

Development, Characterization, Application and Recycling of Novel Construction Materials, 2nd Edition

Edited by
Mouhamadou Amar and Nor Edine Abriak

mdpi.com/journal/applsci

MDPI

Development, Characterization, Application and Recycling of Novel Construction Materials, 2nd Edition

Development, Characterization, Application and Recycling of Novel Construction Materials, 2nd Edition

Guest Editors

Mouhamadou Amar
Nor Edine Abriak

MDPI

Basel • Beijing • Wuhan • Barcelona • Belgrade • Novi Sad • Cluj • Manchester

Guest Editors

Mouhamadou Amar
Institut Mines-Télécom
IMT Nord Europe
Douai
France

Nor Edine Abriak
Institut Mines-Télécom
IMT Nord Europe
Douai
France

Editorial Office
MDPI AG
Grosspeteranlage 5
4052 Basel, Switzerland

This is a reprint of the Special Issue, published open access by the journal *Applied Sciences* (ISSN 2076-3417), freely accessible at: https://www.mdpi.com/journal/applsci/special_issues/519QGV9386.

For citation purposes, cite each article independently as indicated on the article page online and as indicated below:

Lastname, A.A.; Lastname, B.B. Article Title. *Journal Name* **Year**, *Volume Number*, Page Range.

ISBN 978-3-7258-7667-9 (Hbk)
ISBN 978-3-7258-7668-6 (PDF)
https://doi.org/10.3390/books978-3-7258-7668-6

© 2026 by the authors. Articles in this reprint are Open Access and distributed under the Creative Commons Attribution (CC BY) license. The reprint as a whole is distributed by MDPI under the terms and conditions of the Creative Commons Attribution-NonCommercial-NoDerivs (CC BY-NC-ND) license (https://creativecommons.org/licenses/by-nc-nd/4.0/).

Contents

applied sciences

MDPI

Editorial

Recent Advances in the Use of Recycled Materials and SCMs in Construction: Approaches, Microstructure, Durability, and Performance

Mouhamadou Amar [1,*] and Nor-Edine Abriak [2]

[1] Centre for Materials and Processes, Institut Mines-Télécom, IMT Nord Europe, F-59508 Douai, France
[2] Laboratoire de Génie Civil et Géo-Environnement, ULR 4515—LGCgE, Institut Mines-Télécom, University Lille, F-59000 Lille, France
* Correspondence: mouhamadou.amar@imt-nord-europe.fr

1. Introduction

The construction sector is undergoing a profound transition driven by the urgent need to reduce greenhouse gas emissions, preserve natural resources, and enhance infrastructure resilience. Cementitious materials remain at the core of this transformation because of their dominant role in the global built environment and also their versatility. However, conventional Portland cement-based systems are associated with high energy consumption and significant CO_2 emissions. In 2020, global concrete consumption reached the staggering figure of 14 billion m^3. This trajectory is unsustainable: demand for natural aggregates is expected to double by 2060 to reach 60 Gt, while the European Union currently recycles only 9.3% of the 3 Gt of aggregates produced annually. Consequently, there has been an uptick in research on alternative binders, clay-based cement, geopolymers, alkali-activated materials, recycled aggregates, and multi-functional cement-based composites.

This Special Issue, "Recent Advances in the Use of Recycled Materials and SCMs in Construction: Approaches, Microstructure, Durability, and Performance", captures this transition by presenting recent advances that couple material innovation with durability, performance-based design, and circular economy principles. The collected works illustrate how cement and concrete research is evolving from strength-driven optimization toward multi-criteria performance, including durability, sustainability, and end-of-life recovery [1,2].

2. Advances in Cementitious and Alkali-Activated Systems

A major development highlighted across the contributions is the growing maturity of low-clinker and clinker-free binder systems. Supplementary cementitious materials (SCMs) such as fly ash, slag, calcined clays, and industrial by-products are increasingly used not only as partial replacements but as key components in engineered low-carbon binder systems. In parallel, geopolymers and alkali-activated materials are emerging as viable alternatives, offering reduced carbon footprints and promising mechanical and durability performance [3–5].

Progress in hydration science, reaction kinetics, and cement chemistry, supported by advanced characterization tools (e.g., microstructural analysis, thermal methods, and multi-scale mechanical testing) is enabling improved control of setting, strength development, and long-term stability. Particular attention is being paid to the interfacial transition zone, pore structure refinement, and transport properties, which directly govern durability against chloride ingress, carbonation, freeze–thaw cycles, and chemical attack [6].

3. Recycled Aggregates and Circular Construction Materials

Another central theme of this Special Issue is the valorization of construction and industrial waste. The use of recycled concrete aggregates, recycled fine fractions, and other secondary raw materials is being explored to reduce the extraction of natural aggregates and landfill disposal. Research demonstrates that performance limitations traditionally associated with recycled aggregates can be mitigated through optimized mix design, pre-treatment methods, and the incorporation of mineral additions [7–9]. There are also challenges in 3D printing technologies using recycled aggregates [10].

These approaches support the development of circular materials, where product loops are progressively closed. However, the long-term mechanical stability, shrinkage behavior, and durability of such systems under coupled environmental loading represent areas requiring further investigation. The standardization of quality classes for recycled materials and durability-based design frameworks is still evolving.

4. Remaining Knowledge Gaps

Despite rapid progress, several scientific and technical gaps persist. Long-term durability under multi-physics exposure (mechanical loading combined with thermal gradients, moisture transport, and aggressive agents) is not yet fully understood for many novel binders and recycled material systems. Service life prediction models developed for conventional concrete are not always directly transferable to geopolymers or alkali-activated materials.

Furthermore, the variability in secondary raw materials introduces challenges in terms of reproducibility and quality control. Harmonized test protocols and performance-based specifications are needed to support broader industrial adoption. The coupling between microstructural evolution, cracking processes, and transport properties also requires deeper investigation, particularly for fiber-reinforced and hybrid cementitious composites.

5. Contribution of This Special Issue

The contributions in this Special Issue collectively advance the field by combining innovative material formulations with rigorous experimental characterization and application-orientated assessment. An emphasis is placed on durability enhancement, microstructure–property relationships, and the integration of recycled constituents. Several studies also address functional properties beyond mechanical performance, including thermal behavior, shrinkage control, and resistance to aggressive environments.

6. Future Research Directions

Several works focus on long-term field validation of innovative cementitious materials, geopolymers, alkali-activated binders, and recycled aggregate concrete, including the following topics:

- Coupled durability testing under realistic service conditions;
- Development of performance-based standards for low-carbon cementitious systems;
- Multi-scale modeling linking chemistry, microstructure, cracking, and transport;
- Digital tools and data-driven approaches for mix design optimization;
- Design for deconstruction and high-value recycling of cement-based materials.

Stronger collaboration between research institutions, industry, and standardization bodies will be essential to accelerate the safe and reliable implementation of these novel materials in structural and infrastructure applications [2].

https://doi.org/10.3390/app16073417

7. Concluding Remarks

This Special Issue demonstrates that the evolution of cementitious materials is central in achieving sustainable and resilient infrastructure. Advances in alternative binders, geopolymers, and recycled aggregate systems show that significant reductions in environmental impact are achievable without compromising performance. The integration of advanced characterization techniques, durability science, and circular economy principles marks a decisive step toward next-generation concrete technologies.

Author Contributions: M.A.; writing—original draft preparation, N.-E.A.; writing—review and editing. All authors have read and agreed to the published version of the manuscript.

Funding: This research received no external funding.

Informed Consent Statement: Not applicable.

Conflicts of Interest: The authors declare no conflicts of interest.

References

1. Favier, A.; De Wolf, C.; Scrivener, K.; Habert, G. *A Sustainable Future for the European Cement and Concrete Industry Technology Assessment for Full Decarbonisation of the Industry by 2050*; ETH Zurich: Zürich, Switzerland, 1993.
2. Scrivener, K.L.; Gartner, E.M.; John, V.M.; Gartner, E.M.; John, V.M.; Gartner, E.M. Eco-efficient cements: Potential economically viable solutions for a low-CO_2 cement-based materials industry. *Cem. Concr. Res.* **2018**, *114*, 2–26. [CrossRef]
3. Hanein, T.; Thienel, K.C.; Zunino, F.; Marsh, A.T.M.; Maier, M.; Wang, B.; Canut, M.; Juenger, M.C.G.; Haha, M.B.; Avet, F.; et al. Clay calcination technology: State-of-the-art review by the RILEM TC 282-CCL. *Mater. Struct./Mater. Constr.* **2022**, *55*, 3. [CrossRef]
4. Davidovits, J. *Geopolymer Chemistry and Applications*, 5th ed.; Institut Géopolymère: Saint-Quentin, France, 2020.
5. Mehta, A.; Siddique, R. An overview of geopolymers derived from industrial by-products. *Constr. Build. Mater.* **2016**, *127*, 183–198. [CrossRef]
6. Alloul, A.; Amar, M.; Benzerzour, M.; Abriak, N.E. A comparative analysis of ambient-cured metakaolin geopolymer mortar and flash-calcined soil geopolymer. *Constr. Build. Mater.* **2023**, *409*, 134085. [CrossRef]
7. Silva, R.V.; de Brito, J.; Dhir, R.K. Use of recycled aggregates arising from construction and demolition waste in new construction applications. *J. Clean. Prod.* **2019**, *236*, 117629. [CrossRef]
8. Marie, I.; Quiasrawi, H. Closed-loop recycling of recycled concrete aggregates. *J. Clean. Prod.* **2012**, *37*, 243–248. [CrossRef]
9. Abreu, V.; Evangelista, L.; de Brito, J. The effect of multi-recycling on the mechanical performance of coarse recycled aggregates concrete. *Constr. Build. Mater.* **2018**, *188*, 480–489. [CrossRef]
10. Mengistu, G.M.; Nemes, R. Recycling 3D Printed Concrete Waste for Normal Strength Concrete Production. *Appl. Sci.* **2024**, *14*, 1142. [CrossRef]

Disclaimer/Publisher's Note: The statements, opinions and data contained in all publications are solely those of the individual author(s) and contributor(s) and not of MDPI and/or the editor(s). MDPI and/or the editor(s) disclaim responsibility for any injury to people or property resulting from any ideas, methods, instructions or products referred to in the content.

https://doi.org/10.3390/app16073417

applied sciences

MDPI

Article

A Hipocarbonic Binder Strategy Through the Reuse of Crushed Tempered Glass

Maria Teresa Gomes Barbosa [1,*], Mayara Carelli de Paula Costa [1] and Nelson Luis Gonçalves Dias de Souza [2]

[1] Engineering Faculty, Federal University of Juiz de Fora, Juiz de Fora 36036-900, MG, Brazil; eng.mayaracarelli@gmail.com
[2] Chemistry Faculty, Federal University of Tocantins, Palmas 77001-090, TO, Brazil; nelson.luis@mail.uft.edu.br
* Correspondence: teresa.barbosa@ufjf.br

Abstract

The reuse of waste generated in various sectors has become a sustainable alternative. Advances in research highlight its potential as a secondary raw material to produce construction materials, contributing to the reduction in waste disposal while mitigating the intensive exploitation of natural resources. Tempered glass is rarely used in recycling and in the production of new materials. Therefore, this study evaluated the applicability of using it, after glass crushing, as a partial replacement for natural sand in the production of cement products. Thus, natural sand was replaced by 25% and 50% with sand resulting from glass crushing, and the mechanical properties (mechanical strength) and porosity (water absorption and void index) of the cementitious mixtures (mortars) were evaluated at 28 days, as well as their chemical properties and CO_2 emissions. Glass powder (a result of crushing glass) was added to the mixtures to maximize the use of residual materials and improve the performance of the composite. The results demonstrate gains of approximately 10% in the studied properties with the substitution of natural sand with crushed tempered glass sand, and above 24% for the addition of glass powder, i.e., the addition of 20% powder glass tends to contribute favorably to the performance of cementitious mixtures, supporting the production of more sustainable building materials and making it an appropriate strategy for the circular economy.

Keywords: waste reuse; cementitious composite; circular economy; sustainability

1. Introduction

The circular economy is a production and consumption model that reduces waste and maximizes reuse. It aligns with sustainable development by stimulating the reuse and recycling of waste [1,2]. This system allows for the regeneration of nature and the minimization of waste generation, since products and materials are kept in circulation for as long as possible through processes such as maintenance, reuse, and recycling, among others [3,4].

The adoption of the circular economy concept promotes technological innovation in the construction industry. This results in sustainable products that incorporate environmental principles and offer economic benefits to the sector. Several studies [5–9] show that recycled building materials can achieve properties similar to or better than conventional materials. They also offer lower costs compared to those that use natural resources.

In this context, the glass industry has improved and developed multiple strategies for managing its waste, such as high-tech recovery, which even employs artificial intelligence

and collaborative robots to characterize and recover special glass sheets (e.g., smartphone screens) [3], as well as the development of public policies that promote the circular economy, such as specific legislation on the subject, which includes economic incentives [10], waste reuse, efficient waste management [11], among others [12].

In Brazil, a majority of the 7350 tons/day of float glass produced is derived from special glass, such as "safety glass" (59% tempered, 15% laminated). In the case of tempered glass, this results in a 35% waste in civil construction, such as pieces and shavings, leftovers from cutting products (such as doors and windows) [13]. It should be noted that tempered glass, due to the production process and its different chemical composition, is rarely used in recycling.

The addition of waste (crushing tempered glass) into concrete and mortar production, especially as a partial or complete replacement for aggregates, tends to minimize the negative impacts of waste [14], providing an efficient approach to industrial waste management [15], as well as providing benefits to the physical, chemical, and mechanical properties of cementitious composites [16,17]. Some researchers [18,19] have investigated the inclusion of this waste as coarse aggregate in conventional concrete production. However, one of the drawbacks of crushing tempered glass is the shape of the grains, as smooth particles (low surface roughness) [20] require a greater amount of Portland cement due to the increased void coefficient [21].

Therefore, the procedure adopted in this research consists of two stages: the incorporation of glass powder (resulting from crushing) as a supplementary cementitious material [22,23], resulting in eco-efficiency gains (both environmental and economic) in the mixtures [24], as well as the partial replacement of sand by crushed tempered glass, where the efficiency of including glass powder in the densification of the composite and in the performance of the mixtures was evaluated [25].

The experimental program is presented below, where the mechanical properties (compressive strength and diametral compression tensile strength), absorption, and chemical properties in mortar mixtures with/without tempered glass crushing were investigated.

The EMMA (Elkem Materials Mixture Analyzer) computational tool was used to determine the optimal ratio between the materials, i.e., a more efficient composition of the mortar constituents [26,27]. This procedure allows for the proper proportioning of particulate materials, so that larger voids are filled with smaller particles, which are then refilled with even smaller particles, and so on, successively [28,29].

In practice, an ideal (theoretical) particle size distribution curve is adopted through particle packing models, seeking a combination of the particles of the available materials that approximates this ideal curve as closely as possible [26,27]. This is a computational procedure that uses the granular system constituting the mixture [29].

Motivation and Contribution of This Research

(i) Partial replacement of natural sand with crushed tempered glass contributes to more sustainable solutions and minimizes environmental impacts.
(ii) Effective incorporation of waste in the mortar mixture, including crushed powder, contributes to its mechanical properties [8] and intrinsic characteristics of the composite [30,31].
(iii) Employment of the "grain packing" concept through the specific particle size of each material.
(iv) Strengthening the principles of the circular economy by minimizing the extraction of natural materials (i.e., natural sand) and enabling technically viable and environmentally responsible cementitious matrices.

https://doi.org/10.3390/app16031483

The highlight of this research is the reuse of so-called specialty tempered glass waste, investigating various aspects that address the interaction between the components. This approach also shows promise for applications in other cementitious composites, including fiber-reinforced systems.

2. Materials and Methods

2.1. Materials

- Portland cement (C) (type: CPV [32]).
- Sand produced by the Technological Research Institute (IPT/Brazil) [33] (S), (γ = 2.65 kg/dm^3, maximum diameter = 2.36 mm).
- Sand from crushed tempered glass (same grain size S) (G), (γ = 2.70 kg/dm^3, maximum diameter = 2.36 mm).
- Silica fume (SF) (% SiO_2 > 90%, γ_R= 2.22 kg/dm^3, $Ø_{max}$ = 200 nm–1 µm).
- Tempered glass powder (P), (γ = 2.70/dm^3, $Ø_{max}$ = 200 nm–1 µm).
- Additive (superplasticizer): MC-PowerFlow 4001, MC-Bauchemie (γ = 1.12 kg/L).
- Water.

The Elkem Materials Mixture Analyzer (EMMA) computational tool was used to determine the proportion of materials used in the mortar to achieve a more efficient arrangement between material grains, based on data relating to the particle size of the materials and their density [26,27]. The mix proportion reference, by weight, was 1:3:0.25:0.37:0.02 (cement: sand: silica fume: water/cement ratio: superplasticizer additive) (see Figure 1). Table 1 presents the mixture proportions and their nomenclature.

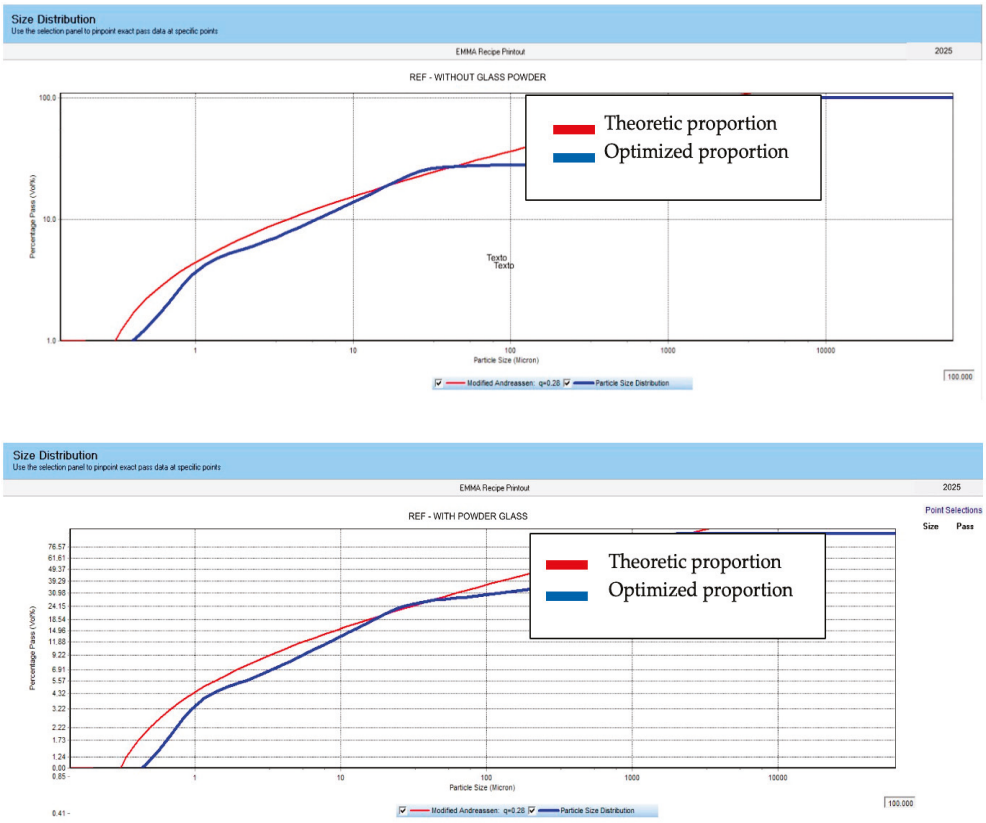

Figure 1. Optimized mix proportion.

https://doi.org/10.3390/app16031483

Table 1. Nomenclature and mix proportion (weight) research.

Nomenclature	C	S	G	SF	P	w/c Ratio	Additive
REF	1	3	-	0.05	-	0.37	0.01
REF25	1	2.25	0.75	0.05	-	0.37	0.01
REF50	1	1.5	1.5	0.05	-	0.37	0.01
REFP	1	3	-	0.05	0.20	0.37	0.02
REF25P	1	2.25	0.75	0.05	0.20	0.37	0.02
REF50P	1	1.5	1.5	0.05	0.20	0.37	0.02

As shown in Table 1, the reference mixture proportion (REF) was studied, and natural sand was partially replaced with sand resulting from the crushing of tempered glass at levels of 25% and 50%, i.e., REF25 and REF50, respectively. It should be noted that the particle size distribution of the crushed tempered glass is the same as that of natural sand. Subsequently, 20% glass powder (resulting from crushing) was added relative to the amount of cement (REFP). This level was adopted as the maximum limit to avoid compromising the mechanical properties of the composite [34]. The addition of glass powder aims to increase the consumption of waste and densify the aggregate/cement paste transition zone, since the shape and texture of the grains obtained in the crushing of tempered glass (low surface roughness) tend to impair the performance of the mixture and/or increase cement consumption [20,21]. The consistency of the mixtures was set at 270 $\pm$ 10 mm, which was determined according to Brazilian standards through the flow table [35].

2.2. Methods

The six specimen tests (10 cm $\times$ 5 cm—high $\times$ diameter) were made for each investigated property. They were subjected to curing in a humid chamber according to Brazilian standards (temperature = 21 °C and air humidity = 95%) [36]. After curing for 28 days, many tests were carried out, including compressive strength ($\mathbf{f_c}$) [37], diametral compression tensile strength ($\mathbf{f_{ct,sd}}$) [38], void index (**Iv**), and immersion absorption (**A**) [39].

For chemical analyses, a Perkin Elmer FTIR spectrometer (PerkinElmer, Waltham, MA, USA) was used in the region of 4000–400 cm^{-1}, with a resolution of 4 cm^{-1}, an average of 64 scans, and using a KBr tablet. The samples were dried in an oven at 110 °C for 24 h before obtaining the spectra to minimize the influence of water absorbed by the samples.

3. Results and Discussion

Table 2 and Figures 2–4 show the average results of the properties along with the variation coefficient (CV). This procedure is used when you want to compare the variability of several samples with their average value; if the CV value is less than 25%, the sample will be accepted.

Table 2. Average result properties in a mixed proportion.

Mix	f_c (MPa)	$f_{ct,\ sd}$ (MPa)	A (%)	Iv (%)
REF	69.23 (CV = 15.5%)	10.20 (CV = 3.0%)	0.28 (CV = 2.0%)	0.44 (CV = 2.10%)
REF25	74.61 (CV = 16.2%)	10.7 (CV = 16.0%)	0.27 (CV = 18.0%)	0.45 (CV = 9.90%)
REF50	43.70 (CV = 19.5%)	9.82 (CV = 17.1%)	0.31 (CV = 22.0%)	0.55 (CV = 15.0%)
REFP	83.70 (CV = 16.3%)	11.03 (CV = 15.2%)	0.23 (CV = 16.3%)	0.39 (CV = 18.0%)
REF25P	86.15 (CV = 16.2%)	12.63 (CV = 18.2%)	0.24 (CV = 17.4%)	0.37 (CV = 17.2%)
REF50P	55.70 (CV = 19.2%)	7.75 (CV = 15.3%)	0.39 (CV = 17.4%)	0.47 (CV = 17.6%)

https://doi.org/10.3390/app16031483

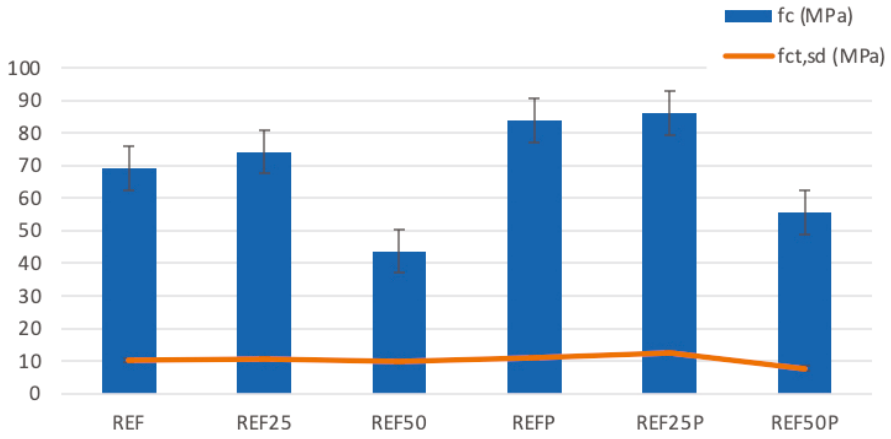

Figure 2. Compressive strength (MPa) × diametral compression tensile strength (MPa).

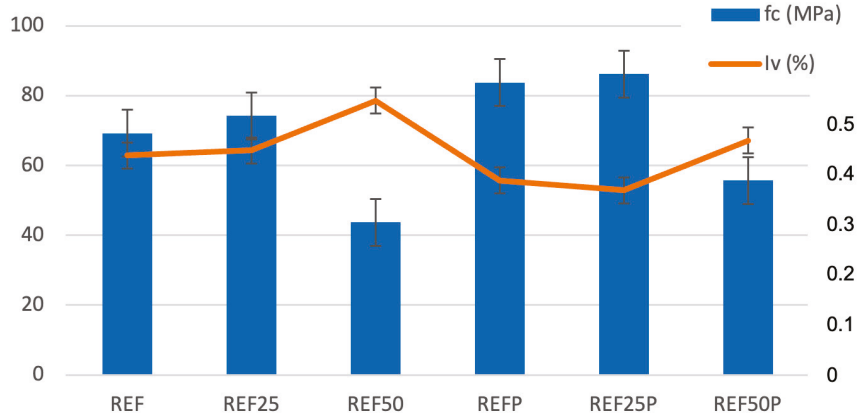

Figure 3. Compressive strength (MPa) × void index (%).

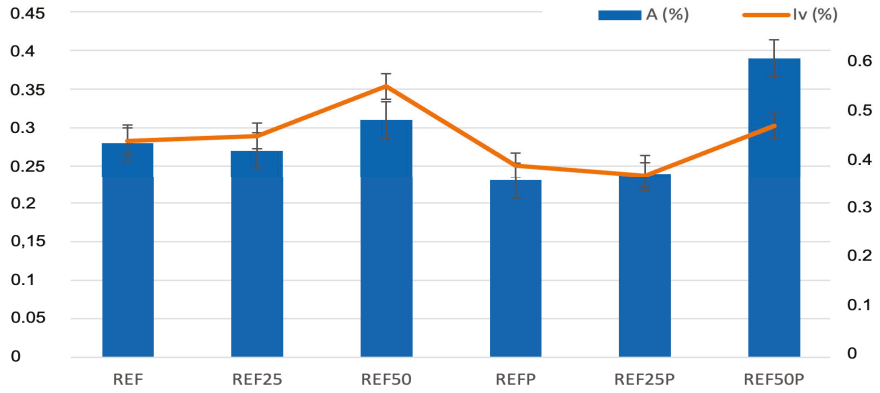

Figure 4. Absorption (%) × void index (%).

Analyzing Table 2 and Figures 2–4, the following can be seen:

The roughness of the surface of the aggregate influences the mechanical properties. As the level of replacement of natural sand with artificial sand (crushed glass) increases, the strength tends to reduce, as this material, when fragmented, does not generate irregularities (the so-called "sharp edges") on the surface of the aggregate, which impairs the adhesion of the cement paste with the aggregate, interfering with the binder/aggregate transition zone. Therefore, one of the possible solutions to be adopted is the "reinforcement" of the mixture, either by increasing the consumption of binder or by using an additional material that allows densification of the transition zone, which in this research consists of the use of glass powder.

https://doi.org/10.3390/app16031483

The replacement of natural sand with crushing glass has been investigated in other research, resulting in improvements in mortar properties, where it was found that 15% replacement of sand with crushing glass results in gains in mixture properties of above 10%, (compressive strength, absorption, among others) [40] as also observed in this study (see Table 2).

Furthermore, the combined use of glass powder and silica fume shows promise, making it possible to reduce cement consumption; that is, the waste is used as a supplementary material, benefiting the properties of cement mixtures, as well as reducing cement consumption, a fact evidenced in the results, as well as in other research [41] even contributing to the reduction in voids in the mixtures studied.

It is noted that as the replacement level of natural sand with glass sand increases, there are losses in mixture properties due to the weakening of the transition zone, caused by the lack of irregularity on the surface of the aggregate, i.e., the mix REF50 proportion, which has a high level of natural aggregate replacement, does not present satisfactory performance of the mixture, presenting a marked loss of properties and little gains from the inclusion of glass powder. Therefore, this mixture was discarded due to the damage caused to the mortar properties.

Figure 5 shows the infrared absorption spectra of the compounds used to obtain the test specimens. Table 3 describes the attempted assignment of cement bands in accordance with the literature [42,43].

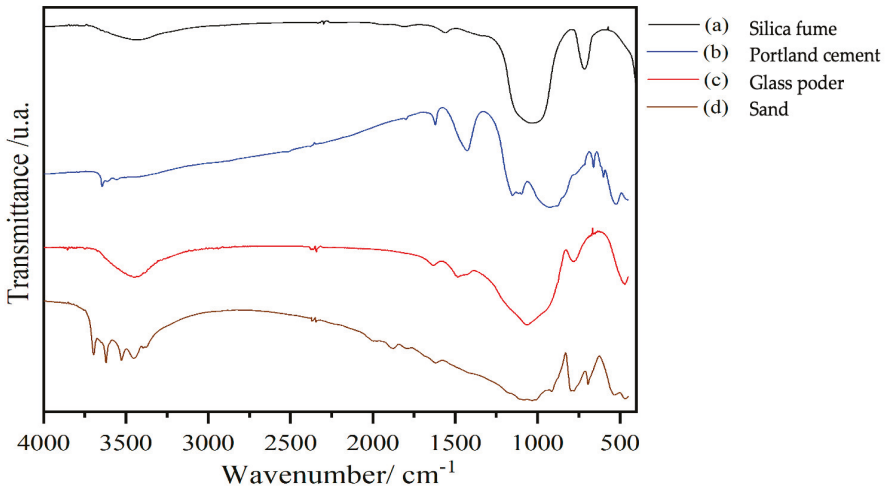

Figure 5. Infrared absorption spectrum.

Table 3. Assignment of the main infrared absorption bands (cm^{-1}).

Portland Cement	Assignment Attempt
3642	ν (OH) Portlandita
3610	ν (OH) Bassanita
3556	ν (OH) $CaSO_4.2H_2O$
1620	δ (OH) $CaSO_4.2H_2O$
1797	ν (C=O) $CaCO_3$
1428	ν_3 (CO_3^{2-})
1151	ν_3(SO_4^{2-})
922	ν_3 (Si-O)
877	ν_2 (CO_3^{2-})
714	ν_4 (CO_3^{2-})
658	ν_4 (SiO_4)
600	ν (S=O) SO_4^{2-}
525	ν_4 (Si-O) C_3S e C_2S

https://doi.org/10.3390/app16031483

Figure 6 shows the infrared absorption spectra of the specimens that were obtained from Portland cement, and by comparing them, it is possible to observe spectral differences that indicate the hydration process of the samples [44]. The band at 922 cm^{-1} in unhydrated cement refers to ν_3 (Si-O); however, during hydration, a polymerization process occurs, which tends to shift to higher wave numbers and become wider, due to the formation of hydrated calcium silicate (CSH). Therefore, this band can be used to evaluate the degree of hydration [45].

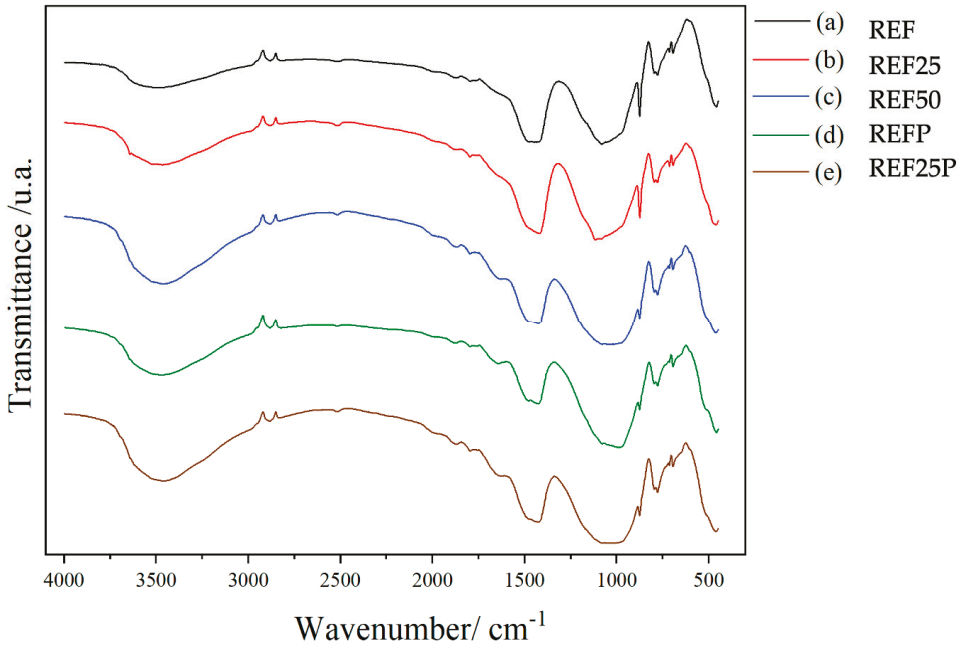

Figure 6. Infrared absorption spectrum.

In relation to the samples, it is observed that REF50, REFP, and REF25P present a band shift from 922 cm^{-1} to the region of 1130 cm^{-1} with greater relative intensity, indicating a greater hydration. The REF and REF25 samples present more similar spectra in relation to this spectral region; therefore, similar hydration stages are expected for both samples. The band at 525 cm^{-1} can also be used to analyze the hydration process, as its intensity decreases during this process [46]. Thus, by analyzing the spectra, it is observed that this band appears in the form of a shoulder that is not very intense in all analyzed samples.

Calcium carbonate is added to cement by the manufacturer, and as hydration progresses, it is consumed due to its reaction with aluminates, which forms less crystalline phases (carboxyaluminates) [46]. Therefore, the bands corresponding to this compound are expected to decrease in intensity as hydration progresses [47]. Thus, the bands corresponding to carbonates at 1428 and 877 cm^{-1} are observed to be less intense in samples REF 50, REFP, and REF 25P, indicating a higher degree of hydration for these samples.

The spectral data indicate that replacing 25% of the sand with glass sand (REF25) does not alter hydration and therefore does not negatively impact the mechanical properties of the specimens. This is consistent with the mechanical strength data, as samples REF and REF25 present similar results. Replacing 50% of the sand with glass sand (REF50) resulted in a spectral profile of a specimen with a higher degree of hydration; however, this did not result in a sample with greater mechanical strength. This can be explained by the lower roughness of the glass sand, which reduces adhesion between the particles that make up the mortar and, consequently, reduces mechanical strength. Finally, the addition of glass powder (REFP) and the replacement of sand with 25% glass sand with glass powder

https://doi.org/10.3390/app16031483

addition (REFP25) resulted in samples with a higher degree of hydration and, therefore, better mechanical properties, as observed in the results presented.

Considering the results obtained, it is also important to evaluate the CO_2 emissions of the new product to contribute to sustainable development [48]. In this sense, the carbon footprint seeks to quantify the amount of equivalent carbon dioxide generated during a process, service, or product. The calculation of total carbon dioxide emissions (Equation (1)) considers the emissions from each unit operation carried out in the process [49].

$$CO = \sum M_i.F_I \quad (1)$$

where CO = CO_2 emissions; M_i—material consumption in unit i; and F_i—carbon emission factor per unit weight of each construction material.

The emissions from the mixtures were based on the Brazilian database, see Figure 7, where the addition of supplementary materials contributes to minimizing carbon emissions; however, mechanical properties must be ensured, with a balance between mechanical and environmental contributions. Thus, waste must contribute effectively to a sustainable built environment and the circular economy, while also ensuring the performance of the product.

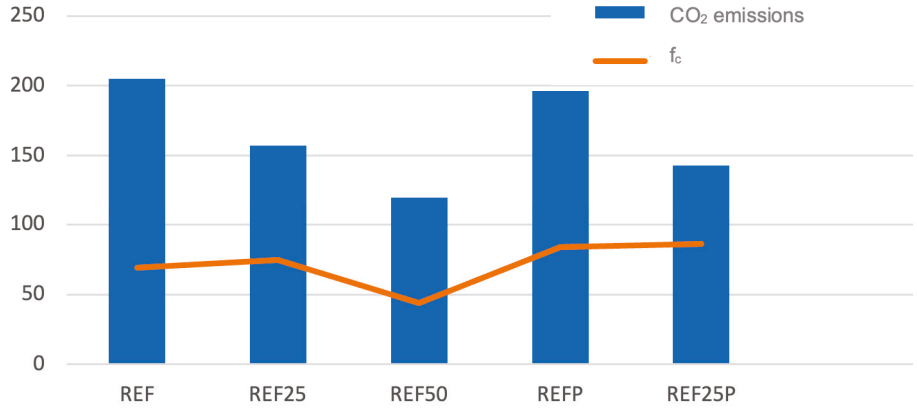

Figure 7. CO_2 emissions ($kgCO_2/m^3$) × compressive strength (MPa).

4. Conclusions

The research, supported by particle packing analyses, experimental testing, and chemical characterization, confirmed the technical feasibility of using crushed tempered glass waste as a partial substitute—up to 25%—for natural sand in the production of cement mortars. The incorporation of glass powder enhanced the densification of the interfacial transition zone between the recycled aggregate and the cement paste, contributing to improved microstructural compactness, reduced carbon emissions, and the promotion of more sustainable building materials.

Regarding mechanical and durability performance, the mixtures exhibited increased compressive strength and durability, demonstrating the potential of this waste material to support the development of more efficient and sustainable construction solutions, in alignment with international guidelines aimed at advancing low-impact and resource-efficient building practices. Finally, further studies are suggested regarding possible alkali–aggregate reactions.

Author Contributions: Conceptualization, M.T.G.B., M.C.d.P.C. and N.L.G.D.d.S.; methodology, M.T.G.B. and M.C.d.P.C.; formal analysis, M.T.G.B., M.C.d.P.C. and N.L.G.D.d.S.; investigation, M.T.G.B., M.C.d.P.C. and N.L.G.D.d.S.; resources, M.T.G.B., M.C.d.P.C. and N.L.G.D.d.S.; writing—original draft preparation, M.T.G.B., M.C.d.P.C. and N.L.G.D.d.S.; writing—review and editing, M.T.G.B.; visualization, M.C.d.P.C. and N.L.G.D.d.S.; supervision, M.T.G.B., M.C.d.P.C. and

https://doi.org/10.3390/app16031483

N.L.G.D.d.S.; project administration, M.T.G.B. All authors have read and agreed to the published version of the manuscript.

Funding: This research received no external funding.

Institutional Review Board Statement: Not applicable.

Informed Consent Statement: Not applicable.

Data Availability Statement: The original contributions presented in this study are included in the article. Further inquiries can be directed to the corresponding author.

Acknowledgments: The Federal University of Juiz de Fora, the Federal University of Tocantins, FAPEMIG (Foundation for Support and Development of Education, Science, and Technology of Minas Gerais), CAPES (Coordination for the Improvement of Higher Education Personnel), and CNPq (Brazilian National Council for Scientific and Technological Development).

Conflicts of Interest: The authors declare no conflicts of interest.

References

1. Nikolova-Minkova, V. The Reuse of Waste Materials in the Context of the Circular Economy. In *Unitech—Selected Papers*; Technical University of Gabrovo: Gabrovo, Bulgaria, 2024. [CrossRef]
2. Okeke, N.K. Na Investigation of how the circular economy's up-cicling, repair, reuse and recycling strategies might increase resource efficiency and reduce fabric waste Generation on Nigeria. *J. Des. Studio* **2025**, *7*, 113–130. [CrossRef]
3. Delbari, S.A.; Hof, L. Glass waste circular economy—Advancing high value glass sheets recovery using industry 4.0 and 5.0 technologies. *J. Clean. Prod.* **2024**, *462*, 142629. [CrossRef]
4. Sancheta, L.N.; Chaves, G.L.D.; Siman, R.R. The use of system dynamics on urban solid waste management: A liter-ature analysis. *Gestão Produção* **2021**, *28*, e5336. [CrossRef]
5. Marques, H.F.; Ribeiro, C.; Oliveira, D.; Bamberg, P.; Almeida, M. Reuse of construction waste: The practice of a recycling plant in the state of Paraná. *Braz. J. Dev.* **2020**, *6*, 21912–21930. [CrossRef]
6. Kabirifar, K.; Mojtahedi, M.; Wang, C.; Tam, V. Construction and demolition waste management contributing factors coupled with reduce, reuse, and recycle strategies for effective waste management: A review. *J. Clean. Prod.* **2020**, *263*, 121265. [CrossRef]
7. Soares Filho, J.; Aurich, J.; Sousa, F.; Nascimento, R.; Paskocimas, C.; Silva, A. Polishing Performance of eco-friendly porcelain stoneware tiles reusing bricks and roof tiles wastes. *J. Clean. Prod.* **2020**, *256*, 120362. [CrossRef]
8. Almada, L.S.; Melo, D.; Bubani, L.; Silva, G.; Santos, W.; Aguilar, M.T. Influence of the heterogeneity of waste from wet processing of ornamental stones on the performance of Portland cement composites. *Constr. Build. Mater.* **2020**, *262*, 120036. [CrossRef]
9. Chien, C.; Aviso, K.; Tseng, M.; Fujii, M.; Lim, M.K. Solid waste management in emerging economies: Opportunities and challenges for reuse and recycling. *Resour. Conserv. Recycl.* **2023**, *188*, 106635. [CrossRef]
10. Wei, K.; Teoh, W.; Xu, X.; Huang, B.; Geng, Y. A review of glass recycling policies in Stockholm, Hong Kong SAR and Shanghai from a circular economy perspective. *J. Clean. Prod.* **2023**, *434*, 140068. [CrossRef]
11. Veja, D.; Bautista-Rodriguez, S. The impact of circular economy strategies on municipal waste management: A system dynamics approach. *Clean. Eng. Technol.* **2024**, *21*, 100761. [CrossRef]
12. Megavand, B.; Cao, W.; Maio, F.; Rem, P. Circularity in practice: Review of main current approaches and strategic propositions for an efficient circular economy of materials. *Sustainability* **2022**, *14*, 962. [CrossRef]
13. Silva, W.; Filgueiras, C. Glass and its importance in life and chemistry. *Chem. New* **2023**, *46*, 491–501. [CrossRef]
14. Moreno, A.; Ponce, C.; Múzquiz, E.; Avalos, F. Marble residues in construction materials: A review of the marble dust in mortars, concrete, and bricks. *Rev. ALCONPAT* **2022**, *12*, 162–183. [CrossRef]
15. Anitha, S.D.; Dinesh, A.; Sarath, B.V. Investigation of waste marble powder in the development of sustainable concrete. *Mater. Today Proc.* **2021**, *44*, 4223–4226. [CrossRef]
16. Singhal, V.; Nagar, R.; Agrawal, V. Use of marble slurry powder and fly ash to obtain sustainable concrete. *Mater. Today Proc.* **2021**, *44*, 4387–4392. [CrossRef]
17. Mirouzi, G.; Houda, A. Effect of mineral additions on the mechanical behavior of polymer concretes. *World J. Eng.* **2023**, *21*, 851–861. [CrossRef]
18. Tretin, P.O.; Manica, J.; Vanzetto, S.C.; Marangoni, B.; Zaleski, A. Partial replacement of small aggregate by ground glass residue in the production of mortar. *Matéria* **2020**, *25*. [CrossRef]
19. Assis, K.; Trindade, J.; Reis, M.J.; Reis, J.C.; Sanjulião, L.; Reis, F. Partial replacement of fine aggregate with ground glass residue in the production of concrete and its interference in compressive strength. *Rev. Bras. Gestão Amb. Sust.* **2023**, *10*, 1495–1505. [CrossRef]

https://doi.org/10.3390/app16031483

20. Pour-Moghaddam, N. Experimental Investigations into the fragmentation of tempered glass. In *On the Fracture Behaviour and the Fracture Pattern Morphology of Tempered Soda-Lime Glass*; Mechanik, Werkstoffe und Konstruktion im Bauwesen; Springer: Wiesbaden, Germany, 2020; Volume 54. [CrossRef]
21. Hussain, S.; Moiz, S. An overview of tempered glass load bearing capability and mechanical behavior. *ENG Trans.* **2022**, *3*, 1–9. [CrossRef]
22. Habert, G.; Miller, S.; John, V.; Provis, A.; Favier, A.; Horvath, K.L. Environmental impacts and decarbonization strategies in the cement and concrete industries. *Nat. Rev. Earth Environ.* **2020**, *1*, 559–573. [CrossRef]
23. Costa, M.C.; Barbosa, M.T.; Sá, R.R.; Sousa, C.D.; Souza, N.L.; Rivelli, L.I. Analysis of the efficiency of adding silica, glass powder, Amazon chestnuts, and biopolymer on the mortar performance. *J. Build. Pathol. Rehabil.* **2024**, *9*, 115. [CrossRef]
24. Anjos, M.; Camões, P.; Campos, G.; Azeredo, G.; Ferreira, R. Effect of high-volume fly ash and metakaolin with and without hydrated lime on the properties of self-compacting concrete. *J. Build. Eng.* **2020**, *27*, 100985. [CrossRef]
25. Campos, H.; Klein, N.; Marques Filho, M.; Bianchini, M. Low-cement high-strength concrete with partial replacement of Portland cement with stone powder and silica fume designed by particle packing optimization. *J. Clean. Prod.* **2020**, *261*, 121228. [CrossRef]
26. Oliveira, S.; Soranço, L.; Pereira, T.; Games, B.; Ferreira, C.; Barbosa, M.T. Research of the addition of N95 facial mask fibers, silica fume, and marble powder in high-performance mortar. *Matéria* **2023**, *28*, e20230042. [CrossRef]
27. Oliveira, S.; Sá, R.; Barbosa, M.T.; Garcia, D.; Costa, M.C.; Souza, N.; Ludwig, Z. Investigation of the influence of the addition of graphene oxide nanoparticles in mortars made with the addition of silica fume, marble powder and fibers from the crushing of the N95 face masks. *Case Stud. Constr. Mater.* **2024**, *21*, e03843. [CrossRef]
28. Pinto, F.; Martins, M.; Werdine, D.; Santos, V.; Gonçlaves, P.; Barros, R.; Mello, M. Mixture design for self-compacting concrete using a virtual particle packing method. *Braz. J. Dev.* **2021**, *7*, 50029–50049. [CrossRef]
29. Lopes, H.; Peçanha, A.; Castro, A. Considerations on the efficiency of Portland cement concrete mixtures based on the particle packing concept. *Matéria* **2020**, *25*. [CrossRef]
30. Janani, R.; Kaveri, V. A critical literature review on reuse and recycling of construction waste in the construction industry. *Mater. Today Proc.* **2021**, *37*, 3077–3081. [CrossRef]
31. Ghaffar, S.; Burman, M.; Braimah, N. Pathways to circular construction: An integrated management of construction and demolition waste for resource recovery. *J. Clean. Prod.* **2020**, *244*, 118710. [CrossRef]
32. *NBR 16697*; Portland Cement—Requirements. Brazilian Standard (ABNT): Rio de Janeiro, Brazil, 2018.
33. *NBR 7214*; Sand for Cement Testing—Specifications. Brazilian Standard (ABNT): Rio de Janeiro, Brazil, 2015.
34. Zanwar, A.B.; Patil, Y.D. Enhancement of sustainable mortar by using fine glass powder. In *Advances in Sustainable Construction Materials and Geotechnical Engineering*; Shukla, S., Barai, S., Mehta, A., Eds.; Lecture Notes in Civil Engineering; Springer: Singapore, 2020; Volume 35. [CrossRef]
35. *NBR 13276*; Consistency Index Determination. Brazilian Standard (ABNT): Rio de Janeiro, Brazil, 2002.
36. *NBR 9479*; Curing Mortar and Concrete Specimens. Brazilian Standard (ABNT): Rio de Janeiro, Brazil, 2006.
37. *NBR 7215*; Cement Portland—Determination of Compressive Strength. Brazilian Standard (ABNT): Rio de Janeiro, Brazil, 2025.
38. *NBR 7222*; Cement Portland—Determination of Diametric Tensile Strength. Brazilian Standard (ABNT): Rio de Janeiro, Brazil, 2011.
39. *NBR 9778*; Mortar and Concrete—Determination of Water Absorption of Immersion. Brazilian Standard (ABNT): Rio de Janeiro, Brazil, 2009.
40. Jamellodin, Z.; Yi, L.; Lafit, Q.; Algaifi, H.; Hamdam, R.; Al-Gheethi, A. Evaluation of fresh and hardened concrete properties incorporating glass waste as partial replacement of fine aggregate. *Sustainability* **2022**, *14*, 15895. [CrossRef]
41. Tyrer, M.; Holmes, N.; Yio, M.; Wong, H. Predicting the hydration of ground granulated blast furnace slag and recycled glass blended cement. *Appl. Sci.* **2025**, *15*, 6872. [CrossRef]
42. Barbosa, M.T.; Innocencio, C.R.; Salzani, L.; Pereira, T.; Souza, N.L.; Oliveira, L.F. Lime-based mortars with added silica fume and bioproducts for restoration and preservation of heritage buildings. *J. Build. Pathol. Rehabil.* **2023**, *8*, 37. [CrossRef]
43. Feitosa, L.; Costa Filho, J.; Sousa, C.; Martins, W.; Barbosa, M.T.; Cavallini, G.; Oliveira, L.F.; Souza, N.L. Crude Glycerin, a By-product of Biodiesel, as Admixture for Concrete Pieces. *Iran. J. Sci. Technol. Trans. Civ. Eng.* **2023**, *47*, 863–872. [CrossRef]
44. Li, Z.; Corr, D.; Han, B.; Shah, P. Investigating the effect of carbon nanotube on early age hydration of cementitious composites with isothermal calorimetry and Fourier transform infrared spectroscopy. *Cem. Concr. Compos.* **2020**, *107*, 103513. [CrossRef]
45. He, S.; Yu, P.; Zou, F. Effect of lime mud under wet grinding on the compressive strength and hydration of cement mortar. *Cem. Concr. Compos.* **2023**, *140*, 105067. [CrossRef]
46. Tararushkin, E.; Shchelokova, T.; Kudryavtseva, V. A study of strength fluctuations of Portland cement by FTIR spectroscopy. *IOP Conf. Ser. Mater. Sci. Eng.* **2020**, *919*, 022017. [CrossRef]
47. Wilinska, I.; Pacewska, B.; Antonovic, V. Hydration Processes of Four-Component Binders Containing a Low Amount of Cement. *Materials* **2022**, *15*, 2192. [CrossRef]

https://doi.org/10.3390/app16031483

48. Wan, O.; Zhao, X.; Liu, H.; Dinçer, H.; Yüksel, S. Assessing the New Product Development Process for the Industrial Decarbonization of Sustainable Economies. *SAGE Open* **2022**, *12*, 1–20. [CrossRef]
49. Cardona, Y.; Ramos, W.; Perez, O. Estimating CO_2 emissions of concrete containing waste glass. *Politec. J.* **2022**, *18*, 52–70. [CrossRef]

Disclaimer/Publisher's Note: The statements, opinions and data contained in all publications are solely those of the individual author(s) and contributor(s) and not of MDPI and/or the editor(s). MDPI and/or the editor(s) disclaim responsibility for any injury to people or property resulting from any ideas, methods, instructions or products referred to in the content.

https://doi.org/10.3390/app16031483

applied sciences

MDPI

Article

The Synthesis and Characterization of Geopolymers Using Metakaolin and Mirror Glass Waste

Ivana Perná *, Martina Nováková, Daniela Řimnáčová, Monika Šupová, Margit Žaloudková and Olga Bičáková

Institute of Rock Structure and Mechanics, Czech Academy of Sciences, V Holešovičkách 94/41, 182 09 Prague 8, Czech Republic; martina.novakova@irsm.cas.cz (M.N.); rimnacova@irsm.cas.cz (D.Ř.); supova@irsm.cas.cz (M.Š.); zaloudkova@irsm.cas.cz (M.Ž.); bicakova@irsm.cas.cz (O.B.)
* Correspondence: perna@irsm.cas.cz; Tel.: +420-266-009-253

Abstract

This study investigates a metakaolin-based geopolymer matrix in which two types of non-recyclable mirror glass waste (MGW) were used as alternative aggregates. The composition, properties and contents of MGW materials as well as their impact on the structure and performance of the geopolymer composites (MGW-Gs) have been characterized using X-ray fluorescence (XRF), X-ray diffraction (XRD), scanning electron microscopy (SEM), thermo-gravimetric analysis (TG), and Fourier transform infrared spectroscopy (FTIR). Mechanical properties, porosity and thermal conductivity have been evaluated, and compared with silica sand reference composites. The results show that MGW-based composites achieved flexural strengths of 3.9–5.7 MPa and compressive strengths of 60–70 MPa, which are lower than those of sand-based materials (8–11 MPa and up to 93.5 MPa, respectively) but remain adequate performance for applications with moderate load. FTIR analysis has indicated that the incorporation of MGW does not adversely affect the geopolymer network. All composites display similar porosity (approximately 18–22%) and water absorption (12–14%), while MGW incorporation has improved their thermal stability and significantly reduced their thermal conductivity to values below 0.53 $W \cdot m^{-1} \cdot K^{-1}$, compared with up to 1.09 $W \cdot m^{-1} \cdot K^{-1}$ for sand-based composites, emphasizing their insulation potential and sustainability benefits. The findings indicate that MGW aggregates can influence the microstructure, mechanical performance, and thermal properties of geopolymer composites, suggesting their potential use in specific construction applications.

Keywords: geopolymer; mirror glass waste; alternative aggregate; characterization

1. Introduction

Since prehistoric times, people have been fascinated by their own image. The earliest primitive mirrors used were natural surfaces of standing water, such as ponds or vessels filled with water. Over time, people developed solid mirrors that were easier to carry and use. The earliest known examples, dating from around 6000 BC, were discovered in Anatolia (modern-day Turkey). They were made of polished obsidian, a type of volcanic glass. In the same period, mirrors made of polished metal—initially mainly bronze and later silver—appeared in Mesopotamia and Egypt. These metal mirrors, however, provided a poorer-quality reflection and required regular maintenance, because their surfaces oxidized and lost their luster over time [1].

Glass mirrors emerged much later. The first were produced in the Roman Empire around the first century AD, when a glass plate was coated with a thin layer of metal.

Nevertheless, truly high-quality glass mirrors did not appear until the Renaissance in Venice. In the sixteenth century, Venetian glassmakers, especially those from the island of Murano, gained renown as Europe's finest mirror makers. Their mirrors were backed with a thin layer of mercury or tin, which ensured an exceptionally clear reflection [2].

A major breakthrough came in the nineteenth century with the discovery of chemical silvering, which enabled mass and affordable mirror production. The process was invented by the German chemist Justus von Liebig in 1835 [3]. This innovation made mirrors widely available, with applications not only in households but also in architecture and industry.

Modern mirrors consist of a thin metal layer applied to the back of a glass pane (commonly silver (Ag), gold (Au), chromium (Cr), copper (Cu) or aluminum (Al)), often protected by an additional coating to prevent metal corrosion and damage.

However, the materials used in mirrors make them difficult to recycle. The main challenge lies in the strong bonding between the glass layer and the thin reflective metal layer, typically aluminum or silver. This bond complicates separation for individual processing. Additionally, the metal can contaminate the glass and damage recycling equipment. The presence of the metal layer and associated chemicals reduces the quality of the recycled glass, further complicating the recycling process. Consequently, alternative methods for the reuse or safe disposal of mirrors are being actively explored. A promising approach is the incorporation of mirror glass waste (MGW) into geopolymer materials.

Geopolymers are amorphous to semi-crystalline inorganic polymers [4,5] formed at the molecular level by a two- or three-dimensional network of tetrahedra, in which central aluminum and silicon atoms are connected via oxygen atoms [6]. The negative charge resulting from the four-fold coordination of aluminum resides on the surrounding oxygen atoms and is neutralized by alkali and alkaline-earth metal cations, primarily originating from the alkaline activating solution [5].

In general, the geopolymerization mechanism depends on the raw materials used [7]. During geopolymer synthesis, the covalent bonds in the aluminosilicate structure are first broken, after which the solid dissolves in an alkaline solution [4,8,9]. This is followed by the formation of reactive oligomers, which subsequently evolve into larger molecules through gelation and crosslinking via polycondensation reactions [4]. As a result of these reactions, geopolymers exhibit a porous structure, with most pores falling within the range of 2–100 nm [10].

In addition to thermally treated natural aluminosilicates (metakaolin), it is possible to prepare geopolymers from various secondary raw materials (e.g., power-plant fly ash, slag, mining residues) [11–16]. When converting kaolin to metakaolin with the release of water molecules, temperatures of approximately 750 °C are sufficient. In comparison with geopolymer cement (of poly(sialate-disiloxo) type), the less environmentally friendly production of Portland cement generates approximately six times more carbon dioxide through decarbonation and combustion of larger amounts of fuel (temperatures of up to 1500 °C) [6], thereby contributing to global warming.

The advantages of geopolymer materials include their high mechanical strength [4,16], excellent resistance to elevated temperatures [4,9], and remarkable thermal stability, with some formulations maintaining structural integrity even at temperatures exceeding 1000 °C and enhanced tensile ductility in certain formulations, as reported by Huang et al. [16]. Furthermore, they exhibit good chemical durability, including resistance to acids such as hydrochloric and sulfuric acid [4,8], as well as the ability to immobilize selected heavy-metal ions (Me^{+} and Me^{2+}) within the matrix [17,18]. These properties make geopolymers attractive for use in harsh environments, including waste stabilization, refractory linings, and fire-resistant construction materials.

https://doi.org/10.3390/app16020667

This article presents a comprehensive characterization of mirror glass waste (MGW), its innovative application as an alternative aggregate in metakaolin-based geopolymers, and a systematic evaluation of the properties of the resulting solid materials. Two different types of MGW have been used. They were crushed using a jaw crusher and incorporated into the geopolymer matrix in the resulting particle size fraction. The geopolymer bonds were analyzed using Fourier-transform infrared spectroscopy (FTIR). In addition, the samples were characterized in terms of their mechanical properties (compressive and flexural strength), mineralogical composition (X-ray diffraction, XRD), water absorption and structure (porosity measurements and scanning electron microscopy, SEM), and thermal properties (thermogravimetric analysis, TGA; thermal conductivity; thermal diffusivity and volumetric-heat capacity).

Recycling waste mirror glass remains highly challenging due to the presence of reflective metal coatings and underlying layers that prevent its inclusion in standard glass-recycling processes. While the overall particle shape of crushed mirror glass is similar to ordinary waste glass, its surface can be affected by metal coatings, introducing potential microstructural heterogeneities. As a result, waste mirrors are typically disposed of as mixed municipal waste, and their reuse is marginal, irregular, or practically non-existent. Only a few studies have explored new uses for this material, such as in the synthesis of ceramic pigments from mirror waste [19].

Compared with ordinary waste glass, mirror glass waste (MGW) presents several additional challenges. Besides its irregular and sharp-edged particle shape, similar to ordinary waste glass, and back layers, typically based on barium or zinc, which can modify the particle surface and promote interface defects in the composite. These coatings can influence particle distribution, porosity, and ultimately the mechanical performance of the resulting materials. In addition, the presence of multilayer coatings contributes to the poor recyclability of MGW and explains why its reuse remains limited and only sporadically addressed in the literature.

This study therefore explores the use of MGW as an aggregate in metakaolin-based geopolymers, focusing on how these specific features of MGW manifest in the resulting materials. The findings provide new insight into the behavior of MGW in alkali-activated systems and demonstrate its potential as a viable secondary raw material.

2. Materials and Methods

2.1. Materials

The clay material L05 (ČLUZ a.s., Prague, Czech Republic) was used as the primary aluminosilicate source for the geopolymer matrix. An alkaline solution was prepared using potassium silicate (Vodní sklo, a.s., Prague, Czech Republic), which provided soluble silica and promoted the polycondensation process, and potassium hydroxide (Penta, Prague, Czech Republic), which increased the alkalinity and facilitated the dissolution of the clay precursor. Chemical composition and particle size distribution of the calcined clay material used are provided in Tables S1 and S2 of the Supplementary Materials. X-ray diffraction (XRD) evaluation indicated that the L05 clay sample is predominantly amorphous. Crystalline phases include significant amounts of quartz (SiO_2) and anatase (TiO_2), with minor presence of muscovite ($KAl_2(AlSi_3O_{10})(OH)_2$) and hematite ($Fe_2O_3$).

The aggregate employed was mirror glass, originating from different waste streams (MGW1 and MGW2). The material was crushed using a jaw crusher and incorporated into the geopolymer matrix as obtained from the crusher. The chemical composition and granulometry of the mirror glass waste are discussed further in the Section 3.

For comparison, reference samples were also prepared using the quartz sands STJ25 and ST03/30, whose chemical composition and particle size distribution are guaranteed

https://doi.org/10.3390/app16020667

by the producer (Sklopísek Střeleč, a.s., Újezd pod Troskami, Czech Republic) [20]. These two types of sand were combined to obtain a particle size distribution approximately matching that of the waste glass.

2.2. Sample Preparation

As the first step, the L05 clay material was heat-activated at 750 °C for four hours. An alkaline solution was then prepared by mixing potassium water glass U-Tonasil K 3150 (K_2SiO_3, Vodní sklo, a.s., Prague, Czech Republic) with potassium hydroxide (KOH, PENTA s.r.o., Prague, Czech Republic). The parameters of the potassium water glass, as guaranteed by the manufacturer, are: K_2O content 12.25%, SiO_2 content 24.04%, density at 20 °C 1358 kg m^{-3}, molar ratio SiO_2/K_2O = 3.20, and solid content 35.40%. KOH was added directly to the potassium water glass under stirring in proportions resulting in molar ratios of K_2O/SiO_2 = 0.72 and H_2O/K_2O = 12.43, and the mixture was allowed to cool to room temperature (20 °C). The cooled components (calcined L05 clay and alkaline solution) were combined in a planetary mixer (Kenwood, Watford, UK) and mixed for 20 min. Aggregates were subsequently added and mixed for an additional 5 min. The fresh geopolymer mixtures (both with waste glass and with reference quartz sand) were cast into molds according to the requirements of the specific tests (see the Section 2.3 for details).

The solid samples were demolded after 24 h and stored in a sealed plastic bag at room temperature (20 °C) for 21 days to limit moisture loss during curing. Afterward, they were conditioned under laboratory conditions (20 °C, 31% relative humidity) for an additional 7 days. To ensure reproducibility of the 7-day mechanical tests, these samples were removed from the bag 2 h prior to testing and equilibrated under laboratory conditions; all other samples were handled according to the standard curing protocol described above. All samples were prepared and conditioned following this same protocol, without further modifications for specific tests. The resulting specimens were subsequently used for all experiments. All physicochemical analyses (see below) were performed on specimens that were at least 28 days old, ensuring that the materials were fully cured prior to testing.

The mix design is summarized in Table 1. The MGW content was selected based on previous experience [21–25] and the observed workability of the mixture during preliminary experiments. The following designations are used: MGW1 and MGW2 are mirror glass waste originating from different waste streams; MGW1-G and MGW2-G denote geopolymers prepared with MGW1 and MGW2, respectively; S-G refers to geopolymers prepared with quartz sand as aggregate. The suffixes I and II indicate different aggregate contents within each formulation.

Table 1. The mix design of geopolymer composites.

Sample	Components (g)						
	L05	**KOH**	**K_2SiO_3**	**MGW1**	**MGW2**	**STJ25**	**ST03/30**
MGW1-G-I	100	20	80	120	-	-	-
MGW1-G-II	100	20	80	160	-	-	-
MGW2-G-I	100	20	80	-	120	-	-
MGW2-G-II	100	20	80	-	160	-	-
S-G-I	100	20	80	-	-	3.3	116.7
S-G-II	100	20	80	-	-	4.4	155.6

2.3. Methods

Non-destructive X-ray fluorescence (XRF) spectrometry was performed using a Spectro IQ instrument (Kleve, Germany) equipped with a palladium target positioned at 90° to the central beam. The focal spot size was 1 × 1 mm, and the maximum anode power was 50 W

https://doi.org/10.3390/app16020667

with forced-air cooling. The spectrometer was fitted with a HOPG Barkla crystal. Samples were prepared as pressed pellets by mixing 4.0 g of powdered material (15–20 μm) with 0.9 g of a wax binder CEREOX (FLUXANA GmbH &Co. KG, Bedburg-Hau, Germany) and homogenizing the mixture for 10 min. The pellets were pressed at 80 kN. The results were automatically converted from elemental composition to oxides using X-LabPro software version 5.1 (Spectro IQ, Kleve, Germany).

Loss on ignition (LOI) was determined at 1000 °C using a gravimetric procedure in accordance with ČSN 72 0103 [26].

Particle size analysis was determined using a Microtrac Sync 5001 particle size analyzer (Microtrac Inc., Montgomeryville, PA, USA) with a measurement range of 0.02–2800 μm. The device is equipped with three red laser resistors and a Flowsync module, which ensures uniform dispersion of the powdered samples in a liquid medium prior to measurement. Approximately 50–100 mg of sample was ultrasound-dispersed in water for 30 s and then transported to the measuring cell. The resulting data represent the average of three measurements.

Strength tests were conducted in accordance with the European Standard EN 196-1 [27] using prisms with standard dimensions of 40 × 40 × 160 mm, tested after 7, 28 and 90 days under laboratory conditions (20 °C, 31% relative humidity). The tests were performed using an E156 motorized press (strain rate: 0.6 ± 0.2 MPa·s^{-1}) equipped with appropriate devices from Matest (Treviolo, Italy). A three-point bending configuration (support span 100 mm) was employed to determine the flexural strength, using an E172-01 testing device. The fractured portions of the 40 × 40 × 160 mm prisms were then utilized to determine compressive strength using an E170 compression device. Each flexural strength value represents the average of three measurements, whereas compressive-strength values represent the average of six measurements.

X-ray diffraction (XRD) analysis as carried out on a Bruker D8 Advance powder diffractometer operating in Bragg–Brentano geometry with a LynxEye XE detector and CuKα radiation (Bruker AXS, Karlsruhe, Germany). Powdered samples were mounted on a planar, diffraction-free silicon holder. Diffraction patterns were acquired over an angular range of 4–80° 2θ (a step size of 0.015°, a counting time of 0.8 s per step). The resulting XRD patterns were qualitatively evaluated using Diffrac.Eva 4.1 software (Bruker AXS, Karlsruhe, Germany, 2015) together with the ICDD PDF-2 database (ICDD version 2018).

The influence of controlled thermal heating on geopolymer composites was investigated under defined conditions using a MOM thermal analyzer (MOM, Budapest, Hungary), which can measure samples in a compact state. The composites were prepared as cubes with the dimensions of 10 × 10 × 10 mm and were heated in air (30 mL·min^{-1}) at a constant rate of 10 °C·min^{-1} up to 1000 °C. The weight loss of each geopolymer composite cube was evaluated based on the recorded data. Each measurement was performed twice to ensure reproducibility. The influence of MGW incorporation on the thermal stability of the composites and the structural changes in the cubes before and after heating were also assessed.

Fourier-transform infrared (FTIR) spectra were recorded using an iS50 spectrometer (Thermo Nicolet Instruments Co., Madison, WI, USA) equipped with an attenuated total reflection (ATR) accessory with a diamond crystal. The spectra were collected over the spectral range of 400–4000 cm^{-1}, with 32 scans averaged at a resolution of 4 cm^{-1}. Spectral processing was performed using OMNIC 9 software (Thermo Electron Scientific Instruments LLC, Madison, WI, USA).

Water absorption of the samples was evaluated in compliance with ČSN 72 2603, employing standardized saturation and weighing procedures [28].

https://doi.org/10.3390/app16020667

Skeletal density (ρ_{He}) of the solid samples was determined using helium gas pycnometry as a non-destructive technique. The measurements were carried out on ground samples at 25 °C using a Pycnomatic ATC instrument (Thermo Fisher Scientific, Monza, Italy). Since helium has a small atomic size and high diffusivity, it can penetrate even the finest open pores within the solid structure.

Porosity and pore-size distribution were characterized using mercury intrusion porosimetry (MIP) with PASCAL 140 and PASCAL 440 instruments (Thermo Fisher Scientific, Waltham, MA, USA). The measurements were conducted on pre-dried intact-sample pieces of approximately 5 mm in size, targeting pores in the range of 7 nm to 112 μm. Each sample was measured twice to minimize the variability caused by internal heterogeneity. Key parameters such as total porosity (φ), total pore volume, and material density were determined [29]. A comprehensive explanation of sample preparation, methodology, and evaluation procedures can be found, for example, in reference [30].

Particle morphology was examined using a Keyence VHX-6000 digital microscope (Keyence International, Osaka, Japan).

EDS and SEM analyses were performed on polished cross-sections, which were attached to aluminum carriers with carbon tape and coated with carbon (18.9 nm, 16.5 nm for sand) using a Leica EM ACE600 sputter coater (Specion s.r.o., Prague, Czech Republic). EDS maps were obtained using a STEM Apreo S LoVac scanning electron microscope (ThermoFisher Scientific, Waltham, MA, USA) equipped with an Octane Elite SDD (EDAX, Ametek, Berwyn, PA, USA) EDS detector under high-vacuum conditions, with an acceleration voltage of 20 keV and a magnification of 200×. Detailed EDS elemental analyses of each mirror layer were carried out on the same samples at 3500× magnification. Data acquisition was done on EDAX TSL OIM software APEX Advanced V3.0.0601.0001 (EDAX, Ametek, Berwyn, PA, USA). SEM images were acquired on the same microscope at 20 keV using a T1 Trinity Inlens detector with BSE electrons to highlight material differences at 200× magnification.

Thermal conductivity (λ), thermal diffusivity (a), and volumetric-heat capacity (Cρ) were measured using an ISOMET 2114 analyzer (Applied Precision, Bratislava, Slovakia), which operates via a dynamic method based on the temperature response to the heat pulses generated within the probe. The measurements were performed on cylindrical specimens with a diameter of 60 mm and a height of 40 mm. Surface probes with the ranges of 0.04–0.3, 0.3–3.0 and 3.0–6.0 $W \cdot m^{-1} \cdot K^{-1}$ were selected according to the thermal properties of each material. To reduce the influence of temperature fluctuations, the probe and sample were placed in a polystyrene thermal box during the measurement. The final values represent the average of three measurements.

3. Results and Discussion

The experimental plan was designed to comprehensively evaluate the suitability of waste mirror glass (MGW) as an aggregate in geopolymer composites by linking the properties of the raw material with the resulting microstructure and performance of the composites. The chemical and phase compositions of the raw MGW and geopolymer composites (MGW-G) were determined using XRF and XRD analyses. The characterization of the metallic layers present on the glass surface and the effect of MGW incorporation on the composite microstructure were investigated using SEM and EDS analyses, while porosity measurements were used to assess changes in pore structure induced by the glass aggregate. Thermogravimetric (TG) and FTIR analyses were employed to evaluate the thermal stability and the formation of geopolymer bonds in the composites, respectively. Mechanical properties were evaluated using flexural and compressive strength tests as the primary performance indicators. In addition, thermal conductivity (λ), thermal diffusivity

https://doi.org/10.3390/app16020667

(α), and volumetric heat capacity were measured to assess the thermal performance of the composites and their potential applicability in construction-related applications.

3.1. The Characterization of Mirror Glass Waste

Figure 1 shows the mirror glass debris MGW1 and MGW2, observed using a digital microscope. The particles exhibit irregular, non-spherical shapes with sharp edges and a wide range of sizes. Residual layers originating from the original mirror coating are visible on the surface of some particles.

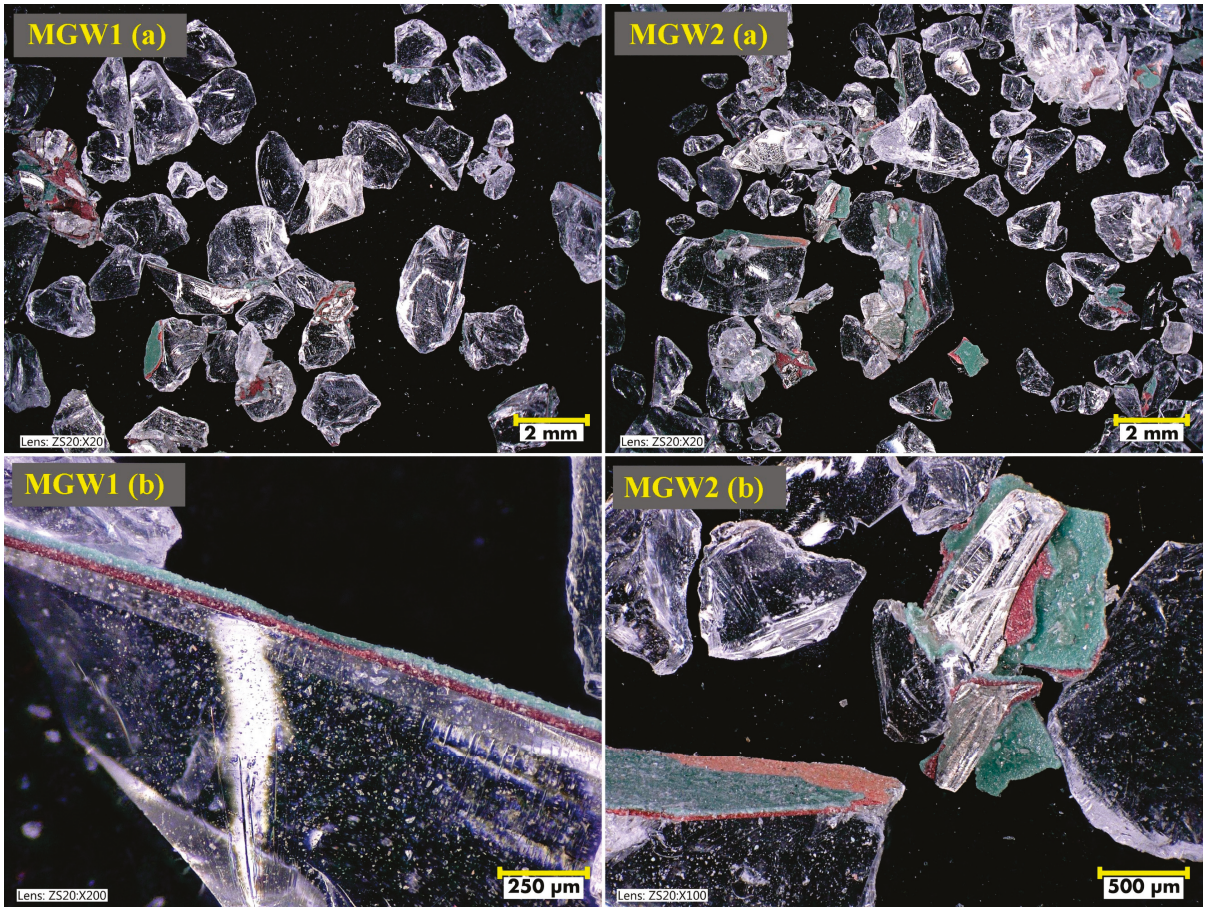

Figure 1. Digital-microscope images of MGW1 and MGW2 ((**a**)—general view, (**b**)—detailed view).

The chemical analysis of two types of mirror glass waste (MGW1 and MGW2), presented in Table 2, has revealed a very similar composition typical of soda-lime glass. Both samples contain approximately 69% of SiO_2, confirming their predominantly silicate character. There is also a significant proportion of Na_2O (about 10%) and CaO (about 11%), which act as fluxing components and glass stabilizers. The MgO content is around 4.6%, whereas Al_2O_3 is present only in low concentrations (0.5–0.6%). The loss on ignition (LOI) is low (~1.5–1.6%), indicating that the material is predominantly inorganic in nature and does not contain significant amounts of volatile components or organic admixtures.

Table 2. Chemical analysis of MGW1 and MGW2 (main oxides in wt.%).

Oxides	Na_2O	MgO	Al_2O_3	SiO_2	SO_3	K_2O	CaO	TiO_2	Fe_2O_3	ZnO	BaO	LOI
MGW1	10.20	4.63	0.53	69.71	0.47	0.10	11.40	0.14	0.32	0.29	0.55	1.54
MGW2	10.43	4.63	0.58	68.90	0.53	0.11	11.35	0.14	0.29	0.34	0.96	1.61

https://doi.org/10.3390/app16020667

The grain-size distributions of the MGW1 and MGW2 fractions determined by sieving show similar characteristics, with slight differences in the proportion of each fraction (Figure 2). In both samples, there is a predominance of particles larger than 1.25 mm, accounting for approximately 72% in MGW1 and 55% in MGW2. MGW2 contains a higher proportion of medium-fine fractions (mainly 0.4–0.8 mm) than MGW1, which may slightly affect its workability or the structure of the resulting material. The proportion of fine particles (<0.4 mm) is relatively low in both materials, with its being slightly higher in MGW2 than in MGW1.

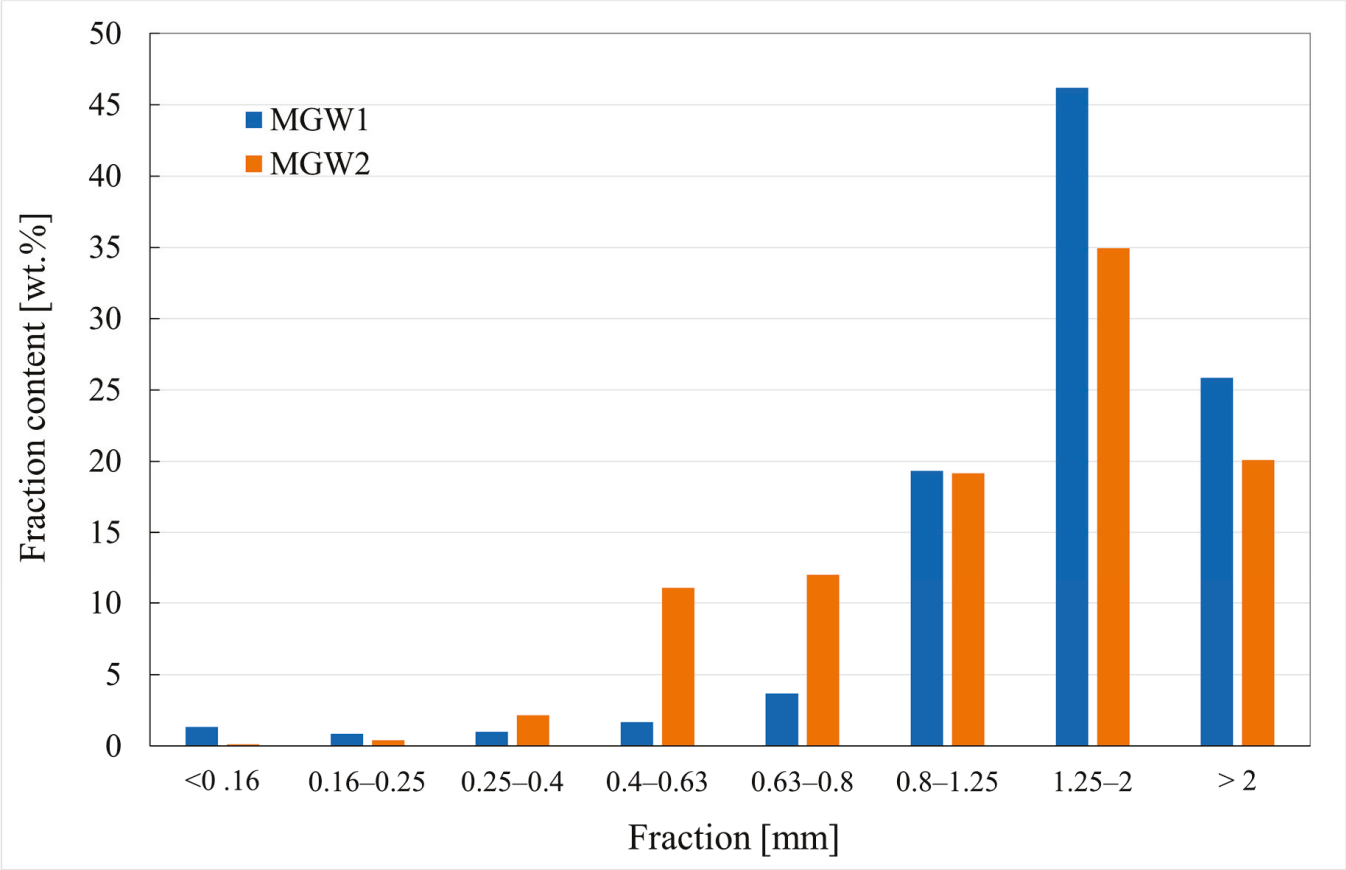

Figure 2. Grain-size distribution of MGW1 and MGW2.

Figure 3 shows SEM images (a) and EDS maps (b) of the mirror glass waste samples MGW1 and MGW2. Detailed EDS analyses of both types of MGW are presented in Figures S1 and S2 and in Tables S3 and S4 of the Supplementary Materials. The results are consistent with the chemical analysis of both types of mirror glass waste (Table 2). The glass matrix consists mainly of silicon, oxygen, sodium and calcium, corresponding to soda-lime glass.

https://doi.org/10.3390/app16020667

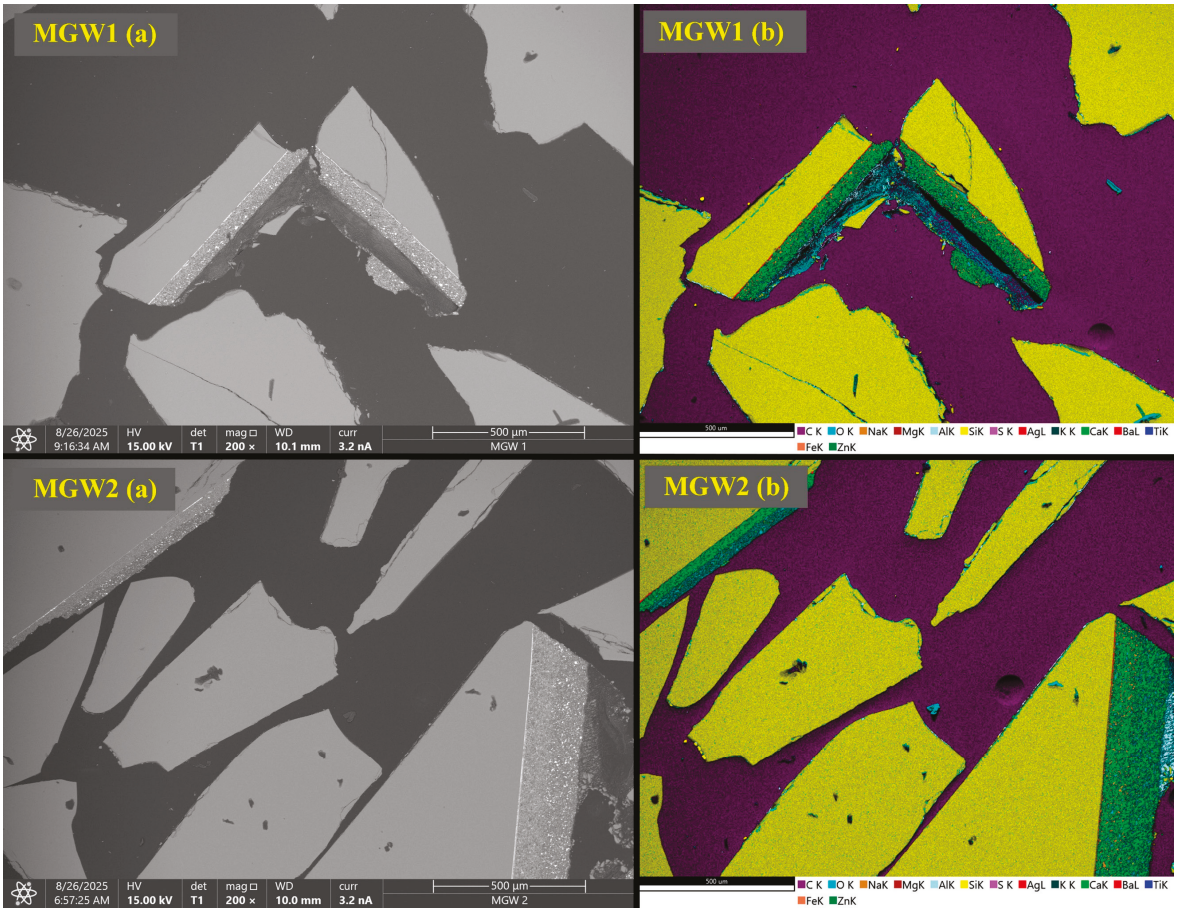

Figure 3. SEM images (**a**) and EDS elemental maps (**b**) of mirror glass waste samples.

The layers forming the mirror are clearly visible in the SEM images. EDS maps of the cross-sections (MGW1 and MGW2, 200×) and EDS analyses reveal the presence of three thin coatings. The first layer contains predominantly silver (Ag) with minor traces of silicon (Si) and sulfur (S). The second layer consists of calcium (Ca) accompanied by zinc (Zn), magnesium (Mg) and silicon (Si). The third layer is formed by barium (Ba), silicon (Si), calcium (Ca), magnesium (Mg), sulfur (S) and titanium (Ti). These elements correspond to a typical mirror structure—a silver reflective layer deposited on barium-based backing layers (likely $BaSO_4$ and/or $BaTiO_3$), possibly covered by a zinc-containing protective paint [31–34]. Minor traces of Fe and Al are also present.

From the mineralogical point of view (Table 3), both MGW samples contain the majority of the amorphous phase (over 98 wt.%) and trace amounts of quartz, calcite and zincite (up to 0.5 wt.%).

Table 3. XRD quantitative phase analyses of MGW1 and MGW2 (wt.%).

Sample	Amorphous Phase	Quartz	Calcite	Zincite
MGW1	98.4	0.5	0.7	0.4
MGW2	98.4	0.6	0.6	0.4

The ATR-FTIR spectra of all input materials and their comparison with the L05 clay material and the geopolymer matrix are shown in Figure 4.

https://doi.org/10.3390/app16020667

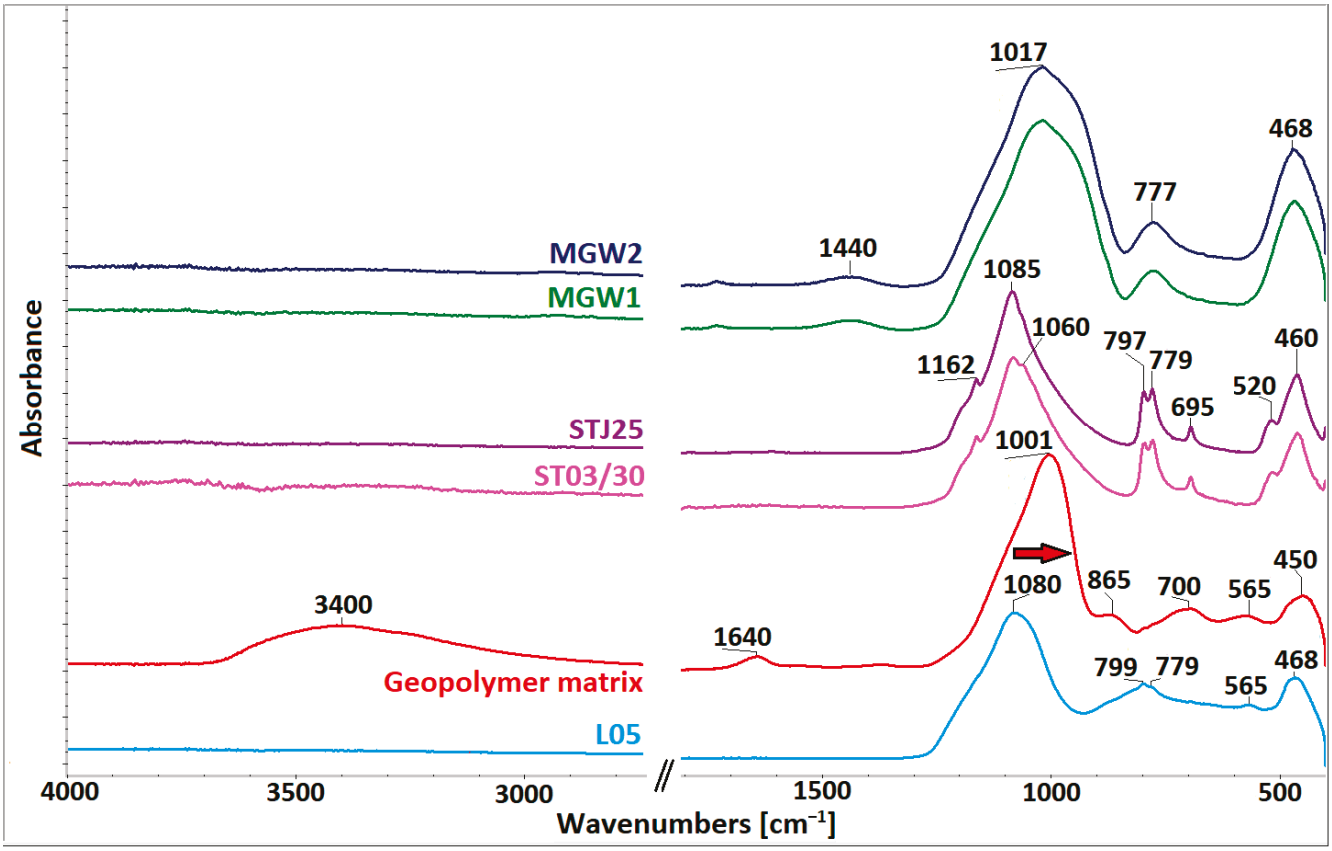

Figure 4. The ATR-FTIR spectra of input materials; clay material (L05), geopolymer matrix, sand fillers (STJ25 and ST03/30) and mirror glass waste (MGW1 and MGW2). The spectral region of 2500–2000 cm^{-1} is not shown because it contains only diamond-crystal noise and carbon-dioxide absorption bands.

The clay material (L05) shows broad bands associated with the asymmetric stretching and bending of Si–O, as well as the asymmetric stretching of Si–O–Al groups, at 1080 cm^{-1}, ~780 cm^{-1}, and 468 cm^{-1}. Distinct peaks at 799 and 779 cm^{-1} indicate the presence of quartz [35] as a minor impurity. Alkaline activation of L05 and the subsequent formation of the geopolymer matrix are indicated by a shift in the main Si–O–T asymmetric stretching band from 1080 cm^{-1} to 1001 cm^{-1} (red arrow in Figure 4). This change reflects the incorporation of AlO_4 units into SiO_4 tetrahedra, forming a Si–O–Al network [36,37]. Additional weak band at 865 cm^{-1} arises from Si–OH bending [38], while the shoulder near 560 cm^{-1} is attributed to silicates or aluminosilicates with long-range order [39]. Bands at 3400 cm^{-1} and 1640 cm^{-1} correspond to the stretching and bending of OH groups in water, indicating residual moisture in geopolymer matrix [40].

The ATR-FTIR spectra of MGW1 and MGW2 mirror glass waste samples exhibit identical spectral features. They display a broad, intense band between 1250 and 840 cm^{-1} with a peak at 1017 cm^{-1}, and a band at 450–470 cm^{-1}, attributed to O–Si–O bending (ν_4) and Si–O asymmetric stretching (ν_3) in SiO_4 tetrahedra [35]. A weak band at 777 cm^{-1} reflects Si–O–Si symmetric stretching of bridging oxygens [41], while another at 1440 cm^{-1} corresponds to the asymmetric stretching of C–O bond and out-of-plane bending of O-C-O in carbonate groups. The major absorption band in the spectra of STJ25 and ST03/30 is located at 1200–850 cm^{-1}. This broad band contains several subbands assigned to asymmetric stretching vibrations belonging to various optically active symmetries (A2 and E) in quartz [42]. The remaining absorption features located in the region of 800–400 cm^{-1} are attributable to symmetric stretching and to the Si–O–Si bending in

https://doi.org/10.3390/app16020667

SiO_4, respectively [43]. The differences in the ST spectra are related to the width of the main absorption band at 1200–850 cm^{-1}; the material ST03/30 exhibits broadening of the entire envelope, which may be attributed to decreased internal order, i.e., reduced crystallinity [44].

3.2. The Characterization of Geopolymer Composites

Digital-microscope images (Figure 5) have revealed clear differences in the distribution and morphology of the aggregates used in geopolymer composites on their fracture surfaces. In both MGW1 and MGW2 systems, mirror glass waste appears as angular, reflective fragments that are well embedded in the geopolymer matrix. An increase in aggregate content from variant I to II results in a visibly denser distribution of MGW particles, although the overall distribution remains relatively uniform. MGW2 exhibits slightly finer and more heterogeneous fragments than MGW1, which is consistent with the granulometric analysis (Figure 2). In contrast, sand-based composites (S-G-I and S-G-II) have displayed a much more homogeneous microstructure with uniformly sized, rounded particles and a more continuous matrix phase. The smoother morphology of sand composites may contribute to their slightly higher mechanical strength observed in the tested systems. Overall, the images confirm the effective incorporation of both types of mirror glass waste while highlighting the internal morphological differences between recycled glass and natural sand.

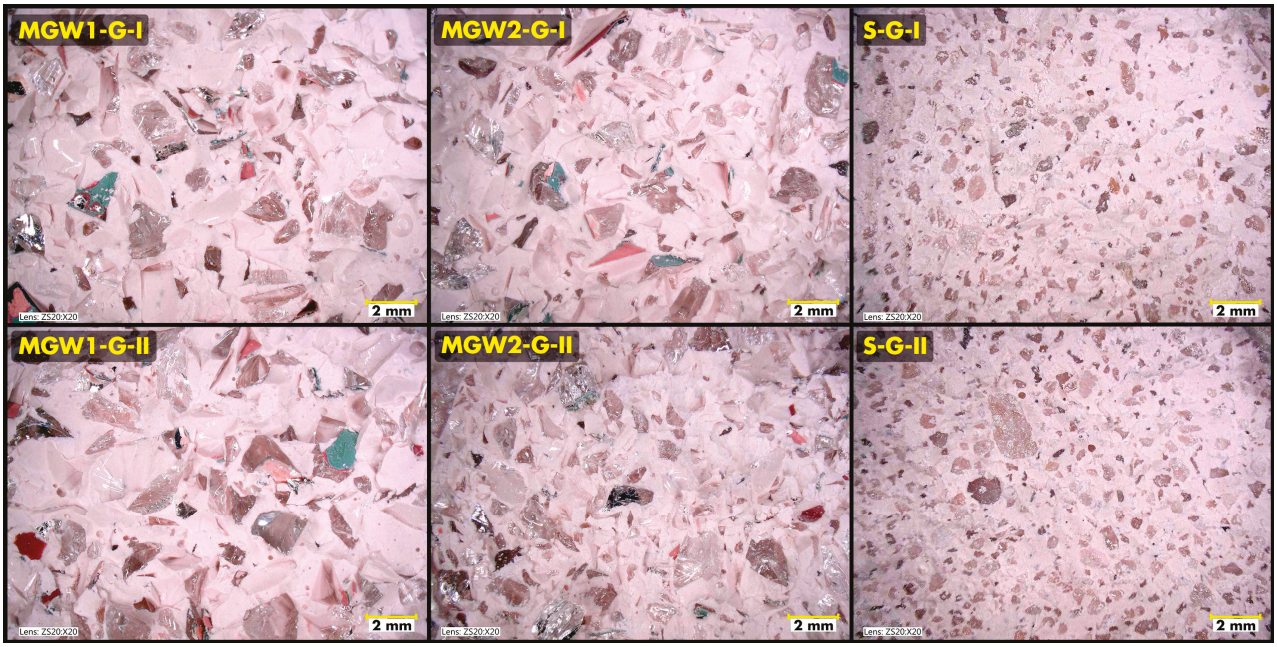

Figure 5. Digital-microscope images of geopolymer composites prepared with MGW and silica aggregates.

The chemical composition of geopolymer samples (Table 4) varies significantly depending on the type and quantity of the aggregate used. Samples with mirror glass aggregate (MGW1-G, MGW2-G) exhibit higher contents of alkali oxides (Na_2O, K_2O) and CaO than samples with silica sand (S-G), indicating partial reactivity of glass aggregate in an alkaline environment [45]. As the aggregate content increases (variant II), there is generally a slight increase in SiO_2 and a corresponding decrease in Al_2O_3 and alkali oxides, consistent with the dilution of the geopolymer matrix by the inactive component. This trend is most pronounced in samples with inert sand, where higher aggregate content leads to a more significant decrease in active components and a parallel increase in SiO_2.

https://doi.org/10.3390/app16020667

Table 4. XRF analyses of the geopolymer composites prepared with MGW and silica aggregates.

Oxides	Na_2O	MgO	Al_2O_3	SiO_2	SO_3	K_2O	CaO	TiO_2	Fe_2O_3	ZnO	BaO	LOI
MGW1-G-I	1.56	0.49	21.40	52.22	0.13	11.44	3.58	0.89	0.71	0.16	0.30	6.94
MGW1-G-II	1.69	0.57	20.73	53.01	0.15	11.10	3.97	0.86	0.72	0.16	0.30	6.59
MGW2-G-I	1.17	0.33	21.94	51.12	0.12	12.37	2.86	0.92	0.78	0.14	0.38	7.70
MGW2-G-II	1.39	0.49	21.51	52.01	0.14	11.71	3.48	0.89	0.74	0.16	0.37	6.91
S-G-I	0.33	<0.17	20.67	55.60	0.02	12.67	0.02	0.90	0.73	0.003	<0.001	8.91
S-G-II	0.28	<0.17	20.33	57.28	0.02	12.1	<0.001	0.83	0.68	0.001	<0.001	8.27

Loss-on-ignition (LOI) observed in the hardened mixtures probably reflects the release of physically and chemically bound water and the decomposition of partially carbonated reaction products in the binder during heating to 1000 °C. For this reason, LOI values are generally higher in samples with lower aggregate content, where the proportion of binder is higher. These assumptions are further discussed and supported by XRD results and thermal analysis presented later in the manuscript.

The data obtained confirm that both the type and the amount of aggregate significantly influence the chemical composition and, consequently, the potential reactivity and properties of geopolymer composites, which is consistent with the literature [46,47].

The results presented in Table 5 show that the flexural strength of samples with waste mirror glass (MGW-G) was significantly lower than that of sand-based reference geopolymers (S-G) at all curing stages. MGW-based samples achieved values between 3.9 and 5.7 MPa, while S-G mixtures reached 8–11 MPa. For all samples, flexural strength increased slightly from 7 to 28 days, indicating ongoing geopolymerization, followed by a slight decrease or stabilization after 90 days.

Table 5. The flexural strength of the geopolymer composites prepared with MGW and silica aggregates.

Sample	Flexural Strength (MPa)		
	7 Days	28 Days	90 Days
MGW1-G-I	4.7 ± 0.0	4.1 ± 0.0	4.10 ± 0.6
MGW1-G-II	4.9 ± 0.3	4.50 ± 0.3	3.90 ± 0.6
MGW2-G-I	5.3 ± 0.6	5.30 ± 0.5	3.90 ± 0.3
MGW2-G-II	5.7 ± 0.3	5.50 ± 0.6	4.30 ± 0.3
S-G-I	8.8 ± 0.4	10.3 ± 1.0	8.6 ± 0.3
S-G-II	8.2 ± 0.5	10.9 ± 0.6	9.2 ± 0.3

Among MGW-based mixtures, MGW2-G variants generally exhibited slightly higher flexural strength than MGW1-G, which may be related to differences in the particle size distribution or surface properties of the glass aggregate, affecting the matrix–aggregate interface. The differences between variants I and II (i.e., lower and higher aggregate contents, respectively) were small, suggesting that the aggregate content had only a limited effect on flexural strength.

The compressive-strength results summarized in Table 6 show a trend similar to that of flexural strength (Table 5). Geopolymers with sand (S-G) achieved the highest values, reaching up to 93.5 MPa after 28 days, whereas samples containing waste mirror glass (MGW-G) exhibited lower strength, typically in the range of 60–70 MPa. All mixtures exhibited an increase in compressive strength between 7 and 28 days, confirming ongoing geopolymerization and matrix densification during this period. Between 28 and 90 days, only minor changes were observed, suggesting that the reaction was nearly complete within the first month of curing. In particular, the slight decrease in compressive strength seen for

https://doi.org/10.3390/app16020667

S-G-II between 28 and 90 days is minor and can be attributed to slight drying, redistribution of internal moisture, or minor microstructural changes over time. In mixtures with higher aggregate content, such effects may become more noticeable due to a more sensitive matrix–aggregate interface, whereas systems with lower aggregate content generally exhibit a more continuous matrix and less pronounced variations. Overall, the mechanical properties of the studied geopolymers remain stable over time.

Table 6. The compressive strength of the geopolymer composites prepared with MGW and silica aggregates.

Sample	Compressive Strength (MPa)		
	7 Days	28 Days	90 Days
MGW1-G-I	60.2 ± 1.8	70.1 ± 3.1	70.8 ± 2.9
MGW1-G-II	64.2 ± 1.9	65.9 ± 2.9	67.4 ± 2.8
MGW2-G-I	70.3 ± 1.2	70.8 ± 1.9	69.5 ± 1.8
MGW2-G-II	68.2 ± 1.2	64.5 ± 4.0	68.5 ± 4.4
S-G-I	81.5 ± 4.4	87.5 ± 7.1	87.0 ± 5.2
S-G-II	92.2 ± 6.4	93.5 ± 3.2	90.9 ± 3.8

The differences between the MGW1-G and MGW2-G mixtures were marginal, indicating that the properties of the two types of mirror glass waste did not significantly affect the compressive strength overall. Similarly, the influence of aggregate content (variants I and II) was limited, although the S-G-II sample exhibited the highest strength of all. Overall, the replacement of sand with mirror glass waste led to a slight decrease in compressive strength, but the values obtained still indicate good mechanical performance for MGW-based geopolymers.

X-ray diffraction (XRD) analysis, presented in Table 7, shows significant differences in the mineralogical composition of geopolymer composites depending on the type of aggregate used. The initial mirror glass (MGW1 and MGW2) exhibits an almost completely amorphous character (98.4% amorphous phase) with only trace amounts of crystalline phases such as quartz, calcite and zincite. In the resulting MGW1-G-II and MGW2-G-II composites, the amorphous content remains high (96.0 and 96.3%), with crystalline phases present in similar concentrations as in the glass itself.

Table 7. XRD quantitative phase analyses of the geopolymer composites prepared with MGW and silica aggregates (wt.%).

Sample	Amorphous Phase	Quartz	Calcite	Anatase
MGW1-G-II	96.0	3	0.5	0.5
MGW2-G-II	96.3	2.8	0.7	0.2
S-G-II	51.0	48.7	-	0.3

In contrast, the S-G-II sample with sand shows a completely different composition: The amorphous fraction is only 51%, while quartz constitutes almost half of the sample (48.7%). This result is consistent with the use of an inert, crystalline aggregate that does not participate in the geopolymer reaction and significantly reduces the relative amount of the geopolymer phase. The presence of other phases originating from the clay material (anatase, calcite) is minimal and does not significantly affect the interpretation.

These XRD results further suggest that the loss on ignition (LOI) values reported in Table 2 are primarily due to the release of physically and chemically bound water, given the low or negligible amount of carbonate phases in the geopolymer samples.

https://doi.org/10.3390/app16020667

Spectroscopically, all final geopolymer materials, both the series MGW1 (Figure 6a) and MGW2 (Figure 6b), are identical. The positions of the principal band in MGW1 and MGW2 are 1017 cm^{-1}, in the geopolymer matrix 1001 cm^{-1}, and the geopolymer composites exhibit positions in the range of 1005–1007 cm^{-1}. These values are within the resolution limit of the method (up to 4 cm^{-1}). This shift (10–12 cm^{-1}, red arrow in Figure 6) is smaller than that observed for automotive glass in our previous research [21], where this shift was 27–29 cm^{-1}. A new weak band at approximately 700 cm^{-1} is attributable to the stretching and bending vibrations of Si–O–Al, providing another fingerprint for the generation of the geopolymer structure [48]. On the other hand, the original band at 777 cm^{-1}, characterizing Si–O bonds in MGW1 and MGW2, disappears due to the geopolymer reaction.

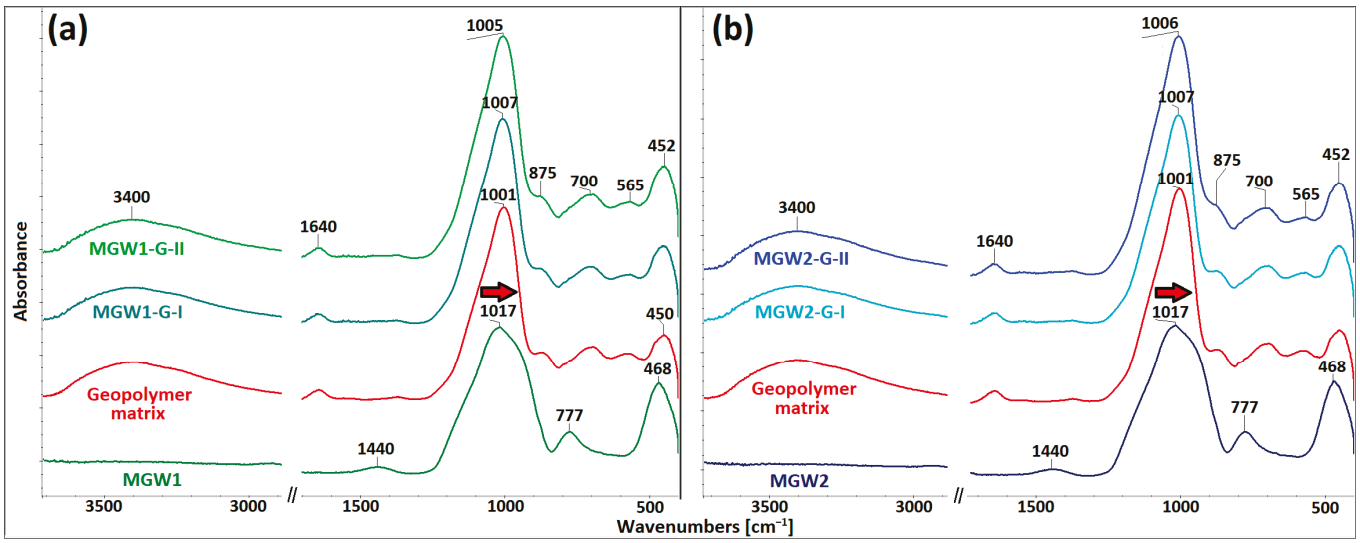

Figure 6. The ATR-FTIR spectra of geopolymer materials: the series MGW1-G (**a**) and MGW2-G (**b**) with variable MGW concentrations (I and II) and their comparison with the two types of mirror glass waste (MGW1/2) and the geopolymer matrix.

The sand filler is a mixture of STJ25 and ST03/30 materials; the positions of the principal bands in both spectra are at 1085 cm^{-1}. The final geopolymer materials S-G-I and S-G-II (Figure 7) are identical, with the principal band in both spectra located at 1009 cm^{-1} and the shift of the principal band after geopolymerization to lower wavenumbers being 76 cm^{-1}. A new weak band at approximately 700 cm^{-1}, corresponding to the vibrations of Si–O–Al, provides further evidence of the generation of the geopolymer structure [48]. Very weak remnants of the bands at 779 and 797 cm^{-1}, which originate from the sand filler, are still visible in the spectra of S-G geopolymers.

All the spectra of geopolymer composites also contain bands of the hydroxy groups (3400 and 1640 cm^{-1}) originating from the geopolymer matrix. ATR-FTIR analysis has confirmed that the content of neither mirror glass waste nor sand filler negatively affects the progress of the geopolymer reaction.

The SEM microstructures in Figure 8 show clear differences between the composites, arising from the distinct morphology of the mirror glass waste (MGW) and silica sand used as aggregates. MGW fragments (2) are sharp-edged and often carry thin metal coatings (3), which remain locally attached to their surfaces and form additional interfacial features. In contrast, silica sand grains (4) are rounded and smoother, resulting in simpler and more uniform interfaces with the geopolymer matrix (1). The matrix (1) forms a continuous phase in all samples; however, in type-II specimens, the higher aggregate content brings the particles into closer contact, reducing the proportion of continuous matrix and creating

https://doi.org/10.3390/app16020667

a more interconnected granular structure. In some cases, microcracks can be observed, which may originate either during the drying and shrinkage of the material or during the preparation of polished cross-sections for SEM analysis. The latter possibility is supported by the fact that some microcracks propagate through glass or quartz grains (e.g., MGW2-G-II and S-G-II). Overall, MGW-containing composites have a microstructure that reflects the angular shape of glass fragments and the presence of metal surface layers, whereas sand-filled composites exhibit a more uniform microstructure due to the rounded shape of quartz grains and their consistent bonding with the matrix. This observation is consistent with Kuri et al. [49], who reported that weak bonding at the interfacial transition zone between glass aggregates and the matrix can reduce compressive strength and increase porosity.

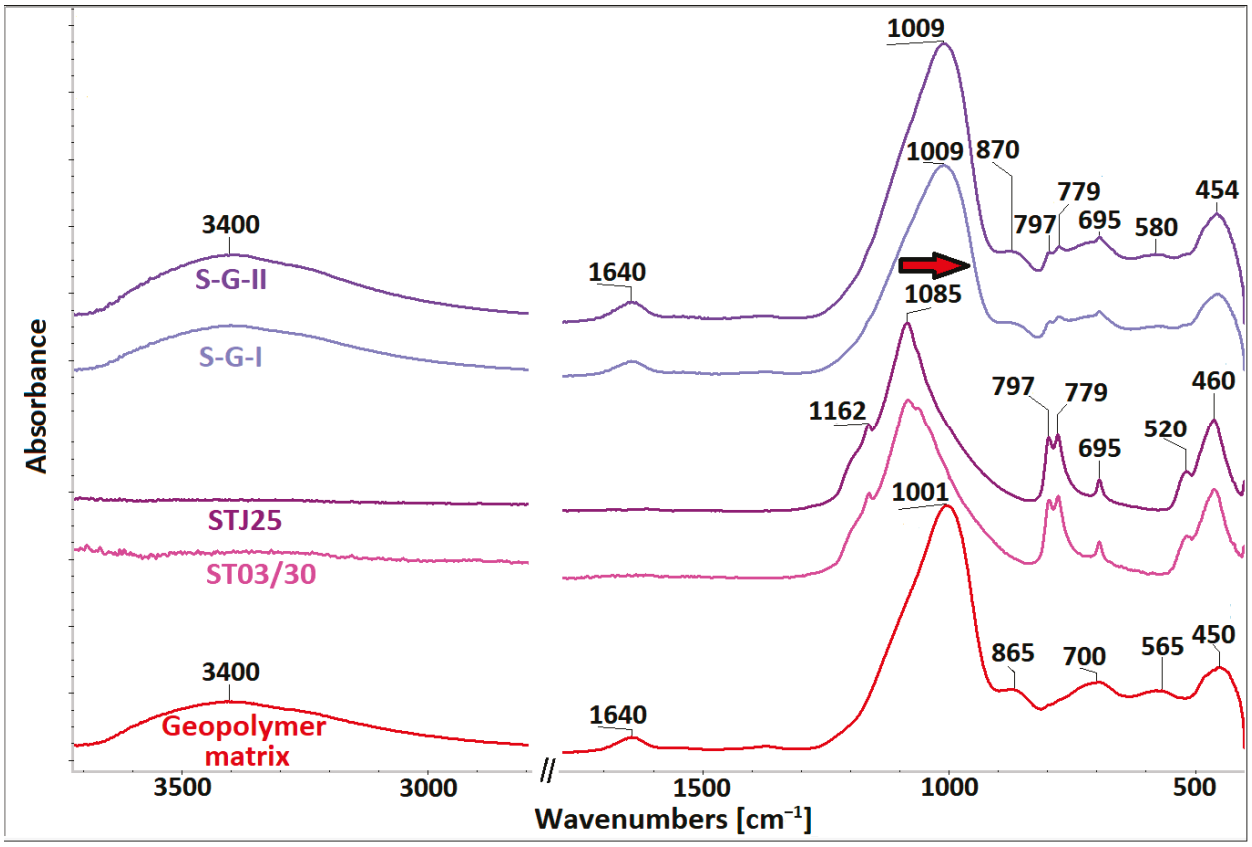

Figure 7. The ATR-FTIR spectra of geopolymer materials: the series S-G with variable ST concentrations (I and II) and their comparison with sand fillers (STJ25, ST03/30) and the geopolymer matrix.

The water absorption values of all geopolymer composites (Figure 9) fall within a narrow range (approximately 12–14% wt.%), indicating comparable overall porosity regardless of the type of aggregate used. Differences between the mixtures with lower (I) and higher (II) aggregate content are only minor within the error ranges, suggesting that aggregate content does not significantly affect water absorption. MGW2-containing composites exhibit slightly lower absorption than those with MGW1, whereas sand-based samples (S-G-I and S-G-II) show values similar to MGW systems. The higher variability observed in MGW1-G-II may be related to the less uniform distribution of waste mirror glass at its higher content. Overall, the results suggest that neither the type nor the amount of aggregate has a significant effect on water absorption in the geopolymers studied.

https://doi.org/10.3390/app16020667

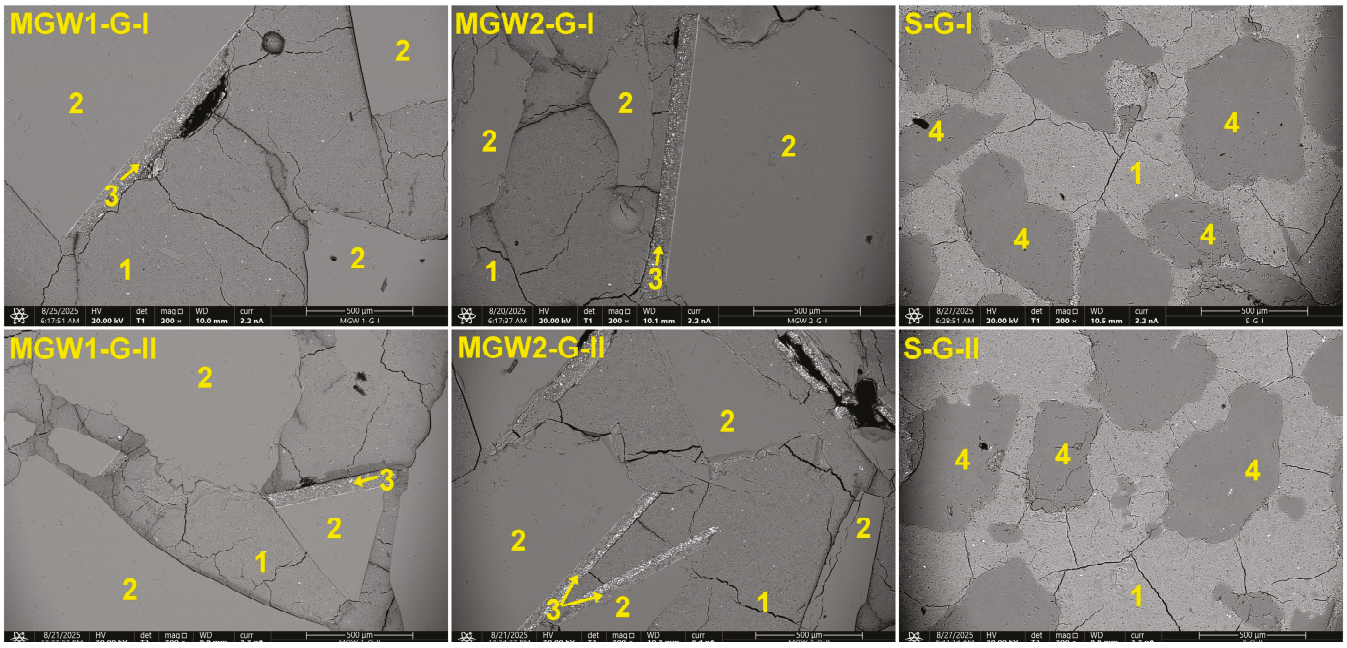

Figure 8. SEM images of the geopolymer composites prepared with MGW and silica aggregates (1—geopolymer matrix, 2—glass, 3—thin metal coatings, 4—silica sand grains).

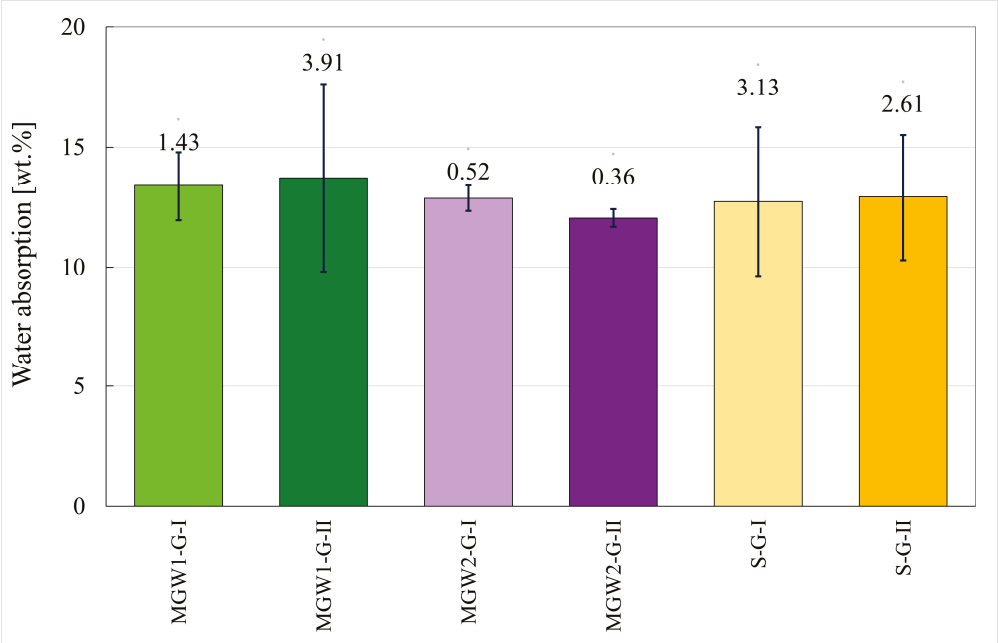

Figure 9. Water absorption of the geopolymer composites prepared with MGW and silica aggregates.

The results of mercury intrusion porosimetry (MIP) measurements reveal the pore volume and overall porosity of the various composites and raw materials (see Table 8). Figure 10 presents the pore-size distributions for all samples, grouped into four categories: <10 nm, 10–50 nm, 50–250 nm, and >250 nm. This classification effectively highlights differences in porosity across the sample set.

As shown in Figure 10, composites containing mirror fragments exhibit similar pore-size distributions. The presence of fine-grained mirror particles or sand does not significantly affect the pore-size profile. In contrast, the addition of a higher proportion of MWG1 (MWG1-G-II) leads to an increase in pores larger than 250 nm. Composites incorporating

https://doi.org/10.3390/app16020667

either type of mirror glass waste maintain similar compressive and flexural strengths, whereas the sand-based composites achieve slightly higher values.

Table 8. The average values of the main textural parameters and calculated parameters.

	V_c ($mm^3 \cdot g^{-1}$)	φ (%)	ρ_{App} ($g \cdot cm^{-3}$)	ρ_{Hg} ($g \cdot cm^{-3}$)	ρ_{He} ($g \cdot cm^{-3}$)	φ_{He} (%)
GP	22.0	3.53	1.663	1.605	2.254	28.81
S-G-I	33.8	6.48	2.053	1.920	2.385	19.52
S-G-II	32.6	6.37	2.088	1.955	2.391	18.22
MGW1	8.6	2.07	2.471	2.420	2.461	1.66
MGW1-G-I	33.4	5.90	1.884	1.773	2.286	22.45
MGW1-G-II	39. 5	7.41	2.027	1.877	2.300	18.38
MGW2	8.3	1.95	2.397	2.350	2.420	2.89
MGW2-G-I	35.3	6.47	1.962	1.835	2.232	17.79
MGW2-G-II	35.6	6.65	2.003	1.869	2.348	20.38

V_c—total pore volume, φ/φ_{He}—total porosity by MIP/calculated porosity using helium density, $\rho_{App}/\rho_{Hg}/\rho_{He}$—apparent/bulk/helium density.

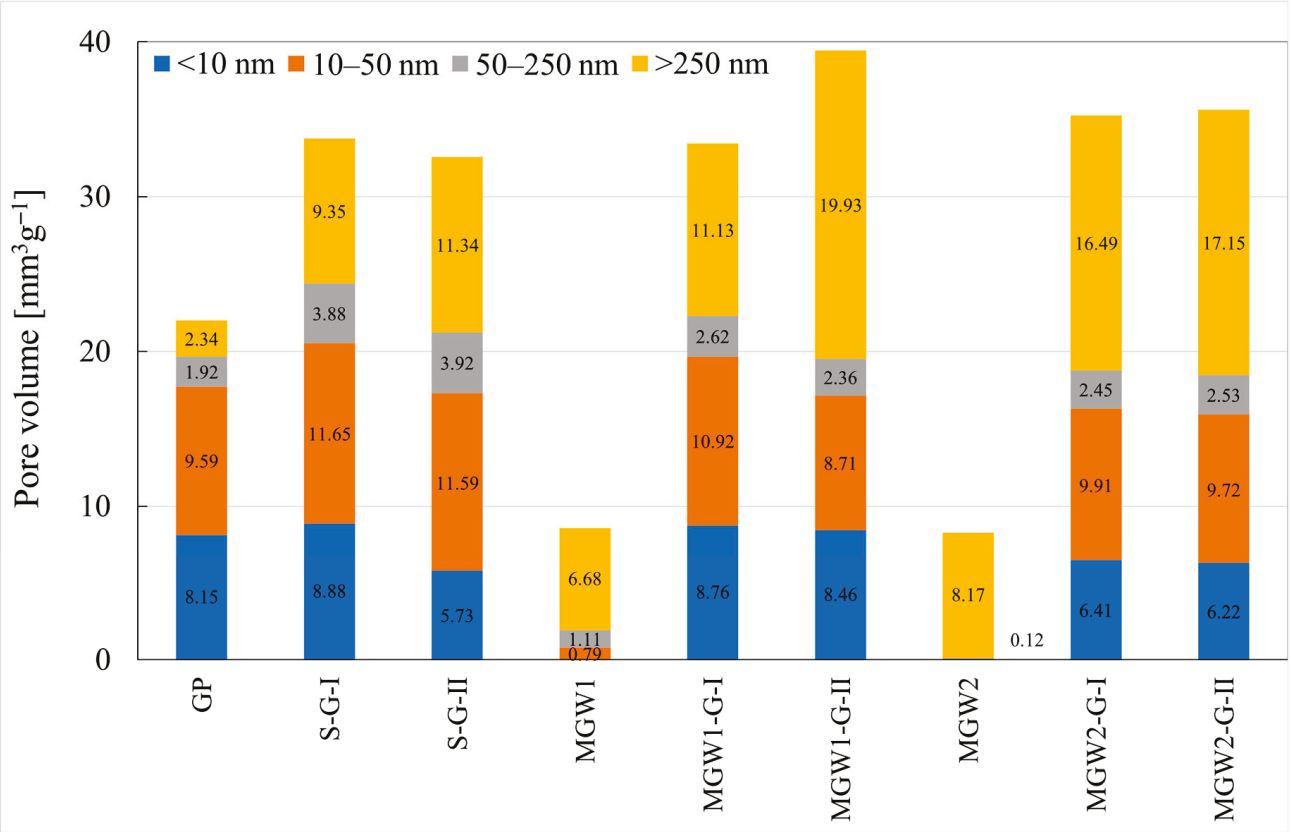

Figure 10. Pore-volume distribution across principal pore-size classes determined by mercury intrusion porosimetry.

For raw mirror samples, the relative pore volume tends to decrease with increasing pore diameter, which may be attributed to the presence of intergranular pores. The total pore volumes of the composites and the geopolymer (GP) matrix exceed 20 $mm^3 \cdot g^{-1}$, with the average pore diameters smaller than 30 nm, whereas the total pore volume of raw mirrors is lower than 9 $mm^3 \cdot g^{-1}$, with the average pore diameters of 400 nm for MWG1 and 3944 nm for MGW2.

The thermal behavior of geopolymer composites was investigated using TGA under controlled heating in air, revealing a gradual weight loss associated with both physically

https://doi.org/10.3390/app16020667

and chemically bound water. The TGA curves (Figure 11) indicate that the pure geopolymer exhibited the highest weight loss, as water is gradually released during heating—physically bound up to 100 °C and chemically bound up to 300 °C—which is consistent with the results presented [50]. At temperatures above 300 °C, water is released through dihydroxylation [51].

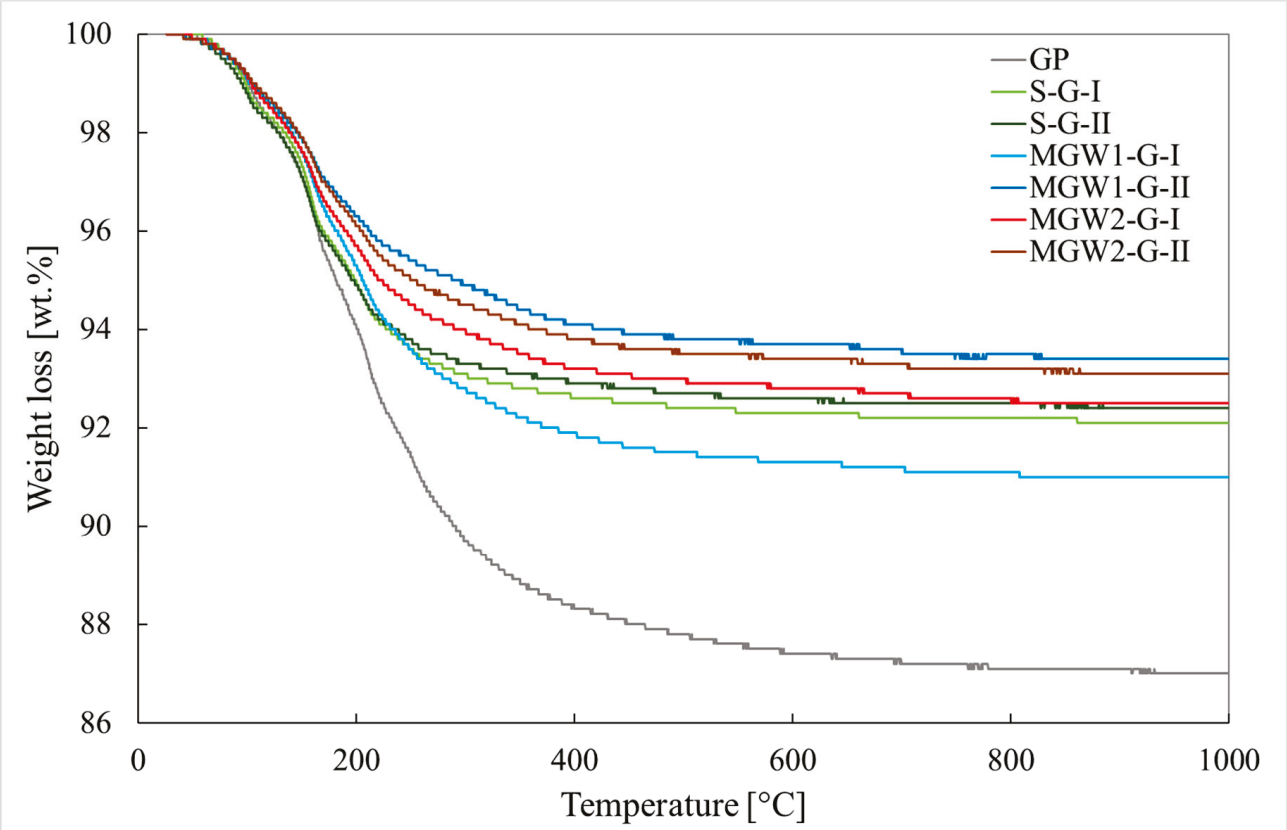

Figure 11. TGA curves of the weight loss (wt.%) of cube samples heated to 1000 °C in an air atmosphere at a flow rate of 30 mL·min^{-1}.

Since MGW is practically an inert material, its addition enhances the thermal stability of the composites, as evidenced by the much lower weight losses. The total weight changes in the pure geopolymer and geopolymer composites may also be influenced by structural modifications occurring at high temperatures (Figure S3 of the Supplementary Materials). This effect is particularly noticeable in MGW-containing samples, which maintain better structural integrity than the pure geopolymer.

A comparison of MGW1 additions shows that a lower amount results in a higher weight loss, corresponding to lower density and increased porosity. This trend confirms the relationship between MGW content, microstructural compactness, and thermal stability, in agreement with previous studies [52,53].

Conversely, MGW2 samples demonstrated slightly better stability (weight loss) than MGW1, which may be attributed to a higher proportion of finer fractions and, consequently, better incorporation into the geopolymer matrix. Composites with MGW2 also exhibit lower porosity than those with MGW1, which is related to the increased density of the geopolymer composite and the higher proportion of MGW, and thus to a lower TGA weight loss [52,53].

As shown in the microstructural analysis (Figure 3; Figures S1 and S2; Tables S3 and S4), the MGW samples contain metallic layers that can locally influence the microstructure at

https://doi.org/10.3390/app16020667

temperatures around 1000 °C by promoting the fusion of glass particles and the formation of a glassy phase, which is evident on the surface of the cubes (Figure S3).

The thermal conductivity (λ), thermal diffusivity (a), and volumetric-heat capacity (Cρ) of metakaolin-based geopolymers containing different aggregates (mirror glass waste and sand) were measured to assess their suitability for thermally resistant applications.

The results (see Table 9) showed that geopolymers with sand (S-G) exhibited significantly higher thermal conductivity and diffusivity than those with mirror glass waste (MGW-G). For example, S-G-II reached a thermal conductivity of 1.0851 $W \cdot m^{-1} \cdot K^{-1}$, whereas MGW-based samples remained below 0.53 $W \cdot m^{-1} \cdot K^{-1}$. Overall, the measured values of thermal conductivity ranged from 0.4487 to 1.0851 $W \cdot m^{-1} \cdot K^{-1}$, those of thermal diffusivity from 0.3008 to 0.7335 $\times 10^{-6}$ $m^2 \cdot s^{-1}$, and those of volumetric-heat capacity from 1.4244 to 1.6733 $\times 10^6$ $J \cdot m^{-3} \cdot K^{-1}$, depending on the specific composition.

Table 9. Thermal properties of the geopolymer composites prepared with MGW and silica aggregates.

Sample	λ ($W \cdot m^{-1} \cdot K^{-1}$)	a·10^6 ($m^2 \cdot s^{-1}$)	Cρ·10^{-6} ($J \cdot m^{-3} \cdot K^{-1}$)	T (°C)
MGW1-G-I	0.4693 ± 0.0006	0.3089 ± 0.0005	1.5190 ± 0.0019	29.197
MGW1-G-II	0.5286 ± 0.0016	0.3711 ± 0.0014	1.4244 ± 0.0034	30.009
MGW2-G-I	0.4487 ± 0.0009	0.3008 ± 0.0008	1.4918 ± 0.0066	30.085
MGW2-G-II	0.5284 ± 0.0006	0.3138 ± 0.0007	1.6733 ± 0.0038	30.206
S-G-I	0.9364 ± 0.0022	0.6125 ± 0.0015	1.5289 ± 0.0027	29.729
S-G-II	1.0851 ± 0.0062	0.7335 ± 0.0033	1.4793 ± 0.0028	30.450

λ—thermal conductivity, a—thermal diffusivity, Cρ—volumetric-heat capacity, T—temperature.

These findings are generally consistent with data reported by Ziejewska et al. [54] for geopolymer foams containing waste glass (thermal conductivity 0.080–0.117 $W \cdot m^{-1} \cdot K^{-1}$), although their samples were highly porous, with total porosity ranging from 58.7% to 67.3%, whereas our dense composites have a porosity of approximately 20%. Despite the differences in porosity and sample type, the trend of lower thermal conductivity for glass-containing geopolymers is similar.

In a broader context, typical thermal-conductivity values for compact geopolymer composites based on slag and/or metakaolin generally fall within the range of 0.2–1.2 $W \cdot m^{-1} \cdot K^{-1}$, depending on porosity, binder composition, and the inclusion of fillers or aggregates [55–58]. In particular, higher slag content and reduced porosity are commonly associated with increased thermal conductivity. Correlations between pore structure, compressive strength, and thermal conductivity have also been reported in similar systems [58], confirming the importance of microstructure optimization for the design of geopolymer composites, as pore distribution and connectivity strongly influence both mechanical and thermal performance.

Compared with traditional construction materials [59–61], such as Portland-cement concrete (0.8–2.0 $W \cdot m^{-1} \cdot K^{-1}$), the studied geopolymers exhibit lower to comparable thermal conductivity. Specifically, S-G samples approached or exceeded 1 $W \cdot m^{-1} \cdot K^{-1}$, suggesting potential for thermal stability, whereas MGW-G samples showed lower conductivity, indicating better thermal insulation potential.

Microscopic observations of thin sections (Figure 8) revealed the presence of microcracks within the geopolymer matrix as well as gaps between mirror particles and the geopolymer binder. These create additional void space that is easily accessible to helium (in ground samples) but may be partially inaccessible to mercury (in intact samples), especially in the case of poorly connected or extremely fine pores. Consequently, helium pycnometry consistently yields higher porosity values than MIP. The discrepancies be-

https://doi.org/10.3390/app16020667

tween these two methods reflect both the physical principles of measurement and the actual morphology of the pore system, as well as the different sensitivities of the techniques.

The replacement of natural sand with MGW in geopolymer composites reduces the consumption of natural resources and decreases landfill waste, thereby supporting circular economy principles. This study on geopolymer composites containing glass-waste additives highlights the potential of these waste materials for sustainable construction applications [45]. The use of geopolymers in mirror recycling is thus not only environmentally friendly but also economically advantageous, with the potential to drive innovation in waste management. Moreover, the mechanical properties and stability of the MGW-based geopolymers indicate that they are suitable for practical applications such as paving elements, protective layers, or other non-load-bearing components, where moderate mechanical performance is sufficient. These findings highlight the feasibility of integrating waste-derived geopolymers into real construction practices, contributing to both sustainability and resource efficiency.

4. Conclusions

This study has demonstrated that geopolymers offer a promising route for recycling mirror glass waste. The characterization of MGW1 and MGW2 has confirmed their typical composition, consisting of an amorphous silicate matrix (>90%) with a silver reflective coating and barium-based backing layers. Both materials have been chemically and structurally stable and exhibited very similar properties.

After crushing, MGW1 contained a higher proportion of coarse particles, whereas MGW2 had more medium-fine fractions, which may influence workability and microstructure. MGW particles appeared as sharp-edged, irregular fragments with heterogeneous spatial distribution, while sand produced a smoother and more homogeneous internal structure. This difference correlated with the higher mechanical strength observed in sand-based composites.

Flexural and compressive strengths of MGW composites were lower than those of sand-based materials. MGW composites reached flexural strength values of 3.9–5.7 MPa and compressive strengths of 60–70 MPa, whereas sand-based composites achieved 8–11 MPa in flexural strength and up to 93.5 MPa in compressive. Nevertheless, the strength values of the MGW composites remain sufficient for applications subjected to moderate mechanical loading, such as paving elements, protective layers, or other non-load-bearing or secondary construction components, where compressive stresses below approximately 60 MPa and flexural stresses below about 4 MPa are expected and are significantly lower than those in primary structural components.

ATR-FTIR analysis demonstrated that the incorporation of either mirror glass waste or sand filler into the geopolymer matrix results in only a slight shift in the main spectral band, while having no adversely effect on the geopolymerization process during the formation of the composite.

All composites exhibited similar water absorption values (~12–14%). The type and amount of additive has only a minor effect. Composites with MGW show similar pore-size distributions, although MGW1 increases the volume of pores larger than 250 nm. The total pore volumes of MGW-G composites and the geopolymer matrix exceeded 20 $mm^3 \cdot g^{-1}$ with average pore diameters below 30 nm. In contrast, the raw MGW materials had much lower pore volumes (<9 $mm^3 \cdot g^{-1}$) and larger average-pore diameters (400 and 4000 nm).

In terms of thermal stability, the pure geopolymer exhibited the highest weight loss associated with water release up to 300 °C. The incorporation of MGW improves thermal stability, resulting in lower overall mass losses, with MGW2 composites showing slightly better performance than MGW1. This improvement is likely related to the higher proportion

https://doi.org/10.3390/app16020667

of finer MGW2 particles, which may enhance the formation of a glassy phase during heating to approximately 1000 °C. All MGW composites showed significantly lower thermal conductivity (<0.53 $W \cdot m^{-1} \cdot K^{-1}$) than the sand-based materials (up to 1.085 $W \cdot m^{-1} \cdot K^{-1}$), demonstrating their superior insulation potential.

Overall, this study indicates that mirror glass waste can be effectively integrated into geopolymer composites, transforming an underutilized material into a valuable resource. While MGW-based composites show lower mechanical strength than sand-based systems, they provide enhanced sustainability and functional advantages, including reduced landfill burden, conservation of natural resources, and markedly improved thermal insulation. These combined benefits highlight MGW as a viable and environmentally meaningful alternative aggregate, particularly for applications where moderate strength, enhanced insulation, and circular economy principles are desirable.

Future research will include leaching tests on the composites under different environmental conditions and a long-term evaluation of potential metal/ion release, in order to more comprehensively verify the environmental safety of MGW-based geopolymers. In addition, the detailed influence of reflective coatings and possible interface defects on geopolymerization and durability remains to be clarified and will be addressed in future studies.

Supplementary Materials: The following supporting information can be downloaded at: https://www.mdpi.com/article/10.3390/app16020667/s1, Table S1. The chemical composition of the clay material used (major oxides in wt.%); Table S2. The particle size distribution of the clay material used; Figure S1. A SEM image for EDS analysis of the layered structure forming the mirror coating on the MGW1 aggregate; Table S3. EDS analysis of MGW1; Figure S2. A SEM image for EDS analysis of the layered structure forming the mirror coating on the MGW2 aggregate; Table S4. EDS analysis of MGW2; Figure S3. Photographs of geopolymer composite cubes before thermal treatment (top row), after heating at 1000 °C (middle row), and detailed views of the thermally exposed cubes (bottom row).

Author Contributions: Conceptualization: I.P.; methodology: I.P., D.Ř., M.Š., M.Ž. and O.B.; formal analysis: I.P., D.Ř., M.Š., M.Ž., M.N. and O.B.; investigation: I.P., D.Ř., M.Š., M.Ž. and O.B.; data curation: I.P.; writing—original draft preparation: I.P., D.Ř., M.Š. and O.B.; writing—review and editing: I.P., D.Ř., M.Š., M.Ž., M.N. and O.B.; supervision: I.P. All authors have read and agreed to the published version of the manuscript.

Funding: This work was supported by the long-term project for the conceptual development of the research organization No. 67985891 and the Strategy AV21 Research Program of the Czech Academy of Sciences: Sustainable Energy (VP27).

Institutional Review Board Statement: Not applicable.

Informed Consent Statement: Not applicable.

Data Availability Statement: The raw data supporting the conclusions of this article will be made available by the authors on request.

Conflicts of Interest: The authors declare no conflicts of interest.

References

1. Enoch, J.M. History of Mirrors Dating Back 8000 Years. *Optom. Vis. Sci.* **2006**, *83*, 775–781. [CrossRef]
2. Venetian Mirrors. History of Venetian Mirrors. Available online: https://www.venetian-mirrors.com/en/content/7-history-of-venetian-mirrors (accessed on 3 December 2025).
3. Anderson, K.J. Reflections on Mirror Coating Materials. *MRS Bull.* **1989**, *14*, 68–69. [CrossRef]
4. Zhang, M.; Deskins, N.A.; Zhang, G.; Cygan, R.T.; Tao, M. Modeling the Polymerization Process for Geopolymer Synthesis through Reactive Molecular Dynamics Simulations. *J. Phys. Chem. C* **2018**, *122*, 6760–6773. [CrossRef]

https://doi.org/10.3390/app16020667

5. Provis, J.L.; Van Deventer, J. (Eds.) *Geopolymers: Structures, Processing, Properties and Industrial Applications*; Woodhead Publishing Limited: Cambridge, UK, 2009.
6. Davidovits, J. *Geopolymer Chemistry and Applications*, 5th ed.; Geopolymer Institute: Saint-Quentin, France, 2020.
7. Siyal, A.A.; Radin Mohamed, R.M.S.; Shamsuddin, R.; Ridzuan, M.B. A Comprehensive Review of Synthesis Kinetics and Formation Mechanism of Geopolymers. *RSC Adv.* **2024**, *14*, 446–462. [CrossRef]
8. Petrus, H.T.B.M.; Hulu, J.; Dalton, G.S.P.; Malinda, E.; Prakosa, R.A. Effect of Bentonite Addition on Geopolymer Concrete from Geothermal Silica. *Mater. Sci. Forum* **2016**, *841*, 7–15. [CrossRef]
9. Castillo, H.; Collado, H.; Droguett, T.; Vesely, M.; Garrido, P.; Palma, S. State of the Art of Geopolymers: A Review. *e-Polymers* **2022**, *22*, 108–124. [CrossRef]
10. Chen, S.; Ruan, S.; Zeng, Q.; Liu, Y.; Zhang, M.; Tian, Y.; Yan, D. Pore Structure of Geopolymer Materials and Its Correlations to Engineering Properties: A Review. *Constr. Build. Mater.* **2022**, *328*, 127064. [CrossRef]
11. Podolsky, Z.; Liu, J.; Dinh, H.; Doh, J.H.; Guerrieri, M.; Fragomeni, S. State of the Art on the Application of Waste Materials in Geopolymer Concrete. *Case Stud. Constr. Mater.* **2021**, *15*, e00637. [CrossRef]
12. Nagaraju, T.V.; Bahrami, A.; Azab, M.; Naskar, S. Development of Sustainable High Performance Geopolymer Concrete and Mortar Using Agricultural Biomass—A Strength Performance and Sustainability Analysis. *Front. Mater.* **2023**, *10*, 1128095. [CrossRef]
13. Toniolo, N.; Boccaccini, A.R. Fly Ash-Based Geopolymers Containing Added Silicate Waste. A Review. *Ceram. Int.* **2017**, *43*, 14545–14551. [CrossRef]
14. Mabroum, S.; Moukannaa, S.; El Machi, A.; Taha, Y.; Benzaazoua, M.; Hakkou, R. Mine Wastes Based Geopolymers: A Critical Review. *Clean. Eng. Technol.* **2020**, *1*, 100014. [CrossRef]
15. Ren, B.; Zhao, Y.; Bai, H.; Kang, S.; Zhang, T.; Song, S. Eco-Friendly Geopolymer Prepared from Solid Wastes: A Critical Review. *Chemosphere* **2021**, *267*, 128900. [CrossRef]
16. Huang, B.T.; Xi, H.; Ma, R.Y.; Zhang, Z.L.; Lao, J.C.; Zhang, H.; Shen, Y.N.; Shi, D.D.; Xu, L.Y. Ultra-High-Strength Engineered Geopolymer Composites (UHS-EGC) with Mineral Processing Waste: Probabilistic Modeling of Cracking Behavior. *Theor. Appl. Fract. Mech.* **2025**, *140*, 105138. [CrossRef]
17. Hanzlicek, T.; Steinerova, M.; Straka, P. Radioactive Metal Isotopes Stabilized in a Geopolymer Matrix: Determination of a Leaching Extract by a Radiotracer Method. *J. Am. Ceram. Soc.* **2006**, *89*, 3541–3543. [CrossRef]
18. Minaříková, M.; Škvára, F. Fixation of Heavy Metals in Geopolymeric Materials Based on Brown Coal Fly Ash. *Ceram.-Silik.* **2006**, *50*, 200–207.
19. Yongvanich, N.; Supanichwatin, K.; Penglan, J.; Triamnak, N. Synthesis and Characterizations of $(Co_xMg_{(2-x)})SiO_4$ Forsterite Ceramic Pigments from Mirror Waste. *Materials* **2018**, *11*, 1210. [CrossRef]
20. Sklopísek Střeleč, a. s. Available online: https://glassand.eu/ (accessed on 23 December 2025).
21. Perná, I.; Havelcová, M.; Šupová, M.; Žaloudková, M.; Bičáková, O. The Synthesis and Characterization of Geopolymers Based on Metakaolin and on Automotive Glass Waste. *Appl. Sci.* **2024**, *14*, 3439. [CrossRef]
22. Perná, I.; Novotná, M.; Řimnáčová, D.; Šupová, M. New Metakaolin-Based Geopolymers with the Addition of Different Types of Waste Stone Powder. *Crystals* **2021**, *11*, 983. [CrossRef]
23. Perná, I.; Novotná, M.; Hanzlíček, T.; Šupová, M.; Řimnáčová, D. Metakaolin-Based Geopolymer Formation and Properties: The Influence of the Maturation Period and Environment (Air, Demineralized and Sea Water). *J. Ind. Eng. Chem.* **2024**, *134*, 415–424. [CrossRef]
24. Perná, I.; Zárybnická, L.; Mácová, P.; Šupová, M.; Ševčík, R. Physico-Mechanical Properties of Geopolymers after Thermal Exposure: Influence of Filler, Temperature and Dwell Time. *Constr. Build. Mater.* **2024**, *451*, 138893. [CrossRef]
25. Perná, I.; Hanzlíček, T.; Straka, P.; Steinerová, M. Acoustic Absorption of Geopolymer/Sand Mixture. *Ceram.-Silik.* **2009**, *53*, 48–51.
26. *ČSN 72 0103*; Základní Postup Rozboru Silikátů-Stanovení Ztráty Žíháním. TECHNOR print, s.r.o.: Hradec Králové, Czech Republic, 2009.
27. *EN 196-1*; Methods of Testing Cement–Part 1. Determination of Strength. European Committee for Standardization: Brusel, Belgium, 2016.
28. *ČSN 72 2603*; Stanovení Nasákavosti. TECHNOR print, s.r.o.: Hradec Králové, Czech Republic, 1979.
29. Washburn, E.W. The Dynamics of Capillary Flow. *Phys. Rev.* **1921**, *17*, 273–283. [CrossRef]
30. Košek, F.; Dudák, J.; Tymlová, V.; Žemlička, J.; Řimnáčová, D.; Jehlička, J. Evaluation of Pore-Fracture Microstructure of Gypsum Rock Fragments Using Micro-CT. *Micron* **2024**, *181*, 103633. [CrossRef]
31. Sutter, F.; Fernández-García, A.; Heller, P.; Anderson, K.; Wilson, G.; Schmücker, M.; Marvig, P. Durability Testing of Silvered-Glass Mirrors. *Energy Procedia* **2015**, *69*, 1568–1577. [CrossRef]
32. Cao, Y.; Liang, H.; Lin, H.L.; Qi, L.; Yang, P.; Fong, X.; Dogheche, E.; Bettiol, A.; Danner, A. Engineering Refractive Index Contrast in Thin Film Barium Titanate-on-Insulator. *Nano Lett.* **2023**, *23*, 7267–7272. [CrossRef] [PubMed]

https://doi.org/10.3390/app16020667

33. SphereOptics GmbH. Barium Sulphate Diffuse Reflectance Coating for Optical Components. Available online: https://sphereoptics.de/products-services-index/optical-materials/barium-sulphate-paint/ (accessed on 3 December 2025).
34. Photonics Media Publications Mirrors: Coating Choice Makes a Difference. Available online: https://www.photonics.com/Articles/Mirrors-Coating-Choice-Makes-a-Difference/a25501 (accessed on 3 December 2025).
35. Torres-Carrasco, M.; Palomo, J.G.; Puertas, F. Sodium Silicate Solutions from Dissolution of Glasswastes. Statistical Analysis. *Mater. Constr.* **2014**, *64*, e014. [CrossRef]
36. Lee, W.K.W.; Van Deventer, J.S.J. Use of Infrared Spectroscopy to Study Geopolymerization of Heterogeneous Amorphous Aluminosilicates. *Langmuir* **2003**, *19*, 8726–8734. [CrossRef]
37. Rees, C.A.; Provis, J.L.; Lukey, G.C.; Van Deventer, J.S.J. Attenuated Total Reflectance Fourier Transform Infrared Analysis of Fly Ash Geopolymer Gel Aging. *Langmuir* **2007**, *23*, 8170–8179. [CrossRef]
38. Kouamo Tchakouté, H.; Henning Rüscher, C.; Hinsch, M.; Noël, J.; Djobo, Y.; Kamseu, E.; Leonelli, C. Utilization of Sodium Waterglass from Sugar Cane Bagasse Ash as a New Alternative Hardener for Producing Metakaolin-Based Geopolymer Cement. *Geochemistry* **2017**, *77*, 257–266. [CrossRef]
39. Sitarz, M.; Mozgawa, W.; Handke, M. Vibrational Spectra of Complex Ring Silicate Anions-Method of Recognition. *J. Mol. Struct.* **1997**, *404*, 193–197. [CrossRef]
40. Sarah, A.-S.; Mohammed, K.; Géber, R.; Simon, A.; Kurovics, E.; Hamza, A. Comparative Study of Metakaolin-Based Geopolymer Characteristics Utilizing Different Dosages of Water Glass in the Activator Solution. *Results Eng.* **2023**, *20*, 101469. [CrossRef]
41. ElBatal, H.A.; Hassaan, M.Y.; Fanny, M.A.; Ibrahim, M.M. Optical and FT Infrared Absorption Spectra of Soda Lime Silicate Glasses Containing Nano Fe_2O_3 and Effects of Gamma Irradiation. *Silicon* **2017**, *9*, 511–517. [CrossRef]
42. Anbalagan, G.; Prabakaran, A.R.; Gunasekaran, S. Spectroscopic Characterization of Indian Standard Sand. *J. Appl. Spectrosc.* **2010**, *77*, 86–94. [CrossRef]
43. Müller, C.M.; Molinelli, A.; Karlowatz, M.; Aleksandrov, A.; Orlando, T.; Mizaikoff, B. Infrared Attenuated Total Reflection Spectroscopy of Quartz and Silica Micro- and Nanoparticulate Films. *J. Phys. Chem. C* **2012**, *116*, 37–43. [CrossRef]
44. Stein, M.; Georgiadis, A.; Gudat, D.; Rennert, T. Formation and Properties of Inorganic Si-Contaminant Compounds. *Environ. Pollut.* **2020**, *265*, 115032. [CrossRef] [PubMed]
45. Hajimohammadi, A.; Ngo, T.; Kashani, A. Glass Waste versus Sand as Aggregates: The Characteristics of the Evolving Geopolymer Binders. *J. Clean. Prod.* **2018**, *193*, 593–603. [CrossRef]
46. Tammam, Y.; Uysal, M.; Canpolat, O.; Kuranlı, Ö.F. Effect of Waste Filler Materials and Recycled Waste Aggregates on the Production of Geopolymer Composites. *Arab. J. Sci. Eng.* **2023**, *48*, 4823–4840. [CrossRef]
47. Joseph, B.; Mathew, G. Influence of Aggregate Content on the Behavior of Fly Ash Based Geopolymer Concrete. *Sci. Iran.* **2012**, *19*, 1188–1194. [CrossRef]
48. Zheng, J.; Li, X.; Bai, C.; Zheng, K.; Wang, X.; Sun, G.; Zheng, T.; Zhang, X.; Colombo, P. Rapid Fabrication of Porous Metakaolin-Based Geopolymer via Microwave Foaming. *Appl. Clay Sci.* **2023**, *249*, 107238. [CrossRef]
49. Kuri, J.C.; Hosan, A.; Shaikh, F.U.A.; Biswas, W.K. The Effect of Recycled Waste Glass as a Coarse Aggregate on the Properties of Portland Cement Concrete and Geopolymer Concrete. *Buildings* **2023**, *13*, 586. [CrossRef]
50. Řimnáčová, D.; Perná, I.; Novotná, M.; Šupová, M.; Nováková, M.; Bičáková, O. Activated Carbon–Geopolymer Composites: Influence of Particle Size and Content on CO_2 Adsorption and Mechanical and Thermal Properties. *Crystals* **2025**, *15*, 892. [CrossRef]
51. Duxson, P.; Lukey, G.C.; van Deventer, J.S.J. Physical Evolution of Na-Geopolymer Derived from Metakaolin up to 1000 °C. *J. Mater. Sci.* **2007**, *42*, 3044–3054. [CrossRef]
52. Schwarz, N.; Cam, H.; Neithalath, N. Influence of a fine glass powder on the durability characteristics of concrete and its comparison to fly ash. *Cem. Concr. Compos.* **2008**, *30*, 486–496. [CrossRef]
53. Rodier, L.; da Costa Correia, V.; Savastano, H., Jr. Elaboration of eco-efficient vegetable fibers reinforced cement-based composites using glass powder residue. *Cem. Concr. Compos.* **2020**, *110*, 103599. [CrossRef]
54. Ziejewska, C.; Bąk, A.; Hodor, K.; Hebda, M. Eco-Friendly Coal Gangue and/or Metakaolin-Based Lightweight Geopolymer with the Addition of Waste Glass. *Materials* **2023**, *16*, 6054. [CrossRef] [PubMed]
55. Agustini, N.K.A.; Triwiyono, A.; Sulistyo, D.; Suyitno. Effects of Water to Solid Ratio on Thermal Conductivity of Fly Ash-Based Geopolymer Paste. *IOP Conf. Ser. Earth Environ. Sci.* **2020**, *426*, 012010. [CrossRef]
56. Prałat, K.; Ciemnicka, J.; Koper, A.; Buczkowska, K.E.; Łoś, P. Comparison of the Thermal Properties of Geopolymer and Modified Gypsum. *Polymers* **2021**, *13*, 1220. [CrossRef]
57. Huang, Y.; Gong, L.; Pan, Y.; Li, C.; Zhou, T.; Cheng, X. Facile Construction of the Aerogel/Geopolymer Composite with Ultra-Low Thermal Conductivity and High Mechanical Performance. *RSC Adv.* **2018**, *8*, 2350–2356. [CrossRef]

https://doi.org/10.3390/app16020667

58. Jaya, N.A.; Yun-Ming, L.; Cheng-Yong, H.; Abdullah, M.M.A.B.; Hussin, K. Correlation between Pore Structure, Compressive Strength and Thermal Conductivity of Porous Metakaolin Geopolymer. *Constr. Build. Mater.* **2020**, *247*, 118641. [CrossRef]
59. Perná, I.; Hanzlíček, T. The Solidification of Aluminum Production Waste in Geopolymer Matrix. *J. Clean. Prod.* **2014**, *84*, 657–662. [CrossRef]
60. Demirboğa, R. Thermal Conductivity and Compressive Strength of Concrete Incorporation with Mineral Admixtures. *Build. Environ.* **2007**, *42*, 2467–2471. [CrossRef]
61. Ukrainczyk, N.; Matusinović, T. Thermal Properties of Hydrating Calcium Aluminate Cement Pastes. *Cem. Concr. Res.* **2010**, *40*, 128–136. [CrossRef]

Disclaimer/Publisher's Note: The statements, opinions and data contained in all publications are solely those of the individual author(s) and contributor(s) and not of MDPI and/or the editor(s). MDPI and/or the editor(s) disclaim responsibility for any injury to people or property resulting from any ideas, methods, instructions or products referred to in the content.

https://doi.org/10.3390/app16020667

applied sciences

MDPI

Article

Performance Evaluation of Conventional and Recycled Ballast Materials: A Coupled FDM-DEM Approach Considering Particle Breakage

Juan Manuel Mayoral * and Nohemí Olivera

Geotechnical Department, Institute of Engineering, National University of Mexico, Mexico City 04510, Mexico; noliveraro@gmail.com

* Correspondence: jmayoralv@iingen.unam.mx

Abstract: The ballast consists of angular particles whose main function is to transmit and distribute train loads to the soil. However, under repeated loads, these particles wear down and break, causing permanent settlement, reducing track stability, and increasing maintenance. Characterizing stresses and deformations under monotonic and cyclic loading is essential to predict short- and long-term performance of railway systems. This numerical study evaluates the behavior of improved ballast materials, considering particle breakage. A hybrid Finite Difference and Discrete Element model was used to simulate the multiscale response of the track system under realistic loading conditions. The model was calibrated using data from laboratory tests conducted by various researchers. The performance of conventional ballast was compared with alternative mixtures, analyzing vertical displacements, stress distribution, safety factor, and particle breakage rates. Results show that the basalt-rubber composite significantly enhances ballast performance by reducing settlements and subgrade stresses while improving resistance to particle breakage. The FDM-DEM coupled approach effectively captures micromechanical interactions and breakage mechanisms, offering valuable insights for optimizing track design based on quantifiable performance criteria. Overall, the findings indicate the hybrid model and breakage–contact criteria approximated system behavior, while alternative ballast compositions improved durability, reduced maintenance, and supported resilient railway solutions.

Keywords: particle size distribution; ballast optimization; particle breakage; recycled material; cyclic load

1. Introduction

The assessment of railway tracks has undergone significant changes in recent decades due to the need to support higher speeds and shaft loads and improve environmental sustainability. The track support transfers loads to the ground within capacity limits, preventing excessive settlements and lateral displacements [1]. Ballast has the structural function of absorbing and dissipating vertical forces from rail traffic, allowing rapid drainage of rainwater, and facilitating the correction of geometric defects [2].

Numerical studies analyzing stress changes in ballast due to train passages have provided a detailed understanding of load distribution patterns [3]. Liu and Zou [4] demonstrate that ballast abrasion significantly impacts strength and deformation. The three-dimensional stress state critically influences substructure design and service life, as the rotation of principal stresses accelerates the accumulation of plastic deformation.

Train-induced cyclic loads also affect material stiffness and permanent deformation development [5,6]. Table 1 presents relevant research on track support analysis and evaluation, covering numerical modeling, laboratory and large-scale testing, field measurements, and proposals to improve railway design methods.

Studies such as [7] show that the parent rock's strength determines its performance: higher values reduce settlement, increase stiffness, and decrease degradation (quantified by the Ballast Breakage Index, BBI) [8]. However, even the most resistant materials face challenges under repeated dynamic loads, driving the search for innovative alternatives and the pursuit of an optimal material.

A promising research line explores the use of recycled materials to comprise more sustainable substructures [9]. Previous studies have indicated that planar polymeric geogrids and cellular inclusions, such as geocells, have the potential to improve track stiffness and reduce lateral dilation [10–12]. Some recent studies have proposed using recycled materials, such as recycled glass, plastics, and demolished construction waste, to replace traditional aggregates in railway substructures. This approach aims to provide a more sustainable solution and meet the requirements outlined by standards [13–15].

Mixes of recycled rubber and steel slag have also been evaluated to improve mechanical properties [16], and in large-scale tests researchers have compared steel slag with conventional crushed ballast [17]. The results showed that steel slag ballast has a higher elastic modulus, less permanent deformation under heavy train loads, and greater shear resistance, consistent with the findings of Kaya [18] and Koh [19]. High-density slag can also enhance track stability by increasing lateral ballast resistance by 27% and vertical stiffness by 64% [20].

Rubber intermixed ballast systems (RIBS) are an innovative solution for railway ballast that combines rubber granules with conventional ballast aggregates [21]. Through large-scale testing, the optimal rubber particle size (9.5–19 mm) and an inclusion ratio (10%) were chosen to meet performance standards, while reducing long-term maintenance. The results show that this 10% rubber substitution significantly decreases degradation and fouling of the coarse aggregates [22].

For the assessment of long-term conditions, large-scale experiments with ballasted track have been designed to gain insight into the behavior of the track bed and the progression of ballast degradation [23]. These studies used validated physical model test platforms to examine settlement and degradation patterns under repeated train loadings. Artificial neural networks have also been incorporated into monitoring to develop simplified numerical models that relate measured parameters to degradation processes [24].

Despite advances in assessing the behavior of materials in the track support system, most laboratory studies do not reproduce the complexity of a real railway system. In these tests, degradation is accelerated through high loads and controlled conditions, which differ from the wear mechanisms observed in the field, where low-amplitude vibrations, localized impacts, and environmental variations influence them. Additionally, the dynamic interaction among the sleeper, ballast, and subgrade is often ignored, even though its effect is crucial in the actual distribution of stresses and the system's response under load. Furthermore, none of the conventional methods have demonstrated an effective capacity to absorb energy and provide adequate damping and resilience to the rails, enabling them to withstand impacts and repeated loads in a sustained manner.

Table 1. Numerical and experimental studies on the assessment of railway tracks.

Authors	Research	Principal Findings
Godson et al. [25]	Large-scale tests were conducted to compare the physical, mechanical, and environmental performance of electric arc furnace slag (EAFS) with conventional material.	The shear strength of EAFS was 15–22% higher than that of granite, with less final vertical deformation and a 20% increase in the load-bearing capacity of the granular layer. In addition, its leaching is within regulatory limits, making it safe for railway use.
Nasrollahi et al. [26]	Real-time monitoring of a zone between a ballasted track and a slab track with fiber Bragg grating (FBG) sensors installed in situ.	The FBG system reliably captures short- and long-term deformations/accelerations of the rail and sleeper; useful data for early diagnosis and model calibration.
Chen et al. [27]	Diametral compression tests by size, large-scale triaxial tests, and numerical modeling using the Discrete Element Method (DEM), to access micromechanical indicators such as coordination number, contact forces, and anisotropy.	The strength of ballast follows a Weibull distribution, and heterogeneous grading improves its performance, although large particles increase the risk of fracture.
Indraratna et al. [14]	Evaluation of recycled material tests: CWRC [1], SEAL [2] (slag + CW + RC), tire cells, and UBM [3] under ballast.	The recycled materials studied increase energy dissipation, reduce degradation, and vibrations.
Li et al. [28]	Full-scale track testing on ballasted track: dynamic responses and cumulative settlements.	They recorded vibration speeds, dynamic stresses, and settlement evolution under moving loads.
Sayeed and Shahin [29]	A design method for ballasted railway track foundations is proposed, combining improved empirical models and 3D numerical analysis, capable of supporting high-speed trains and heavy loads.	The new design method for railway foundations prevents critical failures using empirical models and 3D analysis, offering a more robust solution that is adaptable to various design conditions and modern railway traffic.
Edwards et al. [30]	Laboratory and field tests on concrete sleepers using surface strain gauges to obtain bending moments.	Non-invasive method that quantifies variability between sleepers and provides data for design/service life.
Lu and McDowell [31]	The study uses the Discrete Element Method (DEM) to simulate the behavior of ballast under monotonic and cyclic loads, replicating shear strength and volumetric response, validated experimentally.	The model shows that shear strength varies with confining pressure and ballast size, being less sensitive to pressure in small particles. The number of roughness features influences the peak friction angle, but not the residual friction angle.
Lim et al. [32]	Compression tests were performed on six types of rock to analyze the strength of the ballast, evaluating the results with the Weibull distribution to explore the relationship between size and strength.	The strengths of the ballast conform to the Weibull distribution, but the relationship between size and strength differs from the theory due to factors such as quarry processing and surface fractures, which limit the applicability of the model.
Li and Selig [33]	A design method is proposed to determine the thickness of the granular layer between ballast and subballast, preventing subgrade failure due to repeated loads, using procedures that consider soil strength and railway load.	The method converts traffic conditions into design parameters and defines two criteria to prevent failure and deformation. Validated in the field, it showed good results in tests and real sites.
Cundall and Strack [34]	This research presents the Discrete Element Method (DEM) as a numerical tool designed to describe the mechanical behavior of assemblies of particles represented by disks or spheres.	The numerical results showed a high degree of visual similarity with those obtained experimentally, which supported the validity of the DEM for investigating granular behavior.

[1] Coal wash rubber crumbs. [2] Synthetic energy-absorbing layer. [3] Under ballast mat.

This study evaluates the performance of conventional materials against two sustainable and innovative alternatives for the railway track support system. A three-dimensional

hybrid numerical model combining the Discrete Element Method (DEM) and Finite Difference Method (FDM) was developed and calibrated using large-scale triaxial test data. The model accounts for full interaction among track components (rail, sleeper, ballast, and subgrade) to accurately simulate structural response under dynamic conditions. A particle fracture criterion differentiates volume and contact effects, while a simplified angular-shape model with rolling resistance ensures a balance between accuracy and computational efficiency in evaluating sustainable materials for railway infrastructure.

2. Database

The properties of the five materials evaluated in this study, basalt, granite, limestone, steel slag, and a mixture of basalt and rubber (RIBS), are based on results reported in previous research by other authors. Table 2 summarizes the most relevant characteristics of the selected materials, including the values obtained in the Micro-Deval and Los Angeles abrasion resistance tests. Figure 1 shows the particle size distribution of each material, determined by particle size analysis in accordance with ASTM C136/C136M-19 [35]. This distribution was used directly to define the input particle size in the numerical models developed in this study.

Table 2. Characteristics of materials.

Material	Density	MD [1]	LA [2]	Uniformity Coefficient, C_u	Coefficient of Curvature, C_c	D_{max}	D_{min}
	ρ	(%)	(%)	(-)	(-)	(mm)	(mm)
Basalt [36]	2.60	5.10	12.10	1.48	0.99	53	13
Granite [37]	2.68			1.52	0.90	63	16
Limestone [38]	2.65			1.46	0.97	63	13
Steel Slag [39]	3.20	11.00	23.00	1.94	1.02	28	4
RIBS [40]	2.80	5.20	11.70	2.60	1.40	53	4.75

[1] Micro Deval index test. [2] Los Angeles abrasion index test.

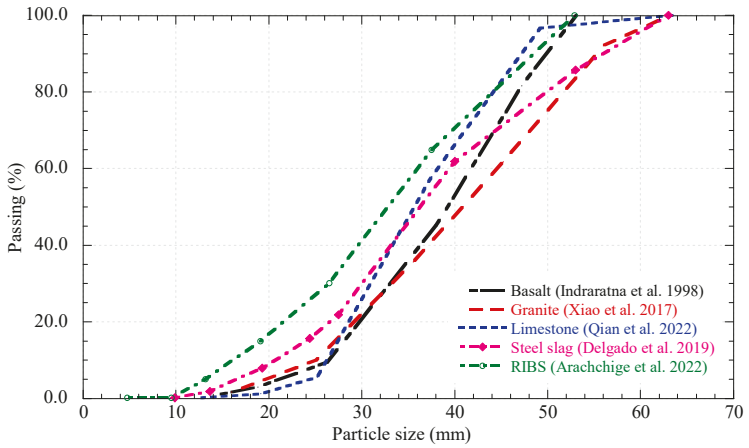

Figure 1. Particle size distribution of materials used in numerical models: Basalt [36], Granite [37], Limestone [38], Steel Slag [39], and RIBS [40].

Figure 2, prepared from data reported in the technical literature, shows the stress–strain curves under different confinement levels for two materials. Steel slag exhibits a stiffer behavior, characterized by a well-defined peak strength, while the basalt-rubber mixture displays a more ductile response, with greater deformations before failure. Table 3 complements this information by including the specific values obtained from the corresponding experimental tests.

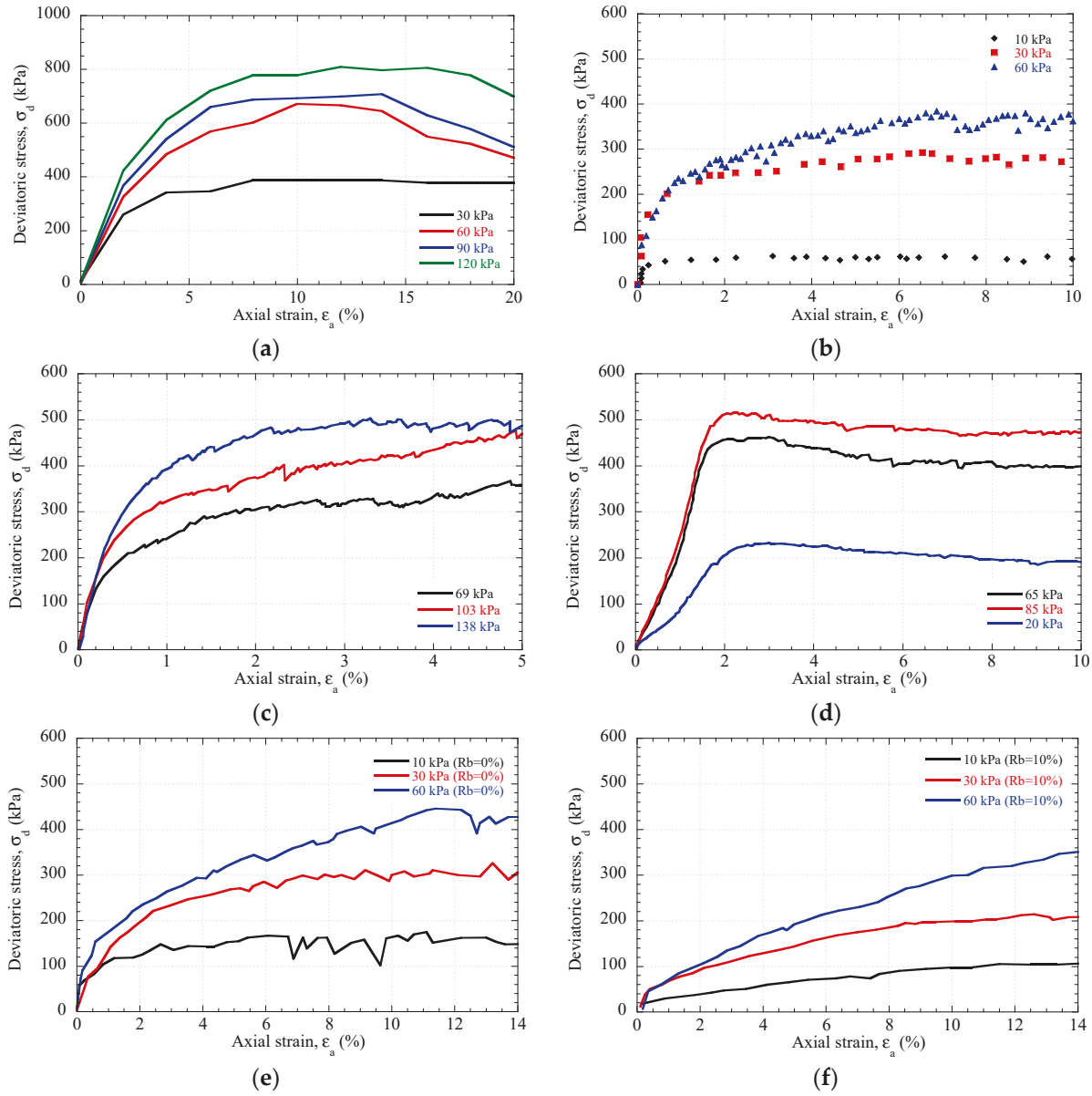

Figure 2. Stress–strain curves reported by various researchers for (**a**) basalt, (**b**) granite, (**c**) limestone, (**d**) steel slag, (**e**) RIBS with 0% rubber, and (**f**) RIBS with 10%.

Table 3. Laboratory test data.

Material	Type of Test	Void Ratio	Confining Pressure, (kPa)	Axial Strain, (%)
Basalt	Triaxial	0.79–0.84	30/60/90/120	20
Granite	Triaxial	-	10/30/60	10
Limestone	Triaxial	-	69/103/138	5
Steel Slag	Triaxial	-	20/65/85	10
RIBS	Triaxial	0.76–0.82	10/30/60	20

Railway ballast inherently exhibits sharp edges and angular corners that significantly influence track mechanics through increased sliding friction, enhanced rolling resistance, and improved particle interlocking. To capture these geometric properties (sphericity, angularity, texture), clumped-sphere aggregates are commonly employed [41]. While this

approach effectively represents multi-contact interactions and realistic rolling resistance behavior [42], it requires a balance between geometric accuracy and computational efficiency for large-scale simulations.

The use of sphere aggregates to represent angular particles is a common simplification in DEM models, aimed at maintaining a balance between geometric fidelity and computational efficiency. While this approximation may partially underestimate the effects of interlocking and shear resistance, the rolling resistance contact model largely compensates for these limitations by reproducing the rotational stiffness and angular restriction mechanisms observed in real particles. Several studies [43–45] support the effectiveness of this strategy in adequately capturing the overall mechanical response of ballast without compromising computational cost.

3. Model Description

3.1. Rolling Resistance Contact Model

To address the issue above, the linear rolling resistance model implemented in PFC^{3D} [45] was adopted as a reference. Particle interactions (particle-particle or particle-facet) are governed by contact forces with normal and shear components, both incorporating spring force (F_n^s) and a damping force (F_n^d). Notably, the normal spring force updates in absolute terms (independent of loading history), while the resultant normal force is limited to prevent tensile stresses. The normal component (F_n) of the contact force follows:

$$F_n = F_n^s + F_n^d = k_n u_n + \beta_n \dot{u}_n \leq 0 \text{ (No tension)} \tag{1}$$

where k_n is the normal contact stiffness, β_n is the damping coefficient in normal direction, u_n y $\dot{u}_n$ are the absolute normal displacement and interparticle velocity, respectively, as shown in Figure 3.

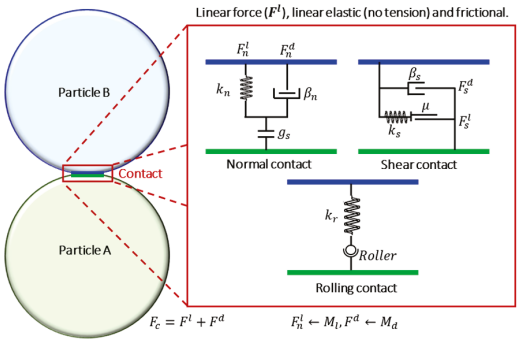

Figure 3. Linear contact with rolling resistance.

3.2. Lineal Model

The Linear Contact Model (LCM), originally developed by Cundall and Strack [34], represents the fundamental contact formulation in DEM simulations. This model combines linear elastic stiffness and viscous damping components to govern energy transfer and dissipation in both normal and tangential directions. The linear component provides tension-free elastic behavior with frictional resistance, while the damping introduces viscous effects, both acting through an infinitesimal contact point that exclusively transmits forces without moments. As illustrated in Figure 4, the resultant contact force emerges from the superposition of these two components, where the elastic stiffness maintains a Hertzian-like contact response while the damping ensures energy dissipation during particle interactions.

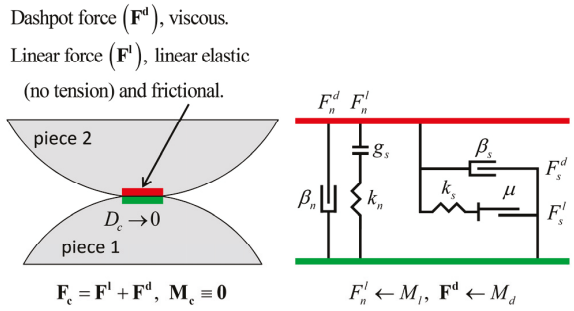

Figure 4. Schematic diagram of the Linear Contact Model.

For ballast materials, particle contacts exhibit negligible viscous behavior, rendering the damping component inactive in most scenarios. Consequently, PFC-based ballast studies typically omit dashpot considerations [46,47]. The linear component combines normal and shear forces as expressed in Equation (2) [48]:

$$F = F^l + F^d \tag{2}$$

$$F_n^l = k_n \beta_n \tag{3}$$

$$F_n^l = \left(F_n^l\right)_0 + k_n \Delta\delta_n \tag{4}$$

$$F_s^l = \left(F_s^l\right)_0 - k_s \Delta\delta_s \tag{5}$$

where F_n^l and F_s^l are the normal and shear components of the linear force, k_n and k_s are the normal and shear stiffnesses, β_n and β_s are the normal and shear critical-damping ratios and, $\Delta\delta_n$ and $\Delta\delta_s$ are the adjusted relative normal and shear-displacement increment.

It should be noted that in most DEM models (using PFC) with the linear contact model, the kinetic energy of particles is dissipated through frictional sliding and local damping, with a default coefficient of 0.7. In PFC, local damping is considered a particle-level attribute, rather than a contact model parameter, and applies a damping force to each particle individually [48].

3.3. Breakage Particle

Railway ballast performance is critically influenced by particle breakage, which alters mechanical properties and track stability. Particle fracture resistance varies due to intrinsic defects, compositional variations, and loading conditions, typically modeled using Weibull distributions. Fractal dimension (D) quantifies fragmentation effects, increasing with progressive breakage and influencing load redistribution. However, excessive fine accumulation compromises drainage, requiring controlled fragmentation.

When studying the fracture of granular particles, it is necessary to define a failure criterion that determines when a particle breaks under specific mechanical conditions. Therefore, this study employs the criterion proposed by Ciantia et al. [49], which unifies contact and volume properties into a single mathematical expression.

The model establishes a limiting condition for normal contact forces, requiring that the force F must not exceed a critical threshold value F_{lim}, as expressed by the following equation:

$$F < \frac{\kappa}{f(\chi, \upsilon)} \pi R^2 sin^2\theta_0 = \sigma_{lim} A_F = F_{lim} \tag{6}$$

The limiting strength σ_{lim} depends on material properties κ, χ y υ, while A_F represents contact area, R is the sphere radius, and θ_0 is a solid angle 'seen' from the center of the particle. This separation between material strength (σ_{lim}) and contact geometry (A_F) allows independent treatment of scenario-dependent contact properties versus intrinsic material behavior. The model accounts for natural soil variability and size effects, with σ_{lim} following a normal distribution (material-specific coefficient of variation). A Weibull-type size correction $f_{size}(d)$ is applied, reflecting increased smaller-particle strength as a hardening rule rather than strict statistical relationship. The size-dependent strength is expressed as

$$\sigma_{lim} = \sigma_{lim,0} f_{size}(d) \tag{7}$$

where $f_{size}(d)$ is given by

$$f_{size}(d) = \left(\frac{d}{d_0}\right)^{-\frac{3}{m}} \tag{8}$$

where $d_0 = 2$ mm is the reference diameter and m is a material parameter. The factor $f_{size}(d)$ scales the limiting strength with particle size, capturing the enhanced resistance of smaller particles. For contact area A_F evaluation, a common approach treats the contact angle θ_0 as a material constant independent of σ_{lim}, yielding the failure contact area:

$$A_F = \frac{\pi}{4} d^2 sin^2 \theta_0 \tag{9}$$

Simulations must incorporate mass loss during fragmentation to accurately model Particle Size Distribution (PSD) evolution. Studies [50,51] show fragmentation generates fractal particle distributions ($\alpha \approx 2.6$), expressed as

$$\frac{M_{(L<d)}}{M_T} = \frac{d^{3-\alpha} - d_{min}^{3-\alpha}}{d_{max}^{3-\alpha} - d_{min}^{3-\alpha}} \tag{10}$$

where M_T is the total mass, $M_{(L<d)}$ is the smallest particle of d, d_{max} is the maximum particle size and d_{min} is the smallest particle observed.

Fragmentation simulations account for mass loss, producing fractal PSDs ($\alpha \approx 2.6$). Apollonian packings (fractal dimension 2.47) model post-fragmentation placement, aligning particles with principal stresses. A minimum particle size threshold optimizes computational efficiency, with analyses showing comminution limits dominate PSD evolution over particle count (14-sphere configurations proving optimal), as shown in Figure 5.

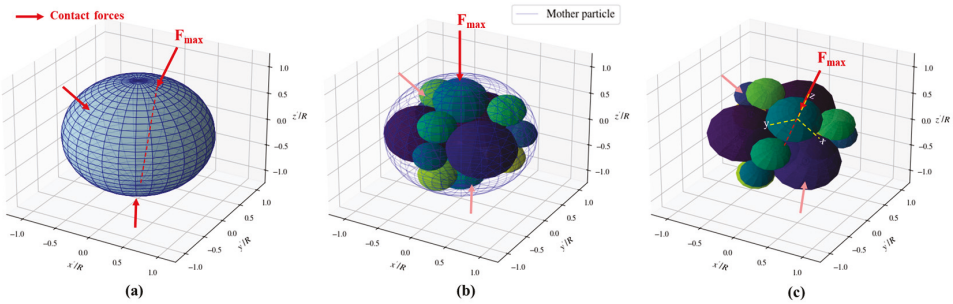

Figure 5. The particle-crushing configuration includes (**a**) intact grain, (**b**) sibling disposition, and (**c**) sibling reorientation, modified from [49].

4. Model Calibration

This section presents the methodology and results of the numerical simulations conducted to replicate triaxial test behavior using the Discrete Element Method (DEM). The obtained calibration parameters are introduced, ensuring the numerical model accurately captures the mechanical response observed in laboratory tests.

The calibration procedure for the simulated triaxial specimens is described in detail, including the adjustment of micromechanical parameters and validation against macroscopic experimental data. Additionally, the key features of the coupled modeling approach combining Finite Difference Method (FLAC^{3D}) and Discrete Element Method (PFC^{3D}) are discussed. This hybrid framework allows for the simulation of geotechnical problems involving both continuous and discontinuous media, enhancing the analysis of soil and rock mechanics under complex loading conditions.

The integration of PFC^{3D} (for particle-scale interactions) and FLAC^{3D} (for continuum modeling) provides a robust numerical tool for studying granular materials and their interaction with larger structural elements, offering insights that are difficult to obtain through purely experimental or analytical approaches.

4.1. Parameter Calibration

The model calibration was based on extensively documented and validated experimental results gathered from the technical literature, derived from carefully selected large-scale triaxial tests. These studies are in good agreement with the recommended properties for materials often used in railway tracks supports. Thus, these data were deemed appropriate for this initial research phase. While the importance of direct experimental validation is acknowledged, the used data allows establishing the soundness of the proposed methodology.

For the calibration process, large-scale triaxial tests previously reported by different authors [36–40] were reproduced numerically. Each simulation was designed to remain consistent with the laboratory configurations described in those studies, ensuring that the numerical response could be directly compared with the experimental results.

Triaxial tests were conducted using cylindrical specimens of different sizes and with a grain size distribution based on previous experimental data. Each specimen, enclosed by two flat plates and a curved wall (Figure 6), was created by randomly placing ballast particles and adjusting the friction coefficient to achieve either dense or loose packing. Isotropic confinement was applied using the PFC^{3D} servo-control algorithm until the target pressure was reached.

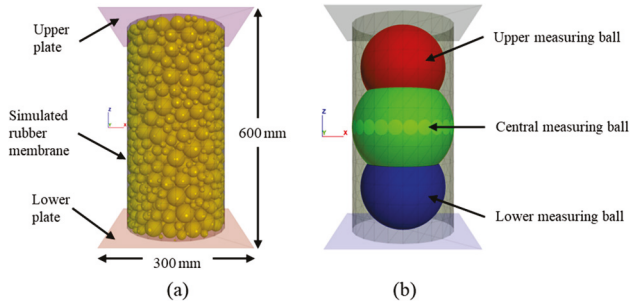

Figure 6. Numerical triaxial model: (**a**) general characteristics and (**b**) measure balls.

Once the sample was obtained, a monotonic triaxial test was conducted by controlling the axial deformation and maintaining constant lateral pressure. During loading, the deviatoric stress and axial deformation were recorded, and measurement spheres were used to assess particle breakage. In the model, three types of contact were considered:

ballast–ballast, rubber–rubber, and ballast–rubber, as shown in Figure 7. Contacts with rubber were modeled using a linear approach, while ballast contacts were simulated with a linear model incorporating rolling resistance to account for the effect of angular shape and to reduce computational cost.

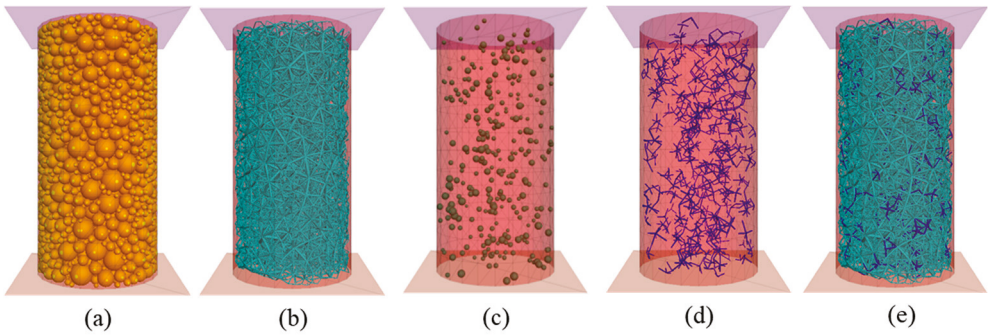

Figure 7. Specimen for DEM simulation: (**a**) ballast particles, (**b**) ball–ball contact, (**c**) rubber particles, (**d**) rubber–rubber contact, and (**e**) ball–rubber contact.

Due to the complexity of directly obtaining DEM simulation parameters from experimental results, most researchers have historically determined these parameters using indirect methods, which are described below and adopted in this study. In the first stage, a comprehensive literature review was conducted to establish reasonable value ranges for the parameters. Subsequently, these values were optimized through trial-and-error iterations to achieve agreement between the simulated macroscopic mechanical behavior and available experimental data. The final parameters used in the DEM simulations are specified in Table 4.

Table 4. Parameters of the PFC models.

Material	Density (kg/m^3)	Normal Stiffness, k_n	Shear Stiffness, k_s	Damping	Friction Coefficient, μ	Rolling Friction Coefficient, μ_r
		(N/m)	(N/m)	-	-	-
Basalt	2650	2×10^6	2×10^6	0.7	0.4	0.8
Granite	2680	3×10^8	3×10^8	0.7	0.5	0.6
Limestone	2600	2×10^7	2×10^7	0.7	0.5	0.7
Steel slag	3200	1×10^9	1×10^9	0.7	0.4	0.4
RIBS	2650	5×10^8	5×10^8	0.7	0.3	0.7

The selection of micro-parameters is a key aspect for achieving an accurate approximation in numerical simulation. Table 5 summarizes the values used in previous studies to represent the behavior of rubber, which served as a reference and starting point for the calibration developed in this study. The calibration procedure was conducted as follows:

First, the basalt-basalt contact parameters were calibrated using particles from a pure basalt sample. Subsequently, a 10% rubber-basalt mixture was employed to calibrate the rubber-basalt contact parameters. Given the established basalt-basalt contact parameters and the limited quantity of large rubber particles, the rubber-basalt contact was found to have minimal contribution to the overall strength. Therefore, specific calibration of the rubber-basalt contact parameters was performed. Finally, the rubber content percentage was varied to validate the simulated macroscopic behavior against available experimental data. The final micro-parameters adopted to represent the rubber are detailed in Table 6.

Notably, following the recommendations of Li and McDowell [52], a local damping coefficient of 0.7 was implemented in the model. This technical measure proved crucial for suppressing numerically unstable oscillations in the system during simulations.

Table 5. Reference parameters for rubber.

Contact Model	Normal Stiffness, k_n	Shear Stiffness, k_s	Young Modulus, E	Friction Coefficient, μ	Rolling Friction Coefficient, μr	Reference
	(N/m)	(N/m)	(Pa)	(-)	(-)	
Linear	1.5×10^5	1.5×10^5	-	1.00	-	Liu et al. [53]
Linear	8.0×10^5	8.0×10^5	-	0.60	-	Wang et al. [54]
Hertz	-	-	1.2×10^7	1.00	-	Perez et al. [55,56]
RRLM	1.0×10^3	1.0×10^3	-	1.50	-	Gong et al. [57]
RRLM	3.28×10^5	2.18×10^5	-	1.00	0.1	Guo et al. [58]
Hertz	-	-	5.0×10^7	1.00	-	Wu et al. [59]
Linear	2.0×10^5	2.0×10^5	-	1.00	-	Zhang et al. [60]
Linear	-	-	1.57×10^7	-	-	Ngo et al. [61]

Table 6. Contact micro-parameters of RIBS.

Contact Type	Normal Stiffness, k_n	Shear Stiffness, k_s	Friction Coefficient, μ	Rolling Friction Coefficient, μ_r
	(N/m)	(N/m)	-	-
Ballast–ballast	3.3×10^7	3.3×10^7	0.45	0.80
Rubber–rubber	4.5×10^3	4.5×10^3	1.00	
Ballast–rubber	2.0×10^6	2.0×10^6	1.00	0.50
Particle–wall	1.7×10^8	1.7×10^8	0.30	

In Figure 8, the calibration results obtained for conventional materials are presented. It is observed that the numerical response satisfactorily reproduces the behavior observed experimentally in large-scale triaxial tests, demonstrating an adequate correspondence between the stress–strain curves for the different levels of confining stress. The specific details of the reference experimental conditions are indicated in Table 3 of Section 2.

The calibration results for the recycled materials are shown in Figure 9. This difference between computed and experimental data is attributed to the intrinsic properties of these materials, especially rubber, whose high deformability and low stiffness cannot be explicitly represented in PFC, which assumes rigid particles. Nevertheless, the calibration is considered acceptable, as it accurately reproduces the overall response and experimental trends.

Based on the model calibration, it was observed that the normal stiffness (kn) and tangential stiffness (ks) are the parameters that have the most significant influence on the model's response, as they directly control the initial slope of the stress–strain curve. When these values are high, the material exhibits a more brittle behavior, reaching its peak strength too early. Reducing kn and ks of the rubber particles decreases the initial stiffness and the friction angle. Conversely, while friction mainly controls the maximum strength of the assembly, the rolling resistance determines the shape of the curve in the post-peak stage, defining the transition between the maximum load state and the residual condition.

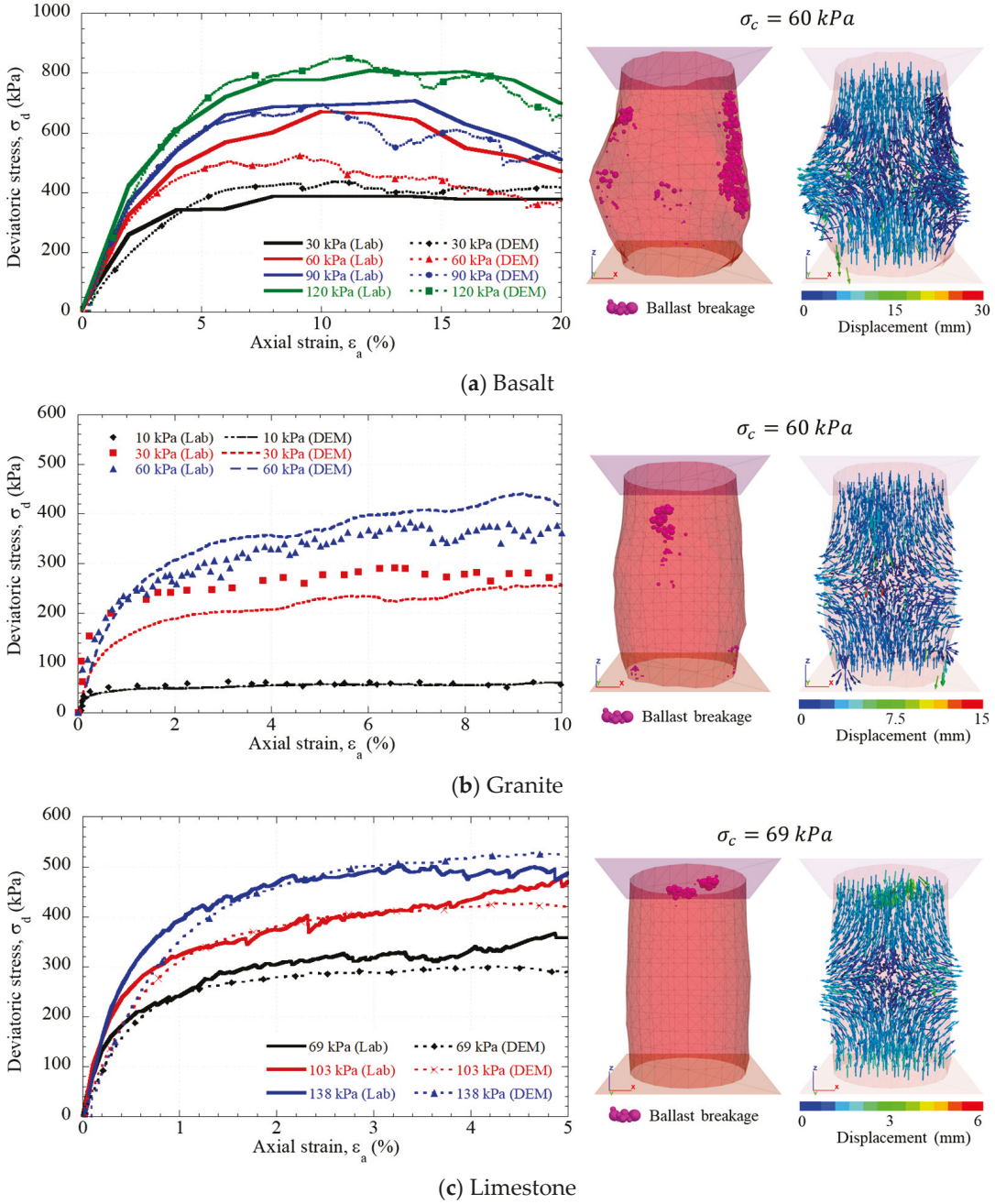

Figure 8. Comparison of the stress–strain curves from the numerical calibration and experimental results, fractured particles within the triaxial specimens, and displacement vectors at different levels of confining stress in conventional materials.

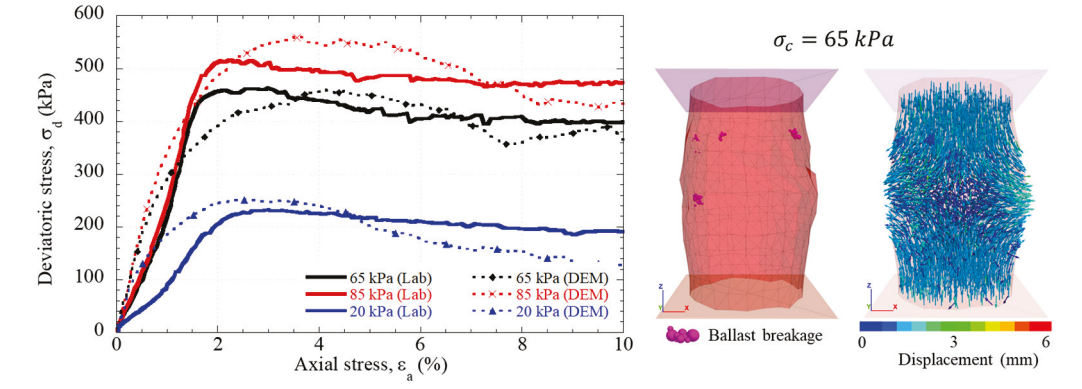

(**a**) Steel slag

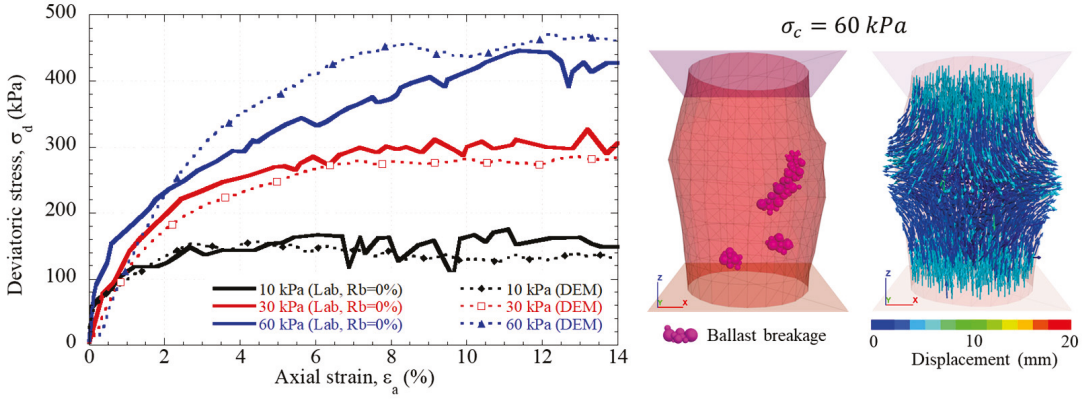

(**b**) RIBS without rubber

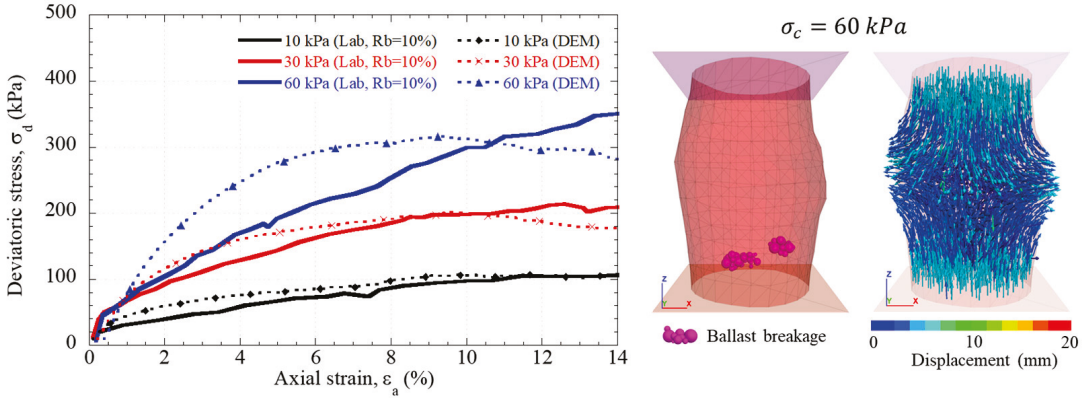

(**c**) Ribs with 10% rubber content

Figure 9. Comparison of the stress–strain curves from the numerical calibration and experimental results, fractured particles within the triaxial specimens, and displacement vectors at different levels of confining stress in recycled materials.

4.2. Coupled Numerical Model PFC^{3D}—FLAC^{3D}

The study evaluated the ballasted track system's behavior at both macroscopic and microscopic scales, a 3D coupled DEM-FDM model was established, as illustrated in Figure 10a. The FDM modeled the subgrade, base, sleepers, and rail, and the DEM simulated the ballast. Moreover, the interactions between the ballast particles and the base or sleepers were simulated by interface elements generated at the contact area between the discrete and continuous elements.

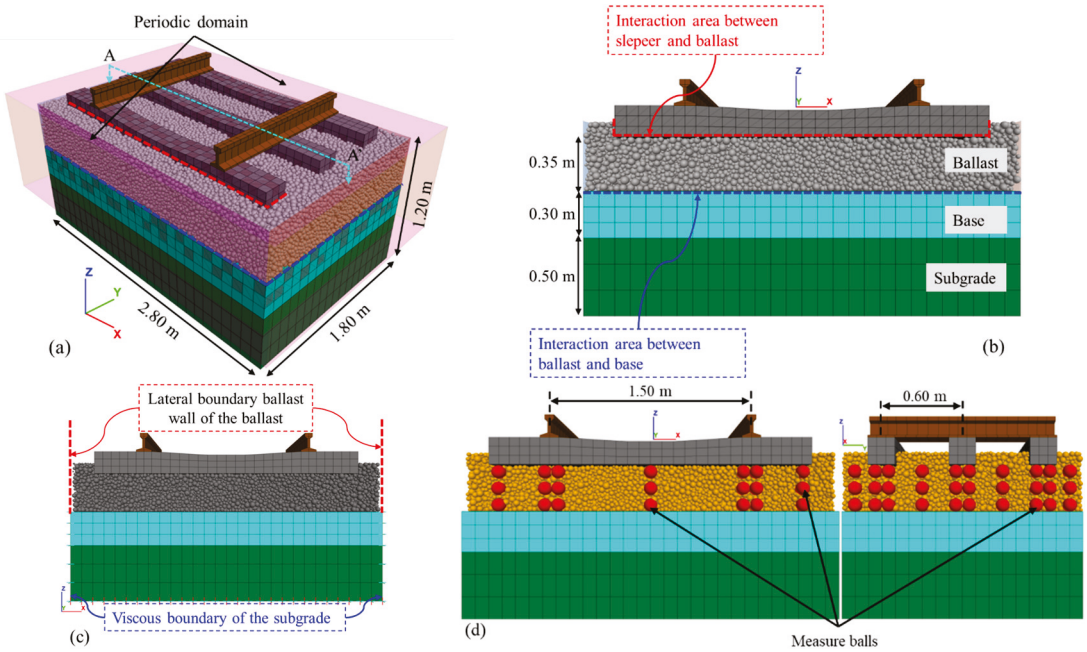

Figure 10. Coupled model (**a**) characteristics, (**b**) between the continuous domain and the discrete domain, (**c**) model boundaries, and (**d**) measuring spheres in the ballast layer.

The track superstructure components (rail and concrete sleeper) are modeled as linear–elastic materials since non-yielding behavior is expected. In the analysis, two different models for the track substructure, elastic and elastoplastic, are considered to study the effect of the material model type on the load and stress path of the railroad. In the case of elastoplastic models, the base is simulated using an elastic-perfect plastic model embracing the Mohr–Coulomb yield criterion, while subgrade is modeled as elastic behavior, the material properties are presented in Table 7.

Table 7. Material properties for the soils.

Group	Constitutive Model	γ (kN/m^3)	c (MPa)	ϕ (°)	E (MPa)	ν (-)
Subgrade	Mohr–Coulomb	22.0	0	43	143	0.30
Base	Elastic	17.6			9,590	0.35
Sleeper	Elastic	24.0			47,500	0.18
Rail	Elastic	79.0			210,000	0.30

Given the critical role of ballasted track compaction conditions in the simulation, this study employed the multilayer compaction method proposed by several researchers [43,44,62], as illustrated in Figure 11. The compaction procedure was initiated with three ballast layers, with compaction pressures exceeding 200 kPa at each stage. Subsequently, excess particles were removed, and auxiliary surfaces were created. The compaction process was repeated to ensure proper particle densification. Finally, sleepers and rails were positioned on top the ballast layer, after which the auxiliary surfaces were removed.

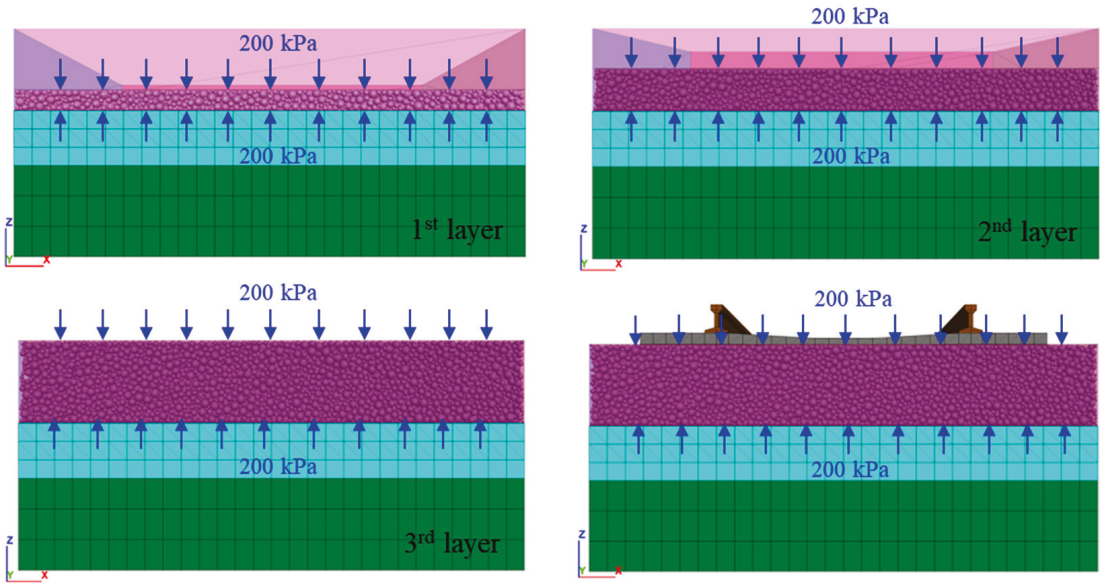

Figure 11. Multilayer compacting procedure.

To characterize the cyclic load transmitted by the bogie, it was considered: (1) the maximum sustained load of 147.15 kN per axle (73.57 kN per wheel), (2) a design speed of 85 km/h, (3) a wheel diameter of 0.914 m, and (4) an Impact Factor, IF (Equation (11)), of 0.48 as recommended by AREMA [63].

$$IF = \frac{33V}{100D} \tag{11}$$

where V = speed in mph; D = wheel diameter in inches.

Thus, the cyclic load was applied 100 times with a frequency of 10 Hz, considering a distance between each axle of 2.40 m.

In this initial phase of the research, a 10 Hz frequency load, and limited number of cycles (100) allows to assess the initial evolution of the stiffness, stress distribution, and fracture mechanisms under controlled conditions, without compromising numerical stability or computational cost. The approach aims to identify relative trends among difference materials. However, it is acknowledged that future studies should include a greater number of cycles, as well as coupled fatigue and progressive damage models, to evaluate long-term response and the accumulation of permanent deformations.

5. Results

For each case analyzed, vertical displacements, the vertical stresses, PSD evolution and breakage index were obtained.

5.1. Monotonic Load

Figure 12 presents the vertical stress distribution versus depth below the loaded sleeper, compared with empirical calculations from AREMA [63]. In 4 of the 5 cases analyzed, the interface stresses at the sleeper-ballast contact exceeded the reference empirical values, reinforcing the need for advanced numerical models in precise track design.

In the present study, it has been observed that both the RIBS material and the steel slag have shown the highest stress concentrations and the lowest vertical displacements, with values below 0.6 mm. However, when considering cyclic loading, these values have increased due to particle rearrangement, breakage, and abrasion. In contrast, the material

that exhibited the highest propensity for displacement was limestone, with values of 0.74 mm. Fracture introduces new contact surfaces, influencing stresses and displacements and confirming their dominant role in the overall behavior of the system. However, these results underline the importance of considering particle fracture, even in cases of minimal fracture, as this can affect the evolution of deformation and long-term strength under repeated loading conditions.

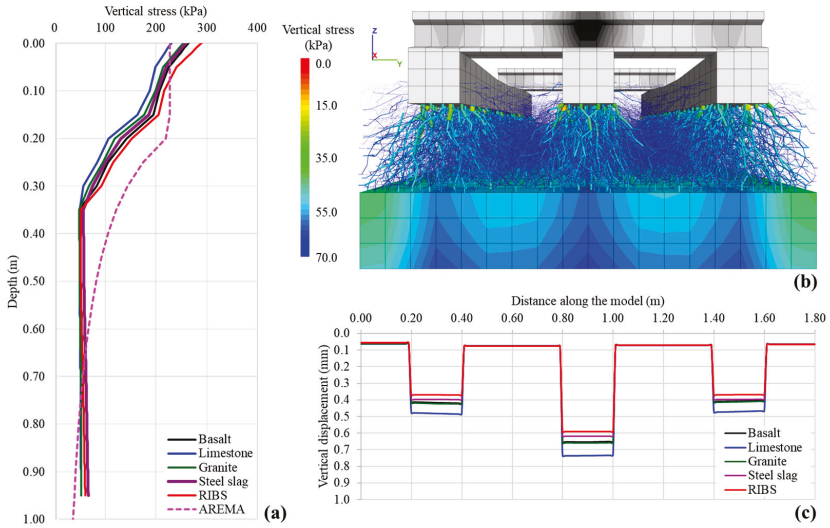

Figure 12. (**a**)Vertical stress distribution with depth beneath the central sleeper, (**b**) stress contours and contact force chains, and (**c**) y-direction displacement profile.

Figures 13 and 14 show the distribution of contact force chains among ballast particles under monotonic load. Each contact force is represented by a cylinder aligned with its direction and with a diameter proportional to its magnitude. The load was applied to both rails on the central sleeper. As shown in the figure, the forces propagate downward into the ballast in a pyramidal pattern, suggesting that the material outside this zone experiences negligible stress. This behavior aligns with findings reported in the literature [64,65]. Additionally, a marked increase in contact forces is observed near the edges of the sleepers, which accounts for the higher particle fracture recorded in these areas.

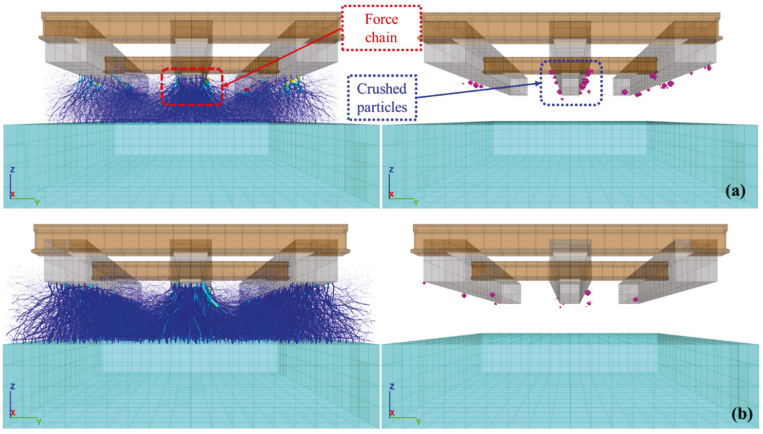

Figure 13. Force chain and crushed particles induced from monotonic load for (**a**) basalt and (**b**) granite.

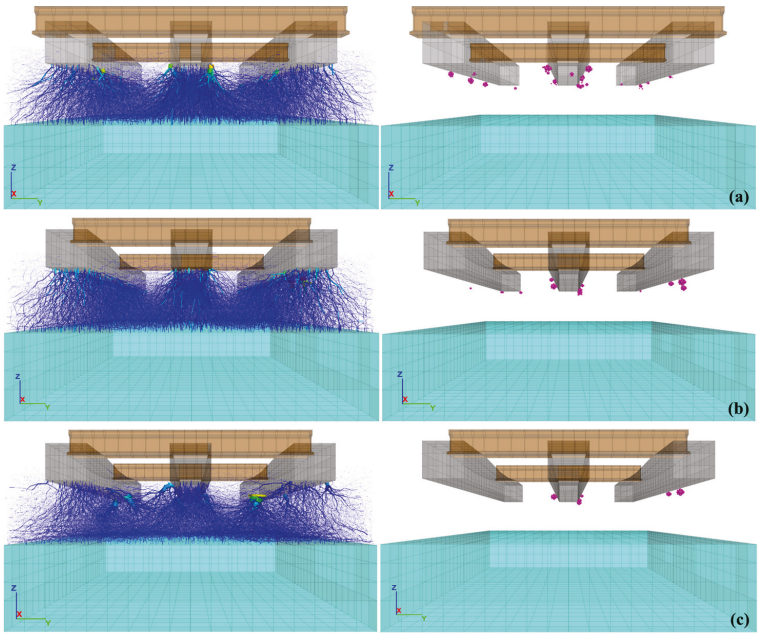

Figure 14. Force chain and crushed particles induced from monotonic load for (**a**) limestone, (**b**) steel slag, and (**c**) RIBS.

5.2. Cyclic Loading

The cyclic load was applied to the center sleeper rail in the same way as the monotonic load. This article presents the results corresponding to 100 load cycles applied at a frequency of 10 Hz.

Figure 15 shows how the deformations evolve with the increase in the number of cycles in the sphere located under the central sleeper (shown in Figure 10d). The vertical deformation of the particles at the interface between the sleeper and the ballast is greater during the first load cycle, and subsequently, a linear increase is observed.

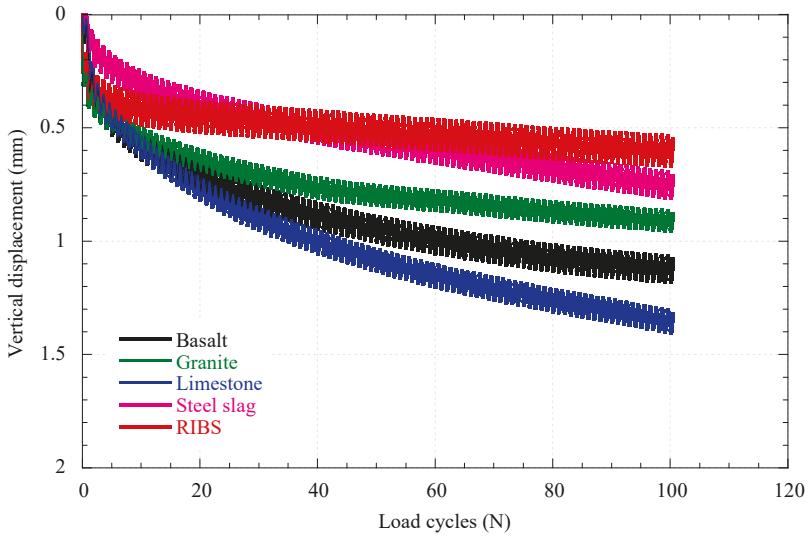

Figure 15. Permanent displacement with the number of load cycles for the materials analyzed.

5.3. Ballast Breakage

Figure 16 shows that contact forces are significantly greater at the edges of the sleeper, leading to increased particle fracture in these areas. In addition, it can be seen that, after

100 load cycles, particle fracture extends to greater depths and is not limited solely to direct contact with the sleeper, as observed in the analysis under sustained load.

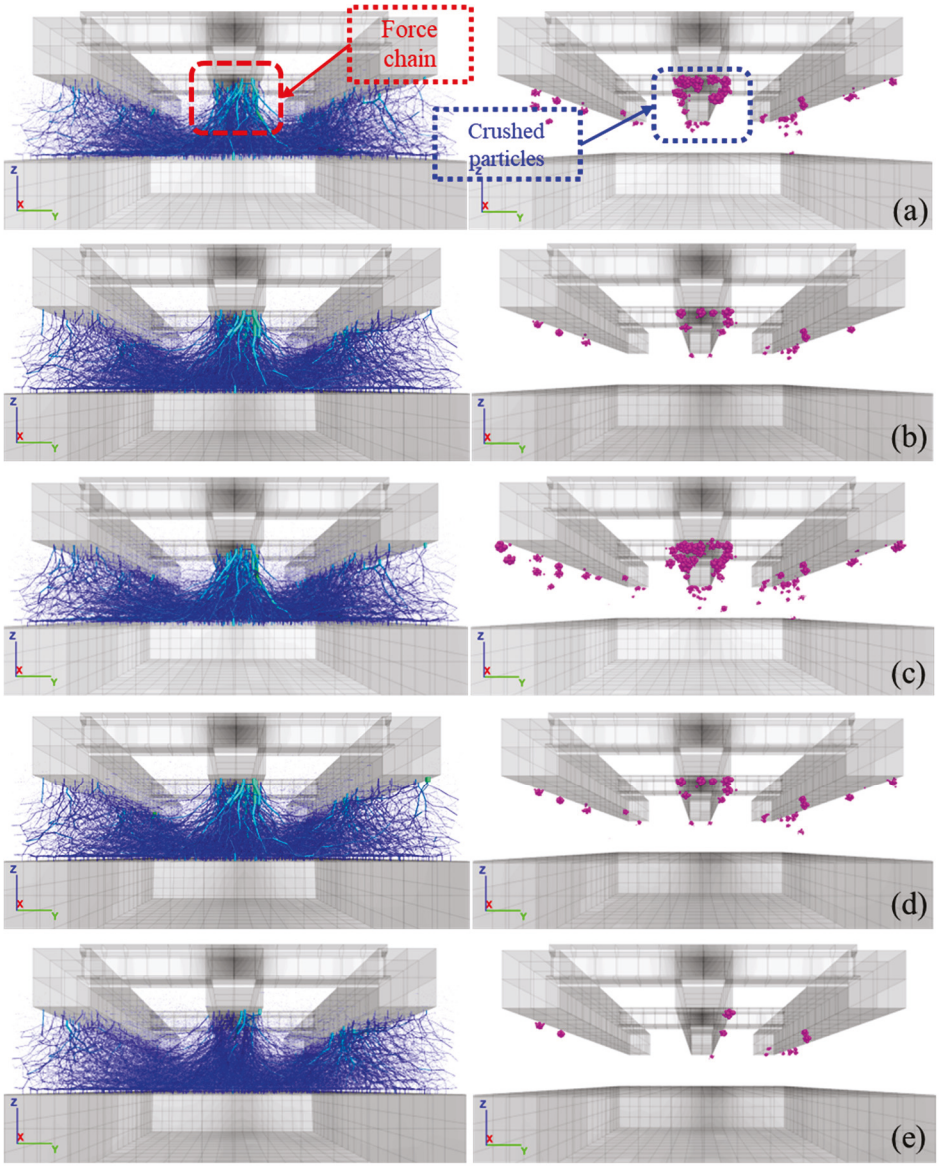

Figure 16. Force chain and crushed particles induced from cyclic load for (**a**) basalt, (**b**) granite, (**c**) limestone, (**d**) steel slag, and (**e**) RIBS with 10% rubber.

This distribution can be attributed to the generation of smaller particles, which are rearranged by gravity and by the general movement of particles toward the bottom of the layer. This behavior has been corroborated in various field studies and is associated with the phenomenon known as fouling.

Finally, Figures 17 and 18 show the behavior of the breakage indices obtained according to the Indraratna, BBI, and Marsal Bg criteria. It can be seen that particle degradation occurs in particles larger than 25 mm. The ballast breakage index (BBI) decreased by 51.04%, from 0.721 to 0.353, when 10% rubber was added to the RIBS model. Similarly, the breakage index according to Marsal's criteria (Bg) decreased by 49.43%, from 7.373 to 3.729. These results reflect a significant improvement in the mechanical behavior of the material, supporting its potential practical application in these track support systems.

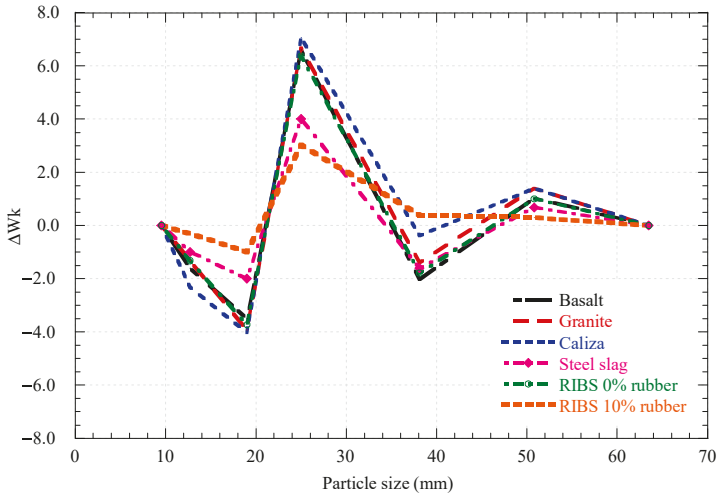

Figure 17. Marsal's breakage index, Bg, for all the samples with cyclic load.

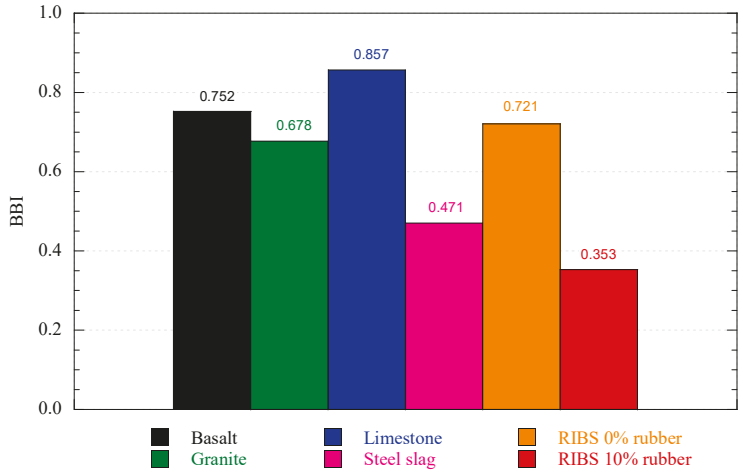

Figure 18. Ballast breakage index, BBI, values all the samples with cyclic load.

The current model does not explicitly incorporate environmental effects, such as the presence of water, freeze–thaw cycles, or material aging. This omission responds to the primary objective of the study: to compare the basic mechanical performance of conventional and alternative materials under controlled conditions, before introducing additional environmental variables.

However, there is agreement on the importance of these factors, especially in the case of rubber, whose response can be affected by temperature or surface degradation. Therefore, future research includes the development of a coupled thermo-hydro-mechanical model that allows for analyzing the combined effects of moisture, temperature, and aging on the durability and long-term response of the railway system.

5.4. Economic Implications

The results of this study show that reducing ballast degradation has direct economic effects on the life cycle of the track. In the RIBS mixture (basalt–rubber), a 51% decrease in the BBI index and a 49.4% reduction in the Bg reduces the generation of fines, maintains permeability, and extends the material's lifespan. This increased durability decreases maintenance frequency, labor and machinery costs, and railway service disruptions, resulting in significant operational savings.

The RIBS system offers the best balance between technical performance and long-term profitability: although its initial cost is higher, the reduction in maintenance offsets the investment. Steel slag is economically viable in regions with local production, while conventional materials have lower initial costs but higher recurring expenses due to degradation.

Additionally, the reuse of waste and the reduced extraction of natural aggregates provide environmental benefits that translate into economic savings and emission reductions. However, the adoption of recycled materials still faces technical, regulatory, and logistical challenges. Therefore, it is recommended to apply life cycle cost analysis (LCCA) tailored to the local context, integrating criteria of cost, performance, and sustainability to guide more efficient and resilient investment decisions.

6. Discussion

One of the main limitations of this study is the simplified geometric modeling of the particles. To optimize calculation time and computational efficiency, a contact model with rotational resistance was used. This model approximately reproduces the effects associated with the angular morphology of the particles.

However, to obtain more realistic simulations, it is recommended to incorporate the actual shape of the particles, whether through agglomerates, polyhedra, or other irregular geometries. Several studies have shown that this representation influences interlocking, shear resistance, and abrasion processes. Adopting this approach would allow for a more detailed analysis of the impact of fines generation and ballast fouling, as well as particle fracture. Finally, applying more advanced contact laws (for example, Newton + Coulomb + Signorini) could improve the simulation of prolonged load cycles and facilitate the study of the long-term behavior of the railway system.

In this context, improving numerical models must be accompanied by a broader understanding of the materials that make up the railway track. The use of recycled materials in the ballast represents an important step toward more sustainable and resilient railway systems. Recent research on steel slag, rubber-ballast mixtures, and tire-derived aggregates has shown improvements in energy absorption and fracture reduction. However, these materials exhibit lower initial stiffness and some uncertainties regarding their durability.

The variability of their properties and the scarcity of long-term tests under real environmental conditions limit their standardization. Therefore, it is essential that predictive models incorporate the effects of temperature, humidity, and aging to more accurately reproduce the behavior of the pathway under actual operational conditions.

Based on this analysis, future research developments should focus on a multiscale understanding of ballast behavior. This should consider both microstructural aspects and environmental and operational effects. The following priority areas are proposed:

- Analyze the combined effects of temperature, humidity, and chemical aging on recycled ballast.
- Study the influence of water, saturation, and freeze–thaw cycles through coupled thermo-hydro-mechanical models.
- Evaluate long-term durability with large-scale cyclic triaxial tests (>10^6 cycles) and DEM simulations that include multigenerational failure.
- Conduct life cycle assessments (LCA) and life cycle cost analyses (LCC) to quantify environmental and economic benefits.
- Develop pilot sections equipped with fiber optic sensors (FBG) and piezometers to validate numerical models and build digital twins that enhance predictive maintenance and performance-based design.

Together, these perspectives drive the transition toward a performance-based, durable, and sustainable railway design framework. This framework should be supported by numerical, experimental, and environmental evidence, and aligned with the principles of circular economy applied to modern railway engineering.

7. Conclusions

The behavior of ballast is closely related to the lithology of the granular material used; therefore, it is essential to analyze a variety of materials in practice to evaluate the structural performance of tracks more comprehensively. There is a broad base of research on ballast materials, including laboratory tests, large-scale trials, and field implementation through pilot tests. However, it is still necessary to deepen the understanding of factors such as the interaction of overall track performance, the effects of extreme environments, advanced multiscale numerical modeling, and rigorous economic-environmental analysis.

This study evaluated three materials conventionally used in track support and two alternatives that, according to bibliographic research, have performed well in different scenarios. The numerical model was calibrated by comparing it with experimental results from large-scale triaxial tests, explicitly considering the particle failure mechanism, and contrasting the stress–strain curves obtained. Once the parameters of each of the materials had been calibrated, they were evaluated under the same confinement stress of 60 kPa, from which the following conclusions were drawn:

- The breakage indices, Bg, obtained from triaxial tests were low for all materials, indicating good mechanical behavior against fracture. It is important to mention that analysis under cyclic loading is recommended.
- Particle degradation was mainly concentrated in the <25 mm fractions, consistent with the ballast breakage index (BBI). Minimal differences were observed between curves, resulting in values of less than 5%, indicating good quality ballast.

Subsequently, a coupled DEM-FDM model was performed to simulate the behavior of the materials under sustained and cyclic loads. The following conclusions can be drawn from this analysis:

- The RIBS system (basalt mixed with rubber) showed the best overall performance, with the lowest fracture rate (0.05%) and reduced vertical displacements (<0.6 mm) under monotonic loading. From a practical perspective, the results question conventional empirical approaches, as in 80% of cases, stresses at the sleeper-ballast interface were higher than expected. In the models subjected to cyclic loading, a significant increase in vertical settlements was observed during the first cycles for the RIBS model. However, this model showed better stabilization of displacements compared to the others.
- The conventional materials (basalt, granite, and limestone) followed similar displacement trajectories, though with distinct magnitudes of settlement. Limestone showed the most significant final displacement (1.32 mm), followed by basalt (1.08 mm) and granite (0.71 mm). After 100 load cycles, all materials produced vertical stresses exceeding empirical estimates, except for the RIBS model, which reached a maximum stress of 177 kPa and exhibited a more uniform stress distribution.
- The incorporation of 10% rubber into the basalt ballast significantly improved mechanical performance: the BBI decreased by 51.0% (from 0.721 to 0.353), and the Marsal breakage index (Bg) reduced by 49.4% (from 7.373 to 3.729). These results confirm the effectiveness of rubber intermixing in reducing particle degradation and enhancing ballast resilience.

The results of this research reaffirm the technical potential of using alternative materials and innovative mixtures for application as railway ballast. In particular, the RIBS system, based on a mixture of basalt and rubber, showed superior performance against degradation and deformation, standing out for its low fracture rate, lower vertical displacements under cyclic loading, and a more uniform distribution of stresses. Conventional materials such as basalt, granite, and limestone also showed acceptable performance, although with notable differences in their shear strength and confinement capacity. Steel slag is presented as a viable alternative, provided it meets regulatory requirements, while the breakage indices (Bg and BBI) confirm the good mechanical quality of most of the materials tested. However, the results also reveal limitations in current empirical methods, as in many cases the measured stresses exceed the predicted theoretical values.

The inclusion of granular mixtures with additives, such as rubber, not only improves the structural performance of the ballast but also opens up new opportunities for developing more sustainable and resilient solutions to repeated loads and demanding operating conditions. Further studies are recommended to evaluate the behavior of these materials under extreme environmental conditions and in long-term applications to strengthen their practical implementation in the track support system.

Author Contributions: Conceptualization, J.M.M.; methodology, J.M.M. and N.O.; software, N.O.; validation, J.M.M.; formal analysis, N.O.; investigation, J.M.M. and N.O.; resources, J.M.M.; data curation, N.O.; writing—original draft preparation, N.O.; writing—review and editing, J.M.M. and N.O.; visualization, N.O. All authors have read and agreed to the published version of the manuscript.

Funding: This research received no external funding.

Institutional Review Board Statement: Not applicable.

Informed Consent Statement: Not applicable.

Data Availability Statement: The original contributions presented in this study are included in the article. Further inquiries can be directed to the corresponding author.

Conflicts of Interest: The authors declare no conflicts of interest.

Abbreviations

The following abbreviations are used in this manuscript:

AREMA	American Railway Engineering and Maintenance-of-Way Association
BBI	Ballast Breakage Index
Bg	Breakage index Marsal
LA	Los Angeles index
MD	Micro-Deval index
DEM	Discrete element method
FDM	Finite difference method
RIBS	Rubber Intermixed ballast Systems

References

1. Selig, E.; Waters, J. *Track Geotechnology and Substructure Management*; Thomas Telford: London, UK, 1994.
2. De Paiva, C.E.L.; Pereira, M.L. Sustainability of the Ballasted Track—A Comprehensive Review on Reducing the Use of Mineral Aggregates and the Role of Sub-ballast as a Protective Layer. In *Sustainable Solutions for Railways and Transportation Engineering*; Springer: Cham, Switzerland, 2018; pp. 67–100.
3. Varandas, J.N.; Paixão, A.; Fortunato, E.; Hölscher, P. A Numerical Study on the Stress Changes in the Ballast Due to Train Passages. *Procedia Eng.* **2016**, *143*, 1169–1176. [CrossRef]

4. Liu, H.; Zou, D. Associated generalized plasticity framework for modeling gravelly soils considering particle breakage. *J. Eng. Mech.* **2013**, *139*, 606–615. [CrossRef]
5. Gräbe, P.J.; Clayton, C.R. Effects of principal stress rotation on permanent deformation in rail track foundations. *J. Geotech. Geoenviron. Eng.* **2009**, *135*, 555–565. [CrossRef]
6. Mayoral Villa, J.M.; Olivera, N.; Tepalcapa, S.; Román, A.; Alcaraz, M. Numerical Assessment of Enhanced Urban-Train Support Systems. In Proceedings of the 10th European Conference on Numerical Methods in Geotechnical Engineering (NUMGE 2023), London, UK, 26–28 June 2023; International Society for Soil Mechanics and Geotechnical Engineering: London, UK, 2023; pp. 2903–2910.
7. Shi, C.; Fan, Z.; Connolly, D.P.; Jing, G.; Markine, V.; Guo, Y. Railway ballast performance: Recent advances in the understanding of geometry, distribution and degradation. *Transp. Geotech.* **2023**, *41*, 101042. [CrossRef]
8. Indraratna, B.; Salim, W. *Mechanics of Ballasted Rail Tracks: A Geotechnical Perspective*; CRC Press: Boca Raton, FL, USA, 2005.
9. Indraratna, B.; Qi, Y.; Tawk, M.; Heitor, A.; Rujikiatkamjorn, C.; Navaratnarajah, S.K. Advances in ground improvement using waste materials for transportation infrastructure. *Proc. Inst. Civ. Eng.-Ground Improv.* **2022**, *175*, 3–22. [CrossRef]
10. Indraratna, B.; Nimbalkar, S.; Rujikiatkamjorn, C. Track stabilisation with geosynthetics and geodrains, and performance verification through field monitoring and numerical modelling. *Int. J. Railw. Technol.* **2012**, *1*, 195–219. [CrossRef]
11. Chen, C.; McDowell, G.R.; Thom, N.H. Investigating geogrid-reinforced ballast: Experimental pull-out tests and discrete element modelling. *Soils Found.* **2014**, *54*, 1–11. [CrossRef]
12. Leshchinsky, B.; Ling, H. Effects of geocell confinement on strength and deformation behavior of gravel. *J. Geotech. Geoenviron. Eng.* **2013**, *139*, 340–352. [CrossRef]
13. Indraratna, B.; Qi, Y.; Malisetty, R.S.; Navaratnarajah, S.K.; Mehmood, F.; Tawk, M. Recycled materials in railroad substructure: An energy perspective. *Railw. Eng. Sci.* **2022**, *30*, 304–322. [CrossRef]
14. Naeini, M.; Mohammadinia, A.; Arulrajah, A.; Horpibulsuk, S. Recycled glass blends with recycled concrete aggregates in sustainable railway geotechnics. *Sustainability* **2021**, *13*, 2463. [CrossRef]
15. Indraratna, B.; Qi, Y.; Ngo, T.; Malisetty, R.; Arachchige, C.K. Innovative and cost-effective rail track construction using recycled rubber. *Railw. Eng. Sci.* **2024**, *33*, 327–341. [CrossRef]
16. Alves, R.; Rios, S.; Fortunato, E.; Viana da Fonseca, A.; Guimarães Delgado, B. Mechanical behaviour of steel slag–rubber mixtures: Laboratory assessment. *Sustainability* **2023**, *15*, 1563. [CrossRef]
17. Sagar, N.; Hussain, A.; Hussaini, S.K.K. Experimental assessment of shear behavior of crumb rubber intermixed steel slag used as railway subballast. In Proceedings of the 4th Asia-Pacific Conference on Physical Modelling in Geotechnics (ACPMG 2024), Abu Dhabi, United Arab Emirates, 11–13 December 2024; International Society for Soil Mechanics and Geotechnical Engineering: London, UK, 2024. [CrossRef]
18. Kaya, M. A Study on the Stress-Strain Behavior of Railroad Ballast Materials by Use of Parallel Gradation Technique. Ph.D. Thesis, Middle Eastern Technical University, Ankara, Turkey, 2004.
19. Koh, T.; Moon, S.W.; Jung, H.; Jeong, Y.; Pyo, S. A feasibility study on the application of basic oxygen furnace (BOF) steel slag for railway ballast material. *Sustainability* **2018**, *10*, 284. [CrossRef]
20. Esmaeili, M.; Nouri, R.; Yousefian, K. Experimental comparison of the lateral resistance of tracks with steel slag ballast and limestone ballast materials. *Proc. Inst. Mech. Eng. Part F J. Rail Rapid Transit.* **2017**, *231*, 175–184. [CrossRef]
21. Arachchige, C.M.; Indraratna, B.; Qi, Y.; Vinod, J.S.; Rujikiatkamjorn, C. Deformation and degradation behaviour of Rubber Intermixed Ballast System under cyclic loading. *Eng. Geol.* **2022**, *307*, 106786. [CrossRef]
22. Arachchige, C.M.K. *Experimental and Numerical Study of Rubber Intermixed Ballast System Subjected to Monotonic and Cyclic Loading*; University of Technology: Sydney, Australia, 2022.
23. Bian, X.; Jiang, H.; Cheng, C.; Chen, Y.; Chen, R.; Jiang, J. Full-scale model testing on a ballastless high-speed railway under simulated train moving loads. *Soil Dyn. Earthq. Eng.* **2014**, *66*, 368–384. [CrossRef]
24. Indraratna, B.; Hunt, H.; Malisetty, R.S.; Alagesan, S.; Qi, Y.; Rujikiatkamjorn, C. Optimization of inputs for the application of ANN to rail track granular materials. *Can. Geotech. J.* **2024**, *62*, 1–22. [CrossRef]
25. Godson, M.D.; Rajesh, B.G.; Kumar, P. Electric arc furnace slag—A prospective alternative for railway sub-ballast layer. *Constr. Build. Mater.* **2025**, *483*, 141702. [CrossRef]
26. Nasrollahi, K.; Dijkstra, J.; Nielsen, J.C.O. Towards real-time condition monitoring of a transition zone in a railway structure using fibre Bragg grating sensors. *Transp. Geotech.* **2024**, *44*, 101166. [CrossRef]
27. Chen, J.; Liu, Y.; Hu, Q.; Gao, R. Effects of particle size and grading on the breakage of railway ballast: Laboratory testing and numerical modeling. *Sustainability* **2023**, *15*, 16363. [CrossRef]
28. Li, W.; Bian, X.; Duan, X.; Tutumluer, E. Full-scale model testing on ballasted high-speed railway: Dynamic responses and accumulated settlements. *Transp. Res. Rec.* **2018**, *2672*, 125–135. [CrossRef]

29. Sayeed, M.A.; Shahin, M.A. Design of ballasted railway track foundations using numerical modelling. *Part I Development. Can. Geotech. J.* **2018**, *55*, 353–368. [CrossRef]
30. Edwards, J.R.; Gao, Z.; Wolf, H.E.; Dersch, M.S.; Qian, Y. Quantification of concrete railway sleeper bending moments using surface strain gauges. *Measurement* **2017**, *111*, 197–207. [CrossRef]
31. Lu, M.; McDowell, G.R. Discrete element modelling of railway ballast under monotonic and cyclic triaxial loading. *Géotechnique* **2010**, *60*, 459–467. [CrossRef]
32. Lim, W.L.; McDowell, G.R.; Collop, A.C. The application of Weibull statistics to the strength of railway ballast. *Granul. Matter* **2004**, *6*, 229–237. [CrossRef]
33. Li, D.; Selig, E.T. Method for railroad track foundation design. I: Development. *J. Geotech. Geoenviron. Eng.* **1998**, *124*, 316–322. [CrossRef]
34. Cundall, P.A.; Strack, O.D.L. A discrete numerical model for granular assemblies. *Géotechnique* **1979**, *29*, 47–65. [CrossRef]
35. *ASTM C136/C136M-19*; Standard Test Method for Sieve Analysis of Fine and Coarse Aggregates. ASTM International: West Conshohocken, PA, USA, 2019.
36. Indraratna, B.; Ionescu, D.; Christie, H.D. Shear behavior of railway ballast based on large-scale triaxial tests. *J. Geotech. Geoenviron. Eng.* **1998**, *124*, 439–449. [CrossRef]
37. Xiao, J.; Zhang, D.; Wei, K.; Luo, Z. Shakedown behaviors of railway ballast under cyclic loading. *Constr. Build. Mater.* **2017**, *155*, 1206–1214. [CrossRef]
38. Qian, Y.; Tutumluer, E.; Hashash, Y.M.; Ghaboussi, J. Triaxial testing of new and degraded ballast under dry and wet conditions. *Transp. Geotech.* **2022**, *34*, 100744. [CrossRef]
39. Delgado, B.G.; da Fonseca, A.V.; Fortunato, E.; Maia, P. Mechanical behavior of inert steel slag ballast for heavy haul rail track: Laboratory evaluation. *Transp. Geotech.* **2019**, *20*, 100243. [CrossRef]
40. Arachchige, C.M.; Indraratna, B.; Qi, Y.; Vinod, J.S.; Rujikiatkamjorn, C. Geotechnical characteristics of a rubber intermixed ballast system. *Acta Geotech.* **2022**, *17*, 1847–1858. [CrossRef]
41. Jiang, M.J.; Yu, H.S.; Harris, D. A novel discrete model for granular material incorporating rolling resistance. *Comput. Geotech.* **2005**, *32*, 340–357. [CrossRef]
42. Lu, M.M.G.R.; McDowell, G.R. The importance of modelling ballast particle shape in the discrete element method. *Granul. Matter* **2007**, *9*, 69–80. [CrossRef]
43. Li, L.; Liu, W.; Ma, M.; Jing, G.; Liu, W. Research on the dynamic behaviour of the railway ballast assembly subject to the low loading condition based on a tridimensional DEM-FDM coupled approach. *Constr. Build. Mater.* **2019**, *218*, 135–149. [CrossRef]
44. Xiao, Y.; Shen, Z.; Tan, P.; Hua, W.; Wang, M.; Jitsangiam, P. Evaluating enhancement effect of bottom groove shape on lateral resistance of frictional sleepers in ballasted railway track via hybrid DEM-FDM approach. *Constr. Build. Mater.* **2024**, *436*, 136755. [CrossRef]
45. Jiang, M.J.; Shen, Z.F.; Wang, J.F. A novel three-dimensional contact model for granulates incorporating rolling and twisting resistances. *Comput. Geotech.* **2015**, *65*, 147–163. [CrossRef]
46. Guo, Y.; Zhao, C.; Markine, V.; Jing, G.; Zhai, W. Calibration for discrete element modelling of railway ballast: A review. *Transp. Geotech.* **2020**, *23*, 100341. [CrossRef]
47. Coetzee, C.J. Calibration of the discrete element method. *Powder Technol.* **2017**, *310*, 104–142. [CrossRef]
48. Itasca Consulting Group. *PFC3D 6.0 Particle Flow Code in Three Dimensions, Theory and Implementation Volume*; Itasca Consulting Group: Minneapolis, MN, USA, 2016.
49. Ciantia, M.O.; Arroyo, M.; Calvetti, F.; Gens, A. An approach to enhance efficiency of DEM modelling of soils with crushable grains. *Géotechnique* **2015**, *65*, 91–110. [CrossRef]
50. Turcotte, D.L. Fractals and fragmentation. *J. Geophys. Res.* **1986**, *91*, 1921–1926. [CrossRef]
51. McDowell, G.R.; Bolton, M.D.; Robertson, D. The fractal crushing of granular materials. *J. Mech. Phys. Solids* **1996**, *44*, 2079–2101. [CrossRef]
52. Li, H.Q.; Mcdowell, G.R. Discrete element modelling of under sleeper pads using a box test. *Granul. Matter* **2018**, *20*, 26. [CrossRef]
53. Liu, F.; Wu, M.; Wang, H. Effect of particle size ratio and mix ratio on mechanical behavior of rubber-sand mixtures. *J. Eng. Geol.* **2019**, *27*, 376–389.
54. Wang, C.; Deng, A.; Taheri, A. Three-dimensional discrete element modeling of direct shear test for granular rubber–sand. *Comput. Geotech.* **2018**, *97*, 204–216. [CrossRef]
55. Perez, J.L.; Kwok, C.Y.; Senetakis, K. Micromechanical analyses of the effect of rubber size and content on sand-rubber mixtures at the critical state. *Geotext. Geomembr.* **2017**, *45*, 81–97. [CrossRef]
56. Perez, J.L.; Kwok, C.Y.; Senetakis, K. Effect of rubber size on the behaviour of sand-rubber mixtures: A numerical investigation. *Comput. Geotech.* **2016**, *80*, 199–214. [CrossRef]

57. Gong, L.; Nie, L.; Xu, Y.; Wang, H.; Zhang, T.; Du, C.; Wang, Y. Discrete element modelling of the mechanical behaviour of a sand-rubber mixture containing large rubber particles. *Constr. Build. Mater.* **2019**, *205*, 574–585. [CrossRef]
58. Guo, Y.; Ji, Y.; Zhou, Q.; Markine, V.; Jing, G. Discrete element modelling of rubber-protected ballast performance subjected to direct shear test and cyclic loading. *Sustainability* **2020**, *12*, 2836. [CrossRef]
59. Wu, H.; Zhu, L.; Song, W.; Xu, Z.; Xu, F.; Gong, H. Impact performance of ballast by incorporating waste tire-derived aggregates. *Constr. Build. Mater.* **2021**, *288*, 122992. [CrossRef]
60. Zhang, F.; Yao, Q.; Wang, H.; Feng, H.; Chang, J.; Lu, L.; Jiang, M. DEM analysis of the cyclic behavior of ballast mixed with crumb rubber. *Constr. Build. Mater.* **2023**, *375*, 130975. [CrossRef]
61. Ngo, T.; Indraratna, B.; Coop, M.; Qi, Y. Behaviour of ballast stabilised with recycled rubber mat under impact loading. *Géotechnique* **2023**, *75*, 192–212. [CrossRef]
62. Tran, V.D.; Meguid, M.A.; Chouinard, L.E. Discrete element and experimental investigations of the earth pressure distribution on cylindrical shafts. *Int. J. Geomech.* **2014**, *14*, 80–91. [CrossRef]
63. AREMA. American Railway Engineering and Maintenance-of-Way Association. *Man. Railw. Eng.* **2013**, *2*, 55–57.
64. Mosayebi, S.A.; Zakeri, J.A.; Esmaeili, M. Some aspects of support stiffness effects on dynamic ballasted railway tracks. *Period. Polytech. Civ. Eng.* **2016**, *60*, 427–436. [CrossRef]
65. Chen, J.; Vinod, J.S.; Indraratna, B.; Ngo, T.; Liu, Y. DEM study on the dynamic responses of a ballasted track under moving loading. *Comput. Geotech.* **2023**, *153*, 105105. [CrossRef]

Disclaimer/Publisher's Note: The statements, opinions and data contained in all publications are solely those of the individual author(s) and contributor(s) and not of MDPI and/or the editor(s). MDPI and/or the editor(s) disclaim responsibility for any injury to people or property resulting from any ideas, methods, instructions or products referred to in the content.

applied sciences

MDPI

Article

Preparation of Ecological Refractory Bricks from Phosphate Washing By-Products

Mariem Hassen [1], Raja Zmemla [2], Mouhamadou Amar [3,*], Abdalla Gaboussa [4], Nordine Abriak [3] and Ali Sdiri [1]

[1] Geomaterials, Structures, Civil Engineering and Environment, National School of Engineers of Sfax (ENIS), Sfax 3052, Tunisia; hassenmariem93@gmail.com (M.H.); ali.sdiri@enis.tn (A.S.)
[2] Laboratory of Environmental Engineering and Ecotechnology, National School of Engineers of Sfax (ENIS), Sfax 3052, Tunisia; tunisiazmemla@yahoo.fr
[3] Civil and Environmental Engineering Department, Civil and Geo-Environmental Engineering Laboratory, IMT Nord Europe, 59000 Lille, France; nor-edine.abriak@imt-nord-europe.fr
[4] Higher Institute of Technological Studies, Gafsa 2112, Tunisia; gaboussaabdallah@gmail.com
* Correspondence: mouhamadou.amar@imt-nord-europe.fr

Abstract: This research is to assess the potential use of phosphate sludge from the Gafsa (Tunisia) phosphate laundries as an alternative raw material for the manufacture of ecological refractory bricks. Feasibility was evaluated through comprehensive physico-chemical and mineralogical characterizations of the raw materials using X-ray diffraction (XRD), X-ray fluorescence (XRF), Fourier-transform infrared spectroscopy (FTIR), and thermal analysis (TGA-DTA). Bricks were formulated by substituting phosphate sludge with clay and diatomite, then activated with potassium silicate solution to produce geopolymeric materials. Specific formulations exhibited mechanical performance ranging from 7 MPa to 26 MPa, highlighting the importance of composition and minimal water absorption values of approximately 17.8% and 7.7%. The thermal conductivity of the bricks was found to be dependent on the proportions of diatomite and clay, reflecting their insulating potential. XRD analysis indicated the formation of an amorphous aluminosilicate matrix, while FTIR spectra confirmed the development of new chemical bonds characteristic of geopolymerization. Thermal analysis revealed good stability of the materials, with mass losses mainly related to dehydration and dehydroxylation processes. Environmental assessments showed that most samples are inert or non-hazardous, though attention is required for those with elevated chromium content. Overall, these findings highlight the viability of incorporating phosphate sludge into fired brick production, offering a sustainable solution for waste valorization in accordance with the circular economy.

Keywords: phosphate sludge; characterization; mining by-products; valorization; fired bricks; geopolymerization

1. Introduction

Phosphate mines generate millions of tons of waste rock in open-pit mining [1]. Furthermore, during phosphate ore processing, fluorapatite is separated from associated gangue minerals through a combination of successive mineral processing steps, including crushing/sieving, washing, and flotation. These operations produce large volumes of phosphate—a mixture of water and fine mineral particles—which are discharged into large surface ponds. Over time, the solids in the mix settle and form phosphate tailings,

while waste rock is dumped into the mine. In general, the mining industry is facing many environmental challenges resulting from the huge quantities of waste that mines engender, such as waste rocks, concentrator tailings, and phosphate sludge (fine-grained waste material generated during phosphate ore washing and beneficiation processes). These wastes are deposited or stockpiled within the mine site and constitute a potential source of pollution because of their chemical characteristics and grain size [2].

Tunisia, with its large phosphate reserves, is the fifth-largest producer of phosphates in the world, which have been mined for more than a century. Nationwide phosphate reserves are estimated at 325 billion tons. These phosphates are transformed into fertilizers for agriculture. The main phosphate deposits are divided into three areas: the northern phosphate area (Srâa El-Ouertane and Kalaâ-Khasba), the phosphate area of the center (Chérahil, Maknassy), and the phosphate area of the south (Gafsa). These three areas represent one of the most important phosphate complexes in the world. Thus, the Tunisian phosphate sector, represented by the Phosphates Company of Gafsa (CPG) and its subsidiary GCT (Tunisian Chemical Group), has stopped growing even representing a large part of the economic activity of Tunisia, 4.5% of GDP [3]. Tunisian natural phosphate is a rock formed approximately 50 million years ago (Eocene), characterized by a beige color, a sandy texture, and a soft consistency, with high porosity. Its microcrystalline structure is composed of carbonated fluorapatite.

This intense mining activity related to natural phosphate beneficiation generates large amounts of sludge. In Tunisia, for instance, 11 million metric tons per year of phosphate sludge were deposited in 2011 [3]. However, this activity, like any mining activity, generates environmental damages related to dust, wastewater, and atmospheric emissions from ore processing plants, which are not without consequences for water resources, wildlife, flora, and human health: air pollution, water, and soil pollution; chronic diseases; and degradation of the vegetation cover and wildlife habitat area [2]. Recently, with the growing environmental awareness and regulatory incentives, mining companies are looking for sustainable and feasible solutions to minimize the high amounts of waste. Consequently, many promising eco-friendly solutions have been established by numerous researchers [4]. Nowadays, several industrial and mining wastes have been studied for their potential use as alternative materials. Although the mining industry still considers most of its waste as materials without any value, recent trends favored by incentive legislation show that the potential mine waste reuse could be beneficial in many cases, especially when they are proven not to be acid-generating. Building materials are supposed to be the utmost efficient way to consume these substantial amounts of waste generated every day [4]. Therefore, the recycling of mining waste as raw materials for the construction industry allows the reduction of the quantity of this waste and also the preservation of natural resources [5].

For Obenaus-Emler et al. [6], alkali-activated materials can be made from mine tailings, geopolymers [7], or in the preparation of concrete blocks using purified tailings [8]. More recently, Boutaleb et al. [9,10] demonstrated that phosphate mine tailings improve the mechanical properties of ceramic tiles. They used industrial mine tailings at a rate of 33% in formulas based on local clays for ceramic material manufacturing. Bricks with up to 30% phosphate sludge exhibited acceptable mechanical properties, meeting industry standards. Environmentally, incorporating sludge reduced clay consumption and waste generation. At the same time, it increased open porosity and water absorption; for example, using 50% sludge resulted in 52% porosity and 32% water absorption [11]. For Inabi et al. [12], the bricks manufactured using phosphate washing sludge exhibit robust mechanical performance, low embodied energy, excellent insulation, and thermal properties. Additionally, it was demonstrated that bricks manufactured with 2.5% phosphate sludge demonstrated

approved compressive strength and met environmental standards, classified as non-inert materials [13]. Valorization of tailings (the process of converting waste materials into valuable products or resources) could be a promising alternative not only to reduce their potential environmental impacts but also to create a path for an eco-commercial profit by making a good business opportunity.

Given the significant environmental challenges posed by the accumulation of phosphate washing by-products in the Gafsa-Métlaoui region, this research aims to explore a sustainable pathway for their valorization through the development of ecological refractory bricks. By systematically characterizing the physical, chemical, and mineralogical properties of local phosphate sludge and evaluating its performance as a primary precursor, alone and in combination with natural clay and diatomite, this study investigates the feasibility of producing high-quality geopolymer bricks activated with potassium silicate. The resulting materials are rigorously assessed for mechanical strength, water absorption, thermal conductivity, and environmental safety to ensure compliance with construction standards. Ultimately, this approach offers a promising solution for transforming mining waste into value-added construction materials, aligning with circular economy principles and contributing to both environmental protection and resource efficiency in the region.

Although extensive research has addressed the reuse of phosphate by-products in construction materials, most previous studies have been limited by relatively low substitution rates—typically between 30% and 50%—due to concerns over mechanical strength, increased porosity, and water absorption. For example, while some works have demonstrated that moderate additions of phosphate sludge or tailings can improve certain properties of bricks or ceramics, higher incorporation rates often result in products that do not meet industry standards for durability and performance. Furthermore, the majority of these studies have focused on traditional fired ceramics, which require significant energy input and contribute to the overall environmental footprint of the material. These limitations highlight the need for alternative approaches that can both maximize waste valorization and minimize environmental impact.

In this context, our research seeks to overcome these challenges by investigating the use of up to 100% phosphate washing sludge in geopolymer brick formulations activated with potassium silicate, entirely avoiding high-temperature firing. This strategy aims to enhance waste utilization, reduce energy consumption, and provide a more sustainable pathway for the production of high-performance, eco-friendly refractory bricks.

2. Mining Site

In Tunisia, the GPG oversees the processing of phosphate ores in ten washing stations, each discharging approximately 284,000 m^3 of sludge into the rivers of the Gafsa region [5]. To optimize water recovery and reduce the volume of sludge for disposal, the GPG has implemented underground pipelines to transfer sludge from the washing stations to storage basins. By 2001, the accumulated sludge in these basins exceeded 11 million m^3, with over 90% not reaching the residue basins but being dispersed outside through an artificial river system. Between 1998 and 2011, around 2.5 million tons of sludge were annually discharged into the Thelja, Sebseb, and El Malah rivers [3].

Our study area is located in the Gafsa mining basin, a region highly impacted by phosphate mining activities. This basin encompasses several key sites critical to understanding the environmental effects of mining sludge disposal. Specifically, we focused on three sampling zones (Figure 1): Métlaoui (also known as Thelja), the first city in the basin and a central hub for mining operations; Redeyef, another major mining town within the basin;

and Oued Etfal, situated approximately 20 km from Gafsa along the regional road R201 connecting Gafsa to Moulares.

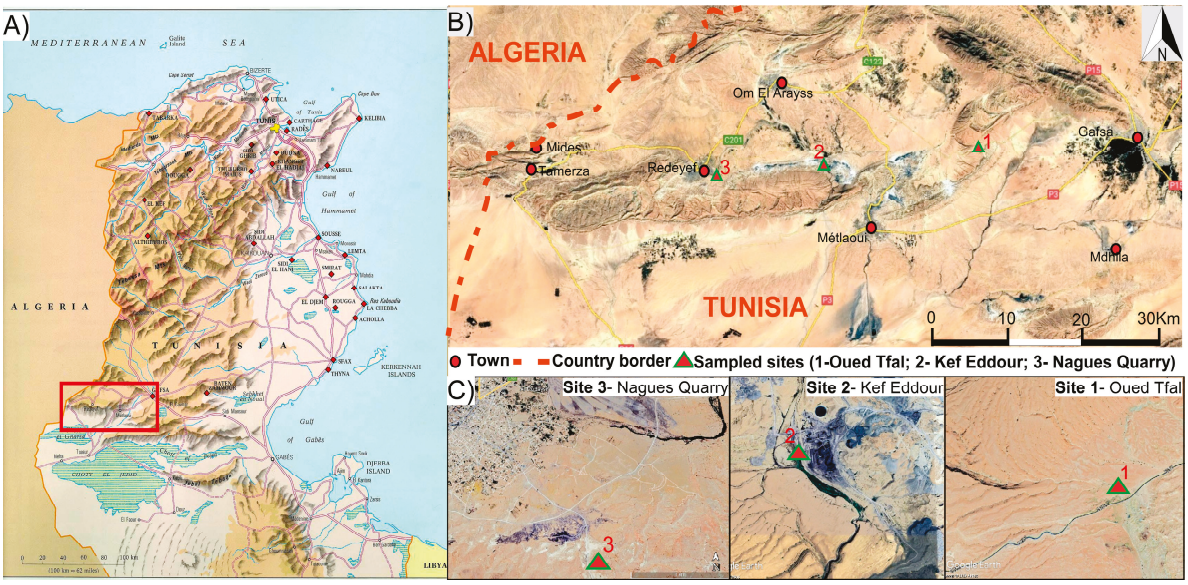

Figure 1. Geographic location of the sampling sites in the Gafsa mining basin: (**A**) general location of the Gafsa mining basin on the relief map of Tunisia (in red); (**B**) satellite view of the entire basin showing the location of the sampling sites; (**C**) high-resolution satellite images of each site showing the positions of phosphate washing sludge, clay, and diatomite samples.

3. Materials and Methods

3.1. Materials Used

Sludge samples were collected from washing station 2 in Métlaoui Gafsa, after the flocculation process to characterize these by-products in the context of our ongoing study.

The materials employed in this study encompassed a selection of constituents: phosphate waste sludge (PWS), natural clay from Oued Tfal near Gafsa (20 km from Gafsa), diatomite from the Nagues quarry in Redeyef, corresponding to the interlayer between layers 6 and 7 of the phosphate series, and alkaline silicate (ALK) (with the product name Geosil). The phosphate sludge, sourced from industrial waste, served as a key precursor after calcination at 850 °C. The kaolinic clay underwent thermal transformation at 700 °C; this temperature was specifically selected based on literature and preliminary tests, as it is optimal for converting kaolinite into highly reactive metakaolin. Calcining at 700 °C ensures complete dehydroxylation of kaolinite, maximizing the availability of amorphous aluminosilicates necessary for geopolymerization, while avoiding excessive energy use or the formation of less reactive crystalline phases.

Geopolymerization refers to the chemical process in which aluminosilicate materials, such as metakaolin and calcined phosphate sludge, react with alkaline activators (here, potassium silicate) to form a three-dimensional amorphous aluminosilicate network. This reaction results in the formation of inorganic polymers known as geopolymers, which are characterized by their durable, cross-linked aluminosilicate structures and excellent mechanical and thermal properties.

Diatomite was calcined at 750 °C to enhance its reactivity and stability. Potassium silicate was employed to initiate geopolymerization, while ensuring the formation of a durable aluminosilicate matrix. This combination of materials aimed to produce sustainable refractory bricks with improved mechanical and thermal properties.

3.2. Mix Proportioning

The use of washing phosphate sludge (WPS), kaolinitic clay (KC), and diatomite (D) as precursors in alkali-activated geopolymer binders promotes sustainable construction practices by repurposing industrial and mining waste. These materials are abundantly available in regions such as Gafsa, Tunisia, where phosphate mining generates significant sludge by-products, while (KC) and (D) are locally sourced natural minerals. Previous studies have limited WPS substitution in refractory materials to 50% due to its lower reactivity [7,14,15]. However, this research expands the substitution range from 50% to 100% to optimize waste valorization. The formulations GBM (PS + KC), GBD (WPS + D), and GBDM (WPS + KC + D) (Figure 2) were designed using potassium silicate (K_2SiO_3) as the alkaline activator to initiate the geopolymerization reaction between the calcined phosphate sludge, clay, and diatomite. Its role is to dissolve aluminosilicate species from the precursors and promote the formation of a stable amorphous geopolymer matrix, which enhances the mechanical strength and durability of the resulting bricks, with its concentration fixed to 15% of the binder weight, as derived from preliminary trials and literature.

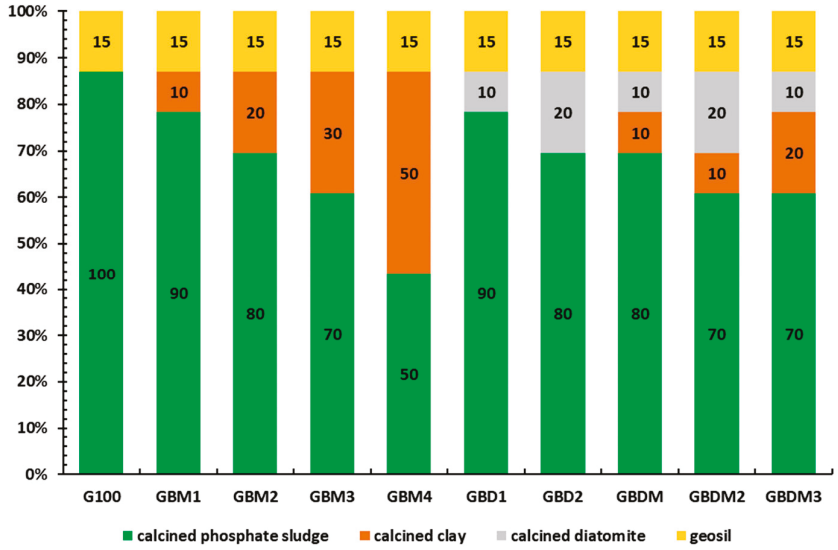

Figure 2. Schematic representation of the brick formulations used in this study. Each formulation combines varying proportions of calcined phosphate sludge (WPS), kaolinitic clay (KC), and diatomite (D), with potassium silicate solution (15% of binder weight) as the alkali activator. The percentages shown reflect the mass ratio of each precursor in the mix.

3.3. Mix Preparation Protocol

The refractory geopolymer bricks were formulated by combining washing phosphate sludge, kaolinitic clay, and diatomite in varying proportions, following a systematic mixing protocol adapted to ensure optimal homogeneity and performance. The preparation process consisted of several structured steps. First, the raw materials were weighed, and the dry components (PS, KC, and D) were mixed for 5 min to achieve a uniform blend. Subsequently, the potassium silicate solution was gradually added over 10 min while maintaining continuous mixing to ensure even distribution and activation of the binders.

The fresh geopolymer bricks were then poured into cylindrical molds (Ø50 mm × 50 mm) for compressive strength testing. This geometry, recommended by the NF EN 196-1 standard and supported by Mkaouar [16], ensures reliable and comparable mechanical results. Although the material is referred to as "brick," cylindrical samples are commonly used in geopolymer research for standardized testing. Each sample was compacted using

a uniaxial pressing force of 10 MPa to enhance density and reduce porosity. The molds were then sealed to prevent moisture loss and cured at ambient temperature (22 ± 2 °C) for 72 h, allowing the geopolymerization process to proceed. After curing, the bricks were demolded and oven-dried at 105 °C for 24 h to remove residual moisture and further improve mechanical properties Figure 3. The composite combines anatase-phase TiO_2 with calcite-phase $CaCO_3$, preserving their individual crystal structures. XRD analysis confirms successful integration without phase transformation. $CaCO_3$ reduces TiO_2 agglomeration, enhancing photocatalytic surface area and stability [17].

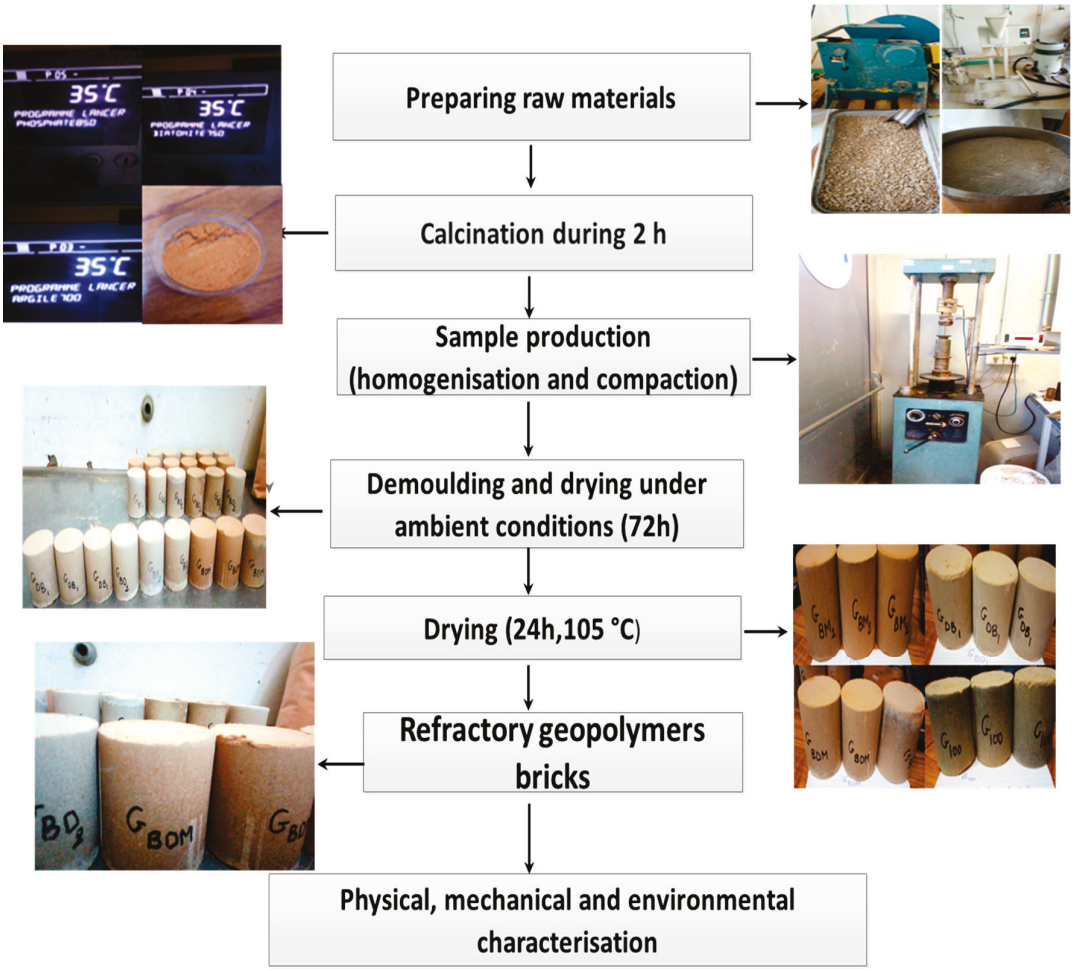

Figure 3. Simplified diagram illustrating the making of refractory geopolymers bricks.

This meticulous procedure ensured consistent mixing, compaction, and curing, which are critical factors in evaluating the structural integrity and durability of geopolymer-based refractory bricks.

3.4. Experimental Methods

3.4.1. Material Characterization

The raw materials were characterized using various analytical techniques to determine their chemical and physical properties. The analyses included the following.

Loss on ignition (LOI) was determined in accordance with NF EN 15169, in order to evaluate the volatile matter content using a static furnace heated at 550 °C. The particle size distribution (PSD) was assessed following NF EN 933-10, providing insights into the granulometric profile of the samples. The = apparatus used is a LS13320 model.

Phase identification and structural analysis were carried out using the following techniques:

(a) X-ray diffraction (XRD) analysis was conducted with a Bruker D2 diffractometer (Bruker Corporation, Billerica, MA, USA) using Cu-Kα radiation (λ = 1.5406 Å), in accordance with NF EN 13925-1 and NF EN 13925-2.

(b) Fourier-transform infrared spectroscopy (FTIR) was performed using a Thermo Scientific Nicolet iS20 spectrometer (Thermo Fisher Scientific, Waltham, MA, USA), based on the methodology outlined in NF ISO 4650.

These analyses provided detailed insights into the mineralogical composition and microstructure of the raw materials and resulting brick specimens.

3.4.2. Mechanical Testing

Compressive strength tests were conducted on cylindrical specimens (Ø50 mm × 50 mm) using an INSTRON 5500 R universal testing machine (Instron, Norwood, MA, USA), following the NF EN 196-1 standard. For each brick formulation, three replicate specimens were tested to ensure reproducibility. Additional mechanical tests were also performed on fired bodies to evaluate the influence of thermal treatment.

3.4.3. Method for Measuring Water Absorption

Water absorption (W_s)was measured in accordance with the NF P51-302 standard. Three brick specimens per formulation were dried to constant mass (M_d), cooled to room temperature (20 °C), and immersed in water for 24 h. After immersion, excess surface water was removed, and the wet mass (M_s) was recorded. The water absorption was calculated as (Equation (1)):

$$W_S(\%) = \frac{M_S - M_d}{M_d} \times 100 \quad (1)$$

3.4.4. Thermal Conductivity Measurement Procedure

Thermal conductivity measurements were carried out using the transient plane source (TPS) method with a hot disk apparatus. A resistive sensor functioning as a planar heat source was positioned between two identical pellets. The temperature rise resulting from heat dissipation was monitored and analyzed using the Hot Disk Thermal Constants Analyser software version 7.6.15 to calculate thermal conductivity. The measurement is based on Fourier's law of thermal conduction (Equation (2)):

$$q(r,t) = -k\Delta T(r,t) \quad (2)$$

where q represents the heat flux density, k the thermal conductivity, and $\Delta T(r,t)$ the temperature gradient.

3.4.5. Thermogravimetric Analysis (TGA)

Thermogravimetric analysis was performed using a NETZSCH STA 409 instrument (NETZSCH Group, Selb, Germany) under a nitrogen atmosphere. The heating program involved a constant rate of 10 °C/min, from 40 to 1000 °C. This test provided information on the thermal stability and decomposition behavior of the samples.

3.4.6. Chemical and Environmental Analysis

For environmental assessment, all samples were ground to a fine powder and then subjected to a leaching test. The powdered samples were agitated in distilled water for 24 h in accordance with the standard protocol. After agitation, the resulting solutions were

filtered prior to analysis. Trace element concentrations were determined by inductively coupled plasma atomic emission spectrometry (ICP-AES), for which 2% nitric acid was added to the filtrates to stabilize dissolved metals and prevent any precipitation or adsorption on the container walls before measurement. In contrast, for ion chromatography (IC), the filtered solutions were analyzed directly—without acid addition—in accordance with best practices for anion determination (chlorides, sulfates, fluorides, etc.), in order to avoid altering ion speciation. The concentrations of water-soluble ions such as sulfate, chloride, and fluoride were thereby quantified by IC. The environmental behavior of the geopolymer bricks was thus assessed via leaching tests and subsequent analyses, following protocols designed to ensure the reliability and reproducibility of results for both cationic and anionic species.

3.4.7. Durability Assessment

The durability of the bricks was evaluated using an efflorescence test, following the NF EN 772-5 standard. This test assessed the potential for the formation of surface crystalline deposits resulting from the migration of soluble salts.

3.4.8. Experimental Protocol

All tests were carried out at the IMT Nord Europe Center for Education, Innovation and Research. Unless otherwise stated, six specimens were prepared and tested for each formulation, in compliance with the relevant technical standards for mechanical, thermal, and physical characterization.

4. Results and Discussion

4.1. Raw Material Characterization

4.1.1. Physical Characterization

The sludges from the Gafsa phosphate washery exhibit distinct granulometric characteristics, with over 90% of particles being smaller than 200 μm (Table 1). Detailed analysis reveals a bright sandy texture, without the presence of particles exceeding 90 μm, indicating an absence of clay components. The particle size distribution, characterized by a conformity coefficient of 5 and a uniformity coefficient of 1.58, suggests marked heterogeneity in the soil composition but also a relative uniformity in particle sizes within the sample. These findings underscore the need for careful management of phosphate sludges to minimize their potential environmental impact. The density of the sludge was 2.85 g/cm^3 and the loss on ignition was 6.23%.

Table 1. Physical characteristics of sludge.

Particle Diameter (μm)	Diameter	Volume %
D10	10	1.2
D25	25	6.0
D50	50	42.7
D75	75	136.7
D90	90	178.4
Bulk Density (γ_s)		2.85 g/cm^3
Loss on Ignition (W_LOI)		6.23%
Water Demand (D_water)		0.243%

4.1.2. Mineralogical Characterization

Raw Materials

X-ray diffraction (XRD) analysis was conducted to determine the mineralogical composition of the raw materials used in this study, revealing that the phosphate sludge (Figure 4) primarily consists of apatite (fluorapatite $Ca_{10}(PO_4)_6F_2$ or carbonated apatite) as the predominant crystalline phase, with minor components of calcite ($CaCO_3$), quartz (SiO_2), and clay minerals, consistent with previous research [5,18], with the XRD patterns suggesting that the clay, calcite, and quartz phases are predominantly associated with the exogangue components of the sludge, while their interference with the fluorapatite peaks may stem from their presence as endogangue constituents; the XRD patterns for the raw natural clay (Figure 4) reveal a complex mineralogical composition, confirming its heterogeneous nature and detecting minerals such as illite, kaolinite, hematite, dolomite, quartz, and calcite, consistent with findings by Bouaziz in a similar natural clay mineralogy study [19]. The XRD spectra for raw diatomite (Figure 4) reveal its composition primarily consists of amorphous silica (SiO_2) phases, along with crystalline quartz and calcium carbonate (calcite and dolomite), also identifying trace amounts of clay minerals and feldspars (albite, orthoclase).

Effect of Thermal Treatment on Raw Materials

Thermal treatment of raw materials induced notable changes in their mineralogical compositions. For phosphate sludge, calcination led to sharper XRD peaks, indicating improved apatite crystallinity, and the disappearance of calcite peaks, signaling its thermal decomposition into calcium oxide, while quartz remained stable (Figure 4). In natural clay, calcination transformed kaolinite into amorphous metakaolinite, evidenced by a broad peak at 27.9° 2θ, with illite, hematite, and quartz peaks persisting (Figure 4). Finally, calcination of diatomite promoted partial recrystallization, reduced clay impurities and calcite peaks, and caused structural rearrangements evident in cristobalite and quartz peak variations (Figures 5 and 6).

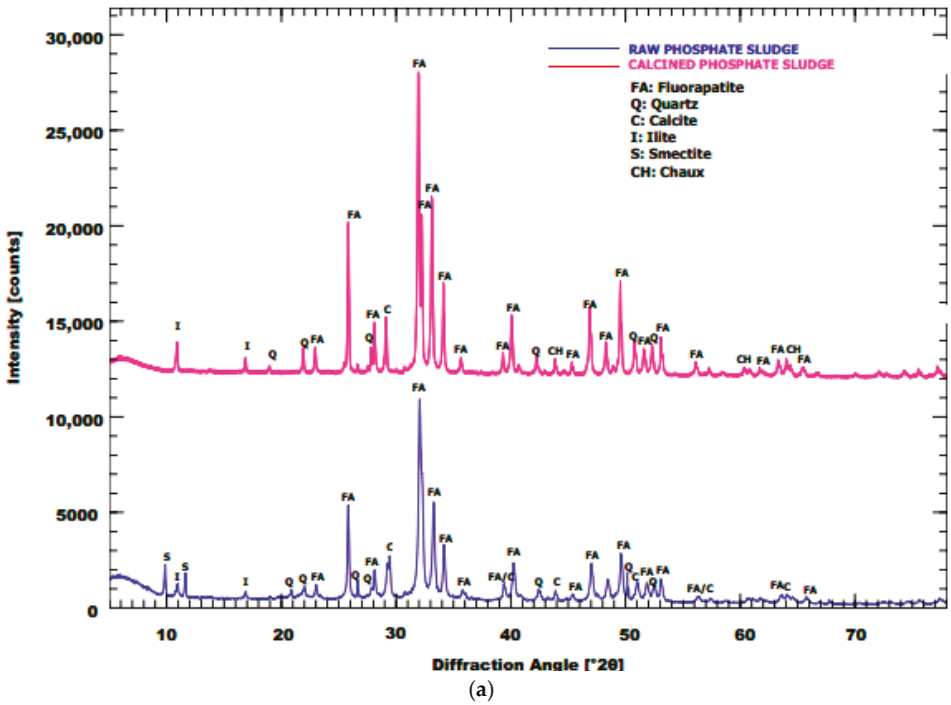

(a)

Figure 4. *Cont.*

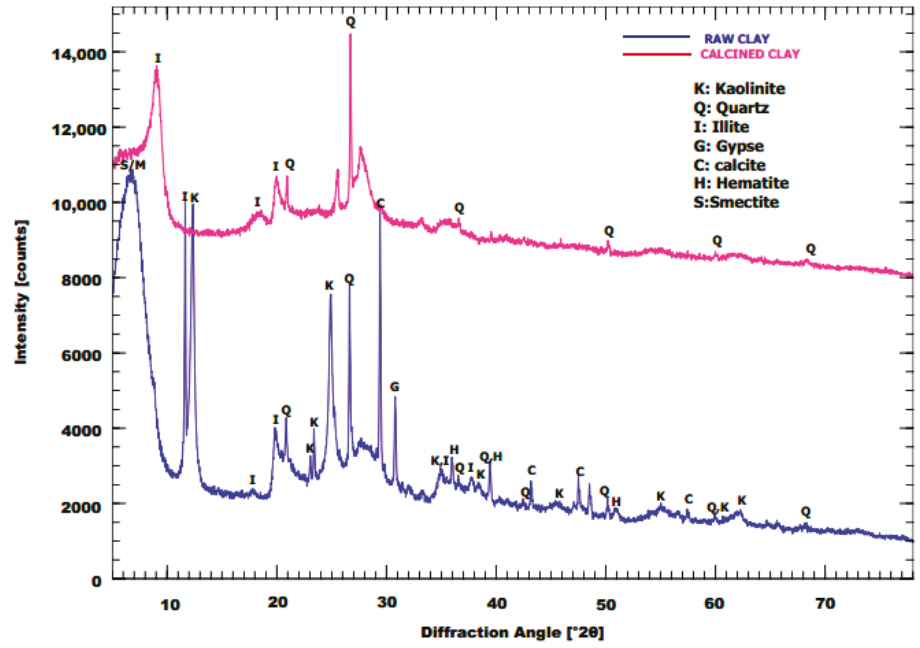

(**b**)

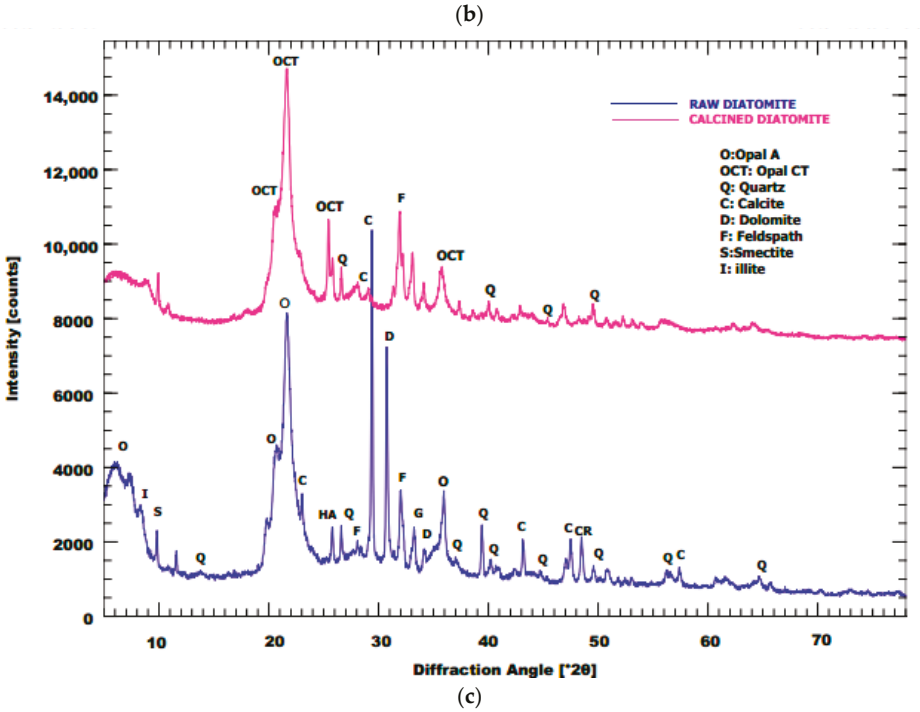

(**c**)

Figure 4. X-ray diffraction (XRD) patterns of the raw and calcined materials used as precursors for geopolymer brick synthesis: phosphate washing sludge (WPS) (**a**), kaolinitic clay (KC) (**b**), and diatomite (D) (**c**). Patterns were recorded at room temperature on finely ground powders. Major peaks are labeled to identify the crystalline phases present in the raw materials (such as quartz, kaolinite, calcite, and cristobalite) and to highlight the mineralogical transformations occurring after calcination (e.g., dehydroxylation of kaolinite to metakaolin, increased amorphous content). These results confirm the effectiveness of the calcination process in enhancing precursor reactivity for subsequent geopolymerization.

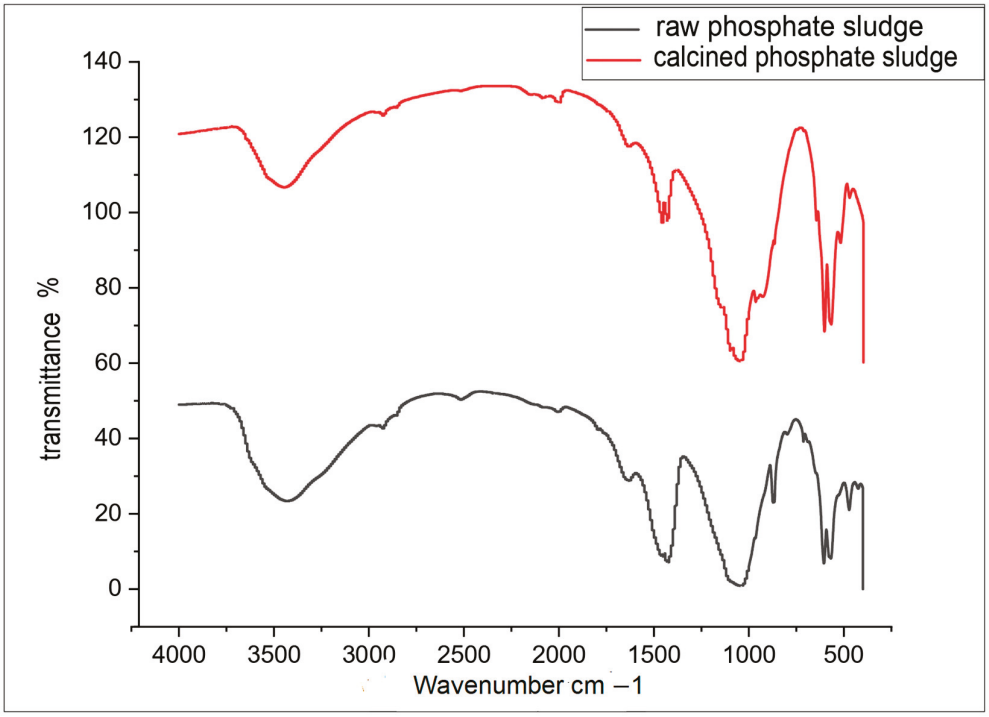

(a)

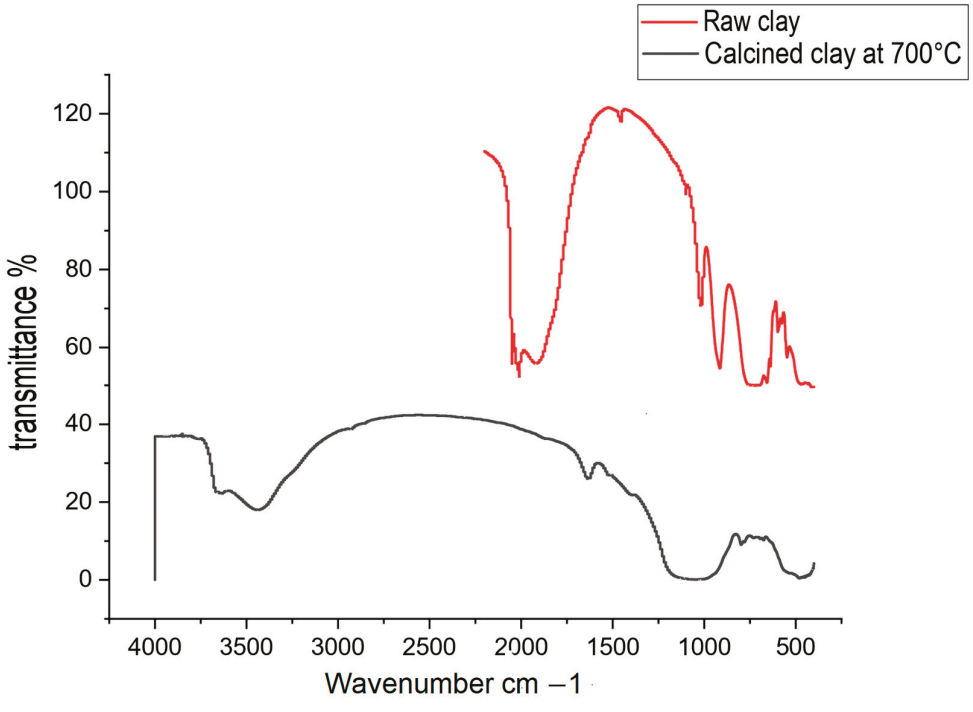

(b)

Figure 5. *Cont.*

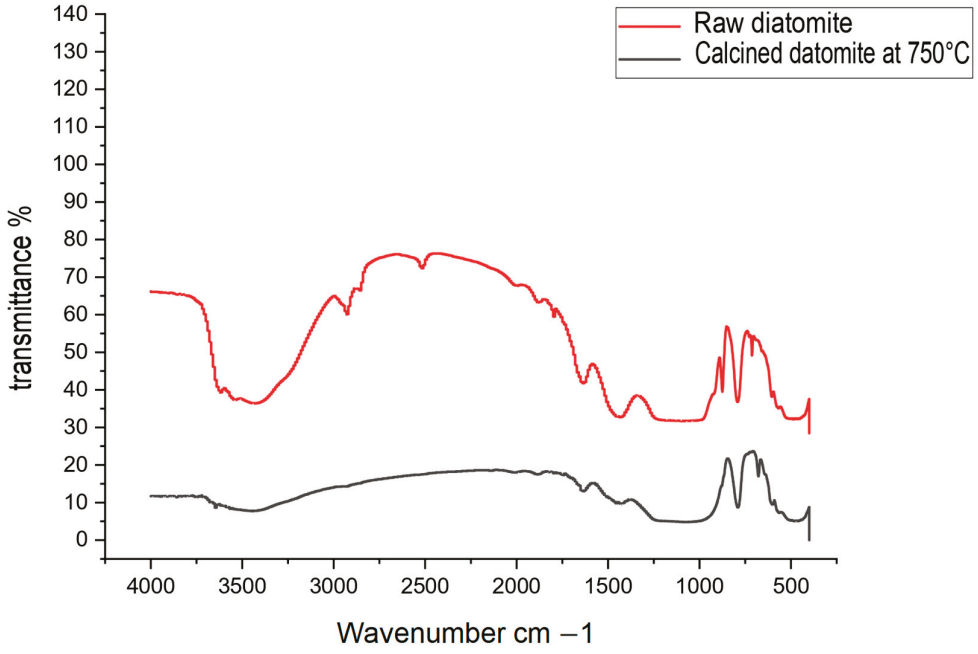

(**c**)

Figure 5. Fourier-transform infrared (FTIR) spectra of the raw and calcined materials used as precursors for geopolymer brick formulation: phosphate washing sludge (WPS) (**a**), kaolinitic clay (KC) (**b**), and diatomite (D) (**c**). Spectra were recorded in the 4000–400 cm^{-1} range at room temperature. The main absorption bands are assigned to functional groups such as Si–O–Si, Al–O, and CO_3^{2-}, characteristic of the mineral phases present. The comparison between raw and calcined materials highlights the structural changes induced by thermal activation, such as the dehydroxylation of kaolinite and the modification of silicate and carbonate bands, which enhance the reactivity of the precursors for subsequent geopolymerization.

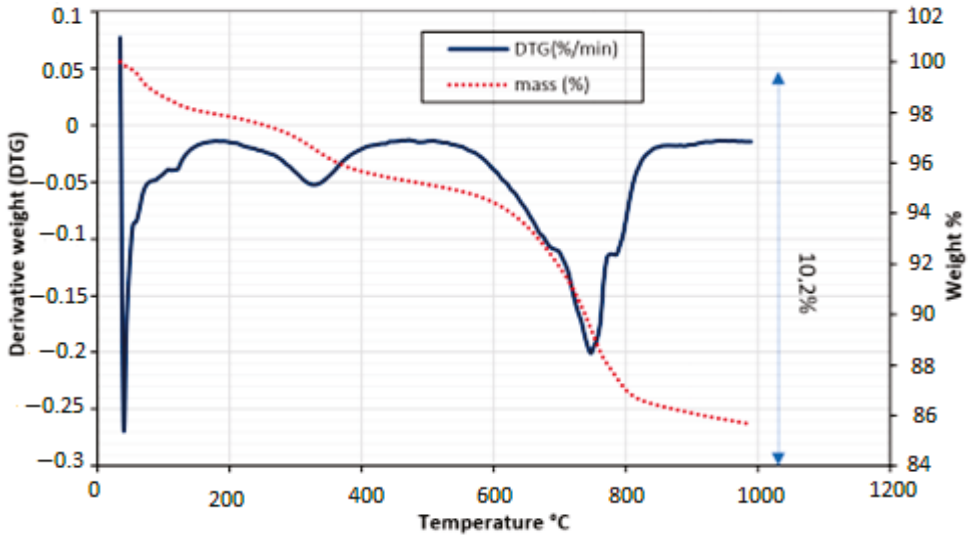

Figure 6. Thermogravimetric analysis (TGA) curve of phosphate washing sludge (WPS) recorded under nitrogen atmosphere from room temperature up to 1000 °C. The mass loss below 200 °C corresponds mainly to moisture evaporation. A significant weight loss observed between 600 and 900 °C is attributed to the decomposition of organic matter and carbonates present in the sludge. The overall mass loss reaches approximately 9%, indicating the thermal stability and decomposition behavior of the phosphate sludge prior to its use in geopolymer formulations.

4.1.3. Fourier-Transform Infrared (FTIR) Spectroscopy

Fourier-transform infrared was employed to reveal key functional groups and the impact of thermal treatment. The FTIR spectrum of raw phosphate sludge exhibited a broad absorption band between 3000 and 3600 cm^{-1}. That is indicative of significant water content, with the region between 1000 and 1200 cm^{-1} suggesting the presence of phosphate groups (PO_4^{3-}) and 1400–1600 cm^{-1} hinting at carbonates or organic matter. After calcination, the water band diminished, and phosphate groups became more defined (Figure 5). Similarly, FTIR analysis of raw clay from Oued Tfal showed a broad band in the 3700–3000 cm^{-1} region, characteristic of O-H stretching vibrations from water and hydroxyl groups within clay minerals, consistent with [19]. This band attenuated after calcination, while Si–O–Si bands initially located between 1000 and 1100 cm^{-1} transformed into a wider, less defined band. The bands associated with kaolinite, such as the Si–O–Al vibration below 800 cm^{-1} (notably around 750 cm^{-1}) and Al-OH (915 cm^{-1}), disappeared, in agreement with Louati et al. [20], indicating dehydroxylation and the disruption of the silicate network. Finally, FTIR spectra of diatomite before calcination displayed a broad, intense band around 3400 cm^{-1}, attributed to O-H stretching vibrations from adsorbed water and silanol groups (Si-OH), and a peak at 1630 cm^{-1} corresponding to water bending; after calcination at 750°C, these bands nearly vanished, indicating the elimination of adsorbed and structural water, while the bands at 1000–1200 cm^{-1}, 800 cm^{-1}, and 460 cm^{-1} representing Si–O–Si stretching and bending vibrations. Zheng et al. [21] showed that the band at 800 cm^{-1} became narrower and more continuous, suggesting an improved silica crystallinity, although the overall silica network structure was retained, aligning with the XRD results.

4.1.4. Thermogravimetric Test

Phosphate Sludge

The TGA of phosphate sludge reveals three main stages of mass loss visible in Figure 6:

- 200 °C to 400 °C: 7.4% loss, attributed to the decomposition of organic matter. This is due to thermolyzing organic compounds in the sludge, such as proteins, lipids, and carbohydrates.
- 400 °C to 600 °C: 1.3% loss, attributed to the decarbonation of calcite. This occurs through dehydration, transforming fluorapatite into hydroxyapatite.
- 600 °C to 800 °C: 1.5% loss, associated with calcite decomposition. This stems from the thermal breakdown of calcite into calcium oxide.

The stability of fluorapatite up to temperatures above 1000 °C is consistent with both our results and the literature. These attributions are further corroborated by XRD and FTIR analyses, which show the disappearance of calcite and organic matter signatures after thermal treatment.

The total mass loss of 10.2% indicates a significant organic content in the phosphate sludge.

An interpretation based on the mineral composition is: 74% organic matter: decomposes between 200 °C and 400 °C; 13% fluorapatite: decomposes between 400 °C and 600 °C; and 15% calcite: decomposes between 600 °C and 800 °C.

Natural Clay

The TG/DTG analysis reveals a thermal decomposition of the natural clay in several stages (Figure 7). Initially, a slight mass loss is observed up to approximately 200 °C, likely due to the desorption of water or residual solvents from the material's surface. The most significant mass loss occurs between 400 °C and 600 °C, with a major peak on the DTG curve around 500 °C (Figure 7). This mass loss corresponds to the dehydroxylation of kaolinite

and the formation of metakaolin. The initial mass loss below 200 °C can be attributed to the loss of water adsorbed by smectite and/or gypsum, while the slower mass loss above 600 °C could correspond to the decomposition of carbonates (calcite) or structural transformations of other mineral phases present. The total mass loss observed over the entire temperature range is approximately 12%, reflecting the total amount of volatile materials or decomposable compounds, including water released during the transformation into metakaolin.

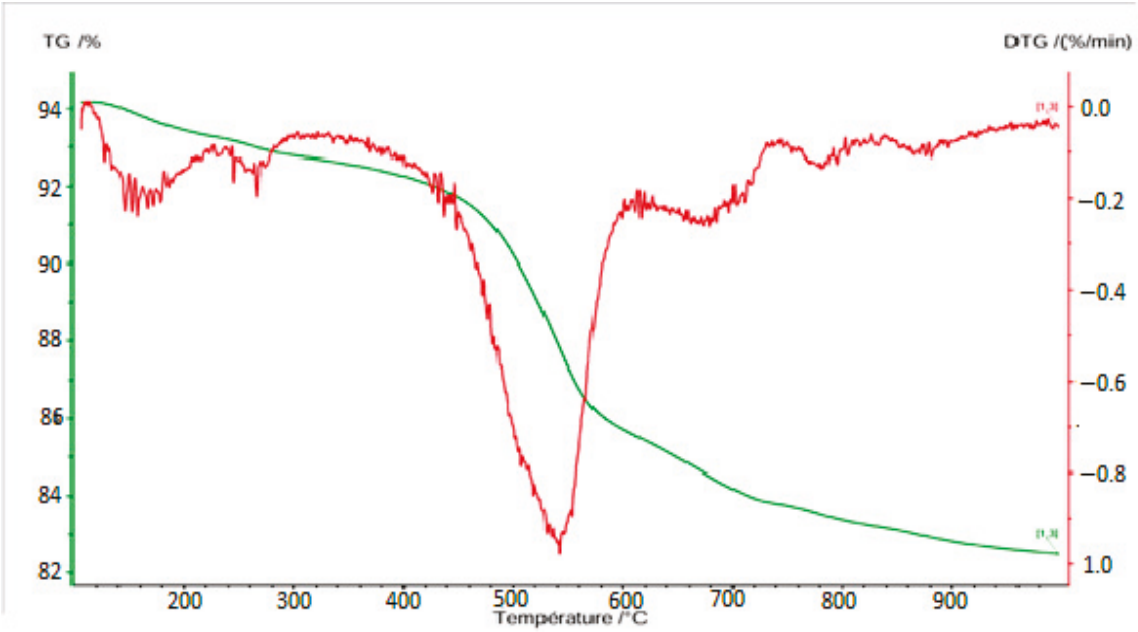

Figure 7. Thermogravimetric analysis (TGA) curve of kaolinitic clay recorded under an air atmosphere from room temperature up to 1000 °C at a heating rate of 5 °C/min. The mass loss below 200 °C corresponds mainly to the removal of adsorbed and structural water. A significant weight loss between 400 and 600 °C is attributed to the dehydroxylation of kaolinite, leading to the formation of metakaolin. Above 900 °C, the mass stabilizes, indicating the formation of thermally stable phases such as mullite. This thermal behavior is typical of kaolinitic clays and is critical for optimizing calcination conditions prior to geopolymer synthesis.

Diatomite Mineral

The DTG thermograph reveals the presence of two endothermic peaks at around 90 °C and 750 °C, respectively. The first peak, which is associated with a mass loss of approximately 2 to 4% at low temperature, is typical of diatomite, which is known for its high porosity and ability to physically adsorb water, a characteristic confirmed in the literature on natural diatomites [22]. The second endothermic peak, correlated with a mass loss of approximately 8%, can be attributed to the decarbonation of calcite (Figure 8). This would contribute to decreasing its thermal conductivity, thereby improving its thermal insulation capacity [22].

The continuous decrease in the TG curve below 800 °C and the increase in the DTG curve after the 750 °C peak may be due to an exothermic reaction. Thus, the formation of compounds results from the destruction of diatomite. Alternatively, the mineralogical rearrangement of the siliceous phase following the transformation of opal-CT to opal-C is more ordered [23]. This phenomenon corresponds to recrystallization.

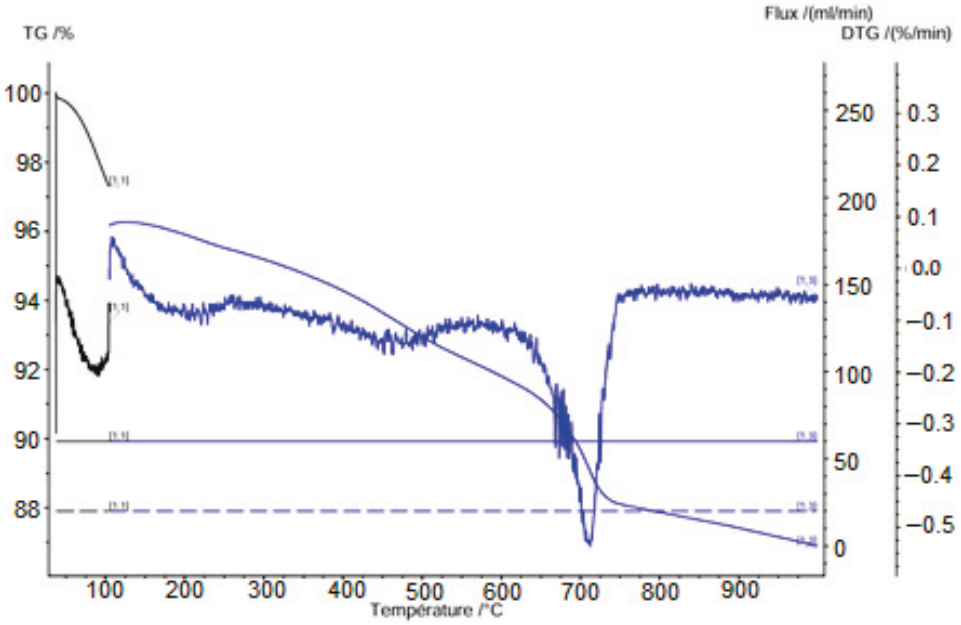

Figure 8. Thermogravimetric analysis (TGA) curve of raw diatomite recorded under nitrogen atmosphere from room temperature up to 1000 °C. The initial mass loss below 150 °C is attributed to the desorption of physically adsorbed water. A gradual weight loss observed between 400 and 600 °C corresponds to the removal of chemically bound water and dehydroxylation processes. The stability of the sample above 600 °C indicates the thermal resistance of the silica-rich diatomite structure. This thermal behavior is typical for diatomaceous earth and is important for optimizing its use as a precursor in geopolymer formulations.

4.2. Environmental Characterization of Raw Materials

The environmental analysis of mining effluents from the phosphate washery, natural clay, and diatomite reveals concentrations of trace elements using inductively coupled plasma atomic emission spectrometry (ICP-AES). The detection limits for various elements indicate method sensitivity, while most heavy metals such as As, Ba, Cd, Cu, Ni, Pb, Sb, and Zn are present at concentrations far below the regulatory limits for inert (ISDI) and non-hazardous (ISDND) waste (see Table 2). However, calcined phosphate sludge shows a significant increase in chromium (Cr) leaching (up to 79 mg/L), exceeding the ISDND limit (10 mg/L) and even surpassing the hazardous waste threshold (ISDD, 70 mg/L). Molybdenum (Mo) and selenium (Se) also increase after calcination, sometimes exceeding the ISDI limits. Sulfate, chloride, and fluoride concentrations are generally high, especially in phosphate sludge, but remain below ISDND thresholds.

Table 2. Heavy metals and anions of raw and calcined materials.

Elements	Phosphate Sludge (mg/l)	Clay Mineral	Diatomite	Calcined Clay	Calcined Phosphate Sludge	Calcined Diatomite	ISDI	ISDND	ISDD
As	<0.1	<0.1	<0.1	0.18	<0.1	<0.1	0.5	2	25
Ba	0.068	<0.008	0.026	<0.008	0.34	0.034	20	100	300
Cd	<0.009	<0.009	<0.009	<0.009	<0.009	<0.009	0.04	1	5
Cr	0.025	<0.004	0.01	15	79	17	0.5	10	70

Table 2. *Cont.*

Elements	Phosphate Sludge (mg/l)	Clay Mineral	Diatomite	Calcined Clay	Calcined Phosphate Sludge	Calcined Diatomite	ISDI	ISDND	ISDD
Cu	<0.02	<0.02	<0.02	<0.02	<0.02	<0.02	2	50	100
Mo	0.55	0.18	2.0	0.88	7.3	6.1	0.5	10	30
Ni	<0.05	<0.05	0.076	<0.05	<0.05	<0.05	0.4	10	40
Pb	<0.03	<0.03	<0.03	<0.03	<0.03	<0.03	0.5	10	50
Sb	<0.06	<0.06	<0.06	0.06	0.34	<0.06	0.06	0.7	5
Se	0.088	0.32	0.48	0.23	5.8	0.99	0.1	0.5	7
Zn	0.63	0.81	0.91	0.82	0.96	0.61	4	50	200
Sulfates	4760	644	724	353	450	1350	1000	20,000	50,000
Chlorides	386	487	80	259	70	13.5	800	15,000	25,000
Fluorides	14	2.0	1.5	2.1	13.4	1.8	10	150	500

4.3. Geopolymer Brick Characterization

4.3.1. Compressive Strength

The compressive strength of geopolymer bricks is an important property in material formulation. Higher resistance to compressive force also indicates a denser and more cohesive internal structure, which is typically associated with improved durability and reduced porosity in the bricks. Figure 9 shows the compressive strength of the developed bricks. As seen, the binary mixture GBM1 (90% calcined phosphate sludge and 10% calcined clay) achieved a remarkable strength of 25.9 MPa, significantly surpassing the 17.8 MPa observed for the G100 formulation (100% calcined phosphate sludge) due to enhanced geopolymerization from reactive aluminosilicates [7,15]. This result shows the efficacy of controlled clay addition in boosting mechanical properties. While higher clay proportions decreased strength (down to 6.8 MPa), the initial benefit of 10% substitution demonstrates a key threshold for maximizing performance. Ternary mixtures (GBDM) and diatomite-based formulations (GBD) exhibited moderate strengths (11.4–15.9 MPa), suggesting their suitability for applications prioritizing thermal insulation over extreme mechanical demands [24]. The study confirms that strategic clay incorporation can significantly elevate geopolymer performance for refractory applications.

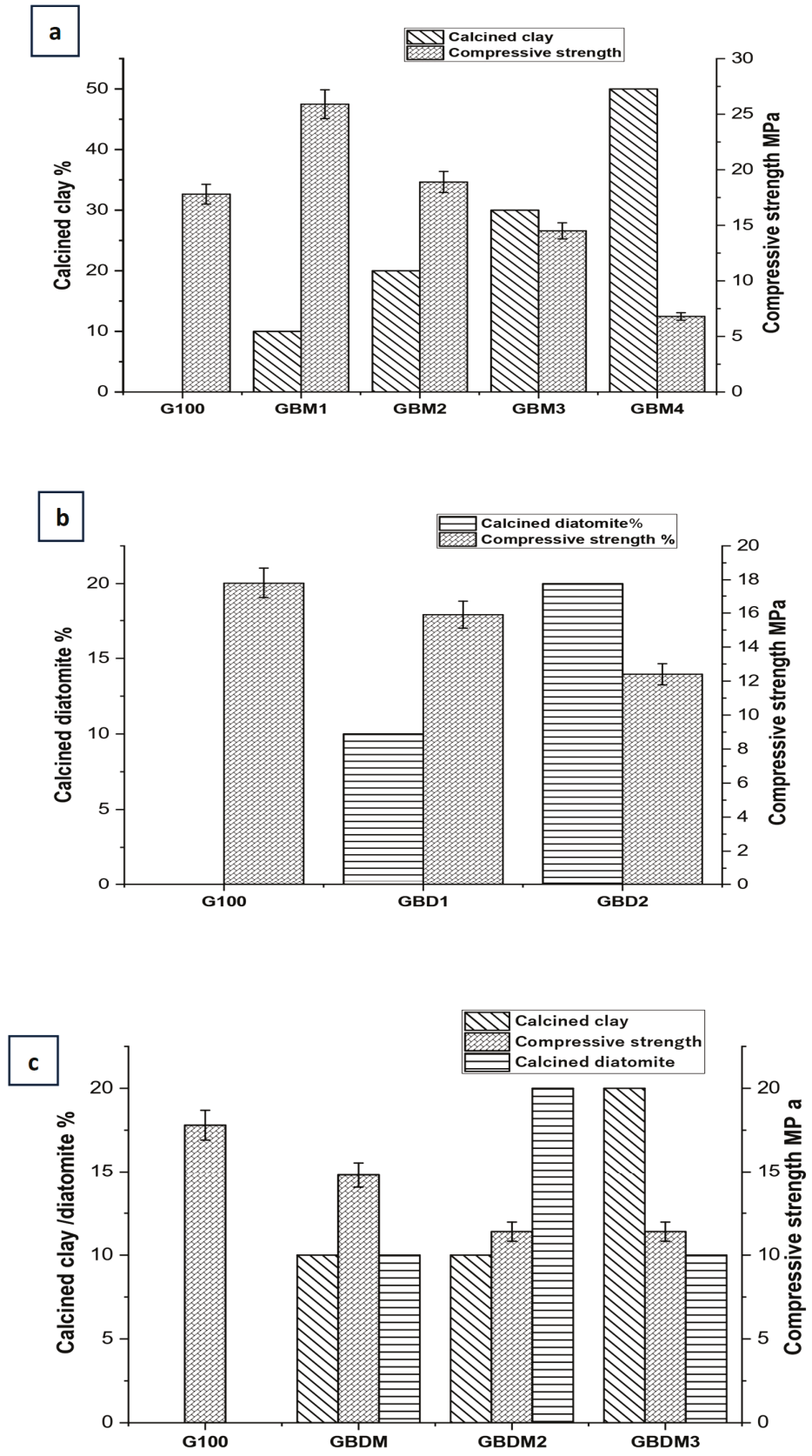

Figure 9. Evolution of the compressive strength of geopolymer bricks as a function of composition (proportions of WPS (**a**) KC (**b**), and D (**c**)). The tests were conducted according to the NF EN 196-1 standard on cylinders (Ø50 mm × 50 mm) after 7 days of curing at room temperature. The error bars represent the standard deviation from three tests.

4.3.2. Water Absorption

Low water absorption is desirable for refractory bricks, as it helps to reduce the risk of cracking and delamination. A recent study examined the influence of formulation composition on the water absorption of refractory bricks. Figure 10 shows that compositions with 100% calcined phosphate (G100) exhibit the lowest water absorption (~8%), indicating a dense microstructure with enhanced water resistance, slightly below values reported by [5]. Additives such as diatomite (GBD series) and clay (GBM series) increase absorption up to 17% (GBDM3/GBM4), attributed to diatomite's inherent porosity and clay's post-calcination structural changes [14]. Key formulations (G100, GBM1-GBM3) comply with NF EN 772-21 standards (17–22% absorption for frost-resistant bricks), aligning with findings that waste-derived additives can stabilize absorption [25], highlighting the need for precise additive control to optimize durability.

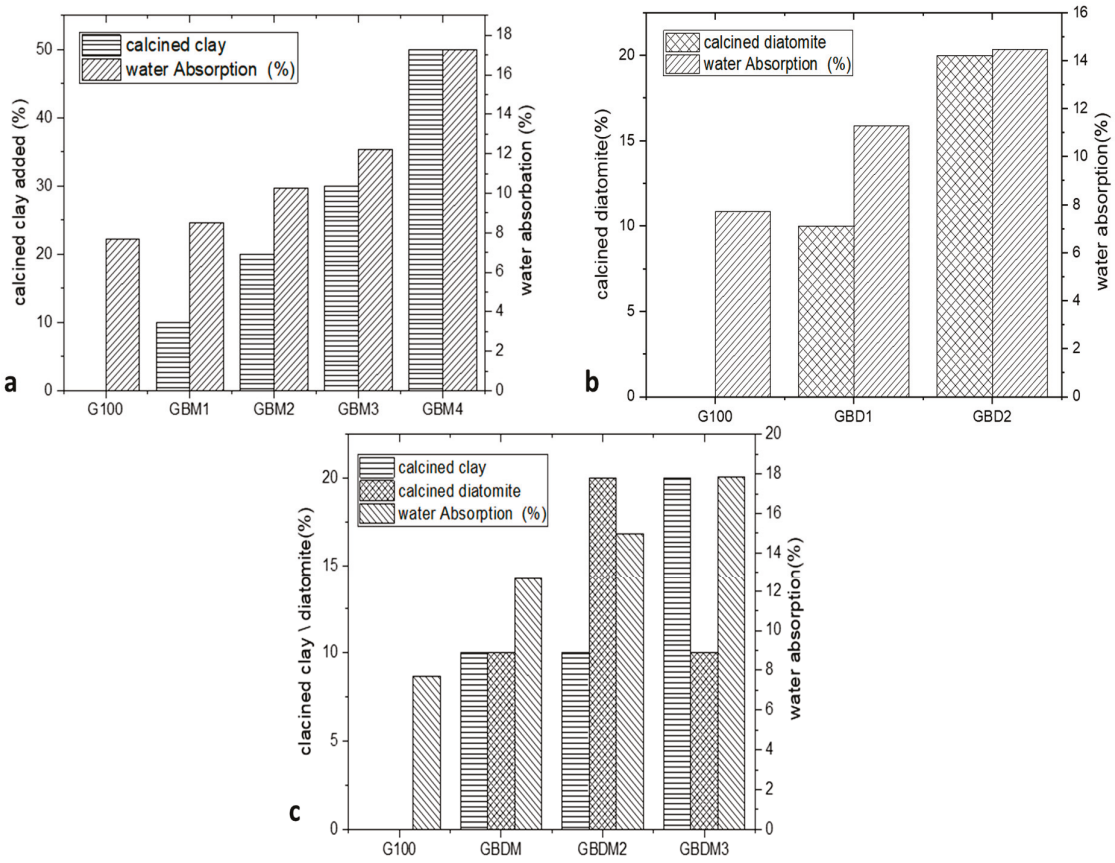

Figure 10. Water absorption rates of different geopolymer brick formulations after 24 h of immersion. The results highlight the influence of composition on the open porosity of the materials: (**a**) the effect of calcined clay, (**b**) the effect of calcined diatomite and (**c**) the combined effect.

Table 3 compares selected results from other studies. That allows us to compare different properties.

Table 3. Comparative studies of some geopolymers brick formulations and results.

References	Valuation Ways	Raw Materials	Origine	Firing Conditions	Water Absorption (%)	Compressive Strength (MPa)
[5]	Fired bricks	100% phosphate sludge	Tunisia Kef schfeir	Air drying for 24 h Oven drying at 60 °C for 24 h Firing at 900 °C, 1000 °Cand 1100 °C for 3 h (heating rate of 120 °C)	12.5–17.2	–
[14]	Ceramics bricks	Indonesian sludge (Banten Province)	25–50% of phosphate sludge + kaolin	Dried in an oven at 110 °C for at least 24 h. a heating rate of 5 °C/min to 500 °C, at 10 °C/min from 500 to 925 °C and at 15 °C/min from 925 °C	>30.23	>à 25
[18]	Ceramics products	Tunisian phosphate Kef eddour	0–50% phosphate sludge + kaolin	Dried at 105 °C for 24 h. The dried pellets were heated at 900, 1000, and 1100 °C for up to 2 h	–	–
[26]	Ceramics industries	Marrocan sludge	0–100% sludge + 0–100% clay	Heating ramp 5 °C/min up to the selected firing temperature (600, 900, 1000, 1100, and 1120 °C) 2 h dwell time at the temperature selected		
[27]	Geopolymer	Marroc phosphate industry	Alkaline solution, metakaolin-in and thermally untreated phosphate sludge (UPS)(of 50%)	Liquid to solid ratio of L/S = 1.2 Left drying at 60 °C for 24 h Hardened matrices for 28 days	–	28.05–46.83
[28]	geopolymer	Fly ash came from the heat and power plant in Skawina (Poland), the metakaolin came from the Czech Republic, and the diatomite came from Jawornik Ruski	Fly ash (FA) + metakaolin (MK) + 1–5% diatomite	Alkaline solution consisted of technical sodium hydroxide flakes with aqueous sodium silicate (a ratio of 1:2.5 was used) and tap water	Not specified	15–31.7
[15]	Geopolymer		Phosphate washing waste and alkaline solution	PPW calcined at 700 °C or 900 °C, activated with NaOH (7 M) and sodium silicate		15–22
[29]	Geopolymer		Geopolymers based on fly ash or metakaolin			20–70
[30]	Fired bricks	China	84% hematite tailings, fly ash, and clay mixed with 12.5–15% water	20–25 MPa of forming pressure, and a suitable firing temperature ranged from 980 to 1030 °C for 2 h	16.54–17.93%	20.03–22.92 MPa
[31]	Hybrid brick	India	70–90% clay + 5–15% ceramic waste powder + 5–15% bagasse ash	The bricks were cast using molds without any pressure being applied to them. In India, the bricks were left to dry in the sun for two days at a temperature of 35 to 40 °C for an 800 °C firing	11.4–18%	20–27.2
Current Study	Geoploymer	Phosphate washing by-product	50–100% phosphate washing by-product + (10–50% calcined clay (GBM)/10–20% Calcined diatomite (GBD)/calcined diatomite + calcined clay (GBDM)) + potassium silicates solution	The materials were calcined at 700 °C, 750 °C, and 800°C, activated with potassium silicate solution, then pressed, cured at ambient temperature for 72 h, and oven-dried at 105 °C for 24 h	7.7–17.8%	7–26 MPa

4.3.3. Thermal Conductivity

The study of thermal conductivity in refractory bricks highlights significant trends influenced by composition. The G100 formulation (100% phosphate sludge) exhibits the highest thermal conductivity (0.55 W/m·K) (see Figure 11). This could be related to its phosphate content. Phosphate-rich sludges, such as phosphogypsum, show high electrical conductivity due to their soluble ion content, mainly Ca^{2+}, Na^{+}, and PO_4^{3-}. Studies [32,33] report conductivity increases from hundreds of μS/cm to several mS/cm with higher phosphate sludge concentrations, confirming their strong impact on salinity levels. Incorporating calcined diatomite (GBDM series) reduces conductivity to 0.38 W/m·K, while clay additions (GBM series) yield intermediate values (~0.50 W/m·K). These results align with the study of Bories et al. [34], who reported conductivity around 0.53 W/m·K for bio-based porous agents in fired clay bricks, and Phonphuak et al. [35] have reached lower conductivity (0.22–0.47 W/m·K) using sawdust, albeit with higher porosity (22.8–32.4%) [35]. This proves the critical role of pore agent type and quantity in modulating thermal and structural properties. Compared to commercial dense (1.0–2.0 W/m·K) and insulating (0.2–0.8 W/m·K) refractory bricks [34], the formulations developed in this study fall within the insulating range (0.38–0.58 W/m·K). Notably, the use of local, sustainable materials reduces the carbon footprint.

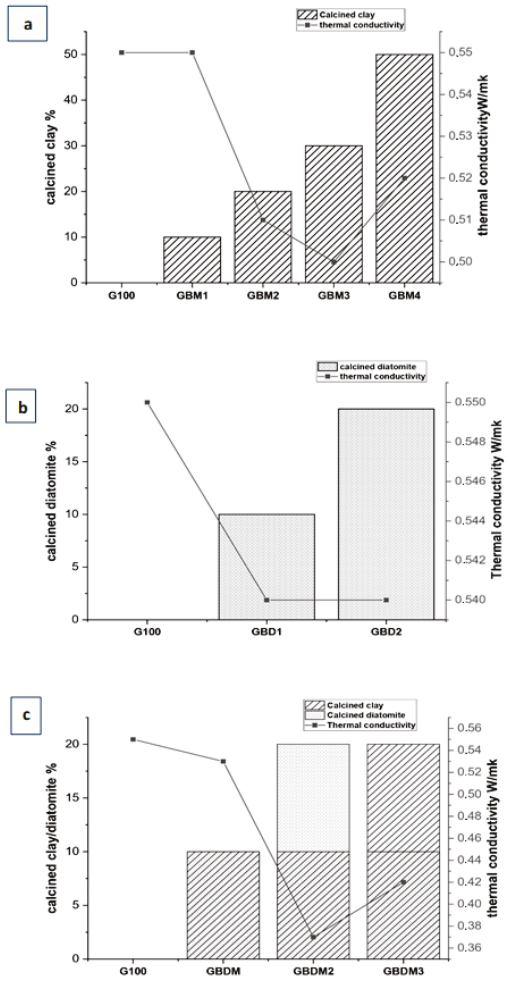

Figure 11. Thermal conductivity of geopolymer bricks as a function of calcined clay and calcined diatomite content, measured at room temperature. (**a**) Effect of calcined clay, (**b**) effect of calcined diatomite, and (**c**) combined effect of both additions. Hatched bars correspond to calcined clay, dotted bars to calcined diatomite, and the solid line with square points indicates thermal conductivity.

4.3.4. X-Ray Diffraction Results

The X-ray diffraction patterns of geopolymer formulations in Figure 12 reveal the mineralogical composition of consolidated materials. While geopolymers are generally considered amorphous materials by XRD, a broad hump centered around 20° to 35° (2θ) indicates the dissolution of SiO_4 and AlO_4 species and the formation of an amorphous phase compared to calcined clays, reflecting polycondensation reactions [19,36,37]. However, the significant intensity of crystalline peaks, particularly quartz, suggests limited reactivity and incomplete dissolution of raw materials [38,39]. Compared to metakaolin-based geopolymers, which typically exhibit more complete amorphization [19], our materials show similarities to fly ash-based geopolymers, which often retain residual crystalline phases [40]. These crystalline phases may contribute to thermal stability, making the materials potentially suitable for refractory applications. Thus, while geopolymerization is evident, optimization of synthesis conditions is needed to enhance precursor reactivity and achieve improved performance for refractory uses.

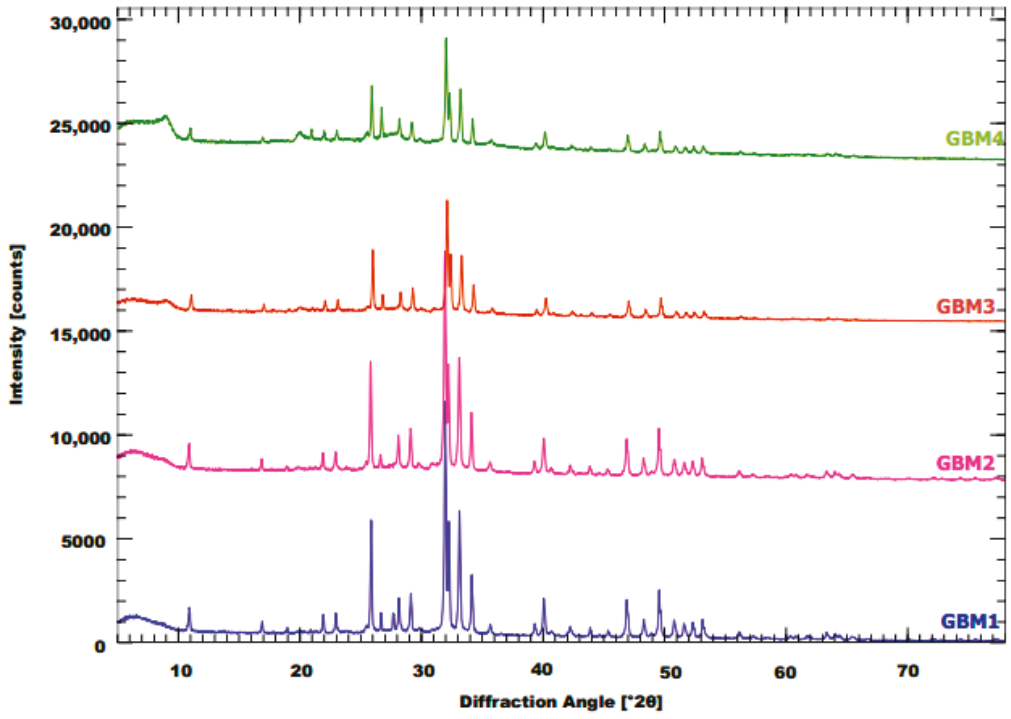

(**A**)

Figure 12. *Cont.*

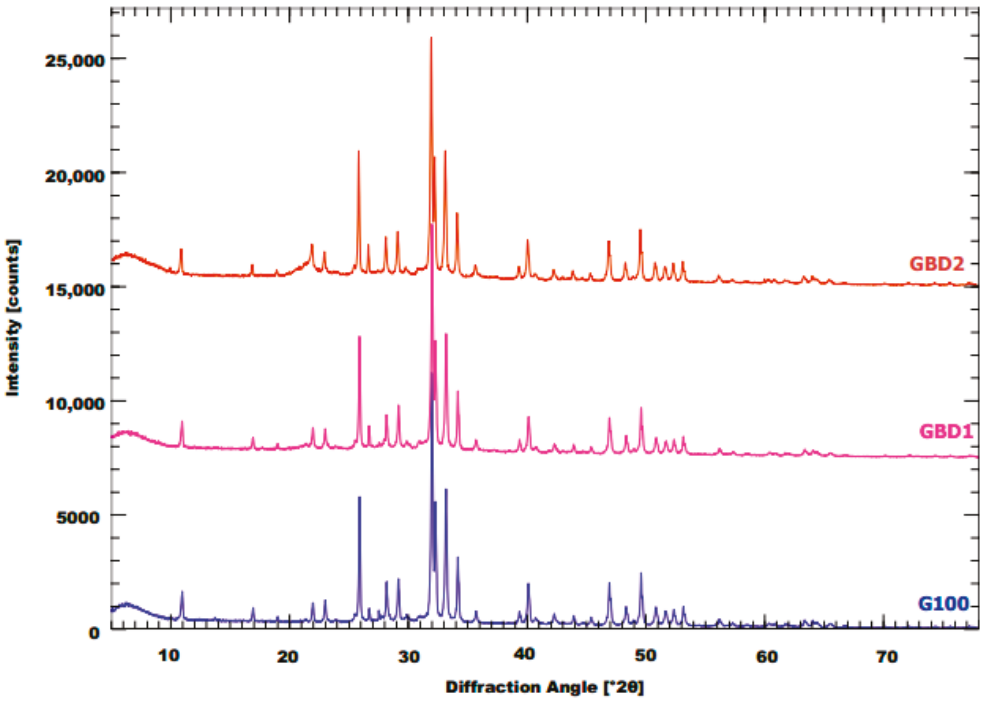

(**B**)

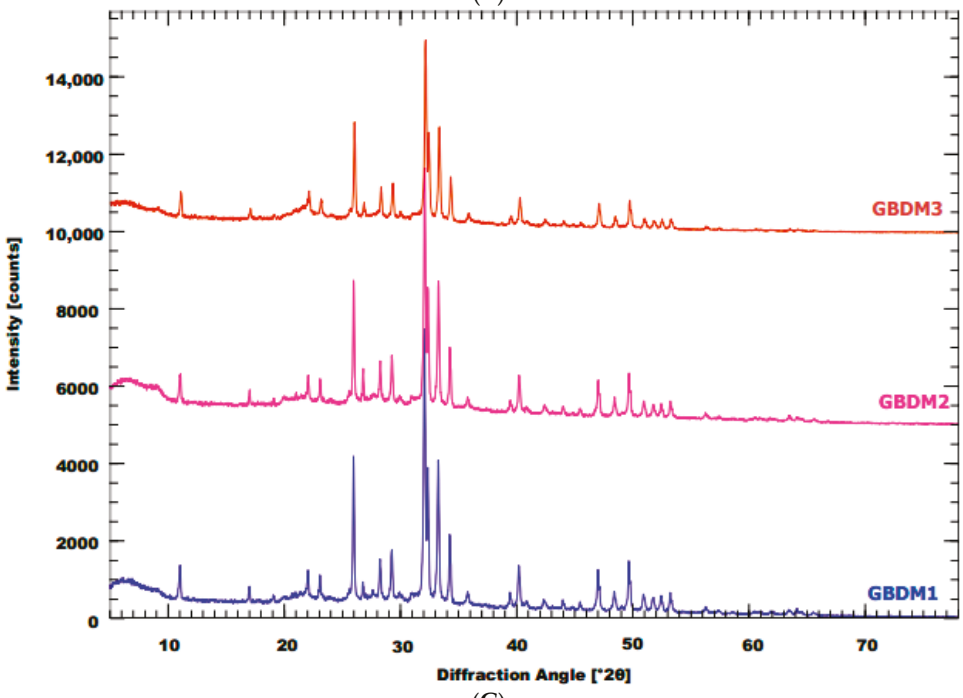

(**C**)

Figure 12. X-ray diffraction (XRD) patterns of geopolymer bricks prepared with different formulations: (**A**) GBM series (phosphate washing sludge and clay), (**B**) GBD series (phosphate washing sludge and diatomite), and (**C**) GBDM series (phosphate washing sludge, clay, and diatomite). Patterns were recorded at room temperature on finely ground samples after 7 days of curing. Major diffraction peaks are labeled to identify crystalline phases such as quartz, calcite, and residual kaolinite. The presence and intensity of amorphous humps and new mineral phases reflect the extent of geopolymerization and the influence of precursor composition on the final structure.

4.3.5. FTIR Analysis

Figure 13 represents the FTIR spectra of the GBM (phosphate sludge + clay), GBD (sludge + diatomite), and GBDM (sludge + diatomite + metakaolin) series and reveals

distinct structural signatures. The Si–O–Si/Al band (1100–950 cm^{-1}) shifts to 980 cm^{-1} (GBM), 950 cm^{-1} (GBD), and 960 cm^{-1} (GBDM), reflecting differential Al incorporation into the silicate network [19,41]. The marked reduction of the 450 cm^{-1} band (Si–O) in GBDM indicates advanced consumption of clay phases [42], while residual peaks at 800 cm^{-1} (illite) [19] and 700 cm^{-1} (quartz) stabilize the matrix at high temperatures [43]. The hydroxyl region (3300–3600 cm^{-1}) shows increased residual porosity for GBD (linked to diatomite) and improved condensation for GBDM (via metakaolin) [44] compared to fly ash-based geopolymers (960 cm^{-1}, low hydroxyl absorption) or slag-based systems (dominant amorphous halo) [45]. These formulations combine residual crystalline phases and complete carbonate decomposition (1470 cm^{-1}) at 400 °C, offering superior thermal stability. The GBDM series, optimizing the Si/Al ratio through metakaolin, outperforms conventional geopolymers in structural stability and dehydration resistance, confirming the efficacy of hybrid systems [46].

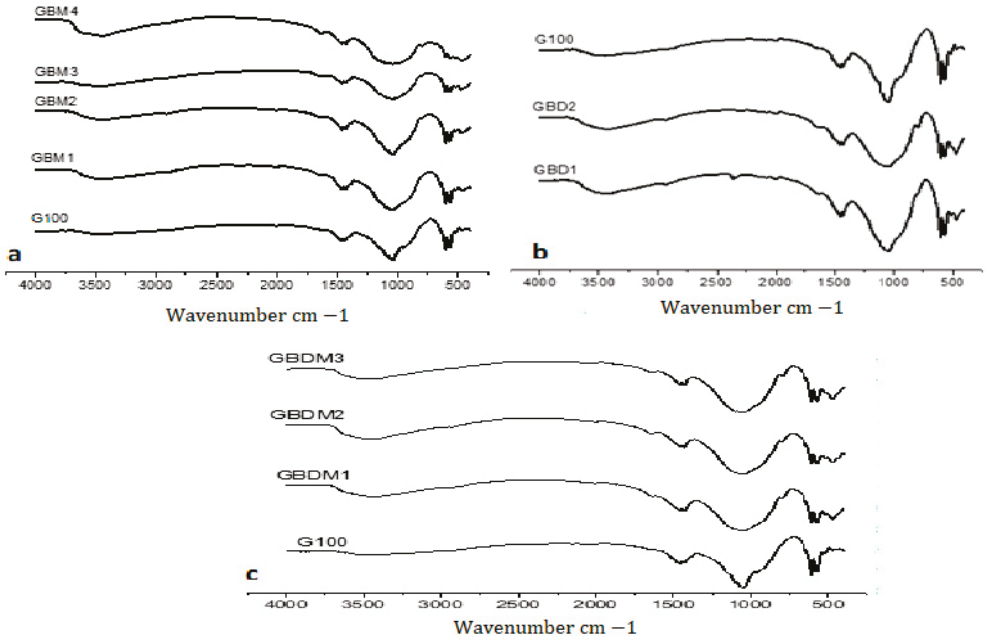

Figure 13. Fourier-transform infrared (FTIR) spectra of geopolymer bricks with different formulations: (**a**) GBM series (phosphate washing sludge and clay), (**b**) GBD series (phosphate washing sludge and diatomite), and (**c**) GBDM series (phosphate washing sludge, clay, and diatomite). Spectra were recorded in the 4000–400 cm^{-1} range at room temperature on powdered samples after 7 days of curing. The main absorption bands are assigned to functional groups such as Si–O–Si, Al–O, and CO_3^{2-}, characteristic of geopolymer structures. Comparative analysis of the spectra reveals the formation of new bonds and the disappearance or shift of certain peaks, indicating successful geopolymerization and the influence of precursor composition on the chemical structure of the final materials.

4.3.6. Thermogravimetric Analysis

The study of the thermal behavior of synthesized geopolymer materials, based on the thermograms of the GBM, GBD, and GBDM series (Figure 14), highlights significant differences depending on the composition and treatment of the raw materials. For the GBM series, the main mass loss occurs between 25 and 600 °C, corresponding to the removal of free water, dehydroxylation of –OH groups, and decomposition of carbonates, with a moderate total mass loss (4–6%) (Figure 14), which could lead to higher porosity at elevated temperatures, indicating good consolidation of the geopolymer network [38]; (Dabbebi

et al., 2018) [15]. The GBD formulations (Figure 14) show contrasting behaviors: GBD1 is exceptionally stable, GBD2 combines low mass loss (~3%) and strong thermal robustness, while G100 (100% calcined phosphate sludge) exhibits a more pronounced mass loss due to carbonate decomposition [39]. Finally, the GBDM series, which incorporates calcined diatomite and clay, exhibits excellent thermal stability, with all samples losing less than 3% of their mass up to 1200 °C. Among them, GBDM2 stands out by offering the best compromise between minimal mass loss and structural robustness, making it particularly suitable for refractory applications. This superior performance is attributed to the optimized combination of calcined diatomite and clay, which enhances the formation of a dense, stable geopolymer network capable of withstanding high temperatures without significant degradation [28,44]. These results confirm the importance of initial composition and the use of calcined diatomite and clay to achieve lightweight, stable, and high-performance geopolymers at high temperatures.

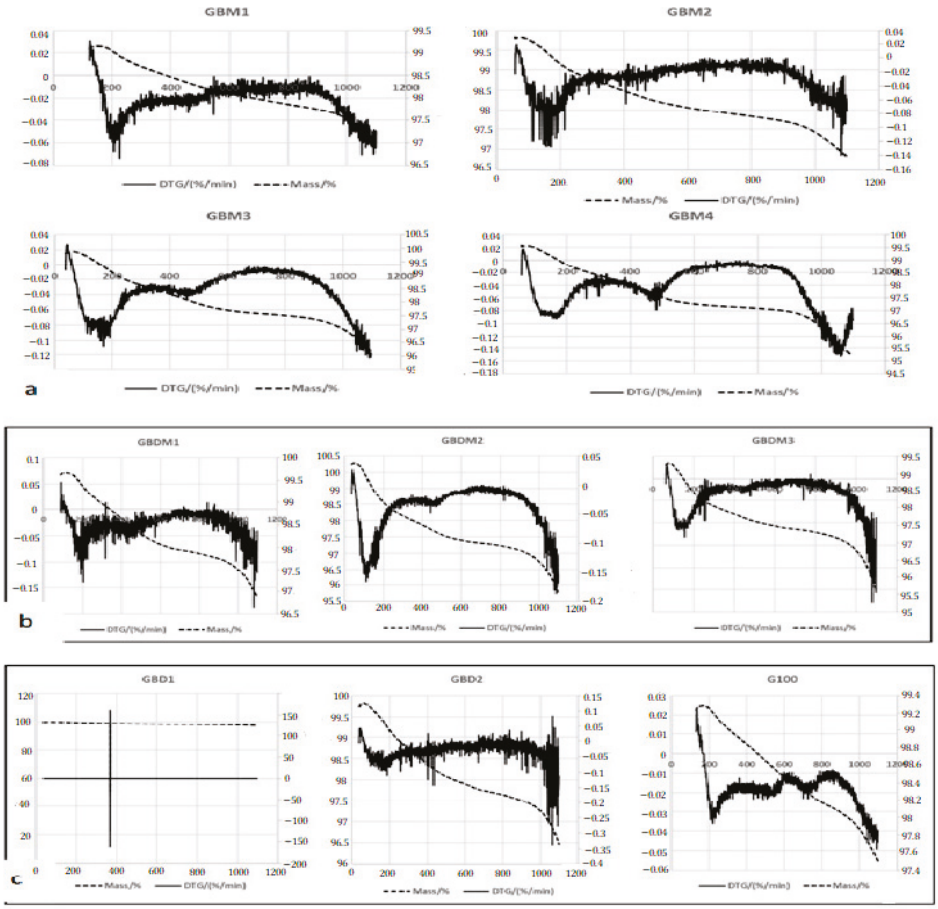

Figure 14. GBD series thermal behavior of geopolymer bricks from different formulations: (**a**) GBM series (phosphate washing sludge and clay), (**b**) GBDM series (phosphate washing sludge, clay, and diatomite), and (**c**) GBD series (phosphate washing sludge and diatomite). Thermogravimetric analysis (TGA) and differential thermal analysis (DTA) were performed under a nitrogen atmosphere from room temperature to 1000 °C at a heating rate of 10 °C/min. The curves illustrate mass loss events corresponding to moisture evaporation below 200 °C, dehydroxylation of aluminosilicate phases between 400 and 600 °C, and decomposition of carbonates or organics at higher temperatures. Differences in thermal stability and phase transformations among the formulations reflect the influence of precursor composition on geopolymer structure and durability.

4.3.7. Environmental Assessment of Heavy Metal and Anion Leaching from Geopolymer Formulations

Across all formulations in Table 4, most heavy metals remain well below ISDND limits, indicating effective immobilization within the geopolymer matrix. Sulfate, chloride, and fluoride levels are sometimes elevated (e.g., sulfate up to 1195 mg/L in GBDM1), but still comply with non-hazardous waste regulations.

Table 4. Heavy metals and anions of geopolymers.

Elements	GBM1	GBM2	GBM3	GBM4	GBD1	GBD2	GBDM1	GBDM2	GBDM3	G100	ISDI	ISDND	ISDD
As	<0.1	<0.1	0.13	0.35	<0.1	0.12	<0.1	0.13	<0.1	<0.1	0.5	2	25
Ba	<0.008	<0.008	<0.008	<0.008	<0.008	<0.008	<0.008	<0.008	0.009	0.012	20	100	300
Cd	<0.009	<0.009	<0.009	<0.009	<0.009	<0.009	<0.009	<0.009	<0.009	0.01	0.04	1	5
Cr	10	13	16	19	13	18	14	16	20	41	0.5	10	70
Cu	<0.02	<0.02	<0.02	<0.02	<0.02	<0.02	<0.02	<0.02	<0.02	<0.02	2	50	100
Mo	0.91	1.7	2.2	2.1	1.7	2.0	1.1	2.1	2.3	2.9	0.5	10	30
Ni	<0.05	<0.05	<0.05	<0.05	<0.05	<0.05	<0.05	<0.05	<0.05	<0.05	0.4	10	40
Pb	<0.03	<0.03	<0.03	<0.03	0.05	<0.03	<0.03	<0.03	<0.03	<0.03	0.5	10	50
Sb	<0.09	0.10	0.10	0.08	0.09	0.12	0.065	<0.06	0.079	0.18	0.06	0.7	5
Se	0.87	2.2	2.7	2.5	2.2	1.9	1.1	2.8	2.2	2.8	0.1	0.5	7
Zn	<0.01	0.74	<0.01	<0.01	<0.01	<0.01	<0.01	<0.01	<0.01	<0.01	4	50	200
Sulfates	243	772	734	151	1033	841	298	1042	1100	595	1000	20,000	50,000
Chlorides	50	70	98	151	34	25	54.5	74.4	40.3	40.8	800	15,000	25,000
Fluorides	4.9	8.4	7.2	7.0	11	6.6	5.2	8.0	7.5	7.0	10	150	500

Chromium (Cr) is the main limiting factor in the formulations; its concentration ranges from 10 to 41 mg/L, exceeding both the inert (ISDI: 0.5 mg/L) and often the non-hazardous (ISDND: 10 mg/L) thresholds, but remaining below the hazardous waste limit (ISDD: 70 mg/L). This elevated Cr content is directly linked to the use of calcined phosphate sludge, which is very rich in leachable Cr. However, the reduction in Cr concentration compared to the pure calcined sludge is due to dilution effects and partial immobilization by the geopolymer matrix. To conclude, the geopolymer formulations can be classified as non-hazardous waste for most elements, but the Cr content remains above the thresholds for inert and non-hazardous waste, limiting their valorization without further treatment. Optimizing the formulation or adding specific stabilizing agents for chromium is recommended to improve environmental performance [47].

5. Comparative Analysis and Selection of Optimal Geopolymer Brick Formulations

To identify the most promising geopolymer brick formulations for refractory applications, a comprehensive comparative analysis was performed, considering mechanical strength, thermal stability, heavy metal immobilization, and thermal conductivity. While all formulations exhibited potential for waste valorization, two distinct categories of high-performing bricks emerged, depending on the specific application requirements: dense and high-strength, or balanced and environmentally optimized.

The GBM1 formulation (with 10% calcined clay) is unequivocally the best choice for producing dense, high-strength refractory bricks. This formulation demonstrated the highest compressive strength in our study, achieving 25.9 MPa (Figure 9). This performance not only significantly surpasses other formulations tested within this study (whose overall mechanical performance ranged from 7 MPa to 26 MPa), but it also renders GBM1 highly competitive with commercial refractory bricks and standard geopolymer materials

reported in the literature [15,45]. Its thermogravimetric analysis (TGA) (as presented in Section 3.4) reveals good thermal stability, with a moderate mass loss of approximately 12%, primarily due to dehydration and dehydroxylation processes, which is crucial for maintaining material integrity at high temperatures. The thermal conductivity of GBM1 is 0.55 W/m·K (Figure 11), a value characteristic of dense refractory bricks, providing a suitable balance between thermal resistance and heat transfer. Furthermore, environmental assessments (Table 4) showed that GBM1's leachate concentrations of heavy metals are among the lowest, classifying it as "non-hazardous" and very close to "inert" for most elements (with the exception of chromium, which, while slightly above the inert limit of 0.5 mg/L, remains well below the non-hazardous threshold of 10 mg/L).

Conversely, the GBDM (phosphate sludge + clay + diatomite) formulation represents the best compromise for a versatile and highly environmentally friendly refractory brick. While its compressive strength (15 MPa, Figure 9) is lower than GBM1, it is still adequate for many non-structural or semi-structural applications. GBDM's main advantage lies in its outstanding thermal stability, exhibiting the lowest TGA mass loss (~9%) among all our formulations (Figure 14), indicating exceptional durability at high temperatures. Moreover, GBDM demonstrates the best environmental performance (Table 4), with the lowest concentrations of leached heavy metals, confirming its "non-hazardous" classification and minimal environmental impact potential. Its thermal conductivity of 0.45 W/m·K (Figure 11) positions it as a good insulator, performing better than GBM1 in this specific property.

In conclusion, the selection of the "best" formulation depends on the specific application requirements. If maximum mechanical performance is the predominant criterion for dense refractory bricks, GBM1 is the most appropriate choice. However, if a balance between good strength, improved thermal insulation, superior thermal stability, and minimal environmental impact is desired, GBDM represents the most balanced and promising solution from our study for a versatile and sustainable refractory brick. These distinctions provide valuable insights for future industrial applications of these eco-friendly materials.

6. Economic Feasibility and Scalability Considerations

The process developed in this study offers several economic and practical advantages compared to traditional fired refractory bricks. All raw materials—phosphate sludge, clay, and diatomite—are abundantly available and locally sourced from the Gafsa mining basin, with diatomite and phosphate sludge being mining by-products or considered as waste. This ensures low material costs and reduces the need for waste management.

Unlike conventional refractory bricks, our method does not require high-temperature firing, but only calcination of raw materials and drying at 105 °C. This significantly lowers energy consumption and production costs and reduces greenhouse gas emissions. The limited use of potassium silicate as an alkaline activator further minimizes chemical input costs. The preparation process (mixing, compacting, ambient curing, and drying) is simple and compatible with existing industrial equipment, facilitating easy scale-up. The abundance of raw materials and the straightforward process make large-scale production feasible and sustainable.

In summary, our approach provides a cost-effective and environmentally friendly alternative to traditional fired bricks, with strong potential for industrial applications in regions with similar resources.

7. Conclusions

This study presents a novel and sustainable approach for the valorization of Tunisian phosphate washing sludge as a primary raw material for ecological refractory bricks. Unlike previous research limited to partial substitution, our work demonstrates for the first time the successful use of up to 100% calcined phosphate sludge, in combination with locally sourced kaolinitic clay and diatomite, to produce geopolymer bricks activated by potassium silicate and cured at ambient temperature.

The developed bricks exhibit outstanding mechanical performance, with compressive strengths reaching up to 25.9 MPa, low water absorption, and favorable thermal insulation properties. These results confirm that careful optimization of precursor composition and activator concentration can yield materials that meet or exceed industry standards for refractory applications.

From an environmental perspective, this process offers significant benefits by transforming mining waste into high-value construction materials. The method reduces the volume of hazardous waste, mitigates risks of soil and water contamination, and substantially lowers both energy consumption and greenhouse gas emissions compared to conventional fired bricks.

Overall, our findings highlight the dual advantage of this approach: it provides a technically robust solution for producing high-performance, durable refractory bricks, while also contributing to environmental protection and circular economy objectives. Future research should focus on scaling up the process, further optimizing formulations for industrial applications, and ensuring the safe management of trace elements to fully realize the environmental and economic potential of this technology.

Author Contributions: Conceptualization, M.H. and R.Z.; methodology, M.A.; software, A.G.; validation, M.H., A.S. and M.A.; formal analysis, R.Z.; Investigation, M.A. and M.H.; resources, N.A.; data curation, A.S.; writing—original draft preparation, M.H. and M.A.; writing—review and editing, M.H.; visualization, A.S.; supervision, N.A.; project administration, R.Z.; funding acquisition, N.A. All authors have read and agreed to the published version of the manuscript.

Funding: This research received no external funding.

Data Availability Statement: No new data were created or analyzed in this study. Data sharing is not applicable to this article.

Conflicts of Interest: No conflict of interest to disclose.

References

1. Idrissi, H.; Taha, Y.; Elghali, A.; El Khessaimi, Y.; Aboulayt, A.; Amalik, J.; Hakkou, R.; Benzaazoua, M. Sustainable use of phosphate waste rocks: From characterization to potential applications. *Mater. Chem. Phys.* **2021**, *260*, 124119. [CrossRef]
2. Hakkou, R.; Benzaazoua, M.; Bussière, B. Valorization of Phosphate Waste Rocks and Sludge from the Moroccan Phosphate Mines: Challenges and Perspectives. *Procedia Eng.* **2016**, *138*, 110–118. [CrossRef]
3. Brahmi, M.; Zouari, S.; Rossi, M. L'industrie minière et ses effets écologiques. État socio-économique et environnemental dans le bassin minier tunisien. *Collect. EDYTEM Cah. Géographie* **2019**, *17*, 109–120. [CrossRef]
4. Bayoussef, A.; Oubani, M.; Loutou, M.; Taha, Y.; Benzaazoua, M.; Manoun, B.; Hakkou, R. Manufacturing of high-performance ceramics using clays by-product from phosphate mines. *Mater. Today Proc.* **2020**, *37*, 3994–4000. [CrossRef]
5. Ettoumi, M.; Jouini, M.; Neculita, C.; Bouhlel, S.; Coudert, L.; Taha, Y.; Benzaazoua, M. Characterization of phosphate processing sludge from Tunisian mining basin and its potential valorization in fired bricks making. *J. Clean. Prod.* **2021**, *284*, 124750. [CrossRef]
6. Obenaus-Emler, R.; Falah, M.; Illikainen, M. Assessment of mine tailings as precursors for alkali-activated materials for on-site applications. *Constr. Build. Mater.* **2020**, *246*, 118470. [CrossRef]

7. Moukannaa, S.; Loutou, M.; Benzaazoua, M.; Vitola, L.; Alami, J.; Hakkou, R. Recycling of phosphate mine tailings for the production of geopolymers. *J. Clean. Prod.* **2018**, *185*, 891–903. [CrossRef]
8. Zeng, R.; Ge, Y.; Sun, W.; Du, X.; Chen, W.; Duan, G. Method for purifying flotation phosphate tailings and preparing concrete blocks. 2019.
9. Boutaleb, F.; Boutaleb, N.; Deblij, S.; El Antri, S.; Bahlaouan, B. Effect of Phosphate Mine Tailings from Morocco on the Mechanical Properties of Ceramic Tiles. *Int. J. Eng. Res. Technol.* **2020**, *9*. [CrossRef]
10. Boutaleb, F.Z.; Boutaleb, N.; Bahlaouan, B.; Sanaa, D.; El Antri, S. Production of ceramic tiles by combining Moroccan phosphate mine tailings with abundant local clays. *Mediterr. J. Chem.* **2020**, *10*, 568–576. [CrossRef]
11. Harech, M.; Labbilta, T.; Anasser, I.; El Hafiane, Y.; Abouliatim, Y.; Nibou, L.; Smith, A.; Mesnaoui, M. From by-product to sustainable building material: Reusing phosphate washing sludge for eco-friendly red brick production. *J. Build. Eng.* **2023**, *78*, 107575. [CrossRef]
12. Inabi, O.; Khalil, A.; Zouine, A.; Hakkou, R.; Benzaazoua, M.; Taha, Y. Investigation of the Innovative Combined Reuse of Phosphate Mine Waste Rock and Phosphate Washing Sludge to Produce Eco-Friendly Bricks. *Buildings* **2024**, *14*, 2600. [CrossRef]
13. Kulakowski, M.P.; Brehm, F.A.; Moraes, C.A.M.; Pampanelli, A.; Reckziegel, V. Monitoring and Evaluation of Industrial Production of Fired-Clay Masonry Bricks with 2.5% of Phosphatization Sludge. *Key Eng. Mater.* **2014**, *634*, 206–213. [CrossRef]
14. Muliawan, J.; Astutiningsih, S. Preparation and characterization of Phosphate-Sludge kaolin mixture for ceramics bricks. *Int. J. Technol.* **2018**, *9*, 317–324. [CrossRef]
15. Dabbebi, R.; Baklouti, S.; de Aguiar, J.L.B.; Pacheco-Torgal, F.; Samet, B. Investigations of geopolymeric mixtures based on phosphate washing waste. *Sci. Technol. Mater.* **2018**, *30*, 1–5. [CrossRef]
16. Tunisienne, R. Ecole Doctorale Sciences et Technologies Thèse de DOCTORAT Nom du Doctorat N° d'ordre: 92–2020 DOCTORAT Dans la discipline Géologie Génie Géo-Ressources, Environnement et Aménagement Par. Available online: https://theses.hal.science/tel-04923554v1/file/These_JuliaCabanes.pdf (accessed on 19 March 2025).
17. Kuppusamy, M.; Kim, S.W.; Lee, K.P.; Jo, Y.J.; Kim, W.J. Development of TiO_2–$CaCO_3$ Based Composites as an Affordable Building Material for the Photocatalytic Abatement of Hazardous NOx from the Environment. *Nanomaterials* **2024**, *14*, 136. [CrossRef]
18. Baccour, H.; Koubaa, H.; Baklouti, S. Phosphate sludge from tunisian phosphate mines: Valorisation as ceramics products. In *Recent Advances in Environmental Science from the Euro-Mediterranean and Surrounding Regions*; Advances in Science, Technology and Innovation; Springer: Cham, Switzerland, 2018; pp. 1479–1480. [CrossRef]
19. Mkaouar, S. Valorisation de Quelques Formations Argileuses Pour la Production de Briques en Terres Crues et de Matériaux Géopolymères. 2021. Available online: http://www.theses.rnu.tn/fr/dynamique/uploads/cfd2b6661e8090e5e6f9672023c2d062.pdf (accessed on 19 March 2025).
20. Louati, S.; Baklouti, S.; Samet, B. Geopolymers Based on Phosphoric Acid and Illito-Kaolinitic Clay. *Adv. Mater. Sci. Eng.* **2016**, *2016*, 2359759. [CrossRef]
21. Zheng, R.; Ren, Z.; Gao, H.; Zhang, A.; Bian, Z. Effects of calcination on silica phase transition in diatomite. *J. Alloys Compd.* **2018**, *757*, 364–371. [CrossRef]
22. Ilia, I.K.; Stamatakis, M.G.; Perraki, T.S. Mineralogy and technical properties of clayey diatomites from north and central Greece. *Cent. Eur. J. Geosci.* **2009**, *1*, 393–403. [CrossRef]
23. Tlili, A.; Saidi, R.; Fourati, A.; Ammar, N.; Jamoussi, F. Mineralogical study and properties of natural and flux calcined porcelanite from Gafsa-Metlaoui basin compared to diatomaceous filtration aids. *Appl. Clay Sci.* **2012**, *62–63*, 47–57. [CrossRef]
24. Zibo Jucos Co., Ltd. Moyens et Méthodes Pour Améliorer la Résistance à la Compression de la Brique Réfractaire—Support Technique—Zibo Jucos Co., Ltd. Available online: https://fr.jucosceramicfiber.com/info/ways-and-methods-of-improving-compressive-stre-48546449.html# (accessed on 19 March 2025).
25. Taha, Y. Valorisation des Rejets Miniers dans la Fabrication de Briques Cuites: Évaluations Technique et Environnementale. Ph.D. Thesis, Université du Québec en Abitibi-Témiscamingue, Ville-Marie, QC, Canada, 2017. [CrossRef]
26. Harech, M.A.; Mesnaoui, M.; Abouliatim, Y.; EL Hafiane, Y.; Benhammou, A.; Abourriche, A.; Smith, A.; Nibou, L. Effect of temperature and clay addition on the thermal behavior of phosphate sludge. *Boletín Soc. Española Cerámica Vidr.* **2020**, *60*, 194–204. [CrossRef]
27. Hamdane, H.; Tamraoui, Y.; Mansouri, S.; Oumam, M.; Bouih, A.; El Ghailassi, T.; Boulif, R.; Manoun, B.; Hannache, H. Effect of alkali-mixed content and thermally untreated phosphate sludge dosages on some properties of metakaolin based geopolymer material. *Mater. Chem. Phys.* **2020**, *248*, 122938. [CrossRef]
28. Nykiel, M.; Korniejenko, K.; Setlak, K.; Melnychuk, M.; Polivoda, N.; Kozub, B.; Hebdowska-Krupa, M.; Łach, M. The Influence of Diatomite Addition on the Properties of Geopolymers Based on Fly Ash and Metakaolin. *Materials* **2024**, *17*, 2399. [CrossRef] [PubMed]

29. Chen, L.; Wang, Z.; Wang, Y.; Feng, J. Preparation and properties of alkali activated metakaolin-based geopolymer. *Materials* **2016**, *9*, 767. [CrossRef]
30. Chen, Y.; Zhang, Y.; Chen, T.; Zhao, Y.; Bao, S. Preparation of eco-friendly construction bricks from hematite tailings. *Constr. Build. Mater.* **2011**, *25*, 2107–2111. [CrossRef]
31. Malkapuram, D.; Ballari, S.O.; Chinta, S.; Rajasekaran, P.; Venkatesan, B.; Vellingiri, S.; Paulraj, P.; Ramaswamy, A.; Ramamurthy, D.; Salam, F.A.; et al. Mechanical, Water Absorption, Efflorescence, Soundness and Morphological Analysis of Hybrid Brick Composites. *Matéria* **2024**, *29*, e20240179. [CrossRef]
32. Luo, A.; Li, J.; Xiao, Y.; He, Z.; Liang, J. Engineering Soil Quality and Water Productivity Through Optimal Phosphogypsum Application Rates. *Agronomy* **2024**, *15*, 35. [CrossRef]
33. Liu, B.; Chen, Z.; Liu, F.; Zhu, J. Characteristics of Modified Complex of Red Mud and Phosphogypsum and Its Soil Substrate Utilization. *Processes* **2025**, *13*, 972. [CrossRef]
34. Bories, C.; Borredon, M.E.; Vedrenne, E.; Vilarem, G. Development of eco-friendly porous fired clay bricks using pore-forming agents: A review. *J. Environ. Manag.* **2014**, *143*, 186–196. [CrossRef]
35. Phonphuak, N.; Teerakun, M.; Srisuwan, A.; Ruenruangrit, P.; Saraphirom, P. The use of sawdust waste on physical properties and thermal conductivity of fired clay brick production. *Int. J. GEOMATE* **2020**, *18*, 24–29. [CrossRef]
36. Raphaëlle, P. Formulation and Durability of Metakaolin-Based Geopolymers. HAL Open SCIENCE. 2015; pp. 1–264. Available online: https://tel.archives-ouvertes.fr/tel-01297848/file/2015TOU30085.pdf (accessed on 19 March 2025).
37. Selmani, S.; Essaidi, N.; Gouny, F.; Bouaziz, S.; Joussein, E.; Driss, A.; Sdiri, A.; Rossignol, S. Physical–chemical characterization of Tunisian clays for the synthesis of geopolymers materials. *J. Afr. Earth Sci.* **2015**, *103*, 113–120. [CrossRef]
38. Essaidi, N. Discipline: Matériaux Céramiques et Traitements de Surface Najet ESSAIDI Le 12 Décembre 2013 Formulation de Liant Aluminosilicaté de Type Géopolymère à Base de Différentes Argiles Tunisiennes. 2013. Available online: https://cdn.unilim.fr/files/theses-doctorat/2013LIMO4030.pdf (accessed on 19 March 2025).
39. Zhang, Z.H.; Zhu, H.J.; Zhou, C.H.; Wang, H. Geopolymer from kaolin in China: An overview. *Appl. Clay Sci.* **2016**, *119*, 31–41. [CrossRef]
40. Luhar, I.; Luhar, S. A Comprehensive Review on Fly Ash-Based Geopolymer. *J. Compos. Sci.* **2022**, *6*, 219. [CrossRef]
41. Zeghichi, L.; Benalia, S. Les géopolymères: Matières premières et influence des paramètres de composition: A review. *J. Eng. Exact Sci.* **2023**, *9*, 18838. [CrossRef]
42. Hassen, M.A.; Benikhlef, Z.A. Synthés et Caractérisation de Liant Hydrauliques Présenté Par. Available online: https://dspace.univ-temouchent.edu.dz/bitstream/123456789/4990/1/inbound3408018541411183319-MahmoudAhmed.pdf (accessed on 19 March 2025).
43. Essaidi, N.; Samet, B.; Baklouti, S.; Rossignol, S. Feasibility of producing geopolymers from two different Tunisian clays before and after calcination at various temperatures. *Appl. Clay Sci.* **2014**, *88–89*, 221–227. [CrossRef]
44. Kouamo, H.T. Elaboration et Caractérisation de Ciments Géopolymères à Base de Scories Volcaniques. 2013. Available online: http://lopesphilippe.free.fr/CimentsGeopolymeresScoriesVolcaniquesTchakouteKouame2013.pdf (accessed on 19 March 2025).
45. Cheng-Yong, H.; Yun-Ming, L.; Al Bakri Abdullah, M.M.; Hussin, K. Thermal Resistance Variations of Fly Ash Geopolymers: Foaming Responses. *Sci. Rep.* **2017**, *7*, 45355. [CrossRef]
46. Alouani, M.E.L. Synthèse et Caractérisation des Matériaux Inorganiques de Type Géopolymères à Base de Cendres Volantes et de Métakaolin: Application en Génie de L'environnement et Génie Civil. Ph.D. Thesis, Université Mohammed V de Rabat, Rabat, Morocco, 2020.
47. Ren, X.; Wang, F.; He, X.; Hu, X. Resistance and durability of fly ash based geopolymer for heavy metal immobilization: Properties and mechanism. *RSC Adv.* **2024**, *14*, 12580–12592. [CrossRef]

Disclaimer/Publisher's Note: The statements, opinions and data contained in all publications are solely those of the individual author(s) and contributor(s) and not of MDPI and/or the editor(s). MDPI and/or the editor(s) disclaim responsibility for any injury to people or property resulting from any ideas, methods, instructions or products referred to in the content.

applied sciences

MDPI

Article

Waste Marble Slurry as Partial Substitution for Cement: Effect of Water-to-Cement Ratio

Zoi S. Metaxa [1,*], Sevasti Koryfidou [1], Lazaros Grigoriadis [1], Effrosyni Christodoulou [2], Athanasios Ekmektsis [2] and Athanasios C. Mitropoulos [1]

[1] Hephaestus Laboratory, School of Chemistry, Faculty of Sciences, Democritus University of Thrace, St. Luke, 65404 Kavala, Greece; sevikoryfidou@hotmail.com (S.K.); grigoriadis_l@yahoo.gr (L.G.); amitrop@chem.duth.gr (A.C.M.)

[2] Alexandros SA, 53 Mix. Karaoli St., 67100 Xanthi, Greece; frosi@alexandrosae.gr (E.C.); sakis@alexandrosae.gr (A.E.)

* Correspondence: zmetaxa@chem.duth.gr

Abstract: This study investigates the potential of waste marble slurry as a partial replacement for ordinary Portland cement, with particular emphases on the influence of the water-to-cement (w/c) ratio and the objectives of determining the effect of water content and the optimum marble slurry concentration. Cement pastes were prepared with three w/c ratios (0.3, 0.4, and 0.5) and five substitution levels of marble slurry (0%, 5%, 10%, 15%, and 20%). Workability was assessed through mini slump flow tests, while mechanical performance was evaluated via compressive and flexural mechanical tests. The initial and final setting times were also investigated. Electrical resistivity measurements, combined with X-ray diffraction (XRD), Fourier-transform infrared spectroscopy (FTIR), and scanning electron microscopy (SEM), were used to examine chemical composition and microstructure. Results showed that marble slurry behaves as an inert filler, rather than a reactive component. Its incorporation, up to 10%, significantly improves the fresh properties and mechanical performance of mixes with higher w/c ratios (0.4 and 0.5). At lower w/c ratios (0.3), strength was adversely affected due to insufficient hydration. Electrical resistivity measurements indicated that pastes with w/c = 0.5 and up to 10% slurry replacement became slightly more resistant to electrical current, whereas mixes with lower w/c ratios (0.3 and 0.4) showed only minor reductions at 5% and 10% cement substitution. SEM imaging demonstrated a denser microstructure when marble slurry was incorporated, consistent with a filler effect. Marble slurry was also found to accelerate the setting of cement pastes, an effect most evident at lower w/c ratios and higher substitution levels. Overall, the findings highlight that waste marble slurry can be effectively utilized at moderate replacement levels in cement-based materials, contributing to sustainable construction practices by reducing cement consumption and marble waste disposal.

Keywords: waste marble slurry; cement paste; partial replacement; workability; mechanical properties; electrical properties

1. Introduction

Waste marble slurry is an industrial by-product resulting from cutting, shaping, and polishing marble blocks. The generated slurry contains water, marble dust, and small pieces of steel from the water saw [1]. Typically, a rate of 20–25% marble waste slurry is produced, based upon the type of sawing and polishing operations [2–4]. Waste marble

slurry is treated to remove as much water as possible. The final product, called marble sludge, is collected, but due to the large quantities produced, storage by the marble industry is not feasible. As a result, this waste is discarded in nature, with controlled or uncontrolled access, causing considerable environmental hazards and health risks [5]. In particular, the porosity and permeability of soil are reduced in the area close to the deposited waste, something that has diverse effects on its morphology, hydrology, and fertility. Also, the waste marble sludge that is left in the environment air-dries and converts into a very fine dust [6], which becomes suspended in air and causes serious health problems, such as respiratory, visual, and skin disorders [7]. For these reasons, the recycling and utilization of waste marble are critical issues, both for environmental sustainability and for financial benefits. So far, marble waste has been used in various fields, such as paper, paint, plastic, glass, and agricultural production of animal feed and lime [5].

Cement is one of the most important materials in the construction industry. Nevertheless, its production is one of the most harmful industrial processes for the environment, because large volumes of CO_2 emissions are released in the atmosphere. According to various studies, 1 tone of clinker production emits 1 tone of CO_2 [8]; as a result, the cement industry is responsible for 7% of total CO_2 emissions globally [9]. Also, the raw materials that are used for the production of cement, such as lime, are depleted continuously, because of their extended utilization.

The construction industry could play a leading role in the reuse of marble waste, due to its scale and material demands. Most related existing studies have focused on the use of marble powder, which is obtained after drying and grinding the waste. Waste marble powder has been incorporated into conventional concrete [10–17], self-compacting concrete (SCC) [18–20], and polymer concrete [21–23]. In these applications, marble powder has been used as a partial replacement for cement, sand, or both, offering environmental, economic, and technical benefits [24].

Marble slurry, however, differs from both marble powder and marble sludge in its physical form and water content. Its direct utilization as a cement replacement in cement paste has been far less studied. It is important to distinguish between marble slurry and marble sludge: slurry refers to the wet suspension of marble particles and water generated during cutting and polishing, whereas sludge denotes the semi-dry residue obtained after dewatering the slurry. In this study, the term 'marble slurry' is used consistently, as the experimental work employed the wet form directly. Research has shown that the addition of marble slurry in a cement mixture may lead to a decrease in workability of fresh mixtures due to the higher surface area of the slurry particles [25–27]. Mechanical strength improvements are often reported up to cement replacement levels of around 10–15%, whereas higher dosages, beyond 20%, lead to strength reduction [28–30]. Reuse of waste marble slurry as is, without any processing, in construction materials as replacement for cement could lower CO_2 emissions, lessen the usage of raw materials that are in great demand, reduce the consumption of fossil fuels and power, offer economic advantages to cement industries, and increase the consumption of a waste material which would otherwise be discarded.

Although previous studies have explored the incorporation of marble waste powder or sludge, most investigations have focused either on its use as a fine aggregate replacement or on its general influence on mechanical properties. Limited attention has been paid to the role of the water-to-cement ratio in controlling the performance of cement pastes containing marble slurry, especially in relation to fresh state properties, mechanical performance, and physicochemical properties. In addition to conventional mechanical testing, electrical resistivity was included in this study to evaluate the pore structure and

matrix connectivity of cement pastes. Resistivity is widely recognized as an indicator of hydration progress, porosity, and durability in cementitious systems, and its correlation with mechanical strength provides additional insight into the microstructural effects of marble slurry incorporation.

The objective of the present study is to systematically examine the combined effects of water-to-cement (w/c) ratio and marble slurry substitution level on the performance of cement pastes. To this end, cement pastes were prepared with three w/c ratios (0.3, 0.4, and 0.5) and five substitution levels of marble slurry (0%, 5%, 10%, 15%, and 20%). This study was conducted at the paste level to provide fundamental insight into hydration behavior, filler effects, and microstructural modifications, without the additional complexity of aggregates. Paste testing enables identification of the intrinsic influences of marble slurry and w/c ratio on the binder matrix, which serves as a basis for future investigations on mortar and concrete systems. The fresh state, setting time, and mechanical, electrical, chemical, and microstructural properties were investigated through mini slump flow tests, Vicat apparatus, compressive and flexural strength testing, electrical resistivity assessments, X-ray diffraction (XRD), Fourier-transform infrared spectroscopy (FTIR), and scanning electron microscopy (SEM). By clarifying the role of marble slurry and identifying the optimum substitution levels under different w/c ratios, this study provides new insights into the effective utilization of marble slurry in sustainable cement-based materials.

2. Materials and Methods

2.1. Materials

The cementitious material used as binder was ordinary Portland cement, type CEM II 32.5R, with a relative density of 3.15 and conforming to ASTM C-150 [31] and EN-197-1/2011 [32]. Marble slurry was obtained as by-product from Democritus S.A., a marble industry located in Eastern Macedonia and Thrace (prefecture of Xanthi, Greece), which exclusively processes a single type of marble excavated in the Kavala region. Marble slurry, with a relative density of 2.75, came from the cutting, shaping, and polishing processes and was slightly air-dried. Samples were collected at different times and from different on-site disposal points of the Democritus S.A. facility, all derived from the same marble source, ensuring consistent material characteristics. The slurry was white in color and used in its wet form without further processing. Marble slurry was characterized to determine its moisture content, chemical structure, and chemical composition.

To determine the moisture content of the slurry, the samples were oven-dried at 150 °C until a constant weight was achieved, defined as the point at which two consecutive measurements yielded the same mass. Samples obtained during the same sampling event showed similar moisture contents. The by-products displayed very consistent values, ranging from 20.61% to 21.61%, with only minor fluctuations. The moisture content of marble slurry, i.e., the proportion of water it contains, is a characteristic factor of the material, as this water participates in the hydration of cement and must be considered when calculating concrete mix proportions.

FTIR spectra of marble slurry were obtained using a Perkin Elmer FT-IR/NIR spectrometer. The spectra were recorded in the wavelength range of 600–4000 cm^{-1}, with a resolution of 0.4 cm^{-1}. All measurements were performed at room temperature, and, to ensure reproducibility, at least three samples were examined. The typical transmittance spectrum of marble slurry is presented in Figure 1. As expected, the spectrum exhibits the typical features of calcium carbonate. In particular, distinct absorption peaks are observed at 1400–1405 cm^{-1}, 875–878 cm^{-1}, and 710–715 cm^{-1}, which are characteristic of the calcite structure.

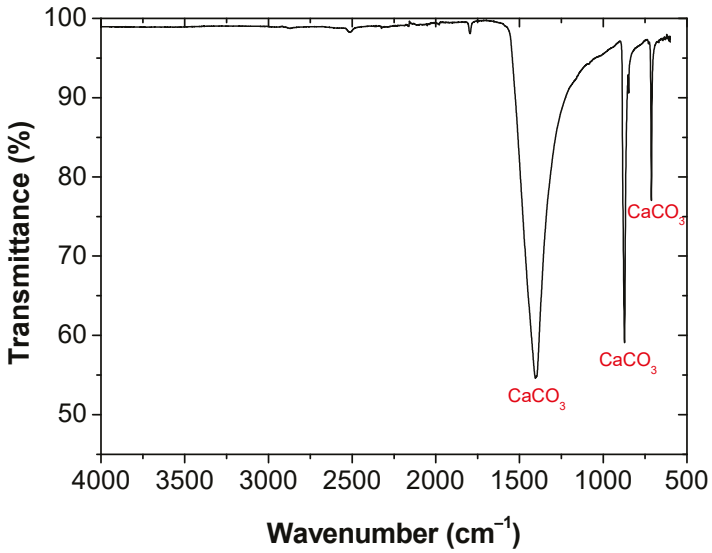

Figure 1. FTIR spectrum of marble slurry.

The chemical composition of marble slurry was investigated with X-ray diffraction (XRD). The analysis was carried out using a D8 FOCUS diffractometer (Bruker AXS GmbH, Karlsruhe, Germany), equipped with a nickel filter and operated at a scanning speed of 0.5 min^{-1}. The X-ray wavelength was Cu Kα radiation (λ = 1.5406 Å). The X-ray tube was operated at 40 kV and 40 mA. Prior to testing, to ensure proper sample preparation, marble by-products were dried and ground into a fine powder using a mortar, and then pressed into the sample holder. Phase identification was performed using the instrument's XRD software (DIFFRACplus XRD Commander V6.0) and its reference library (DIFFRAC.EVA V2.0). The XRD results for marble by-products are presented in Figure 2. The material was found to consist mainly of calcite crystalline phases, with a minor presence of dolomite, identified at 31.5° 2θ in low concentration.

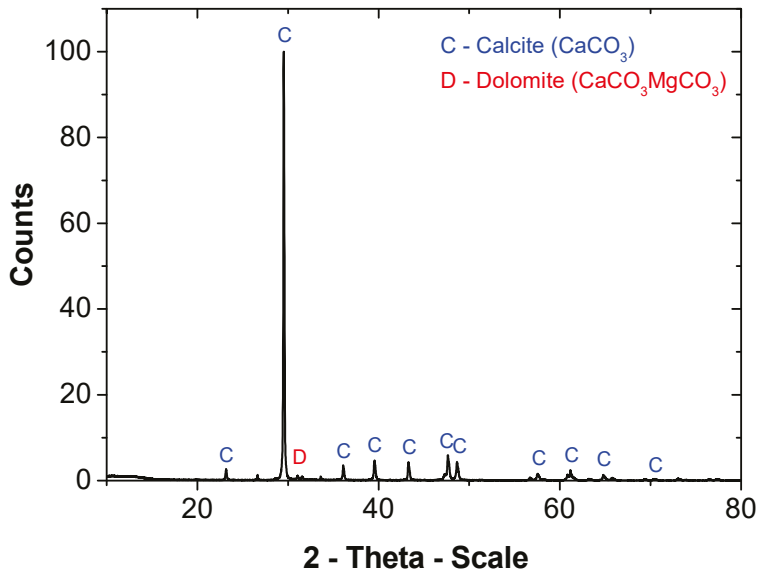

Figure 2. X-ray diffraction (XRD) results of marble by-products.

2.2. Mix Proportions

The experimental procedure of the present study was separated into 3 stages, with 15 cement paste mixes in total. Three water/cement proportions (0.3, 0.4, 0.5) were chosen

for each set of cement paste specimens. Replacement levels of marble slurry were 0%, 5%, 10%, 15%, and 20% by weight of binder for every group of samples. The marble slurry was used for substitution of the cement powder. To ensure that the targeted w/c ratios (0.3, 0.4, 0.5) were maintained, the water present in the slurry was accounted for in the mix design. Four mixtures of cement pastes with the addition of marble slurry, as well as the control mixture without marble slurry, were prepared for every experimental stage. The mix proportions of the different samples produced are provided in Table 1. The raw materials that were used are presented in Figure 3.

Table 1. Mix proportions of cement pastes.

Mix	Water/Cement Ratio	Substitution Ratio (%)	Cement (g)	Marble Slurry (g)	Water (g)
0.3-M0	0.3	0	600	0	180
0.3-M5	0.3	5	570	36.37	173.63
0.3-M10	0.3	10	540	72.74	167.26
0.3-M15	0.3	15	510	109.11	160.89
0.3-M20	0.3	20	480	145.48	154.52
0.4-M0	0.4	0	600	0	240
0.4-M5	0.4	5	570	36.37	233.63
0.4-M10	0.4	10	540	72.74	227.26
0.4-M15	0.4	15	510	109.11	220.89
0.4-M20	0.4	20	480	145.48	214.52
0.5-M0	0.5	0	600	0	300
0.5-M5	0.5	5	570	36.37	293.63
0.5-M10	0.5	10	540	72.74	287.26
0.5-M15	0.5	15	510	109.11	280.89
0.5-M20	0.5	20	480	145.48	274.52

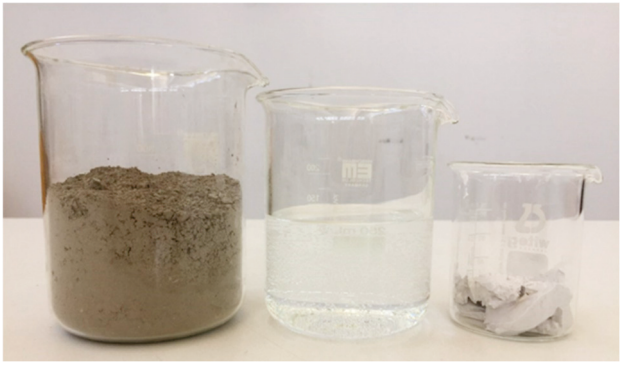

Figure 3. Raw materials: ordinary Portland cement (**left**), water (**middle**), and waste marble slurry (**right**).

2.3. Mixing, Casting, and Curing

Materials were mixed in a standard mixer to produce fresh cement paste specimens according to ASTM C305 [33]. The mixing materials used to prepare the cement paste composites are presented in Figure 3. In the case of control mixes, cement was placed in the mixer and water was added slowly. Afterwards, cement and water were left together for 30 s. Then, the mixer was turned on at low speed for another 30 s, after which the mixer was stopped to clean its internal surface, so as to achieve a better blend. Finally, the mixer was turned on again at high speed for 1 min. The same procedure was followed in the case of marble-blended cement pastes, with the only difference being that marble slurry was dissolved in the mixing water before entering the mixer. Immediately after

the end of mixing, the samples were cast in well-oiled molds. The molds were circular, with dimensions of 150 × 300 mm, and prismatic, with dimensions of 20 × 20 × 80 mm (Figure 4a,b). After 24 h, specimens were removed from the molds and cured in water saturated with calcium hydroxide (lime) at room temperature for 28 days, until testing.

(**a**) (**b**) (**c**)

Figure 4. Casting of cement paste specimens in (**a**) cylindrical and (**b**) prismatic molds and (**c**) with embedded grids for resistivity measurements.

2.4. Characterization Methods

A series of tests was carried out in order to investigate the fresh and hardened properties, such as workability, setting time and mechanical behavior, as well as the chemical and mineralogical compositions, of cement pastes with the incorporation of waste marble slurry. The workability of the fresh mixtures was tested using the mini slump flow test (Figure 5). The mini slump flow test was conducted on three replicate samples per mixture. To conduct the test, the standard metallic truncated cone, opened at both ends, was placed on a metallic plate and filled with material (Figure 5a), after which it was removed, and vibration was applied via 25 rotations in a period of 15 s. To calculate the workability, the diameters of the mixtures were measured at 3 different points (Figure 5b), and the average value was calculated.

(**a**) (**b**)

Figure 5. Flow test experimental setup: (**a**) test initiation and (**b**) test completion.

Initial and final setting times were determined according to EN 196-3 [34] using a Vicat apparatus (MATEST S.p.A., Arcore, Italy). Three replicate tests were performed for each mixture.

Compressive tests were conducted according to ASTM C39/C39M-20 [35] using a servo-hydraulic INSTRON 8801 Testing Device (Instron Corporation, Norwood, MA, USA). For each mixture, three cylindrical specimens (30 mm diameter × 60 mm height) were tested. A constant displacement rate of 0.25 mm/min was used. Load, displacement, and time were recorded during testing. The modulus of elasticity was calculated by setting the slope of the straight line in the stress–strain diagram. The compressive toughness was determined by calculating the area under the stress–strain curve up to a specific point (strain: 0.012 mm/mm). Results are reported as the average of three specimens.

Flexural strength was assessed by four-point bend testing on 20 × 20 × 80 mm prisms. The supporting distance was 70 mm, while the mechanical load was applied at two points, with a total distance of 35 mm, placed symmetrically with the specimen. A 10 kN MTS Insight load frame was used, and the measurements were performed by applying a constant displacement rate of 0.001 mm/sec. Three replicate specimens were tested per condition, and the average values are reported.

Electrical resistivity in cementitious materials can be measured using either non-destructive or intrusive electrical techniques. In this study, bulk resistance of hardened paste specimens was measured with a low-current, four-electrode configuration; under these conditions, the test is considered non-destructive because it does not alter the specimens. Microstructures of cement-based materials, such as pore size distribution and form of interconnections, define their durability and can be investigated through electrical resistivity tests [36–38]. In general, the denser the microstructure of a material is, the more resistant it is and, by extension, the better durability it has [39]. In the present study, a four-probe resistivity measurement technique was used. Immediately after mixing, four rectangular stainless steel electrodes were placed along the cross-sections of the samples, as presented in Figure 4c. After 24 h, the cement pastes were demolded and cured in water saturated with calcium hydroxide for 28 days, after which the samples were cleaned with tap water and dried in an oven at 80 °C for 72 h to remove the free water. Electrical resistance of the samples was measured using a 34450A Keysight Laboratory Digital Bench Multimeter (Keysight Technologies, Santa Rosa, CA, USA). During testing, the internal electrodes were used to record the voltage, while the external electrodes supplied the current. Measurements were recorded every 2 s over a period of 30 min to minimize deviations due to polarization effects. Resistance measurements were performed on three replicate specimens per mixture. Average values were calculated after stabilization. The average resistivity was then calculated according to Ohm's law, based on the mean resistance values obtained during the final five minutes of the measurement period. Calculated electrical resistivity is an intrinsic, geometry-independent property of a material that quantifies how readily an electrical current can flow through its structure [40].

A D8 FOCUS X-ray diffractometer (XRD) (Bruker AXS GmbH, Karlsruhe, Germany) with Ni filter, at a scan speed of 0.5 min^{-1}, was used in order to determine the crystalline phases present, as well as the hydration reactions in the cement paste/marble slurry specimens. The wavelength of X-rays used was Cu radiation, λ = 1.5406 Å. The X-ray tube was operated at 40 kV with 40 mA. After compressive testing, the broken pieces of the cement/marble samples were grinded to a fine powder with the help of a mortar and placed into the sample holder. Then, a slice of glass was placed on the sample holder to achieve a completely smooth surface. Subsequently, the sample holder was placed in the diffractometer and the analysis began. The analysis of the results was performed through the XRD software library.

Fourier-transform infrared (FTIR) spectra of cement pastes with various dosages of marble slurry were obtained using a Perkin Elmer FT-IR/NIR Spectrometer (PerkinElmer, Waltham, MA, USA). The IR spectra were displayed from 600 to 4000 cm^{-1}, at a resolution of 0.4 cm^{-1} at room temperature. The samples used were obtained after the compressive strength tests, in the form of crushed pieces, and grinded to a fine powder. Then, several milligrams of sample powder were placed on the diamond crystal, pressured with the swivel pressure tower, and scanned in order to produce the FTIR patterns. Microstructural analyses (XRD, FTIR) were performed on representative specimens of each mixture. Measurements were repeated on at least two samples to confirm reproducibility.

Fresh fractured samples of various concentrations of marble slurry and reference samples were coated with Chromium using a Quorum Q 150T ES Sputter Coater (Quorum Technologies Ltd., Laughton, East Sussex, UK). A Jeol 6390LV (JEOL Ltd., Tokyo, Japan) scanning electron microscope (SEM) was used. Spot size was set as 40, working distance was at 19.000, and magnification was displayed at 50 μm.

3. Results and Discussion

3.1. Workability

The workability of different mixtures is shown in Figure 6. As expected, the workability increases with increasing water-to-cement ratio (w/c). The results have shown high reputability with mostly minimal variations. In specimens with a w/c = 0.3, it is observed that, when the cement powder is replaced with up to 10% marble slurry, the workability of the material remains constant. In contrast, at higher replacement rates (15 and 20%) there is a decline, and then an increase in workability, which is accompanied by a higher standard deviation. The mixtures with w/c = 0.4 and 0.5 show similar behaviors. It is shown that, for replacement ratios up to 10%, the use of marble slurry for the replacement of cement does not affect the workability of the material. The introduction of higher contents of marble paste results in a slight reduction in workability, especially for water-to-cement ratios of 0.4 and 0.5.

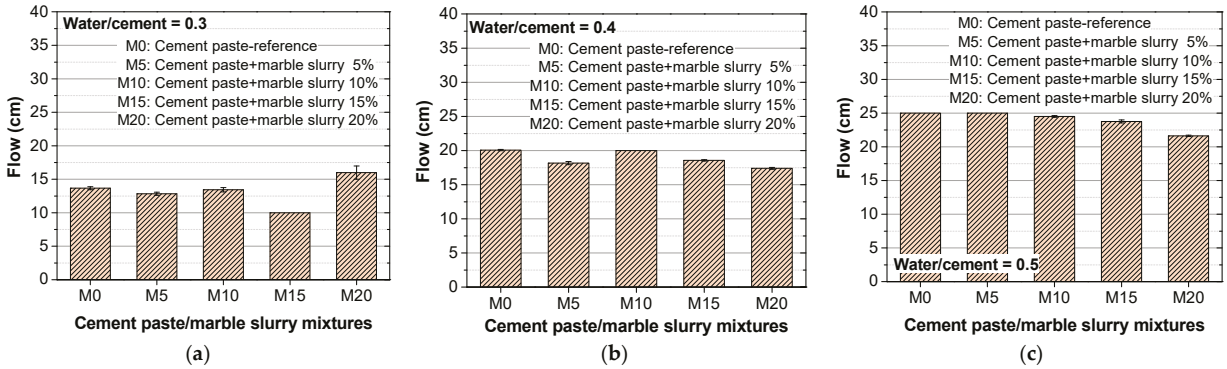

Figure 6. Flow values of cement paste mixtures with different marble slurry concentrations at water/cement ratios of (**a**) 0.3, (**b**) 0.4, and (**c**) 0.5.

To date, most of the research on the workability of cementitious composites with marble by-products have focused on the use of marble powder, rather than marble slurry, and on its effects on self-compacting concrete (SCC). Uysal and Yilmazh [41] have shown that the addition of marble powder has positive effects on the workability of SCC, especially at cement substitution levels of up to 20%. On the contrary, Shawki et al. [42] report that the addition of marble powder slightly decreases the workability of SCC.

In the present study, the results show that marble slurry, at a cement substitution level of up to 10%, does not alter workability, while higher replacement levels tend to slightly reduce flowability, particularly at conventional w/c ratios of 0.4 and 0.5. On the contrary, for w/c = 0.3 and 20% substitution, higher flow values were measured. This behavior may be explained by the balance between the filler effect and the increased water demand associated with the marble particles included in the slurry. At low replacement levels, up to 10% of cement, marble slurry acts primarily as a fine filler, improving particle packing and reducing interparticle friction. Beyond this threshold, however, possibly, the increased specific surface area and water demand of the marble slurry becomes more significant, reducing the amount of free water available for lubrication and, thereby, lowering slump

flow [15]. The slight recovery at 20% replacement and w/c = 0.3 may be attributed to localized segregation or variability in the slurry–water interaction, as reflected in the higher standard deviations.

3.2. Setting Time

The effects of marble slurry addition on the setting time of cement pastes are presented in Figure 7. As expected, both the initial and final setting times increased with higher w/c ratio, reflecting the higher water content available. For example, the control mixes showed final setting times of 202, 351, and 417 min for w/c = 0.3, 0.4, and 0.5, respectively.

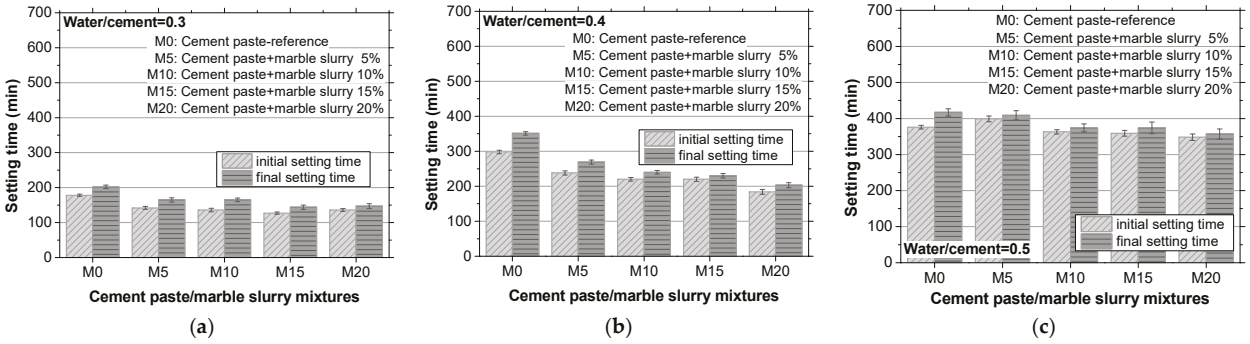

Figure 7. Initial and final setting times of cement paste mixtures with different marble slurry concentrations at water/cement ratios of (**a**) 0.3, (**b**) 0.4, and (**c**) 0.5.

At w/c = 0.3, the setting time decreases progressively with increasing marble slurry content. The final setting time ranges from 165 min at 5% to 147 min at 20% cement replacement with marble slurry. A maximum reduction of approximately 28% is observed with the incorporation of marble slurry at substitution levels of 15 to 20%. For w/c = 0.4, a similar reduction trend was observed, with the final setting time decreasing from 269 min at 5% substitution to 201 min at 20% substitution. At w/c = 0.5, the setting time also decreased with slurry incorporation, although the effect was less pronounced, from 409 min at 5% to 357 min at 20% cement replacement, representing a maximum reduction of approximately 14% compared to the control.

Reductions in the initial and final setting times of cement composites with marble powder and sludge have been reported previously [43–45]. There are two possible mechanisms that these reductions can be attributed to. The filler effect of marble slurry provides nucleation sites that accelerate the formation of hydration products. The calcite particles present in the slurry, as confirmed by XRD analysis, can act as nucleation sites for calcium silicate hydrate formation [44]. Additionally, the use of marble sludge has been shown to raise the water demand and subsequently lower the available free water in the paste [25]. The influence is strongest at low w/c ratios, where water is already limited, leading to more significant reductions in setting time, and less pronounced at higher w/c ratios, where additional water compensates for slurry demand. Overall, the results confirm that marble slurry accelerates the setting of cement pastes, particularly at lower w/c ratios, possibly due to its filler effect and increased water demand.

3.3. Mechanical Performance

3.3.1. Compressive Strength

The typical stress–crosshead displacement curves for all the samples tested, with water-to-cement ratios of 0.3, 0.4, and 0.5 at the age of 28 days, are illustrated in Figure 8. Comparing the results of the reference samples, it is observed that, as expected, the cement

paste specimens with a w/c = 0.3 display higher strength values compared to the specimens with w/c = 0.4 and w/c = 0.5. Control cement pastes with w/c = 0.3 demonstrate a compressive strength equal to 31.7 MPa, while the ones with w/c = 0.4 and w/c = 0.5 have compressive strengths equal to 30.8 MPa and 23.3 MPa, respectively. This happens due to the effect of water-to-cement ratio on the mechanical properties of cement-based products [46–48]. However, when marble slurry is added in the mixes, alterations are noticed considering the mechanical attributes of specimens.

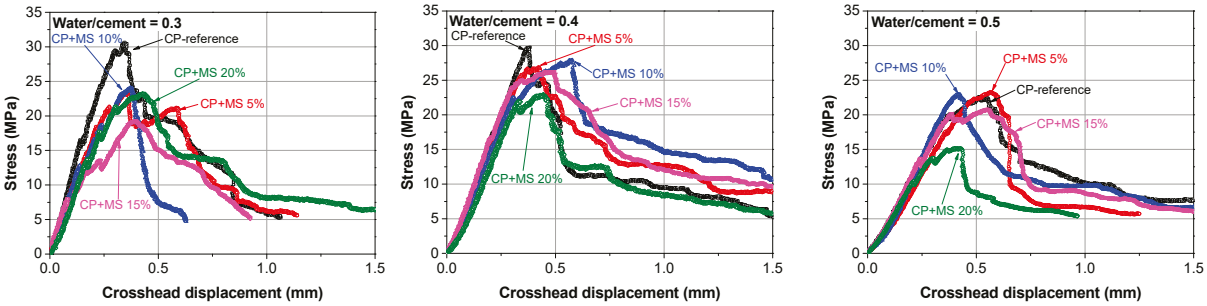

Figure 8. Stress–displacement curves of cement paste (CP) specimens with different marble slurry (MS) concentrations at water/cement ratios of (**a**) 0.3, (**b**) 0.4, and (**c**) 0.5.

The results of the average compressive strengths for different percentages of marble slurry replacement and different water-to-cement ratios are shown in Figure 9. Cement pastes with w/c = 0.3 displayed the highest performance regarding compressive strength of control samples. However, a decrease in the compressive strength was noticed when marble slurry was included as cement replacement. A reduction of approximately 28% occurred at a 5% substitution of cement with marble slurry. At 10% replacement, similar results were observed, with a 25% decrease in strength. Greater strength reduction was observed for cement paste specimens with 15% marble slurry, which was 47% lower compared to the control sample. Generally, the cement paste/marble slurry mixtures that were produced with w/c = 0.3 displayed lower compressive strength values compared to the control mix. Possibly, this occurs due to the limited amount of water used, which potentially obstructed the composite materials from being mixed properly.

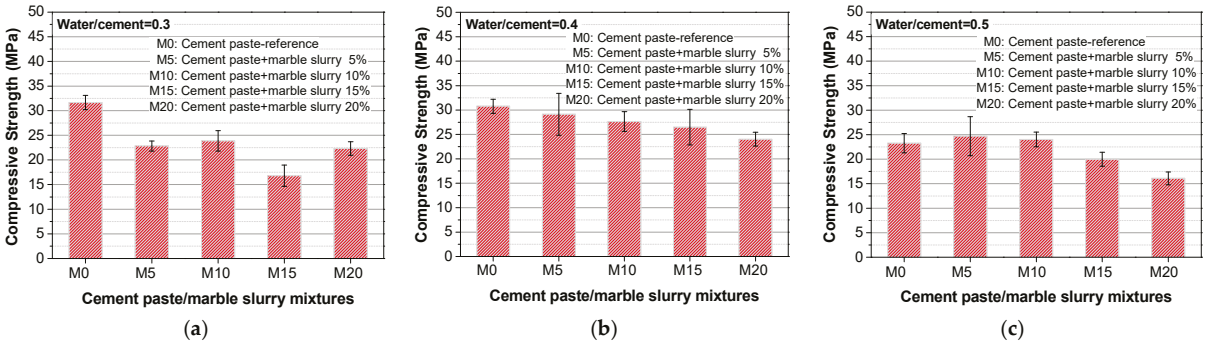

Figure 9. Compressive strengths of cement paste specimens with different marble slurry concentrations at w/c ratios of (**a**) 0.3, (**b**) 0.4, and (**c**) 0.5.

In the case of cement paste/marble slurry specimens with a w/c = 0.4, when 5% and 10% of marble slurry were added, the results are very similar to the reference samples, having a very slight reduction in strength, by 5.5% and 10%, respectively. Further decrease in compressive strength was noticed when the replacement level of marble slurry increased.

Particularly, 15% and 20% additions of marble slurry caused 14% and 22% strength decreases, respectively.

On the other hand, the mechanical results indicate that, at a w/c = 0.5, the compressive strength increases for a marble slurry replacement level up to 10%, and then it begins to decrease. In particular, 5% replacement of ordinary Portland cement with marble slurry leads to an increase in compressive strength of about 6%. Similarly, strength values increase by around 3% in the case of 10% replacement. This increase can possibly be attributed to a pore-filling effect of marble slurry, providing suitable nucleus for the development of hydration products [39]. The compressive strengths of cement pastes with the incorporation of marble slurry at 15% and 20% substitution ratios are decreased by almost 14% and 31% respectively, compared to the reference cement paste specimens. This decrease possibly happens due to a potential reduction in cementitious materials (C3S, C2S), which are responsible for the strength development of cement-based products [49]. This reduction is more intense for higher replacement levels of cement and is commonly known as the dilution of the pozzolanic reactions [50].

3.3.2. Modulus of Elasticity

The modulus of elasticity offers valuable information on the abilities of cement-based materials to deform elastically. The experimental results of the modulus of elasticity for the cement paste specimens with marble slurry at the age of 28 days are shown in Figure 10. The modulus of elasticity demonstrated was normalized by the average modulus of elasticity of the reference samples for each w/c ratio.

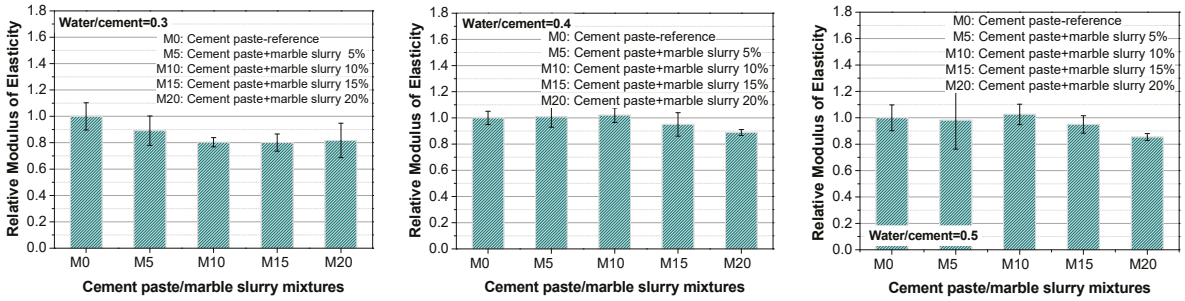

(**a**) (**b**) (**c**)

Figure 10. Modulus of elasticity of cement paste specimens with different marble slurry concentrations at w/c ratios of (**a**) 0.3, (**b**) 0.4, and (**c**) 0.5.

Cement paste specimens with w/c = 0.3 exhibit a gradual drop in elasticity values for all replacement levels of cement by marble slurry. In the case of samples with w/c = 0.4, the modulus of elasticity seems to be almost unaltered, with a slight increase until 10% substitution level of marble slurry compared to the control samples, but it decreases when further amounts of marble slurry are incorporated into the mixes. Considering cement pastes with various marble concentrations and w/c ratio equal to 0.5, the modulus of elasticity appears to have an increased trend up to 10% replacement level and declines for greater dosages of marble slurry (15% and 20%). It is observed that the modulus of elasticity results have close relations to the compressive strength results for all the different samples tested, as almost all the specimens displayed similar behaviors in both attributes [8].

3.3.3. Compressive Toughness

The results of the compressive toughness obtained at different replacement levels of cement by marble slurry and w/c ratios are presented in Figure 11. Starting from the samples with w/c

= 0.3, there is a gradual reduction in compressive toughness for all substitution levels against the control sample. This could be ascribed to the very low water content and, by extension, to the inadequate amount of cement for the composition of cement pastes. Considering cement paste specimens with w/c = 0.4, the compressive toughness remains almost unaltered until 10% replacement with marble slurry compared to the control samples. Above that level, a gradual decrease in the compressive toughness is noticed. In the case of samples with w/c = 0.5, compressive toughness slightly improved up to a 5% substitution level, but it decreased when further amounts of marble slurry were incorporated into the mixes. In general, the results show that there is a good correlation among the compressive toughness, modulus of elasticity, and compressive strength for the majority of the cement paste samples.

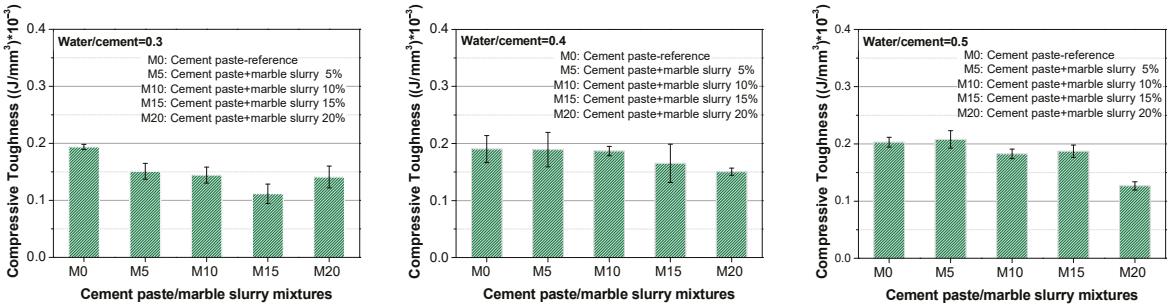

(**a**) (**b**) (**c**)

Figure 11. Compressive toughness of cement paste specimens with different marble slurry concentrations at w/c ratios of (**a**) 0.3, (**b**) 0.4, and (**c**) 0.5.

3.3.4. Flexural Strength

The results of the average flexural strength for different percentages of marble slurry replacement and different water-to-cement ratios are shown in Figure 12. The addition of marble slurry to the cement paste with w/c = 0.3 did not significantly affect the flexural strength of the specimens. All the different samples with marble slurry had flexural strengths of 1.6 MPa and above. The flexural strengths for different marble slurry replacement ratios for w/c = 0.4 were also quite stable. There is a slight deviation in the specimens for 10% replacement ratio (slightly reduced flexural strength), but the results are considered within the range of the standard deviation. In the case of a higher water-to-cement ratio (0.5) for low percentages of marble slurry replacement (e.g., 5% and 10%), a significant increase in flexural strength is shown, taking values of 2.4 and 2.2 MPa, respectively. The results of flexural strength are in absolute correspondence with those of compressive strength, where a similar relative increase in mechanical strength was observed. For higher marble slurry replacement rates, the flexural strengths are significantly reduced.

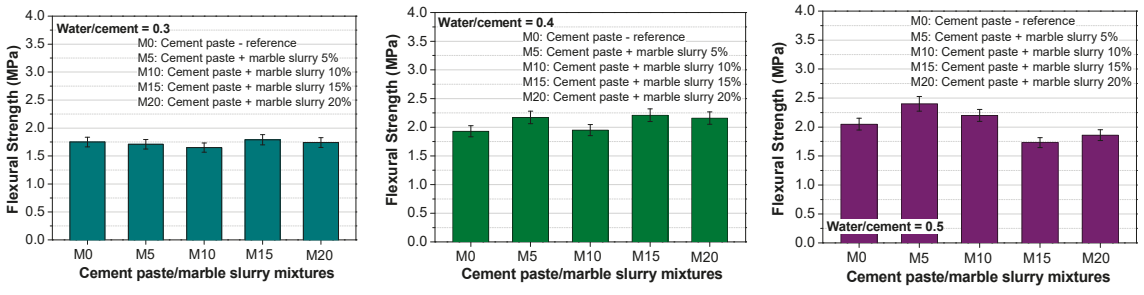

(**a**) (**b**) (**c**)

Figure 12. Flexural strengths of cement paste specimens with different marble slurry concentrations at w/c ratios of (**a**) 0.3, (**b**) 0.4, and (**c**) 0.5.

The influence of marble slurry on the mechanical properties of cement pastes becomes more pronounced under two conditions: at lower w/c ratios and at higher substitution levels. At low w/c ratio, the limited availability of water reduces the hydration potential of the system. When marble slurry is added, even in small amounts, the additional surface area further increases the water demand. As a result, the beneficial filler effect is not fully developed, and strength values decrease. This possibly explains why the reductions are sharper at lower than at higher ratios.

At higher slurry replacement levels ($\geq$15%), the dilution effect dominates across all w/c ratios. The reduction in cement content leads to fewer hydration products and weaker matrix formation. In addition, the interfacial transition zones (ITZs) around the inert marble particles may act as stress concentration sites, reducing stiffness and toughness. This explains the simultaneous declines in compressive strength, elastic modulus, and toughness observed at higher substitution levels. By contrast, at moderate marble slurry contents ($\leq$10%) and higher w/c ratios (0.5), the filler effect contributes to a denser microstructure, supporting the slight improvements observed in compressive and flexural strengths. Marble particles fill voids, refine pore connectivity, and possibly provide nucleation sites for hydration products, thereby supporting the modest increases observed in compressive and flexural strengths [25,44].

3.4. Electrical Resistivity

Figure 13 illustrates the electrical resistivity test results conducted on cement paste specimens with three w/c ratios (0.3, 0.4, 0.5) and various replacement levels of marble slurry (0%, 5%, 10%, 15%, 20%). For comparison purposes, relative electrical resistivity values are reported. It can be observed that the two mixes (w/c = 0.3, w/c = 0.4) present decreased tendencies in electrical resistivity with the incorporation of marble slurry, compared to control samples without marble. However, these reductions are very slight for replacement levels 5% and 10%. On the other hand, the resistivity values are slightly increased for up to 10% replacement levels in the case of cement paste mix with w/c = 0.5 (Figure 13c). The electrical resistivity results can be directly correlated with the observed mechanical performance. Slightly higher resistivity values, as measured in mixes with w/c = 0.5 and up to 10% slurry replacement, indicate possible reductions in the porosity by filling the voids and reducing the interconnections of the pore structure [39,51]. As a result, the composites become slightly denser and more resistant in the electrical current. This also corresponds to the observed improvement in the compressive and flexural strengths at these replacement levels and w/c ratio. Conversely, the reduced resistivity observed at lower w/c ratios (0.3 and 0.4) suggests that slurry addition possibly increases the porosity, which is consistent with the slight reduction in strength under these conditions. This correlation confirms that resistivity is a reliable indicator of microstructural refinement and mechanical performance [3,7].

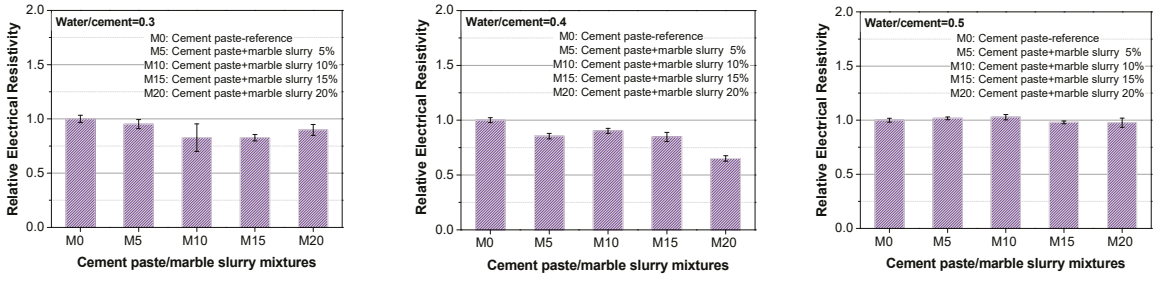

(**a**) (**b**) (**c**)

Figure 13. Relative electrical resistivity of cement paste specimens with different marble slurry concentrations at w/c ratios of (**a**) 0.3, (**b**) 0.4, and (**c**) 0.5.

3.5. X-Ray Diffraction Analysis

X-ray diffraction tests were conducted on control samples with 0% marble slurry and samples with various marble concentrations (5%, 10%, 15%, and 20%). This process was carried out for every water-to-cement ratio (0.3, 0.4, and 0.5) tested. The purpose of XRD analysis was to investigate whether or not marble slurry participates in the chemical reactions that take place during the hydration process. XRD spectra of the mixtures of cement pastes with marble slurry for w/c = 0.3, 0.4, and 0.5 are presented in Figure 14. The major peaks that are recognized are of calcite, calcium hydroxide (portlandite), ettringite, and calcium silicate hydrate. XRD analysis of cement pastes after 28 days of curing demonstrated that there is no noticeable difference among the investigated samples. This is evident for all the w/c ratios studied. Some minor alterations in the intensity of the hydration products (C2S), (C3S), and $Ca(OH)_2$ can be observed as the replacement ratio of marble slurry increases, something that could possibly be attributed to the higher necessity of water for higher substitution levels of marble [3]. On the other hand, there is a slight increase in the proportion of calcite as the substitution percentage of marble increases, due to the calcium content of the marble slurry [52]. All in all, it is clear that marble slurry is an inert material and does not contribute to the chemical processes that occur throughout the hydration of the cement paste [7,51–53].

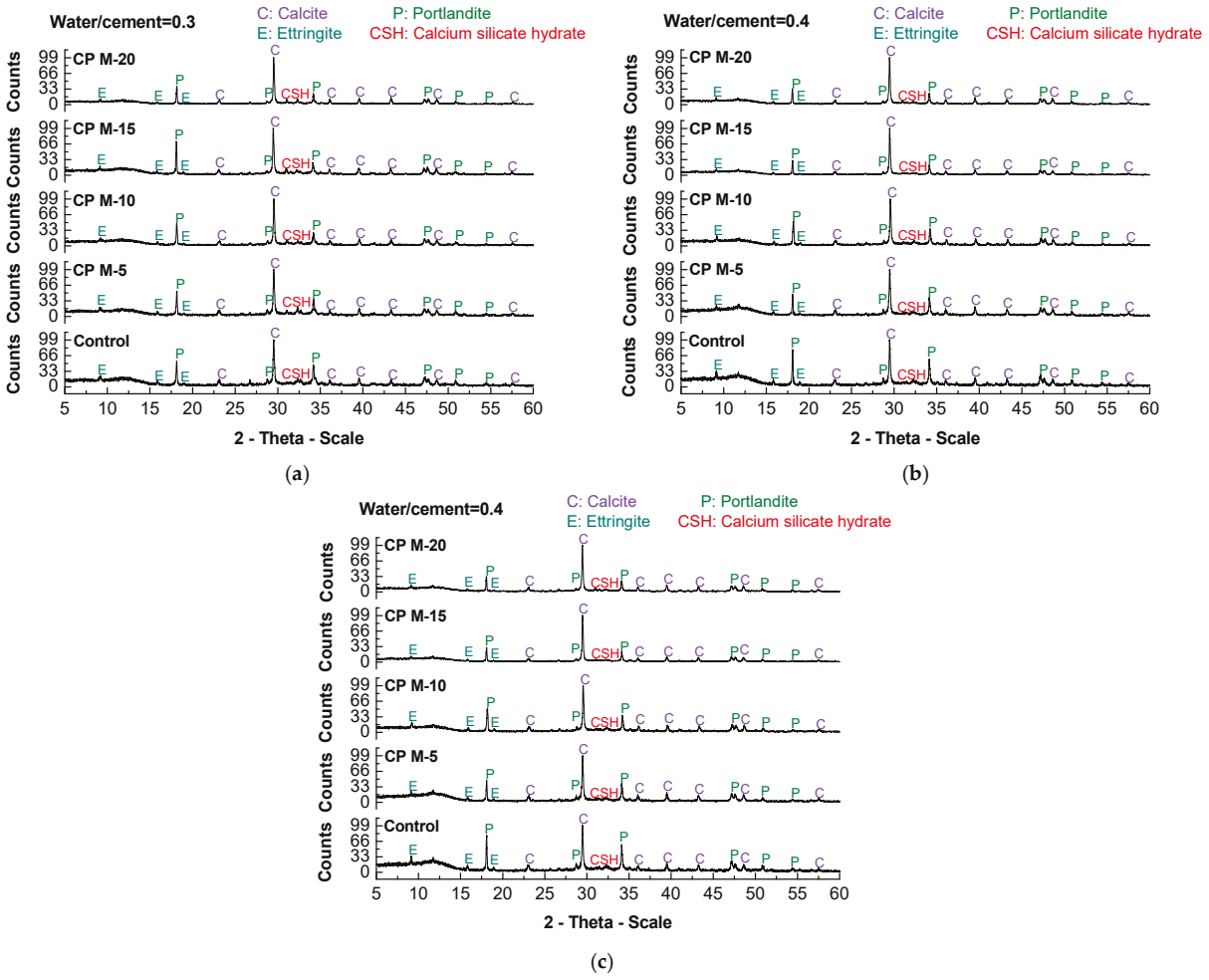

Figure 14. XRD patterns of cement paste specimens with different marble slurry concentrations at w/c ratios of (**a**) 0.3, (**b**) 0.4, and (**c**) 0.5.

3.6. Fourier-Transform Infrared Spectroscopy Analysis

Infrared spectroscopy (IR) was used in order to investigate the molecular structures and characterize the chemical classes of materials qualitatively and quantitatively. The frequencies of waves measured by IR can offer information about the silicate, sulphate, and carbonate phases [54]. IR spectra of cement pastes without marble slurry (control), as well as cement pastes with different marble concentrations (5%, 10%, 15%, and 20%), for the three water-to-cement ratios (0.3, 0.4, and 0.5) are presented in Figure 15. Seven principal bands have been identified for cement paste samples, which were identical across all spectra, showing only minor variations in peak intensity. Starting from the left, the peak at around 3642 cm^{-1} corresponds to the internal hydroxyl group in Portlandite ($Ca(OH)_2$), which is formed while silicate phases of cement disintegrate to form calcium silicate hydrate (C-S-H) phases during hydration. The broad peak close to 1650 cm^{-1} is associated with O-H stretch of forcefully polarized H-bonded water, related to cementitious minerals. The peaks at approximately 1415 cm^{-1}, 874 cm^{-1}, and 712 cm^{-1} represent CO_3^{2-} bands which occur due to C–O stretch of $CaCO_3$. Characteristic sulphate absorption bands are visible near to 1113 cm^{-1}, due to the vibration of the SO_4^{2-} group in sulphates. A last peak, at 960 cm^{-1}, is referred to as the SiO_4^{4-} band, caused by Si-O stretch, basically signifying C–S–H gel and other silicate phases [54]. In general, supplementary powder materials that participate in hydration reactions can cause shifts in the characteristic absorption peaks of cement pastes. However, in the present study, no such shifts were observed. The spectra of all mixtures remained essentially unchanged, confirming that marble slurry acts as an inert filler and does not chemically participate in the hydration process.

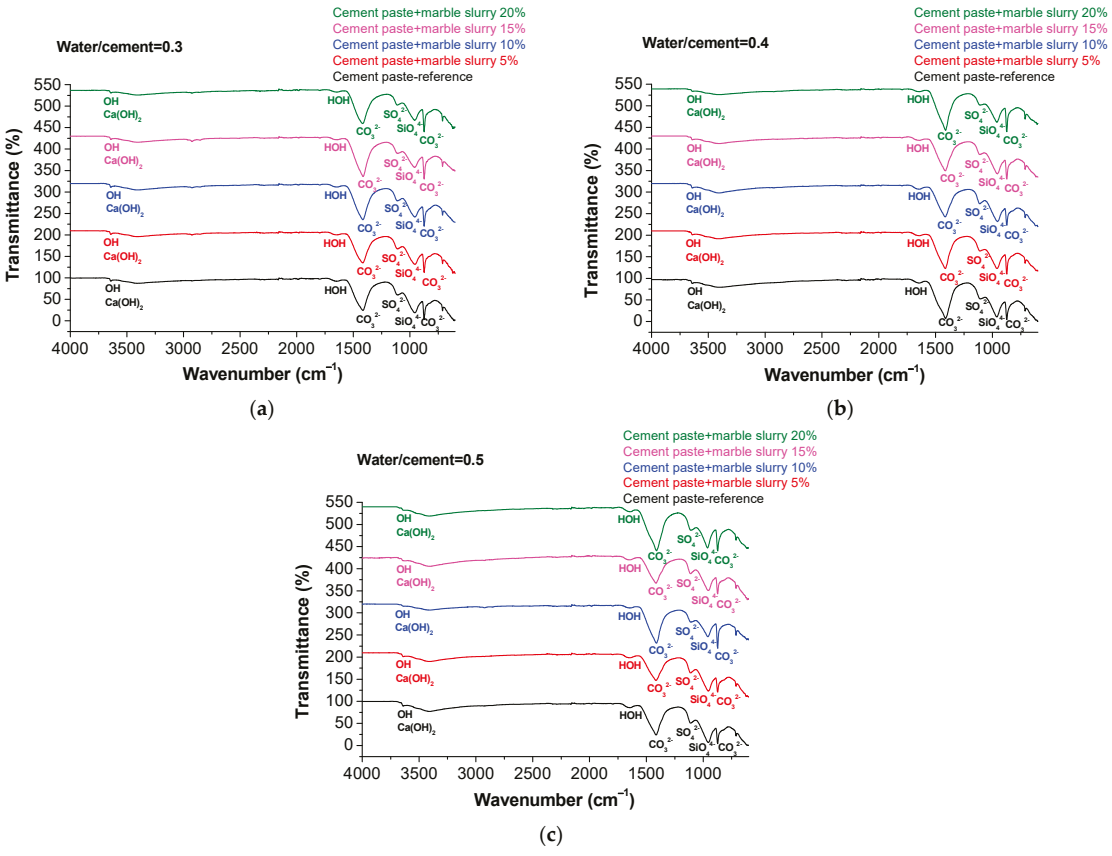

Figure 15. FTIR patterns of cement paste specimens with different marble slurry concentrations at w/c ratios of (**a**) 0.3, (**b**) 0.4, and (**c**) 0.5.

3.7. Microscopy Analysis

Scanning Electron Microscopy (SEM) micrographs of cement pastes including marble slurry as a replacement of cement at 10% and 20% substitution levels, and reference cement paste with 0% marble slurry, are shown in Figure 16. Fresh fractured surfaces of cement paste samples were examined, considering their microstructure at the age of 28 days. It should be noted that the SEM images presented in this study were obtained at 450× magnification. While this level of magnification does not allow for detailed visualization of hydration products, it provides useful information on the general morphology of the cement matrix. SEM images of cement pastes with the incorporation of marble slurry indicate that their structures are less porous compared to control cement paste. The capillary pores, visible in specimens without marble slurry, are decreased significantly as the replacement of cement by waste marble slurry increases up to the 10% replacement level. Pore volume reduction likely happens due to the filling property of marble, which fills the voids and results in a denser microstructure [51]. This leads to enhanced durability and strength in cement pastes.

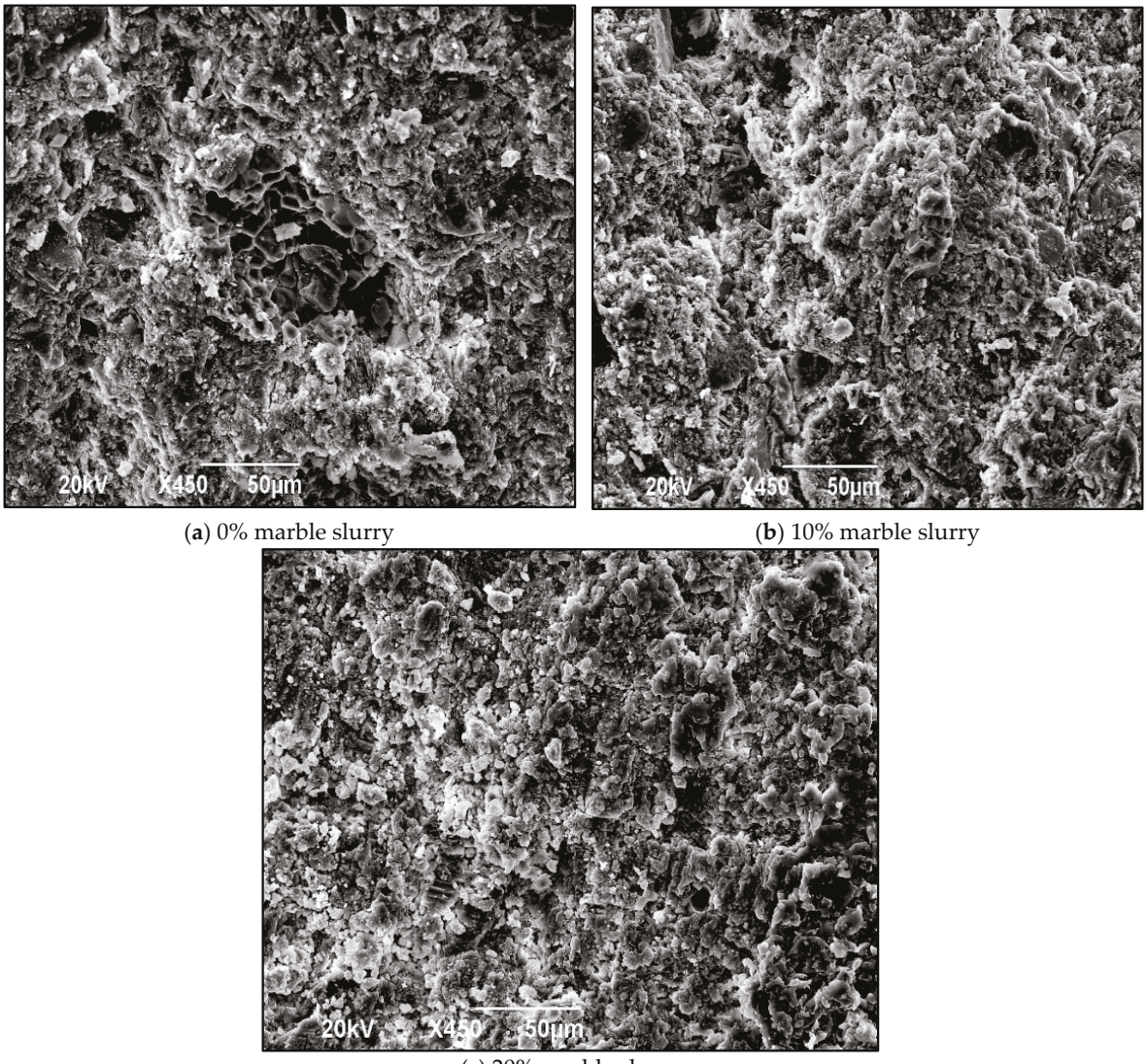

(**a**) 0% marble slurry (**b**) 10% marble slurry

(**c**) 20% marble slurry

Figure 16. SEM micrographs of cement paste specimens with different marble slurry concentrations (w/c = 0.5), namely (**a**) 0%, (**b**) 10%, and (**c**) 20% marble slurry concentrations.

4. Conclusions

This study investigated the partial replacement of cement with waste marble slurry in cement pastes at different w/c ratios (0.3, 0.4, 0.5) and substitution levels (0–20%). The following conclusions can be drawn:

1. Workability results showed that marble slurry, at substitution levels up to 10%, has minimal influence on the flowability of cement pastes, while higher replacement levels slightly reduce workability, especially at w/c ratios of 0.4 and 0.5.
2. Initial and final setting times of cement pastes are reduced with the incorporation of marble slurry, with the effect being most pronounced at lower w/c ratios and higher substitution levels. This acceleration could be attributed to the combined actions of the marble slurry particle filler effect and increased water demand.
3. At w/c = 0.5, compressive and flexural strengths, modulus of elasticity, and toughness improve at moderate marble slurry substitution levels ($\leq$10%). At w/c = 0.4, changes are minor up to 10% substitution, with reductions at higher cement substitution levels. At w/c = 0.3, all three properties decline with slurry addition, reflecting the limited water available for hydration.
4. Electrical resistivity trends were consistent with the mechanical results, confirming the link between microstructural refinement at moderate slurry levels and improved performance.
5. Microstructural analysis (XRD, FTIR, SEM) confirmed that marble slurry is chemically inert, acting as a filler that enhances particle packing at moderate contents.

Overall, marble slurry is not recommended for low w/c ratios (<0.4), but up to 10% substitution at higher w/c ratios improves both fresh and hardened properties. As an inert material, its effects are mainly physical, enhancing packing and pore refinement, rather than chemical reactivity. Thus, marble slurry can be effectively utilized in cementitious systems at moderate levels, supporting sustainability by reducing cement consumption, lowering CO_2 emissions, and utilizing marble industry waste. Future work should extend these findings to mortars and concretes to evaluate combined effects with aggregates.

Author Contributions: Conceptualization, A.E. and E.C.; methodology, Z.S.M. and A.C.M.; investigation, Z.S.M., S.K., L.G. and E.C.; resources, A.E.; writing—original draft preparation, Z.S.M., S.K. and L.G.; writing—review and editing, Z.S.M., E.C. and A.E.; supervision, A.E. and A.C.M.; project administration, A.E.; funding acquisition, A.E. All authors have read and agreed to the published version of the manuscript.

Funding: This research has been co-financed by the European Regional Development Fund of the European Union and Greek national funds through the Operational Program East Macedonia and Thrace 2014–2020: 'Investment innovation plans for research and development for companies in the quarrying sector' (project code: MIS5034823).

Institutional Review Board Statement: Not applicable.

Informed Consent Statement: Not applicable.

Data Availability Statement: The raw data supporting the conclusions of this article will be made available by the authors on request.

Conflicts of Interest: Authors Effrosyni Christodoulou and Athanasios Ekmektsis were employed by the company Alexandros SA. The remaining authors declare that the research was conducted in the absence of any commercial or financial relationships that could be construed as a potential conflict of interest.

References

1. Anwar, A.; Ahmad, J.; Khan, M.A.; Ahmad, S.; Ahmad, S.A. Study of compressive strength of concrete by partial replacement of cement with marble dust powder. *Int. J. Curr. Eng. Technol.* **2014**, *4*, 4162–4166.
2. Aruntaş, H.Y.; Gürü, M.; Dayı, M.; Tekin, İ. Utilization of waste marble dust as an additive in cement production. *Mater. Des.* **2010**, *31*, 4039–4042. [CrossRef]
3. Aliabdo, A.A.; Abd Elmoaty, M.; Auda, E.M. Re-use of waste marble dust in the production of cement and concrete. *Constr. Build. Mater.* **2014**, *50*, 28–41. [CrossRef]
4. Gesoğlu, M.; Güneyisi, E.; Kocabağ, M.E.; Bayram, V.; Mermerdaş, K. Fresh and hardened characteristics of self-compacting concretes made with combined use of marble powder, limestone filler, and fly ash. *Constr. Build. Mater.* **2012**, *37*, 160–170. [CrossRef]
5. Demirel, B.; Alyamaç, K.E. Waste marble powder/dust. In *Waste and Supplementary Cementitious Materials in Concrete*; Elsevier: Amsterdam, The Netherlands, 2018; pp. 181–197.
6. Sarkar, R.; Das, S.K.; Mandal, P.K.; Maiti, H.S. Phase and microstructure evolution during hydrothermal solidification of clay–quartz mixture with marble dust source of reactive lime. *J. Eur. Ceram. Soc.* **2006**, *26*, 297–304. [CrossRef]
7. Vardhan, K.; Goyal, S.; Siddique, R.; Singh, M. Mechanical properties and microstructural analysis of cement mortar incorporating marble powder as partial replacement of cement. *Constr. Build. Mater.* **2015**, *96*, 615–621. [CrossRef]
8. Khodabakhshian, A.; De Brito, J.; Ghalehnovi, M.; Shamsabadi, E.A. Mechanical, environmental and economic performance of structural concrete containing silica fume and marble industry waste powder. *Constr. Build. Mater.* **2018**, *169*, 237–251. [CrossRef]
9. Naik, T.R.; Moriconi, G. Environmental-friendly durable concrete made with recycled materials for sustainable concrete construction. In Proceedings of the International Symposium on Sustainable Development of Cement, Concrete and Concrete Structures, Toronto, ON, Canada, 5–7 October 2005; Volume 5.
10. Demirel, B. The effect of the using waste marble dust as fine sand on the mechanical properties of the concrete. *Int. J. Phys. Sci.* **2010**, *5*, 1372–1380.
11. Arel, H.Ş. Recyclability of waste marble in concrete production. *J. Clean. Prod.* **2016**, *131*, 179–188. [CrossRef]
12. Mangi, S.A.; Raza, M.S.; Khahro, S.H.; Qureshi, A.S.; Kumar, R. Recycling of ceramic tiles waste and marble waste in sustainable production of concrete: A review. *Environ. Sci. Pollut. Res. Int.* **2022**, *29*, 18311–18332. [CrossRef]
13. Babouri, L.; Biskri, Y.; Khadraoui, F.; El Mendili, Y. Mechanical performance and corrosion resistance of reinforced concrete with marble waste. *Eur. J. Environ. Civ. Eng.* **2022**, *26*, 4112–4129. [CrossRef]
14. Hou, W.; Zhang, Q.; Zhuang, Z.; Zhang, Y. Sustainable reusing marble powder and granite powder in cement-based materials: A review. *ACS Sustain. Chem. Eng.* **2024**, *12*, 2484–2510. [CrossRef]
15. Abbas, M.M.; Muntean, R. Marble powder as a sustainable cement replacement: A review of mechanical properties. *Sustainability* **2025**, *17*, 736. [CrossRef]
16. Ramteke, J.; Rathore, K.; Supe, J.D. Green concrete incorporating industrial waste and E-waste: A review of compressive strength, CO_2 emissions, and replacement levels. *Asian J. Civ. Eng.* **2025**, *26*, 1881–1906. [CrossRef]
17. Moolchandani, K. Industrial byproducts in concrete: A state-of-the-art review. *Next Mater.* **2025**, *8*, 100593. [CrossRef]
18. Alyamaç, K.E.; İnce, R. Study on the usability of waste marble mud in self-compacting concrete as a powder material. In *Proceedings of the TÇMB Third International Symposium*; Turkish Cement Manufacturers' Association: Ankara, Turkey, 2007; pp. 821–832.
19. Kore, S.D.; Vyas, A.K.; Kabeer, S.A.K.I. A brief review on sustainable utilisation of marble waste in concrete. *Int. J. Sustain. Eng.* **2020**, *13*, 73–84. [CrossRef]
20. Prakash, B.; Saravanan, T.J.; Kabeer, K.I.S.A.; Bisht, K. Exploring the potential of waste marble powder as a sustainable substitute to cement in cement-based composites: A review. *Constr. Build. Mater.* **2023**, *401*, 132887. [CrossRef]
21. Tawfik, M.E.; Eskander, S.B. Polymer concrete from marble wastes and recycled poly(ethylene terephthalate). *J. Elastomers Plast.* **2006**, *38*, 65–79. [CrossRef]
22. Solouki, A.; Viscomi, G.; Lamperti, R.; Tataranni, P. Quarry waste as precursors in geopolymers for civil engineering applications: A decade in review. *Materials* **2020**, *13*, 3146. [CrossRef]
23. Metwally, G.A.M.; Elemam, W.E.; Mahdy, M.; Ghannam, M. A comprehensive review of metakaolin-based ultra-high-performance geopolymer concrete enhanced with waste material additives. *J. Build. Eng.* **2025**, *103*, 112019. [CrossRef]
24. Singh, M.; Choudhary, K.; Srivastava, A.; Sangwan, K.S.; Bhunia, D. A study on environmental and economic impacts of using waste marble powder in concrete. *J. Build. Eng.* **2017**, *13*, 87–95. [CrossRef]
25. Rashwan, M.A.; Al-Basiony, T.M.; Mashaly, A.O.; Khalil, M.M. Behaviour of fresh and hardened concrete incorporating marble and granite sludge as cement replacement. *J. Build. Eng.* **2020**, *32*, 101697. [CrossRef]

26. Ahmad, J.; Zaid, O.; Shahzaib, M.; Abdullah, M.U.; Ullah, A.; Ullah, R. Mechanical properties of sustainable concrete modified by adding marble slurry as cement substitution. *AIMS Mater. Sci.* **2021**, *8*, 166–185. [CrossRef]
27. Verma, P.; Kumar, R.; Mukherjee, S.; Sharma, M. Sustainable self-compacting concrete with marble slurry and fly ash: Statistical modeling, microstructural investigations, and rheological characterization. *J. Build. Eng.* **2024**, *94*, 109785. [CrossRef]
28. Prošek, Z.; Nežerka, V.; Tesárek, P. Enhancing cementitious pastes with waste marble sludge. *Constr. Build. Mater.* **2020**, *255*, 119372. [CrossRef]
29. Allam, M.E.; Amin, S.K.; Garas, G. Testing of cementitious roofing tile specimens using marble waste slurry. *Int. J. Sustain. Eng.* **2020**, *13*, 151–157. [CrossRef]
30. Siddique, S.; Jang, J.G.; Gupta, T. Developing marble slurry as supplementary cementitious material through calcination: Strength and microstructure study. *Constr. Build. Mater.* **2021**, *293*, 123474. [CrossRef]
31. *ASTM C150/C150M-18*; Standard Specification for Portland Cement. ASTM International: West Conshohocken, PA, USA, 2018. [CrossRef]
32. *EN 197-1*; Cement—Part 1: Composition, Specifications and Conformity Criteria for Common Cements. European Committee for Standardization: London, UK, 2011.
33. *ASTM C305-20*; Standard Practice for Mechanical Mixing of Hydraulic Cement Pastes and Mortars of Plastic Consistency. ASTM International: West Conshohocken, PA, USA, 2020.
34. *EN 196-3*; Methods of Testing Cement—Part 3 Determination of Setting Time and Soundness. Comité Européen de Normalisation: Brussels, Belgium, 2016.
35. *ASTM C39/C39M-20*; Standard Test Method for Compressive Strength of Cylindrical Concrete Specimens. ASTM International: West Conshohocken, PA, USA, 2020.
36. Tang, S.W.; Cai, R.J.; He, Z.; Cai, X.H.; Shao, H.Y.; Li, Z.J.; Yang, H.M.; Chen, E. Continuous microstructural correlation of slag/superplasticizer cement pastes by heat and impedance methods via fractal analysis. *Fractals* **2017**, *25*, 1740003. [CrossRef]
37. Liao, Y.; Wang, S.; Qunaynah, S.A.; Wan, S.; Yuan, Z.; Xu, P.; Tang, S. Hydration behavior and thermodynamic modelling of ferroaluminate cement blended with steel slag. *J. Build. Eng.* **2024**, *97*, 110833. [CrossRef]
38. Liao, Y.; Wang, S.; Qunaynah, S.A.; Tang, S. A study on the hydration of calcium aluminate cement pastes containing silica fume using non-contact electrical resistivity measurement. *J. Build. Eng.* **2023**, *24*, 8135–8149.
39. Khodabakhshian, A.; Ghalehnovi, M.; De Brito, J.; Shamsabadi, E.A. Durability performance of structural concrete containing silica fume and marble industry waste powder. *J. Clean. Prod.* **2018**, *170*, 42–60. [CrossRef]
40. Akinlabi, E.T.; Mahamood, R.M. *Solid-State Welding: Friction and Friction Stir Welding Processes*; Springer: Cham, Switzerland, 2020; ISBN 978-3-030-37015-2.
41. Uysal, M.; Yilmaz, K. Effect of mineral admixtures on properties of self-compacting concrete. *Cem. Concr. Compos.* **2011**, *33*, 771–776. [CrossRef]
42. Shawki, M.A.; Elnemr, A.; Koenke, C.; Aboul-Fotouh, S.; Shoukry, H.; Koenders, E. Rheological properties of high-performance SCC using recycled marble powder. *Innov. Infrastruct. Solut.* **2024**, *9*, 176. [CrossRef]
43. Mashaly, A.O.; El-Kaliouby, B.A.; Shalaby, B.N.; El-Gohary, A.M.; Rashwan, M.A. Effects of Marble Sludge Incorporation on the Properties of Cement Composites and Concrete Paving Blocks. *J. Clean. Prod.* **2016**, *112*, 731–741. [CrossRef]
44. Kırgız, M.S. Fresh and Hardened Properties of Green Binder Concrete Containing Marble Powder and Brick Powder. *Eur. J. Environ. Civ. Eng.* **2016**, *20*, S64–S101. [CrossRef]
45. Biricik, Ö.; Aytekin, B.; Mardani, A. Effect of Waste Binder Material Usage Rate on Thixotropic Behaviour of Cementitious Systems. *Constr. Build. Mater.* **2023**, *403*, 133197. [CrossRef]
46. Apebo, N.S.; Shiwua, A.J.; Agbo, A.P.; Ezeokonkwo, J.C.; Adeke, P.T. Effect of water–cement ratio on the compressive strength of gravel-crushed over burnt bricks concrete. *Civ. Environ. Res.* **2013**, *3*, 74–81.
47. Varma, M.B. Effect of change in water–cement ratio on wet density, dry density, workability and compressive strength of M-20 grade concrete. *Int. J. Eng. Res.* **2015**, *5*, 43–59.
48. Hranice, C. The effect of water ratio on microstructure and composition of the hydration products of Portland cement pastes. *Ceram.–Silik.* **2002**, *46*, 152–158.
49. Singh, J.; Bansal, R.S. Partial replacement of cement with waste marble powder with M25 grade. *Int. J. Tech. Res. Appl.* **2015**, *3*, 202–205.
50. Ergün, A. Effects of the usage of diatomite and waste marble powder as partial replacement of cement on the mechanical properties of concrete. *Constr. Build. Mater.* **2011**, *25*, 806–812. [CrossRef]
51. Singh, M.; Srivastava, A.; Bhunia, D. An investigation on effect of partial replacement of cement by waste marble slurry. *Constr. Build. Mater.* **2017**, *134*, 471–488. [CrossRef]

52. Ashish, D.K. Feasibility of waste marble powder in concrete as partial substitution of cement and sand amalgam for sustainable growth. *J. Build. Eng.* **2018**, *15*, 236–242. [CrossRef]
53. Ashish, D.K.; Verma, S.K.; Kumar, R.; Sharma, N. Properties of concrete incorporating sand and cement with waste marble powder. *Adv. Concr. Constr.* **2016**, *4*, 145–160. [CrossRef]
54. Hanna, R.A.; Barrie, P.J.; Cheeseman, C.R.; Hills, C.D.; Buchler, P.M.; Perry, R. Solid state 29Si and 27Al NMR and FTIR study of cement pastes containing industrial wastes and organics. *Cem. Concr. Res.* **1995**, *25*, 1435–1444. [CrossRef]

Disclaimer/Publisher's Note: The statements, opinions and data contained in all publications are solely those of the individual author(s) and contributor(s) and not of MDPI and/or the editor(s). MDPI and/or the editor(s) disclaim responsibility for any injury to people or property resulting from any ideas, methods, instructions or products referred to in the content.

applied sciences

MDPI

Article

Integrated Digital Twin and BIM Approach to Minimize Environmental Loads for In-Situ Production and Yard-Stock Management of Precast Concrete Components

Junyoung Park [1], Sunkuk Kim [2] and Jeeyoung Lim [3,*]

[1] Architecture Division, Hyundai Development Company, Hangang-daero 23-gil, Seoul 04377, Republic of Korea; jundrag@naver.com
[2] Department of R&D, Earth Turbine Co., Ltd., Daegu 41057, Republic of Korea; kimskuk@khu.ac.kr
[3] Department of Architectural Engineering, Kyung Hee University, Yongin-si 17104, Republic of Korea
* Correspondence: jyounglim@khu.ac.kr

Abstract: Digital twin (DT) technology, integrated with building information modeling (BIM), enables real-time feedback and predictive analytics in construction. This study presents a BIM-enabled DT framework to optimize in situ production and yard-stock management of precast concrete (PC) components with a focus on minimizing CO_2 emissions. Using Oracle Crystal Ball, scenario-based simulations revealed up to an 8.9% reduction in environmental impact. Distinct from prior research that largely emphasized cost or off-site strategies, this study uniquely addresses on-site sustainability by embedding carbon metrics into the decision-making process. The framework was validated through a large-scale logistics warehouse project that showcased its practical utility. This research contributes a replicable method for enhancing sustainability in precast construction through digital technologies.

Keywords: digital twin; building information modeling; precast concrete; environmental impact; in situ production

1. Introduction

The construction industry is undergoing a paradigm shift, driven by the emergence of digital technologies that enable the management of complexity, uncertainty, and sustainability [1,2]. As projects grow more intricate with the addition of diverse stakeholders, sustainability imperatives, and unpredictable site conditions, digital transformation has become essential. Among these advancements, digital twin (DT) technology stands out as a pivotal tool, enabling the real-time synchronization of physical assets with virtual models to support simulation-driven and predictive decision-making [3,4].

The integration of DT with building information modeling (BIM) has garnered increasing attention. BIM provides a foundational platform for data-driven project coordination, design management, and stakeholder collaboration [5–9]. While BIM offers a comprehensive static representation of a facility, DT technology augments this by incorporating real-time data streams to enable dynamic responses, such as anomaly detection, maintenance forecasting, and risk evaluation, within a closed-loop feedback system [10,11].

Despite these technological advances, significant research gaps remain, particularly in applying BIM–DT integration to optimize the production and yard-stock of precast concrete (PC) components. Prior research has often focused on modular production systems or

factory-based simulation models, which tend to lack the flexibility required for resource-constrained, site-specific scenarios [12,13].

Moreover, the existing studies have largely overlooked real-time planning for in situ production and yard layout of PC components [14–16]. Efficient management of these components demands precise coordination of production, transportation, and temporary storage, all of which are susceptible to spatial limitations, scheduling conflicts, and environmental considerations [17]. A comprehensive and real-time platform is urgently needed to monitor, predict, and optimize these tasks.

In particular, the studies on in situ PC production have primarily focused on production area and layout planning [18–22]. However, yard-stock areas are reported to require more than five times the space of production areas [23–26], and inefficient stockyard layouts can lead to material congestion, schedule delays, and increased environmental burden [27–29]. Nonetheless, research on operational strategies and layout management for yard-stock areas remains limited [30,31]. In other words, the previous studies do not incorporate a simulation-based decision-making framework utilizing digital tools such as BIM, DT, or Monte Carlo methods. Moreover, there is a lack of empirical case studies involving CO_2 emission analysis based on actual field data or the application of optimized yard-stock space management.

In situ production replicates the processes of factory manufacturing, rebar placement, formwork, concrete pouring, curing, and temporary storage on the construction site [32–35]. This method has been shown to reduce environmental loads by over 14.58% and construction costs by up to 39.4% compared to factory production, without sacrificing quality [20,21,36,37]. These benefits highlight the need for intelligent, real-time scheduling and layout planning using BIM-integrated DT systems and simulation tools. Studies also show that in situ production can yield quality levels equal to or exceeding those of in-plant production, which makes it competitive in terms of convenience, quality, cost, and schedule [21,36].

Lim and Kim (2024) [21] and Lim and Kim (2020) [36] are foundational studies focusing on in situ production optimization that offer a reference point for time and CO_2 comparisons in their work. Gao (2024) [37] provides practical cases of BIM–DT integration and digital tracking applicable to yard-stock management component. Su (2025) [38] contributes an advanced multi-objective optimization framework that is methodologically aligned with the use of Monte Carlo-based simulations. Pradhan (2025) [39] highlights lifecycle and method selection criteria that enrich comparative perspectives. Cotoarbă et al. (2025) [40] offer innovative approaches to uncertainty management and DT-based collaboration that may broaden existing research scopes.

Traditional methods for managing PC production and yard layouts often result in inefficient material flows and space usage, leading to increased environmental burdens, particularly CO_2 emissions. While prior research has utilized building information modeling (BIM) and digital twin (DT) technologies, most have been limited to design coordination and visualization, lacking execution-level frameworks for real-time environmental optimization on construction sites. This study proposes a BIM–DT integrated framework that aims to reduce environmental loads, especially CO_2 emissions, by optimizing yard layouts and minimizing transportation distances between production and installation zones. Grounded in real-world construction data, the model not only demonstrates significant quantitative improvements in sustainability metrics but also proves its applicability in practical construction scenarios.

To gain advantages in in situ production, it is essential to optimize real-time production and layout planning based on site conditions, which requires the integration of BIM-based

DT technology and probabilistic simulation tools. Accordingly, this study proposes a BIM-based DT framework designed to optimize the in situ production and yard-stock layout of PC components. The objectives are to minimize carbon emissions from construction through predictive modeling and simulation.

This paper emphasizes the importance of an integrated platform that simultaneously addresses layout efficiency and carbon reduction strategies as a key enabler for sustainable construction. The scope of this study is confined to steel-reinforced concrete (SRC) precast components. Accordingly, this study demonstrates a comprehensive distinction from previous studies in the following key aspects:

- Development of a BIM–DT integrated model for environmental load reduction;
- Shift in focus from cost/schedule efficiency (common in prior studies) to environmental performance enhancement;
- Validation using data from a large-scale, real-world project.

2. Literature Review

2.1. In Situ Production and Yard-Stock PC Components

In construction sites with spatial constraints, a designated area is required to facilitate the in situ production and yard-stock of PC components without hindering ongoing construction activities. The spatial requirements are determined by the size and quantity of PC members, and ensuring consistent quality demands dedicated site managers and skilled labor. Moreover, considering the advantages of in situ production, such as reductions in CO_2 emissions and construction costs, this approach may be preferentially selected by clients who seek direct control over the production process, as opposed to relying on factory-based manufacturing. The yard layout process follows the sequence of production, yard-stock, and installation [20,21,41]. As illustrated in Figure 1a, components are first produced based on zone-specific requirements identified from design drawings. Since component shapes and sizes vary, multiple mold types are required. Zones are classified by component type (e.g., beams, columns, slabs), and production is planned to meet the earliest possible installation deadline within each zone. As the production, yard-stock, and installation quantities are the same, the components to be installed are identified. The quantity is calculated to determine the target quantity for in situ production. The location of the column and beam components for each zone of in situ production is analyzed through design drawing analysis.

(a) **(b)** **(c)**

Figure 1. Production-stock yard-erection process of PC components: (**a**) in situ production; (**b**) yard-stock; (**c**) erection.

The number of members and area for the yard-stock in Figure 1b are calculated. And the required yard-stock area is calculated by multiplying the number of members. The available area for production and yard-stock is calculated for each process, and the yard-stock and production arrangement plans are simulated based on the reviewed area. If

the yard-stock and production are not satisfied, the arrangement simulation is completed through repeated modifications (feedback routine). For yard-stock simulation, first, the crane movement path is analyzed and the possibility of utilizing the yard space is reviewed. At this time, the yard space is determined by dividing it into before and during the installation of PC members. The yard-stock utilization order is determined and the possibility of utilizing the yard-stock space according to the in situ production schedule is reviewed.

As illustrated in Figure 1c, the number of cranes required for the installation of PC components is determined based on the in situ production schedule. Crane specifications are selected by considering the radius of rotation and lifting capacity [41,42]. Based on the number of cranes, a zoning plan is established in which crane operating zones are defined to prevent spatial interference during simultaneous operations. Subsequently, the installation sequence of PC components, such as columns, beams, and slabs, is determined by analyzing crane movement paths within each zone. The installation duration per component is then calculated based on type-specific productivity metrics. A simulation of the installation schedule is carried out in weekly or daily units in accordance with the overall site construction plan. This simulation supports decision-making for optimal resource allocation and construction sequencing. In practice, PC components produced in situ are first placed in the stockyard and then installed sequentially according to the predefined order and zoning constraints.

2.2. Previous Studies

2.2.1. Integration of BIM and DT in the Construction Industry

BIM has become a foundational platform for construction information management, supporting tasks such as design coordination, scheduling, and resource allocation [10,31]. However, BIM traditionally functions as a static system, lacking the ability to reflect real-time conditions on site. To address this limitation, DT technology is increasingly being adopted to create dynamic, real-time representations of physical environments [3,4].

The integration of BIM and DT technology has significantly improved decision-making across the project lifecycle by enhancing visualization, operational control, and performance monitoring. For instance, Opoku et al. (2021) utilized DT technology to improve site visibility and adaptive decision-making [43], while Kassem et al. (2015) applied IoT-based DT frameworks for real-time equipment tracking [44]. Other studies, such as those by Xu et al. (2024), have reviewed the technical challenges and strategic benefits of integrating digital technologies in construction [45].

Importantly, recent research has expanded DT applications to include environmental impact assessment through life cycle assessment (LCA) [46]. Chen et al. (2021) [47] and Tagliabue et al. (2023) [48] demonstrate how DT technology can be linked to LCA metrics to promote low-carbon construction and compliance with environmental regulations.

For LCA, Chen et al. (2021) [47] adopt a process-based approach to quantify the embodied carbon of buildings across their entire lifecycle, encompassing cradle-to-cradle boundaries and including the product, construction, use, end-of-life, and beyond stages (i.e., reuse and recycling). In the product stage, emissions are calculated based on raw material inputs, machinery operations, and energy consumption, all of which are measured in appropriate units such as mass, volume, or area. The construction stage accounts for emissions from transportation, on-site waste, and site activities. The use stage incorporates emissions from surface-level CO_2 exchanges, routine maintenance, repairs, component replacement, and refurbishments throughout a standard reference study period of 60 years. End-of-life emissions include those arising from demolition, off-site transport, waste processing, and final disposal. The beyond stage quantifies the net benefits or burdens

resulting from the substitution of primary products with recovered or recycled materials. Each lifecycle stage is analytically subdivided into specific sub-processes, and corresponding emission factors are systematically applied. By explicitly presenting detailed equations that were omitted in the previous literature, this framework provides a comprehensive and accurate methodology for life-cycle-based embodied carbon estimation.

Lu et al. (2020) further illustrated the value of integrating sensor data into BIM–DT systems to enable anomaly detection in facility monitoring [11]. Opoku et al. (2021) emphasized the use of real-time data from IoT and machine learning models to enhance the predictive capabilities of DT technology [43]. According to Xu et al. (2024), the transition from BIM to DT represents a fundamental evolution in construction workflows, one that enables system-wide intelligence and predictive control [45].

2.2.2. DT for Predictive Planning and Risk Management

DT technology's core strength lies in its ability to simulate future scenarios and support proactive decision-making in complex environments. For example, Lu et al. (2020) developed a DT-based approach to improve coordination and productivity in on-site construction processes [11]. Zhang et al. (2024) applied DT technology for real-time environmental monitoring and integrated lifecycle carbon footprint analysis into planning workflows [49].

Case studies have shown that time and cost management using 4D and 5D BIM models has enabled stakeholders to prepare simulations and predict scenarios to achieve resource optimization [50]. It can also play a critical role in establishing predictive maintenance and energy management strategies [51]. In the port area, this process has led to strategic asset management for risk and safety management activities [52,53].

More recently, scenario-based and probabilistic simulation tools have been embedded within DT frameworks. Bakhshi et al. (2024) introduced a DT platform that incorporates simulation techniques for proactive risk mitigation and emission tracking [54]. The integration of optimization algorithms with DT technology has proven especially useful in improving the responsiveness and reliability of construction project control systems.

2.2.3. In Situ PC Production and Stockyard Management

Effective management of in situ production and temporary storage is critical in precast construction, where just-in-time assembly and spatial optimization are essential. Kosse et al. (2023) proposed a simulation-based model for optimizing yard layouts in precast construction [55], while Lim and Kim (2024) explored the integration of scheduling and spatial constraints in PC logistics planning [21].

However, many existing models remain static and are not responsive to real-time conditions. To overcome this limitation, it is essential to incorporate sensor inputs and intelligent simulation platforms within DT systems. Environmental optimization is an area that has not yet been adequately addressed in the literature.

2.2.4. Reducing Carbon Emissions Using DT

Recent advancements in DT technologies have demonstrated substantial potential in reducing carbon emissions across the entire lifecycle of built environments. Several studies have shown that integrating DT technology with real-time sensing and AI-driven analytics enables dynamic monitoring and optimization of energy usage and CO_2 emissions in both construction and operation phases [56,57]. For instance, cognitive digital twins applied to HVAC (heating, ventilation, and air conditioning) systems in smart buildings have achieved up to 30–50% carbon reduction by adapting to occupant behavior and

environmental conditions [58]. Moreover, city-scale digital twin platforms, such as those implemented in Sydney and the European "Destination Earth" project, allow for urban-level simulation of emission sources and inform sustainable policy planning [59]. These findings underscore the importance of embedding DT-enabled carbon intelligence within construction workflows, from design to operation, as a pathway to achieving low-carbon and climate-resilient infrastructure.

2.2.5. Holistic Lifecycle Carbon Assessment Frameworks Using BIM

ISO 14040 [60], ISO 14044 [61] and EN 15978 [62] provide a foundational basis for life cycle assessment (LCA), encompassing goal and scope definition, inventory analysis, impact assessment, and interpretation phases [63]. These frameworks promote consistency and transparency in quantifying environmental impacts over a building's entire lifecycle. Berges-Álvarez et al. (2024) [64] have explored the integration of LCA with building information modeling (BIM), enabling extraction of design geometry and material specifications for automated environmental calculations. Mazur and Olenchuk (2023) [65] applied BIM-driven LCA to quantify CO_2 footprint reductions across housing typologies. While BIM-based LCA workflows have demonstrated value, they are often static in nature, focusing on early design phases without capturing real-time updates or site-level data during the construction phase. This presents a key limitation in responding dynamically to carbon-intensive activities on site.

2.2.6. Precedents in DT–BIM for Environmental Performance Optimization

Badenko (2024) [66] demonstrated how coupling BIM and DT allowed for predictive energy optimization and real-time operation feedback, achieving up to 15% energy savings in building operation. Kosse (2022) [67] applied Industry 4.0-based digital twins to automate precast component production and integrate real-time data into logistics optimization. Widjaja (2025) [68] expanded this to include BIM-based reinforcement layout optimization via DT feedback loops, achieving waste reduction and enhanced coordination. Although these studies demonstrate the potential of DT–BIM in performance monitoring, they have not fully addressed environmental impact minimization, especially in terms of in situ CO_2 reduction and dynamic yard-stock scenarios. Most research focuses on energy or operational parameters without integrating material-specific carbon tracking in precast workflows.

2.2.7. PC Sustainability Strategies: In Situ vs. Off-Site Trade-Offs

Comparative analyses reveal that PC typically yields around 10% lower CO_2 emissions per cubic meter compared to cast-in-place equivalents [69]. Another study revealed that, although prefabricated systems generate the highest carbon emissions during the installation phase, they can still achieve a reduction of approximately 86 kg-CO_2 per square meter [70]. In situ production methods, depending on project-specific conditions, have been shown to realize more than a 14.3% reduction in CO_2 emissions compared to off-site (factory-based) production [36]. Producing directly in situ can further reduce carbon emissions associated with logistics by minimizing transportation distances, improving operational flexibility, and optimizing construction workflows [71]. In contrast, factory-based production excels in terms of process speed, quality control, and safety. Some case studies have demonstrated that off-site methods can achieve reductions of over 50% in waste and emissions, reduce construction time by up to one-third, and maintain defect rates below 5% [72]. Generally, off-site precast production is advantageous in terms of resource efficiency and schedule acceleration, while in situ production, when coupled with proper planning and appropriate

equipment, can outperform it in terms of carbon emissions. Particularly, factors such as transportation distances, equipment efficiency, site layout, and material reuse significantly influence the sustainability outcome, which underscores the need for project-specific optimization strategies.

2.2.8. Research Gap

Despite growing interest in DT applications, there remains a lack of fully integrated BIM–DT systems specifically tailored to the complexities of PC logistics. In particular, few frameworks support simulation-based optimization of CO_2 emissions in tandem with production and yard management. This study aims to address this gap by proposing a unified platform that enables environmentally conscious decision-making for in situ PC component production.

3. Methodology

In general, DT technology is considered a virtual mirror that describes the physical characteristics of a system and transmits and receives information for control, monitoring, and decision-making processes [73]. DT technology should be connected and synchronized while running simulations of physical counterparts over time. DT technology is defined as a model that pairs physical and digital models by automatically exchanging data between them [74].

However, in this study, we apply DT technology that is different from general models by using an optimization tool. The conceptual diagram in Figure 2 shows a framework for efficiently managing the in-situ production and installation of PC structures based on DT technology, while achieving sustainability (carbon reduction) goals at the same time. The DT model consists of a bidirectional link between the actual physical site and the BIM-based DT that virtually implements it. The BIM model is updated based on real-time on-site data using Dynamo, and simulation and analysis are made possible through the BIM model.

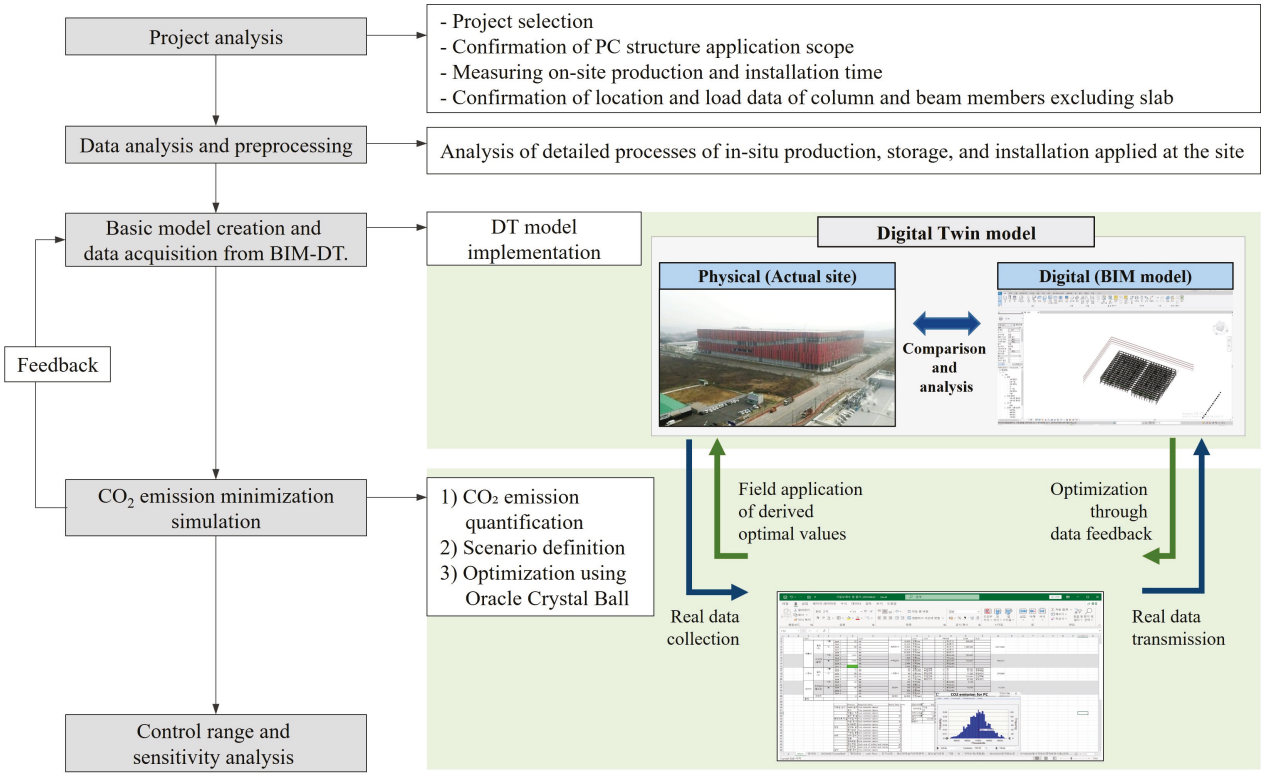

Figure 2. Research flow.

The digital twin system is linked to optimization tools such as Oracle Crystal Ball to achieve the goals of minimizing carbon dioxide (CO_2) emissions. The optimization tool uses information derived from the BIM model and actual field data to perform sensitivity analysis and control variable settings, thereby deriving the optimal scenario. The results are fed back into the digital twin model and reflected in decision-making in the field, which continuously improves the accuracy of the model.

3.1. Project Analysis

To validate the effectiveness and practical applicability of the proposed BIM-based DT framework, a real construction project was selected as a case study. The project involves the construction of a large-scale logistics warehouse located in A City. The structure consists of four above-ground floors, with PC slabs installed from level 1 to level 4. The building's core structure is composed of reinforced concrete (RC), and the ramp areas utilize a combination of steel and SRC systems. This study focuses primarily on the PC slab construction processes across the four floors. The positional and loading data of column and beam elements, excluding the slab, are collected.

3.2. Data Analysis and Preprocessing

In the data analysis and preprocessing phase, the detailed procedures of in situ production, storage, and installation applied on-site are analyzed, as illustrated in Figure 3. The construction process of PC buildings consists of PC component production, transportation, and installation. The production process begins with formwork preparation, including mold cleaning, mold assembly, embedded hardware installation, and rebar placement followed by inspection. Subsequently, concrete is cast after the application of release agent, which is followed by steam curing and demolding, which completes the production of the components. Once produced, components undergo lifting, cleaning, and finishing operations before being placed in the yard for storage. The installation process begins with preparation for erection, including connection with lifting equipment, upending, hoisting to the designated installation position, and temporary fixation. This is followed by verticality inspection and final alignment using a plumb-down operation. The installation planning for PC components is conducted during the preparation stage, based on the working radius and lifting capacity of the crane. The crane also influences mold allocation and schedule-related factors. Idle cranes not utilized for installation are employed for in situ production processes. Therefore, the production and installation workflows were analyzed based on actual field-applied data that reflect practical operational constraints and resource allocation.

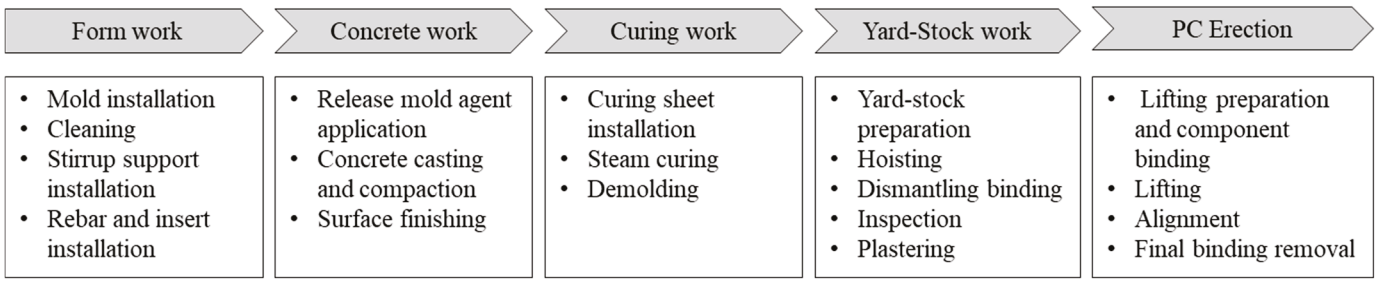

Figure 3. Process analysis of in situ production.

3.3. Basic Model Creation and Data Acquisition from BIM–DT

In the basic model creation and data acquisition from BIM–DT phase, the DT model is implemented and linked with actual site information and BIM models. The model is

used for simulation-based optimization. This study aims to optimize the in situ production and yard-stock management of PC components through the integration of BIM and DT technologies. While BIM captures the physical attributes and design information of each component, the DT functions as a system for simulation-based operational decision-making and process optimization. The two technologies serve complementary roles, forming a real-time or near-real-time feedback loop that enhances the sustainability and responsiveness of on-site operations. Figure 4 shows a BIM model implemented using Dynamo. The software used in this study was Autodesk Revit 2022. A Dynamo script was created to obtain real-time information, and the BIM model was structured based on the IFC schema to ensure data consistency and interoperability. The IFC class and property set assigned to the selected member in the BIM model can be retrieved.

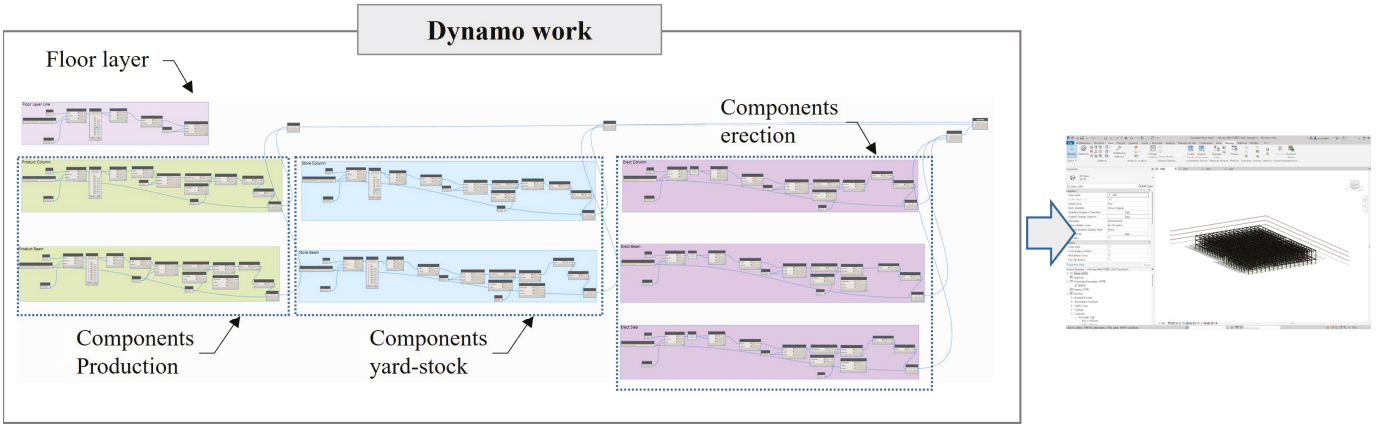

Figure 4. BIM model divided into production, yard-stock, and erection implemented using Dynamo.

Initially, information such as the location, geometry, quantity, type, and installation sequence of PC components is extracted from the BIM model and transformed into a data structure suitable for DT-based simulation. This data processing step is automated using Dynamo, and the refined dataset is subsequently exported in Excel format for integration with the external simulation tool, Oracle Crystal Ball. Figure 5 shows the 4D simulation of the site after the installation of PC members has started, which was built using BIM. PC members are not installed during the lead time from D + 1 to D + 86. Therefore, only the construction from D + 87 to D + 134 is shown. In D + 98, the production areas of zone A and B are determined to be 630 m^2 and 580 m^2 in real time using Dynamo, respectively, and the yard-stock areas of zone A and B are determined to be 7124 m^2 and 6812 m^2 in real time, respectively. In the case of a general in situ production system, since the erection area is added, it is difficult to produce and store PC members in the same location, so the production and yard-stock locations have to be moved. However, in this study, only the production location was moved, and the yard-stock location was set up to be the closest location to the installation location. The monthly site plans obtained using BIM are consistent with those presented in our parallel study [75].

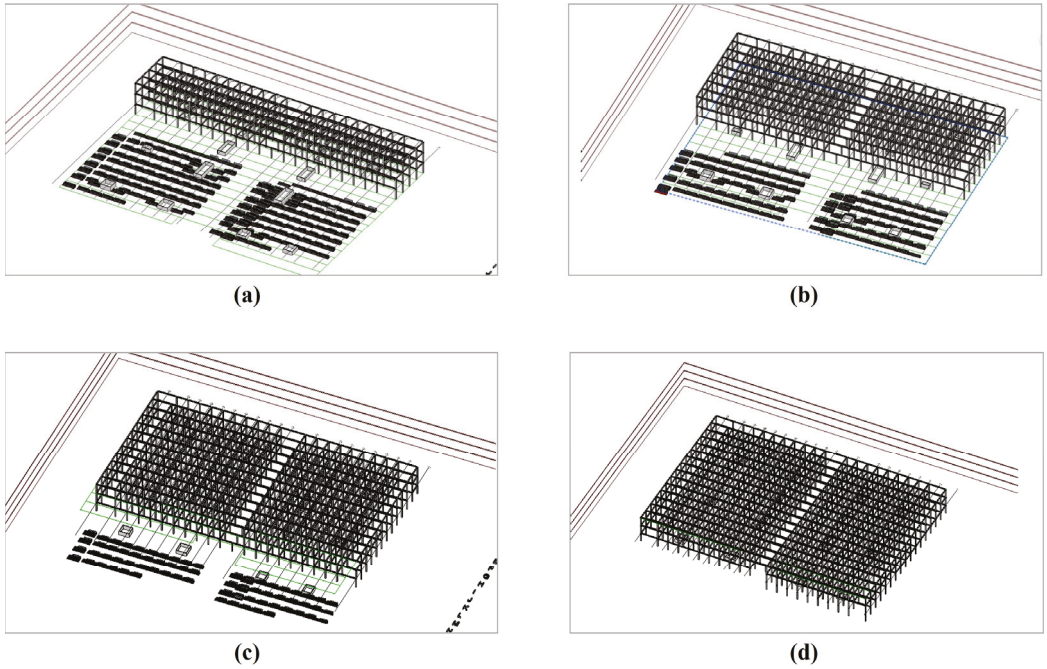

Figure 5. Monthly site plan using BIM: (**a**) D + 98; (**b**) D + 110; (**c**) D + 122; (**d**) D + 134.

3.4. CO_2 Emission Minimization Simulation

3.4.1. CO_2 Emission Quantification

To estimate CO_2 emissions, it is essential to first perform a detailed quantity takeoff. As shown in Table 1, the material quantities for key columns and beams were calculated. For instance, for Column A and Column B, the quantities were determined as follows: concrete volumes of 6.444 m^3 and 6.745 m^3, steel weights of 2.129 tons and 2.382 tons, and form steel weights of 0.016 tons, respectively. Similarly, for Beam A and Beam B, the calculated quantities were concrete volumes of 20.957 m^3 and 21.238 m^3, steel weights of 3.647 tons and 3.965 tons, and form steel weights of 0.010 tons. When aggregated, the total material quantities amounted to 30.457 m^3 of concrete, 7.070 tons of steel, and 0.038 tons of form steel.

Table 1. Quantity of columns and beams.

Work	Item	Unit	A Column	B Column	A Girder	B Girder	Total
Concrete work	Concrete	m^3	6.444	6.745	20.957	21.238	30,457
Reinforcement work	HD10	t	0.302	0.333	0.171	0.156	729
	HD13	t	0.104	0.175	0.314	0.238	609
	HD16	t	0.050	0.112	-	-	441
	HD 19	t	-		-	-	254
	HD 22	t	1.212	1.301	0.971	1.117	2284
	HD 32	t	-	-	1.269	1.532	1110
	Steel joint	t	0.461	0.461	0.922	0.922	1797
	Sub-total	t	2.129	2.382	3.647	3.965	7070
Form work	Steel form	t	0.016	0.016	0.010	0.010	38

In the case project, steel molds were utilized for the production process. As illustrated in Figure 6, the steel molds applied in the in situ production are identical in specification and configuration to those used in conventional in-plant production. These molds are ordered with the same technical specifications from the manufacturers that supply the precast plant. Columns are produced in sets of two units and, similar to beam production, a spacing of 0.1 m is maintained between adjacent molds to ensure sufficient working space during on-site operations.

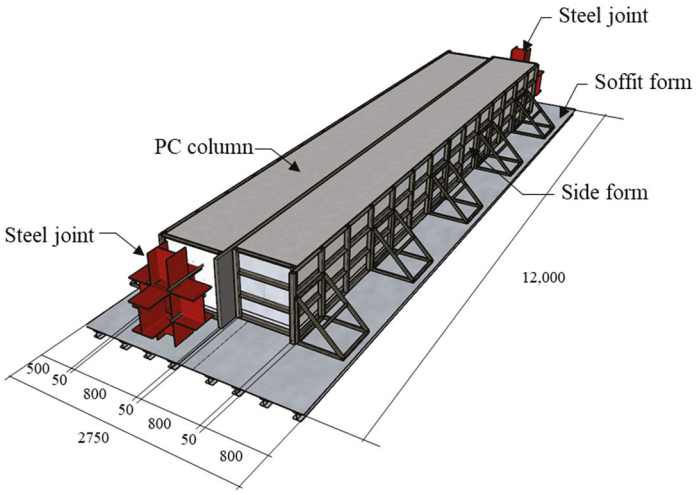

Figure 6. Steel mold for in situ production.

CO_2 emissions are calculated using actual labor inputs, along with oil and electricity consumption during the production and yard-stock processes. CO_2 emission calculation formulas are provided in Equations (1) and (2). The CO_2 emission factors for steel and concrete were observed to be 3500 kg-CO_2 per ton and 140 kg-CO_2 per cubic meter, respectively. The CO_2 emission factor for labor is 0.02 kg-CO_2 per person-hour. Equation (3) presents the estimation of CO_2 emissions associated with each construction activity based on oil consumption during the construction phase. This estimation builds upon the energy consumption calculated using Equation (4). Furthermore, CO_2 emissions derived from electricity usage at the construction stage are estimated using Equation (5), which is based on the energy consumption model described in Equation (6). Based on these calculations, the total CO_2 emissions are determined as follows:

$$CE_c = \sum_{i=1}^{n} [Q_{ci} \times (CE_{ul} + CE_{uo} + CE_{uel} + CE_{ulh} + CE_{uec})] \quad (1)$$

$$CE_b = \sum_{i=1}^{m} [Q_{bi} \times (CE_{ul} + CE_{uo} + CE_{uel} + CE_{ulh} + CE_{uec})] \quad (2)$$

$$E_{CO} = 0.0017 \times A_f + 37.5 \quad (3)$$

$$Q_{CO_2o} = E_{co} \times 3.06 \quad (4)$$

$$E_{ce} = 0.0247 \times A_f^{0.79} \quad (5)$$

$$Q_{CO_2e} = E_{ca} \times 1.64 \quad (6)$$

CE_t: total CO_2 emission, CE_{ci}: CO_2 emission of column, CE_{bj}: CO_2 emission of beam, Q_{ci}: ith column quantity, CE_{ul}: unit CO_2 emission of labor, CE_{uo}: unit CO_2 emission of oil, CE_{uel}: unit CO_2 emission of electricity, CE_{ulh}: unit CO_2 emission of lighting and heating, CE_{uec}: unit CO_2 emission of environmental conservation, Q_{bi}: ith beam quantity, i: number of installed ith column (1,. . ., n), j: number of installed ith beam (1,. . ., m), E_{CO}: energy (oil) consumption during the construction stage (TOE), A_f: total floor area (m^2), Q_{CO_2O}: CO_2 emission based on oil use in the construction stage (T-CO_2), E_{ce}: power consumption in the construction stage (TOE), Q_{CO_2e}: CO_2 emission based on power consumption in the construction stage (T-CO_2).

In the actual case project, the average unit installation times for PC components were recorded as 19 min for columns, 8 min for girders, and 10 min for slabs. The total number of components installed included 850 columns, 1371 girders, and 4032 slabs. The overall installation period, based on calendar days, amounted to 48 days, during which the crane operated with a rotational coverage of 20 m per minute. Excluding the time required for fixing the component positions, the net installation time for PC components was also calculated to be 48 days, as shown in Table 2. For reference, in conventional RC structures, the standard installation times are, similarly, 19 min for columns, 8 min for girders, and 10 min for slabs; however, in the case of PC structures, the installation durations for columns and girders are reduced by approximately 50%. Based on crane performance data [76], the estimated total installation time for PC components in RC construction scenarios was 172 days. Additionally, the average unit yard-stock time for PC columns and beams was recorded as 13 min, with a total yard-stock handling period of approximately 11 days, as shown in Table 3. CO_2 emission calculation formulas for yard-stock and erection are provided in Equations (7)–(10).

Table 2. Actual resource for yard-stock and erection.

Item		Unit	Quantity
Labor	Equipment operator	Day	59
	common labor	Day	144
Material	Diesel	L	12,900
Equipment	Crane (550 ton)	Day	430

Table 3. CO_2 emission calculation for in situ production (unit: T-CO_2).

Classification	Production	Yard-Stock and Erection
Material use	37,940	-
Labor use	243	120
Oil use	987	23,785
Electricity use	543	146
Lighting, and heating use	287	65
Environmental conservation	202	37
Total	40,002	24,153

$$CEYE_t = CEYE_c + CEYE_b + CEYE_s \quad (7)$$

$$CEYE_c = \sum_{i=1}^{n}[Q_{ci} \times (CEYE_{ul} + CEYE_{uo} + CEYE_{uel} + CEYE_{ulh} + CEYE_{uec})] \quad (8)$$

$$CEYE_b = \sum_{i=1}^{m}[Q_{bi} \times (CEYE_{ul} + CEYE_{uo} + CEYE_{uel} + CEYE_{ulh} + CEYE_{uec})] \quad (9)$$

$$CEYE_s = \sum_{i=1}^{l}[Q_{si} \times (CEYE_{ul} + CEYE_{uo} + CEYE_{uel} + CEYE_{ulh} + CEYE_{uec})] \quad (10)$$

$CEYE_t$: total CO_2 emission for yard-stock and erection, $CEYE_c$: CO_2 emission of column for yard-stock and erection, $CEYE_b$: CO_2 emission of beam for yard-stock and erection, $CEYE_s$: CO_2 emission of slab for yard-stock and erection, Q_{ci}: ith column quantity, $CEYE_{ul}$: unit CO_2 emission of labor for yard-stock and erection, $CEYE_{uo}$: unit CO_2 emission of oil for yard-stock and erection, $CEYE_{uel}$: unit CO_2 emission of electricity for yard-stock and erection, $CEYE_{ulh}$: unit CO_2 emission of lighting and heating for yard-stock and erection, $CEYE_{uec}$: unit CO_2 emission of environmental conservation for yard-stock and erection, Q_{bi}: ith beam quantity, Q_{si}: ith slab quantity, i: number of installed ith column (1,. . ., n), j: number of installed ith beam (1,. . ., m), k: number of installed ith slab (1,. . ., l).

3.4.2. Scenario Definition and CO_2 Emission Optimization Process

Table 4 shows the assumptions for 4D simulation using BIM. The total cost and time are not considered because they satisfy the client's requirements. All PC components are produced, stored, and installed in situ. The PC member production and yard-stock location can always be located near the installation location. As this site has a large floor area and a low number of floors, it is difficult to use a tower crane. Hence, a mobile crane is used.

Table 4. Assumptions for 4D simulation.

No.	Assumptions
1	The cost and time satisfy the client's requirements.
2	All PC components are produced, stored, and installed in situ.
3	The PC components production and yard-stock location is near the installation location.
4	As this site has a large floor area and not many floors, a mobile crane is used.
5	The production cycle for each PC component is consistently maintained at two days.
6	For material transportation routes and each individual transport line, both transport efficiency and unit cost can be applied.

The entire area and each yard-stock yard are defined along the X- and Y-axes and simplified into rectangles with parallel boundaries. For material transportation routes and each individual transport line, both transport efficiency and unit cost can be applied. The assumptions related to transportation are described in detail in the study by Lim and Kim [21]. In this paper, only the aspects directly associated with CO_2 emissions are addressed.

Table 5 shows the constraints for 4D simulation using BIM. To minimize environmental loads, unnecessary secondary transportation should be avoided and equipment utilization should be limited to prevent excessive energy consumption. Formworks are assumed to be reused at least 40–50 times to reduce environmental impacts from material production and disposal. Furthermore, the production and yard-stock of all columns and beams, as well as the installation of all columns, beams, and slabs, must be incorporated.

Table 5. Constraints for 4D simulation.

No.	Constraints
1	During the estimation of yard-stock areas, unnecessary secondary transport must be minimized to reduce energy consumption from equipment operation.
2	The use of cranes and transport equipment must be limited to the minimum level required to prevent excessive energy waste.
3	Formworks must be reused at least 40–50 times as a principle.
4	The production and yard-stock processes of all columns and beams must be included, and the installation processes of all columns, beams, and slabs shall be incorporated.

The number of required molds is calculated based on production quantity, production cycle, and total production duration. Similarly, the number of cranes is determined by the unit erection time, total installation quantity, and allowable erection period. The total yard area is estimated by multiplying the number of stored components by the unit of yard area per component type. These calculations are formalized in Equations (11)–(14).

$$Q_s = Q_{sc} + Q_{sb} \tag{11}$$

Q_s: in situ production quantity, Q_{sc}: in situ column quantity production, Q_{sb}: in situ beam quantity production.

$$N_m = \sum_{i=1}^{n} \frac{Q_{Mi} \times T_{PC}}{T_s} \tag{12}$$

N_m: number of molds; Q_{Mi}: in situ production quantity of each mold type; T_{PC}: production cycle time; T_s: in situ production time; i: number of mold types (1,. . ., n).

$$N_c = \frac{(T_{UE} \times Q_S)}{T_e} \tag{13}$$

$$\text{Subject to } N_C \geq 1, \text{integer}$$

N_C: number of cranes; T_{UE}: unit erection time; Q_S: in situ production quantity; T_e: erection time.

$$A_{YS} = \sum_{i=1}^{n} (Q_{YSi} \times A_{YSi}) \tag{14}$$

A_{YS}: yard-stock area, Q_{YSi}: yard-stock quantity of each mold type, A_{UYSi}: unit of yard-stock area of each mold type, *i*: number of mold types (1,. . ., n).

Figure 7 illustrates the optimization process proposed in this study. Based on structural component data extracted from a Revit-based BIM–DT model, this study estimates the production quantity of PC columns and beams. Subsequently, it quantifies CO_2 emissions across three major stages: production, yard-stock, and installation. This quantification considers workload per stage, number of workers, productivity rates, and contingency factors to compute total work time. By multiplying these values by stage-specific CO_2 emission factors, the emissions for each phase are calculated. Furthermore, the model integrates Monte Carlo simulation results generated via Oracle Crystal Ball, specifically incorporating stockyard area as a constraint. The cumulative results from these analyses yield the total CO_2 emissions, enabling the identification of the optimal configuration. The algorithmic structure of this process is detailed in Algorithm A1 of Appendix A.

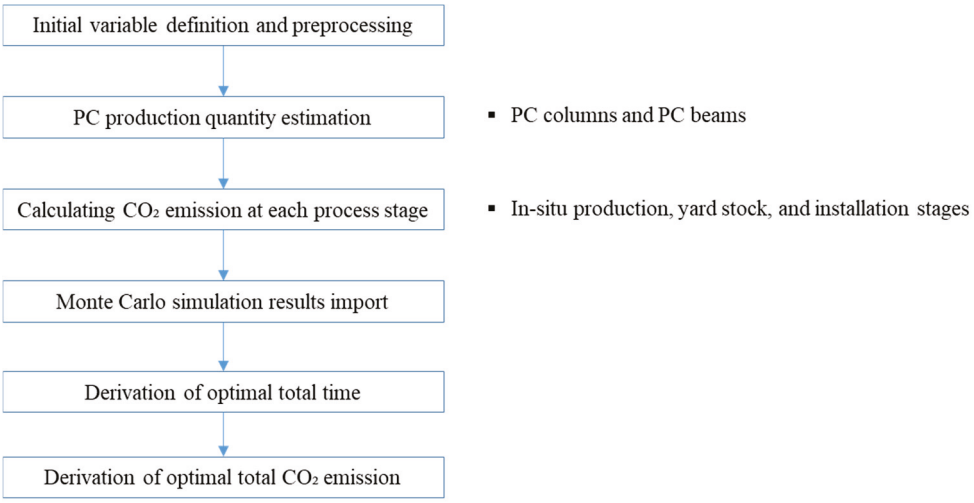

Figure 7. CO_2 emission optimization process.

3.4.3. Optimization Model Design Using Oracle Crystal Ball

Lim et al. (2020) [41] explained six assumptions about the available area, selected as the main influencing factor, and derived the highest cost reduction rate among the scenarios applicable to the field. In addition, Lim et al. (2020) [42] derived the Min and Max for each factor such as in situ production quantity, lead time, number of molds, and number of cranes, and analyzed the effect of quantity on cost and CO_2. However, this study assumes that all members are produced and derives factors affecting CO_2 emission. In addition, the goal of this study is to reduce environmental loads by 10%.

This study presents a procedure for quantifying and optimizing CO_2 emissions generated during the production and yard-stock processes for precast concrete (PC) components by utilizing quantity data extracted from the BIM model in conjunction with Oracle Crystal Ball. The CO_2 emission objective function applied in this procedure is as shown in Equation (15).

$$\text{Minimize } (CE_t) = CE_c + CE_b \tag{15}$$

The range of control variables is set for each scenario. The optimal values applicable to the actual site are derived from the simulation results, and these are fed back into the model to enable iterative improvement.

For efficient in situ production and yard layout, implementation of DT using BIM and optimal space planning strategies based on time series analysis are required. These values were established based on actual site conditions during the preparation stage of in situ production. The assumption conditions of the main factors for BIM implementation are as shown in Table 6. These values were chosen considering the on-site conditions during the in situ production preparation stage. The required construction period presented by the client is 18 months, and the applied quantity is 1035 ea of columns and 1906 ea of beams.

The number of molds applied is 32 ea for columns and 90 ea for beams. Two cranes were assigned, corresponding to the number of designated work zones. The maximum yard-stock area derived by reflecting these conditions was calculated to be 15,235 m^2. The construction period applied on site is set at 8 months to comply with the client's requested conditions. The factors used as parameters are quantity, number of molds, and number of cranes.

Table 6. Input values for CO_2 emission optimization.

Category			Details	Units	Distribution Types
Fixed Variables	Required Construction Duration		18	month	-
	Quantity	Column	850	ea	-
		Beam	1371	ea	-
Parameters	Planned Construction Duration		8	month	Normal Distribution
	Number of Molds	Column	32	ea	Normal Distribution
		Beam	90	ea	Normal Distribution
	Number of Cranes		3	ea	Normal Distribution
	Maximum Yard-Stock Area		15,235	m^3	Normal Distribution
	CO_2 emission		113,744	T-CO_2	Normal Distribution

4. Result and Sensitivity Analysis

The production and yard-stock areas for a unit of area are calculated in real time, as shown in Table 7, using Dynamo. The following equations, Equations (16) and (17), were applied for the area. The production area, installation area, and yard-stock areas for one member are 16.5 m^2 and 9.6 m^2, respectively. The maximum yard-stock area of 15,235 m^2 was derived in real time at lead-time D + 86. The reason why the highest number of yard-stock members is shown during this period is because the PC members produced during the lead-time were accumulated. And since the yard-stock members are installed, the number of PC members decreases as they are installed. The period from D + 86 to D + 134 is the time-lag, which is 3 months. That is, when construction begins, the yard-stock area gradually increases, and the largest yard-stock area is recorded just before the start of installation (D + 86). When installation begins, the yard-stock area decreases, and when the area becomes 0, the PC construction is finished. The daily areas are consistent with those presented in our parallel study [65].

Table 7. Daily area (unit: 1000 m^2).

Daily area	D + 17	D + 34	D + 51	D + 68	D + 85	D + 102	D + 119	D + 134
Production area	12.1	12.1	12.1	12.1	12.1	0.0	0.0	0.0
Yard-stock area	2.8	5.7	8.5	11.3	13.9	8.2	4.1	0.0

$$Ap(t) = 1\sum n\{Ai \mid t \in [Si, Ei)\} \quad (16)$$

$$Ay(t) = 1\sum n\{Ai \mid t \in [Ei, Ii)\} \quad (17)$$

$A_p(t)$: In situ production area occupied at time t, $A_y(t)$: yard-stock area occupied at time t, S_i: production start date of the ith component, E_i: production completion date of the ith component, I_i: installation date of the ith component

In the same way as schedule optimization, CO_2 emission optimization was performed through maximum repetition simulation (1,000,000 times) in the Oracle Crystal Ball Release 11.1.3.0.0 program. All possible cases of crane and CO_2 occurrence were derived to derive the Min and Max for each factor. The factors used as parameters at this time were quantity, production cycle, lead-time, number of molds, and number of cranes. As a result of deriving the Min–Max management range of the crane as shown in Figure 8, the Min was set to

2.00 ea and the Max was set to 3.270 ea. The reason why the crane does not decrease below 2.00 months is because the minimum number of cranes is required to match the process. As a result of analyzing the management range, the crane and CO_2 emissions, according to the change in each factor, were generally proportional, so they appeared in graphs of a similar shape.

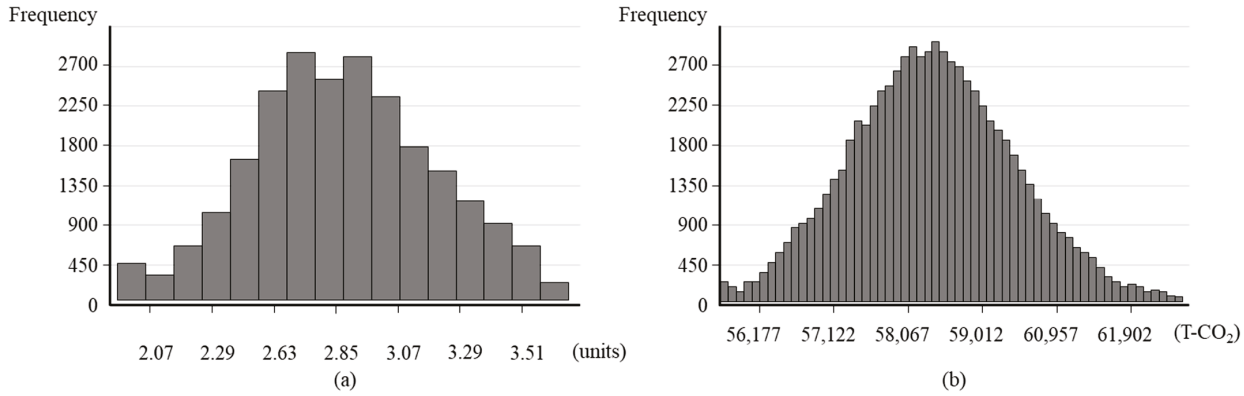

Figure 8. Control range of crane and CO_2 emissions: (**a**) crane; (**b**) CO_2 emission.

Using the management scope of the crane and CO_2 emissions derived through Monte Carlo simulation, the optimal case is derived as shown in Table 8. The CO_2 emissions are derived in real time as 64,355T- CO_2, the construction time is 6.5 months, and this value is the smallest value among the derived CO_2 emission values. The number of molds is 30 columns, there are 91 beams, the number of cranes is two, and the yard-stock area is 15,729 m^2. Upon completion of the simulation, the optimized results are fed back into the BIM environment through Dynamo. This feedback loop enables iterative improvements between design and operation, fostering continuous optimization and enhancing decision-making accuracy in construction planning. When the derived values are applied to the DT model and explained in Figure 9, (a) is modified to (a) D + 96, (b) D + 106, (c) D + 116, and (d) D + 127. The proposed system is designed to divide the entire process into four phases, with the data being updated accordingly. This configuration ensures systematic synchronization between each stage. Through the results, it is determined that the CO_2 emissions increase as the number of cranes increases, which means that the crane is a factor that increases CO_2 emissions. In the future, the values of various factors can be determined on-site, considering the minimum CO_2 emissions, by considering various factors. The number of forms according to the yard-stock area is derived, the lead time and total construction period applied to the number of forms are derived, and the yard-stock area is calculated. CO_2 emissions were calculated by applying these results step by step.

Table 8. Optimization result for schedule.

Item		Unit	Value
CO_2 emission		T-CO_2	64,355
Construction time		month	6.5
Number of molds	Column	ea	30
	Beam	ea	91
Cranes		ea	2
Yard-stock area		m^2	15,729

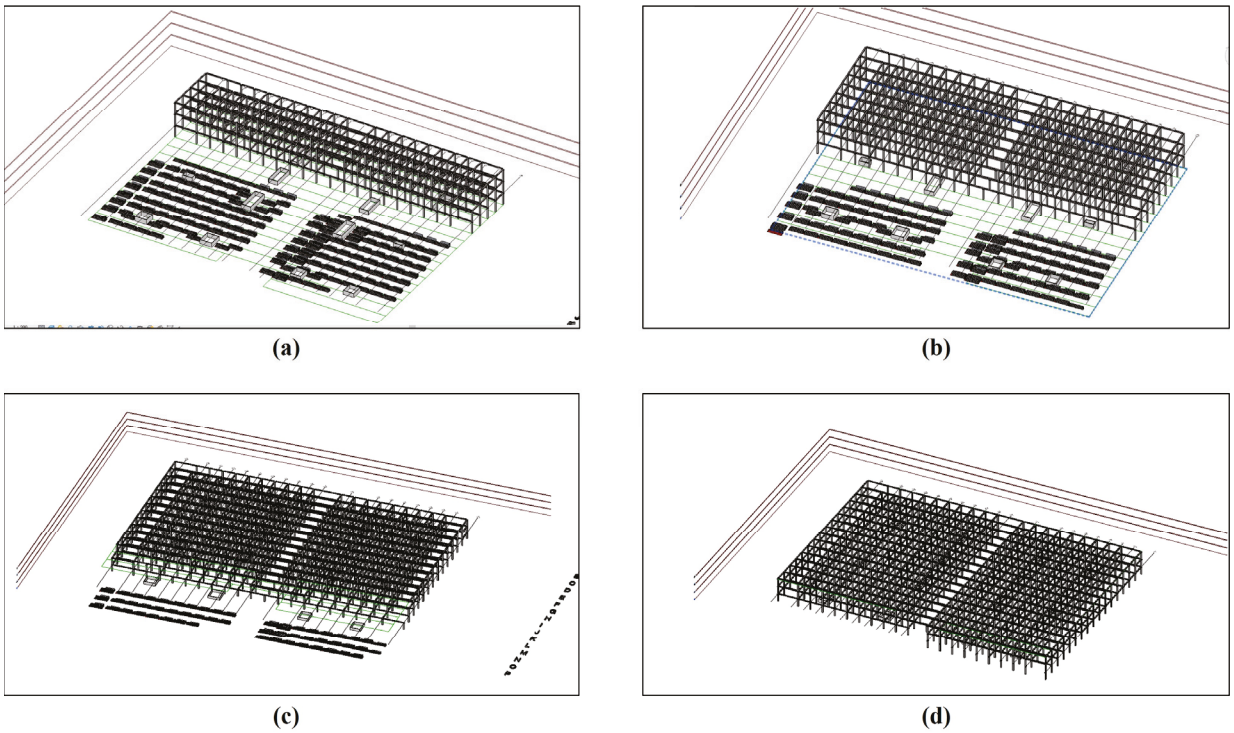

Figure 9. Monthly site plan using BIM: (**a**) D + 96; (**b**) D + 106; (**c**) D + 116; (**d**) D + 127.

Table 9 shows the sensitivity analysis. The number of cranes and the CO_2 emissions exhibited the most pronounced correlation ($r \approx 0.47$). This result indicates that equipment operation is directly associated with increased energy consumption and carbon emissions. It also implies that, as the number of cranes increases, additional waiting time between tasks can be required, which thereby extends idle periods. Furthermore, the project duration showed a negative correlation with the yard-stock area ($r \approx -0.12$), which suggests that longer durations tend to improve yard efficiency and reduce spatial occupation. The relationships among the remaining variables were weak, and the duration and CO_2 emissions appeared largely independent. Table 10 indicates that the CO_2 emissions were calculated with a minimum of 55,603 T-CO_2, a mean of 58,297 T-CO_2, a maximum of 62,862 T-CO_2, and a standard deviation of 1421.12 T-CO_2.

Table 9. Sensitivity analysis.

Variable Pair	Correlation (r)	*p*-Value	R^2
Cranes—CO_2 Emission	0.47	0.000076	0.22
Molds—CO_2 Emission	0.22	0.00051	0.05
Duration—CO_2 Emission	0.00	0.00054	0.00
CO_2 Emission—Yard-stock Area	−0.05	0.00023	0.00

Table 10. Descriptive statistics (unit: T-CO_2).

Item	Min	Mean	Max	Std. Dev.
CO_2 Emission	55,603	58,297	62,862	1421.12

5. Discussion

5.1. CO_2 Emission Result Assessment

This study proposes a BIM-based DT framework for optimizing in situ production and yard-stock management of PC components. Oracle Crystal Ball simulation was used to perform probabilistic CO_2 emissions optimization. The results showed that the environmental impact can be reduced by 8.9%.

In this study, SRC precast components were applied. In previous studies, it was found that SRC precast components can reduce the construction period by at least 18.7% compared to RC structure precast components [77,78] and emit at least 11.7% less CO_2 [79,80]. It is noteworthy that, when comparing RC and SRC structures, a maximum reduction of up to 32.02% in construction duration can be achieved [78]. However, this result was derived from a study conducted on non-PC structural systems, and therefore does not directly apply to PC structures. If process optimization is applied to actual sites, it is expected that CO_2 emissions will be minimized up to 8.9%.

While this study primarily focuses on optimizing carbon emissions, it is essential for future research to recognize the potential trade-offs between carbon reduction and project schedule acceleration objectives. Shortening the construction duration may increase CO_2 emissions as more equipment and resources are required. On the other hand, reducing equipment operation time to reduce CO_2 emissions can require an extension of the construction period. Accelerating the schedule can lead to increased carbon emissions due to intensified equipment use, while minimizing emissions can require extended timelines. Therefore, a multi-objective optimization model was considered, and the most eco-friendly layouts were introduced to support informed decision-making.

5.2. Comparison with Previous Studies of This Case Site

This study conducted Monte Carlo simulations using Oracle Crystal Ball and achieved an optimized CO_2 emission reduction of 8.9%. As shown in Table 11, CO_2 emission values derived from the same case study in previous research were compared. Lim and Kim (2020) [36] estimated the CO_2 emissions for the total number of columns and girders as 33,699 T-CO_2 for in situ production and 39,095 T-CO_2 for in-plant production. The differences in CO_2 emission values between this study and Lim and Kim (2020) [36] for in situ production are attributed to the following factors: (1) Lim and Kim did not consider labor use, lighting and heating use, or environmental conservation in their calculations and, (2) while Lim and Kim (2020) [36] applied RC structural systems, this study applied an SRC system, which resulted in different material usage.

Additionally, Kim et al. (2023) [76] estimated CO_2 emissions for the erection phase using actual inputs for labor, oil, electricity, lighting and heating, and environmental conservation, yielding a total of 74,110 T-CO_2. By applying the model developed in this study, a 25.99% reduction in CO_2 emissions was achieved compared to the actual construction. In contrast, this study demonstrated a reduction of 8.9%, which appears to be smaller than that of Kim et al. (2023) [76]. However, it should be noted that Kim et al. (2023) [76] only assessed the erection phase and did not include material use, which constitutes a significant portion of CO_2 emissions. When material use is included in Kim et al. (2023) [76]'s analysis, the resulting reduction is 8.2%, which is lower than the 8.9% reduction achieved in this study.

Table 11. CO_2 emission comparison with previous studies (unit: T-CO_2).

Classification	This Study		Lim and Kim (2020) [36]		Kim et al. (2023) [76]	
	In Situ Production, Yard-Stock and Erection	CO_2 Optimization	In Situ Production	In-Plant Production	Actual Erection	Simulation-Calculated Erection
Material use	37,940	37,940	32,169	32,169	-	-
Labor use	363	283	-	-	372	341
Oil use	24,772	19,371	987	987	73,004	53,965
Electricity use	689	538	543	543	427	307
Transport equipment use	-	-	-	5397	-	-
Lighting, and heating use	352	275	-	-	197	153
Environmental conservation	239	186	-	-	110	83
Total	64,355	58,597	33,699	39,095	74,110	54,850

As shown in Table 11, rebar and structural steel materials account for the highest CO_2 emissions among all components. Therefore, the most effective approach to reducing total CO_2 emissions is to minimize the material usage of rebar and steel. However, in this study, the material quantity and structural design were not considered as influencing factors. Instead, the parameters used in the simulation model included the planned construction time, number of molds, number of cranes, and maximum yard-stock area. Accordingly, in order to achieve a more substantial reduction in CO_2 emissions—particularly addressing the material use, which accounts for over 33% of total emissions—future research should focus on the development of low-carbon structural materials and design strategies that minimize rebar and steel consumption.

5.3. Mechanisms by Which DT–BIM Integration Reduced CO_2

The integrated BIM–DT system is structured around three core mechanisms for reducing carbon emissions on construction sites: precise data utilization based on full-process modeling, simulation-based optimization, and the incorporation of real-time operational information. Firstly, BIM enables detailed modeling of PC components, such as columns and beams, by defining their geometry, quantity, and material specifications. This accurate quantification helps prevent overproduction and unnecessary stockpiling, thereby reducing resource waste and, indirectly, associated carbon emissions.

Subsequently, the digital twin reflects actual site conditions and operational parameters, such as crane deployment and task durations, in real time, enabling holistic optimization of production, yard-storage, and installation workflows. Analytical tools like Oracle Crystal Ball are employed to model variables such as working time, mold count, and crane allocation using probability distributions (normal distribution) and to simulate outcomes under multiple scenarios. This process facilitates the derivation of optimal work plans that minimize fuel-intensive operations, directly contributing to CO_2 emission reduction.

The introduction of in situ production, in particular, eliminates long-distance transportation from factories and shortens the movement paths of cranes and equipment. This leads to a significant decrease in fuel consumption, one of the major sources of carbon emissions. This study's simulation results indicate a CO_2 reduction effect of approximately 8.9%.

Additionally, the integrated framework quantitatively calculates resource consumption and CO_2 emissions at each process stage (production, yard-stock, erection) by applying

LCA coefficients. These results are visualized through a dashboard interface, enabling stakeholders, such as clients and contractors, to clearly understand each process's environmental contribution and adopt carbon-reduction strategies accordingly.

In summary, the DT–BIM integration offers a scientific mechanism for carbon mitigation on construction sites through production planning precision, simulation-based optimization, reduced material transport distances, efficient yard-space utilization, LCA-based emissions quantification, and real-time feedback systems. This framework serves not merely as a design aid but as a next-generation digital decision-making system that simultaneously addresses environmental performance and construction efficiency.

5.4. Decision-Making Suggestion

The decision-making process for minimizing environmental loads, as conducted in this study, is detailed in Figure 10. This process can be partially modified and adapted for practical implementation on construction sites, depending on the specific objectives and goals.

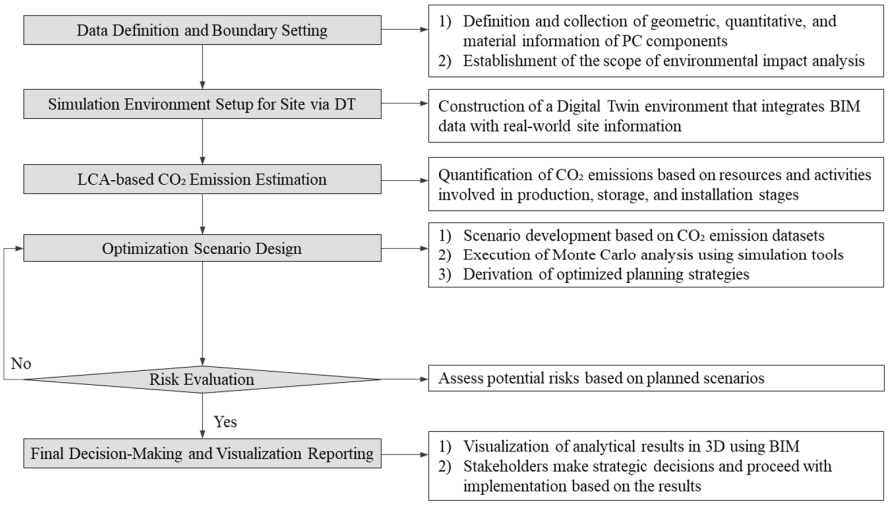

Figure 10. Decision-making suggestion process.

(1) In the data definition and boundary setting phase, the geometry, quantity, and material properties of precast concrete (PC) elements such as columns and beams are defined and extracted from the BIM model. Concurrently, real-time field sensor data and operational information are collected through the digital twin system. This stage also involves clearly delineating the boundaries of environmental load analysis by defining the scope of the life cycle assessment (LCA), for example as cradle-to-gate or cradle-to-site.

(2) The simulation environment setup for in situ production via the DT phase involves constructing a simulation environment that integrates BIM data with real-world site information using a DT platform. Key variables such as the production time, number of workers, productivity rates, transportation paths, and storage area dimensions are modeled. This simulation framework enables real-time tracking of resource inputs and environmental impacts across each construction phase and serves as a basis for scenario-based comparative evaluations.

(3) In the LCA-based CO_2 emission estimation phase, CO_2 emissions are quantified for each process phase—production, yard-stock, and installation—based on its respective resource and activity inputs (e.g., materials, labor, electricity, and fuel consumption). Each phase's contribution to total carbon emissions is analyzed to identify major emission drivers, which provides insights for targeted environmental interventions.

(4) In the optimization scenario design phase, based on the calculated CO_2 emission data, various optimization scenarios are developed (e.g., carbon-reduction-oriented, schedule-driven, cost-saving, or multi-objective scenarios). Monte Carlo simulations are conducted using tools such as AI-based models or Oracle Crystal Ball. Input variables (e.g., working hours, manpower, storage area) are treated as probabilistic distributions—typically normal distributions—that reflect their statistical characteristics. The output includes optimized plans for in situ production, yard storage allocation, and installation sequencing.

(5) The risk evaluation phase evaluates potential risks associated with each scenario, including spatial congestion, scheduling delays, and material interference. Through the DT, dynamic feedback mechanisms are established, which enables real-time scenario adjustments. For example, if excessive stacking occurs in a yard area, simulation reruns can automatically reallocate PC components to alternative zones or revise installation sequences.

(6) In the final decision-making and visualization reporting phase, all analytical outcomes are visualized in 3D using the BIM environment. Dashboards provide real-time insights into CO_2 emission contributions by phase as a result of space utilization rates, process durations, and scenario comparisons. Stakeholders, including owners, contractors, and engineers, can use this information to select and implement the most sustainable and operationally efficient strategies.

5.5. Discuss Trade-Offs (Digital Overhead vs. Savings)

This study demonstrates a concrete effort to strike a balance between productivity and environmental sustainability by integrating DT and BIM systems. However, while this approach offers clear benefits in terms of reducing environmental loads, it also entails significant costs and technical complexities associated with the deployment of digital systems. In this context, this study serves as a representative case for analyzing the trade-offs between digital overhead, stemming from initial implementation costs and ongoing maintenance, and the environmental and operational benefits of reduced CO_2 emissions and optimized production planning.

Digital overhead begins to accumulate from the initial stages of system implementation. Establishing BIM data and integrating them with a digital twin environment requires advanced modeling, real-time site data synchronization, the deployment of IoT sensors, and the application of simulation-based analytical tools such as Oracle Crystal Ball. These technical requirements increase upfront costs and demand considerable time and resources to build the necessary digital infrastructure. Moreover, such systems require continuous maintenance and data synchronization during operation, including regular updates of BIM tools (e.g., RVT, IFC) and personnel support for reflecting real-time sensor data into the DT environment. These factors collectively contribute to the high managerial complexity of digital-based systems.

Despite these challenges, the integrated DT–BIM framework proposed in this study yields significant advantages. The most notable achievement is the reduction in CO_2 emissions: through simulation-based optimization of production, yard-stock, and installation processes, this study demonstrates a potential reduction of approximately 8.9% compared to conventional methods. Particularly in in situ production scenarios, material transport is minimized, and equipment movement is reduced, which leads to a notable decrease in fuel consumption—a key source of CO_2 emissions. Furthermore, the dashboard visualization of the resource input and carbon output per process stage enables both clients and contractors

to gain a clear understanding of each stage's environmental contribution, facilitating more strategic decision-making.

Additionally, this framework contributes to schedule and spatial optimization. Zoning plans that account for crane rotation radii and operating capacities, sequencing of precast component placements within the yard, and installation planning based on crane logistics are shown to improve productivity even in space-constrained urban construction sites. Scenario-based evaluation using Monte Carlo simulations enhances resilience to uncertain site variables and allows for proactive risk mitigation (e.g., material congestion, spatial limitations).

In conclusion, this study illustrates that, while the integration of digital twin and BIM systems entails certain costs and complexities, the long-term benefits, such as CO_2 emissions reduction, construction efficiency, and risk mitigation, can be substantial. Such integrated strategies are especially valuable in the current industrial landscape, where enhanced ESG (environment, social, governance) evaluation criteria, carbon taxation, and green-smart construction practices are gaining traction. Therefore, the proposed approach not only represents a technological innovation but also exemplifies a digital decision-making framework capable of driving the environmental and operational transformation of the construction industry.

5.6. Present Limitations and Future Research Directions

This study presents a practical framework aimed at reducing environmental loads, particularly carbon dioxide emissions, through the integration of DT technology and BIM in the in situ production and yard-stock management of PC components. However, the proposed system also entails several technical and operational limitations, along with areas for potential improvement:

(1) One significant challenge lies in the reliability and accuracy of the real-time data provided by the digital twin system, which is susceptible to variables such as sensor coverage, data transmission stability, and discrepancies between the actual site and the digital model. If the real-time field conditions are not accurately reflected in the BIM environment, simulation-based decision-making may result in errors. Incomplete or imprecise data inputs undermine the effectiveness of the digital twin.

(2) From the perspective of environmental impact analysis (LCA), this study primarily focuses on CO_2 emissions, excluding multidimensional environmental indicators such as total energy consumption, material lifecycle, water usage, and fine particulate matter. This narrows the scope of result interpretation and suggests a need to expand the analytical framework for more comprehensive sustainability evaluations.

(3) The decision-making model does not incorporate multi-agent simulations that account for interactions among multiple stakeholders. Complex decision structures involving resource competition and schedule conflicts among cranes, equipment, and laborers are difficult to capture using a single optimization algorithm.

To enhance the framework, future research may take the following directions:

(1) Simulation methods that employ Bayesian analysis or probabilistic LCA models should be introduced to address uncertainties inherent in construction environments. These approaches can generate more robust decisions by accounting for variable fluctuations and risk. Furthermore, the development of multi-objective optimization algorithms that balance carbon reduction, cost savings, and schedule compression is necessary. Machine learning or reinforcement learning techniques may improve prediction accuracy and automation levels.

(2) Integrating the BIM–DT system with supply chain management (SCM) or enterprise resource planning (ERP) systems could enable the prediction of material arrival times, the adoption of just-in-time (JIT) supply strategies for yard logistics, and the minimization of

material waste. Another critical task is securing long-term empirical data to quantitatively validate the framework's applicability and performance in actual projects.

(3) Expanding the set of environmental assessment indicators is essential. This includes incorporating factors such as energy consumption, on-site health and safety (e.g., noise, vibration, dust), and material recyclability. The development of a dashboard that can visualize and quantify these indicators would enhance decision-making transparency and stakeholder confidence.

(4) Ultimately, the development of internationally standardized open BIM–DT protocols is necessary to ensure interoperability across platforms and to streamline sensor metadata structures. Such standardization would improve scalability and maintenance efficiency. This evolution goes beyond mere technological advancement and contributes to establishing a strategic digital construction management system aligned with the era of carbon neutrality.

6. Conclusions

This study proposed a BIM-based DT framework to optimize in situ production, yard-stock management, and installation of PC components in large-scale construction projects. By integrating probabilistic simulation with BIM-derived data based on data that are actually applied in the field, the framework effectively addressed the core constraints of environmental impact assessment within a unified digital environment.

Using Oracle Crystal Ball, this study conducted Monte Carlo simulations to evaluate CO_2 emissions. CO_2 emissions were optimized to 64,355 T-CO_2, which highlights the significant environmental benefits achievable through intelligent layout and production planning. Notably, increased crane use was associated with a higher carbon output, which indicates that equipment operation is a key driver of environmental load.

Overall, the results validate the feasibility of predictive and simulation-driven planning in managing complex construction variables. By enabling real-time synchronization of production, yard layout, and installation processes, the proposed framework contributes to more sustainable and resilient construction strategies. This study was conducted by utilizing data that were actually applied in the field and presenting assumption conditions. The optimization model can be used to control carbon emissions, and the DT model can be used to reflect real-time feedback in the field.

From an academic perspective, this research advances the application of DT technology in construction by holistically integrating environmental performance into a single model. Practically, it provides actionable insights for project managers and policy makers seeking to implement smart, low-carbon construction practices. However, the findings are limited to a single case project and do not yet incorporate real-time sensor feedback or automated 3D yard modeling.

Future research should focus on expanding the applicability of the framework in the following ways:

- Integrating real-time sensor data for dynamic feedback control;
- Applying machine learning techniques to improve CO_2 emission forecasting;
- Enhancing safety and risk management through predictive analytics;
- Developing cloud-based visualization dashboards for intelligent site monitoring.

By addressing these directions, the framework can evolve into a fully autonomous, adaptive DT system capable of supporting the next generation of sustainable construction management.

Author Contributions: Conceptualization, S.K. and J.L.; methodology, J.L.; software, J.P. and J.L.; validation, J.L.; formal analysis, J.P. and J.L.; investigation, S.K. and J.L.; resources, J.P., S.K. and J.L.;

data curation, J.P. and J.L.; writing—original draft preparation, J.P. and J.L.; writing—review and editing, J.P., S.K. and J.L.; visualization, J.L.; supervision, S.K. and J.L.; project administration, S.K. and J.L.; funding acquisition, S.K. and J.L. All authors have read and agreed to the published version of the manuscript.

Funding: This work was supported by the National Research Foundation of Korea (NRF) grant funded by the Korea government (MOE) (No. 2021R1C1C2094527 and No. 2022R1A2C2005276).

Institutional Review Board Statement: Not applicable.

Informed Consent Statement: Not applicable.

Data Availability Statement: The raw data supporting the conclusions of this article will be made available by the authors on request.

Conflicts of Interest: Author Junyoung Park was employed by Hyundai Development Company. Author Sunkuk Kim was employed by Earth Turbine Co., Ltd. The remaining author declares that the research was conducted in the absence of any commercial or financial relationships that could be construed as a potential conflict of interest.

Abbreviations

The following abbreviations are used in this manuscript:

DT	Digital Twin
BIM	Building Information Modeling
PC	Precast concrete
SRC	Steel-reinforced concrete
RC	Reinforced concrete

Appendix A

Algorithm A1. The framework of CO_2 emission optimization.

```
Require: CO2 emission of each stage and each parameter.
Ensure: Optimal CO2 emission
def calculate_ CO2 emission(N_m, N_c, N_w, A_y, L_t, stage_params, A_m, CO2_factors):
    """
    Calculate total CO2 emission for PC production stages.
     Parameters:
     - N_m: Number of molds (dict: {'column': int, 'beam': int})
     - N_c: Number of cranes
     - N_w: Number of workers per stage (dict: {stage: int})
     - A_y: Stockyard area (m2)
     - stage_params: Dict of stage parameters {stage: {'workload': float, 'productivity': float, 'contingency': float}}
     - A_m: Area per mold (m2)
     - CO2_factors: CO2 emission factors {stage: float} (kg CO2 per workhour)
     Returns:
     - Total CO2 emissions (kg), stage-wise breakdown
     """
     # Initialize variables
     stage_CO2 = {}
     total_CO2 = 0
     days_per_month = 30 # Assumption for conversion
     # Maximum molds based on stockyard area
     N_m_max = A_y // A_m
     batch_count = max(1, (N_m['column'] + N_m['beam']) / N_m_max)
     # Process each stage
     for stage in ['MP', 'RP', 'CP', 'CU', 'DM', 'FI']:
          workload = stage_params[stage]['workload'] # hours per mold
          productivity = stage_params[stage]['productivity'] # mold per worker-hour
          contingency = stage_params[stage]['contingency']

 # Time per mold for the stage
          T_s = workload / (N_w[stage] * productivity) # hours per mold considering number of workers

# Total time for stage
```

```
            T_s_total = (N_m['column'] + N_m['beam']) / (N_w[stage] * productivity) * T_s * (1 + contingency)
            T_s_total *= batch_count # batch effect
            # CO2 emission calculation
            CO2_stage = T_s_total * CO2_factors[stage] # kg CO2
            stage_CO2[stage] = CO2_stage
            total_CO2 += CO2_stage
    # Installation stage (IN)
    T_IN_unit = stage_params['IN']['workload'] # Time per component (hours)
    C_c = stage_params['IN']['crane_capacity'] # Components per crane per unit time
    T_IN = ((N_m['column'] + N_m['beam']) / (N_c * C_c)) * T_IN_unit
    CO2_IN = T_IN * CO2_factors['IN'] # kg CO2
    stage_CO2['IN'] = CO2_IN
    total_CO2 += CO2_IN
    return total_CO2, stage_CO2
# Example usage
stage_params = {
    'MP': {'workload': 8, 'productivity': 1, 'contingency': 0.1},
    'RP': {'workload': 6, 'productivity': 1, 'contingency': 0.1},
    'CP': {'workload': 4, 'productivity': 1, 'contingency': 0.1},
    'CU': {'workload': 24, 'productivity': 1, 'contingency': 0.1},
    'DM': {'workload': 4, 'productivity': 1, 'contingency': 0.1},
    'FI': {'workload': 3, 'productivity': 1, 'contingency': 0.1},
    'IN': {'workload': 2, 'crane_capacity': 1, 'contingency': 0.1}
}
CO2_factors = {
    'MP': 5.0, # kg CO2 per workhour
    'RP': 4.0,
    'CP': 3.0,
    'CU': 6.0,
    'DM': 3.5,
    'FI': 2.5,
    'IN': 7.0
}
N_m = {'column': 30, 'beam': 91}
N_c = 2
N_w = {'MP': 10, 'RP': 8, 'CP': 6, 'CU': 4, 'DM': 6, 'FI': 5, 'IN': 10}
A_y = 15729
A_m = 50
L_t = 5.1
total_CO2, stage_CO2 = calculate_CO2_emission(N_m, N_c, N_w, A_y, L_t, stage_params, A_m, CO2_factors)
print(f"Total CO2 Emission: {total_CO2:.2f} kg")
print("Stage-wise CO2 Breakdown:")
for stage, co2 in stage_CO2.items():
    print(f"{stage}: {co2:.2f} kg")
```

References

1. Merschbrock, C.; Munkvold, B.E. The digital transformation of the construction industry: A review. *Ind. Commer. Train.* **2024**, *56*, 123–140. [CrossRef]
2. Nyqvist, R.; Peltokorpi, A.; Lavikka, R.; Ainamo, A. Building the digital age: Management of digital transformation in the construction industry. *Constr. Manag. Econ.* **2025**, *43*, 262–283. [CrossRef]
3. Qi, Q.; Tao, F. Digital twins and big data towards smart manufacturing and Industry 4.0: 360-degree comparison. *Adv. Eng. Inform.* **2021**, *59*, 101542. [CrossRef]
4. Boje, C.; Guerriero, A.; Kubicki, S.; Rezgui, Y. Towards a semantic construction digital twin: Directions for future research. *Autom. Constr.* **2020**, *114*, 103179. [CrossRef]
5. Jeong, S.-H.; Kim, G.-H. Development of BIM Utilization Level Evaluation Model in Construction Management Company. *Korean J. Constr. Eng. Manag.* **2024**, *25*, 24–33. [CrossRef]
6. Hwang, J.; Song, S.H.; Lee, C.; Ahn, H.; Cho, H.; Kang, K.-I. BIM and OpenAI-based Model for Supporting Initial Construction Planning of Bridges and Tunnels. *Korean J. Constr. Eng. Manag.* **2024**, *25*, 24–33. [CrossRef]
7. Kang, H.; Seong, H. Conceptual Model for Quality Risk Assessment and Reserve Cost Estimation for Construction Projects based on BIM. *Korean J. Constr. Eng. Manag.* **2025**, *26*, 62–71. [CrossRef]
8. Kim, H.; Nam, J. Applying BIM Standard Guideline to Expressway BIM Results and Drawing Its Improvement Measure for Project Management. *Korean J. Constr. Eng. Manag.* **2025**, *26*, 82–88. [CrossRef]
9. Kim, I.; Shah, S.H. A Proposal for Evaluation Criteria of Decision Support System for BIM. *Korean J. Constr. Eng. Manag.* **2025**, *26*, 89–102. [CrossRef]

10. Sacks, R.; Brilakis, I.; Pikas, E.; Xie, H.S.; Girolami, M. Construction with digital twin information systems. *Data-Centric Eng.* **2020**, *1*, e14. [CrossRef]
11. Lu, Q.; Parlikad, A.K.; Woodall, P.; Ranasinghe, G.D.; Xie, Y.; Liang, Z.; Konstantinou, E. Developing a digital twin at building and city levels: Case study of West Cambridge campus. *J. Manag. Eng.* **2020**, *36*, 05020004. [CrossRef]
12. Jiang, Y.; Li, M.; Guo, D.; Wu, W.; Zhong, R.Y.; Huang, G.Q. Digital twin-enabled smart modular integrated construction system for on-site assembly. *Comput. Ind.* **2022**, *136*, 103594. [CrossRef]
13. Guo, J.; Zhao, N.; Sun, L.; Zhang, S. Modular based flexible digital twin for factory design. *J. Ambient. Intell Hum. Comput.* **2019**, *10*, 1189–1200. [CrossRef]
14. Al-Kahwati, K.; Birk, W.; Nilsfors, E.F.; Nilsen, R. Experiences of a digital twin based predictive maintenance solution for belt conveyor systems. *PHM Soc. Eur. Conf.* **2022**, *7*, 1–8. [CrossRef]
15. Chen, Z.; Tan, Y.; Zhang, A. Integrating digital twin and blockchain for smart building management. *Sustain. Cities Soc.* **2023**, *99*, 104514. [CrossRef]
16. Lim, J.; Kim, J.J. Dynamic optimization model for estimating in-situ production quantity of PC members to minimize environmental loads. *Sustainability* **2020**, *12*, 8202. [CrossRef]
17. Hong, W.-K.; Lee, G.; Lee, S.; Kim, S. Algorithms for in-situ production layout of composite precast concrete members. *Autom. Constr.* **2014**, *41*, 50–59. [CrossRef]
18. Na, Y.J.; Kim, S.K. A process for the efficient in-situ production of precast concrete members. *J. Reg. Assoc. Archit. Inst. Korea* **2017**, *19*, 153–161.
19. Lim, C. Construction Planning Model for In Situ Production and Installation of Composite Precast Concrete Frame. Ph.D. Thesis, Kyung Hee University, Seoul, Republic of Korea, 2016.
20. Lim, J.; Son, C.-B.; Kim, S. Scenario-based 4D dynamic simulation model for in situ production and yard stock of precast concrete members. *J. Asian Arch. Build. Eng.* **2022**, *22*, 2320–2334. [CrossRef]
21. Lim, J.; Kim, S. Environmental Impact Minimization Model for Storage Yard of In-situ Produced PC Components: Comparison of Dung Beetle Algorithm and Improved Dung Beetle Algorithm. *Buildings* **2024**, *14*, 3753. [CrossRef]
22. Jung, H.T.; Lee, M.S. A Study on the Site-production Possibility of the Prefabricated PC Components. In Proceedings of the 1992 Autumn Annual Conference of the Architectural Institute of Korea, Seoul, Republic of Korea, 24 October 1992; Volume 12, pp. 629–636.
23. Li, H.; Love, P.E. Genetic search for solving construction site-level unequal-area facility layout problems. *Autom. Constr.* **2000**, *9*, 217–226. [CrossRef]
24. Won, I.; Na, Y.; Kim, J.T.; Kim, S. Energy-efficient algorithms of the steam curing for the in situ production of precast concrete members. *Energy Build.* **2013**, *64*, 275–284. [CrossRef]
25. Kim, S.; Kim, G.; Kang, K. A Study on the effective inventory management by optimizing lot size in building construction. *J. Korea Inst. Build. Constr.* **2004**, *4*, 73–80. [CrossRef]
26. Lee, J.M.; Yu, J.H.; Kim, C.D. *A Economic Order Quantity (EOQ) Determination Method Considering Stock Yard Size*; Korea Institute of Construction Engineering and Management: Seoul, Republic of Korea, 2007; pp. 549–552.
27. Lee, J.M.; Yu, J.H.; Kim, C.D.; Lee, K.J.; Lim, B.S. Order Point Determination Method considering Materials Demand Variation of Construction Site. *J. Archit. Inst. Korea* **2008**, *24*, 117–125.
28. Thomas, H.R.; Horman, M.J.; Minchin, R.E.; Chen, D. Improving labor flow reliability for better productivity as lean construction principle. *J. Constr. Eng. Manag.* **2003**, *129*, 251–261. [CrossRef]
29. Yun, J.-S.; Yu, J.-H.; Kim, C.-D. Economic Order Quantity (EOQ) Determination Process for Construction Material considering Demand Variation and Stockyard Availability. *Korean J. Constr. Eng. Manag.* **2011**, *12*, 33–42. [CrossRef]
30. Dobson, D.W.; Sourani, A.; Sertyesilisik, B.; Tunstall, A. Sustainable construction: Analysis of its costs and benefits. *Am. J. Civ. Eng. Archit.* **2013**, *1*, 32–38.
31. Volk, R.; Stengel, J.; Schultmann, F. Building Information Modeling (BIM) for existing buildings—Literature review and future needs. *Autom. Constr.* **2014**, *38*, 109–127. [CrossRef]
32. Osman, H.M.; Georgy, M.E.; Ibrahim, M.E. A hybrid CAD-based construction site layout planning system using genetic algo-rithms. *Autom. Constr.* **2003**, *12*, 749–764. [CrossRef]
33. Ning, X.; Lam, K.-C.; Lam, M.C.-K. Dynamic construction site layout planning using max-min ant system. *Autom. Constr.* **2009**, *19*, 55–65. [CrossRef]
34. Abdul-Rahman, H.; Wang, C.; Eng, K.S. Repertory grid technique in the development of Tacit-based Decision Support System (TDSS) for sustainable site layout planning. *Autom. Constr.* **2011**, *20*, 818–829. [CrossRef]
35. Lee, G.J. A Study of In-Situ Production Management Model of Composite Precast Concrete Members. Ph.D. Thesis, Kyung Hee University, Seoul, Republic of Korea, 2012.

36. Lim, J.; Kim, S. Evaluation of CO_2 Emission Reduction Effect Using In-situ Production of Precast Concrete Components. *J. Asian Arch. Build. Eng.* **2020**, *19*, 176–186. [CrossRef]
37. Gao, M.Y.; Han, J.; Yang, Y.; Tiong, R.L.; Zhao, C.; Han, C. BIM-based and IoT-driven smart tracking for precast construction dynamic scheduling. *J. Constr. Eng. Manag.* **2024**, *150*, 04024117. [CrossRef]
38. Su, R.; Aviles, J.S. Construction Scheduling Optimization of Prefabricated Buildings Under Resource Constraints Based on an Improved Whale Optimization Algorithm. *Int. J. Comput. Intell. Syst.* **2025**, *18*, 166. [CrossRef]
39. Pradhan, P.; Verma, M.S.; Sahu, M.S. Optimization of Cast-In-Situ and Precast Concrete Methods Through BIM and Structural Simulations. *Optimization* **2025**.
40. Cotoarbă, D.; Straub, D.; Smith, I.F. Probabilistic digital twins for geotechnical design and construction. *Data-Centric Eng.* **2025**, *6*, e30. [CrossRef]
41. Lim, J.; Kim, S.; Kim, J.J. Dynamic simulation model for estimating in-situ production quantity of pc members. *Int. J. Civ. Eng.* **2020**, *18*, 935–950. [CrossRef]
42. Lim, J.; Park, K.; Son, S.; Kim, S. Cost reduction effects of in-situ PC production for heavily loaded long-span buildings. *J. Asian Arch. Build. Eng.* **2020**, *19*, 242–253. [CrossRef]
43. Opoku, D.G.J.; Perera, S.; Osei-Kyei, R. Digital Twins for the Built Environment: Learning from Conceptual and Process Models in Manufacturing. *Smart Sustain. Built Environ.* **2021**, *10*, 557–575.
44. Kassem, M.; Kelly, G.; Dawood, N.; Serginson, M.; Lockley, S. BIM in Facilities Management Applications: A Case Study of a Large University Complex. *Built Environ. Proj. Asset Manag.* **2015**, *5*, 261–277. [CrossRef]
45. Xu, Q.; Wang, J.; Gao, W.; Ren, S.; Li, Z. Digital Twin: State-of-the-Art and Future Perspectives. In Proceedings of the 2024 5th International Conference on Computer Science and Management Technology, Xiamen, China, 18–20 October 2024; pp. 731–740.
46. Alizadehsalehi, S.; Hadavi, A.; Huang, J.C. From BIM to Extended Reality in AEC Industry. *Autom. Constr.* **2020**, *116*, 1–13. [CrossRef]
47. Chen, C.; Zhao, Z.; Xiao, J.; Tiong, R. A conceptual framework for estimating building embodied carbon based on digital twin technology and life cycle assessment. *Sustainability* **2021**, *13*, 13875. [CrossRef]
48. Tagliabue, L.C.; Brazzalle, T.F.; Rinaldi, S.; Dotelli, G. Cognitive Digital Twin Framework for Life Cycle Assessment Supporting Building Sustainability. In *Cognitive Digital Twins for Smart Lifecycle Management of Built Environment and Infrastructure*; CRC Press: Boca Raton, FL, USA, 2023; pp. 177–205.
49. Zhang, Z.; Wei, Z.; Court, S.; Yang, L.; Wang, S.; Thirunavukarasu, A.; Zhao, Y. A review of digital twin technologies for enhanced sustainability in the construction industry. *Buildings* **2024**, *14*, 1113. [CrossRef]
50. Agostinelli, S.; Cinquepalmi, F.; Ruperto, F. 5D BIM: Tools and methods for digital project construction management. *WIT Trans. Built Environ.* **2019**, *192*, 205–215. [CrossRef]
51. Gonzalez, J.; Soares, C.A.P.; Najjar, M.; Haddad, A.N. BIM and BEM methodologies integration in energy-efficient buildings using experimental design. *Buildings* **2021**, *11*, 491. [CrossRef]
52. Rodrigues, F.; Baptista, J.S.; Pinto, D. BIM approach in construction safety—A case study on preventing falls from height. *Buildings* **2022**, *12*, 73. [CrossRef]
53. Muzi, F.; Marzo, R.; Nardi, F. Digital information management in the built environment: Data-driven approaches for building process optimization. In *Technological Imagination in the Green and Digital Transition*; Springer International Publishing: Cham, Switzerland, 2022; pp. 123–132. [CrossRef]
54. Bakhshi, S.; Ghaffarianhoseini, A.; Ghaffarianhoseini, A.; Najafi, M.; Rahimian, F.; Park, C.; Lee, D. Digital twin applications for overcoming construction supply chain challenges. *Autom. Constr.* **2024**, *167*, 105679. [CrossRef]
55. Kosse, S.; Forman, P.; Stindt, J.; Hoppe, J.; Konig, M.; Mark, P. Industry 4.0 enabled modular precast concrete components: A case study. In *International RILEM Conference on Synergising Expertise Towards Sustainability and Robustness of CBMs and Concrete Structures*; Springer Nature: Cham, Switzerland, 2023; pp. 229–240.
56. Wang, Q.; Yin, Y.; Chen, Y.; Liu, Y. Carbon peak management strategies for achieving net-zero emissions in smart buildings: Advances and modeling in digital twin. *Sustain. Energy Technol. Assess.* **2024**, *64*, 103661. [CrossRef]
57. Filippova, E.; Hedayat, S.; Ziarati, T.; Manganelli, M. Artificial Intelligence and Digital Twins for Bioclimatic Building Design: Innovations in Sustainability and Efficiency. *Preprints* **2025**. [CrossRef]
58. Hosamo, H.; Hosamo, M.H.; Nielsen, H.K.; Svennevig, P.R.; Svidt, K. Digital Twin of HVAC system (HVACDT) for multiobjective optimization of energy consumption and thermal comfort based on BIM framework with ANN-MOGA. *Adv. Build. Energy Res.* **2023**, *17*, 125–171. [CrossRef]
59. Sohail, A.; Shen, B.; Cheema, M.A.; Ali, M.E.; Ulhaq, A.; Babar, M.A.; Qureshi, A. Beyond data, towards sustainability: A Sydney case study on urban digital twins. *PFG J. Photogramm. Remote Sens. Geoinf. Sci.* **2025**, *93*, 365–377. [CrossRef]

60. *ISO 14040*; Environmental Management-Life Cycle Assessment-Principles and Framework. International Organization for Standardization: Geneva, Switzerland, 2006. Available online: https://www.iso.org/standard/37456.html (accessed on 25 August 2025).
61. *ISO 14044*; Environmental Management-Life Cycle Assessment-Requirements and Guidelines. International Organization for Standardization: Geneva, Switzerland, 2006. Available online: https://www.iso.org/standard/38498.html (accessed on 25 August 2025).
62. *EN 15978*; Sustainability of Construction Works—Assessment of Environmental Performance Of Buildings—Calculation Method. The British Standards Institution: London, UK, 2011. Available online: https://shop.bsigroup.com/ProductDetail?pid=00000000 0030256638 (accessed on 25 August 2025).
63. Hollberg, A.; Genova, G.; Habert, G. Evaluation of BIM-based LCA results for building design. *Autom. Constr.* **2020**, *109*, 102972. [CrossRef]
64. Berges-Alvarez, I.; Martinez-Rocamora, A.; Marrero, M. A Systematic Review of BIM-Based Life Cycle Sustainability Assessment for Buildings. *Sustainability* **2024**, *16*, 11070. [CrossRef]
65. Mazur, Ł.; Olenchuk, A. Life cycle assessment and building information modeling integrated approach: Carbon footprint of masonry and timber-frame constructions in Single-Family houses. *Sustainability* **2023**, *15*, 15486. [CrossRef]
66. Badenko, V.; Bolshakov, N.; Celani, A.; Puglisi, V. Principles for Sustainable Integration of BIM and Digital Twin Technologies in Industrial Infrastructure. *Sustainability* **2024**, *16*, 9885. [CrossRef]
67. Kosse, S.; Vogt, O.; Wolf, M.; Konig, M.; Gerhard, D. Digital twin framework for enabling serial construction. *Front. Built Environ.* **2022**, *8*, 864722. [CrossRef]
68. Widjaja, D.D.; Lim, J.; Kim, S. Integrating Digital Twin and BIM for Special-Length-Based Rebar Layout Optimization in Reinforced Concrete Construction. *Buildings* **2025**, *15*, 2617. [CrossRef]
69. Dong, Y.H.; Jaillon, L.; Chu, P.; Poon, C.S. Comparing carbon emissions of precast and cast-in-situ construction methods—A case study of high-rise private building. *Constr. Build. Mater.* **2015**, *99*, 39–53. [CrossRef]
70. Zhou, F.; Ning, Y.; Guo, X.; Guo, S. Analyze differences in carbon emissions from traditional and prefabricated buildings combining the life cycle. *Buildings* **2023**, *13*, 874. [CrossRef]
71. Afsahi, I. Comparison Between Precast Versus In Situ Structures in Terms of Sustainability. Master's Thesis, Universitat Politecnica de Catalunya, Barcelona, Spain, 2024.
72. Gong, T.; Yang, J.; Hu, H.; Xu, F. Construction technology of off-site precast concrete buildings. *Front. Eng. Manag.* **2015**, *2*, 122. [CrossRef]
73. Tharma, R.; Winter, R.; Eigner, M. An approach for the implementation of the digital twin in the automotive wiring harness field. In Proceedings of the DS 92: DESIGN 2018 15th International Design Conference 2018, Dubrovnik, Croatia, 21–24 May 2018; pp. 3023–3032. [CrossRef]
74. Kritzinger, W.; Karner, M.; Traar, G.; Henjes, J.; Sihn, W. Digital Twin in manufacturing: A categorical literature review and classification. *IFAC-Pap.* **2018**, *51*, 1016–1022. [CrossRef]
75. Lim, J.; Kim, S. BIM-Driven Scheduling Optimization for In-situ Production and Yard-stock Integration of Precast Concrete Members. *Ain Shams Eng. J.* 2025; *manuscript in preparation*.
76. Kim, S.; Oh, J.; Lim, J. Development of an algorithm for crane trajectory distance calculation for erection of precast concrete members. *Buildings* **2023**, *14*, 11. [CrossRef]
77. Hong, W.K.; Park, S.C.; Lee, H.C.; Kim, J.M.; Kim, S.I.; Lee, S.G.; Yoon, K.J. Composite beam composed of steel and precast concrete (modularized hybrid system). Part III: Application for a 19-storey building. *Struct. Des. Tall Spec. Build.* **2010**, *19*, 679–706. [CrossRef]
78. Rajput, B.L.; Hussain, M.A.; Shaikh, N.N.; Vadodaria, J. Time and Cost Comparison of Construction of RCC, Steel and Composite Structure Building. *IUP J. Struct. Eng.* **2013**, *6*, 50. Available online: https://research.ebsco.com/c/akl6ox/viewer/pdf/lxkljxp5 wn (accessed on 4 June 2025).
79. Ghayeb, H.H.; Razak, H.A.; Sulong, N.R. Evaluation of the CO_2 emissions of an innovative composite precast concrete structure building frame. *J. Clean. Prod.* **2020**, *242*, 118567. [CrossRef]
80. Kudo, S.; Kapfudzaruwa, F.; Broadhurst, J.L.; Edusah, S.E.; Awere, K.G.; Matsuyama, K.; Nagao, M.; Mino, T. Moving towards Transdisciplinarity: Framing Sustainability Challenges in Africa. *Sustain. Dev. Afr. Concepts Methodol. Approaches* **2019**, *5*, 1.

Disclaimer/Publisher's Note: The statements, opinions and data contained in all publications are solely those of the individual author(s) and contributor(s) and not of MDPI and/or the editor(s). MDPI and/or the editor(s) disclaim responsibility for any injury to people or property resulting from any ideas, methods, instructions or products referred to in the content.

applied sciences

MDPI

Article

Utilization of Waste Clay–Diatomite in the Production of Durable Mullite-Based Insulating Materials

Svetlana Ilić [1,*], Jelena Maletaškić [1], Željko Skoko [2], Marija M. Vuksanović [1], Željko Radovanović [3], Ivica Ristović [4] and Aleksandra Šaponjić [1,*]

[1] Vinča Institute of Nuclear Sciences, National Institute of the Republic of Serbia, University of Belgrade, Mike Petrovića Alasa 12-14, 11000 Belgrade, Serbia; jelena.pantic@vin.bg.ac.rs (J.M.); marija.vuksanovic@vin.bg.ac.rs (M.M.V.)
[2] Department of Physics, Faculty of Science, University of Zagreb, Bijenička 32, 10000 Zagreb, Croatia; zskoko@phy.hr
[3] Innovation Centre of the Faculty of Technology and Metallurgy, Karnegijeva 4, 11000 Belgrade, Serbia; zradovanovic@tmf.bg.ac.rs
[4] Faculty of Mining and Geology, University of Belgrade, Đušina 7, 11000 Belgrade, Serbia; ivica.ristovic@rgf.bg.ac.rs
* Correspondence: svetlanailic@vin.bg.ac.rs (S.I.); acavuc@vin.bg.ac.rs (A.Š.)

Featured Application: Due to their low thermal conductivity, mullite-based materials obtained from mining waste might be successfully used as insulating materials, while designing and texturing their microstructure can further enhance their insulating properties.

Abstract: Microstructural, mechanical and qualitative phase identification of durable mullite-based ceramics obtained by utilization of waste clay–diatomite has been studied. Mullite-based ceramics were fabricated using waste clay–diatomite from the Baroševac open-cast coal mine, Kolubara (Serbia). The raw material consists mainly of SiO_2 (70.5 wt%) and a moderately high content of Al_2O_3 (13.8 wt%). In order to achieve the stoichiometric mullite composition ($3Al_2O_3$-$2SiO_2$), the raw material was mixed with an appropriate amount of $Al(NO_3)_3 \cdot 9H_2O$. After preparing the precursor powder, the green compacts were sintered at 1300, 1400 and 1500 °C for 2 h. During the process, rod-shaped mullite grains were formed, measuring approximately 5 μm in length and a diameter of 500 nm (aspect ratio 10:1). The microstructure of the sample sintered at 1500 °C resulted in a well-developed, porous, nest-like morphology. According to the X-ray diffraction analysis, the sample at 1400 °C consisted of mullite, cristobalite and corundum phases, while the sample sintered at 1500 °C contained mullite (63.24 wt%) and an amorphous phase that reached 36.7 wt%. Both samples exhibited exceptional compressive strength—up to 188 MPa at 1400 °C. However, the decrease in compressive strength to 136 MPa at 1500 °C is attributed to changes in the phase composition, the disappearance of the corundum phase and alterations in the microstructure. This occurred despite an increase in bulk density to 2.36 g/cm^3 (approximately 82% of theoretical density) and a complete reduction in open porosity. The residual glassy phase (36.7 wt% at 1500 °C) is probably the key factor influencing the mechanical properties at room temperature in these ceramics produced from waste clay–diatomite. However, the excellent mechanical stability of the samples sintered at 1400 and 1500 °C, achieved without binders or additives and using mined diatomaceous earth, supports further research into mullite-based insulating materials. Mullite-based materials obtained from mining waste might be successfully used in the field of energy-efficient refractory materials and thermal insulators. for high-temperature applications

Keywords: mullite; mining waste; diatomaceous earth/diatomite; sintering; compressive strength; thermal insulators

1. Introduction

Guided by economic and ecological approaches, many scientists and professionals are increasingly utilizing industrial, construction and mining waste in accordance with the Sustainable Development Goals (SDGs), which are implemented through the concept of the circular economy. Since the circular economy of materials has a long-term impact on minimizing negative environmental impacts such as air, soil and groundwater pollution, the utilization of natural and waste materials is increasingly being used in the production of lightweight concretes (LWCs) as lightweight aggregates [1,2]. In recent years, significant attention has also been directed toward geopolymer concretes, which are considered a sustainable and environmentally friendly alternative to conventional Portland cement in traditional cementitious systems. Recent comprehensive studies have emphasized the potential of these environmentally friendly building materials, which are produced from extracted soils and sediments such as clays, mining waste, slags, etc. In particular, these mining wastes have proven to be effective precursors for geopolymer binders [3–5]. Given their promising properties, such materials could be used in the construction of highways, tunnels and embankments, enhancing roadway performance of roads, including improved fire and frost resistance [6–8].

Another valuable application of industrial waste and natural materials, including mining waste such as kaolin, diatomite, bauxite and other minerals that accumulate in landfills, is in the production of highly durable refractories. As already mentioned, the use of such materials for the production of high-performance technical ceramics remains a challenge. It requires innovative strategies for the management of sustainable post-mining landscapes and balanced societal decisions to promote a green economy—one that provides equitable solutions for both people and the planet. At the same time, the proper design of ceramic materials is essential to achieve the appropriate technological properties (i.e., thermal, mechanical and chemical) and performance (e.g., highly resistant mullite refractories) for various industries such as iron, steel, cement, glass, petrochemicals, etc. Solving the problem of industrial, construction and mining waste not only mitigates air and soil pollution but also enables economic savings through the production of highly durable mullite refractories [9–11]. One of the most common industrial waste materials used for the production of mullite refractories is coal fly ash, which remains one of the most significant environmental problems in today's society [12,13]. The utilization of coal fly ash, which is typically located at uncontrolled landfills, supports the implementation of a circular economy, thereby mitigating growing pollution and depletion of natural resources. In addition, natural and mining-derived materials such as kaolin, diatomaceous earth and bauxite are also used extensively in the production of lightweight bricks, panels and precast elements. These materials significantly reduce structural loads and enable the design and construction of more efficient high-rise buildings and structures. In addition, precast elements can be designed to fulfill specific project requirements, including acoustic performance, fire resistance and thermal insulation [14–17].

The applicability of natural materials and waste/by-products in the production of mullite-based refractories has already been confirmed. Highly vitreous bodies offer specific advantages in processing [18]. First, the high viscosity of the glassy phase (high content of SiO_2) allows the ionic diffusion of nucleating agents essential for the formation of mullite.

This promotes the growth of mullite within the network and forms a loose framework of randomly arranged needle-like structures. This characteristic microstructure prevents deformation at high temperatures (shape retention) and ensures excellent long-term dimensional stability at temperatures above 1500 °C. However, a potential drawback arises when excessive amounts of the glassy phase accumulate at triple points, which can negatively affect mechanical performance. Engineering the microstructure, for example, by introducing closed spherical pores, can reduce thermal conductivity while improving mechanical performance and high compressive strength due to controlled porosity [19]. In addition, natural and waste-derived materials often contain alkali, alkaline earth and transition metal oxides (such as FeO, Fe_2O_3, TiO_2, MnO, MgO, CaO, Na_2O, K_2O and P_2O_5), as well as rare earth elements, all of which significantly influence the properties of the final product. These components promote anisotropic grain growth and thus increase the strength and toughness of the resulting interlocked microstructure. This microstructure typically consists of intertwined orthorhombic acicular mullite grains, needles or whiskers with an aspect ratio of over 30 [14,19,20]. Furthermore, the high content of glassy phases in naturally occurring hydroxy-aluminosilicates (kaolinite, halloysite, pyrophyllite, sericite), alumosilicates (kyanite, sillimanite), mineral sources (albite, mining waste, kaolinite) and processing conditions (e.g., precipitation of aluminum oxide on kaolinite) is a significant factor; precipitation of aluminum oxide on the surface of waste sand particles) and the temperature of mullite formation (mullitization) could be reduced to the range of 1200–1400 °C [21,22].

This study aims to determine the suitability of waste clay–diatomite powder from mine tailings as a precursor, coupled with the $Al(NO_3)_3 \cdot 9H_2O$, in order to obtain durable mullite-based ceramics that could be applied as thermal insulators and/or refractory materials. The qualitative phase identification, microstructure, pore size distribution, porosity percentage content, bulk density, relative density, open porosity, linear shrinkage, and compressive strength of the resulting mullite ceramics were investigated. Following the simple preparation of precursor powders and earlier investigations [23] where mullite compacts were pressed at 2 MPa and sintered at 1300, 1400, and 1500 °C for 2 h [24], further research has been undertaken. In the present study, the prepared powder was pressed into green compacts at 50 MPa and sintered at three different temperatures (1300, 1400 and 1500 °C) for 2 h.

2. Materials and Methods

The starting diatomite was sourced from the surface coal mine Baroševac, Lindfield D, Kolubara (Serbia), and obtained via the air flotation method, commonly used in mining. Its chemical composition (Table 1) was determined using standard silicate rock analysis, as described in a previous study [23]. A flowchart of the synthesis process is shown in Figure 1.

Table 1. Chemical composition of starting material waste clay–diatomite.

Oxides	SiO_2	Al_2O_3	CaO	MgO	Fe_2O_3	K_2O	Na_2O	TiO_2	Loss on Ignition (1000 °C)
wt.%	70.48	13.78	3.01	0.74	2.89	0.89	0.13	0.34	7.70

These sintering temperatures were chosen to achieve a balance between phase composition and mechanical performance.

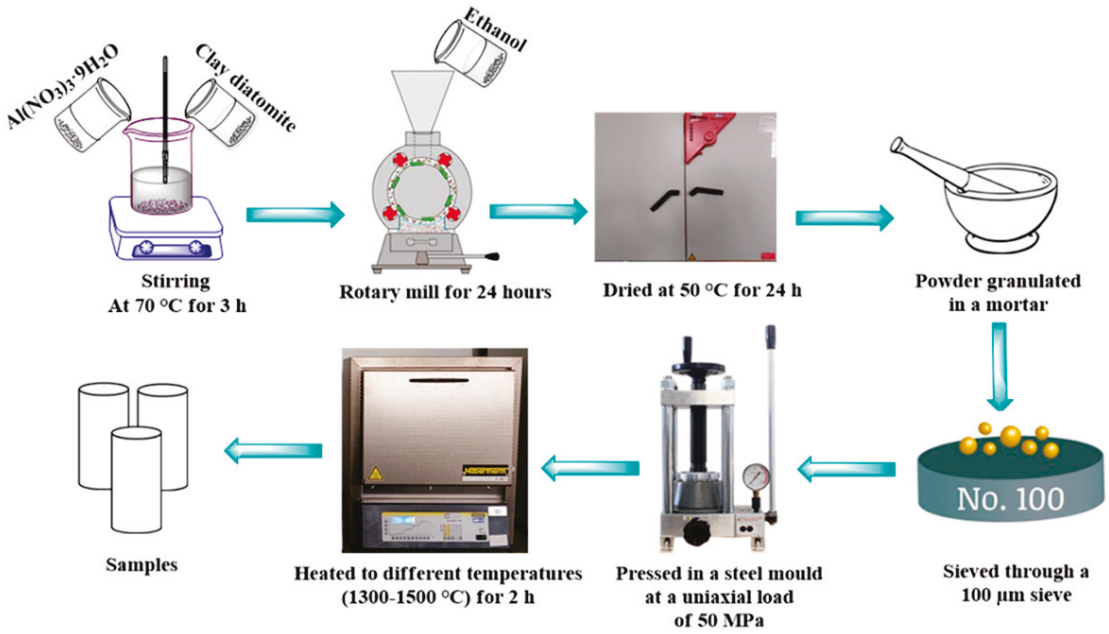

Figure 1. Flowchart of the synthesis process.

The XRD (X-ray diffraction) patterns of the heat-treated compacts were scanned with a Rigaku Ultima IV diffractometer using Cu Kα radiation at 40 kV and 40 mA in the 2θ range between 10° and 80° with a step of 0.02° and a scan rate of 10°/min. Phase analysis was performed with PDXL2 software (version 2.0.3.0) [25] using reference diffraction patterns from the International Centre for Diffraction Data (ICDD) database [26], version 2012. The average crystallite size (D) and the internal lattice strain (Δd/d) of the sintered samples were estimated from the Williamson–Hall diagrams [27]. In addition to the quantification of the crystalline phase (Table 2), the X-ray diffraction patterns were subjected to a semi-quantitative evaluation of the amorphous phase using the EVA v.7.1 software package (Bruker AXS). After an automatic polynomial background fit, the program separates the broad diffuse scattering ("amorphous halo") from the Bragg peaks. The ratio between the integrated halo intensity and the total diffracted intensity is then used to estimate the amorphous fraction so that no external standard is required.

Table 2. Volume fraction of phases, mullite lattice parameters (*a*,*b*,*c*), crystallite size, and lattice strain of mullite samples sintered at 1300, 1400, and 1500 °C for 2 h.

Sintering Temperature (°C)	Volume Fraction (vol.%)	Mullite Lattice Parameters (Å)	Crystallite Size (nm)	Lattice Strain (%)
1300	53.42 (M) 10.76 (Cr) 4.01 (C) 6.09 (Q)	7.5550(2) ***a*** 7.7053(4) ***b*** 2.8918(2) ***c***	68 ± 0.2	0.001115
1400	58.13 (M) 7.87 (Cr) 1.47 (C) 2.67 (Q)	7.5488(3) ***a*** 7.7028(3) ***b*** 2.8916(6) ***c***	70 ± 0.4	0.000958
1500	63.24 (M) 0.06 (Q)	7.5391(2) ***a*** 7.6914(1) ***b*** 2.8885(4) ***c***	72 ± 0.3	0.000801

The apparent density and open porosity of sintered mullite samples were determined using the Archimedes method. Linear shrinkage was calculated by measuring the diameter of the samples before and after heat treatment.

A Tescan Mira 3 XMU FESEM (Field Emission Scanning Electron Microscopy, TESCAN, Kohoutovice, Czech Republic) was used for the microstructural characterization of the sintered mullite samples. Prior to FE-SEM analysis, the powders were coated with Au using a Polaron SC502 sputter coater. EDS analysis was performed using an INCAx-act LN2-free analytical silicon drift characteristic X-ray detector with PentaFET® Precision and the AZtec 4.3 software package (Oxford Instruments, Abingdon, Oxfordshire, UK) connected to a TESCAN Mira 3 XMU using a generator voltage (20.0 kV) and a working distance of 15 mm.

The images obtained from the FESEM were used to examine the porosity of the material. The assessment of the porosity of the material as well as the distribution of the pore diameters was performed using the Image Pro Plus software 6.0 (Media Cybernetics, Rockville, MD, USA).

The mechanical stability of sintered cylindrical mullite ceramics, i.e., with a diameter of 7.4–8.6 mm and a height of 15.4–17.4 mm, was assessed by compression testing in a universal testing machine, Instron 1185, using the Test Instrument Explorer software. The cylindrical specimens were compressed for 1 min at a test speed of 1 mm until they broke. The compressive strength was determined by dividing the maximum force by the cross-sectional area of the test. At least four replicates were tested for each sample.

3. Results

Starting from diatomite, the formation of the mullite phase has occurred at a relatively low sintering temperature, which is primarily due to the presence of small amounts of alkali and alkaline earth oxides, as well as Fe_2O_3. These components promote viscous flow sintering and facilitate mullitization reaction by reducing the viscosity of the molten glassy phase. As shown in Table 1, the diatomaceous earth used in this study consists mainly of SiO_2 and Al_2O_3, with the missing Al_2O_3 content being supplemented by aluminum nitrate [24]. The moderately high Al_2O_3 content in diatomite originates from kaolinite and muscovite phases, while SiO_2 appears as quartz and silicate glass (evidenced by a broad hump around 2θ of 25° in the XRD pattern, Figure 2a). Quartz particles surrounded by a liquid, glassy phase during heating are more readily transformed into cristobalite, as previously reported [23]. Other studies have also confirmed that the mullitization temperature is lowered due to eutectic reactions promoted by these oxides [28–30]. Kaolinite ($Al_4[Si_4O_{10}](OH)_8$), serves as a binder for other compacted components in glass-ceramics made from clay, the initial mixture of which usually contains clays, fluxes and fillers. Meanwhile, quartz remains stable at processing temperatures and plays a role as a filler by reducing shrinkage and deformation. The presence of muscovite (mica), which contains potassium (K), promotes the formation of a liquid phase during firing and enables the crystallization of elongated mullite grains at lower temperatures [31,32]. In addition, K_2O together with CaO and Fe_2O_3 contributes to grain growth, so their presence in the starting material is beneficial for mullite formation [33].

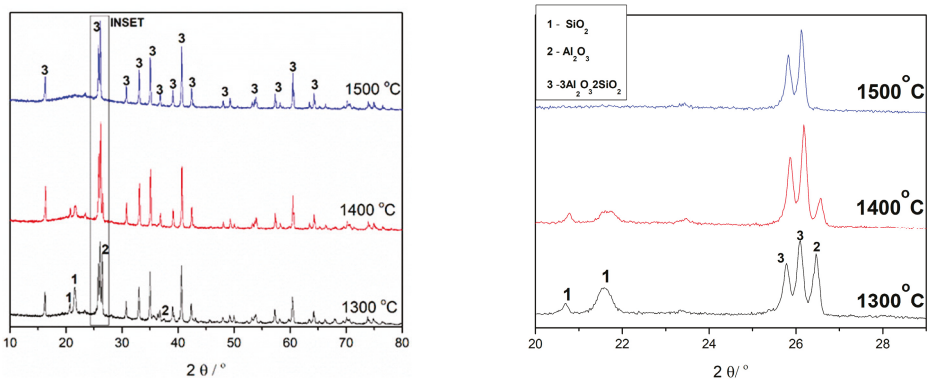

(**a**) (**b**)

Figure 2. XRD patterns of mullite samples sintered at 1300, 1400, and 1500 °C for 2 h (**a**) and the inset of splitting of diffraction peaks at around 2θ = 26° (**b**).

3.1. The Structural (XRD) Analysis

According to the results of the XRD analysis (Figure 2 and Table 2), the primary phases detected at 1300 °C and 1400 °C are mullite ($3Al_2O_3 \cdot 2SiO_2$, ICDD NO. 01-088-2049, M), cristobalite (SiO_2, ICDD PDF No. 01-071-6248, Cr), corundum (α-Al_2O_3, ICDD PDF No. 00-046-1212, C) and quartz (SiO_2, ICDD PDF No.01-089-8936, Q). The presence of a liquid phase at higher temperatures (above 1300 °C) facilitates mullite formation by reaction with Al_2O_3. At temperatures above 1400 °C, the increased intensity of the mullite peaks indicates a higher mullite content and improved crystallinity. After sintering at 1500 °C for 2 h, the cristobalite and corundum peaks disappeared (Figure 2b, inset), confirming the formation of single-phase mullite at this temperature.

The splitting of the diffraction peaks (120) and (210) at around 26° is a well-known indicator of the mullite transformation from a metastable tetragonal phase into a stable orthorhombic structure [34]. The clear separation of these peaks, which can be observed even at the lowest sintering temperature (1300 °C), confirms the onset of mullite formation at this temperature. However, the split diffraction peaks are accompanied by an intense corundum reflection (labeled as 2 in Figure 2b). This corundum peak is most pronounced at 1300 °C, decreases gradually at 1400 °C, and disappears completely at 1500 °C. This disappearance is attributed to the diffusive dissolution of corundum into the silica-rich glassy phase (such as soda–lime–silica glasses) [35], which simultaneously promotes further mullite formation.

The volume fractions of the crystalline phases in the sintered samples as well as the mullite lattice parameters, crystallite sizes and lattice strains are listed in Table 2. With increasing sintering temperature, all lattice parameters of the mullite phase decreased, indicating improved crystallinity at higher temperatures. This observation is consistent with the findings of Chakraborty [36], according to which mullite, which initially crystallizes in silica-rich gels, appears as small, highly strained crystals.

The reduction in lattice parameters reflects enhanced crystallinity rather than a change in chemical composition. In addition, the lattice strain, estimated from the slope of the Williamson-Hall diagrams, gradually decreases with temperature, indicating the relaxation of strain introduced during the initial phase of mullite formation. This strain typically arises from structural imperfections such as impurities, interstitial atoms or vacancies [37], so its reduction implies a decreasing defect concentration. Such behavior indicates a progressive rearrangement of atoms and improved structural coherence during sintering, which is consistent with the observed grain growth. Accordingly, the samples sintered at 1400 °C and 1500 °C exhibit well-crystallized and structurally ordered mullite. In addition, the semi-quantitative analysis revealed a systematic increase in amorphous phase content with

temperature: 25.8 wt.% at 1300 °C, 29.8 wt.% at 1400 °C, and 36.7 wt.% at 1500 °C, as shown in Figure 3. This trend supports the disappearance of corundum and cristobalite reflections (Figure 2b) and suggests that their dissolution in the silica-rich melt contributes to the formation of a more continuous glassy matrix at higher temperatures.

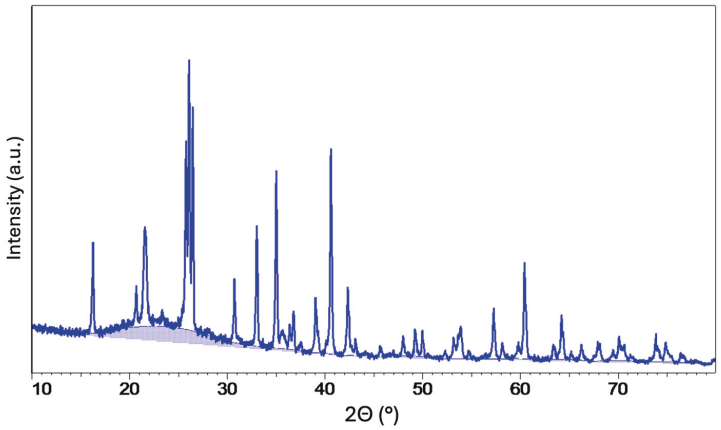

(**a**)

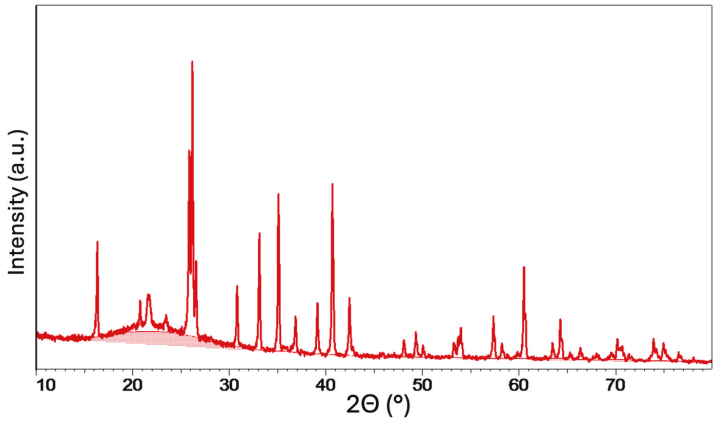

(**b**)

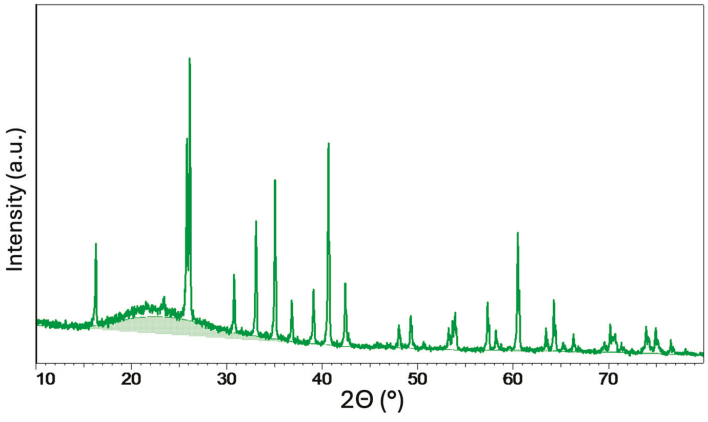

(**c**)

Figure 3. X-ray diffraction (XRD) patterns of the samples heat-treated at 1300 °C (**a**), 1400 °C (**b**), and 1500 °C (**c**). The broad hump between ~15° and 35° 2θ indicates the presence of an amorphous component, while the shaded area represents the fitted background and amorphous halo, used for semi-quantitative estimation of the amorphous phase content.

3.2. The Microstructural (FE-SEM/EDS) and Mechanical Analysis

The development of the characteristic mullite microstructure is shown in Figure 4. At 1300 °C, the sample consists mainly of round, equiaxed grains distributed in a glassy matrix (Figure 4a,d). During sintering at 1400 °C, grow larger and begin to coalesce, resulting in a denser and more compact matrix (Figure 4b,e). At 1500 °C, a well-developed microstructure of defined, interlocked mullite rods emerges (Figure 4c,f). These rod-shaped mullite grains are generally around 5 μm long and have a diameter of around 500 nm (Figure 4c). Closer inspection reveals that they are shaped as regular rectangular prisms with side lengths of about 300–400 nm (Figure 4f). In contrast, the grains formed at lower sintering temperatures (1300 °C and 1400 °C) are smaller and thinner, indicating slower grain growth. As the samples exhibited some porosity, the pore size and distribution were estimated using Image-Pro Plus software in accordance with previously published methodologies in similar studies [38–40].

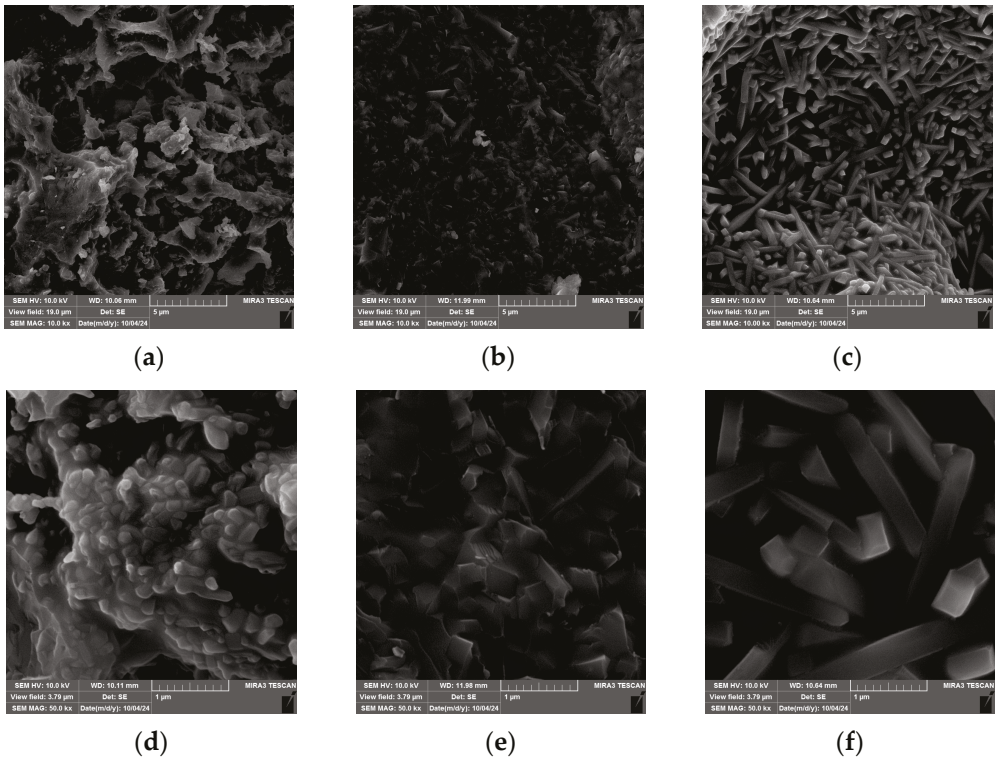

Figure 4. FE-SEM images of the mullite samples sintered at 1300 °C (**a**,**d**), 1400 °C (**b**,**e**), and 1500 °C (**c**,**f**).

The results presented in Table 3 show that the sintered mullite monoliths are dense, hard and structurally reliable materials. The density of the mullite bodies increases at higher sintering temperatures. The relative density was calculated on the basis of the theoretical densities of mullite (3.17 g/cm^3), cristobalite (2.35 g/cm^3), quartz (2.65 g/cm^3) and corundum (4.00 g/cm^3). A theoretical density of 2.4 g/cm^3 was taken from the literature for the amorphous silicate phase [41]. Using the rule of mixtures and the volume fractions obtained from the XRD data (Table 2), the theoretical densities of the samples sintered at 1300, 1400 and 1500 °C were determined, with the sample at 1500 °C having the highest amorphous phase content (36.7 wt%). As shown in Table 3, the relative density increases sharply from 1300 to 1400 °C and gradually from 1400 to 1500 °C, finally reaching 82% of the theoretical density (TD) for the 1500 °C sample, where the open porosity approaches zero. Linear shrinkage also increases with sintering temperature and stabilizes

at around 20%, which is consistent with previously reported values [24]. The compressive strength of the mullite bodies reaches a peak value of 188 MPa at 1400 °C. This increase is due to the favorable phase composition, optimized microstructural properties (e.g., grain morphology and size), increased bulk density and the almost complete elimination of open porosity. At 1500 °C, the formation of a continuous glassy matrix promotes densification and eliminates open porosity but also reduces the integrity of the crystalline mullite framework. This microstructural shift probably explains the decrease in compressive strength to 136 MPa. The mechanical performance of these ceramics produced from waste is therefore strongly determined by the balance between the supporting crystalline mullite needles and the intergranular glassy phase.

Table 3. Bulk density, relative density, open porosity, linear shrinkage, and compressive strength of mullite bodies sintered at 1300, 1400, and 1500 °C.

Sintering Temperature (°C)	1300	1400	1500
Bulk density (g/cm^3)	1.69	2.20	2.36
Relative density (TD%)	58	76	82
Open porosity (%)	37	16	0
Linear shrinkage (%)	14.1	21.1	20.5
Compressive strength (MPa)	52.80	188.67	136.35

When porous materials are produced, their structural characteristics are typically assessed using key parameters such as void content, average pore diameter, and specific surface area, which together provide valuable insights into the material's porosity and performance [42,43]. Evaluation of these properties often relies on image analysis techniques. For example, the Image Pro Plus software facilitates this process by enabling precise extraction and distinction of the light and dark regions within microscopic images. This allows researchers to clearly identify the solid portions of the sample in contact with the surface and to quantify the empty spaces or pores distributed throughout the material [44]. The pores represent the dark part of the image. Pore size measurements obtained using the Image-Pro Plus image analysis software are presented in Figure 5, where the distinct separation and distribution of the pores within the material can be clearly observed.

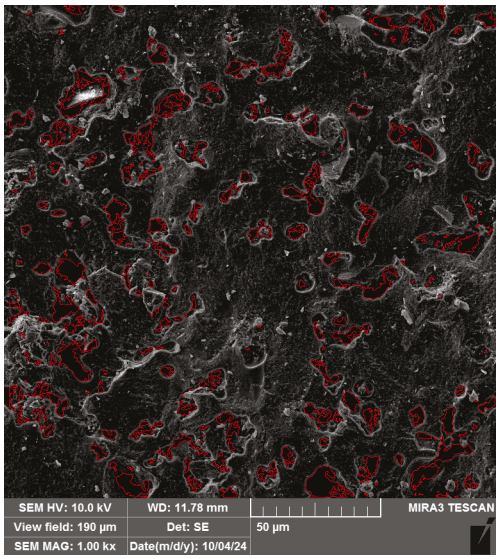

Figure 5. Extracting pores in an image using Image Pro Plus.

A series of FE-SEM images with a magnification of 1.00 kx (field of view: 190 µm) were used to evaluate the pore diameter distribution in the samples sintered at different temperatures, as shown in Figure 6.

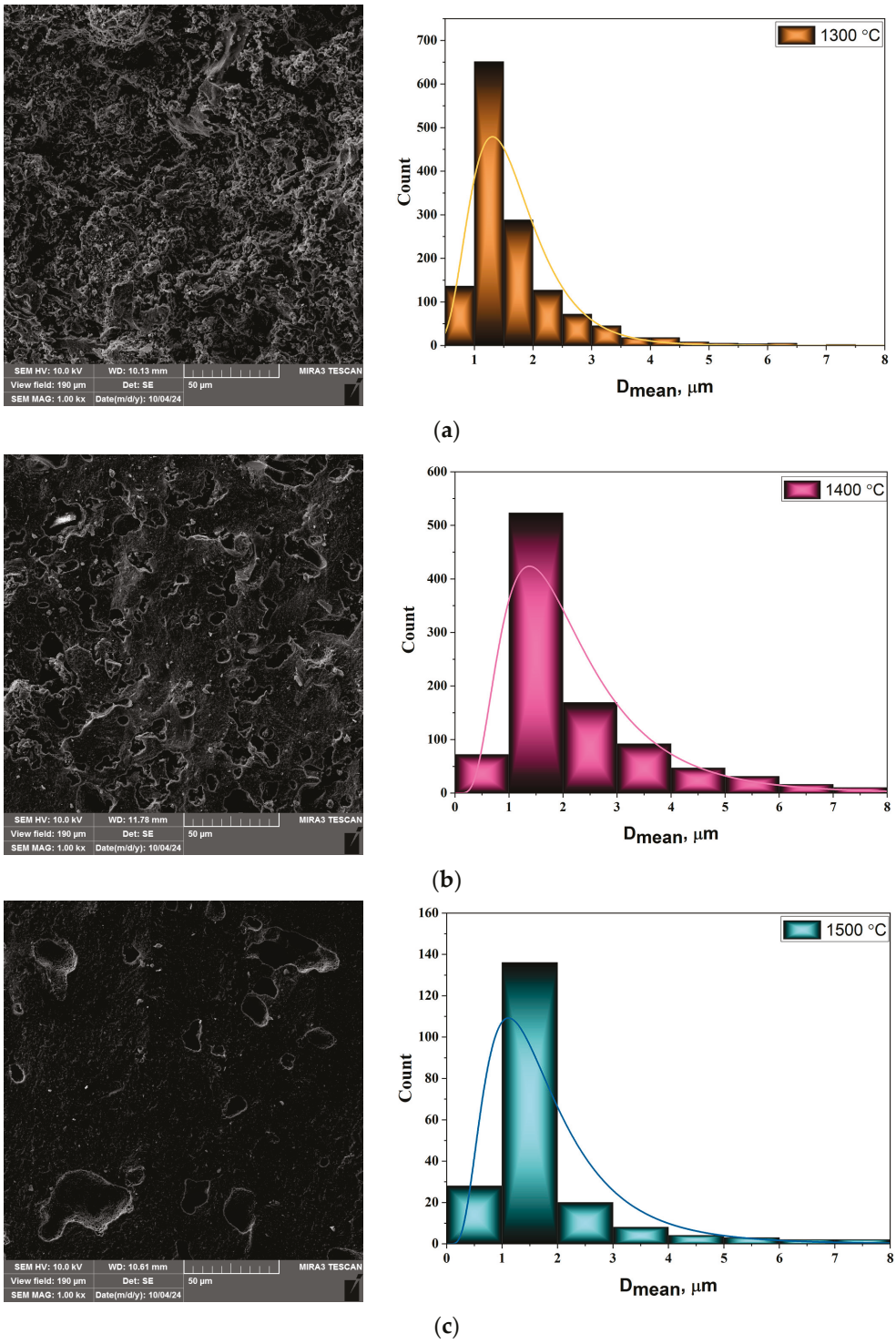

Figure 6. FE-SEM micrographs of the mullite samples sintered at (**a**) 1300 °C: (**b**) 1400 °C, and (**c**) 1500 °C with appropriate histograms of pore size diameter distribution.

The differences in the mullite obtained at different sintering temperatures are also evident in the size and distribution of the pores, as shown in the microstructures shown in Figure 6. The pore sizes were measured using image analysis, and the corresponding

histograms of the pore size distribution (D_{mean}) are shown for each sample. In Figure 6a, the mullite sample sintered at 1300 °C has the highest frequency of pores with average diameters between 1 and 1.5 μm. In contrast, for the samples sintered at 1400 °C and 1500 °C, the majority of pore diameters are in the 1–2 μm range. The FE-SEM analysis reveals that with increasing sintering temperature, the average pore diameter increases, although the overall porosity decreases, as shown in Figure 7.

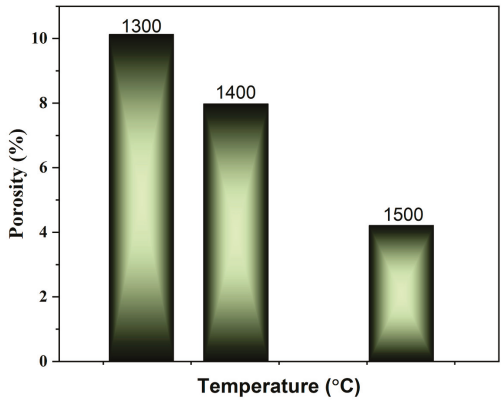

Figure 7. Porosity percentage content of mullite samples sintered at 1300, 1400, and 1500 °C for 2 h.

The porosity of the sample sintered at 1400 °C decreased by 21.3% compared to the sample sintered at 1300 °C. For the sample sintered at 1500 °C, the reduction in total porosity is even more significant, amounting to 58.4% (Figure 7).

3.3. EDS Analysis

Energy dispersive X-ray spectroscopy (EDS) was performed over wide surface areas of the specimens to determine the elemental composition of the mullite samples sintered at 1300, 1400 and 1500 °C for 2 h (Figures 7–10). The EDS elemental maps confirmed the presence of key phases previously identified by X-ray diffraction. In particular, silicon, aluminum and oxygen were found to be constituents of the crystalline phases—mullite, corundum, quartz and cristobalite. Notably, segregation of the SiO_2 phase into isolated glassy areas was observed in the sample sintered at 1300 °C (Figure 6), a phenomenon that was not observed in the samples sintered at 1400 °C and 1500 °C (Figures 9 and 10). Other elements detected, such as Al, K, Fe and Ca, exhibited a uniform spatial distribution across all samples.

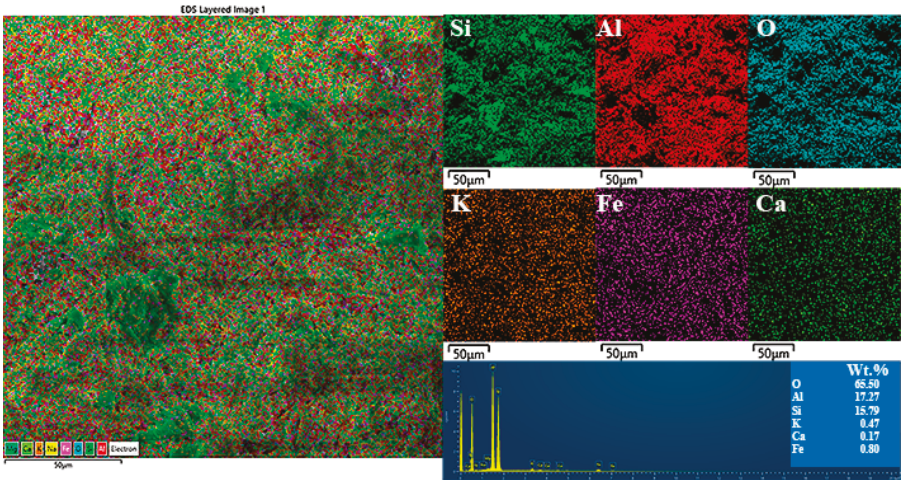

Figure 8. EDS spectrum of the mullite sample sintered at 1300 °C.

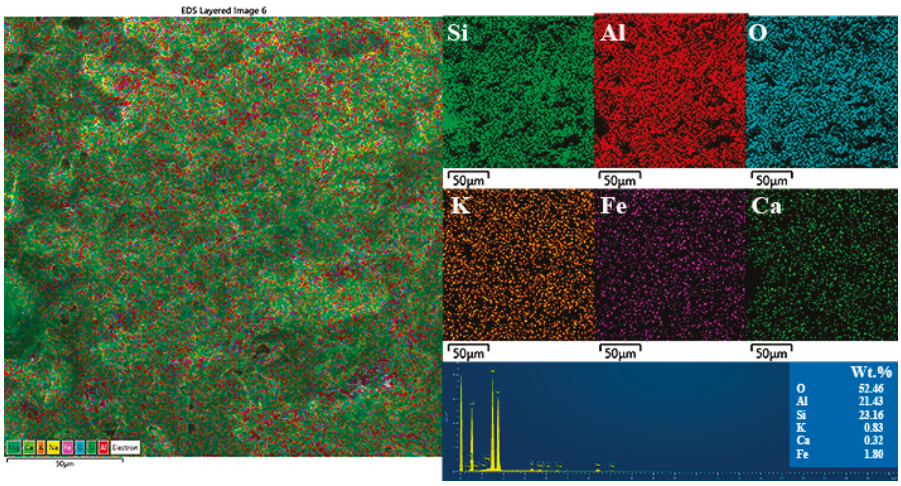

Figure 9. EDS spectrum of the mullite sample sintered at 1400 °C.

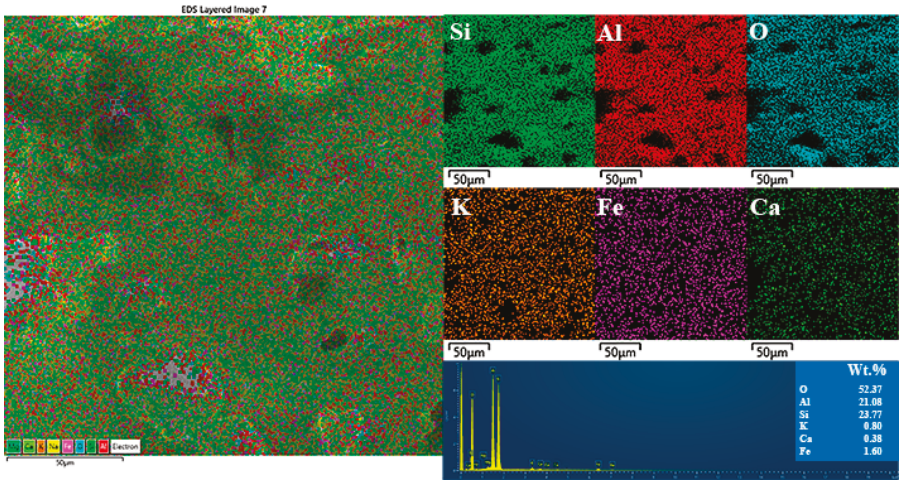

Figure 10. EDS spectrum of the mullite sample sintered at 1500 °C.

4. Discussion

The utilization of natural materials—in particular, mining waste such as kaolin, diatomite, bauxite, and other material residues from landfills—offers both environmental and economic advantages. The production of structural and functional ceramics from this waste contributes significantly to the conservation of natural resources and at the same time reduces environmental pollution. Moreover, the appropriate design of these ceramics ensures that high-performance standards are met without relying on cost-intensive production methods. Mullite ceramics, especially in the form of refractory materials, are among the most promising candidates for use in various high-temperature industrial processes. As mentioned above, a wide range of natural and waste-derived materials have been successfully employed in their production, which have exceptional long-term dimensional stability at temperatures above 1500 °C.

In this study, diatomaceous earth from the Kolubara open-face coal mine (Serbia), specifically from the Baroševac (Lindfield D) in Serbia, was used as the starting material. The chemical composition of the diatomite revealed a notably high Al_2O_3 content of 13.78 wt%, which is atypical for diatomaceous earth, as it usually consists mainly of SiO_2 with a minimal alumina content. The XRD analysis confirmed the presence of clay minerals, especially kaolinite and muscovite, which confirms the high alumina content. In addition, morphological analysis using SEM identified the characteristic fossilized diatom frustules,

confirming the diatomaceous origin of the material [23]. The presence of other oxides in the composition served as fluxing agents and promoted the diffusion of reactive species during thermal processing. Following powder preparation and subsequent fabrication steps, durable mullite monoliths were successfully produced.

The structural characterization of the sintered mullite samples confirmed that at the highest processing temperature of 1500 °C, a mechanically stable, single-phase mullite compact was achieved. Despite a slight increase in density, the elimination of open porosity, and a reduction in overall and surface porosity compared to the sample sintered at 1400 °C, the compressive strength decreased to 136 MPa. At 1500 °C, the mullite grains exhibited a well-developed morphology, forming an interconnected network of thicker and longer rod-like structures compared to the finer tubular grains observed at 1400 °C. Although image analysis and porosity measurements revealed a very low total porosity (~4%) and no open pores, the decrease in compressive strength is likely due to the increased presence of a glassy phase. This hypothesis is supported by the nature of the aluminosilicate-based starting system, which contained numerous alkalis, alkaline earth, and transition metal oxides—components typical of soda–lime–silica-type glasses. The sample sintered at 1500 °C had a bulk density of 2.36 g/cm^3 (82% theoretical density) and contained 63.24 wt.% crystalline mullite but retained a significant content of amorphous phase. The semi-quantitative analysis revealed a steady increase in amorphous phase content with sintering temperature, from 25.8 wt.% at 1300 °C to 29.8 wt.% at 1400 °C and up to 36.7 wt.% at 1500 °C. While EDS mapping performed over areas of ~200 μm did not allow a clear distinction between crystalline and amorphous regions, especially in the sample sintered at 1500 °C—the increased glassy content is evident. These results indicate that the intergranular glass phase plays a crucial role in governing the mechanical behavior of these ceramics produced from clay waste. While the glass phase promotes densification, it can simultaneously weaken the supporting crystalline mullite network, emphasizing the importance of a balanced ratio between glassy and crystalline components in glassy ceramic systems.

The results presented in this study have focused future research on thermal conductivity and thermal shock resistance, which are of crucial importance for refractory materials. Preliminary results on thermal conductivity have shown that this material is promising for further investigation with a thermal conductivity of approximately 0.24 W/(m·K) (unpublished results). These values are significantly better than previously published results [45,46]. However, the design of a sintered mullite matrix composite (magnesia-stabilized zirconia/WO_3), known as hollow mullite grains [47], lowered the thermal conductivity to 0.4 W/(m·K) at room temperature and 900 °C. However, this material also has excellent properties, including thermal shock resistance, as evidenced by a decrease in Young's modulus of only 0.5% after 10 cycles [46]. The detected phases with low (zircon, $ZrSiO_4$) or even negative value (aluminum tungstate, $Al_2(WO_4)_3$) of thermal expansion coefficient [48] reduced the thermal expansion coefficient and improved the thermal shock resistance of the resulting material.

The reduced thermal conductivity observed in the sintered mullite materials can be attributed to several microstructural and compositional features. Specifically, the loosely packed mullite grains, along with the presence of pores and intergranular cavities, contribute to the suppression of thermal conduction by interrupting the continuous thermal paths. Furthermore, these structural voids hinder convective heat transfer by restricting air movement within the closed porosity. In addition to porosity, grain boundaries, triple junctions and the intergranular glassy phase also have a significant influence on heat transfer. These disordered regions, particularly the amorphous phase, act as effective phonon scattering centers, restricting phonon propagation and significantly reducing the overall thermal

conductivity of the ceramic [49]. Given the promising thermal behavior observed, future research will focus on a more detailed compositional and structural characterization. This will include Rietveld refinement of the mullite phase, quantification of the amorphous and crystalline components, analysis of macroporosity and systematic evaluation of thermal shock resistance and thermal conductivity. These efforts are aimed at further optimizing the performance of waste-derived mullite ceramics for high-temperature applications, particularly in the field of energy-efficient refractory materials and thermal insulators.

5. Conclusions

In this study, sintered mullite ceramics were successfully produced from diatomaceous earth and aluminum nitrate at temperatures ranging from 1300 to 1500 °C for 2 h. The resulting mullite monoliths showed remarkable mechanical stability over the entire temperature range, with the sample sintered at 1400 °C achieving the highest compressive strength of 188 MPa. Interestingly, although the sample sintered at 1500 °C exhibited well-formed rod-shaped mullite grains (~5 μm in length and ~500 nm in diameter) and increased density (82% of theoretical density), its compressive strength decreased to 136 MPa. This decrease is due to the increased content of the intergranular glassy phase, which promotes densification but impairs the load-bearing crystalline framework.

The microstructural analysis revealed a clear trend of pore refinement with increasing sintering temperature. The pore size decreased from ~1.5 μm at 1300–1400 °C to ~1 μm at 1500 °C, accompanied by a reduction in total porosity from 10% to 4%, as estimated from FESEM images. However, the presence of a few large, irregularly shaped pores indicates that further porosity characterization is required using techniques such as mercury intrusion porosimetry or helium pycnometry.

Preliminary measurements of thermal conductivity (~0.24 W/(m·K)) suggest that these mullite ceramics possess excellent insulating properties. Coupled with their mechanical robustness and the sustainable utilization of industrial by-products, such as mine tailings from the Kolubara coal basin, these materials are very promising for high-temperature insulation and refractory applications. Future work will focus on thermomechanical characterization, including detailed porosity profiling, thermal shock resistance, and evaluation of long-term performance under service conditions.

Author Contributions: Conceptualization, S.I. and A.Š.; methodology, S.I., M.M.V. and A.Š.; software, J.M., Ž.S. and M.M.V.; validation, I.R. and A.Š.; formal analysis, Ž.S., Ž.R. and J.M.; investigation, S.I., A.Š. and M.M.V.; resources, S.I., M.M.V. and A.Š.; data curation, S.I., M.M.V., Ž.S. and A.Š.; writing—original draft preparation, S.I., M.M.V. and A.Š.; writing—review and editing, J.M., Ž.R., Ž.S. and I.R.; visualization, S.I., M.M.V. and Ž.S.; supervision, A.Š.; project administration, S.I. and A.Š.; funding acquisition, A.Š., M.M.V., J.M. and I.R. All authors have read and agreed to the published version of the manuscript.

Funding: This work was financially supported by the Ministry of Science, Technological Development and Innovation of the Republic of Serbia (Contract Nos. 451-03-136/2025-03/200017, 451-03-136/2025-03/200287, and 451-03-136/2025-03/200126) and gratefully acknowledges the support of project CeNIKS co-financed by the Croatian Government and the European Union through the European Regional Development Fund—Competitiveness and Cohesion Operational Programme (Grant No. KK.01.1.1.02.0013).

Institutional Review Board Statement: Not applicable.

Informed Consent Statement: Not applicable.

Data Availability Statement: The data presented in this study are available on request from the corresponding author or co-authors. The data are not publicly available.

Conflicts of Interest: The authors declare no conflict of interest. The funders had no role in the design of the study; in the collection, analyses, or interpretation of data; in the writing of the manuscript; or in the decision to publish the results.

References

1. Mahmmod, L.M.R.; Dulaimi, A.; Bernardo, L.F.A.; Andrade, J.M.D.A. Characteristics of Lightweight Concrete Fabricated with Different Types of Strengthened Lightweight Aggregates. *J. Compos. Sci.* **2024**, *8*, 144. [CrossRef]
2. Abbas, M.M.; Muntean, R. Marble Powder as a Sustainable Cement Replacement: A Review of Mechanical Properties. *Sustainability* **2025**, *17*, 736. [CrossRef]
3. Amar, M.; Ladduri, B.; Alloul, A.; Benzerzour, M.; Abriak, N.-E. Geopolymer Synthesis and Performance Paving the Way for Greener Building Material: A Comprehensive Study. *Case Stud. Constr. Mater.* **2024**, *20*, e03280. [CrossRef]
4. Bouchikhi, A.; Amar, M.; Arroug, L.; Safhi, A.e.M.; Haddaji, Y. Characterizing Nano-Indentation and Microstructural Properties of Mine Tailings-Based Geopolymers. *Case Stud. Constr. Mater.* **2024**, *21*, e03899. [CrossRef]
5. Amar, M.; Ladduri, B.; Alloul, A.; Benzerzour, M.; Abriak, N.-E. Microstructure and Mechanical Properties of Geopolymers Utilizing Excavated Soils, Metakaolin and Slags. *J. Build. Eng.* **2024**, *86*, 108755. [CrossRef]
6. Kathirvel, P.; Sreekumaran, S. Sustainable Development of Ultra High Performance Concrete Using Geopolymer Technology. *J. Build. Eng.* **2021**, *39*, 102267. [CrossRef]
7. Manzoor, T.; Bhat, J.A.; Shah, A.H. Performance of Geopolymer Concrete at Elevated Temperature—A Critical Review. *Constr. Build. Mater.* **2024**, *420*, 135578. [CrossRef]
8. Zhang, B. Durability of Low-Carbon Geopolymer Concrete: A Critical Review. *Sustain. Mater. Technol.* **2024**, *40*, e00882. [CrossRef]
9. Herrington, R.J. The Raw Material Challenge of Creating a Green Economy. *Minerals* **2024**, *14*, 204. [CrossRef]
10. Romero, M.; Padilla, I.; Contreras, M.; López-delgado, A. Mullite-based Ceramics from Mining Waste: A Review. *Minerals* **2021**, *11*, 332. [CrossRef]
11. Sánchez-Soto, P.J.; Eliche-Quesada, D.; Martínez-Martínez, S.; Pérez-Villarejo, L.; Garzón, E. Study of a Waste Kaolin as Raw Material for Mullite Ceramics and Mullite Refractories by Reaction Sintering. *Materials* **2022**, *15*, 583. [CrossRef]
12. Yan, H.; Chen, S.; Lang, Y.; Wei, H.; Tian, C.; Wang, C. Near-net-size Preparation of Porous Mullite Matrix Ceramics with in Situ Formed 3D Mullite Whisker Network. *Int. J. Appl. Ceram. Technol.* **2022**, *19*, 3116–3126. [CrossRef]
13. Khalil, N.M.; Algamal, Y. Recycling of Ceramic Wastes for the Production of High Performance Mullite Refractories. *Silicon* **2020**, *12*, 1557–1565. [CrossRef]
14. Choo, T.F.; Mohd Salleh, M.A.; Kok, K.Y.; Matori, K.A. A Review on Synthesis of Mullite Ceramics from Industrial Wastes. *Recycling* **2019**, *4*, 39. [CrossRef]
15. Burinskienė, A.; Lingaitienė, O.; Jakubavičius, A. Core Elements Affecting the Circularity of Materials. *Sustainability* **2022**, *14*, 8367. [CrossRef]
16. Singh, N.; Raza, J.; Colangelo, F.; Farina, I. Advancements in Lightweight Artificial Aggregates: Typologies, Compositions, Applications, and Prospects for the Future. *Sustainability* **2024**, *16*, 9329. [CrossRef]
17. Khater, G.A.; Romero, M.; López-Delgado, A.; Padilla, I.; El-Kheshen, A.A.; Farag, M.M.; Elmaghraby, M.S.; Shendy, H.; Nasralla, N.H.S. Utilizing Ceramic Factory Waste to Produce Low-Cost Refractory Ceramics. *Recycling* **2024**, *9*, 98. [CrossRef]
18. Reka, A.; Kosanovic, D.; Ademi, E.; Aggrey, P.; Berisha, A.; Pavlovski, B.; Jovanovski, G.; Rexhepi, B.; Jashari, A.; Makreski, P. Fabrication of Ceramic Monoliths from Diatomaceous Earth: Effects of Calcination Temperature on Silica Phase Transformation. *Sci. Sinter.* **2022**, *54*, 495–506. [CrossRef]
19. Koshy, P.; Ho, N.; Zhong, V.; Schreck, L.; Koszo, S.A.; Severin, E.J.; Sorrell, C.C. Fly Ash Utilisation in Mullite Fabrication: Development of Novel Percolated Mullite. *Minerals* **2021**, *11*, 84. [CrossRef]
20. Gu, X.; Chen, P.; Wang, T.; Liu, S.; Zhu, S.; Zhu, Y.; Liu, Y. Analysis of Influencing Factors in the Preparation of Mullite Whiskers from Recovering Silicon-Rich Waste under Low-Temperature Conditions. *Nanomaterials* **2023**, *13*, 1143. [CrossRef]
21. Sánchez-Soto, P.J.; Garzón, E.; Pérez-Villarejo, L.; Angelopoulos, G.N.; Eliche-Quesada, D. Mining Wastes of an Albite Deposit as Raw Materials for Vitrified Mullite Ceramics. *Minerals* **2021**, *11*, 232. [CrossRef]
22. Badanoiu, A.-I.; Stoleriu, S.-P.; Carocea, A.-C.; Eftimie, M.-A.; Trusca, R. Influence of Synthesis Route on Composition and Main Properties of Mullite Ceramics Based on Waste. *Materials* **2025**, *18*, 1098. [CrossRef]
23. Saponjic, A.; Maletaskic, J.; Zildzovic, S.; Radovanovic, Z.; Kuzmanovic, M.; Maslovara, S.; Ilic, S. Calcined Mullite Powder Produced from Waste Clay-Diatomite. *Sci. Sinter.* **2024**, 15. [CrossRef]
24. Saponjic, A.; Maletaškić, J.; Radovanović, Ž.; Pošarac-Marković, M.; Gordić, M. Properties of Durable Mullite Bodies Manufactured from Waste Clay-Diatomite. *Metall. Mater. Data* **2024**, *2*, 55–58. [CrossRef]
25. *PDXL Version 2.0.3.0 Integrated X-Ray Powder Diffraction Software*; Rigaku Corporation: Tokyo, Japan, 2011.

26. Gates-Rector, S.; Blanton, T. The Powder Diffraction File: A quality materials characterization database. *Powder Diffr.* **2019**, *34*, 352–360. [CrossRef]
27. Giacovazzo, C. *Fundamentals of Crystallography*, 3rd ed.; IUCr texts on crystallography; Oxford University Press: Oxford, UK, 2011; ISBN 978-0-19-957366-0.
28. Dong, L.; Zhang, C.; Chen, Y.; Cao, L.; Li, J.; Luo, L. Acicular Porous Mullite from Diatom Frustules. *Mater. Lett.* **2016**, *171*, 108–111. [CrossRef]
29. Rana, A.P.S.; Aiko, O.; Pask, J.A. Sintering of α-Al_2O_3/Quartz, and α-Al_2O_3/Cristobalite Related to Mullite Formation. *Ceram. Int.* **1982**, *8*, 151–153. [CrossRef]
30. Akhtar, F.; Vasiliev, P.O.; Bergström, L. Hierarchically Porous Ceramics from Diatomite Powders by Pulsed Current Processing. *J. Am. Ceram. Soc.* **2009**, *92*, 338–343. [CrossRef]
31. Lee, W.E.; Souza, G.P.; McConville, C.J.; Tarvornpanich, T.; Iqbal, Y. Mullite Formation in Clays and Clay-Derived Vitreous Ceramics. *J. Eur. Ceram. Soc.* **2008**, *28*, 465–471. [CrossRef]
32. Ghorbel, A.; Fourati, M.; Bouaziz, J. Microstructural Evolution and Phase Transformation of Different Sintered Kaolins Powder Compacts. *Mater. Chem. Phys.* **2008**, *112*, 876–885. [CrossRef]
33. Yamuna, A.; Devanarayanan, S.; Lalithambika, M. Phase-Pure Mullite from Kaolinite. *J. Am. Ceram. Soc.* **2002**, *85*, 1409–1413. [CrossRef]
34. Song, K.; Kim, W.; Suh, C.-Y.; Bang, J.-H.; Ahn, J.-W. Preparation of Mullite-Silica Composites Using Silica-Rich Monophasic Precursor Obtained as a Byproduct of Mineral Carbonation of Blast-Furnace Slag. *Minerals* **2018**, *8*, 219. [CrossRef]
35. Yoshizawa, F.T.; Garel-Laurin, A.-C.; Burov, E.; Toplis, M.J. Diffusive Dissolution of α -Alumina in Industrial Soda-Lime Silica Glass. *J. Non-Cryst. Solids* **2025**, *650*, 123351. [CrossRef]
36. Chakraborty, A.K. Structural Parameters of Mullite Formed During Heating of Diphasic Mullite Gels. *J. Am. Ceram. Soc.* **2005**, *88*, 2424–2428. [CrossRef]
37. Völkl, J. Stress in Cooling Crystals. In *Handbook of Crystal Growth*; Hurle, D.T.J., Ed.; Elsevier: Amsterdam, The Netherlands, 1994; Volume 2b.
38. Alazreg, A.; Vuksanović, M.M.; Egelja, A.; Mladenović, I.O.; Radovanović, Ž.; Petrović, M.; Marinković, A.; Heinemann, R.J. Mechanical Properties of Acrylate Matrix Composite Reinforced with Manganese-aluminum Layered Double Hydroxide. *Polym. Compos.* **2023**, *44*, 6783–6792. [CrossRef]
39. Mohamed, S.S.M.; Vuksanović, M.M.; Vasiljević-Radović, D.G.; Janković Mandić, L.; Jančić Heinneman, R.M.; Marinković, A.D.; Mladenović, I.O. Sol–Gel Derived Alumina Particles for the Reinforcement of Copper Films on Brass Substrates. *Gels* **2024**, *10*, 648. [CrossRef]
40. Edkheil, A.; Vuksanović, M.M.; Savić, A.; Šaponjić, A.; Petrović, M.; Radojević, V.; Heinemann, R.J. Dental composite materials based on Zn/Al-layered double hydroxide and their physical mechanical properties. *Polym. Compos.* **2025**, *46*, 1617–1625. [CrossRef]
41. Pfleiderer, P.; Horbach, J.; Binder, K. Structure and Transport Properties of Amorphous Aluminium Silicates: Computer Simulation Studies. *Chem. Geol.* **2006**, *229*, 186–197. [CrossRef]
42. Hyväluoma, J.; Kulju, S.; Hannula, M.; Wikberg, H.; Källi, A.; Rasa, K. Quantitative Characterization of Pore Structure of Several Biochars with 3D Imaging. *Environ. Sci. Pollut. Res.* **2018**, *25*, 25648–25658. [CrossRef]
43. Le, T.; Le Saout, G.; Garcia-Diaz, E.; Betrancourt, D.; Rémond, S. Hardened Behavior of Mortar Based on Recycled Aggregate: Influence of Saturation State at Macro- and Microscopic Scales. *Constr. Build. Mater.* **2017**, *141*, 479–490. [CrossRef]
44. Dimitrijevic, M.; Veljovic, D.; Posarac-Markovic, M.; Jancic-Heinemann, R.; Volkov-Husovic, T.; Zrilic, M. Mechanical Properties Correlation to Processing Parameters for Advanced Alumina Based Refractories. *Sci. Sinter.* **2012**, *44*, 25–33. [CrossRef]
45. Liu, H.; Xiong, X.; Li, M.; Wang, Z.; Wang, X.; Ma, Y.; Yuan, L. Fabrication and Properties of Mullite Thermal Insulation Materials with In-Situ Synthesized Mullite Hollow Whiskers. *Ceram. Int.* **2020**, *46*, 14474–14480. [CrossRef]
46. Mahnicka-Goremikina, L.; Svinka, R.; Svinka, V.; Grase, L.; Juhnevica, I.; Rundans, M.; Goremikins, V.; Tolendiuly, S.; Fomenko, S. Thermal Properties of Porous Mullite Ceramics Modified with Microsized ZrO_2 and WO_3. *Materials* **2022**, *15*, 7935. [CrossRef]
47. Kong, X.Y.; Wang, Z.L.; Wu, J. Rectangular Single-Crystal Mullite Microtubes. *Adv. Mater.* **2003**, *15*, 1445–1449. [CrossRef]
48. Mahnicka-Goremikina, L.; Svinka, R.; Svinka, V.; Goremikins, V.; Ilic, S.; Grase, L.; Juhnevica, I.; Rundans, M.; Eiduks, T.V.; Pludons, A. Porous Mullite Ceramic Modification with Nano-WO_3. *Materials* **2023**, *16*, 4631. [CrossRef]
49. Wang, H.; Du, X.; Shi, Y.; Deng, M.; Wang, J.; Qi, J.; Huang, Z. Grain-Size Dependent Thermal Conductivity of $Gd_2Zr_2O_7$ Ceramics. *Ceram. Int.* **2022**, *48*, 16444–16448. [CrossRef]

Disclaimer/Publisher's Note: The statements, opinions and data contained in all publications are solely those of the individual author(s) and contributor(s) and not of MDPI and/or the editor(s). MDPI and/or the editor(s) disclaim responsibility for any injury to people or property resulting from any ideas, methods, instructions or products referred to in the content.

applied sciences

MDPI

Article

Experimental Analysis of Creep and Shrinkage of Self-Compacting Concrete with Recycled Concrete Aggregates

Marijan Skazlić [1], Hamdo Mešić [2] and Ivan Gabrijel [1,*]

[1] Materials Department, Faculty of Civil Engineering, University of Zagreb, Fra Andrije Kačića Miošića 26, 10000 Zagreb, Croatia; marijan.skazlic@grad.unizg.hr
[2] Independent Researcher, Ulica 502. Viteške Brigade 25, 77000 Bihać, Bosnia and Herzegovina; hamdo.mesic@hotmail.com
* Correspondence: ivan.gabrijel@grad.unizg.hr

Featured Application: The loading of specimens during the creep deformation test was performed at an age of 2 days in order to simulate the process of introducing the pre-stressing force into precast, prestressed concrete elements. The results presented can serve as input for the calibration and verification of existing models for predicting the creep behaviour of concrete with recycled concrete aggregates.

Abstract: The recycling of old concrete from the demolition of concrete structures is necessary for the rational use of natural aggregate resources. Recycled concrete aggregates (RCAs) are the highest quality recycled aggregates as they are the closest to natural aggregates. However, the use of RCAs is always associated with greater fluctuations and usually with a deterioration in workability, mechanical properties and long-term properties. The use of RCA in self-compacting concrete (SCC), where the proportion of aggregate is lower than in conventional concrete, is one way of mitigating the effects of RCAs. In this paper, the effects of coarse and fine RCA are investigated, focusing on dimensional changes due to shrinkage and creep. SCC mixes were developed in which the dolomite aggregates were partially or completely replaced by RCAs and additionally mixes in which 50% of the cement was replaced by fly ash. The average shrinkage strain measured after 180 days increased from 0.34 mm/m for a mix with natural aggregates to 1.04 mm/m for a mix made entirely with RCAs, showing an almost proportional increase in strain with RCA content. At the same age, the creep compliance ranged from 0.07 GPa^{-1} for the mix with natural aggregates to 0.34 GPa^{-1} for the mix made entirely with RCAs, and is most strongly correlated with hardened concrete density.

Keywords: recycled concrete aggregate; self-compacting concrete; fly ash; creep strain

1. Introduction

Nowadays, the construction sector is confronted with two specific circumstances that influence its sustainability and will become increasingly important in the future. On the one hand, intensive construction activity requires larger quantities of concrete, which leads to an increased consumption of natural resources and energy. It is estimated that 14 billion m^3 of concrete was produced worldwide in 2020 [1]. In terms of natural resources, there is a particular focus on aggregates for concrete, the increasing use of which is leading to environmental degradation. Sand, gravel and crushed stone for construction alone account for almost 24% of the global extraction of non-metallic materials, and volumes are

expected to double by 2060, reaching around 60 Gt [2]. In 2019, a total of around 3 Gt of aggregates was produced in EU countries, including UK and EFTA countries, of which 9.3% were recycled aggregates [3]. The production of concrete consumed around 5.5% of total primary energy demand in 2015 and was responsible for 8.5% of global greenhouse gas emissions [2]. On the other hand, the high intensity of construction means that more and more construction waste is being generated. For this reason, the recycling and reuse of construction waste as a new building product is becoming increasingly important in many industrialised countries around the world. Data show that around 30 to 50% of construction waste consists of concrete [4,5]. It is estimated that 50 million tonnes of concrete waste are generated in China every year [6]. In the EU, concrete accounted for the largest share of construction and demolition waste (CDW) in 2020, estimated at around 56% or 74 million tonnes [7].

One of the sustainable ways to reuse concrete waste is to produce recycled concrete aggregate (RCA) and use it as a substitute for part of the aggregate in new concrete. In this way, several benefits are achieved, such as reducing the consumption of natural aggregates, reducing the amount of construction waste, and reducing the cost of transportation, energy consumption and overall CO_2 emissions [8–10]. Today, however, the majority of concrete waste is downcycled, by being used mainly for road construction and backfilling [7], or disposed of in landfills [6]. Whether this practice will change depends on national regulations.

Numerous studies on RCA show that its quality can vary greatly, but also that its properties always fall short of those of natural aggregates. The density of RCA is up to 10% lower than that of natural aggregates, the water absorption of recycled aggregates is several times higher, the crushing coefficient according to the Los Angeles method is lower etc. [11–13]. In addition, recycled aggregates often contain microcracks due to the crushing process and are considerably more porous [14]. The results of experimental studies on concrete with RCA have shown that the incorporation of RCA into concrete reduces workability, reduces strength and stiffness, and increases porosity. The main reason for this is the poorer properties of the recycled aggregate due to the presence of old cement paste, which leads to higher absorption and the formation of several different interfaces (contact zones) in the concrete [15–17].

Since the matrix of self-compacting concrete (SCC) is adjusted to have better workability properties than normal concrete, the idea was brought up that the SCC paste matrix would serve as a better medium for RCA [18]. Compared to normal concrete, SCC contains more fine particles originating from cement, finest aggregate fraction and fillers, which affect the inter-particle forces in the fresh state and result in a refined microstructure and pore network in hardened concrete. Much research, particularly in the last twenty years, has focused on determining the effects of partial or complete replacement of natural coarse aggregate with RCA. In general, the addition of RCA decreases the flowability, reduces the mechanical properties and increases the permeability properties [18–22]. It has been shown that the flow properties of SCC can be maintained even if all natural aggregates are replaced by RCA [23–26]. The research conducted has shown that RCA–SCC can be used for structural reinforced concrete and that the incorporation of RCA into SCC is ecologically and economically feasible [9,27–29].

When designing structural concrete elements, the long-term structural deformation due to shrinkage and creep must be considered. The incorporation of RCA in concrete increases both shrinkage and creep, which is due to the porosity and reduced stiffness of the mortar adhering to the aggregates [30–32]. To date, there are only a minimal number of studies addressing the shrinkage [23,33,34] and creep [35,36] of SCC with RCA, and it

should be emphasised that no research has yet fully investigated the deformation properties of this material.

This paper presents the results of testing the mechanical (compressive strength, static Young's modulus) and deformation (shrinkage, creep) properties of SCC with RCA obtained by crushing precast concrete elements. The tests were carried out with nine concrete mixtures. The influence of the water/cement ratio (w/c), the type of cement matrix, the amount of recycled aggregate and the cement replacement by fly ash were investigated. The knowledge gained can serve as input for the calibration and verification of existing models for predicting creep behaviour and contribute to an increased application of RCA in the construction industry.

2. Materials and Methods

2.1. Materials

The cement used for the production of concrete meets the conformity criteria of the European standard EN 197-1:2011 for rapid hardening Portland cement without mineral additives and is designated as CEM I 42,5 R [37]. In two concrete mixtures, the cement was partially replaced by siliceous fly ash from pulverised coal combustion. The density of the cement was 3.17 g/cm^3 and that of the fly ash was 2.11 g/cm^3.

The natural aggregate was crushed dolomite, and the recycled aggregate was produced from prefabricated concrete elements. Three fractions—0/4, 4/8 and 8/16 mm—of both aggregates were used for the tests (Figure 1). The density, absorption and particle size distribution of the aggregates are shown in Table 1 and Figure 2. Recycled aggregates produced from concrete elements exhibit less variation in physical and mechanical properties than recycled aggregates containing brick or masonry mortar particles in addition to concrete.

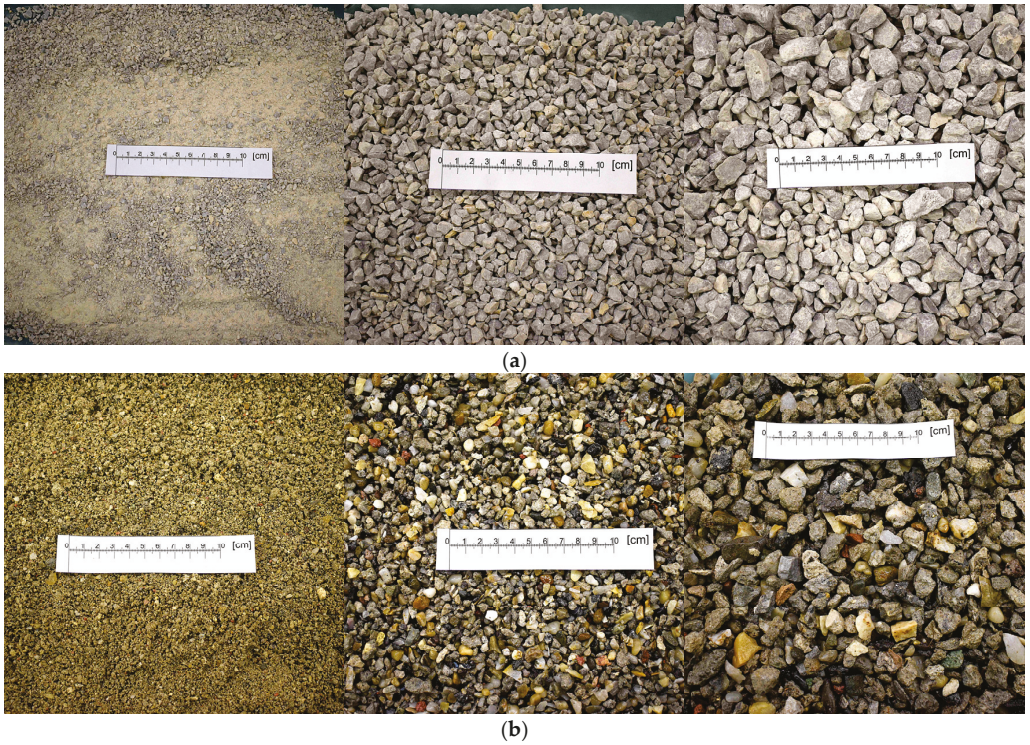

(**a**)

(**b**)

Figure 1. Aggregate fractions of 0/4, 4/8 and 8/16 mm used for concrete: (**a**) natural crushed aggregate; (**b**) recycled concrete aggregate.

Table 1. Density and absorption of natural and RCA.

Property	Natural Aggregate Fraction			Recycled Aggregate Fraction		
	0/4 mm	4/8 mm	8/16 mm	0/4 mm	4/8 mm	8/16 mm
Density (kg/dm^3)	2.62	2.77	2.78	2.25	2.30	2.34
Absorption (% of mass)	0.5	0.4	0.3	7.5	6.1	4.7

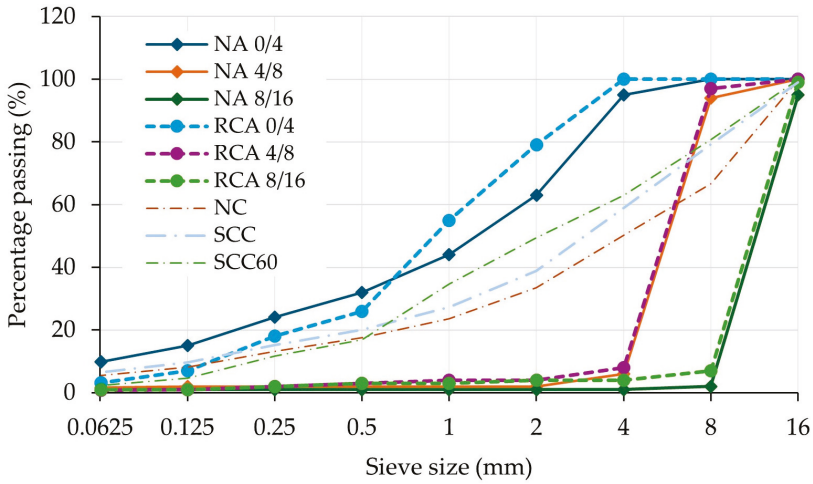

Figure 2. Particle size distribution of natural aggregate fractions (NA 0/4, NA 4/8 and NA 8/16), RCA fractions (RCA 0/4, RCA 4/8 and RCA 8/16) and cumulative curves for NC mixes (NC1 and NC2), SCC mixes (SCC0–SCC50) and SCC60 mix.

In SCC mixtures, a dolomite filler was used that was produced in the same quarry as the natural aggregate. The dry density of the filler is 2.85 g/cm^3 and its particle size distribution is given in Table 2. Polycarboxylate superplasticizer was used to achieve adequate flow properties of SCC. According to the production specification, the density of the superplasticizer is in the range of 1.06–1.1 g/cm^3.

Table 2. Results of sieve analysis of dolomite filler particles.

Sieve (mm)	0.063	0.09	0.125	0.25	0.5	1.0
Passing percentage (%)	76	84	93	97	100	100

2.2. Concrete Mix Design

Nine concrete mixtures were designed (Table 3). The empirical mix design method for SCC was used, in which cohesion is achieved by the addition of fillers [34]. All mixtures had the same binder quantity of 400 kg. The mixes NC1 and NC2 were normal concrete mixes with a w/c ratio of 0.5, in which the coarse aggregates were partially or completely replaced by RCA. The SCC0, SCC10, SCC20 and SCC30 mixes were SCC mixes with a w/c ratio of 0.5. The SCC0 mix was produced with natural aggregate, while in the SCC10, SCC20 and SCC30 mixes, the coarse aggregates were partially or completely replaced by RCA. In the SCC30 mix, 50% of the cement is replaced by fly ash. The SCC40, SCC50 and SCC60 mixes were SCC mixes with a w/c ratio of 0.4. In the SCC40 and SCC50 mixes, the coarse aggregates were partially or completely replaced by RCA. The SCC60 mix was an eco-mix, as it was produced entirely with RCA and 50% of the cement was replaced by fly ash. When calculating the aggregate/paste volume in Table 3, the volume of the aggregate is calculated as the volume of three aggregate fractions (0–4 mm, 4–8 mm and 8–16 mm)

and the volume of the cement paste as the sum of the volumes of cement, fly ash, water and superplasticizer.

Table 3. Concrete mix composition quantities per 1 m^3.

Component	Concrete Mixture								
	NC 1	**NC 2**	**SCC0**	**SCC10**	**SCC20**	**SCC30**	**SCC40**	**SCC50**	**SCC60**
Cement (kg)	400	400	400	400	400	200	400	400	200
Natural aggregate 0/4 mm (kg)	930	930	970	970	970	970	970	970	-
Natural aggregate 4/8 mm (kg)	267	-	310	310	-	-	310	-	-
Natural aggregate 8/16 mm (kg)	-	-	320	-	-	-	-	-	-
Recycled aggregate 0/4 mm (kg)	-	-	-	-	-	-	-	-	970
Recycled aggregate 4/8 mm (kg)	-	267	-	-	310	310	-	310	310
Recycled aggregate 8/16 mm (kg)	644	644	-	320	320	320	320	320	320
Water (l)	200	200	200	200	200	200	160	160	160
Superplasticizer (kg)	2.4	2.0	16.1	7.6	10.5	8.6	12.6	16.9	20.6
Filler (kg)	-	-	200	200	200	200	200	200	200
Fly ash (kg)	-	-	-	-	-	200	-	-	200
Water/cement ratio	0.5	0.5	0.5	0.5	0.5	0.5	0.4	0.4	0.4
Aggregate/paste ratio (by volume)	2.21	2.28	1.75	1.86	1.91	1.75	2.08	2.13	2.09

2.3. Specimen Mixing, Casting and Curing

Due to its high absorption capacity, the recycled aggregate was partially saturated with water. This reduced the amount of additional water that had to be added during mixing to compensate for the saturated surface dry condition of the moisture. All concrete constituents were conditioned at 20 ± 2 °C. Mixing was carried out in a compulsory mixer with a capacity of 75 litres. Since the amount of concrete for each mix was 108 litres, two batches were made for each mix, first the batch of 48 litres and then the second batch of 60 litres. Care was taken to reduce the time between mixing the two batches to around 45 to 60 min.

In the normal concrete mixes, the aggregates were first mixed with about half of the mixing water for two minutes. At the end of the two-minute standing time, the cement was added and mixed with the aggregate, followed by the addition of the remaining water mixed with superplasticizer. For SCC mixtures, aggregate and filler were mixed with about one-third of the water. After 30 s, cement or cement and fly ash were added, followed by the addition of the second third of the water. After two minutes of mixing, the remaining water, premixed with superplasticizer, was added and mixed for 1.5 min. Mixing was then interrupted for two minutes and continued for a further three minutes. For SCC mixtures, a slump flow test was carried out to check whether sufficient flowability of the mixture was achieved. An additional amount of superplasticizer was added to the first batch, if necessary, to achieve the desired slump or slump flow, and it was mixed for a further two minutes. In all cases, the second batch of mix was prepared with the same total amount of superplasticizer as the first batch, which was added premixed with water. Therefore, there is a difference in the type of superplasticizer dosage between the first and second batches.

The concrete specimens made from the NC1 and NC2 mixes were compacted on a vibrating table, while no vibration was used for the specimens made from SCC. After casting, the specimens were stored at a temperature of 20 ± 5 °C and covered with a plastic sheet. After 24 h, the specimens were demoulded. The specimens for the compressive

strength test and Young's modulus test were stored in the curing chamber at a relative humidity of >95% and a temperature of 20 ± 2 °C. The specimens for the shrinkage and creep tests were prepared for testing and transported to the test room where the relative humidity was kept at 60 ± 5%.

2.4. Testing Methods

After mixing, the following properties of the fresh concrete were evaluated: density (EN 12350-6), temperature and air content (EN 12350-7) [38,39]. For the NC1 and NC2 mixes, the consistency was evaluated using a slump test (EN 12350-2) [40]. For the SCC mixtures, the workability was evaluated by testing the flowability with the slump flow test (EN 12350-8), the viscosity with the V-funnel test (EN 12350-9), the passing ability with the L-box test (EN 12350-10) and the resistance to segregation with the sieving test (EN 12350-11) [41–44]. Figure 3 shows the L-box test and the measurement of the flowability of SCC.

(**a**) (**b**)

Figure 3. Testing of fresh SCC properties: (**a**) passing ability using L-box test; (**b**) slump flow test.

Concrete cylinders with a diameter of 150 mm and a length of 300 mm were used to determine the compressive strength of the concrete, the static Young's modulus in compression and to measure shrinkage and creep strain. For each test, one specimen was taken from the first batch and two specimens from the second batch of concrete. The compressive strength was tested at a concrete age of 2 and 28 days in accordance with standard EN 12390-3 [45]. The Young's modulus was determined at the age of 28 days as the secant modulus after three loading–unloading pre-cycles in accordance with EN 12390-13 [46]. The compressive strength at the specimen age of 2 days was determined with the aim of assessing the development of the early compressive strength and to obtain the characteristic value of the strength required for the compressive loading of the specimens during the creep deformation test.

Drying shrinkage length change was determined in accordance with ISO 1920-8 [47]. After demoulding, measuring pins were glued to opposite sides of each cylinder at a distance of 200 mm and the initial value was recorded. The change in length was measured with a length comparator and the displacement was measured with a digital indicator. Parallel to the samples for shrinkage measurement, pins were also attached to the samples for creep test. The samples were loaded at an age of 2 days to a value of 30% of the achieved compressive strength. The load after 2 days was chosen to simulate the process of introducing the prestressing force into prefabricated, prestressed structural elements. The creep test was carried out in accordance with the ISO 1920-9 standard [48]. The load frame for the creep test consisted of a spring system to maintain the load and a permanently installed load cell to read and adjust the load force. Figure 4 shows some details of the measurement procedures. During the creep and shrinkage measurements, the ambient temperature was kept at 20 ± 2 °C and the relative humidity at 60 ± 5%.

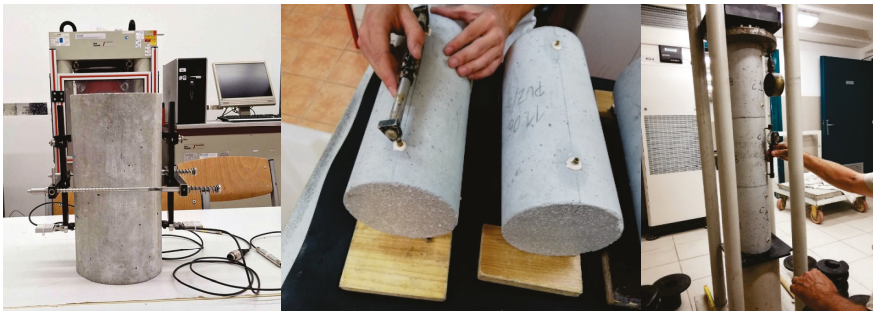

(a) (b) (c)

Figure 4. (**a**) System for measuring Young's modulus under compression; (**b**) adjusting spacing of measuring pins using length comparator; (**c**) reading of length between measuring pins on samples loaded in creep loading frame.

The measurement of shrinkage and creep was carried out up to a concrete age of 180 days. An exception is the SCC50 mixture, for which the measurements were carried out up to a concrete age of 90 days. Previous investigations of the deformation properties of SCC with recycled aggregate have shown that the shrinkage and creep deformations become stable after 180 days and approach the asymptotic final value [35].

The creep coefficient of concrete under compressive load is calculated as follows:

$$\Phi(t, t_0) = \frac{\varepsilon_p(t, t_0)}{\varepsilon_{el}(t_0)} \tag{1}$$

$$\varepsilon_p(t, t_0) = \varepsilon_{tot}(t, t_0) - \varepsilon_{el}(t_0) - \varepsilon_s(t) + \varepsilon_s(t_0) \tag{2}$$

where $\Phi(t,t_0)$, $\varepsilon_p(t,t_0)$ and $\varepsilon_{tot}(t,t_0)$ are the creep coefficient, the creep strain and the total strain of the specimens under load, respectively, at concrete age t, which were subjected to a constant load at age t_0. $E_{el}(t_0)$ is the elastic strain at loading, while $\varepsilon_s(t)$ and $\varepsilon_s(t_0)$ are the shrinkage strains at age t and t_0 respectively.

3. Results

3.1. Fresh Concrete Properties

The results of the fresh concrete properties are shown in Table 4. The density of the fresh concrete decreases with the increase in the proportion of recycled aggregate, but also with the addition of fly ash, which is due to the lower density of these constituents compared to natural aggregate and cement. A reduction in the w/c ratio increased the density, as the reduction in the w/c ratio was achieved by reducing the water content. The air content varied between 1.5% and 3.5%. In SCC mixtures, the air content increased with the increase in RCA content, except in the SCC30 mixture, which contained fly ash.

The results listed in Table 4 for the slump of the NC mixtures and the workability properties of SCC refer to the second batch, in which the entire amount of superplasticizer was added premixed with water. This allowed for better dispersion of the superplasticizer and resulted in better flowability than the first batch. Therefore, the authors believe that these results are more meaningful for evaluating the effects of RCA on workability.

The slump values of the NC1 and NC2 mixes show that the concrete has a plastic consistency. Taking into account the amount of superplasticizer and the slump, RCA reduced the water requirement in the NC2 mix. The slump flow of the SCC mixes was classified according to the European standard for concrete HRN EN 206:2021 [49], which shows that the criteria for SCC were met (Table 4). From the dosage of superplasticizer and

the results of the slump flow and V-funnel test, it can be seen that replacing the 8/16 mm fraction with recycled aggregate increases flowability and decreases viscosity. This is particularly evident in the SCC40 mix, where the amount of water was reduced by 40 litres compared to the SCC0 mix. The replacement of the 4/8 mm fraction increased the water requirement and viscosity in the SCC20 and SCC50 mixtures. It can be seen from Table 4 that the density of the SCC50 mix was almost the same as that of the SCC40 mix, although it contained a greater proportion of lower density aggregates. The results of the compressive strength tests (Table 5) support the possibility that mixtures in which both coarse aggregates were replaced with recycled aggregates have a denser packing of particles. It is known that denser packing of coarse aggregates can increase flow resistance [50]. Most of the results reported show that recycled concrete aggregates reduce the flowability of SCC [19,51–54]. The reduction in flowability is often attributed to the increased internal friction between the aggregates due to the increased angularity. The comparison of natural and recycled aggregates shown in Figure 1 indicates that this was not the case with the RCA used in this work.

The partial replacement of cement with fly ash improved fluidity, mainly due to the reduced friction caused by the spherical shape and smooth surface of the fly ash particles [55]. Apart from the SCC0 mixture, only mixtures with fly ash were able to fulfil the criteria for passing ability. It has been shown that the addition of pulverised coal fly ash increases the flowability and passing ability of SCC RCA mixes [23]. In the SCC60 mix, the highest superplasticizer dosage was required to achieve adequate flow properties. The particle size distribution of natural and recycled aggregate fractions differs, with the greatest difference being in the fine aggregates (Figure 2). The quantities of the individual fractions in the concrete mix were optimised for natural aggregate, which was then replaced by the same quantity of recycled aggregate. This leads to deviations from the optimised particle grading and can result in changes in the packing density and, consequently, changes in the water requirement.

Table 4. Fresh concrete properties.

Fresh Concrete Properties	**Concrete Mixture**								
	NC1	**NC2**	**SCC0**	**SCC10**	**SCC20**	**SCC30**	**SCC40**	**SCC50**	**SCC60**
Density (kg/m^3)	2330 (±10)	2295 (±9)	2460 (±1)	2365 (±31)	2299 (±40)	2259 (±20)	2392 (±40)	2378 (±7)	2163 (±22)
Temperature (°C)	19.8 (±1.6)	20.1 (±2.1)	23.7 (±0.3)	23.1 (±1.4)	23.1 (±0.6)	22.2 (±0.5)	23.2 (±0.6)	23.1 (±1.5)	21.7 (±0.2)
Air content (%)	3.5 (±0.8)	2.8 (±0.1)	1.6 (±0.3)	2.2 (±0.7)	3.0 (±0.9)	1.5 (±0.2)	1.8 (±0.2)	2.3 (±0.6)	3.1 (±0.5)
Slump (mm)	90	95	-	-	-	-	-	-	-
Slump flow (mm)	-	-	745 (SF2)	735 (SF2)	690 (SF2)	715 (SF3)	800 (SF3)	755 (SF3)	725 (SF2)
Slump flow time, t_{500} (s)	-	-	1.7 (VS1)	0.5 (VS1)	1.4 (VS1)	0.6 (VS1)	1.0 (VS1)	1.9 (VS1)	2.4 (VS2)
L-box (3 bars) (-)	-	-	0.81 (PL2)	0.82 (PL2)	0.75 (−)	0.72 (−)	0.71 (−)	0.78 (−)	0.80 (PL2)
V-funnel (s)	-	-	5.6 (VF1)	2.5 (VF1)	2.7 (VF1)	3.1 (VF1)	7.4 (VF1)	11.8 (VF2)	9.4 (VF2)
GTM sieve (%)	-	-	5.2 (SR2)	11.6 (SR2)	6.0 (SR2)	8.8 (SR2)	11.0 (SR2)	3.5 (SR2)	0.0 (SR2)

For the density, the temperature and air content numbers in parentheses represent the half-span of two measurements. Classification of SCC mixes according to standard EN 206 is given in parentheses. For the L-box test, (−) means that the criteria are not met.

Table 5. Hardened concrete properties at an age of 2 and 28 days.

Hardened Concrete Properties	Concrete Mixture									
	Unit	**NC 1**	**NC 2**	**SCC0**	**SCC 10**	**SCC 20**	**SCC 30**	**SCC 40**	**SCC 50**	**SCC 60**
Density	kg/m^3	2343 (±18)	2290 (±6)	2478 (±10)	2374 (±24)	2323 (±17)	2297 (±23)	2407 (±24)	2389 (±12)	2150 (±34)
Compressive strength, 2 days	MPa	27.3 (±0.7)	24.3 (±0.3)	46.0 (±0.4)	29.4 (±0.6)	24.6 (±0.2)	9.4 (±0.2)	37.6 (±0.9)	40.4 (±3.5)	9.3 (±0.1)
Compressive strength, 28 days	MPa	45.1 (±1.3)	45.9 (±0.7)	57.6 (±0.7)	51.1 (±0.6)	52.6 (±0.4)	25.3 (±0.7)	56.3 (±0.4)	65.4 (±1.0)	30.0 (±2.2)
* Young's modulus, 2 days	GPa	15.4 (±1.9)	17.8 (±3.1)	36.8 (±1.4)	23.9 (±1.9)	19.5 (±1.9)	8.7 (±1.3)	24.3 (±0.8)	32.8 (±2.0)	9.3 (±1.0)
Young's modulus, 28 days	GPa	31.0 (±0.6)	27.5 (±0.3)	40.6 (±2.9)	30.5 (±0.1)	30.6 (±0.2)	25.8 (±2.0)	35.3 (±0.8)	34.9 (±0.6)	23.5 (±0.9)

* Calculated from load and deformation measured at initial loading of samples for creep test. Numbers in parentheses represent standard deviation.

3.2. Hardened Concrete Properties

Table 5 shows the results of the compressive strength and Young's modulus tests. Each test was performed on three samples and the average value is given. The density was determined from the measured dimensions and mass of the samples for the compressive strength test. Figure 5 shows averaged values of the shrinkage strain and the total strain under compressive load. Both normal concrete and SCC appear to exhibit similar trends in strain development, regardless of the type of aggregate. It was found that the hyperbolic Equation (3), which is often used to represent the increase in the compressive strength of concrete [56], could be fitted fairly accurately to the shrinkage and total strain data.

$$y(t) = A\frac{B(t-C)}{1+B(t-C)} \tag{3}$$

where $y(t)$ is the strain at age t (shrinkage strain or total strain), A is the limiting strain, and B and C are coefficients that determine the shape of the curve. Figure 5 also shows the best fit equations. The coefficients of determination were above 0.95 in all cases. The primary purpose of fitting the equations to the measured strains here is to smooth out the fluctuations in the average values that normally occur in this type of measurement. It is not intended to use these fitted curves to extrapolate data, particularly to estimate long-term strains, as these values would likely underestimate the actual strains that would be measured in a long-term experiment of 1 year or longer [57].

The creep coefficients calculated according to Equation (1) are shown in Figure 6a–c. The creep coefficient was calculated using measured data for $\varepsilon_{tot}(t,t_0)$ and $\varepsilon_s(t)$, with linear interpolation between the data points to match the age of the concrete. The measurement uncertainty intervals of the creep coefficient are shown in Figure 6 and are determined according to the methodology described in JCGM 100:2008 [58]. These intervals represent the combined standard uncertainty of the creep coefficient $u_c(\Phi)$ given by Equation (4).

$$u_c^2(\Phi) = \sum_{i=1}^{N}\left(\frac{\partial\Phi}{\partial\varepsilon_i}\right)^2 u^2(\varepsilon_i) \tag{4}$$

where ε_i are the parameters of the measurement model and u(ε_i) are the associated standard uncertainties. The measurement model used here is assumed to be equivalent to Equation (2), where the parameters used to calculate the creep coefficient are $\varepsilon_{tot}(t,t_0)$, $\varepsilon_{el}(t_0)$, $\varepsilon_s(t)$ and $\varepsilon_s(t_0)$ and their standard uncertainties are determined from the standard deviations of the experimental data. It should be emphasised that the measurement uncertainty intervals

shown in Figure 6 are mainly derived from the differences between the samples and are used here to assess the confidence in the averaged creep coefficients. Analysing the measurement uncertainty of the creep or shrinkage tests would require a more comprehensive discussion, which is beyond the scope of this paper.

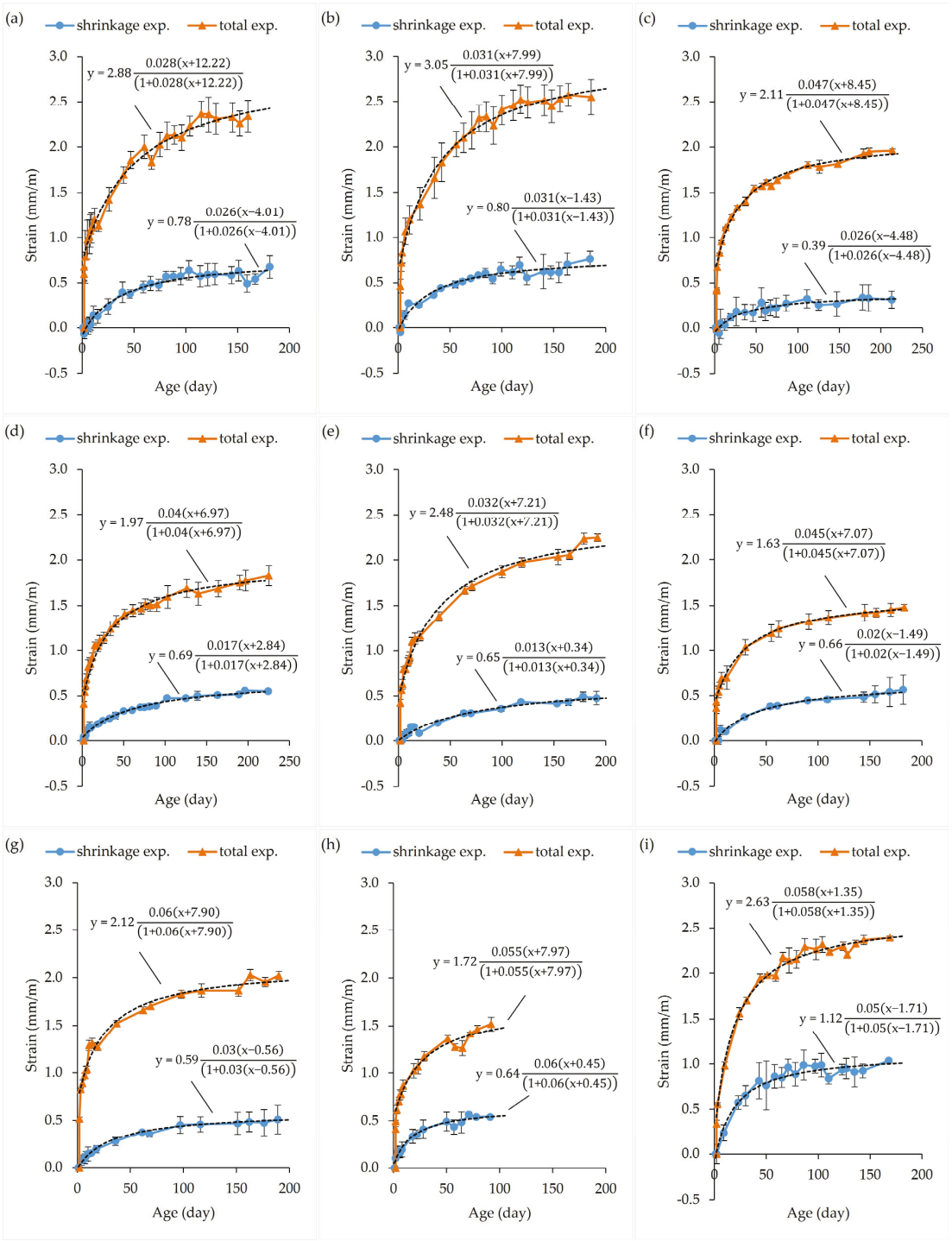

Figure 5. Shrinkage strain (circles) and total strain (triangles) measured on different mix compositions: (**a**) NC1; (**b**) NC2; (**c**) SCC0; (**d**) SCC10; (**e**) SCC20; (**f**) SCC30; (**g**) SCC40; (**h**) SCC50; (**i**) SCC60. (Error bars represent standard deviation of experimental data. Dashed lines represent best fit hyperbolic equation curve, and best fit equations are placed above corresponding curve).

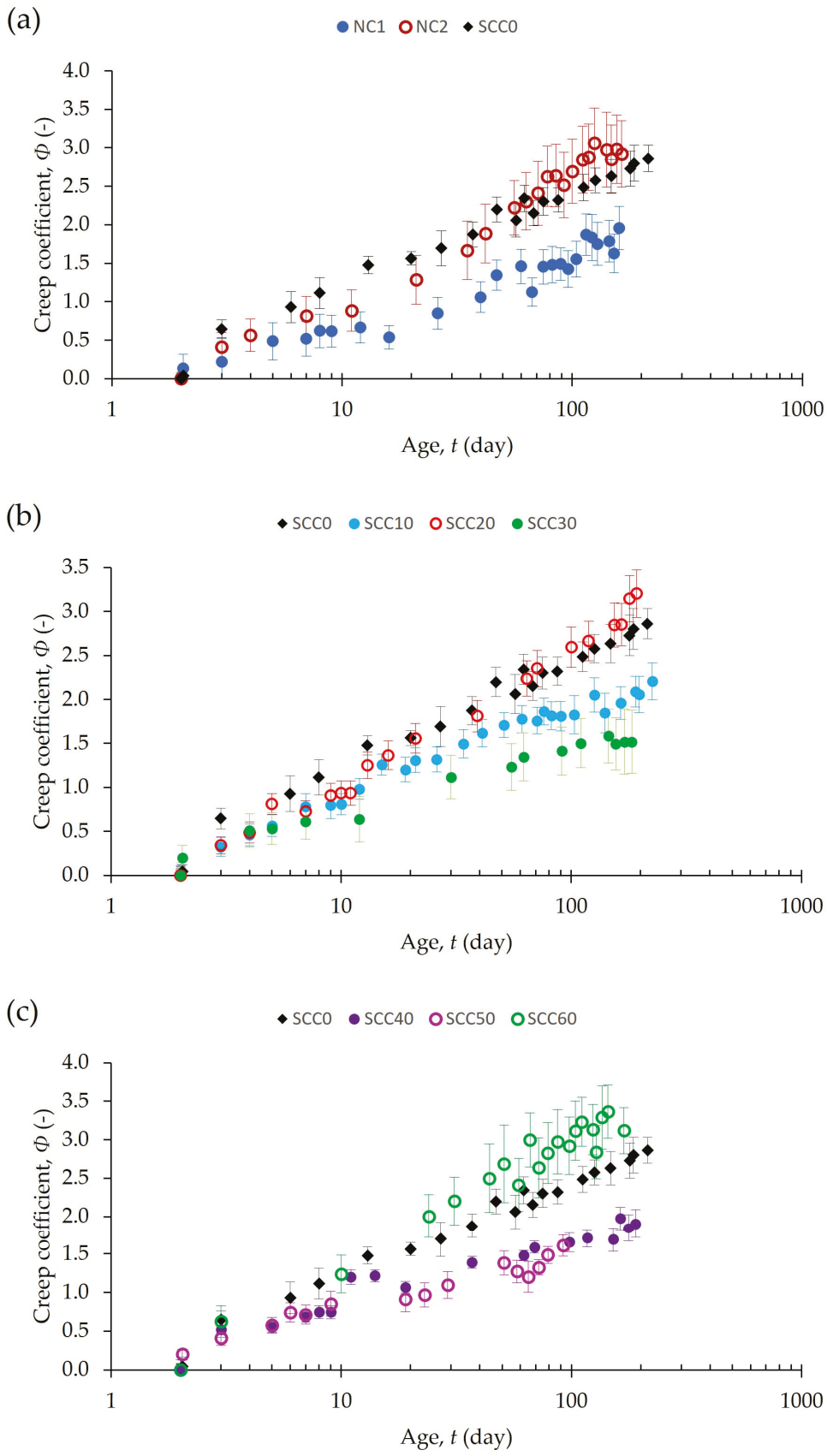

Figure 6. Comparison of creep coefficients of concrete mixes with mix SCC0: (**a**) normal concrete mixes; (**b**) SCC mixes with w/c ratio 0.5; (**c**) SCC mixes with w/c ratio 0.4.

4. Discussion

4.1. Impact of Variations in Concrete Mix Composition on Mechanical Properties

The mechanical properties at the age of 28 days show that replacing natural aggregate with recycled aggregate had different effects on the Young's modulus and compressive strength (Figure 7). The SCC0 mix had the highest Young's modulus. Replacing the coarse aggregate resulted in a reduction in Young's modulus by 25% for mixes SCC10 and SCC20, regardless of whether only one or both fractions of the coarse aggregate were replaced. This reduction is primarily due to the lower stiffness of the recycled aggregate compared to the natural aggregate. The compressive strength in the SCC10 mix was reduced by 11% and in the SCC20 mix by 9%. Replacing 50% of the cement with pulverised coal fly ash in mix SCC30 resulted in a further 36% reduction in stiffness and 56% reduction in compressive strength compared to mix SCC0. This could be due to the slower pozzolanic reactions that dominate at an age of more than 28 days [59], but also to the lower stiffness of fly ash particles compared to cement particles [60,61]. The reduction of the cement paste volume by lowering the water content by 40 litres and the reduction of the capillary porosity due to the lower w/c ratio both increased the stiffness of the cement paste matrix in the SCC40 and SCC50 mixes. However, the introduction of recycled aggregate resulted in a reduction in Young's modulus by 13% and 14% for the SCC40 and SCC50 mixes, respectively, compared to SCC0 mix. At the same time, the compressive strength was reduced by 2% in the SCC40 mix and increased by 14% in the SCC50 mix. It is noteworthy that the replacement of 4/8 mm aggregate in the SCC20 and SCC40 mixes had almost no effect on the Young's modulus compared to the replacement of only 8/16 mm aggregate, but at the same time it increased the compressive strength (Figure 7a). For the normal concrete mix NC2, the replacement of both coarse aggregates also resulted in an increase in compressive strength compared to the NC1 mix. This could be related to the lower stiffness of the recycled aggregate, which reduces the stress concentrations, i.e., reduces the difference in the stiffness of the cement matrix and the aggregate, resulting in a more favourable stress distribution under loading [62]. Xiao et al. numerically determined that the magnitude of tensile and shear stresses in the interfacial transition zone increases rapidly with the increase in the modulus of elasticity of the aggregate [63]. This also means that the introduction of fly ash into the cement matrix in the SCC30 mix increased the difference between the stiffness of the aggregate and the matrix, resulting in higher stress concentrations compared to the SCC20 mix and consequently contributing to lower compressive strength. In the SCC60 mix, all the above effects are present, resulting in a 42% reduction in Young's modulus and 48% reduction in compressive strength compared to the SCC0 mix. Carro-Lopez et al. compared the compressive strength of SCC with natural fine aggregate and with 100% replacement of the fine aggregate with recycled aggregate and found a 47% reduction in strength [52].

At an age of 2 days, the SCC10 and NC1 mixtures exhibited a higher compressive strength than the SCC20 and NC2 mixtures. The "crossover" in compressive strength for these mixtures therefore took place in the period between 2 and 28 days. This could also be related to the gradual increase in stiffness of the cement matrix caused by cement hydration and the associated redistribution of stress between the matrix and aggregates.

The increase in compressive strength in the mixtures SCC20, SCC50 and NC2 compared to the mixtures SCC10, SCC40 and NC1 shows that the replacement of all coarse aggregates by RCA is more favourable than the replacement of only one coarse fraction. The results allow the conclusion that incorporation of RCA reduces the compressive strength. However, this reduction can be partially compensated for if the natural aggregates are replaced by recycled aggregates in a sufficiently large particle size range. On the other

hand, the workability and density results indicate that, in addition to differences in stiffness, the effect of denser particle packing on compressive strength should not be ruled out.

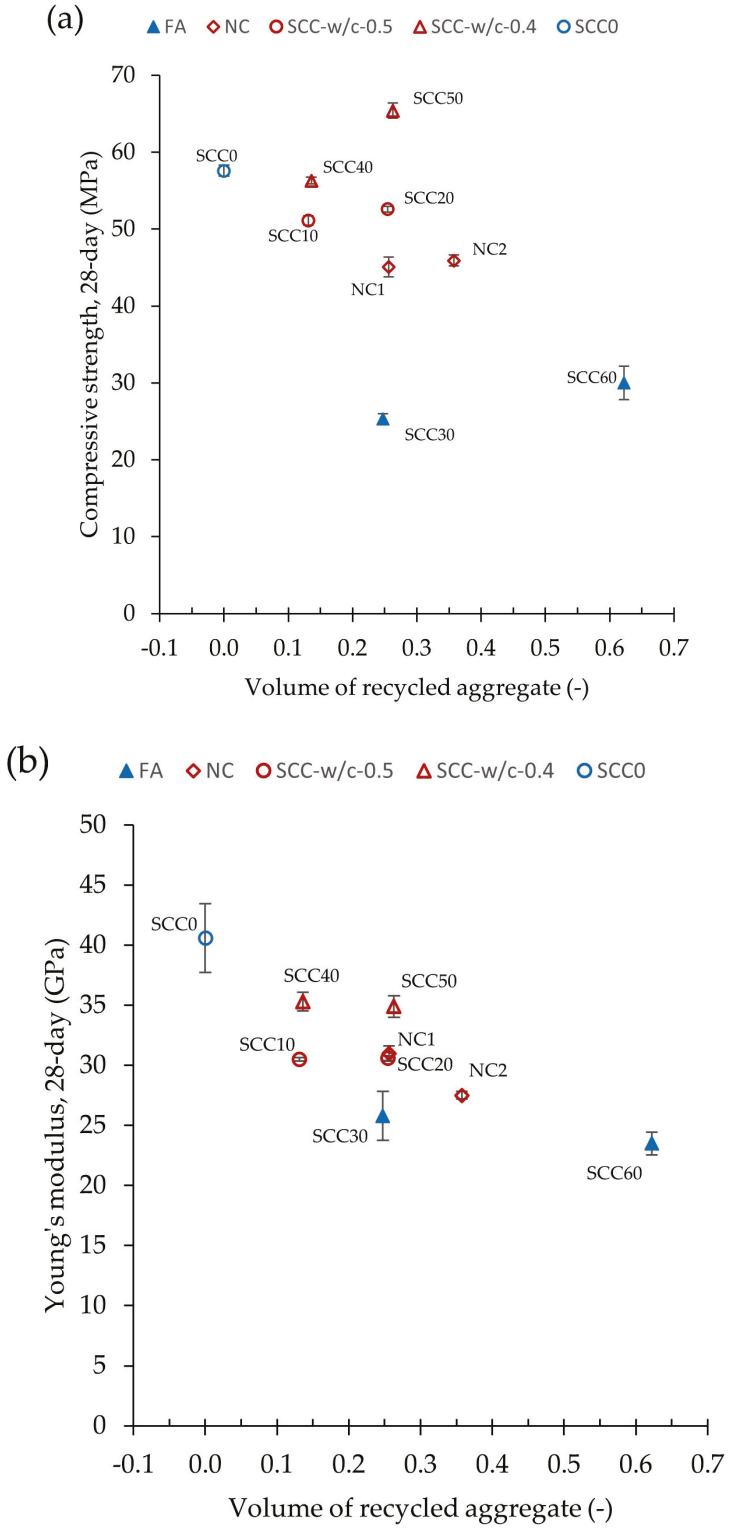

Figure 7. Dependence of mechanical properties on recycled aggregate content: (**a**) 28-day compressive strength; (**b**) 28-day Young's modulus.

To achieve the transformation from normal to self-compacting concrete, part of the coarse aggregate contained in normal concrete mixes is replaced by dolomite filler. The

volume of total coarse aggregate in SCC mixes is approximately equal to the volume of 8/16 mm aggregate in normal concrete. Therefore, the recycled aggregate content (by volume) in the NC1 mix is approximately equal to the volume of recycled aggregate in the SCC20, SCC30 and SCC50 mixes (Figure 7). Comparing the mechanical properties of the SCC20 and NC1 mixes, which both have the same w/c ratio of 0.5, it can be seen that replacing the normal cement matrix with the cement matrix of SCC leads to an increase in compressive strength (Figure 7a), while the Young's modulus is approximately the same (Figure 7b). This could be related to the increased stiffness of the SCC cement matrix due to filling effects, i.e., increased cohesion and improved particle packing due to the addition of fine mineral admixture [62,64].

4.2. Shrinkage Deformation

Dimensional changes measured on unloaded concrete cylinders are not only caused by the evaporation of water from the surface, but also by self-desiccation, which is present throughout the specimens. Self-desiccation phenomena are associated with cement hydration and lead to so-called autogenous shrinkage [65]. Autogenous shrinkage develops faster than drying shrinkage and occurs mainly at an early age. Gabrijel et al. measured the autogenous shrinkage of SCC produced with the cement type CEM I 42,5 R with a w/c ratio in the range 0.4–0.47 and found that the autogenous deformation was most intense within the first 20 h and only a moderate increase was measured in the following 4 days [66]. It was also found that the change in length of concrete specimens subjected to drying 1 day after casting was mainly due to drying shrinkage for a mix with a w/c ratio of 0.4 [67]. The same study also found that the contribution of autogenous deformation to overall shrinkage increased with decreasing w/c ratio [67]. Therefore, the change in length of the unloaded specimens in this work can be largely attributed to drying shrinkage.

Regardless of the shrinkage mechanism, the internal restraints that counteract deformation are the same and are usually related to the quantity of aggregates and their drying shrinkage [65,68,69]. For concrete produced with natural aggregates, shrinkage depends only on the shrinkage of the cement paste and the volume of the aggregates, as most aggregates are non-shrinking [65]. RCAs contain hardened cement paste, which is the reason for the higher water absorption (Table 1). Since the recycled aggregate was partially saturated before mixing and further saturated during mixing, it is expected that this aggregate will show a reduction in volume due to water loss. Fathifazl et al. used pre-saturated RCA and concluded that the higher early shrinkage of the RCA mixtures could be due to the relatively easier moisture loss from the RCA particles [70]. This explains why the concrete mix SCC0 exhibited the lowest shrinkage strain. In addition, the SCC0 concrete mix exhibited the highest Young's modulus (Figure 7) and thus the greatest internal restraint to shrinkage. The lowest Young's modulus and the highest recycled aggregate content can also explain the highest shrinkage of mix SCC60. NC mixes contain a larger volume of recycled aggregate compared to SCC mixes with the same w/c ratio, which could explain their slightly larger shrinkage strain.

The regression line fitted to the experimental data shows that an increasing RCA content leads to an increase in shrinkage strain. As a first approximation, it can be assumed that this increase is proportional to the volume of RCA in the concrete mix, which can be seen from the slope coefficient of the regression line (Figure 8). The slope of the regression curve is almost the same when the 180-day shrinkage values are plotted. Domingo-Cabo et al. found that the shrinkage strain of mixes containing 100% recycled coarse concrete aggregate was 70% higher than that of the control mixture at 180 days [71].

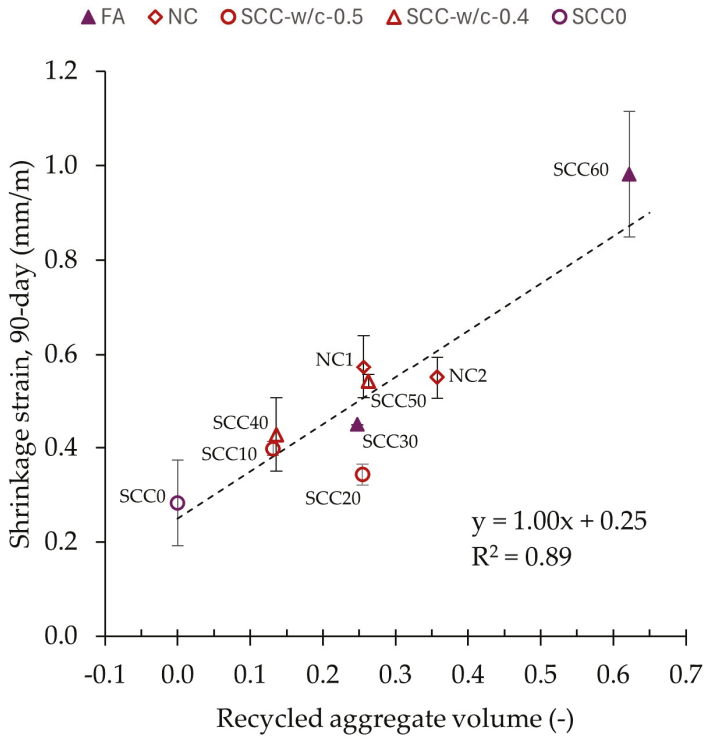

Figure 8. The shrinkage strain of concrete mixes at an age of 90 days (the error bars represent the standard deviation).

The comparison of the shrinkage curves of the mixes SCC10, SCC20, SCC40 and SCC50 shows a higher shrinkage rate for mixes with a w/c ratio of 0.4 during the first weeks (Figure 5). This could be related to the greater contribution of the self-desiccation to the shrinkage strain in mixes with a lower w/c ratio. Mixes with a w/c ratio of 0.5 have a lower internal restraint and contain a greater amount of evaporable water, and at a later age, their shrinkage rate becomes greater than that of mixes with a w/c ratio of 0.4.

The replacement of cement with fly ash in the SCC30 mix increased the initial shrinkage strain, possibly due to a slow stiffness development. However, the long-term shrinkage strain is not significantly different from the shrinkage strain of the SCC20 mix. Qin et al. measured the shrinkage strain of concrete containing 50% and 100% recycled coarse concrete aggregate and in which 50% of the cement was replaced with fly ash [35]. They found that the presence of fly ash reduced the shrinkage strains by approximately 15% after 420 days compared to mixes containing recycled aggregate without fly ash.

4.3. Load-Induced Strain

The interpretation of the creep deformation of concrete based only on the creep coefficient $\Phi(t,t_0)$ can be misleading, especially when these coefficients are used for the creep analysis of concrete structures [57]. It should be noted that the creep coefficient is a normalised quantity. It depends not only on the actual creep strain $\varepsilon_p(t,t_0)$, but also on the elastic deformation $\varepsilon_{el}(t_0)$, which in turn depends on the magnitude of the applied stress and the Young's modulus of the concrete at the age of loading $E(t_0)$. The creep coefficients in Figure 6 are calculated assuming that the initial strain measured immediately after loading the test cylinders to the prescribed stress level $\sigma(t_0)$ corresponds to the elastic deformation $\varepsilon_{el}(t_0)$. The Young's moduli at the age of 2 days (Table 5) are calculated as $E(t_0) = \sigma(t_0)/\varepsilon_{el}(t_0)$. For a complete description of concrete material under load, at least one more parameter must be known in addition to the creep coefficient.

Another way of expressing the response of a viscoelastic material to a long-term load is the compliance function $J(t,t_0)$. Using the compliance function, the time-dependent strain of samples under constant compressive load is expressed as $\varepsilon(t) = J(t,t_0)\ \sigma(t_0)$, where $\sigma(t_0)$ is the compressive load applied at age t_0. $\varepsilon(t)$ consists of the instantaneous (or elastic) strain at the moment of loading and the time-dependent strain, i.e., $\varepsilon(t) = \varepsilon_{el}(t_0) + \varepsilon_p(t,t_0)$. It follows that $J(t,t_0) = [1 + \Phi(t,t_0)\ ]/E(t_0)$. The compliance function, or simply compliance, is the sum of the elastic compliance, which is constant and equal to $1/E(t_0)$, and the creep compliance, which is time-dependent and is expressed as $\Phi(t,t_0)/E(t_0)$. In contrast to $\Phi(t,t_0)$, compliance function is a material property that provides a complete description of the concrete under the applied load, at least for linear creep analysis [57]. Figure 9 shows the compliance function for the concrete mixes analysed in this work. Error bars in Figure 9 represent the combined measurement uncertainty of the compliance function calculated from the standard measurement uncertainty of the creep coefficient Equation (4) and the standard deviation of the 2-day Young's modulus (Table 5).

The physical interpretation of the compliance function is that it represents the strain per unit stress and is expressed in units 1/unit stress. Therefore, at the same stress level, greater compliance corresponds to greater strain. The initial value of compliance measured during the experiment appears at about 15 min (0.01 days), which corresponds to the time required to apply a load and measure the initial change in length. Since the measured compliance spans several orders of magnitude of time, these values are plotted on a logarithmic scale (Figure 9). For SCC mixes with a w/c ratio of 0.5, the lowest compliance is measured for mixture SCC0 (Figure 9b). The initial compliance depends on the concrete stiffness, so it is expected that the mix with the highest Young's modulus will have the lowest initial compliance. Recycled aggregate increases compliance, especially when both coarse aggregate fractions are replaced. The effect of replacing both coarse fractions with recycled aggregate became evident after the 10th day under load, when the slope of the compliance curve started to deviate from the compliance measured for the SCC0 and SCC10 mixes (Figure 9b). This shows that the rate of creep strain after an initial period of 10 days is higher in the mix SCC20 than in the mix SCC10. The replacement of cement with fly ash in the mix SCC30 resulted primarily in an increase in initial compliance while the shape of the compliance curve is very similar to that of the mix SCC20. For normal concrete mixes, the effect of the amount of recycled aggregate is also visible after the initial 10-day period under load (Figure 9a). Even if only the creep compliance is analysed, the replacement of cement with fly ash is found to increase the creep strain. Kou and Poon tested concrete with 25% and 35% fly ash replacement and found that for samples loaded at 28 days, the creep strain measured after 120 days decreased with increasing fly ash content [72]. This phenomenon was attributed to the greater increase in strength due to pozzolanic reactions after loading. The contribution of fly ash to strength development depends on both the w/c ratio and the fly ash replacement ratio [73]. With a high proportion of fly ash (>45%) and a high w/c ratio, the compressive strength of concrete with fly ash cannot exceed the compressive strength of control concrete [73].

The comparison of the creep coefficients shown in Figure 6b shows that the creep coefficients are lowest for the mix SCC30, which could lead to the false conclusion that strain under load is lowest for this mixture. But as already mentioned, this is because the creep coefficient does not contain complete information about the behaviour of the concrete under load.

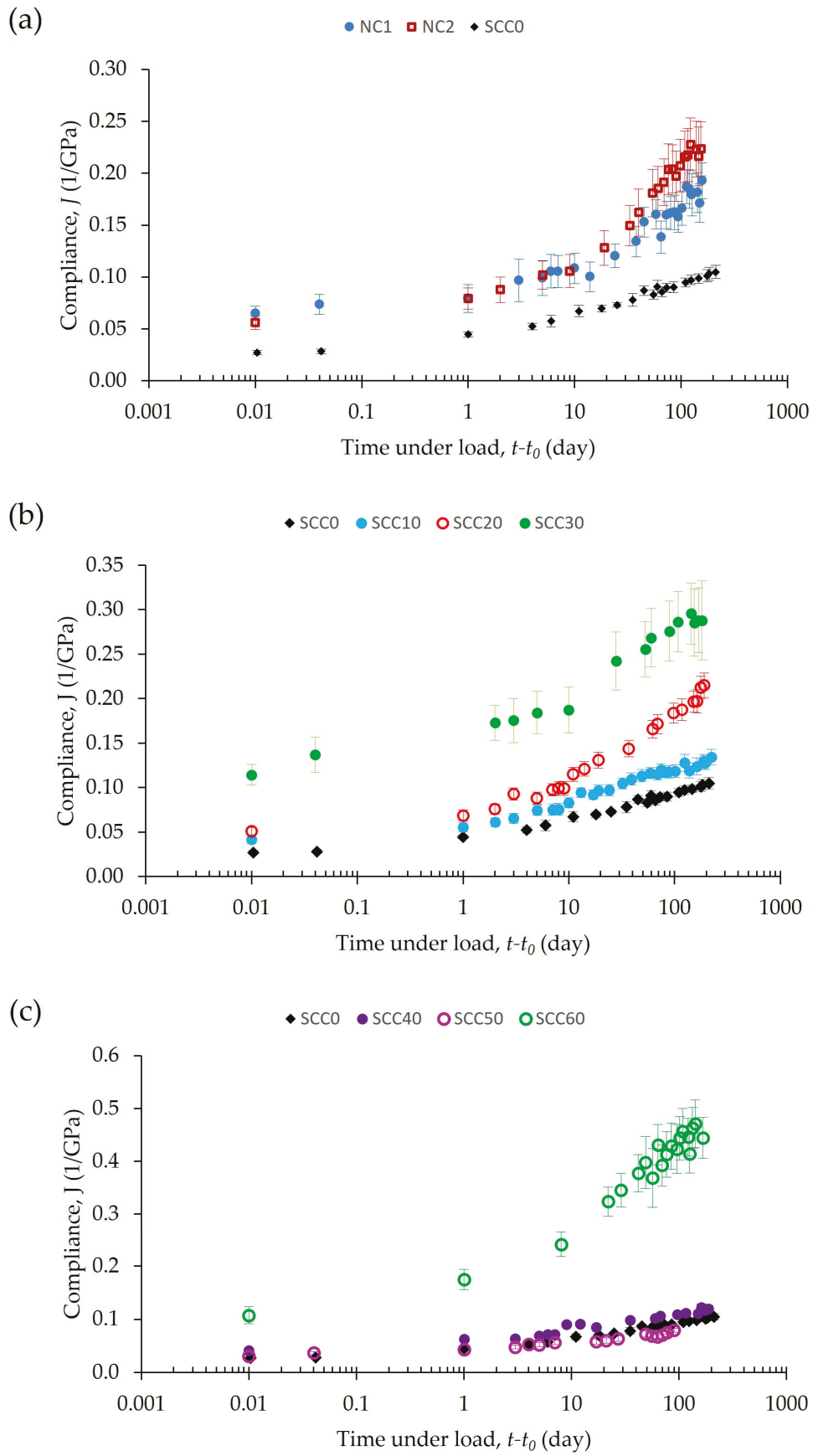

Figure 9. Comparison of the compliance function of mixes subjected to constant compressive load at the age of 2 days with mix SCC0: (**a**) normal concrete mixes; (**b**) SCC mixes with w/c ratio 0.5; (**c**) SCC mixes with w/c ratio 0.4.

Since creep originates from hydrated cement paste [62], mixes with a lower cement paste content and less water available for hydration exhibit a lower creep strain. This led to a lower load-induced strain of the SCC40 and SCC50 mixes compared to the SCC10 and SCC20 mixes. However, this cannot explain the lower strain of mix SCC50 compared to mix SCC40, as the test results of the other mixes clearly show that the incorporation of a higher amount of recycled aggregate increases the creep strain. A look at the results of the compressive strength test after 2 and 28 days (Table 5) shows that the mix SCC50 exhibited a greater increase in strength of 25 MPa compared to 18.7 MPa measured on samples from mix SCC40 in that period. In addition, the mix SCC50 has a higher aggregate/cement ratio compared to the mix SCC40 (Table 3). Both effects, the lower cement paste content and the greater increase in strength, counteracted the effect of the greater volume of recycled aggregate, so the measured load-induced strain of the mix SCC50 was lower overall than that of the mix SCC40.

For the mix SCC60, the initial compliance is comparable to the stress-induced strain measured for the mix SCC30, which is due to the lower initial stiffness at 2 days of age due to the cement replacement by fly ash. At longer load duration mix SCC60 shows the highest rate of creep strain which can be attributed to the incorporation of fine recycled aggregate. Although very little data are available on the influence of fine RCA on creep, studies have shown that it increases creep strain [31].

Manzi et al. found that the lowest creep in SCC with RCA occurred in the mix with the highest compressive strength and the smallest pore size distribution [36]. Figure 10 shows the creep compliance after 28, 90 and 180 days under load together with the 28-day compressive strength. The initial compliance can be derived from Table 5 as the reciprocal value of the 2-day Young's modulus. The data in Figure 10 confirm that creep was lowest in the mix with the highest compressive strength. However, the mixes NC2 and SCC20 exhibited higher creep values than the NC1 and SCC10 mixes despite their higher compressive strength. Both mixes, NC2 and SCC20, had a lower cement paste content and consequently a higher aggregate/cement paste volume (Table 3), which should also contribute to the lower creep strain. This indicates that the increased creep strain in these mixes can only be attributed to the presence of recycled aggregate. Replacing cement with 50% fly ash increased the creep strain in the mix SCC30 but not as much as the decrease in compressive strength would suggest. On the other hand, replacing the fine aggregate with RCA doubled the creep strain compared to the mix SCC30 despite the lower cement paste content. When considering whether the influence of the fine RCA is greater than the influence of coarse RCA, it should be borne in mind that the fine RCA in the SCC mix accounted for 60% of the total aggregate. Therefore, it is not obvious that fine RCA makes a greater contribution to creep than coarse RCA.

Figure 10 also shows the average density of the concrete samples for the compressive strength test. With the exception of the mix SCC50, the decrease in concrete density corresponds well with the increase in creep strain. The linear correlation between density and 28-day, 90-day and 180-day creep compliance has coefficients of determination of 0.81, 0.87 and 0.90, respectively. In comparison, the linear correlation between compressive strength and creep compliance has coefficients of determination of 0.64, 0.62 and 0.56 for 28, 90 and 180 days under load, respectively.

Most models for predicting the creep of concrete use the 28-day compressive strength as input [74]. ACI 209R-92 requires the concrete density in addition to the compressive strength to evaluate Young's modulus [74]. It is therefore known that both compressive strength and density are strongly correlated with creep and both are governed by porosity. What concretes with recycled aggregates have in common is their increased porosity, which

is caused by the porosity of the recycled aggregate. For the concrete mixtures analysed in this work, the volume of the pores contained in the aggregate can be calculated from density and absorption properties (Table 1) and the concrete mix composition (Table 3). This calculation shows that the volume of pores contained in the aggregate alone, excluding air voids and cement paste porosity, ranges from 0.69% for the SCC0 mix to 9.45% for the SCC60 mix. The creep strain measured in this work is the total creep, which is a sum of basic creep and drying creep which is strongly influenced by moisture movement [57]. This implies that the incorporation of RCA in concrete affects the moisture movement, which also affects the creep deformation, and that this process could be the origin of differences in the measured creep deformation between concrete with natural aggregate and concrete made with RCA.

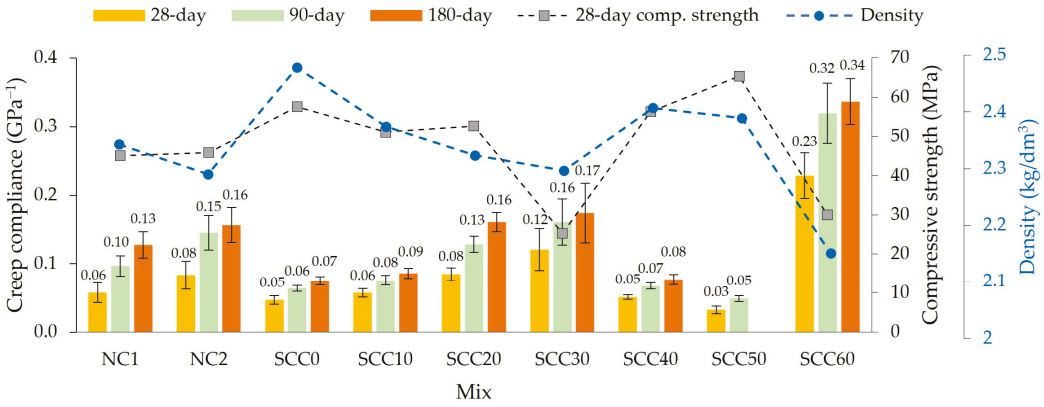

Figure 10. Creep compliance at 28, 90 and 180 * days under load (* for mix NC1, creep compliance after 160 days is presented and for mix SCC60, creep compliance was measured after 168 days); 28-day compressive strength; and hardened concrete density (error bars represent combined uncertainty for creep compliance).

5. Conclusions

Recycled concrete aggregates are considered "high quality" recycled aggregates for concrete production in terms of their mechanical and physical properties and their variability. Of particular interest in this work was the influence of RCA on long-term dimensional stability, i.e., shrinkage and creep deformation. The addition of RCA instead of natural crushed aggregate leads to a change in the fresh and hardened concrete properties:

- When only the 8–16 mm fraction was replaced, the flowability increased, most likely due to the fact that the RCA used contains a certain amount of river gravel particles that were detached from the cement matrix during the crushing process, reducing the overall angularity of the coarse aggregate. A further increase in the RCA content led to a decrease in the flowability of SCC mixes. The greatest increase in the water demand was observed when the fine aggregate was replaced with RCA.
- RCA reduced the Young's modulus and generally also reduced the compressive strength. The increase in compressive strength in the mixes SCC20, SCC50 and NC2 compared to the mixes SCC10, SCC40 and NC1 indicates that replacing all coarse aggregate with recycled aggregate concrete is more favourable than replacing only one coarse fraction. The main reasons for this are a more favourable stress distribution under load due to a smaller difference in the stiffness of the cement matrix and aggregate, or a higher packing density.
- An increasing RCA content leads to an approximately proportional increase in shrinkage strain. This is due to the greater absorbed water content in the RCA and the

simultaneous reduction in stiffness. The presence of fly ash did not cause a significant deviation in shrinkage strain.

- An increase in the coarse and fine fraction of RCA increases creep deformation. Although the highest creep strain was measured on test specimens made from a mix that contained fine RCA, it is not obvious that fine RCA makes a greater contribution to creep than coarse RCA.
- The replacement of aggregate and cement with RCA and fly ash led to a relatively large change in concrete density. Density had a stronger linear correlation with creep strain than compressive strength.

The European standard for concrete production EN 206 allows the use of up to 50% replacement of coarse aggregates with RCA. Nevertheless, the data show that RCA is rarely used as an aggregate in concrete. This is understandable, as there are a number of parameters that need to be considered when deciding whether the use of RCA is appropriate. One technological limitation is that relatively small quantities of RCA come from a demolition site. Or if concrete with natural aggregates meets a certain compressive strength class, it is not sufficient to simply replace the natural aggregates with recycled aggregates, as RCA concrete is likely to have a lower strength. To compensate for the lower strength, some modification of the concrete composition is required, probably by increasing the cement content.

However, it is possible that the use of recycled aggregates in concrete will be enforced by regulations. Concrete already accounts for more than 50% of demolition materials, and the need to recycle these into concrete aggregates will direct demolition activities towards prior characterisation and more careful separation of each type of material.

The experimental investigations carried out in this work have confirmed that SCC–RCA is feasible. The mechanical properties of SCC–RCA, even when 100% of the aggregate is RCA, can be utilised for structural applications. The w/c ratio range of 0.4–0.5 covers most concrete mixes used in construction, so the results presented in this paper can be widely applied. The design rules for concrete structures allow the use of RCA and the results presented in this paper can be used to re-evaluate the resistance reduction factors, especially for structural elements where deformations are of concern.

Author Contributions: Conceptualisation, M.S. and I.G.; methodology, M.S., H.M. and I.G.; formal analysis, I.G. and H.M.; investigation, I.G. and H.M.; resources, M.S.; data curation, H.M.; writing—original draft preparation, M.S. and H.M.; writing—review and editing, I.G.; visualisation, I.G.; supervision, M.S.; project administration, M.S.; funding acquisition, M.S. All authors have read and agreed to the published version of the manuscript.

Funding: This research received no external funding.

Institutional Review Board Statement: Not applicable.

Informed Consent Statement: Not applicable.

Data Availability Statement: The original contributions presented in the study are included in the article, further inquiries can be directed to the corresponding author.

Conflicts of Interest: The authors declare no conflicts of interest.

References

1. Global Cement and Concrete Association. *Concrete Future The GCCA 2050 Cement and Concrete Industry Roadmap for Net Zero Concrete*; Global Cement and Concrete Association: London, UK, 2021.
2. OECD. *Global Material Resources Outlook to 2060: Economic Drivers and Environmental Consequences*; OECD Publishing: Paris, France, 2019.

3. European Aggregates Association. *Annual Review 2020/2021*; European Aggregates Association: Brussels, Belgium, 2021.
4. Garcia-Troncoso, N.; Li, L.; Cheng, Q.; Hung Mo, K.; Ling, T. Comparative study on the properties and high temperature resistance of self-compacting concrete with various types of recycled aggregate. *Case Stud. Constr. Mater.* **2021**, *15*, e00678. [CrossRef]
5. Fanijo, E.O.; Kolawole, J.T.; Babafemi, A.J.; Liu, J. A comprehensive review on the use of recycled concrete aggregate for pavement construction: Properties, performance, and sustainability. *Clean. Mater.* **2023**, *9*, 100199. [CrossRef]
6. Wang, S.; Wang, A.; Fu, X.; Zhang, X.; Li, Z.; Guo, Y.; Li, S.; Wang, M. Experimental Research on the Performance of Recycled Waste Concrete Powder (RWCP) on Concrete. *Materials* **2024**, *17*, 5319. [CrossRef] [PubMed]
7. Cristóbal García, J.; Caro, D.; Foster, G.; Pristerà, G.; Gallo, F.; Tonini, D. *Techno-Economic and Environmental Assessment of Construction and Demolition Waste Management in the European Union*; Publications Office of the European Union: Luxembourg, 2024.
8. Caro, D.; Lodato, C.; Damgaard, A.; Cristobal, J.; Foster, G.; Flachenecker, F.; Tonini, D. Environmental and socio-economic effects of construction and demolition waste recycling in the European Union. *Sci. Total Environ.* **2024**, *908*, 168295. [CrossRef]
9. Pacheco, J.; de Brito, J.; Lamperti Toronaghi, M. *Use of Recycled Aggregates in Concrete*; Publications Office of the European Union: Luxembourg, 2023.
10. Hossain, M.U.; Poon, C.S.; Lo, I.M.C.; Cheng, J.C.P. Comparative environmental evaluation of aggregate production from recycled waste materials and virgin sources by LCA. *Resour. Conserv. Recycl.* **2016**, *109*, 67–77. [CrossRef]
11. Pacheco, J.; de Brito, J. Recycled Aggregates Produced from Construction and Demolition Waste for Structural Concrete: Constituents, Properties and Production. *Materials* **2021**, *14*, 5748. [CrossRef] [PubMed]
12. Artoni, R.; Cazacliu, B.; Hamard, E.; Cothenet, A.; Parhanos, R.S. Resistance to fragmentation of recycled concrete aggregates. *Mater. Struct.* **2017**, *50*, 11. [CrossRef]
13. de Juan, M.S.; Gutierrez, P.A. Study on the influence of attached mortar content on the properties of recycled concrete aggregate. *Constr. Build. Mater.* **2009**, *23*, 872–877. [CrossRef]
14. Tam, V.W.Y.; Wattage, H.; Le, K.N.; Buteraa, A.; Soomro, M. Methods to improve microstructural properties of recycled concrete aggregate: A critical review. *Constr. Build. Mater.* **2021**, *270*, 121490. [CrossRef]
15. McNeil, K.; Kang, T.H.-K. Recycled Concrete Aggregates: A Review. *Int. J. Concr. Struct. Mater.* **2013**, *7*, 61–69. [CrossRef]
16. Wang, B.; Yan, L.; Fu, Q.; Kasal, B. A Comprehensive Review on Recycled Aggregate and Recycled Aggregate Concrete. *Resour. Conserv. Recycl.* **2021**, *171*, 105565. [CrossRef]
17. Wang, D.; Lu, C.; Zhu, Z.; Zhang, Z.; Liu, S.; Ji, Y.; Xing, Z. Mechanical performance of recycled aggregate in green civil engineering: Review. *Case Stud. Constr. Mater.* **2023**, *19*, e02384. [CrossRef]
18. Singh, A.; Duan, Z.; Xiao, J.; Liu, Q. Incorporating recycled aggregates in self-compacting concrete: A review. *J. Sustain. Cem.-Based Mater.* **2020**, *9*, 165–189. [CrossRef]
19. Revilla-Cuesta, V.; Faleschini, F.; Skaf, M.; Manso, J.M. Self-compacting concrete manufactured with recycled concrete aggregate: An overview. *J. Clean. Prod.* **2020**, *262*, 121362. [CrossRef]
20. Santos, S.; da Silva, P.R.; de Brito, J. Self-compacting concrete with recycled aggregates—A literature review. *J. Build. Eng.* **2019**, *22*, 349–371. [CrossRef]
21. Fiol, F.; Revilla- Cuesta, V.; Thomas, C.; Manso, J.M. Self-compacting concrete containing coarse recycled precast-concrete aggregate and its durability in marine-environment-related tests. *Constr. Build. Mater.* **2023**, *377*, 131084. [CrossRef]
22. Tang, W.; Khavarian, M.; Yousefi, A.; Cui, H. Properties of self-compacting concrete with recycled concrete aggregates. In *Self-Compacting Concrete: Materials, Properties, and Applications*; Woodhead Publishing Series in Civil and Structural Engineering; Woodhead Publishing: Sawston, UK, 2020; pp. 219–248.
23. Kou, S.C.; Poon, C.S. Properties of self-compacting concrete prepared with coarse and fine recycled concrete aggregates. *Cem. Concr. Compos.* **2009**, *31*, 622–627. [CrossRef]
24. Revilla-Cuesta, V.; Faleschini, F.; Pellegrino, C.; Skaf, M.; Ortega-Lopez, V. Simultaneous addition of slag binder, recycled concrete aggregate and sustainable powders to self-compacting concrete: A synergistic mechanical-property approach. *J. Mater. Res. Technol.* **2022**, *18*, 1886–1908. [CrossRef]
25. Revilla-Cuesta, V.; Faleschini, F.; Zanini, M.A.; Skaf, M.; Ortega-Lopez, V. Porosity-based models for estimating the me-chanical properties of self-compacting concrete with coarse and fine recycled concrete aggregate. *J. Build. Eng.* **2021**, *44*, 103425. [CrossRef]
26. Revilla-Cuesta, V.; Ortega-Lopez, V.; Skaf, M.; Khan, A.R.; Manso, J.M. Deformational behaviour of self-compacting concrete containing recycled aggregate, slag cement and green powders under compression and bending: Description and prediction adjustment. *J. Build. Eng.* **2022**, *54*, 104611. [CrossRef]
27. Yu, X.; Zhao, X.; Xie, T.; Wang, X. Eco-, economic- and mechanical–efficiencies of using precast rejects as coarse aggregates in self-compacting concrete. *Case Stud. Constr. Mater.* **2022**, *17*, e01591. [CrossRef]

28. Sua-iam, G.; Makul, N. Recycling prestressed concrete pile waste to produce green self-compacting concrete. *J. Mater. Res. Technol.* **2023**, *24*, 4587. [CrossRef]
29. Ortiz-Lozano, J.A.; Mena-Sebastia, F.; Segura, I.; Fuente, A.; Aguado, A. Structural use of fiber-reinforced self-compacting concrete with recycled aggregates: Case study of a foundation wall in Spain. *Case Stud. Constr. Mater.* **2022**, *17*, e01334. [CrossRef]
30. Tošić, N.; de la Fuente, A.; Marinković, S. Creep of recycled aggregate concrete: Experimental database and creep prediction model according to the fib Model Code 2010. *Constr. Build. Mater.* **2019**, *195*, 590–599. [CrossRef]
31. Lye, C.-Q.; Dhir, R.K.; Ghataora, G.S.; Li, H. Creep strain of recycled aggregate concrete. *Constr. Build. Mater.* **2016**, *102*, 244–259. [CrossRef]
32. Tošić, N.; de la Fuente, A.; Marinković, S. Shrinkage of recycled aggregate concrete: Experimental database and application of fib Model Code 2010. *Mater. Struct.* **2018**, *51*, 126. [CrossRef]
33. Nadour, Y.; Bouziadi, F.; Hamrat, M.; Boulekbache, B.; Amziane, S.; Haddi, A.; Labed, A. Short- and long-term properties of self-compacting concrete containing recycled coarse aggregate under different curing temperatures: Experimental and numerical study. *Mater. Struct.* **2023**, *56*, 83. [CrossRef]
34. Wang, J.; Zhou, J.; Kangwa, J. Self-compacting concrete adopting recycled aggregates. In *Multi-Functional Concrete with Recycled Aggregates*; Woodhead Publishing Series in Civil and Structural Engineering; Woodhead Publishing: Sawston, UK, 2023; pp. 267–288.
35. Qin, D.; Dong, C.; Zong, Z.; Guo, Z.; Xiong, Y.; Jiang, T. Shrinkage and Creep of Sustainable Self-Compacting Concrete with Recycled Concrete Aggregates, Fly Ash, Slag, and Silica Fume. *J. Mater. Civ. Eng.* **2022**, *34*, 04022236. [CrossRef]
36. Manzi, S.; Mazzotti, C.; Bignozzi, M.C. Self-compacting concrete with recycled concrete aggregate: Study of the long-term properties. *Constr. Build. Mater.* **2017**, *157*, 582–590. [CrossRef]
37. *EN 197-1*; Cement—Part 1: Composition, Specifications and Conformity Criteria for Common Cements. European Committee for Standardization (CEN): Brussels, Belgium, 2011.
38. *EN 12350-6*; Testing Fresh Concrete—Part 6: Density. European Committee for Standardization (CEN): Brussels, Belgium, 2019.
39. *EN 12350-7*; Testing Fresh Concrete—Part 7: Air Content—Pressure Methods. European Committee for Standardization (CEN): Brussels, Belgium, 2019.
40. *EN 12350-2*; Testing Fresh Concrete—Part 2: Slump-Test. European Committee for Standardization (CEN): Brussels, Belgium, 2019.
41. *EN 12350-8*; Testing Fresh Concrete—Part 8: Self-Compacting Concrete—Slump-Flow Test. European Committee for Standardization (CEN): Brussels, Belgium, 2019.
42. *EN 12350-9*; Testing Fresh Concrete—Part 9: Self-Compacting Concrete—V-Funnel Test. European Committee for Standardization (CEN): Brussels, Belgium, 2010.
43. *EN 12350-10*; Testing Fresh Concrete—Part 10: Self-Compacting Concrete—L-Box Test. European Committee for Standardization (CEN): Brussels, Belgium, 2010.
44. *EN 12350-11*; Testing Fresh Concrete—Part 11: Self-Compacting Concrete—Sieve Segregation Test. European Committee for Standardization (CEN): Brussels, Belgium, 2010.
45. *EN 12390-3*; Testing Hardened Concrete—Part 3: Compressive Strength of Test Specimens. European Committee for Standardization (CEN): Brussels, Belgium, 2019.
46. *EN 12390-13*; Testing Hardened Concrete—Part 13: Determination of Secant Modulus of Elasticity in Compression. European Committee for Standardization (CEN): Brussels, Belgium, 2013.
47. *ISO 1920-8*; Determination of Drying Shrinkage of Concrete for Samples Prepared in the Field or in the Laboratory. International Organization for Standardization: Geneva, Switzerland, 2009.
48. *ISO 1920-9*; Determination of Creep of Concrete Cylinders in Compression. International Organization for Standardization: Geneva, Switzerland, 2009.
49. *EN 206:2013+A2:2021*; Concrete—Specification, Performance, Production and Conformity. European Committee for Standardization (CEN): Brussels, Belgium, 2021.
50. De Larrard, F. *Concrete Mixture Proportioning A Scientific Approach*; CRC Press: London, UK, 1999.
51. Grdic, Z.J.; Toplicic-Curcic, G.A.; Despotovic, I.M.; Ristic, N.S. Properties of self-compacting concrete prepared with coarse recycled concrete aggregate. *Constr. Build. Mater.* **2010**, *24*, 1129–1133. [CrossRef]
52. Carro-Lopez, D.; Gonzalez-Fonteboa, B.; De Brito, J.; Martínez-Abella, F.; Gonzalez-Taboada, I.; Silva, P. Study of the rheology of self-compacting concrete with fine recycled concrete aggregates. *Constr. Build. Mater.* **2015**, *95*, 491–501. [CrossRef]
53. Gonzalez-Taboada, I.; Gonzalez-Fonteboa, B.; Martínez-Abella, F.; Seara-Paz, S. Analysis of rheological behaviour of self-compacting concrete made with recycled aggregates. *Constr. Build. Mater.* **2017**, *157*, 18–25. [CrossRef]
54. Assaad, J.J. Influence of recycled aggregates on dynamic/static stability of self-consolidating concrete. *J. Sustain. Cem.-Based Mater.* **2017**, *6*, 345–365. [CrossRef]

55. Ramachandran, V.S. (Ed.) *Concrete Admixtures Handbook: Properties, Science and Technology*, 2nd ed.; Noyes Publication: Park Ridge, NJ, USA, 1995.
56. Carino, N.J. The maturity method: Theory and application. *J. Cem. Concr. Aggreg.* **1984**, *6*, 61–73. [CrossRef]
57. Bažant, Z.P.; Jirasek, M. *Creep and Hygrothermal Effects in Concrete Structures*; Springer: Dordrecht, The Netherlands, 2018.
58. BIPM; IEC; IFCC; ILAC; ISO; IUPAC; IUPAP; OML. *Evaluation of Measurement Data—Guide to the Expression of Uncertainty in Measurement*; JCGM 100; Joint Committee for Guides in Metrology: Paris, France, 2008.
59. Lawrence, P.; Cyr, M.; Ringot, E. Mineral admixtures in mortars effect of type, amount and fineness of fine constituents on compressive strength. *Cem. Concr. Res.* **2005**, *35*, 1092–1105. [CrossRef]
60. Das, S.; Yang, P.; Singh, S.S.; Mertens, J.C.E.; Xiao, X.; Chawla, N.; Neithalath, N. Effective properties of a fly ash geopolymer: Synergistic application of X-ray synchrotron tomography, nanoindentation, and homogenization models. *Cem. Concr. Res.* **2015**, *78*, 252–262. [CrossRef]
61. Hu, C.; Li, Z. Micromechanical investigation of Portland cement paste. *Constr. Build. Mater.* **2014**, *71*, 44–52. [CrossRef]
62. Mehta, P.K.; Monteiro, P.J.M. *Monteiro Concrete Microstructure, Properties, and Materials*, 3rd ed.; The McGraw-Hill Companies: New York, NY, USA, 2006.
63. Xiao, J.; Li, W.; Corr, D.J.; Shah, S.P. Simulation Study on the Stress Distribution in Modeled Recycled Aggregate Concrete under Uniaxial Compression. *J. Mater. Civ. Eng.* **2013**, *25*, 504–518. [CrossRef]
64. Gabrijel, I.; Jelčić Rukavina, M.; Štirmer, N. Influence of Wood Fly Ash on Concrete Properties through Filling Effect Mechanism. *Materials* **2021**, *14*, 7164. [CrossRef]
65. Bentz, D.P.; Jensen, O.M. Mitigation strategies for autogenous shrinkage cracking. *Cem. Concr. Compos.* **2004**, *26*, 677–685. [CrossRef]
66. Gabrijel, I.; Jelčić Rukavina, M.; Bjegović, D. Autogenous deformations of dolomite based self-compacting concretes with different mineral. In Proceedings of the RILEM International Workshop on Performance-Based Specification and Control of Concrete Durability, Zagreb, Croatia, 11–13 June 2014; pp. 507–514.
67. Technical Committee on Autogenous Shrinkage of Concrete, Japan Concrete Institute. Committee Report. In *Autogenous Shrinkage of Concrete, Proceedings of the International Workshop Organized by JCI (Japan Concrete Institute), Hiroshima, Japan, 13–14 June 1998*; Japan Concrete Institute: Tokyo, Japan, 1999; pp. 1–69.
68. Hobbs, D.W. Influence of aggregate restraint on the shrinkage of concrete. *ACI J. Proc.* **1974**, *71*, 445–450.
69. Lura, P.; Wyrzykowski, M. Influence of aggregate restraint on volume changes: Experiments and modelling. In Proceedings of the 10th International Conference on Mechanics and Physics of Creep, Vienna, Austria, 21–23 September 2015; pp. 17–23.
70. Fathifazl, G.; Ghani Razaqpur, A.; Burkan Isgor, O.; Abbas, A.; Fournier, B.; Foo, S. Creep and drying shrinkage characteristics of concrete produced with coarse recycled concrete aggregate. *Cem. Concr. Compos.* **2011**, *33*, 1026–1037. [CrossRef]
71. Domingo-Cabo, A.; Lázaro, C.; López-Gayarre, F.; Serrano-López, M.A.; Serna, P.; Castaño-Tabares, J.O. Creep and shrinkage of recycled aggregate concrete. *Constr. Build. Mater.* **2009**, *23*, 2545–2553. [CrossRef]
72. Kou, S.C.; Poon, C.S. Enhancing the durability properties of concrete prepared with coarse recycled aggregate. *Constr. Build. Mater.* **2012**, *35*, 69–76. [CrossRef]
73. Wang, X.-Y.; Park, K.-B. Analysis of compressive strength development of concrete containing high volume fly ash. *Constr. Build. Mater.* **2015**, *98*, 810–819. [CrossRef]
74. *ACI 209.2R-08*; Guide for Modeling and Calculating Shrinkage and Creep in Hardened Concrete. American Concrete Institute: Farmington Hills, MI, USA, 2008; pp. 1–45.

Disclaimer/Publisher's Note: The statements, opinions and data contained in all publications are solely those of the individual author(s) and contributor(s) and not of MDPI and/or the editor(s). MDPI and/or the editor(s) disclaim responsibility for any injury to people or property resulting from any ideas, methods, instructions or products referred to in the content.

applied sciences

MDPI

Article

Reutilization of Recycled CDW Sand in Mortars, Paving Blocks, and Structural Concrete

Ángel M. Pitarch, Ana Piquer, Lucía Reig *, Marta Roig-Flores, Vicente Albero, David Hernández-Figueirido and Antonio Melchor-Eixea

Department of Mechanical Engineering and Construction, Universitat Jaume I, 12071 Castellón de la Plana, Spain; pitarcha@uji.es (Á.M.P.); ana.piquer@uji.es (A.P.); roigma@uji.es (M.R.-F.); valbero@uji.es (V.A.); hernandd@uji.es (D.H.-F.); amelchor@uji.es (A.M.-E.)
* Correspondence: lreig@uji.es

Featured Application: This study examines the technical viability of using industrially processed construction and demolition waste (CDW) with a limestone–ceramic composition, washed to remove sulphates, as a fine aggregate (sand) in mortars, paving blocks, and structural concrete.

Abstract: Reusing construction and demolition waste (CDW) as recycled aggregate reduces environmental impact and enhances resource efficiency. While previous research has mainly focused on the use of recycled aggregates (RAs) in concrete, this study evaluates the use of CDW-derived sand in mortars, paving blocks, and structural concrete. Natural and CDW aggregates were characterized, and samples were prepared with two types of Portland cement, replacing up to 100% of the natural limestone sand. Tests were conducted to assess workability, density, strength, and durability. CDW aggregates, primarily composed of limestone and ceramics, reduced sample density as their content increased. Workability improved in the mortars and concrete with higher CDW contents, peaking at 20% CDW in paving blocks. Although the permeability of concrete increased with CDW content, the developed recycled aggregate concrete (RAC) met structural code requirements for all the exposure classes. Despite the decline in strength with higher CDW content, the paving blocks maintained a relative tensile splitting strength above 80%, and the relative compressive strength of the mortars cured for 28 days exceeded 70%. The RAC compressive strength remained within the required range for reinforced concrete (>25–30 MPa). These results validate the feasibility of using CDW-derived sand in various sustainable construction applications with minimal strength loss. Furthermore, they contribute to the development of standardized guidelines for RAs in non-structural applications, fostering broader industry adoption and environmental benefits.

Keywords: construction and demolition waste; recycled aggregates; paving blocks; recycled aggregate mortars; recycled aggregate concrete; physico-mechanical properties

1. Introduction

The reutilization of construction and demolition waste (CDW) as recycled aggregates (RAs) has been paid considerable attention in recent years for its potential to address environmental concerns and to enhance resource efficiency in the construction industry. Global urbanization and industrialization have led to an increasing demand for infrastructure

and housing, which results in the generation of vast quantities of CDW. Over 3 billion tons of CDW waste are generated globally each year [1,2], and in the European Union, CDW constitutes about one-third of the total waste produced annually [3]. According to Alhawamdeh et al. [4], the construction industry is responsible for approximately 36% of the global solid waste found in landfills. CDW can be classified into waste generated during the construction phase, and that generated during demolition, which typically accounts for over 50% of the total waste produced by the construction industry [5]. Additionally, the construction sector is a major consumer of natural resources, accounting for approximately 50% of all extracted materials, including metals, stones, gravel, sand, or wood. It is also responsible for the release of approximately 6 billion tons of CO_2 into the atmosphere [6]. Consequently, the development of sustainable practices to reduce the sector's environmental footprint is imperative. In this context, disposing of CDW in landfills is becoming increasingly unsustainable and necessitates the development of innovative waste management solutions that align with circular economy principles. These solutions should prioritize the reuse of CDW in higher-value-added applications, such as employing it as raw material in the production of new building materials, rather than restricting its use to lower-value applications like road sub-bases. To mitigate the environmental impact of CDW, researchers such as Trancone et al. [2] developed a sustainable bioleaching method to reduce the volume of concrete in CDW. This innovative approach offers an efficient and environmentally friendly strategy for CDW management, facilitating its reuse in the production of new building materials.

The RAs that derive from CDW are a promising alternative to natural aggregates (NAs) in construction applications, including recycled aggregate concrete (RAC), road construction, and embankments. Apart from reducing the volume of waste disposed in landfills, reusing CDW as RAs helps to keep natural resources and to mitigate the environmental impacts associated with resource extraction, habitat destruction, water pollution, and carbon emissions [7–10]. Although RA use can result in cost savings by decreasing the demand for natural materials and lowering waste disposal costs, the initial investment in processing facilities and equipment can be substantial. As highlighted by Vegas et al. [11], the implementation of landfill taxes could be crucial in promoting RA use by offsetting initial processing costs and improving the competitiveness of recycled materials compared to NAs.

The properties and performance of RAs have been extensively researched [12–14]. Recent studies have shown that, when appropriately processed, the properties of RAs can be comparable to those of NAs, which makes them a viable substitute in many structural and non-structural applications [10,13–18]. Elchalakani and Elgaali [12] observed that the impact of RAs on concrete strength is influenced more by the recycled material quality than by its quantity. Some studies have reported a reduction in compressive strength when NAs are replaced with RAs [8,19–21], but other research works have indicated that mechanical properties remain largely unaffected or even improve with the incorporation of RAs [22–26].

This variability in material properties, in addition to the perception of reduced quality compared to NAs, poses challenges of widespread RA adoption. Additionally, the potential for contamination in CDW-derived RAs is significant because materials like concrete, rubble, bricks, tiles, and asphalt, which are common components of CDW, can be processed into RAs. Consequently, the variability in the composition of CDW presents the challenges of ensuring the consistency and reliability of RAs, particularly in structural applications where material performance is critical [13]. To address these challenges, research has focused on optimizing processing techniques to enhance the quality and performance of

RAs. Advanced crushing, sieving, and washing processes have been developed to remove contaminants, to reduce variability in particle size distribution, and to improve overall RA quality. In the present study, CDW-derived sand was subjected to multiple washing cycles to reduce its sulphate content, along with pre-separation, controlled crushing, and sieving. Investigating the properties of this specific CDW and its behavior as raw material in the development of more sustainable building materials will contribute to expanding the current knowledge base and to advancing toward a more sustainable and circular construction industry.

Despite advancements made in processing and treatment, adopting RAs in the construction industry remains limited. One of the main obstacles for the widespread RA use is the perception that they are of lower quality than Nas, and they are, therefore, mainly used in landfills [27]. This perception is often reinforced by the absence of standardized guidelines and regulations that govern RA use in construction [28]. For instance, the Spanish Structural Concrete Code restricts RA use to those that exclusively derive from structural concrete, limiting their use to a maximum of 20% by weight of natural gravel. However, other European standards, such as DS 2426 from Denmark [29], NEN 8005 from the Netherlands [30], and NB 26 from Norway [31], allow the use of moderate and high-quality fine RAs. Additionally, Standard NF EN 206-1/CN from France [32] allows high-quality fine RA use, albeit with specific limitations [27]. To overcome these obstacles, it is important to conduct more studies that generate new knowledge and contribute to establishing consistent standards that guarantee the quality and safety of RAs. This will help to build trust and will encourage their use in a wider variety of applications because, although many studies have investigated CDW aggregate use in concrete [6], very few studies have examined their reutilization in non-structural elements, such as paving blocks or mortars. Previous studies by Ferro et al. [33] investigated mortars incorporating recycled sand with a particle size of less than 8 mm, primarily composed of calcite and quartz. The results indicated a slight reduction in both compressive and flexural strength. Borges et al. [16] developed mortars that replaced natural sand with RAs from CDW at rates of up to 100%. Although the results showed that higher RA content resulted in higher primary energy demand and greater water consumption, mortars containing 50% RA exhibited the best overall performance. This was characterized by higher carbon capture potential, improved compressive strength, and acceptable tensile adhesion strength. The mortars developed by Kepniak and Lukowski [34] reused recycled sand consisting of 88.5% concrete- or mortar-based materials, 4.7% natural stones and aggregates, and approximately 6.5% other compounds. These mortars also showed a positive environmental impact, particularly when replacing 40% to 60% of natural sand. Although a slight reduction in strength was noted, this was balanced by a significant conservation of natural resources. Poon et al. [17] investigated the use of RAs from CDW as replacements for coarse and fine aggregates in concrete bricks and blocks. The two types of RAs used consisted primarily of old concrete rubble, along with small amounts of natural stones, clay bricks, and other impurities such as wood, tiles, and metals. One RA was predominantly composed of concrete (98.8%), while the other contained 77.7% concrete and 21.8% natural stones. Their findings showed that replacing NAs with 25% or 50% RA had a negligible effect on compressive strength, whereas higher replacement levels caused a reduction in compressive strength. Additional tests, including assessments of shrinkage, skid resistance, and plant trials, yielded positive results. In later research, Chu et al. [18] identified particle packing as a key factor influencing the performance of concrete paving blocks. The appropriate packing optimization led to a significant increase in the compressive strength of concrete paving blocks made entirely

with RAs, rising from approximately 30 MPa to 79 MPa. This strength was close to the maximum strength achieved in samples made with only NA, which was 84.8 MPa.

According to the report on a Sustainable Future for the European Cement and Concrete Industry [35], mortars and plasters comprise 24% of cementitious downstream products in Europe, while non-reinforced cement-based products represent 19%. Additionally, currently there are no standards that address the incorporation of CDW into non-structural elements. Therefore, this study aims to characterize one particular CDW RA and to evaluate its performance when used to partially replace natural calcareous aggregates in the manufacture of paving blocks, mortars, and structural concrete. The findings of this study aim to encourage the reuse of this particular CDW as raw material for high-value applications, thereby fostering a construction industry aligned with circular economy principles.

2. Material and Methods

2.1. Experimental Process

The experimental work conducted to explore the potential of reutilizing CDW RAs was divided into three primary stages:

1. Characterization of NA and RA;
2. Design, preparation, and characterization of mortars and paving blocks;
3. Design, preparation, and characterization of structural concrete.

2.2. Materials Used

The aggregates used in this study consisted of natural calcareous sand and one RA derived from CDW, supplied by the local company Hope and Effort S.L. The RA was pre-separated, control-crushed, and sieved, and it underwent multiple washing cycles to reduce its sulphate content. The treatments were conducted by the aggregate supplier, and the CDW RA sand was characterized and used as received, without any further processing.

Mortars and paving blocks were prepared with two different types of Portland cement (PC): CEM I 52.5R, Elite Cementos S.L. (Grao de Castellón, Spain) containing more than 95% clinker, to evaluate the potential for pozzolanic reactions that might enhance the interaction between aggregates and the cementitious matrix; and CEM II/B-M(Q-L) 42.5R, Elite Cementos S.L. (Grao de Castellón, Spain) a more sustainable option with a lower clinker content. Both PC types met the European Standard UNE-EN 197-1 [36] and were provided by Elite Cementos S.L. (Grao de Castellón, Spain). Mortars, paving blocks, and concrete were mixed and cured using tap water. Superplasticizer SKP380, supplied by SIKA (Madrid, Spain), was incorporated into all the prepared mixes.

2.3. Characterization of Aggregates

The aggregates were oven-dried at 100 °C for 24 h and subsequently characterized according to the test methods and standards summarized in Table 1. Each property was determined as the average of at least two tests. The Micro-Deval test was conducted by adapting the procedure outlined in Standard UNE 146404 [37]. During this test, a 500 g dry-weight sample was sieved and washed to obtain particle sizes between 0.125 and 2 mm. This sample was mixed with 2500 g of abrasive load (steel balls approximately 10 mm in diameter) and 2.5 kg of water, and then subjected to 1500 revolutions at 100 ± 5 rpm. After the test, the sample was sieved through an 8 mm sieve to collect the steel balls, and then through 250 micron and 63 micron sieves. The material retained in the last two sieves was then dried and weighed.

The chemical composition of the NA and RA was analyzed by X-ray fluorescence (XRF) in a Bruker S4 Pionner spectrometer (Bruker, Karlsruhe, Germany). Their mineralogical composition was examined through X-ray diffraction (XRD) in a Brucker AXS D4 Endeavor powder diffractometer with Cu Kα radiation at 20 mA and 40 kV, covering 5° to 70° 2 theta degrees. Thermogravimetric (TG) analyses of the aggregates were conducted with a TGA/SDTA851e/LF/1600 by Mettler Toledo up to 1000 °C. Samples were heated at a rate of 20 °C/min in alumina crucibles in an air atmosphere.

Table 1. Properties analyzed, procedures, and standards used to characterize the aggregates.

Property	Test	Standard
Particle size distribution	Sieve analysis	UNE-EN 933-1 [38]
Percentage of fines (<0.063 mm)	Sieve analysis	UNE-EN 933-1 [38]
Assessment of fines	Sand equivalent	UNE-EN 933-8 [39]
Specific weight	Pycnometer	UNE-EN 1097-6 [40]
Water absorption	Sand absorption cone	UNE-EN 1097-6 [40]
Resistance to wear	Micro-Deval *	UNE 146404 [37]

* 500 g material, 2.5 kg stainless steel balls, 2.5 kg water, 1500 revolutions at 100 ± 5 rpm.

2.4. Design, Preparation, and Characterization of Mortars and Paving Blocks

After characterizing the natural and recycled sand, mortars and paving blocks were prepared to assess the suitability of the CDW aggregate as a partial replacement for natural sand in these applications. The applied mix proportions are summarized in Table 2. Both mortars and paving blocks were produced using two PC types: CEM I 52.5R and CEM II/B-M(Q-L) 42.5R. A reference mix (labeled "REF") containing only natural limestone aggregates was prepared, while recycled CDW replaced up to 100% of the NA sand volume (vol.%). In addition to the reference mix, four natural sand replacement levels were investigated. Given the two analyzed cement types, there was a total of 10 series: 5 using CEM I 52.5R and 5 using CEM II/B-M(Q-L) 42.5R. For clarity, they are referred to as CEM I and CEM II, respectively, throughout this work.

Table 2. Mix proportions for mortars and paving blocks. (*) Note: this table applies to the series produced using both cement types (CEM I and CEM II).

Aggregate	Substitution Vol.%	Designation	Cement (*) kg/m^3	Effective Water, L	Effective w/c	NA kg/m^3	CDW kg/m^3
Limestone	0	REF	586	264	0.45	1757.8	0
CDW	25	CDW25				1318.4	381.9
	50	CDW50				878.9	763.8
	75	CDW75				439.5	1145.6
	100	CDW100				0	1527.5

All the mortar and paving block mixes were prepared at a constant cement-to-sand-to-water (c:s:w) weight ratio of 1:3:0.45, along with a constant amount of fluidizing agent SKP380, provided by Sika (1.46 kg/m^3, equivalent to 0.25% by weight of cement). The total amount of water was adjusted to maintain consistent effective water content, which, as defined by UNE EN 206:2013 [32], is the water available for the cement hydration process, excluding the water absorbed by aggregates. In this study, the effective water-to-cement ratio (w/c) was kept constant in all the prepared samples (mortars, paving blocks, and concrete). To achieve this, all the mixes were designed by considering the weight of aggregates saturated with a dry surface, and the water absorption coefficient and humidity content of the aggregates were contemplated to calculate the total amount

of water required for each mix. To simulate real fabrication conditions, the packing block aggregates were used with their natural moisture content. In contrast, to minimize the influence of aggregate moisture and to achieve better control over the effective w/c ratio, the aggregates used for mortar production were pre-dried.

The mortar samples were mixed using an automatic mortar mixer, following the specifications of Section 6.2 of Standard UNE EN 196-1 [41]. Each designed mix was cast into molds with three cavities, each measuring $40 \times 40 \times 160\ mm^3$. The molds were filled in two layers, with each layer compacted using an automatic horizontal jolting table, applying 60 drops at a rate of one per second. The paving blocks were cast in molds measuring $400 \times 400 \times 40\ mm^3$, each with eight cavities of $100 \times 200 \times 40\ mm^3$, as shown in Figure 1.

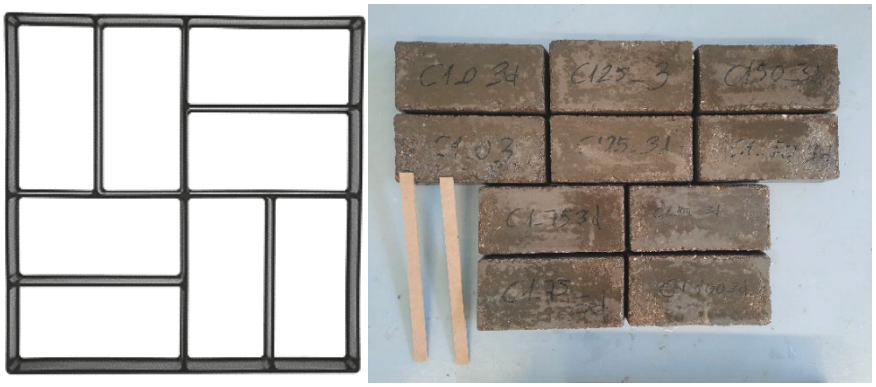

(**a**) (**b**)

Figure 1. Paving blocks made with the NA and CDW aggregates: (**a**) molds; (**b**) developed paving blocks.

Paving blocks were prepared using a mortar mixing rod, with a total mixing time of 9 min. Initially, the aggregates were mixed with cement, followed by the addition of water for 1 min. Mixing continued for 4 min before incorporating the fluidizing additive. The mixture was then mixed for a further 4 min. Finally, the samples were compacted on a vibrating table, as depicted in Figure 2.

(**a**) (**b**)

Figure 2. Preparation of paving blocks made with NA and CDW sand: (**a**) mixing; (**b**) compaction.

Both paving blocks and mortars were cured for up to 28 days at 20 °C and 100% relative humidity in a controlled temperature and humidity chamber until the testing age.

The density of the mortar and paving block samples was determined by weighing and measuring them. Their workability was evaluated by adapting the procedure outlined in Standard UNE-EN 1015-3 [42], using Vicat test molds with a truncated cone shape and a bottom diameter of 80 mm. The molds were first moistened and filled in two layers. Each layer was compacted with 10 strokes, applied at a constant frequency of one stroke per second, using a circular tamper (40 mm diameter, 200 mm long, and a mass of 250 ± 15 g). After 30 s, the mold was lifted vertically and slowly, and the plate was tapped 15 times, at a rate of one tap per second. Workability was assessed in two perpendicular directions by measuring the diameter of spread on a glass plate. For the mortars, workability was measured immediately after mixing (4 min and 30 s after mixing began). For the paving blocks, workability was measured immediately after mixing (10 min) and once again 20 min after mixing commenced. The water absorption of the paving blocks was assessed according to Annex E of Standard UNE EN 1338:2004 [43]. The specimen was first conditioned at a temperature of 20 ± 5 °C. It was then submerged in water for at least 3 days until it reached a constant mass. After this, the specimen was dried in an oven at 105 ± 5 °C for a minimum of 3 days, until a constant mass was attained. The water absorption of each specimen was calculated as the mass loss relative to the dry mass.

The compressive strength of the mortar samples was assessed in a universal testing machine MEH-3000PT/W by Ibertest (Madrid, Spain), after 7 and 28 curing days, in accordance with Standard UNE EN 196-1 [41]. Six samples per mix and curing age were tested. The splitting tensile strength of the paving blocks was measured after 3, 7, and 28 curing days using the same equipment, but following Annex F of Standard UNE EN 1338:2004 [43], as illustrated in Figure 3. Two samples per mix and curing age were tested.

(**a**) (**b**)

Figure 3. Splitting tensile strength testing of the paving blocks made with NA and CDW aggregates: (**a**) equipment used; (**b**) fragments after the test.

2.5. Design, Preparation, and Characterization of Structural Concrete

The mix proportions for the concrete samples designed to evaluate the influence of CDW recycled sand on the performance of structural concrete are summarized in Table 3. Mixes were prepared using the CEM II/B-M(Q-L) 42.5 cement. Consistently with the preparation of the mortars and paving blocks, the amount of PC (370 kg/m^3) and superplasticizer (SKP380 provided by Sika, 0.7% by weight of cement, equivalent to 2.59 kg/m^3) and the effective w/c ratio (0.50) were left constant across all the concrete mixes. The CDW volume used to replace NAs varied. The total amount of water in the mix was adjusted according to the water absorption and humidity of aggregates in order to have constant effective water. A reference mix with no CDW sand (labelled "REF") was also prepared, and 50 vol.% and 100 vol.% of natural sand were replaced with recycled CDW.

Table 3. Mix proportions for structural concrete.

Aggregate	Subs. Vol.%	Desig.	Cement kg/m^3	Effective Water, L	Effective w/c	Gravel NA kg/m^3	Sand	
							NA kg/m^3	CDW kg/m^3
Limestone	0	REF	370	185	0.5	890	890	0
CDW	50	CDW50					445	386.7
	100	CDW100					0	773.5

Concrete mixes were prepared using a concrete pan mixer. The workability, density, compressive strength, shrinkage, and permeability of the developed concrete were evaluated. Workability was determined using the Abrams cone test in accordance with Standard UNE-EN 12350-2 [44], with measurements taken 10 and 30 min after mixing started. For compressive strength testing, eight cubic specimens with dimensions of $100 \times 100 \times 100$ mm^3 were used. Two prismatic specimens measuring $100 \times 100 \times 300$ mm^3 were employed for shrinkage testing, while three cylindrical specimens, each 150 mm in diameter and 300 mm high, were employed for permeability testing. The utilized molds met Standard UNE-EN 12390-1 [45]. The concrete specimens were cured for up to 28 days in a temperature and humidity-controlled chamber at 20 °C and 100% relative humidity.

Density was determined by weighing the cylindrical specimens after 28 curing days. Compressive strength was evaluated using the cubic specimens, cured for 7 and 28 days, in accordance with Standard UNE-EN 12390-3 [46]. Testing was conducted with a hydraulic press by applying a load rate of 0.6 MPa/s until failure. Four specimens per concrete mix and curing period were tested, and the mean compressive strength values, along with their corresponding standard deviations, were calculated. The relative strength (RS) of the concrete containing CDW was calculated as the ratio of the strength of the RAC to that of the REF mix.

The shrinkage of the concrete samples was measured according to Standard UNE-EN 12390-16 [47], using prismatic specimens (dimensions of $100 \times 100 \times 200$ mm^3). Measurements were taken at 1, 7, 14, 18, and 28 curing days, using reference points placed on two faces of samples, as illustrated in Figure 4. In accordance with Standard UNE-EN 12390-16 [47], which specifies a relative humidity range of 50–70% $\pm$ 5%, these concrete specimens were cured in a temperature and humidity-controlled chamber, at 20 °C and 70% relative humidity.

Figure 4. Concrete samples for shrinkage measurements. Reference points marked with red circles.

To assess the durability of the concrete mixes, water penetration tests were performed in accordance with Standard UNE-EN 12390-8 [48]. This procedure involves applying pressurized water at 500 kPa (5 bars) on the lower hardened concrete surface for 72 h. After this period, samples were split in half under indirect tensile stress, as depicted in Figure 5. Both the maximum and average water penetration depths were then measured, following the method detailed in Annex A of the standard.

Figure 5. Concrete samples after water penetration depth measurements.

3. Results and Discussion

3.1. Properties of Aggregates

3.1.1. Morphology and Chemical and Mineralogical Composition of Aggregates

The morphology of the natural calcareous sand and recycled CDW sand used in the study is illustrated in Figure 6. Both sand types exhibited irregular particles characterized by rough surfaces and sharp edges.

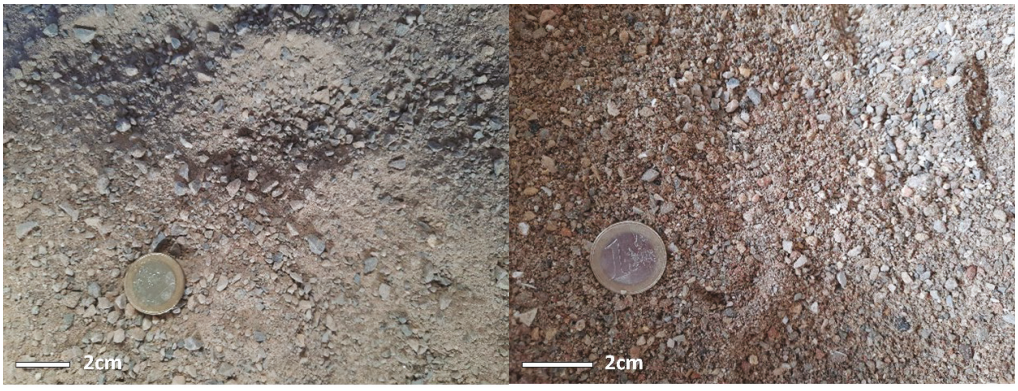

(**a**) (**b**)

Figure 6. Aggregates used in this study: (**a**) natural calcareous; (**b**) CDW.

The chemical composition of the NA and CDW aggregates is listed in Table 4. The CDW sand primarily consisted of SiO_2 and CaO, with relatively large amounts of Al_2O_3, and low contents of Fe_2O_3, Na_2O, MgO, and K_2O. The total amount of SiO_2, Al_2O_3, and Fe_2O_3 was 41.3%, which is less than 70%, the value established by Standard UNE EN 450-1:2013 [49] for other pozzolanic materials commonly used in concrete, such as fly ashes. Additionally, to present pozzolanic activity, Standard UNE EN 450-1:2013 [49] establishes that loss on ignition (LOI) must be below 5% of the total composition. Therefore, the CDW sand was not expected to exhibit pozzolanic activity, or at least not significantly, and

behaved more like an inert aggregate. Although this aggregate size is too large to exhibit pozzolanic activity with PC, pozzolanic behavior could enhance the aggregate–matrix interface. The X-ray fluorescence tests (XRF) did not detect significant amounts of sulfur.

Table 4. Chemical composition of the recycled CDW aggregate, weight % (wt.%).

	Al_2O_3	SiO_2	CaO	MgO	K_2O	Na_2O	Fe_2O_3	SO_3	Other	LOI *
CDW	8.2	32.1	30.5	1.8	1.1	1.1	1.0	0.5	0.4	23.4

* Determined at 1000 °C.

The LOI was determined at 1050 °C for 45 min and closely matched the obtained thermogravimetry results, as shown in Figure 7 (total weight losses expressed as a percentage). The calcareous aggregate exhibited significant weight loss between 630 °C and 920 °C, and reached approximately 45%, which is attributed to the decomposition of $CaCO_3$ and $MgCO_3$. Although this mass loss generates several overlapping peaks that cannot be separately evaluated, previous studies [50] indicate that the first band is associated with the decomposition of magnesium carbonate, and the second with calcium. The mass loss observed in the CDW aggregate (23.4%) is primarily attributed to the decomposition of limestone ($CaCO_3$), as it predominantly occurred between 650 °C and 900 °C. The lower mass loss observed in the CDW waste, compared to the natural dolomitic limestone, is attributed to its lower limestone content, as the CDW waste was mixed with other materials, primarily ceramics. Notably, no mass loss related to the decomposition of cement hydrates was observed. The dehydration of calcium silicates (CSH) or ettringite (AfT) would generate a band between 100 °C and 180 °C, while calcium aluminates (CAH) or calcium aluminosilicates (CASH) would generate a band between 180 °C and 240 °C [51]. Similarly, no mass loss associated with portlandite dehydration, which typically occurs between 520 °C and 600 °C, was observed. These results indicate that the quantity of the concrete waste in the CDW recycled sand was minimal. Thermogravimetric results indicate that the recycled CDW aggregate was expected to show improved stability at high temperatures. Finally, although ceramic residues typically experience minimal mass losses up to 1000 °C, their presence in the sample was confirmed by the X-ray diffraction analysis, as depicted in Figure 8.

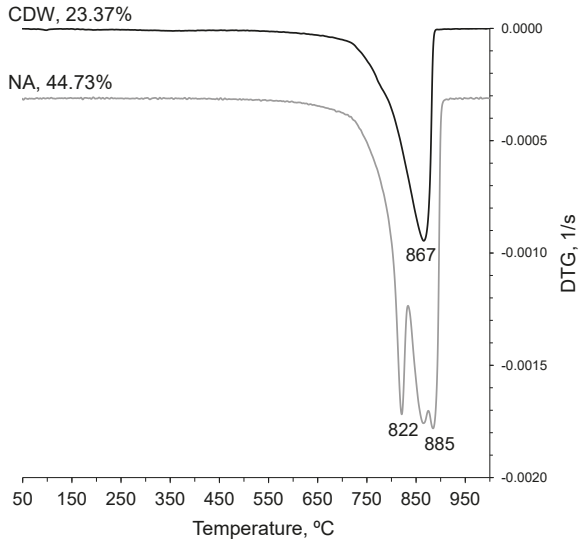

Figure 7. DTG curves for the NA and CDW aggregates.

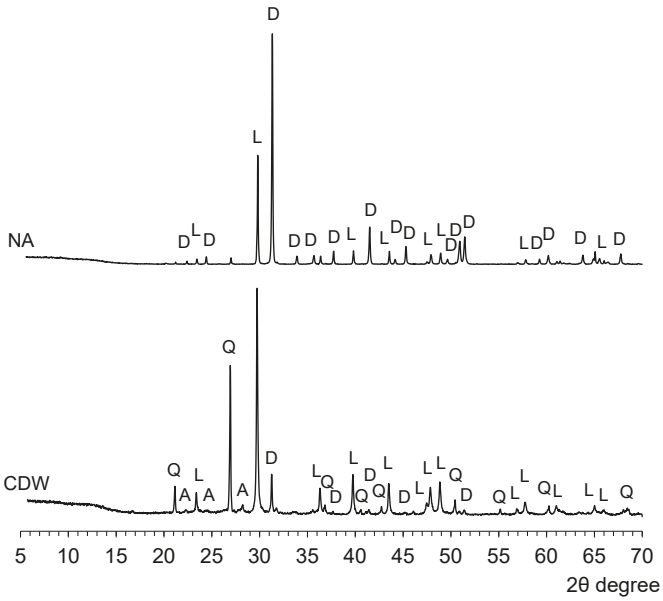

Figure 8. X-ray diffractogram of CDW and calcareous NA sand. D: dolomite ($CaMg(CO_3)_2$; L: limestone ($CaCO_3$); Q: quartz; A: albite ($NaAlSi_3O_8$).

The diffractogram of the CDW aggregate, shown in Figure 8, reveals the presence of quartz (Q, SiO_2, PDFcard 46-1045), limestone (L, $CaCO_3$, PDFcard 83-578), and magnesium carbonate dolomite (D, $CaMg(CO_3)_2$, PDFcard 75-1760). This suggests that the CDW aggregate is composed of natural limestone and ceramic products. Traces of sodium feldspar albite (A, $NaAlSi_3O_8$, PDFcard 9-466), a phase commonly found in ceramic products, were also identified. However, mullite, a crystalline compound typically found in ceramics sintered at high temperatures, was not detected. This indicates that there was a small amount of ceramic products in the CDW recycled aggregate. Consistent with the thermogravimetric analyses, no peaks attributed to portlandite, a typical compound of hydrated cement, were identified, confirming that the RA used did not contain significant amounts of concrete. Additionally, neither aggregate type showed deviation from the baseline within the 15–30 degrees 2θ range, which confirms a minimal presence of amorphous phases that could react with portlandite during PC hydration. As a result, the CDW aggregate was expected to have limited pozzolanic activity. Although it may be suitable as an RA, its low reactivity when used as a partial PC replacement would likely reduce binder strength. Consistently with the XRF and TG results, no crystalline phases associated with sulfur compounds were detected.

The morphology and chemical and mineralogical composition of both the natural and CDW aggregates analyzed were similar. Therefore, the CDW sand characterized in this study has the potential to be effectively reused in the production of sustainable construction materials. This reuse would help reduce environmental impact and enhance resource efficiency.

3.1.2. Particle Size Distribution of Aggregates, Percentage and Quality of Fine Particles

The particle size distribution and percentage of fines in the NA and CDW aggregates, determined by sieving according to Standard UNE-EN 933-1 [38], are presented in Figure 9. The recommended particle size distribution range from the previous Structural Concrete Instruction EHE-08, as defined in the comments of Article 28.4.1, is also included in the figure for reference. Although this reference range is not incorporated in the current Spanish Structural Code, it remains a useful granulometric reference for fine aggregates. At the

upper limit of the 0.063 mm sieve, a cumulative retained percentage of 16% was considered, which, according to Article 30.4.1 of the Structural Code, corresponds to limestone crushed aggregates intended for use in structural concrete exposed to general non-aggressive exposure classes (X0 and XC, as defined in Article 27). The particle size distribution of both the NA and CDW aggregates falls within the reference limits established by EHE-08. This indicates that, based on their particle size distribution, both NA and RA would be suitable for use in structural concrete. However, it is important to note that, since the RA used in this study was not sourced from concrete waste and pertains to a fine aggregate fraction rather than a coarse aggregate fraction, it falls outside the scope of the current Spanish Structural Code.

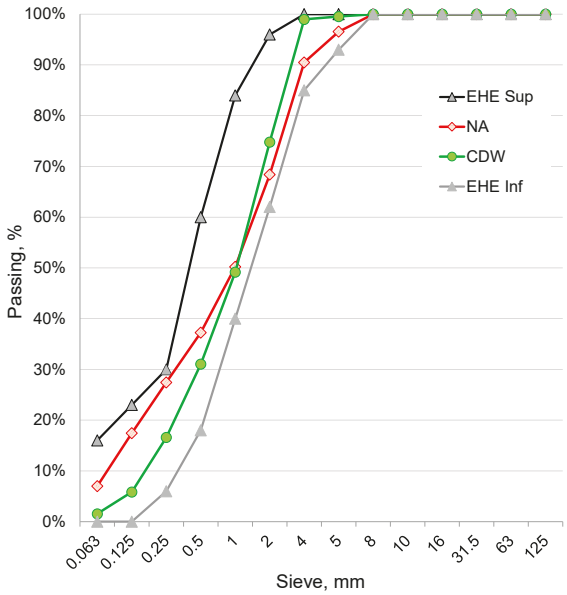

Figure 9. Particle size distribution of natural limestone and CDW aggregates.

The percentage and quality of fine particles, as well as the fineness modulus (FM) of the aggregates, are presented in Table 5. Below 1 mm, the CDW particles were larger than the NA particles (see Figure 9), which was due to the repeated washing to remove sulphates. However, both aggregate types had a similar FM (3.1–3.2), because within the 1–4 mm range, NA particles were coarser than those of the recycled CDW, which balanced the overall modulus value. Slightly higher FM values are reported by Pitarch et al. [52] for natural sand (3.64) and recycled sand obtained from ceramic tiles (3.76), sanitaryware (3.84), and red clay bricks (4.04) intended for use in structural concrete.

Table 5. Particle size distribution, percentage, and quality of fine particles.

Property	NA	CDW
FM	3.1	3.2
Percentage of fine particles, wt.%	14.4	4.4
Sand equivalent	53	73

Article 30.4.1 of the Spanish Structural Code specifies the environmental conditions under which aggregates can be used based on their maximum fine content. Thus, according to the percentage of fines, the CDW recycled sand is suitable for use in structural concrete exposed to the following classes: X0 (no carbonation risk), XC (carbonation-induced corrosion), XS (chloride-induced corrosion from seawater), XD (chloride-induced corrosion

not from seawater), XA (chemical attack), XF (freeze–thaw), or XM (erosion). These classifications correspond to non-calcareous aggregates with a fine content below 6%. In contrast, the calcareous sand is restricted to use in X0 or XC environments because its fines content exceeds 16%, which makes it unsuitable for structural concrete exposed to more severe exposure classes.

When assessing the quality of fines by the sand equivalent test (Annex A of Standard UNE-EN 933-8 [39]), certain particles in suspension were identified. Additionally, the observation of black particles during the oven drying of the CDW recycled aggregate suggests the presence of organic matter. According to the requirements established in Article 30.4.2 of the Structural Code, the recycled CDW aggregate is suitable for use in structural concrete exposed to general classes X0 (no risk) or XC (carbonation), because the sand equivalent value exceeded 70. However, it is unsuitable for structural concrete exposed to specific classes, such as XS, XD, XA, XF or XM, because the obtained sand equivalent value was below 75.

Although the sand equivalent value of limestone sand was below 70, its suitability for use in structural concrete would depend on the methylene blue test results. Additionally, both sand types could be employed in roadbed layers, because the sand equivalent requirements are lower (>30–40, depending on the vehicle weight category) according to the Spanish PG-3 General Technical Specifications for Road and Bridge Works.

3.1.3. Physico-Mechanical Properties of Aggregates

Table 6 summarizes the physico-mechanical properties of both the NA and CDW aggregates. The CDW particles exhibited lower specific weight than the NA sand, which indicates higher porosity and water absorption for the recycled sand versus the NA calcareous particles. This difference is attributed to the presence of ceramic particles in the CDW recycled sand. Pitarch et al. [52] observed significant variation in water absorption values among different types of ceramic materials. They report water absorption values of 0.69%, 6.28%, and 15.76% for the fine ceramic sand obtained from ceramic sanitaryware, ceramic tiles, and red clay bricks, respectively. Medina et al. [25] also report water absorption values ranging from 2.0% to 17.2% for fine recycled aggregates derived from different types of ceramic tiles, which they used in concrete.

Table 6. Physico-mechanical properties of the NA and CDW aggregates.

Property	NA	CDW
Specific weight, kg/m^3	2808.9	2441.2
Water absorption, wt.%	2.01	5.62
Resistance to wear, wt.%	29.2	23.9

The natural sand meets the maximum water absorption requirement outlined in the Spanish Structural Concrete Code for NAs used in structural concrete (5% for both fine and coarse aggregates, as per Article 30.6). According to Article 30.8.3.1. Physical-mechanical conditions of recycled aggregates, the water absorption of the recycled coarse aggregate must not exceed 7%, while that of the natural coarse aggregates to be mixed with should remain below 4.5%. Although the Spanish Structural Code does not contemplate recycled sand use, the CDW RA would meet the requirements established for coarse RAs in structural concrete.

As shown in Table 6, the CDW recycled aggregate exhibited slightly better wear resistance compared to natural limestone, as indicated by the lower mass loss after the Micro-Deval test. These results were due to the presence of ceramic particles in the CDW,

which may be harder than calcareous aggregates. A study by Medina et al. [25] also indicates greater resistance to fragmentation, measured by the "Los Ángeles" test, in RAs obtained from ceramic sanitaryware compared to NAs.

The results indicate that the properties of the analyzed CDW aggregate are comparable to those of the NA limestone and suggest its suitability for use in structural concrete exposed to environmental classes X0 (no carbonation risk) and XC (carbonation-induced corrosion). However, the current structural code permits RA use in structural concrete only if sourced from concrete, with a maximum replacement of natural coarse aggregates limited to 20% by weight. Removing sulfates at the source before CDW disposal could facilitate the production of aggregates with larger particle sizes. Nevertheless, these aggregates would still remain ineligible for concrete applications under current regulations, which restrict the use of RAs to those derived from concrete. While RAs from non-concrete sources are currently excluded from structural concrete, further research is essential to assess their potential and to extend their reuse opportunities. Additionally, this CDW recycled aggregate could be considered for non-structural applications, such as mortars or paving blocks.

3.2. Properties of the Developed Mortars

3.2.1. Workability and Density of the Mortar Samples

Figure 10 illustrates the workability and density of the developed mortars. Workability (Figure 10a) was assessed immediately after mixing, 4 min and 30 s after starting the mixing process. It was slightly better in the mortars prepared with CEM I 52.5R and improved with increasing CDW content, but the overall the results were similar. The density of the mortar samples (Figure 10b) ranged between 2.10 g/cm^3 and 2.35 g/cm^3 and decreased as CDW content increased. The density values were slightly lower in the mortars made with CEM II/B-M(Q-L) 42.5R compared to CEM I 52.5R, which implies that the CEM I 52.5R mixes were more compact.

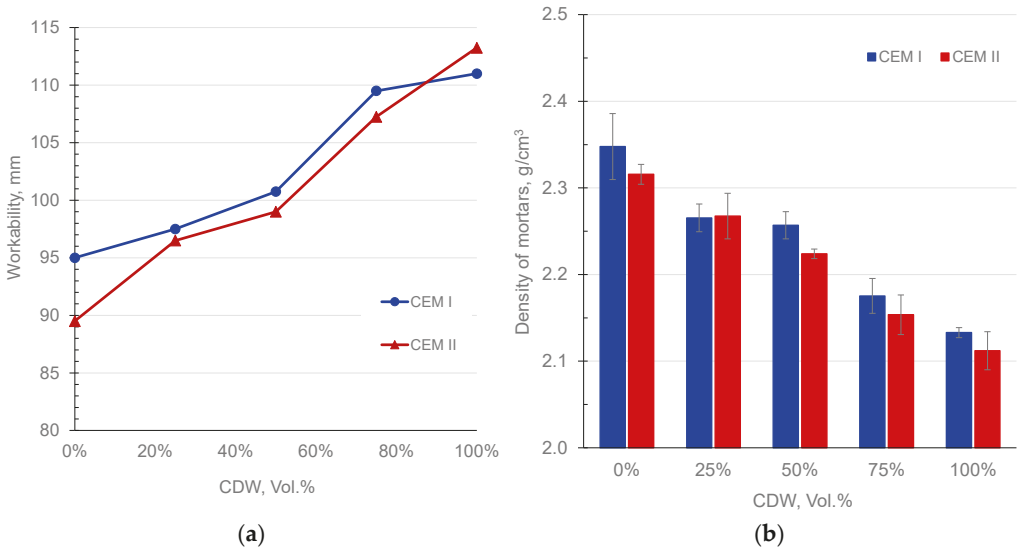

(**a**) (**b**)

Figure 10. Properties of the mortars made with the NA and CDW aggregates: (**a**) workability; (**b**) density.

3.2.2. Compressive Strength of the Mortar Samples

Figures 11a and 11b present the compressive strength and RS of the developed mortars, respectively. Compressive strength progressively decreased as the CSW content increased. The RS remained above 80% with NA substitutions of up to 50 vol.% regardless of curing

age, and above 70% for all the mortars cured for 28 days, which indicates a strength loss of less than 30%.

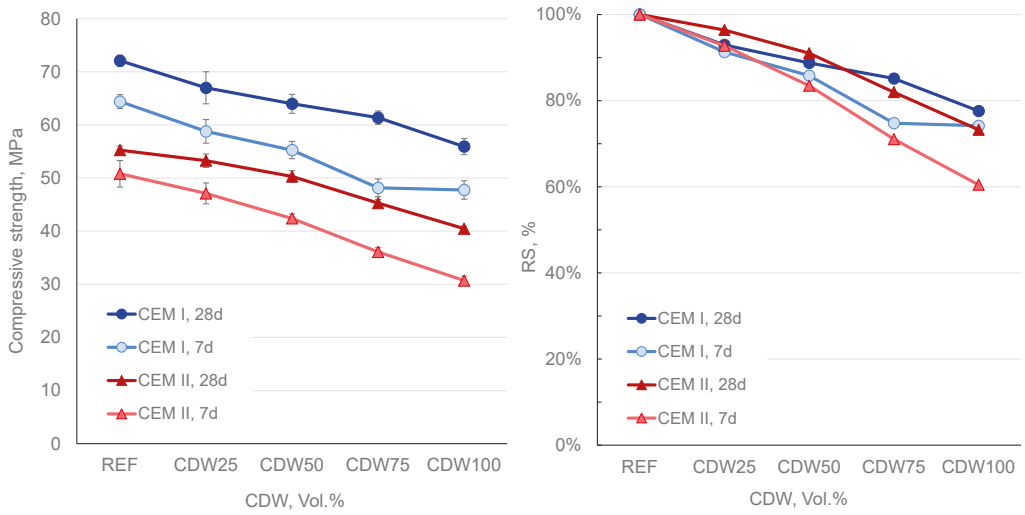

Figure 11. Compressive strength of the mortars made with NA and CDW aggregates: (**a**) compressive strength; (**b**) relative strength.

The results obtained in this study differ from those reported by Borges et al. [16], who prepared mortars using RAs composed of 46% old mortar, 32% ceramics, and 22% basaltic coarse aggregates. While Borges et al. [16] observed a slight increase in the 28-day compressive strength at replacement rates of 25% and 50%, the compressive strength of the reference mix in their study was significantly lower, approximately 2 MPa. In contrast, the results obtained by Kępniak and Łukowski [34] were more consistent with those of the present study, showing a progressive decrease in both compressive and flexural strength as the replacement rate of RAs increased. Although they used recycled sand of a different composition (primarily recycled concrete), the compressive strength of the reference mortar (52 MPa) was closer to that of the mortars prepared in this study using CEM II/B-M(Q-L) 42.5R (~55 MPa). A more pronounced decrease in compressive strength was observed by Ferro et al. [33], who employed recycled sand predominantly composed of calcite and quartz, with traces of cement compounds. This reduction is partly attributed to a significant decrease in the mix's consistency.

3.3. Properties of the Developed Paving Blocks

3.3.1. Workability of Paving Blocks

Figure 12 illustrates the workability of the developed paving blocks. Those produced with CEM II/B-M(Q-L) 42.5R generally showed greater workability compared to those made with CEM I 52.5R. This improvement in workability can be attributed to the larger particle size of the former cement type and the presence of limestone filler, which enhanced workability and delayed the onset of initial chemical reactions. Workability generally decreased with increasing mixing time. A slight improvement was observed with 25 vol.% CDW, but workability progressively decreased with higher CDW RA contents. This reduction is attributed to the higher water absorption of the RA, which caused water retention during mixing. This issue could be addressed by pre-saturating the aggregates.

These findings contrast with those observed in the mortar samples (Figure 10a), which exhibited slightly higher workability with CEM I 52.5R than with CEM II/B-M(Q-L) 42.5R, with values progressively improving as CDW content increased. These differences are

attributed to the higher standardization of the mortar preparation process, whereas paving blocks were produced by a more manual method (mixing, mold filling, and compaction). Additionally, minor variations in the total w'/c ratio may have occurred because, to minimize the influence of aggregate humidity and to better control the effective w/c ratio, aggregates were dried before mortar preparation, whereas sands were used with their natural moisture content for paving block production. Furthermore, given the faster hydration reactions and higher heat of hydration of CEM I 52.5R compared to CEM II/B-M(Q-L) 42.5R cement, the differences in testing times likely contributed to the observed variations in workability. Specifically, mortar workability was measured after 4 min and 30 s, whereas it was assessed after 10 and 30 min for the paving blocks.

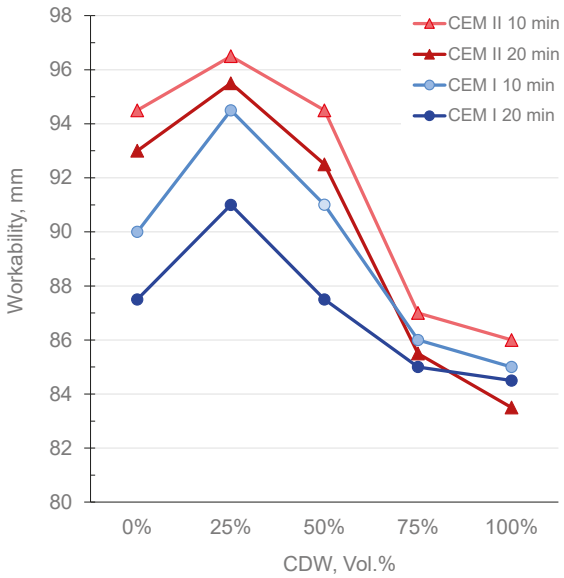

Figure 12. Workability of the paving blocks made with the NA and CDW aggregates.

3.3.2. Density and Water Absorption of Paving Blocks

Similar to the results obtained for the mortars, the density of the paving blocks generally decreased with increasing CDW aggregate content; see Figure 13a. A slightly lower density was observed in the paving blocks made with CEM II/B-M(Q-L) 42.5R compared to those prepared with CEM I 52.5R. However, this difference was insignificant, as all the values ranged between 2.11 g/cm^3 and 2.32 g/cm^3. The high deviation observed in the density of the paving blocks, compared to the variation seen in the mortar results (Figure 10b), is attributed to differences in the preparation process, which was more manual for the paving blocks than for the mortars. Additionally, the dimensional variability of the paving blocks was significantly greater. Specifically, the volume of each paving block was determined as the average of three measurements for each dimension: length, width, and thickness. In contrast, the mortar samples were assumed to have a constant volume of $40 \times 40 \times 160$ mm^3.

As expected, the water absorption coefficient was higher for the paving blocks made with CEM II/B-M(Q-L) 42.5R than for those prepared with CEM I 52.5R, which is attributed to the lower clinker content. As shown in Figure 13b, the coefficient progressively increased with the CDW RA content, with values ranging from 8.94% to 12.05%. According to the specifications outlined in Table 4.1 of Standard UNE EN 1338:2004 [43], the produced paving blocks should be classified as Type A, for which water absorption measurement is not required. Regardless of the aggregate used, all the water absorption values exceeded

6%, the threshold to be classified as Class 2 with a B marking. Consequently, these paving blocks would not be suitable for use in areas prone to frost.

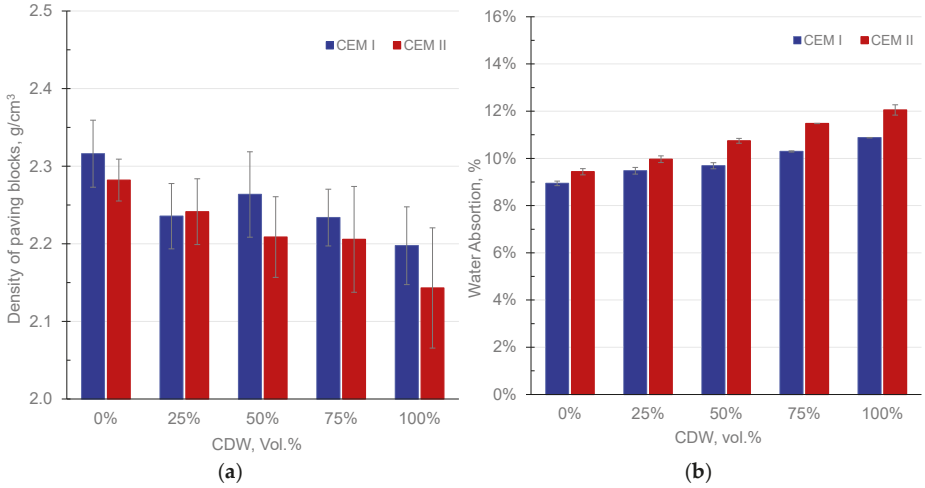

Figure 13. Properties of the paving blocks made with the NA and CDW aggregates: (**a**) density; (**b**) water absorption.

3.3.3. Splitting Tensile Strength of Paving Blocks

Figures 14–16 illustrate the splitting tensile strength of the developed paving blocks. Figure 14 presents the splitting tensile strength (Figure 14a) and breaking load (Figure 14b) of the paving blocks produced with CEM I 52.5R, incorporating increasing amounts of CDW. Figure 15 depicts these properties for the paving blocks made with CEM II/B-M(Q-L) 42.5R. According to Section 5.3.3.2 of Standard UNE EN 1338:2004 [43], the splitting tensile strength of paving blocks must exceed 3.6 MPa, with no individual values falling below 2.9 MPa. Additionally, breaking load must be above 250 N/mm of breaking length (184.1 ± 0.9 mm). These minimum thresholds are indicated in the figures. The paving blocks produced with CEM I 52.5R met these specifications after only 3 curing days, regardless of the percentage of CDW recycled sand used. However, those made with CEM II/B-M(Q-L) 42.5R generally met these requirements only after 28 curing days. The wide variability in the results is primarily attributed to the sample preparation process and the testing methodology.

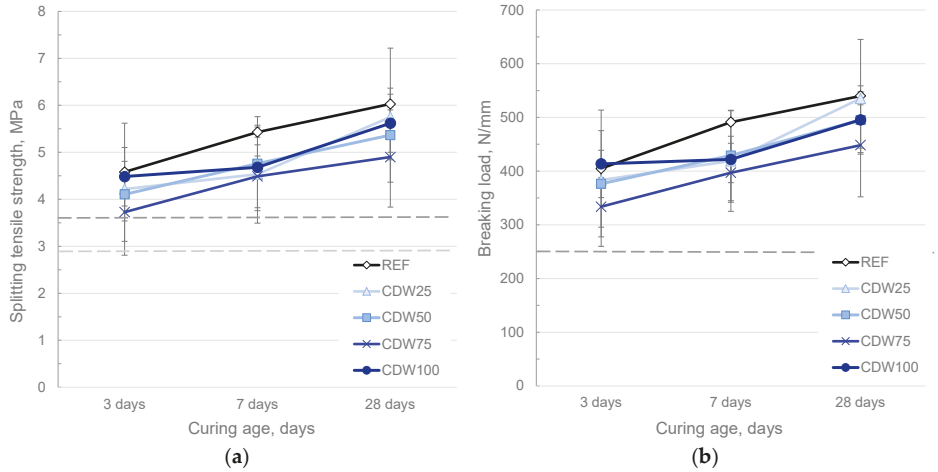

Figure 14. Splitting tensile strength of the paving blocks developed with CEM I 52.5R and increasing amounts of CDW: (**a**) splitting tensile strength; (**b**) breaking load. Limits established by Standard UNE EN 1338:2004 [43] indicated with striped lines.

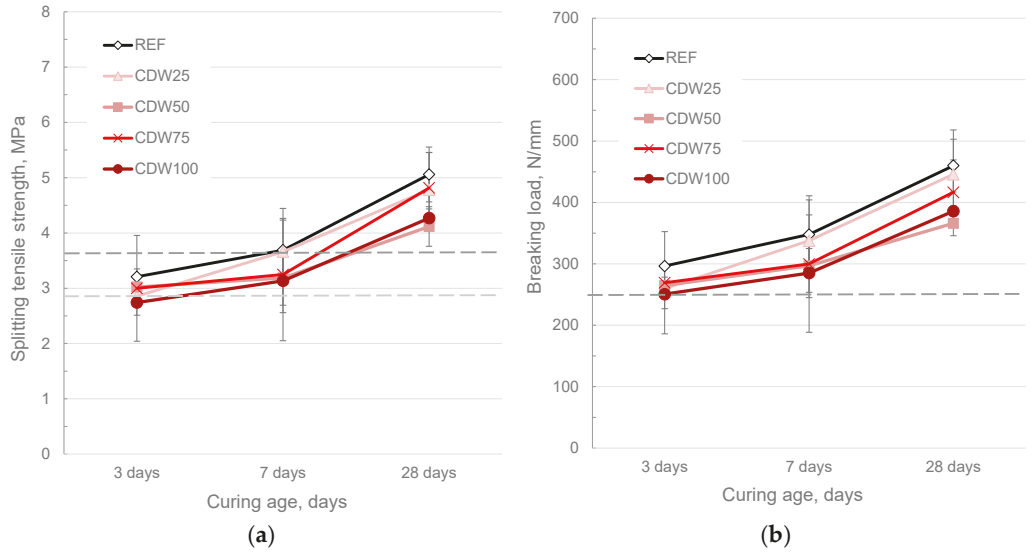

Figure 15. Splitting tensile strength of the paving blocks developed with CEM II/B-M(Q-L) 42.5R and increasing amounts of CDW: (**a**) splitting tensile strength; (**b**) breaking load. Limits established by Standard UNE EN 1338:2004 [43] indicated with striped lines.

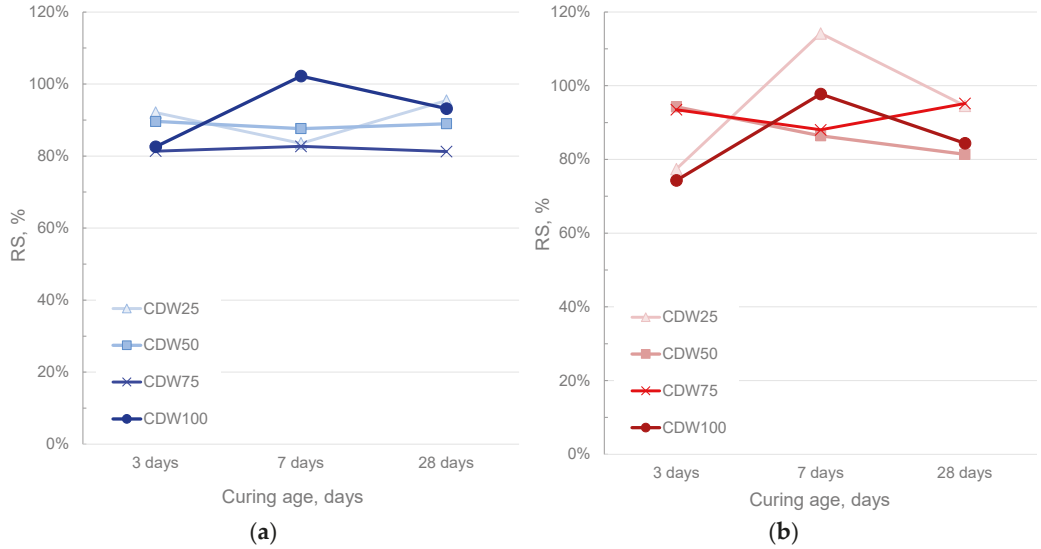

Figure 16. Relative splitting tensile strength between the paving blocks incorporating CDW RA and the REF paving blocks: (**a**) CEM I 52.5R; (**b**) CEM II/B-M(Q-L) 42.5R.

Figure 16 illustrates the RS (RS = R_{CDW}/R_{REF}) between the paving blocks that incorporated CDW aggregates and the REF samples, made with 100% natural calcareous aggregates. Although no significant variation was observed with increasing CDW aggregate content, the RS values generally ranged between 80 and 100%, which denotes a maximum 20% strength reduction compared to the REF samples.

Both the mortars and the paving blocks generally exhibited a progressive strength reduction with increasing CSW content. This trend was more pronounced in mortars than in paving blocks (see Figure 11, Figure 14 and Figure 15), with mortars displaying greater homogeneity and less variation in the strength results. This is attributed to the higher uniformity and standardization of the mortar preparation process, and also to the more precise testing methodology. Figure 17 illustrates the correlation between the strength of the paving blocks and mortars, which enables paving block splitting tensile strength based

on mortar compressive strength, and vice versa, to be estimated. The relatively wide data dispersion (R^2 = 0.74) is due primarily to the variability in the paving blocks results, which can be attributed to their manual preparation process and the challenges associated with adjusting the splitting tensile strength testing method.

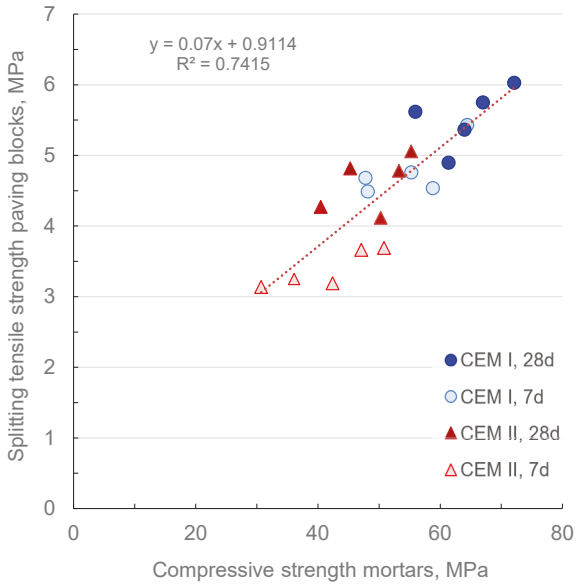

Figure 17. Correlation between the splitting tensile strength of the paving blocks and mortars with increasing CDW content.

The results differ from previous research on concrete blocks [17], where the replacement of natural sand with recycled aggregates (RAs) led to only slight reductions in compressive strength, particularly at replacement rates of 25% or 50%. However, at higher replacement rates, an increase in transverse strength was observed. These discrepancies may be attributed to the higher strength of the reference mixes used in the present study, as well as variations in the type and particle size distribution of the RAs employed in both studies.

3.4. Properties of the Developed Concrete

3.4.1. Workability

Table 7 summarizes the workability of the developed concrete as measured by the Abrams cone test. An improvement in workability was observed in the concrete samples containing CDW recycled sand. As the total water content in the mixes was adjusted based on the water absorption capacity and moisture content of the aggregates, similar workability values were expected. The observed variations can be attributed to differences in the rate of water absorption by aggregates and the additional water added to compensate for this absorption. Furthermore, the mixing process, which affects particle dispersion and consequently influences workability, also played a role.

Table 7. Workability of concrete mixes.

Designation	Cone, mm
REF	100
CDW50	190
CDW100	170

Despite a slight reduction in workability in sample CDW100 compared to CDW50, all the mixes had a fluid (100–150 mm) or liquid (160–210 mm) consistency in accordance with the classification in Chapter 8 of the Structural Code (Table 33.5.a). Previous studies on RAC, in which the amount of water was also adjusted based on that absorbed by aggregates [8,20,23,53], also report similar or slight variations in slump test values. In contrast, other studies [26,54] maintain the water content constant across all the concrete mixes, regardless of the amount of RA used. This method usually results in a reduction in RAC consistency as the proportion of RAs increases due to the higher water absorption typically exhibited by recycled particles.

3.4.2. Density and Compressive Strength of the Developed Concrete Samples

Table 8 summarizes the density and compressive strength of the developed concrete samples. RAC density decreased by 4.2% with the 50 vol.% substitution and by 6.8% with the 100 vol.% replacement of NA with CDW. This reduction is attributed to the lower density of the CDW particles (see Table 6), which led to a smaller RA mass for a given substitution percentage in volume. These findings are consistent with previous studies about RA use in concrete [23,25,52,55], which report a gradual decline in the density of hardened concrete as the proportion of RAs rises. Our results also align with a previous study by Pitarch et al. [52], in which natural limestone aggregates are replaced with various types of ceramic materials (bricks, tiles, and sanitaryware) in RAC. This substitution led to a reduction in density of up to 3.3% when incorporating up to 30% ceramic waste.

Table 8. Density and compressive strength of the developed concrete samples.

		Compressive Strength					
		7 Days			**28 Days**		
	Density, kg/m^3	**Mean MPa**	**Std. Deviation MPa**	**RS %**	**Mean MPa**	**Std. Deviation MPa**	**RS %**
REF	2343.4	37.2	0.8	-	45.7	1.8	-
CDW50	2245.3	28.9	0.5	77.7	39.0	1.7	85.3
CDW100	2184.9	24.9	1.5	66.9	33.7	2.1	73.7

The compressive strength of the concrete samples decreased as the percentage of CDW increased, Figure 18, with minimal variability in the results. The RS of the RAC cured for 28 days exceeded 70%, which indicates that strength loss was less than 30% when completely replacing natural sand with the CDW recycled sand. These findings, along with the higher workability observed in the CDW concrete samples, are consistent with the results obtained for mortars (Figures 10 and 11, mortars with CEM II/B-M(Q-L) 42.5R). Despite having a lower density, the CDW aggregate exhibited slightly higher wear resistance than NA (see Table 6). Consequently, the lower RAC strength cannot be attributed to lower RA particles quality, but may have resulted from the reduced fine content of the CDW aggregate, which might have led to a less compact matrix, along with a delay in PC hydration caused by the gradual release of water absorbed by the aggregates.

The RS of the developed concrete improved with curing time. Previous studies using ceramic materials as RAs in concrete have attributed this improvement to a pozzolanic reaction between the fine ceramic particles and portlandite formed during PC hydration, which enhances the interface between the aggregate and the cementitious matrix [8,52,56]. However, the chemical composition and LOI of the CDW used in this study (see Section 3.1.1) suggest only limited pozzolanic activity. The improvement in RS with curing time herein observed is attributed mainly to greater CDW aggregate absorption. This likely facilitates a slower release of water, which results in more gradual PC hydration over time.

Previous studies into RAC demonstrate that the compressive strength of concrete is significantly influenced by the type of aggregate used. Consistently with the results obtained in this study, several researchers [8,19–21,55] report decreased compressive strength when using RAs in comparison to samples with NAs. Conversely, some studies, like those by Cachim [23], Medina et al. [25], and López et al. [57], observed improved compressive strength when incorporating ceramic RAs. Roig-Flores et al. [58] investigated the use of RAs from stoneware ceramic tiles and report a slight reduction in strength when replacing natural limestone sand. However, when 20% to 100% (by volume) of natural coarse aggregates were substituted, strength was either maintained or slightly improved. Similar studies by Malesev et al. [24] and Evangelista and de Brito [22] report only minor enhancements in compressive strength when replacing NAs with recycled concrete aggregates.

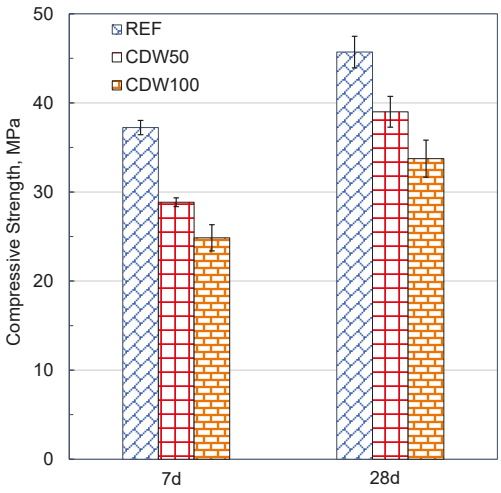

Figure 18. Compressive strength of the developed concrete samples.

As reviewed by Xiao et al. [7], RAC typically exhibits lower mechanical properties than traditional concrete. This limitation is likely one of the primary reasons why the Spanish Structural Code for Concrete restricts the use of RAs to those that derive from concrete, allowing a maximum replacement of 20% by weight of natural coarse aggregates. For higher replacement levels or the incorporation of different RA types, additional studies are required. Despite the reduction in compressive strength observed with the incorporation of the CDW recycled sand herein employed, the obtained strength values still meet the minimum requirements for reinforced concrete production. These findings suggest that the CDW recycled sand has the potential for use as RA in structural concrete applications.

3.4.3. Concrete Shrinkage

Linear shrinkage is presented in Figure 19. The CDW50 concrete exhibited the highest shrinkage values, which surpassed those of the REF sample. In contrast, the CDW100 concrete displayed the least shrinkage, with even lower values than those observed in the REF concrete. As the employed CDW primarily consisted of limestone and ceramic particles, the variation in the shrinkage values among mixes can be attributed to differences in aggregate type, the absorption ratio, and the specific surface of the CDW sand compared to natural sand. As previously reported by Zhang et al. [59], these factors significantly influence concrete shrinkage. Furthermore, the higher porosity of RAC may have also influenced the results. The greater shrinkage observed in the CDW50 series compared to the REF mix can be attributed to the increased porosity (indicated by higher permeability) of RAC, which resulted in fewer restrictions in movement or shrinkage. In the CDW100 samples, slight

expansion was measured one day after demolding, which suggests a minor delay in hydration reactions due to the gradual release of water absorbed by aggregates. In the CDW50 samples, this expansion was not recorded, likely because it occurred before the first measuring date. Nevertheless, greater shrinkage should have also been observed in the CDW100 series given its higher permeability. Therefore, shrinkage should be further investigated, particularly at early ages, to better understand the underlying causes of this behavior.

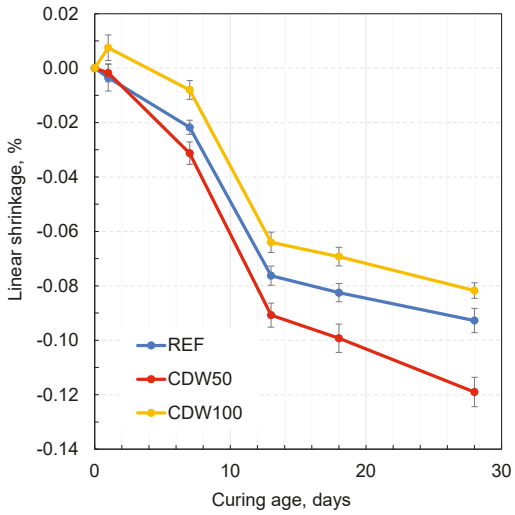

Figure 19. Linear shrinkage of the developed concrete at various curing ages.

3.4.4. Concrete Permeability

Figure 20 shows the maximum and average water penetration depths, measured in accordance with Annex A of UNE-EN 12390-8 [48]. Consistent with the compressive strength values, which decreased as CDW content increased, concrete permeability results showed a slightly more permeable matrix with the incorporation of CDW sand. Both the maximum and the average water penetrations increased with CDW recycled sand incorporation, with a respective rise from 18 mm to 26 mm and from 10.2 mm to 19.5 mm. Despite the increase, the penetration values remained below the limits specified in Table 43.3.2 of the Structural Code for concrete. This code establishes that, for any concrete exposed to highly aggressive environments XS3 (marine corrosion in tidal zones) and XA3 (highly aggressive chemical attack), the maximum water penetration must be less than 30 mm and the average penetration less than 20 mm.

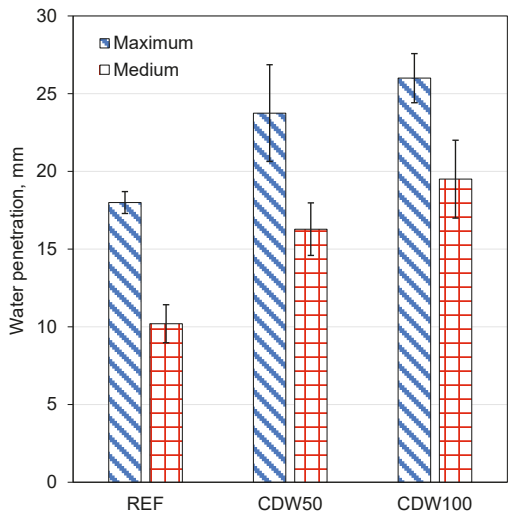

Figure 20. Average and maximum water penetration depths.

4. Conclusions

This study evaluates using CDW-derived sand as RA in mortars, paving blocks, and concrete. The key findings are as follows:

- The CDW aggregate was composed of mainly limestone and ceramics, with low sulfur content, lower fine content, and no pozzolanic activity. It was slightly harder than natural limestone, and had lower density and higher water absorption. The similar properties of NA and RA suggest that the CDW sand can be effectively reused in sustainable construction materials.
- The workability of paving blocks slightly improved with 20 vol.% CDW, but decreased with higher content, while mortars and concrete showed improved workability with the CDW sand.
- The density of all the samples decreased as CDW content increased, and ranged from 2.35 g/cm^3 in the REF sample to 2.10 g/cm^3 with 100% CDW recycled sand.
- The water absorption in the paving blocks increased with the CDW content, limiting their suitability to non-frost areas. Water permeability was higher in RAC, but the water penetration values met the Structural Code limits for all the environmental exposure classes.
- The paving blocks made with CEM I 52.5R met splitting tensile strength requirements after 3 curing days, while those with CEM II/B-M(Q-L) 42.5R met the standard after 28 curing days.
- Compressive strength generally decreased with higher CDW content. The RS of the mortars with up to 50 vol.% CDW remained above 80% at all curing ages, and the RS of all the mortars cured for 28 days exceeded 70%, regardless of the CDW content. The compressive strength of the RAC samples met the minimum requirements for reinforced concrete.

The use of RAs is a key strategy for sustainable construction because it reduces environmental impacts and improves resource efficiency. This study confirms that the CDW-derived sand used can effectively replace natural limestone sand in both structural and non-structural applications. Although regulatory restrictions limit the use of RAs in structural concrete, the study highlights opportunities for reusing this significant waste material, with the optimal replacement percentage determined by specific application requirements. The results support the development of standardized guidelines for RAs in non-structural applications, encouraging broader industry adoption and providing environmental benefits. Further research, along with supportive policies and economic incentives, is essential to overcome the current challenges of using RAs and to promote circular construction practices.

Author Contributions: Conceptualization, L.R., Á.M.P., A.P., M.R.-F. and D.H.-F.; data curation, L.R., V.A., D.H.-F. and A.M.-E.; formal analysis, M.R.-F., V.A. and A.M.-E.; funding acquisition, A.P., M.R.-F. and D.H.-F.; investigation, L.R., M.R.-F., V.A. and A.M.-E.; methodology, L.R., Á.M.P. and A.P.; project administration, Á.M.P., A.P., M.R.-F. and D.H.-F.; resources, A.P. and D.H.-F.; supervision, L.R., Á.M.P. and V.A.; writing—original draft, V.A., D.H.-F. and A.M.-E.; writing—review and editing, L.R., Á.M.P., A.P. and M.R.-F. All authors have read and agreed to the published version of the manuscript.

Funding: This research was funded by Generalitat Valenciana, the regional government of Valencia, through project INVEST/2022/243, and by Universitat Jaume I (UJI) through project UJI-B2021-34.

Data Availability Statement: The raw data supporting the conclusions of this article will be made available by the authors on request.

Acknowledgments: The authors are grateful to HOPE & EFFORT S.L. for supplying the CDW recycled sand and to Élite Cementos for providing the cement used in this research. They would also like to express their gratitude to the Universitat Jaume I (UJI) for providing the means to conduct this research and the Scientific Instrumentation Centre of the UJI for conducting the microstructural characterization tests.

Conflicts of Interest: The authors declare no conflict of interest.

Abbreviations

The following abbreviations are used in this manuscript:

CDW	Construction and demolition waste
NAs	Natural aggregates
PC	Portland cement
RAs	Recycled aggregates
RAC	Recycled aggregate concrete
Vol.%	Percentage in volume
Wt.%	Percentage in weight
WA	Water absorption
w/c	Effective water-to-cement ratio
w'/c	Total water-to-cement ratio
RS	Relative strength
XRD	X-ray diffraction
XRF	X-ray fluorescence
TG	Thermogravimetric analysis
LOI	Loss on ignition
FM	Fineness modulus

References

1. Lyu, Y.; Xiong, N.; Liang, Y.; Lin, S.; Wang, J. Estimation of Construction and Demolition Waste and Assessment of Disposal Facility Location: An Integrated Material Flow Analysis and Geographic Information System Approach. *Resour. Conserv. Recycl.* **2025**, *218*, 108226. [CrossRef]
2. Trancone, G.; Policastro, G.; Spasiano, D.; Race, M.; Parrino, F.; Fratino, U.; Fabbricino, M.; Pirozzi, F. Treatment of Concrete Waste from Construction and Demolition Activities: Application of Organic Acids from Continuous Dark Fermentation in Moving Bed Biofilm Reactors. *Chem. Eng. J.* **2025**, *505*, 159536. [CrossRef]
3. European Commission; Joint Research Centre; Institute for Environment and Sustainability. Supporting Environmentally Sound Decisions for Construction and Demolition (C&D) Waste Management a Practical Guide to Life Cycle Thinking (LCT) and Life Cycle Assessment (LCA). Available online: https://eplca.jrc.ec.europa.eu/uploads/waste-Guide-to-LCTLCA-for-C-D-waste-management-Final-ONLINE.pdf (accessed on 20 March 2025).
4. Alhawamdeh, M.; Ferriz-Papi, J.A.; Lee, A. Examining the Drivers to Support Improved Construction and Demolition Waste Management for a Circular Economy: A Comprehensive Review Using a Systematic Approach. *Sustainability* **2024**, *16*, 6014. [CrossRef]
5. Lee, S.; Chang, H.; Lee, J. Construction and Demolition Waste Management and Its Impacts on the Environment and Human Health: Moving Forward Sustainability Enhancement. *Sustain. Cities Soc.* **2024**, *115*, 105855. [CrossRef]
6. de Andrade Salgado, F.; de Andrade Silva, F. Recycled Aggregates from Construction and Demolition Waste towards an Application on Structural Concrete: A Review. *J. Build. Eng.* **2022**, *52*, 104452. [CrossRef]
7. Xiao, J.; Lu, D.; Ying, J. Durability of Recycled Aggregate Concrete: An Overview. *J. Adv. Concr. Technol.* **2013**, *11*, 347–359. [CrossRef]
8. Alves, A.V.; Vieira, T.F.; De Brito, J.; Correia, J.R. Mechanical Properties of Structural Concrete with Fine Recycled Ceramic Aggregates. *Constr. Build Mater.* **2014**, *64*, 103–113. [CrossRef]
9. Akhtar, A.; Sarmah, A.K. Construction and Demolition Waste Generation and Properties of Recycled Aggregate Concrete: A Global Perspective. *J. Clean Prod.* **2018**, *186*, 262–281. [CrossRef]
10. Chen, Y.; Chen, C.; Cai, Z.; Zhu, P.; Liu, R.; Liu, H. Effect of Strength of Parent Concrete on Utilization of Recycled Aggregate Concrete: A Review. *J. Build. Eng.* **2025**, *103*, 112187.

11. Vegas, I.; Ibañez, J.A.; Lisbona, A.; Sáez De Cortazar, A.; Frías, M. Pre-Normative Research on the Use of Mixed Recycled Aggregates in Unbound Road Sections. *Constr. Build Mater.* **2011**, *25*, 2674–2682. [CrossRef]
12. Elchalakani, M.; Elgaali, E. Sustainable Concrete Made of Construction and Demolition Wastes Using Recycled Wastewater in the UAE. *J. Adv. Concr. Technol.* **2012**, *10*, 110–125. [CrossRef]
13. De Brito, J.; Saikia, N. *Recycled Aggregate in Concrete: Use of Industrial, Construction and Demolition Waste, Green Energy and Technology*, 1st ed.; Springer: London, UK, 2013; ISBN 9781447145400. [CrossRef]
14. Tam, V.W.Y.; Soomro, M.; Evangelista, A.C.J. A Review of Recycled Aggregate in Concrete Applications (2000–2017). *Constr. Build Mater.* **2018**, *172*, 272–292. [CrossRef]
15. Palii, O.; Sirico, A.; Belletti, B.; Bernardi, P. Building a Sustainable Future: Database of Concrete with Recycled Aggregates from Construction and Demolition Waste. *Procedia Struct. Integrity.* **2024**, *59*, 167–174.
16. Borges, P.M.; Rother, L.A.; da Silva, S.R.; Possan, E.; de Oliveira Andrade, J.J. Environmental and Technical Assessment of Mortars Produced with Recycled Aggregate from Construction and Demolition Waste. *Constr. Build Mater.* **2025**, *467*, 140407. [CrossRef]
17. Poon, C.S.; Kou, S.C.; Lam, L. Use of Recycled Aggregates in Molded Concrete Bricks and Blocks. *Constr. Build Mater.* **2002**, *16*, 281–289. [CrossRef]
18. Chu, S.H.; Poon, C.S.; Lam, C.S.; Li, L. Effect of Natural and Recycled Aggregate Packing on Properties of Concrete Blocks. *Constr. Build Mater.* **2021**, *278*, 122247. [CrossRef]
19. De Brito, J.; Pereira, A.S.; Correia, J.R. Mechanical Behaviour of Non-Structural Concrete Made with Recycled Ceramic Aggregates. *Cem. Concr. Compos.* **2005**, *27*, 429–433. [CrossRef]
20. Medina, C.; Zhu, W.; Howind, T.; Sánchez De Rojas, M.I.; Frías, M. Influence of Mixed Recycled Aggregate on the Physical—Mechanical Properties of Recycled Concrete. *J. Clean Prod.* **2014**, *68*, 216–225. [CrossRef]
21. Topçu, I.B.; Şengel, S. Properties of Concretes Produced with Waste Concrete Aggregate. *Cem. Concr. Res.* **2004**, *34*, 1307–1312. [CrossRef]
22. Evangelista, L.; de Brito, J. Mechanical Behaviour of Concrete Made with Fine Recycled Concrete Aggregates. *Cem. Concr. Compos.* **2007**, *29*, 397–401. [CrossRef]
23. Cachim, P.B. Mechanical Properties of Brick Aggregate Concrete. *Constr. Build Mater.* **2009**, *23*, 1292–1297. [CrossRef]
24. Malešev, M.; Radonjanin, V.; Marinković, S. Recycled Concrete as Aggregate for Structural Concrete Production. *Sustainability* **2010**, *2*, 1204–1225. [CrossRef]
25. Medina, C.; Juan, A.; Frías, M.; Sánchez de Rojas, M.I.; Morán, J.M.; Guerra, M.I. Characterization of Concrete Made with Recycled Aggregate from Ceramic Sanitary Ware. *Mater. Construcción* **2011**, *61*, 533–546. [CrossRef]
26. Torkittikul, P.; Chaipanich, A. Utilization of Ceramic Waste as Fine Aggregate within Portland Cement and Fly Ash Concretes. *Cem. Concr. Compos.* **2010**, *32*, 440–449. [CrossRef]
27. Pacheco, J.; de Brito, J.; Lamperti Tornaghi, M. *Use of Recycled Aggregates in Concrete: Opportunities for Upscaling in Europe*; Publications Office of the European Union: Luxembourg, 2023. [CrossRef]
28. Poon, C.S.; Chan, D. The Use of Recycled Aggregate in Concrete in Hong Kong. *Resour. Conserv. Recycl.* **2007**, *50*, 293–305. [CrossRef]
29. *EN 206-1*; Concrete—Materials—Rules for Application of EN 206-1 in Denmark. Danish Standards: Copenhaga, Denmark, 2011.
30. *NEN-EN 206*; Concrete—Specification, Performance, Production and Conformity. Beton: Hardenberg, The Netherlands, 2022.
31. Mehus, J.; Petkovic, G.; Engelsen, C.J.; Karlsen, J.; Lillestol, B. Recycled Aggregates a Viable Alternative for the Norwegian Building and Construction Industry. Available online: https://www.researchgate.net/profile/Christian-Engelsen-2/publication/228474590_Recycled_Aggregates_a_Viable_Alternative_for_the_Norwegian_Building_and_Construction_Industry/links/02e7e52a576e48c0ca000000/Recycled-Aggregates-a-Viable-Alternative-for-the-Norwegian-Building-and-Construction-Industry.pdf (accessed on 20 March 2025).
32. *UNE-EN 206:2013+A2*; Concrete Specification, Performance, Production and Conformity. Asociación Española de Normalización y Certificación (AENOR): Madrid, Spain, 2021.
33. Ferro, G.A.; Spoto, C.; Tulliani, J.M.; Restuccia, L. Mortar Made of Recycled Sand from C&D. *Procedia Eng.* **2015**, *109*, 240–247. [CrossRef]
34. Kępniak, M.; Łukowski, P. Multicriteria Analysis of Cement Mortar with Recycled Sand. *Sustainability* **2024**, *16*, 1773. [CrossRef]
35. Favier, A.; De Wolf, C.; Scrivener, K.; Habert, G. *A Sustainable Future for the European Cement and Concrete Industry*; ETH Zurich: Zürich, Switzerland, 2018. [CrossRef]
36. *UNE-EN 197-1*; Cement. Part 1: Composition, Specifications and Conformity Criteria for Common Cements. Asociación Española de Normalización y Certificación (AENOR): Madrid, Spain, 2012.
37. *UNE 146404*; Áridos Para Hormigones Medida Del Coeficiente de Friabilidad de Las Arenas. Asociación Española de Normalización y Certificación (AENOR): Madrid, Spain, 2018.

38. *UNE-EN 933-1*; Tests for Geometrical Properties of Aggregates. Part 1: Determination of Particle Size Distribution. Sieving Method. Asociación Española de Normalización y Certificación (AENOR): Madrid, Spain, 2013.
39. *UNE-EN 933-8:2012+A1*; Tests for Geometrical Properties of Aggregates. Part 8: Assessment of Fines. Sand Equivalent Test. Asociación Española de Normalización y Certificación (AENOR): Madrid, Spain, 2015.
40. *UNE-EN 1097-6*; Tests for Mechanical and Physical Properties of Aggregates. Part 6: Determination of Particle Density and Water Absorption. Asociación Española de Normalización y Certificación (AENOR): Madrid, Spain, 2014.
41. *UNE-EN 196-1:2018*; Methods of Testing Cement. Part 1: Determination of Strength. Asociación Española de Normalización y Certificación (AENOR): Madrid, Spain, 2018.
42. *UNE-EN 1015-3:2000/A2*; Methods of Test for Mortar for Masonry. Part 3: Determination of Consistence of Fresh Mortar (by Flow Table). Asociación Española de Normalización y Certificación (AENOR): Madrid, Spain, 2007.
43. *UNE-EN 1338:2004*; Concrete Paving Blocks. Requirements and Test Methods. Asociación Española de Normalización y Certificación (AENOR): Madrid, Spain, 2004.
44. *UNE-EN 12350-2:2020*; Testing Fresh Concrete. Part 2: Slump Test. Asociación Española de Normalización y Certificación (AENOR): Madrid, Spain, 2020.
45. *UNE-EN 12390-1:2022*; Testing Hardened Concrete. Part 1: Shape, Dimensions and Other Requirements for Specimens and Moulds. Asociación Española de Normalización y Certificación (AENOR): Madrid, Spain, 2022.
46. *UNE-EN 12390-3:2020*; Testing Hardened Concrete. Part 3: Compressive Strength of Test Specimens. Asociación Española de Normalización y Certificación (AENOR): Madrid, Spain, 2020.
47. *UNE-EN 12390-16:2020*; Testing Hardened Concrete. Part 16: Determination of the Shrinkage of Concrete. Asociación Española de Normalización y Certificación (AENOR): Madrid, Spain, 2020.
48. *UNE-EN 12390-8:2020*; Testing Hardened Concrete. Part 8: Depth of Penetration of Water under Pressure. Asociación Española de Normalización y Certificación (AENOR): Madrid, Spain, 2020.
49. *UNE-EN 450-1*; Fly Ash for Concrete Part 1: Definition, Specifications and Conformity Criteria. Asociación Española de Normalización y Certificación (AENOR): Madrid, Spain, 2013.
50. Gunasekaran, S.; Anbalagan, G. Thermal Decomposition of Natural Dolomite. *Bull. Mater. Sci.* **2007**, *30*, 339–344.
51. Pitarch, A.M.; Reig, L.; Tomás, A.E.; Forcada, G.; Soriano, L.; Borrachero, M.V.; Payá, J.; Monzó, J.M. Pozzolanic Activity of Tiles, Bricks and Ceramic Sanitary-Ware in Eco-Friendly Portland Blended Cements. *J. Clean Prod.* **2021**, *279*, 123713. [CrossRef]
52. Pitarch, A.M.; Reig, L.; Tomás, A.E.; López, F.J. Effect of Tiles, Bricks and Ceramic Sanitary-Ware Recycled Aggregates on Structural Concrete Properties. *Waste Biomass Valorization* **2019**, *10*, 1779–1793. [CrossRef]
53. Debieb, F.; Kenai, S. The Use of Coarse and Fine Crushed Bricks as Aggregate in Concrete. *Constr. Build Mater.* **2008**, *22*, 886–893. [CrossRef]
54. Tavakolia, D.; Heidari, A. Properties of Concretes Produced with Waste Ceramic Tile Aggregate. *Asian J. Civ. Eng.* **2013**, *14*, 369–382.
55. Cabral, A.E.B.; Schalch, V.; Molin, D.C.C.D.; Ribeiro, J.L.D. Mechanical Properties Modeling of Recycled Aggregate Concrete. *Constr. Build Mater.* **2010**, *24*, 421–430. [CrossRef]
56. Etxeberria, M.; Vegas, I. Effect of Fine Ceramic Recycled Aggregate (RA) and Mixed Fine RA on Hardened Properties of Concrete. *Mag. Concr. Res.* **2015**, *67*, 645–655. [CrossRef]
57. López, V.; Llamas, B.; Juan, A.; Morán, J.M.; Guerra, I. Eco-Efficient Concretes: Impact of the Use of White Ceramic Powder on the Mechanical Properties of Concrete. *Biosyst. Eng.* **2007**, *96*, 559–564. [CrossRef]
58. Roig-Flores, M.; Reig, L.; Albero, V.; Hernández-Figueirido, D.; Melchor-Eixea, A.; Pitarch, Á.M.; Piquer, A. Utilisation of Ceramic Stoneware Tile Waste as Recycled Aggregate in Concrete. *Buildings* **2023**, *13*, 1968. [CrossRef]
59. Zhang, W.; Zakaria, M.; Hama, Y. Influence of Aggregate Materials Characteristics on the Drying Shrinkage Properties of Mortar and Concrete. *Constr. Build Mater.* **2013**, *49*, 500–510. [CrossRef]

Disclaimer/Publisher's Note: The statements, opinions and data contained in all publications are solely those of the individual author(s) and contributor(s) and not of MDPI and/or the editor(s). MDPI and/or the editor(s) disclaim responsibility for any injury to people or property resulting from any ideas, methods, instructions or products referred to in the content.

applied sciences

MDPI

Article

Digital Image Correlation and Reliability-Based Methods for the Design of Structural Beams Made from Recycled Concrete Using Aggregates from Precast Rejects

Jorge López-Rebollo [1,*], Evelio Teijón-López-Zuazo [2], Roberto García-Martin [3], Luis Javier Sánchez-Aparicio [1,4] and Diego González-Aguilera [1,*]

[1] Department of Cartographic and Land Engineering, Higher Polytechnic School of Ávila, University of Salamanca, Hornos Caleros, 50, 05003 Ávila, Spain; lj.sanchez@upm.es
[2] Department of Construction and Agronomy, Higher Polytechnic School of Zamora, University of Salamanca, Campus Viriato, Avenida Requejo, 33, 49022 Zamora, Spain; eteijon@usal.es
[3] Department of Mechanical Engineering, Higher Polytechnic School of Zamora, University of Salamanca, Campus Viriato, Avenida Requejo, 33, 49022 Zamora, Spain; toles@usal.es
[4] Department of Construction and Technology in Architecture (DCTA), Escuela Técnica Superior de Arquitectura de Madrid (ETSAM), Universidad Politécnica de Madrid, Av. Juan de Herrera 4, 28040 Madrid, Spain
* Correspondence: jorge_lopez@usal.es (J.L.-R.); daguilera@usal.es (D.G.-A.)

Abstract: The use of recycled aggregates in the manufacture of concrete is presented as a solution to reduce the consumption of resources and waste in the construction sector and contribute to a lower environmental impact. This work aims to explore the possibility of producing structural beams from recycled concrete using aggregates from precast concrete rejects and to improve their design using advanced characterisation techniques. To this end, the experimental data coming from mechanical test and the use of the digital image correlation approach are combined with a robust reliability-based method. The full-field data provided by the digital image correlation approach allow to determine the probabilistic density functions of the mechanical data. From these data, a predictive analysis of the maximum strength and deflection of flexural beams is carried out based on robust design techniques. This approach uses analytical theoretical models and a Monte Carlo-based simulation strategy that allows the prediction of the behaviour of the beams. This methodology was validated by manufacturing six beams with the previously analysed recycled concrete, HA-30, and testing them in the laboratory. All the beams showed behaviour within the predicted range: around 49.7 kN maximum load and just over 9.3 mm maximum deflection. These results demonstrate the robustness of the approach as well as the feasibility of using precast rejects for the manufacture of structural elements.

Keywords: recycled concrete; structural concrete; digital image correlation; realiability-based method; recycled beams

1. Introduction

Sustainability in construction is one of the Sustainable Development Goals (SDGs) established by the United Nations (UN) [1]. In order to prevent the negative environmental impacts of this industry, it is necessary to address the problem both from the point of view of building sustainable infrastructures and cities and from a vision of responsible production and consumption. In general, construction uses non-renewable materials, requiring a

high consumption of natural resources for its production and generates a large amount of waste at the end of its useful life [2]. In Europe, construction and demolition waste (CDW) accounts for between 25% and 30% of all waste generated in the European Union, amounting to 800 million tonnes per year [3]. In Spain, 14,341,183 tonnes of waste were produced annually on average in the period of 2018–2020 from construction [4]. The main component of CDW is concrete [5], responsible for 4–8% of the world's CO_2 emissions [6]. In turn, waste concrete infrastructure comes mainly from Public Works, which is supervised by the transport minister. Supervision is the responsibility of government administration and amounts to 6,140,009 tonnes on average per year, representing 39.76% of total production. Therefore, one of the main solutions proposed is the use of recycled materials in the production of concrete. This solution reduces the use of virgin aggregates and eliminates the presence of waste in landfills [7].

European guidelines indicate the need for a sustainable use of resources, as well as the need to ensure recycling of at least 70% of CDW [8]. Nevertheless, country regulations for the manufacture of structural concrete significantly restrict the use of recycled aggregates, limiting it to a portion of coarse aggregates and preventing the use of fine recycled aggregates [9]. Consequently, most studies for the re-use of CDW have focused on applications requiring lower mechanical performance with non-structural concretes [10–13]. Nevertheless, exhaustive research into the properties of recycled concrete aggregates [14] has demonstrated their viability for use in higher performance applications when properly treated [15] or when sourced from higher quality elements such as precast structural elements [16]. This type of element generally presents a characteristic concrete strength of more than 40 MPa, so its waste allows obtaining recycled aggregates of higher quality to be used in structural concretes [17]. The use of these recycled aggregates makes it possible to achieve strength and bonding properties comparable or superior to those of other structural concretes [18] whose minimum strength value is 20 MPa for mass concretes and 25 MPa for reinforced or prestressed concretes [19]. In addition, the use of precast concrete rejects as recycled aggregate results in up to 15% less energy consumption and carbon dioxide emissions compared to other recycled materials [20].

Due to regulatory constraints, studies in structural concrete are not very common. Nevertheless, research such as that of Perez et al. [21] affirms the potential of these rejects from precast elements even for self-consumption in the same precast plants. Zengfeng et al. [22] validate this theory by manufacturing new building blocks from precast block rejects on an industrial scale. Soares et al. [23] agree that this type of recycled aggregates have a higher quality than average, allowing them to achieve similar characteristics to conventional concrete and propose the elimination of restrictions on their use. Regarding the amount of aggregates to be used, Thomas et al. [24] highlight in their research that substitution percentages up to 20% do not affect the properties of the concrete, and higher substitution percentages cause an increase in the amount of cement. Nevertheless, according to the optimisation analysis of the mix design of these recycled concretes carried out in [25], a minimum substitution of 60% of the aggregates is recommended to achieve a balance between concrete strength and environmental impact.

In any case, recent industrial applications have been limited to the replacement of coarse aggregates, either in the manufacture of beams [26] or precast concrete plants [27]. In this sense, the replacement of all natural aggregates by recycled aggregates can be interesting from the point of view of a greater amount of resources and waste saved. In the same way, it would allow to improve the operational process if the aggregates granulometry allows to use them as all-in-one without the need to distinguish between coarse and fine aggregates. Nevertheless, this solution poses a challenge in terms of characterisation

and definition due to the variation in their behaviour, especially in properties related to deformability or modulus of elasticity [24]. The wide variability in the type of aggregates, their origin or mode of use are some of the factors that lead to this heterogeneity in the behaviour of recycled concrete [28].

For this reason, the mechanical characterisation and obtaining of the properties of these materials requires the use of techniques adapted to their behaviour, in this case heterogeneous. Similarly, the design of structural elements requires the uncertainty in their properties to be taken into account. In this context, the displacement and strain measurement techniques traditionally used, such as strain gauges or LVDT, have a local nature [29], obtaining punctual measurements that do not fully represent the real behaviour of the samples. In contrast to traditional techniques, new full-field techniques allow monitoring the complete behaviour of samples even without contact. Digital image correlation (DIC) [30] is the technique with the greatest potential due to its non-invasive and non-destructive characteristics, the accuracy and the adaptability to different test typologies through its two-dimensional and three-dimensional approach [31]. It is a technique that allows a complete field of displacements and strains to be obtained by capturing images in different load states during the testing process. DIC is a well-proven technique that has been used to characterise materials with variability in their properties such as wood [32], composites [33] or reinforced cementitious materials [34]. Regarding concrete, numerous studies can be found for the measurement of surface displacements or strains using 2D-DIC and 3D-DIC [35–38].

Based on the above-mentioned heterogeneity of the material and the possibility of full-field monitoring of DIC, the use of this technique is proposed for the mechanical characterisation of concrete manufactured by aggregates from precast concrete rejects. Whether in tensile, compression or elastic tests using cubic or cylindrical specimens, DIC can be used in its two-dimensional or three-dimensional variants for the measurement of displacements and strains. In all specimens, their surface can be monitored and values can be obtained that more adequately represent their actual behaviour, regardless of whether cracking is present or in which zone the failure occurs. In addition, the obtained full-field data facilitate a statistical treatment to estimate not only a mean value for the properties, but also a dispersion and distribution that represents the heterogeneity. This type of characterisation is proposed in order to achieve a more detailed definition of the material to introduce their uncertainty and heterogeneity using robust design techniques without the need for excessive over-dimensioning. In contrast to deterministic methods, reliability-based analysis is considered to be the most robust strategy for the design of concrete structures [39,40]. This type of strategy ensures safety by introducing the random uncertainties that occur in practical engineering with new materials, such as reinforced beams [41,42]. The main objective of these approaches is to determine the failure probability of a mechanical system under the influence of different uncertainties, such as loads or material properties, among others [33]. This can be achieved using approximation methods such as the First-Order Reliability (FORM) and Second-Order Reliability (SORM) methods or even simulation strategies such as the Monte Carlo Sampling (MCS) method [39]. The MCS is characterised by its simple and straightforward implementation to carry out a large number of simulations and to mathematically replicate the behaviour. Furthermore, when these simulation strategies are combined with one or more design objectives or cost functions, it is possible to achieve Reliability-Based Design Optimisations (RBDOs) [43].

While most previous works have focused on lower performance applications or partial replacement of aggregates, this work aimed to advance the understanding of the mechanical characterisation of structural concretes made from precast concrete rejects

for the manufacture of structural elements such as beams. In addition, it incorporated advanced characterisation techniques and reliability-based design methods, adding a level of rigour and precision to the assessment of the uncertainties and variability inherent in recycled materials. In pursuit of this objective, a characterisation of the recycled aggregates was initially carried out in order to define an optimised concrete dosage. Then, tensile, compression and elasticity mechanical characterisation tests were carried out using the DIC technique to obtain their properties. Experimentally obtained full-field data from DIC were used along with robust design techniques to predict the behaviour of bending beams. Subsequently, prototypes of structural beams were manufactured using the same concrete. Finally, these beams were subjected to experimental bending tests to compare the results of these tests with the prediction made according to the properties obtained previously.

Following this introduction, Section 2 describes the materials and methodology used in the tests of this research. In Section 3, the experimental results of the mechanical characterisation tests are shown, as well as a discussion of these results. An analysis of the validation tests performed on the manufactured beams is also presented. Finally, Section 4 draws the main conclusions on the suitability of the introduction of these recycled aggregates for the fabrication of structural elements and discusses future lines of research.

2. Materials and Methods

2.1. Materials and Mix Proportions

For reinforced concrete with steel reinforcement, the recommended minimum strength depends on the durability requirements according to the general exposure classes for corrosion of the reinforcement, with a minimum of 25 MPa. Nevertheless, for bending elements such as beams, this requirement is increased to 30 or 35 MPa. These specifications have been evaluated with good quality aggregates in accordance with the usual durability considerations.

On the other hand, this research evaluates the case of low-quality aggregates, such as those obtained from recycling, in this case referring to those obtained from the crushing of rejected elements in the manufacture of prefabricated with siliceous aggregates from the Duero river basin (Figure 1). Specifically, the analysed aggregates come from the factory of the company Prefabricados Duero located in the town of Toro (Zamora, Spain), produced specifically for this research.

Figure 1. Rejection of the manufacture of prefabricated products with siliceous aggregates: (**a**) prefabricated elements; and (**b**) crushed aggregates.

This research used prefabricated elements that failed quality control or were stored for long periods due to restrictions on the movement of goods during the SARS-CoV-2

virus pandemic, COVID-19. As a result, these elements were exposed to high levels of environmental degradation.

Specifically, the aggregate was obtained from the total crushing of prefabricated parts, without any dosing system in the sense that no aggregate fraction is added or removed; the economic viability, and therefore the use of recycled materials, involves processing the material as a whole aggregate of continuous granulometry, regardless of dosing in different sizes.

This research did not evaluate basic properties of the aggregates that initially form the precast elements used in the crushing process for their subsequent recovery as recycled aggregates, as it is assumed that characteristics such as chemical composition or other properties such as shape, resistance to fragmentation or cleanliness are evaluated in the quality systems for the reception of materials in any factory that has to present the mandatory CE marking for construction products in the European Union.

In this study, for practical purposes, the aggregate from the crushing of precast concrete products was considered as precast construction and demolition waste (CDWPrec). To check the suitability of the aggregate for the particle size conditions required for reinforced concrete, the Fuller method [44], was used (Figure 2), which uses the Gessner parabola as a reference curve, representing a continuous particle size.

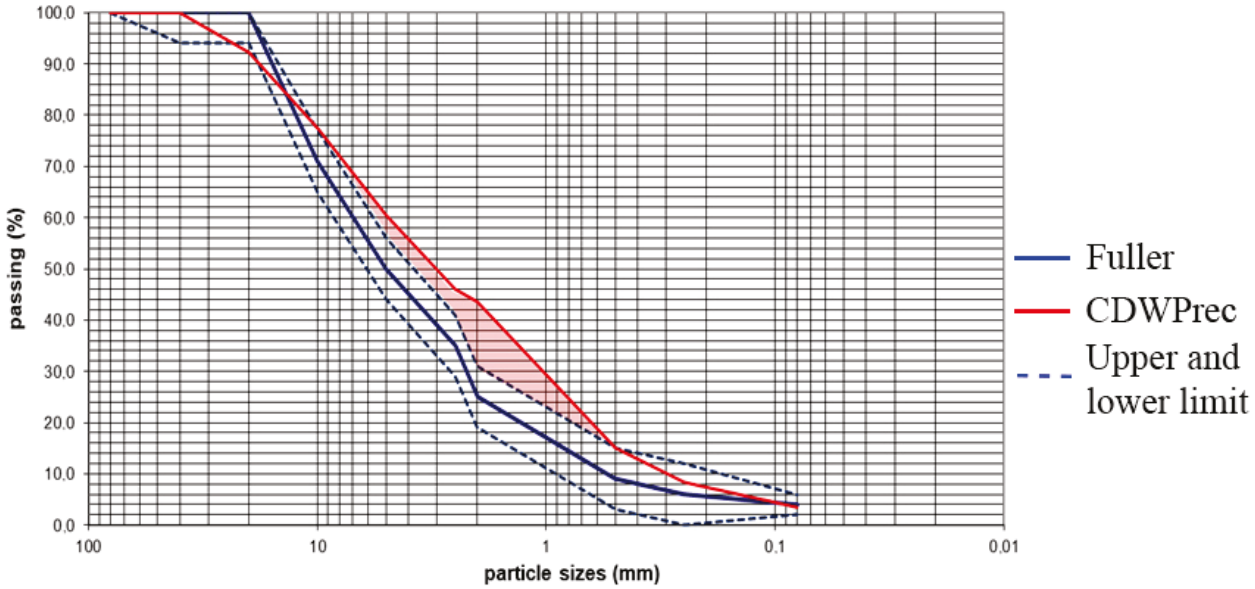

Figure 2. CDWPrec versus Fuller granulometric curve.

Figure 2 shows the lack of continuity of the precast aggregate curve, especially in the intermediate sizes, with the largest deviations of 14% in the 2 mm sieve and 6% in the 1 mm sieve. In any case, as shown later, the intermediate sizes are the least representative in terms of obtaining the strength and compactness of the concrete, so these aggregates have not been ruled out for the production of structural concrete. As repeatedly stated, the advantages of these CDWPrec aggregates must be considered in the context of a sustainable future with Industry 4.0, moving towards zero waste models and maximum sustainability.

In order to evaluate the performance of CDWPrec for concrete production, its granulometric curve was also compared with that of the Bolomey method [45] (Figure 3) for bulk concrete dosing. In this case, the reference curve is the Gessner parabola modified by a coefficient depending on the consistency and type of aggregate.

Table 1 shows the particle size distribution. In CDWPrec, values of uniformity coefficient, Cu = 20.0, and curvature coefficient, Cc = 0.8, were obtained. The high value of the uniformity coefficient shows the high size variation obtained in the unclassified crushing. On the other hand, the low value of the curvature coefficient Cc = 0.8 does not allow it to be classified as well graded, $1.0 \leq Cc \leq 3.0$.

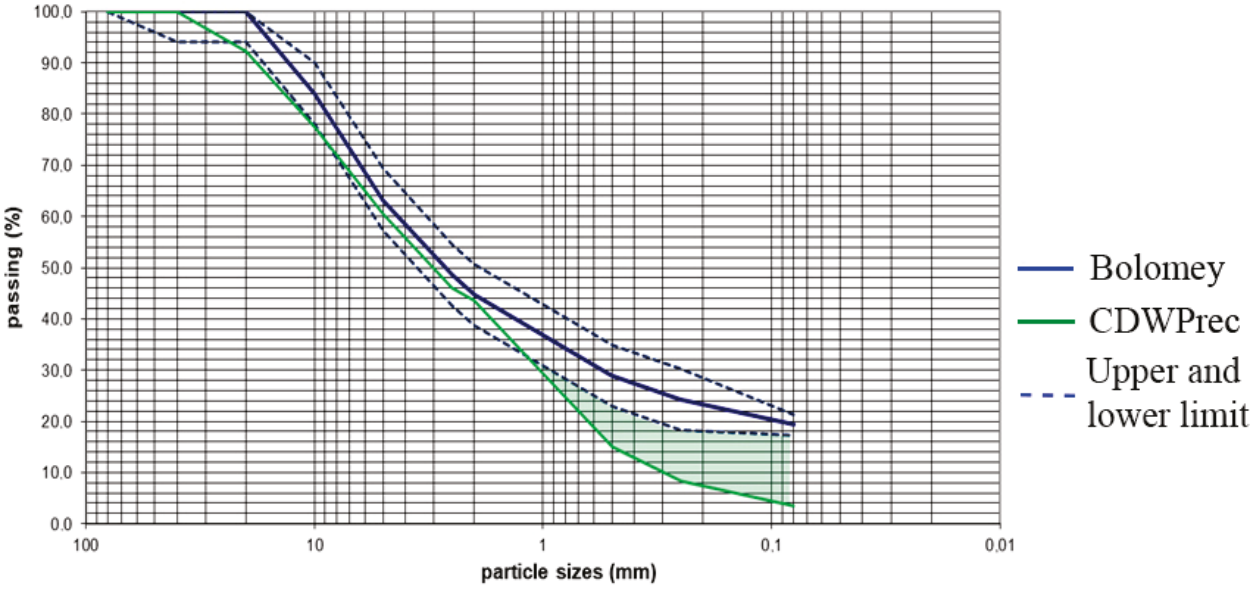

Figure 3. CDWPrec versus Bolomey granulometric curve.

Table 1. Aggregate type and particle size distribution characteristics of CDWPrec.

Material	D_{10} (mm)	D_{30} (mm)	D_{50} (mm)	D_{60} (mm)	C_u	C_c	% Fines	% Sand Size	% (4.75–9.5) mm	% (9.5–40.0) mm
CDWRCer	0.25	1.0	3.0	5.0	20	0.8	3.4	60	16	24

The high absorption associated with the porosity of the recycled aggregates is reflected in the high water–cement ratio W/C of 0.52, 2% higher than that recommended for resistant concretes with natural or artificial aggregates.

In this case, it can be seen in Figure 3 that there is a lack of fines above 1 mm, with the greatest difference being 14% in the 0.063 mm sieve, although it should be noted that this is later corrected when calculating the composite curve for this dosage method, calculating that the cement is an additional aggregate and therefore increasing the percentage of fines.

Finally, the dosage for one cubic metre of concrete was 1400 kg of CDWPrec, 410 kg of cement (C), 210 litres of water (W) and 5 litres of admixture, resulting in a ratio W/C = 0.51. The blinder used for manufacturing the concrete was cement type BL II/B-LL 42.5 R. This cement has the following components: (i) a clinker content comprising between 65 and 79%; (ii) a limestone content of 21–35%; (iii) a chloride content of $\leq$0.10; (iv) a sulphate content of $\leq$4.0; and (v) a soluble toilet chromium VI content of $\leq$0.0002%. It has a beginning setting of $\geq$60 min and an end setting of $\leq$720 min. The expansion is lesser than 10 mm. Resistance at 2 days is $\geq$20 MPa and resistance at 28 days is in the interval $42.5 \leq R \leq 62.5$ MPa. A white cement with a whiteness of $\geq$85% was chosen as an additional characteristic in the search for the best termination.

2.2. Mechanical Characterisation of the Concrete

2.2.1. Test Set up and Specimens

The proposed recycled concrete dosage was characterised by mechanical tests in order to obtain its properties and to define the material behaviour for the subsequent design of structural elements. Specifically, tests were carried out on tensile [46], compression [47] and the determination of the modulus of elasticity [48] of the concrete.

For this purpose, cylindrical and cubic specimens were manufactured in accordance with the Spanish standard UNE-EN 12390-2 [49]. The dimensions were 150 mm in diameter and 300 mm in height for the cylindrical specimens and 150 mm on each side for the cubic specimens. For the first 24 h after manufacture, the specimens were kept in their moulds at a controlled temperature of 20 ± 5 °C and then a humid chamber was used to store the specimens for the 28-day curing period. This chamber allowed controlled temperature conditions of 20 ± 2 °C and a relative humidity of more than 9% to be maintained.

The so-called Brazilian indirect tensile test was used to determine the tensile strength. During this test, a cylindrical specimen is subjected to a compressive load applied in a thin strip along its entire length. The resulting orthogonal tensile load causes the specimen to break in tensile. For this tensile test, a loading rate of 0.05 MPa/s was set.

The compressive strength test was carried out using both cylindrical and cubic specimens in order to determine the relationship between the different types of geometry and to calculate a conversion factor to extrapolate the results obtained for each test. In addition, the strain at the moment before failure, known as peak strain, was recorded in order to obtain the maximum strain. For this compressive test, a loading rate of 0.6 ± 0.2 MPa/s was set.

The modulus of elasticity was obtained from tests with compression cycles. Initially, three preload cycles were applied to stabilise the specimen, starting from an initial stress of 0.5 MPa up to a stress corresponding to 10% of the compressive strength, obtained from the previous tests. Then, three loading cycles are applied, from a lower stress corresponding to 10% of the compressive strength to a higher stress corresponding to one third of the compressive strength. The strain at the upper and lower peaks of each cycle is recorded in order to calculate the initial and stabilised secant modulus of elasticity. For both load application and load reduction, a loading rate of 0.6 ± 0.2 MPa/s was set.

Since the determination of the tensile strength was carried out by indirect methods, all tests were performed on a compression machine. In particular, a Servosis electromechanical testing machine PCD 1065W equipped with a 1500 kN load cell and corresponding compression platens was used.

2.2.2. Digital Image Correlation Fundaments and Prototype

The mechanical characterisation tests were complemented with the digital image correlation technique to measure the displacements and strains of the specimens. DIC allows these measurements to be calculated from images acquired during the testing process, comparing an initial reference image without strain with that corresponding to each of the loading states [30].

Taking into account the type of specimens used and the existence of flat and curved specimens, a different approach was used for each of them. A 2D-DIC approach was used to measure the in-plane displacements and strains of the cubic specimens, while a 3-DIC approach was used for the cylindrical specimens.

In both cases, it is necessary to carry out a preliminary preparation of the specimens. Firstly, the surface is primed with a matt white paint, and after that a speckle pattern is generated on it. In this case, the spray technique with matt black paint was used, which

makes possible to generate a stable greyscale pattern on the surface whose speckle is random, unique and non-periodic [50]. In order to evaluate the quality of the generated pattern, the Mean Intensity Gradient (MIG) parameter [51] and the coverage factor were calculated. The value obtained for the MIG was higher than 30 for all samples, with a coverage factor between 45 and 55%, considered optimal according to Lecompte et al. [52].

The prototype used for image acquisition consisted of high-resolution cameras Manta G-917B 1" (Allied Vision, Stadtroda, Germany) Monochrome CCD equipped with 50 mm macro lens and neutral LED lights to enhance illumination and facilitate acquisition (Figure 4). The synchronisation of the image acquisition and the data provided by the test machine was achieved using a Quantum data acquisition system plus an Omron CP1H programmable logic controller (PLC) that allowed the synchronisation and programming of the triggering of the different cameras.

Figure 4. Digital image correlation prototype: (**a**) 2D-DIC; and (**b**) 3D-DIC.

For the 2D-DIC approach (Figure 4a), a single camera was used and positioned perpendicular to the measurement plane using a micrometric ball joint. For the 3D-DIC approach (Figure 4b), two cameras with a stereo angle of 15° were used. In order to achieve the highest possible accuracy in the measurements, similar to a strain gauge [53], in both cases the device was placed at a distance of 1.25 m from the specimens, which allowed capturing the entire specimen surface with a GSD of 0.09 mm/px. A lens aperture of f8 and a shutter speed of 1/100 s were set to allow image acquisition with adequate illumination, depth of field and sharpness.

Once images were captured, image analysis was performed for subsets of pixels within a region of interest (ROI). DIC uses Zero mean Normalised Cross-Correlation (ZNCC) [54] to analyse and compare the subsets. This process is facilitated by the greyscale speckle pattern. The application of this criterion to all subsets of the ROI and successive images is performed by optimisation algorithms, which are combined with interpolations to achieve sub-pixel accuracy [55].

While for the 2D-DIC approach this process is carried out directly for flat images, in the 3D-DIC approach, it is necessary to carry out an orientation process prior to image acquisition that allows the conversion of image coordinates to three-dimensional coordinates. In this case, an approach similar to the one established by Solav et al. [56] was used, which combines the Bundle Adjustment (BA) algorithm with the Direct Liner Transformation (DLT) algorithm. This methodology allows obtaining the distortion and the internal and external parameters of the cameras, which are used for the three-dimensional reconstruction of the ROI points for which the displacements and strains were calculated using the procedure described above.

2.3. Structural Beam Prototype

2.3.1. Manufacture of Prototypes and Test

In order to study the feasibility of using this type of recycled concrete in structural elements, the fabrication and testing of structural beams was proposed, using a prototyping approach and test setup similar to that used by Visintin et al. [57]. Specifically, it was decided to fabricate beams with dimensions of 1200 mm, 100 mm and 125 mm for length, width and height, respectively. These beams were then subjected to four-point bending tests.

The concrete dosage used for the construction of the beams was the same as the one analysed in the mechanical tests, described in Section 2.1. In addition, the beams were reinforced trying to locate the failure in the centre and avoiding shear failure outside the central third. For this purpose, a reinforcement was designed (Figure 5) with two 10 mm ribbed bars raised to 25 mm and 6 mm wire stirrups with 40 mm spacing in the extreme thirds.

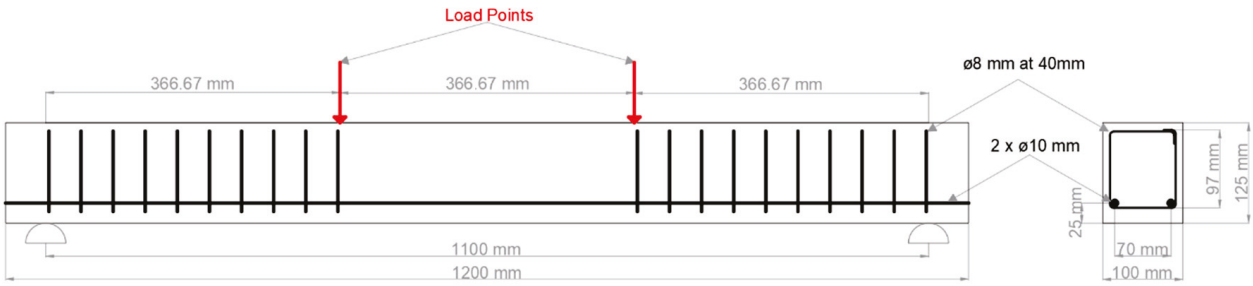

Figure 5. Dimensions and reinforcement of beam prototypes.

The beams were constructed using ad hoc formwork moulds manufactured from coated plywood panels. The reinforcements were then placed inside them and concrete spacers were used to ensure correct placement. Subsequently, the concrete mix manufactured in a concrete mixer was poured into the formwork, applying the corresponding vibration and compaction to ensure uniform distribution throughout the beam. The curing process was similar to that described for the specimens in Section 2.2.1, although in this case the moulds were removed two days after manufacture. The specimens were kept for 28 days in a humid chamber at a controlled temperature of 20 $\pm$ 2 °C and a relative humidity of more than 95%.

A platform was designed to carry out the bending tests in order to adapt the test press (Figure 6). In this case, an electromechanical test machine Servosis ME-405/50/5 was used with a 500 kN load cell. A specific bench performed by structural profiles was designed; for the specimen support, two mobile 45 mm rollers were placed at a distance of 1100 mm, working as punctual loads. In addition, a load plate was fabricated with two 13 mm rollers

welded at one third of the span (366.67 mm) for the application of the load at the two corresponding points.

2.3.2. Prediction of Flexural Performance

Taking into account the mechanical characterisation of the recycled concrete carried out in this work, it is proposed to predict the flexural performance of the manufactured beams in order to subsequently validate the experimental tests. In particular, the flexural strength and deflection of the beams are studied. For this purpose, an approach based on Eurocode 2 for the design of concrete structures [58] is proposed.

Figure 6. Platform and set up for four-point bending test of beam prototypes.

According to the design configuration proposed for the beams and their reinforcement, the equilibrium equation that determines the ultimate moment of their section is the following Equation (1):

$$M_u = f_{ck} \cdot \lambda \cdot x \cdot b \cdot \left(\frac{h}{2} - \lambda \cdot \frac{x}{2} \right) - A_s \cdot \sigma_s \cdot \left(\frac{h}{2} - d \right) \quad (1)$$

where f_{ck} is the characteristic compressive strength of concrete; λ is the coefficient defining the effective depth of the compression zone (λ = 0.8 for $f_{ck} \leq 50$ MPa); x is the depth of the neutral axis; b and h are the base and height of the beam section, respectively; A_s is the area corresponding to the reinforcement; and σ_s is the characteristic strength of concrete steel.

Based on the test and load configuration, the maximum total load and maximum deflection of the beam under ultimate moment conditions can be calculated using the following Equations (2) and (3):

$$F_{max} = 2 \cdot \frac{M_u}{a} \tag{2}$$

$$y_{max} = \frac{M_u}{24 \cdot E \cdot I_{ef}} \cdot \left(3 \cdot L^2 - 4 \cdot a^2\right) \tag{3}$$

where M_u is the ultimate moment; E is the elastic modulus of concrete; L is the beam length; a is the shear span and I_{ef} is the effective moment of inertia, defined by Equation (4):

$$I_{ef} = \frac{I_{cr}}{1 - \left(1 - \frac{I_{cr}}{I_g}\right) \cdot \left(\frac{M_{cr}}{M_u}\right)^2} \tag{4}$$

where I_{cr} is the cracked moment of inertia; I_b is the gross moment of inertia; and M_{cr} is the moment to cause cracking, which depends on the tensile strength of the concrete.

In order to provide a more accurate calculation, the usual design safety coefficients for concrete and steel strength are not used. Instead, robust design techniques are implemented to incorporate material uncertainty by adopting a probabilistic approach based on reliability. This approach takes advantage of the larger population of data obtained by the DIC technique to calculate a significant mean and covariance associated with each of the parameters. In this way, a probabilistic density function (PDF) of the main mechanical properties can be extracted.

The simulation strategy is based on using a Monte Carlo Sampling (MCS) method to generate a large set of random numbers that match the previously calculated PDFs. The proposed ultimate moment and maximum load equations are then evaluated for each of these parameters to obtain a probability density function for the corresponding results. Considering the reliability analysis, the probability of failure can be evaluated according to the following Equation (5):

$$P_f = Prob[G(Y) \leq 0] = \int\limits_{G(Y) \leq 0} p_y(Y) dY \tag{5}$$

where P_f is the probability of failure; G is the performance function; Y is the variable's vector and p_y is the joint probability density function.

Taking into account that the analytical theoretical models include several variables and that a probabilistic analysis is chosen, it is important to know the influence of each input on the final result. To this end, the MCS strategy allows an adequate sampling of the parameters used in the model, thus generating equiprobable situations to carry out a sensitivity analysis. The strategy used is based on the estimation of so-called Sobol indices [59], which assume that the sum of the variances of the input parameters represents the variance of the model output, Equation (6). Sobol indices of different orders (from 1 to 2n − 1) can be obtained by considering the normalisation of each variance with respect to the total variance, Equation (7). The sum of these indices is the overall Sobol index. Likewise, the sum of all their values is equal to 1.

$$V(Y) = \sum_i V_i + \sum_i \sum_{j>i} V_{ij} + \sum_i \sum_{j>i} \sum_{k>j} V_{ijk} + \ldots V_{123..N} \tag{6}$$

where $V(Y)$ is the variance of the model; $V_i = V(E(Y \mid X_i))$ is the first-order partial variance; $V_{ij} = V(E(Y \mid X_i,X_j))$ is the second-order partial variance, etc.

$$S_i = \frac{V_i}{V(Y)}, S_{ij} = \frac{V_{ij}}{V(Y)} \tag{7}$$

where S_i is the first-order Sobol index and S_{ij} is the second-order Sobol indices.

3. Experimental Results

3.1. Mechanical Properties of the Recycled Concrete Evaluated

A total of 20 specimens were tested for indirect tensile, compression and elasticity according to UNE-EN 12390-6 [46], UNE-EN 12390-3 [47] and UNE-EN 12390-13 [48], respectively. Additionally, the compressive strength tests were duplicated as they were performed for both cylindrical and cubic specimens. Finally, to determine the workability of the concrete, two slump tests were carried out according to UNE-EN 12350-2 [60], with a result of 16 cm, which corresponds to a fluid consistency.

The DIC technique described in Section 2.2.2 was used to obtain displacements and strain values. A 2D-DIC approach was used for cubic specimens using the open source software Ncorr (Version 1.2) [55] and a 3D-DIC approach was used for cylindrical specimens using the open source software MultiDIC (Version 1.0) [56]. The processing parameters were similar in both cases, defining an ROI covering the entire specimen and using a subset size of 20 × 20 pixels with a step of 7 pixels, which ensured an overlap of 65%. In addition, a checkerboard calibration target was used to remove image distortion and perform 3D reconstruction using the DLT algorithm.

To obtain the longitudinal strains, several virtual extensometers were placed in order to analyse the entire surface of the region and exploit the potential of DIC. Nevertheless, due to regulatory restrictions, the strain cannot be measured over the entire surface, but it has to be considered in the central third of the specimen. Taking into account the dimensions of the specimens, a total of 10 virtual extensometers with a spacing of 15 mm were placed on each specimen (Figure 7) to analyse their behaviour and spatial influence.

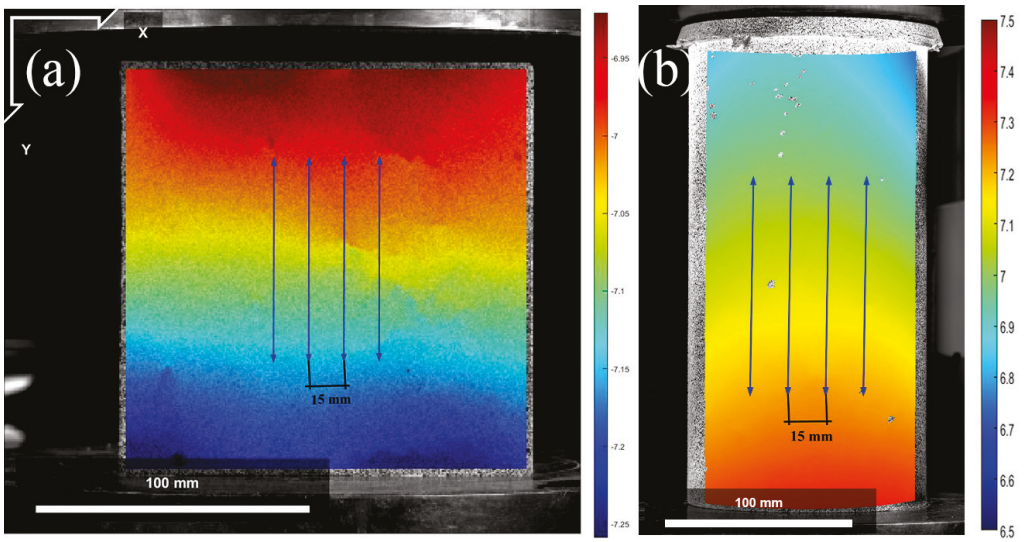

Figure 7. Longitudinal displacements obtained using DIC and extraction of longitudinal strain using the virtual strain gauge: (**a**) cubic specimens with 2D-DIC approach; and (**b**) cylindrical specimens with 3D-DIC approach.

For the compression tests, the peak longitudinal strain at maximum load prior to failure was recorded on virtual extensometers placed over the entire surface. For the elasticity tests, the strain at the maximum and minimum of the applied load and unloading cycles was obtained, as well as over the entire surface.

Considering all the test types and specimens, as well as the virtual extensometers placed on them, the results of the mechanical characterisation are shown in Table 2. Along with the mean values, the main statistical parameters such as standard deviation (STD), coefficient of variation (CoV) and lower and upper bounds are also presented, which allow the behaviour and heterogeneity of these properties to be analysed.

Table 2. Results obtained from the mechanical characterization.

Property	Mean	STD	CoV (%)	Lower Bound	Upper Bound
$f_{c\text{-}cyl}$	36.5	4.3	11.8	29.1	39.4
$f_{c\text{-}cub}$	40.5	2.2	5.4	37.8	43.5
f_{ti}	2.8	0.3	11.2	2.5	3.1
E	27.62	4.56	16.5	21.18	36.82
$\varepsilon_{p\text{-}cyl}$	0.0021	0.0002	11.6	0.0017	0.0026
$\varepsilon_{p\text{-}cub}$	0.0034	0.0006	18.3	0.0023	0.0048

$f_{c\text{-}cyl}$ = Compressive strength of cylindrical specimens (MPa). $f_{c\text{-}cub}$ = Compressive strength of cubic specimens (MPa). f_{ti} = Indirect tensile strength (MPa). E = Secant modulus of elasticity in compression (GPa). $\varepsilon_{p\text{-}cyl}$ = Peak strain at time of maximum stress of cylindrical specimens. $\varepsilon_{p\text{-}cub}$ = Peak strain at time of maximum stress of cubic specimens.

The dosed concrete offered a compressive strength, related to cylindrical specimens, of $f_{c\text{-}cyl}$ = 36.5 MPa. On the other hand, a compressive strength of $f_{c\text{-}cub}$ = 40.5 MPa was obtained from tests carried out on 15 cm cubic specimens. This implies a conversion coefficient from cubic to cylindrical specimens, γ = 0.90, which is similar to the coefficient usually used for conventional concretes with a strength value UCS < 60 MPa. It is worth noting that the results for the cubic specimens showed less variation, with a CoV of 5.4% compared to a CoV of 11.8% for the cylindrical specimens. The larger contact surface for the cubes may be one of the reasons for the greater homogeneity of these results. In any case, very high compressive strength values were obtained, with only one specimen below 30 MPa, allowing the sustainable concrete studied to be classified as HA-30 according to the Spanish Structural Code [19].

The high minimum resistance of 30 MPa obtained makes it possible to meet the durability requirements for all environmental exposure classes and, in all cases, to comply with the dosage parameters for the minimum cement content, with a high cement content C > 400 kg/m^3, thus obtaining a concrete with reduced permeability.

Tensile strength f_{ct} is usually obtained from indirect tensile strength f_{ci}, which for concretes made with CDWPrec has an average value of f_{ti} = 2.8 MPa, i.e., tensile strength f_{tk} = 2.5 MPa.

The modulus of elasticity showed an outcome of 27.6 GPa, which is very similar to the experimental value obtained when strains in concretes made by conventional aggregates is calculated.

The peak strain at the time of maximum stress was 0.0021 for cylindrical specimens and 0.0034 for cubic specimens. In this case, the conversion coefficient between the two types of specimens is approximately 0.6. While for cylindrical specimens the value is similar to the 2‰ generally considered for conventional concrete, for cubic specimens the strain is higher, also associated with the higher strength that this type of specimen achieves due to its geometry.

The high CoV in the modulus of elasticity and ultimate strain results show the heterogeneous behaviour of these materials. Although heterogeneity is present in conventional

concrete, particularly in the strains produced by the phase change between aggregates of different sizes, recycled aggregates accentuate this irregularity due to their own characteristics, such as in the case of greater disaggregation of aggregates and cement [61]. It should also be noted that the compressive and tensile strength data are unique to each specimen. Nevertheless, the ultimate strain and modulus of elasticity data also take into account the spatial variability of the material within the specimen itself. This is because DIC allows multiple measurements to be taken within a single specimen. Issues such as manufacturing heterogeneity, inaccuracies in the alignment of the press during the test, or edge effects can lead to higher variability and therefore increase the CoV of these data.

3.2. Beam Performance

The approach proposed in Section 2.3.2 for predicting the bending behaviour through reliability analysis allows the uncertainty in the behaviour to be quantified. To introduce this uncertainty, the populations of results obtained in the previous section were fitted to probabilistic distributions functions by performing goodness-of-fit tests. The candidate PDFs were selected based on physical considerations and other experimental campaigns with similar methodologies [33,62]. To obtain a larger population size, both cylindrical and cubic sample values were used, applying conversion factor $\gamma = 0.90$. Considering that most of the data accepted all the tests, a lognormal distribution was chosen, including the mean and the deviation for each of the parameters, as shown in Table 2. In particular, after goodness-of-fit tests, a lognormal distribution was selected since, in contrast to the normal distribution, these physical parameters cannot reach negative values.

Taking into account the model defined to obtain the maximum theoretical load, the variables related to the properties of the concrete were introduced as probabilistic variables, except for the tensile strength. In this case, due to its low value in relation to the steel used, the tensile strength of the concrete was not included in the calculation. In the case of the steel parameters, the properties corresponding to a B400S steel were used as a constant input. The ultimate strain of the recycled concrete was also used for the ultimate stress testing domain.

With regard to the model for obtaining the deflection, the experimentally obtained compressive and tensile strengths and the modulus of elasticity were taken into account according to Equations (3) and (4). Due to the difficulty of knowing exactly the effective moment of inertia, a probabilistic coefficient of uniform distribution in the range of 30 to 50% was also introduced in this case and applied to the gross moment of inertia. The uniform distribution was chosen in this case due to the complexity of knowing this parameter and to achieve an equiprobable and uniform sampling. The higher uncertainty of this parameter is a handicap in accurately predicting the deflection result.

In order to obtain a probabilistic density function for the maximum load and deflection supported by a beam manufactured with the recycled concrete studied, a total of 10^6 simulations were carried out using MCS for the previously defined model parameters. The distribution of the simulation results is shown in Figure 8a for the maximum load and in Figure 8b for the deflection.

Both graphs show how the results are distributed according to a distribution that can be considered lognormal, with the modal value close to the mean. The most frequent value for the maximum load is 49.65 kN, while the most frequent value for the deflection is 9.32 mm.

In order to validate the model and obtain the real behaviour of the recycled concrete bending beams, the experimental tests described in Section 2.3.1 were carried out. A total of six beams made of the studied recycled concrete were tested with the proposed config-

uration. A sample of six beams was used to strike a balance between representativeness of results and practical constraints such as available resources. This sample size ensures a variety of representative conditions from which meaningful conclusions can be drawn. This representative sample allows the model to be validated so that it can be scaled up and generalised to larger populations through further statistical analysis, such as Monte Carlo simulations.

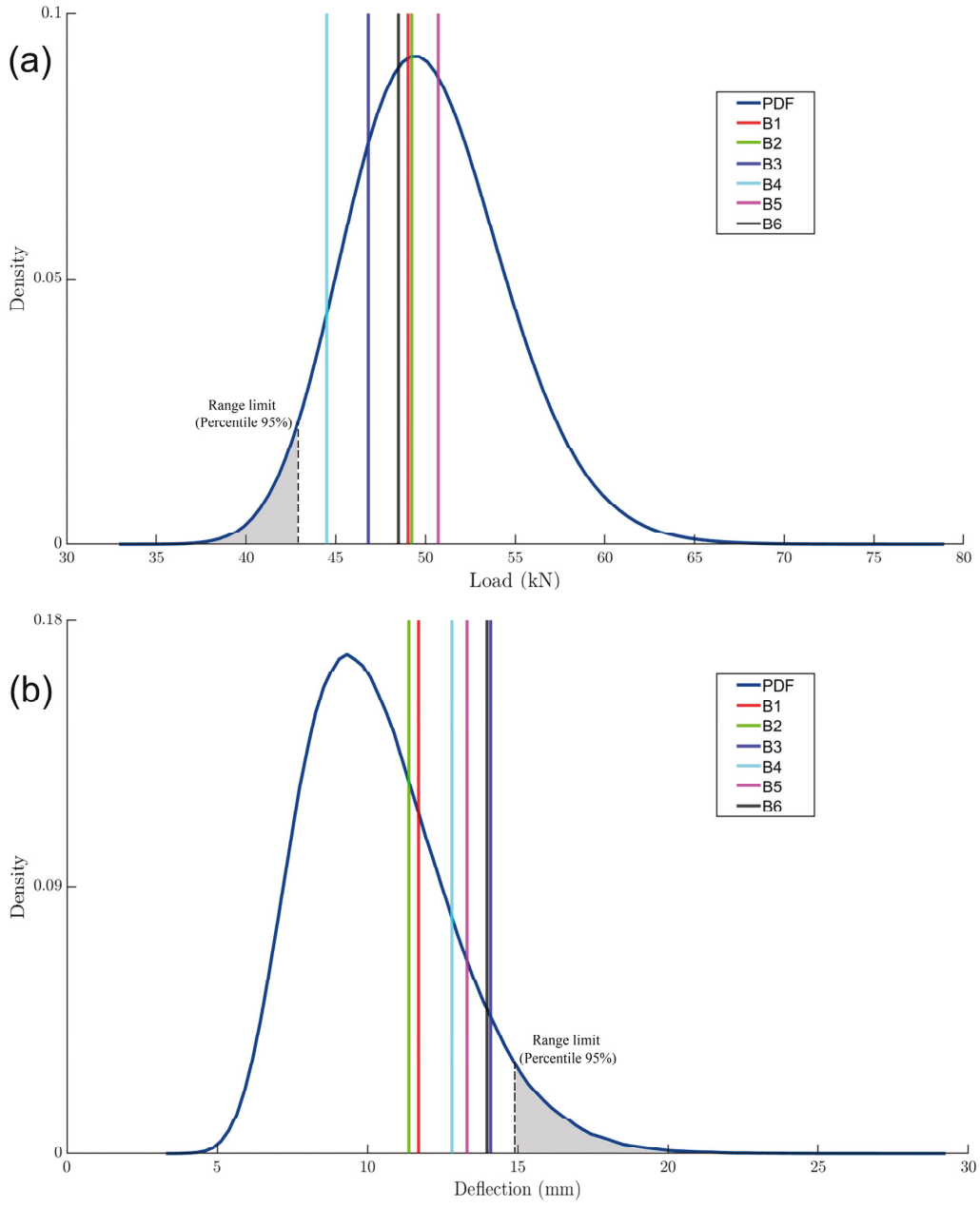

Figure 8. Graphical representation of the probabilistic density function (PDF) obtained from the simulation results together with the values obtained from the experimental tests of the six beams (B1–B6): (**a**) maximum load; and (**b**) deflection.

The results corresponding to the maximum load and deflection of each of the beams are also shown in Figures 8a and 8b, respectively. The DIC technique was also used to calculate the deflection experimentally. Due to the span of the beam, only a central ROI

was selected where the largest displacements occur. A set of 5 × 5 px under the midpoint was then taken to obtain the average deflection.

The behaviour of all tested beams is within the PDF obtained from the simulation. For the case of the maximum load, the experimental results are close to the modal value. Only beams B3 and B4 are slightly further away from this central value. In the case of deflection, the experimental results are further apart and in all cases exceed the modal value of deflection. One of the reasons for this greater dispersion is the greater number of probabilistic parameters involved in this simulation. In addition, the difficulty of predicting deflection in reinforced concrete is greater because parameters such as the effective moment of inertia or the moment to cause cracking are less accurately estimated. Even some factors such as creep or shrinkage are not taken into account in the theoretical analytical models for calculating deflection. In any case, all the results were within the range predicted by the reliability analysis, so it can be assumed that the model is valid and reliable.

From the reliability analysis and the probability of failure corresponding to each load and deflection, the percentile in which the behaviour of each beam is located was calculated. The results of the maximum load and deflection of each beam, together with their corresponding, are shown in Table 3.

Table 3. Experimental test results for the bending beams tested.

Beam	Load (kN)	P_{load} (%)	Deflection (mm)	P_{def} (%)
B1	49.02	58.2	11.70	73.2
B2	49.23	56.3	11.38	69.4
B3	46.83	77.1	14.11	92.0
B4	44.51	91.0	12.81	84.0
B5	50.72	42.8	13.31	87.6
B6	48.50	63.0	13.98	91.4

The following criteria were used to calculate the percentiles: higher maximum load values correspond to better behaviour and lower percentiles; higher deflection values correspond to worse behaviour and higher percentiles. The results obtained in calculating the percentiles allow us to quantify the above for the behaviour of the experimental tests. The experimental results for maximum load show percentiles close to the mean, except for specimen B4, which is in the last decile. The experimental deflection results show higher percentiles, mostly in the last quartile.

It should be noted that the analytical models used did not include safety coefficients, so it is understandable that the results are not in the first percentiles. Other factors other than the main properties obtained experimentally, such as creep or shrinkage deformation, which should be taken into account to improve the accuracy of the model, were also not included. In addition, all the tests were within an acceptable range, as none of them exceeded what could be considered a limit of 5%.

In order to understand which variables are most relevant in the theoretical analytical performance model of recycled concrete, a Sobol sensitivity analysis was carried out. As the prediction of deflection was the most complex model with the most variables and the most dispersed behaviour, the analysis was performed on this model. The same analytical model used for the reliability-based design analysis was employed, with input variables including the compressive strength, tensile strength, and modulus of elasticity of the recycled concrete, as well as the coefficient for calculating the effective moment of inertia. Similarly, the variability of these parameters was introduced by means of their corresponding PDF. In order to carry out this sensitivity analysis, a total of 10^6 simulations were carried out using MCS. For each of these simulations, the input parameters were

given a random value based on the distributions and ranges obtained in the experimental tests. The variances of the input parameters were analysed with respect to the variance of the model outputs, which allowed Sobol indices to be obtained. The results of this analysis are shown in Figure 9 for both the first-order and total indices. It can be seen that both indices are practically similar, so the second-order indices can be discarded.

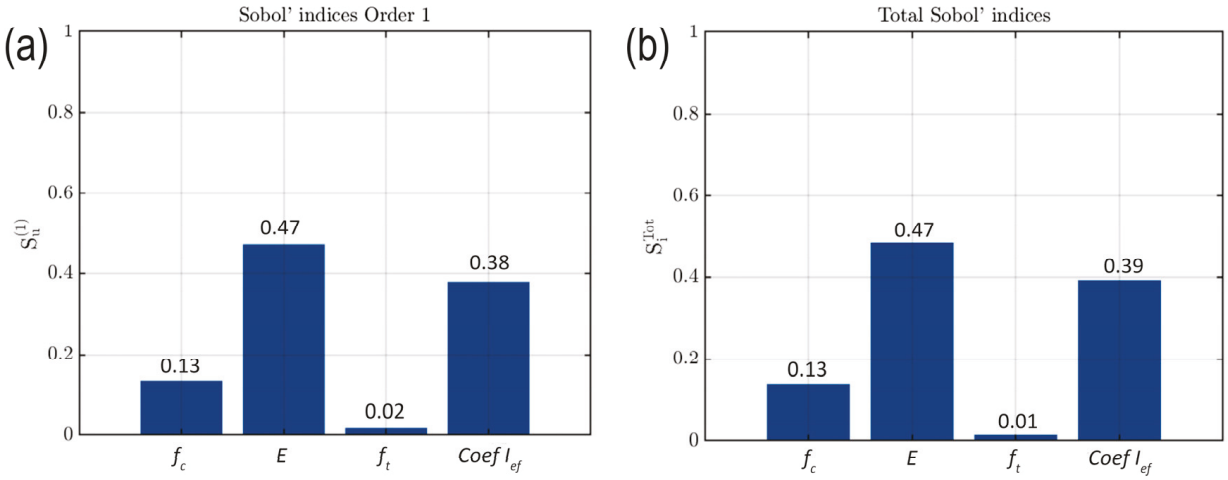

Figure 9. Results obtained during the sensitivity analysis of the deflection model: (**a**) first-order Sobol indices; and (**b**) total Sobol indices.

According to these results, the most relevant parameter in the deflection model is the modulus of elasticity of the concrete, accounting for 47% of the total variance. On the other hand, the parameter with the least influence is the tensile strength of the concrete, with an index of 0.01 (1%), as it is only used for the calculation of the moment to cause cracking. It is also worth mentioning the high influence (39%) of the coefficient used to calculate the effective moment of inertia. Considering that this is a complex parameter to calculate experimentally, this may explain the lower accuracy of the model.

4. Conclusions

This work aimed to investigate the characterisation of structural recycled concrete for the production of beams. The concrete was produced by replacing all the natural aggregates with recycled aggregates from precast concrete rejects. These aggregates have been considered as all-in-one, which represents an advantage in terms of economy and operability for the manufacturing process, in addition to the already known environmental benefits due to the reduction of waste and the lower extraction of raw materials, as set out in the targets of "Goal 12: Responsible consumption and production" of the Sustainable Development Goals established by the United Nations.

Firstly, the analysis of the recycled aggregates showed the adaptability of their granulometric curve to the Fuller method, which allows them to be used in the production of concrete. Subsequently, a large number of cubic and cylindrical specimens were made in order to obtain the main mechanical properties of the recycled concrete. These tests allowed the definition of a HA-30 structural recycled concrete. In addition, the digital image correlation technique was used to obtain more accurate and full-filed strains. Thanks to this technique, the high heterogeneity of the material and the difference found between the results of the cylindrical and cubic specimens were analysed.

The results of the experimental characterisation were then used to define an analytical theoretical model to obtain the maximum load and deflection in bending beams. The

data provided by DIC allowed a reliability-based probabilistic approach to be adopted, performing one million simulations by modifying the input parameters according to the distributions calculated from the experimental tests. This allowed to obtain a probabilistic density function for the maximum load and deflection of the recycled concrete beams studied.

Finally, the theoretical simulations were validated by experimental tests, in which six beams were manufactured and tested in the laboratory. In all cases, the results were in agreement with the model, and the predicted values were within the acceptable range. These results demonstrate the great potential of the proposed methodology to characterise and predict the behaviour of recycled concrete structural elements. Nevertheless, the strength prediction model was more accurate than the deflection model, so a sensitivity analysis of the parameters included in the model was carried out to better understand its behaviour. The results showed a higher influence of the modulus of elasticity (47%), followed by the arbitrary coefficient used to calculate the effective moment of inertia (39%). The difficulty in precisely determining this parameter may account for the model's lower accuracy and represents one of its potential weaknesses. Furthermore, it should be noted that a simple analytical theoretical model was chosen for this study, which presents a limitation when incorporating certain indirect factors. Factors such as interfacial slippage, creep or shrinkage, although having less direct influence, can affect the result and limit the accuracy of the model if they are not taken into account.

One of the main future works will focus on improving the analytical theoretical model, trying to include some of these factors that could improve the accuracy of the results, e.g., creep or shrinkage deformation, and even using a Bayesian approach to adjust the results from the experimental data with a larger number of samples and variability in loading or experimental conditions such as temperature and humidity. In addition, adaptation of the model parameters to material properties and configurations from existing studies could help to validate its extrapolation so that it can be generalised and its use extended to the scientific community. The next step will be to apply this methodology to more complex models by carrying out simulations using the finite element method, in which a more thorough analysis of the behaviour of the elements can be carried out. The results of these full-field models are intended to be compared with full-field experimental measurements obtained through digital image correlation.

Author Contributions: Conceptualization, J.L.-R.; methodology, J.L.-R.; formal analysis, J.L.-R., E.T.-L.-Z., R.G.-M. and L.J.S.-A.; investigation, J.L.-R. and E.T.-L.-Z.; writing—original draft preparation, J.L.-R.; writing—review and editing, J.L.-R., E.T.-L.-Z., R.G.-M., L.J.S.-A. and D.G.-A.; supervision, L.J.S.-A. and D.G.-A.; funding acquisition, R.G.-M. and D.G.-A. All authors have read and agreed to the published version of the manuscript.

Funding: This research was funded by Junta of Castilla y León through the TCUE 2021–2023 program within the framework of the DUTIMEC project (Nº Ref. PC-TCUE21-23_068).

Institutional Review Board Statement: Not applicable.

Informed Consent Statement: Not applicable.

Data Availability Statement: Data are contained within the article.

Acknowledgments: The authors want to thank the Spanish Ministry of Education, Culture and Sports for providing an FPU grant (Training Program for Academic Staff) to the corresponding author of this paper (grant number FPU20/01376).

Conflicts of Interest: The authors declare no conflicts of interest.

References

1. United Nations. *Transforming Our World: The 2030 Agenda for Sustainable Development*; United Nations: New York, NY, USA, 2015.
2. Akhtar, A.; Sarmah, A.K. Construction and demolition waste generation and properties of recycled aggregate concrete: A global perspective. *J. Clean. Prod.* **2018**, *186*, 262–281. [CrossRef]
3. Gálvez-Martos, J.-L.; Styles, D.; Schoenberger, H.; Zeschmar-Lahl, B. Construction and demolition waste best management practice in Europe. *Resour. Conserv. Recycl.* **2018**, *136*, 166–178. [CrossRef]
4. Eurostat. Generation of Waste by Waste Category, Hazardousness and NACE Rev. 2 Activity. Available online: https://ec.europa.eu/eurostat/databrowser/view/env_wasgen/default/table?lang=en (accessed on 1 September 2024).
5. Xiao, J.; Xie, H.; Zhang, C. Investigation on building waste and reclaim in Wenchuan earthquake disaster area. *Resour. Conserv. Recycl.* **2012**, *61*, 109–117. [CrossRef]
6. de Brito, J.; Kurda, R. The past and future of sustainable concrete: A critical review and new strategies on cement-based materials. *J. Clean. Prod.* **2021**, *281*, 123558.
7. Arezoumandi, M.; Smith, A.; Volz, J.S.; Khayat, K.H. An experimental study on flexural strength of reinforced concrete beams with 100% recycled concrete aggregate. *Eng. Struct.* **2015**, *88*, 154–162. [CrossRef]
8. Regulation, E.U. *No 305/2011 of the European Parliament and of the Council of 9 March 2011 Laying down Harmonised Conditions for the Marketing of Construction Products and Repealing Council Directive 89/106*; European Parliament and of the Council: Brussels, Belgium, 2011.
9. Gonçalves, P.; Brito, J.D. Recycled aggregate concrete (RAC)—Comparative analysis of existing specifications. *Mag. Concr. Res.* **2010**, *62*, 339–346. [CrossRef]
10. Juan-Valdés, A.; Rodríguez-Robles, D.; García-González, J.; Guerra-Romero, M.I.; Morán-del Pozo, J.M. Mechanical and microstructural characterization of non-structural precast concrete made with recycled mixed ceramic aggregates from construction and demolition wastes. *J. Clean. Prod.* **2018**, *180*, 482–493. [CrossRef]
11. Guo, Z.; Tu, A.; Chen, C.; Lehman, D.E. Mechanical properties, durability, and life-cycle assessment of concrete building blocks incorporating recycled concrete aggregates. *J. Clean. Prod.* **2018**, *199*, 136–149. [CrossRef]
12. Tamashiro, J.R.; Kinoshita, A.; Silva, L.H.P.; de Paiva, F.F.G.; Antunes, P.A.; Simões, R.D. Compressive resistance of concrete produced with recycled concrete aggregate and sugarcane vinasse waste-water. *Clean. Eng. Technol.* **2022**, *6*, 100362. [CrossRef]
13. Rodríguez, C.; Parra, C.; Casado, G.; Miñano, I.; Albaladejo, F.; Benito, F.; Sánchez, I. The incorporation of construction and demolition wastes as recycled mixed aggregates in non-structural concrete precast pieces. *J. Clean. Prod.* **2016**, *127*, 152–161. [CrossRef]
14. Datta, S.D.; Sobuz, M.H.R.; Akid, A.S.M.; Islam, S. Influence of coarse aggregate size and content on the properties of recycled aggregate concrete using non-destructive testing methods. *J. Build. Eng.* **2022**, *61*, 105249. [CrossRef]
15. Martín-Morales, M.; Zamorano, M.; Ruiz-Moyano, A.; Valverde-Espinosa, I. Characterization of recycled aggregates construction and demolition waste for concrete production following the Spanish Structural Concrete Code EHE-08. *Constr. Build. Mater.* **2011**, *25*, 742–748. [CrossRef]
16. Fiol, F.; Thomas, C.; Muñoz, C.; Ortega-López, V.; Manso, J.M. The influence of recycled aggregates from precast elements on the mechanical properties of structural self-compacting concrete. *Constr. Build. Mater.* **2018**, *182*, 309–323. [CrossRef]
17. Velay-Lizancos, M.; Vazquez-Burgo, P.; Restrepo, D.; Martinez-Lage, I. Effect of fine and coarse recycled concrete aggregate on the mechanical behavior of precast reinforced beams: Comparison of FE simulations, theoretical, and experimental results on real scale beams. *Constr. Build. Mater.* **2018**, *191*, 1109–1119. [CrossRef]
18. Liao, Z. Bond-Slip Behavior and Tensile Stiffness of FRP Reinforcement and Precast Recycled Aggregate Concrete. Master's Thesis, Guangdong University of Technology, Guangzhou, China, 2023.
19. *Real Decreto 470/2021, de 29 de junio, por el que se aprueba el Código Estructural*; Ministerio de Fomento, Gobierno de España: Madrid, Spain, 2021.
20. Yu, Y.; Pacheco-Torgal, F.; Zhao, X.-Y.; Wang, X.-L. Cleaner production of the precast concrete industry: Comparative life cycle analysis of concrete using recycled aggregates from crushed precast rejects. *Eur. J. Environ. Civ. Eng.* **2024**, *28*, 1014–1038. [CrossRef]
21. Pérez Benedicto, J.Á.; del Río Merino, M.; Canudo, J.L.P.; La Mata, M.d.l.R. Características mecánicas de hormigones con áridos reciclados procedentes de los rechazos en prefabricación. *Mater. Construcción* **2012**, *62*, 25–37. [CrossRef]
22. Zhao, Z.; Courard, L.; Groslambert, S.; Jehin, T.; Leonard, A.; Xiao, J. Use of recycled concrete aggregates from precast block for the production of new building blocks: An industrial scale study. *Resour. Conserv. Recycl.* **2020**, *157*, 104786. [CrossRef]
23. Soares, D.; De Brito, J.; Ferreira, J.; Pacheco, J. Use of coarse recycled aggregates from precast concrete rejects: Mechanical and durability performance. *Constr. Build. Mater.* **2014**, *71*, 263–272. [CrossRef]

24. Thomas, C.; Setién, J.; Polanco, J.A. Structural recycled aggregate concrete made with precast wastes. *Constr. Build. Mater.* **2016**, *114*, 536–546. [CrossRef]
25. Yu, Y.; Fang, G.-H.; Kurda, R.; Sabuj, A.R.; Zhao, X.-Y. An agile, intelligent and scalable framework for mix design optimization of green concrete incorporating recycled aggregates from precast rejects. *Case Stud. Constr. Mater.* **2024**, *20*, e03156. [CrossRef]
26. Fiol, F.; Revilla-Cuesta, V.; Skaf, M.; Thomas, C.; Manso, J.M. Scaled concrete beams containing maximum levels of coarse recycled aggregate: Structural verifications for precast-concrete building applications. *Struct. Concr.* **2023**, *24*, 3476–3497. [CrossRef]
27. Revilla-Cuesta, V.; Fiol, F.; Perumal, P.; Ortega-López, V.; Manso, J.M. Using recycled aggregate concrete at a precast-concrete plant: A multi-criteria company-oriented feasibility study. *J. Clean. Prod.* **2022**, *373*, 133873. [CrossRef]
28. Pedro, D.; De Brito, J.; Evangelista, L. Influence of the use of recycled concrete aggregates from different sources on structural concrete. *Constr. Build. Mater.* **2014**, *71*, 141–151. [CrossRef]
29. Xiao, J.; Zhang, K.; Akbarnezhad, A. Variability of stress-strain relationship for recycled aggregate concrete under uniaxial compression loading. *J. Clean. Prod.* **2018**, *181*, 753–771. [CrossRef]
30. Sutton, M.A.; Orteu, J.J.; Schreier, H.X. *Image Correlation for Shape, Motion and Deformation Measurements: Basic Concepts, Theory and Applications*; Springer Science & Business Media: New York, NY, USA, 2009.
31. Pisonero, J.; López-Rebollo, J.; García-Martín, R.; Rodríguez-Martín, M.; Sánchez-Aparicio, L.J.; Muñoz-Nieto, A.; González-Aguilera, D. A comparative study of 2D and 3D digital image correlation approaches for the characterization and numerical analysis of composite materials. *IEEE Access* **2021**, *9*, 160675–160687. [CrossRef]
32. Villarino, A.; López-Rebollo, J.; Antón, N. Analysis of Mechanical Behavior through Digital Image Correlation and Reliability of Pinus halepensis Mill. *Forests* **2020**, *11*, 1232. [CrossRef]
33. Garcia-Martin, R.; López-Rebollo, J.; Sánchez-Aparicio, L.J.; Fueyo, J.G.; Pisonero, J.; Gonzalez-Aguilera, D. Digital image correlation and reliability-based methods for the design and repair of pressure pipes through composite solutions. *Constr. Build. Mater.* **2020**, *248*, 118625. [CrossRef]
34. María, R.-M.; Paula, V.-L.; Jaime, F.-G.; Jorge, L.R. Improvement of tensile properties of carbon fibre-reinforced cementitious matrix composites with coated textile and enhanced mortars. *Constr. Build. Mater.* **2023**, *369*, 130552. [CrossRef]
35. Le, D.B.; Tran, S.D.; Torero, J.L.; Dao, V.T.N. Application of digital image correlation system for reliable deformation measurement of concrete structures at high temperatures. *Eng. Struct.* **2019**, *192*, 181–189. [CrossRef]
36. Dzaye, E.D.; Tsangouri, E.; Spiessens, K.; De Schutter, G.; Aggelis, D.G. Digital image correlation (DIC) on fresh cement mortar to quantify settlement and shrinkage. *Arch. Civ. Mech. Eng.* **2019**, *19*, 205–214. [CrossRef]
37. Abdulqader, A.; Rizos, D.C. Advantages of using digital image correlation techniques in uniaxial compression tests. *Results Eng.* **2020**, *6*, 100109. [CrossRef]
38. Liu, B.; Guo, J.; Wen, X.; Zhou, J.; Deng, Z. Study on flexural behavior of carbon fibers reinforced coral concrete using digital image correlation. *Constr. Build. Mater.* **2020**, *242*, 117968. [CrossRef]
39. Ni, P.; Li, J.; Hao, H.; Yan, W.; Du, X.; Zhou, H. Reliability analysis and design optimization of nonlinear structures. *Reliab. Eng. Syst. Saf.* **2020**, *198*, 106860. [CrossRef]
40. Zhou, Y.; Zhang, J.; Li, W.; Hu, B.; Huang, X. Reliability-based design analysis of FRP shear strengthened reinforced concrete beams considering different FRP configurations. *Compos. Struct.* **2020**, *237*, 111957. [CrossRef]
41. Huang, X.; Zhou, Y.; Li, W.; Hu, B.; Zhang, J. Reliability-based design of FRP shear strengthened reinforced concrete Beams: Guidelines assessment and calibration. *Compos. Struct.* **2023**, *323*, 117421. [CrossRef]
42. Ramamoorthy, D.; Guo, B.; Kazmi, S.M.S.; Wu, Y. A Reliability-Based Design Approach for the Flexural Resistance of Compression Yielded Fibre-Reinforced Polymer (FRP)-Reinforced Concrete Beams. *Buildings* **2024**, *14*, 2415. [CrossRef]
43. Meng, Z.; Yıldız, B.S.; Li, G.; Zhong, C.; Mirjalili, S.; Yildiz, A.R. Application of state-of-the-art multiobjective metaheuristic algorithms in reliability-based design optimization: A comparative study. *Struct. Multidiscip. Optim.* **2023**, *66*, 191. [CrossRef]
44. Fuller, W.B.; Thompson, S.E. The laws of proportioning concrete. *Trans. Am. Soc. Civ. Eng.* **1907**, *59*, 67–143. [CrossRef]
45. Bolomey, J. Détermination de la Résistance à la Compression des Mortiers et Bétons. *Bull. Tech. la Suisse Rom.* **1925**, *51*, 126–132.
46. *UNE-EN 12390-6:2010*; Ensayos de Hormigón Endurecido. Parte 6: Resistencia a Tracción Indirecta de Probetas. AENOR: Madrid, Spain, 2010.
47. *UNE-EN 12390-3:2020*; Ensayos de Hormigón Endurecido. Parte 3: Determinación de la Resistencia a Compresión de Probetas. AENOR: Madrid, Spain, 2020.
48. *UNE-EN 12390-13:2022*; Ensayos de Hormigón Endurecido. Parte 13: Determinación del Módulo Secante de Elasticidad en Compresión. AENOR: Madrid, Spain, 2022.
49. *UNE-EN 12390-2:2020*; Ensayos de Hormigón Endurecido. Parte 2: Fabricación y Curado de Probetas para Ensayos de Resistencia. AENOR: Madrid, Spain, 2020.

50. Dong, Y.L.; Pan, B. A review of speckle pattern fabrication and assessment for digital image correlation. *Exp. Mech.* **2017**, *57*, 1161–1181. [CrossRef]
51. Pan, B.; Lu, Z.; Xie, H. Mean intensity gradient: An effective global parameter for quality assessment of the speckle patterns used in digital image correlation. *Opt. Lasers Eng.* **2010**, *48*, 469–477. [CrossRef]
52. Lecompte, D.; Sol, H.; Vantomme, J.; Habraken, A. Analysis of speckle patterns for deformation measurements by digital image correlation. In *SPECKLE06: Speckles, From Grains to Flowers*; SPIE: Bellingham, WA, USA, 2006; pp. 80–85.
53. Garcia-Martin, R.; Bautista-De Castro, Á.; Sánchez-Aparicio, L.J.; Fueyo, J.G.; Gonzalez-Aguilera, D. Combining digital image correlation and probabilistic approaches for the reliability analysis of composite pressure vessels. *Arch. Civ. Mech. Eng.* **2019**, *19*, 224–239. [CrossRef]
54. Pan, B.; Qian, K.; Xie, H.; Asundi, A. Two-dimensional digital image correlation for in-plane displacement and strain measurement: A review. *Meas. Sci. Technol.* **2009**, *20*, 062001. [CrossRef]
55. Blaber, J.; Adair, B.; Antoniou, A. Ncorr: Open-source 2D digital image correlation matlab software. *Exp. Mech.* **2015**, *55*, 1105–1122. [CrossRef]
56. Solav, D.; Moerman, K.M.; Jaeger, A.M.; Genovese, K.; Herr, H.M. MultiDIC: An open-source toolbox for multi-view 3D digital image correlation. *IEEE Access* **2018**, *6*, 30520–30535. [CrossRef]
57. Visintin, P.; Dadd, L.; Alam, M.U.; Xie, T.; Bennett, B. Flexural performance and life-cycle assessment of multi-generation recycled aggregate concrete beams. *J. Clean. Prod.* **2022**, *360*, 132214. [CrossRef]
58. *UNE-EN 1992-1-1:2010*; Eurocode 2: Design of Concrete Structures—Part 1-1: General Rules and Rules for Buildings. AENOR: Madrid, Spain, 2010.
59. Sobol, I.M. Sensitivity estimates for non-linear mathematical models. *Math. Model. Comput. Exp.* **1993**, *1*, 407–414.
60. *UNE-EN 12350-2:2020*; Ensayos de Hormigón Fresco. Parte 2: Ensayo de Asentamiento. AENOR: Madrid, Spain, 2020.
61. Teijón-López-Zuazo, E.; López-Rebollo, J.; Sánchez-Aparicio, L.J.; Garcia-Martín, R.; Gonzalez-Aguilera, D. Compression and strain predictive models in non-structural recycled concretes made from construction and demolition wastes. *Materials* **2021**, *14*, 3177. [CrossRef]
62. Sasikumar, P.; Suresh, R.; Vijayaghosh, P.K.; Gupta, S. Experimental characterisation of random field models for CFRP composite panels. *Compos. Struct.* **2015**, *120*, 451–471. [CrossRef]

Disclaimer/Publisher's Note: The statements, opinions and data contained in all publications are solely those of the individual author(s) and contributor(s) and not of MDPI and/or the editor(s). MDPI and/or the editor(s) disclaim responsibility for any injury to people or property resulting from any ideas, methods, instructions or products referred to in the content.

applied sciences

MDPI

Article

Utilization of Phosphogypsum and Sediment in Subgrade Material for Pavement Construction

Dragana Tomašević Pilipović [1,*], Nataša Slijepčević [1], Dunja Rađenović Veselić [1], Miloš Šešlija [2], Vesna Bulatović [2] and Nataša Duduković [1]

[1] Department of Chemistry, Biochemistry and Environmental Protection, Faculty of Sciences, University of Novi Sad, Trg Dositeja Obradovića 2, 21000 Novi Sad, Serbia; natasa.slijepcevic@dh.uns.ac.rs (N.S.); dunja.radjenovic@dh.uns.ac.rs (D.R.V.); natasa.dudukovic@dh.uns.ac.rs (N.D.)

[2] Department of Civil Engineering and Geodesy, Faculty of Technical Sciences, University of Novi Sad, Trg Dositeja Obradovića 6, 21000 Novi Sad, Serbia; sele@uns.ac.rs (M.Š.); vesnam@uns.ac.rs (V.B.)

* Correspondence: dragana.tomasevic@dh.uns.ac.rs

Featured Application: Incorporating phosphogypsum and sediment into subgrade material for pavement construction offers a promising solution for waste management and resource conservation while potentially enhancing the performance and cost-effectiveness of pavement systems.

Abstract: (1) Background: The construction industry continuously seeks sustainable alternatives to traditional materials for subgrade material in pavement construction, aiming to mitigate environmental impact while maintaining performance standards. This study investigates the feasibility of incorporating phosphogypsum (PG) and contaminated sediment into subgrade materials, focusing on their physico-chemical and physico-mechanical properties. (2) Methods: The physico-chemical and physico-mechanical properties, performance, and mechanisms of solidified sediment with phosphogypsum (3% and 5% of phosphogypsum in mixture) were studied using long-term leaching tests (ANS 16.1), uniaxial compressive strength (UCS), California Bearing Ratio (CBR), X-ray fluorescence (XRF), and thermogravimetric analysis (TGA). (3) Results: Based on the pseudo-total metal content (Cr, Ni, Cu, Zn, As, Cd, Pb), the sediment is classified as third- and fourth-class, indicating it is polluted and requires treatment before disposal in the environment. To assess the long-term behavior of the sediment treated with phosphogypsum (S/S), a semi-dynamic ANS 16.1 leaching test was performed. The results showed that the metals exhibit moderate mobility, with average diffusion coefficients (De) ranging from 10^{-8} cm^2/s for Zn (in both mixtures) to 10^{-12} cm^2/s for Cr (in mixture F-3). The leaching index (LX) values for both mixtures were above 9 for most metals, confirming their suitability for "controlled" use. Granulometric analysis indicated a predominance of fine particles, which enhances the material's plasticity and mechanical properties. Atterberg consistency tests showed that increasing phosphogypsum content improved both the Liquid Limit and Plastic Index. However, UCS tests indicated that neither the 3% nor 5% phosphogypsum mixtures met the minimum strength requirements for subgrade material. On the other hand, CBR values demonstrated promising performance, with 12.5% for the 3% phosphogypsum mixture and 22.9% for the 5% phosphogypsum mixture. Overall, phosphogypsum positively influenced the strength development of the sediment-PG mixtures, as confirmed by XRF and TGA analyses. (4) Conclusions: Environmental considerations, such as leachability of contaminants, were investigated to ensure the sustainability of the proposed subgrade materials. Leaching tests indicated minimal pollutant release, suggesting the potential for safe utilization of PG and sediment in subgrade material. This study provides valuable insights into the

physico-chemical and physico-mechanical properties of pavement mixes incorporating PG and sediment, supporting the feasibility of using these alternative materials in sustainable subgrade material for pavement construction and offering a viable solution to mitigate waste generation while enhancing pavement performance.

Keywords: sediment; phosphogypsum; solidification/stabilization; toxic metals; subgrade material for pavement construction

1. Introduction

Industrialization has undoubtedly driven significant economic growth globally, but it has also resulted in the generation of large quantities of waste that pose serious environmental risks [1]. Managing this waste presents a formidable challenge, particularly within critical industries such as the food sector. Fertilizer production plays a crucial role in maintaining agricultural productivity and ensuring food security. Fertilizers replenish the nutrients that crops deplete from the soil, and without them, agricultural yields would be severely impacted. The fertilizer production process begins with the extraction of phosphate rock (PR), which is then converted into phosphoric acid. Typically, about 85% of PR is processed using either wet or thermal methods. This results in the generation of approximately 4–5 tons of phosphogypsum (PG) as a by-product for every ton of phosphoric acid produced. The phosphoric acid is then used to produce fertilizers, which account for up to 95% of the total phosphate rock output [2,3]. The characteristics of PG, including its chemical composition and mineralogical properties, are influenced by factors such as the type of phosphate rock used, the production process, the efficiency of the industrial process, and the chemical quality of reagents [4]. The nature of the phosphate ore—whether magmatic or sedimentary—affects the impurities found in the PG [5,6].

Another pressing environmental issue is the pollution of sediments with heavy metals, a problem that is increasingly prevalent [7,8]. These metals, due to their persistence, toxicity, and potential for bioaccumulation, pose long-term threats to ecosystems and human health [9–13]. Sediment removal from watercourses is often part of routine maintenance to mitigate flooding risks and maintain waterway functionality. However, it is also undertaken when significant aquatic degradation occurs, which could have adverse ecological effects [14,15]. Heavy metals in aquatic systems are primarily bound to suspended particles and sediment, with only a small fraction existing as free ions in the water. These metals can become immobilized through processes such as coagulation, flocculation, or adsorption onto sediment surfaces and may form insoluble compounds like metal sulfides [16]. When restoring aquatic environments, sediment removal often necessitates remediation, especially if the sediment is heavily polluted [17].

To address these challenges, stabilization and solidification (S/S) technologies have emerged as effective methods for immobilizing hazardous constituents in contaminated materials [18,19]. These methods involve mixing binder materials (e.g., Portland cement, lime, kaolin) with contaminated materials to reduce environmental risks associated with the mobility of harmful components. Through S/S, toxic constituents of waste are physically and chemically immobilized, thus minimizing their environmental threat and ensuring compliance with regulatory standards. Stabilized wastes, when adhering to regulations, may be suitable for controlled utilization in landfills or as construction materials for applications such as road subgrade and backfill.

In recent years, various approaches have explored the recycling of PG in construction and building materials. PG has been used as a substitute for natural gypsum in producing plaster, wallboard, and cement [20]. The EU Renewable Energy Directive has highlighted the importance of PG due to the shortage of natural and flue gas desulfurization (FGD) gypsum [21]. Although PG is more accessible and cost-effective than natural gypsum, and its use can help reduce the environmental impact of gypsum mining, several challenges persist. These include the presence of soluble phosphorus, fluorine, and organic compounds in PG, which may hinder its reuse in construction materials.

The unsolved problems in this field include the environmental and logistical challenges of managing polluted sediments and the limited reuse options for PG due to its chemical composition. There is also a lack of studies that explore the potential of PG-sediment mixtures for sustainable construction applications, particularly as subgrade material in pavement construction. These issues point to a significant research gap: the need for environmentally friendly, cost-effective solutions that address both waste management and the demand for sustainable construction materials.

The study goal is to explore the feasibility of using PG as an immobilizing agent in the S/S treatment of contaminated sediments, with a specific focus on its potential as a subgrade material in pavement construction. By investigating the physical, chemical, and mechanical properties of PG–sediment mixtures, this research aims to offer a sustainable solution that addresses both the environmental challenges associated with contaminated sediments and the growing need for alternative materials in the construction industry.

2. Materials and Methods

2.1. Framework of the Experimentation

To evaluate the efficacy of stabilization and solidification (S/S) techniques in the remediation of contaminated sediments, an empirical investigation utilizing sediment samples from the Begej Canal was conducted. This canal, a crucial waterway linking the Danube River in Vojvodina, Serbia, with the city of Timisoara in Romania's Tamis County, has been heavily impacted by industrial and agricultural activities. Since 1945, the rapid development in these regions has led to significant pollution of both the sediment and water in the canal. In Serbia, the Begej Canal primarily serves as a discharge conduit for untreated municipal and industrial wastewater, exacerbating its pollution issues. It is estimated that around 700,000 m^3 of sediment needs to be dredged from this canal.

Phosphogypsum is a by-product generated during the production of phosphoric acid at a local facility. As phosphoric acid is extracted from raw phosphate rock, phosphogypsum is formed and requires careful management due to its chemical properties and potential environmental impacts. Phosphogypsum is stored in facilities designed according to national and European standards. The storage floor features a mineral barrier topped with a waterproof membrane, and drainage pipes are installed on the membrane to collect any accumulated water. These meticulous measures reflect the industry's commitment to mitigating the environmental footprint of phosphogypsum, underscoring the importance of sustainable practices in chemical manufacturing. Additionally, the ongoing need for disposal solutions has sparked interest in exploring potential further uses for phosphogypsum. The primary mineral in PG is gypsum, also known as calcium sulfate, which exists in three distinct forms based on the level of hydration: dihydrate ($CaSO_4 \cdot 2H_2O$), hemihydrate ($CaSO_4 \cdot 0.5H_2O$), and anhydrite ($CaSO_4$) [1].

The primary goal of our study was to evaluate the feasibility of repurposing sediment and phosphogypsum treated through S/S methods as potential subgrade material. A thorough examination of contamination levels in the canal's sediment was undertaken,

with a specific focus on metal concentrations and associated toxicity. Given the extent of metal pollution, implementing effective remediation strategies is imperative to mitigate ongoing environmental damage [22].

2.2. Sample Preparation

In Figure 1, the block diagram illustrates all the analyses conducted throughout the experimental work. First, the physico-mechanical experiments and thermal analysis was performed.

To assess the contamination of sediment, analysis of the pseudo-total trace metal contents using nitric acid digestion was done, following the US EPA standard method [23]. Accuracy was ensured by analyzing triplicate samples, with relative standard deviations (RSD) consistently below 10%. Metal concentrations were determined using atomic absorption spectroscopy (AAS) with a Perkin Elmer AAnalyst™ 700 (PerkinElmer Inc., Shelton, CT, USA), adhering to standard procedures [24].

In Serbia, sediment quality is classified based on specific criteria, including 10% organic matter and 25% clay. Sediment quality assessments were adjusted based on Official Gazette of the Republic of Serbia, No. 50/2012 [25] by converting values to reflect the actual sediment conditions, considering both organic material and clay content. Metal concentrations were first corrected to align with standard sediment parameters and then classified according to Serbian national evaluation schemes. The overall sediment quality was determined using the most stringent classification parameters [25].

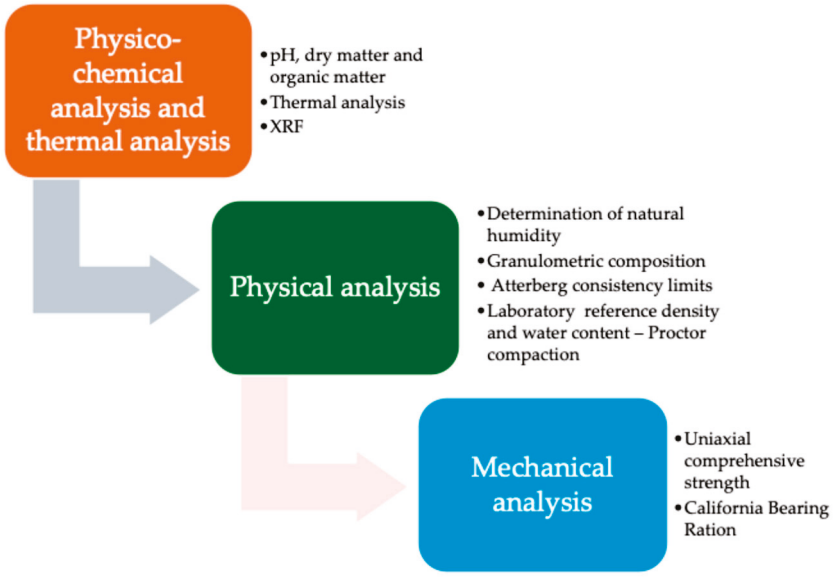

Figure 1. Block diagram for sample analysis.

For the leaching tests, prepared various sample types, denoted by capital letters (F for phosphogypsum, S for sediment) and numbers indicating the percentage weight of each component. The phosphogypsum and sediment content were expressed as a percentages of the total solid weight. The tested samples included F-3 and F-5. Each sample was prepared as monolithic cubes with dimensions of (3 ± 0.1) cm per side. These cubes were compacted at an optimal water content, which maximizes the dry density for the given compactive effort, according to ASTM D1557-00 standards [26], achieving a compactive effort of 2700 kN·m/m^3 [26]. The density of the specimens ranged from 1.38 to 1.54 g/cm^3. After curing at 20 °C in sealed bags for 28 days, the samples were subjected to various tests to evaluate their performance.

For physical analysis, three mixtures were analyzed. The first represents the examination of pure sediment without the addition of 0% binder and then with the addition of 3 and 5% phosphogypsum. Their application is reflected in their use as a road embankment and whether they fulfill the properties for the construction of such a layer. The idolized test is shown in the following block diagram (Figure 1).

We then sampled the material, which was dried, and determined its natural humidity. After that, the preparation of the granulometric composition of the material started, which was tested according to the standard SRPS EN ISO 17892-4:2017 [27]. Then, the plasticity of the material was determined, and Atterberg's consistency limits were defined. The next step was to determine the maximum compaction at the optimal moisture content of the material, i.e., Proctor's test. At the defined optimal moisture content of the material, bodies were made to test the load capacity of the material (California load capacity index) and uniaxial compressive strength after 7 and 28 days. The uniaxial compressive strength test was performed on 3 and 5% binder samples. It is impossible to test on pure sediment because it does not have sufficient strength.

2.3. Physico-Chemical Analysis and Thermal Analysis

2.3.1. pH, Dry Matter and Organic Matter

The content of dry matter and organic matter was determined by drying a 5 g sample at 105 °C to a constant mass and then annealing at 550 °C in order to determine the loss of mass by annealing in accordance with the so-called NEN procedure of the Netherlands Normalization Institute (NNI): NEN 5754 [28]. The pH value was determined according to the standard method SRPS ISO 10390:2007 [29], using a Sentix®21 electrode (pH-meter 340i, WTW, Washington, DC, USA). The SRPS ISO 11265:2007 [30] method was used to determine the specific electrical conductivity (TetraCon electrode and Cond 3210 conductometer).

2.3.2. Thermal Analysis

The TGA (thermogravimetric analysis) method was used to measure the changes in weight and to obtain phase changes of the material (contaminated sediment and sediment with phosphogypsum-PG) as a function of temperature and time under controlled conditions using Labsys Evo (Setaram, Austin TX, USA). Along with TGA, DTA (differential thermal analysis) was also applied, which allows us better identification of weight loss. The sample (ap-proximately 30 mg) was placed in an alumina crucible and TGA/DTA measurements were performed in the temperature range from 25 °C to 1000 °C with a heat change of 10 K/min in an argon atmosphere.

2.3.3. XRF

The chemical composition of samples was determined using SPECTRO XEPOS XRF, Kleve, Germany, using TurboQuant (TQ) method (range of elements: Na-U, air-cooled low power X-ray tube with a Pb/Co anode). The samples for XRF analysis were dried, and then 5 g of sample and 1 g of micropowder C (CEREOX BM-0002-1, Fluxana, Bedburg-Hau, Germany) were mixed together and homogenized, and then a pellet with a diameter of 32 mm was formed.

2.3.4. Leaching Test

To assess the long-term leachability of heavy metals from the stabilization and solidification (S/S)-treated materials, the ANS method 16.1 was utilized [26]. This method allows us to track how the cumulative fraction of these metals leached from the treated materials changes over time. An applied mathematical diffusion model was based on Fick's second

law to analyze the leaching rate as a function of time, providing insights into how metals migrate from the material. The leachability index (LX), derived from the ANS 16.1 test results [26], is a crucial performance metric used by Environment Canada to evaluate the effectiveness of waste treatment for disposal or utilization [31]. This index measures the relative mobility of contaminants, with values ranging from 5, indicating highly mobile contaminants (De = 10^5 cm^2/s), to 15, suggesting very low mobility (De = 10^{15} cm^2/s) [32]. To understand the leaching mechanisms controlling the release of metals, the relationship between the logarithm of the cumulative fraction of metals released (log(Bt)) and the logarithm of time (log(t)) was analyzed. According to De Groot and van der Sloot (1992) [33], this relationship helps identify the dominant leaching mechanism. A slope close to 1 (ranging from 0.60 to 1.00) indicates that dissolution is the primary mechanism, where the material dissolves from the surface more quickly than it diffuses through the pore spaces of the soil matrix. Conversely, a slope of approximately 0.5 (ranging from 0.40 to 0.60) suggests that diffusion controls the leaching process, leading to a slower release of heavy metals. A slope less than 0.40 typically points to surface wash-off as the main release mechanism. For our study, samples were meticulously prepared, and leachate was collected and replaced following the procedures outlined in the ANS 16.1 test [26]. This approach provided a comprehensive understanding of how effectively the treated materials contain or release heavy metals over time.

2.4. Physical Analysis

The following tests were performed from the physical analysis, and are shown in Table 1 and given according to the appropriate standard and number of samples that were tested for a specific test.

Table 1. Type of physical analysis test, scope of test, and applied standards.

Type of Testing	Number of Samples	Applied Standards
Geotechnical investigation and testing—Laboratory testing of soil—Part 4: Determination of particle size distribution	1	SRPS EN ISO 17892-4:2017 [27]
Geotechnical investigation and testing—Laboratory testing of soil—Part 12: Determination of liquid and plastic limits	9	SRPS EN ISO 17892-12:2018 [34]
Unbound and hydraulically bound mixtures—Part 2: Test methods for laboratory reference density and water content—Proctor compaction	12	SRPS EN 13286-2:2022 [35]
Unbound and hydraulically bound mixtures—Part 50: Method for the manufacture of test specimens of hydraulically bound mixtures using Proctor equipment or vibrating table compaction	12	SRPS EN 13286-50:2012 [36]

2.4.1. Granulometric Composition

To classify the material (sediment), the granulometric composition and distribution of fine particles as a function of grain size were examined. The wet sowing method was applied using distilled water. The main objective of this standard is to determine a sufficient amount of sample fraction for the construction of a reliable particle size distribution curve. Determination of particle size distribution is based on a combination of sieving and sedimentation of the sample. Fractions larger than 0.063 mm are determined by a combination of dry and wet sowing, while fractions smaller than 0.063 mm are determined by sedimentation using the pipette method.

2.4.2. Consistency Limits

The consistency limit was determined for all samples, reflecting the plasticity index of the material. This information is crucial for understanding the material's characteristics and assessing the feasibility of using phosphogypsum as a binder. Figure 1 illustrates the

determination of both the material's yield strength and plasticity. Consistency limits, also known as Atterberg limits, are widely used in geotechnical engineering to characterize and classify fine-grained soils. These limits consist of three standardized tests designed to evaluate the plasticity and consistency of materials such as clay and silt. The Liquid Limit and Plastic Limit are critical components of this classification, providing insights into soil behavior in response to moisture variations. The liquid limit indicates the water content at which soil transitions from a liquid state to a plastic state, acquiring modest shear strength. It represents the minimum water content that maintains the soil in a liquid state or the maximum water content at which it remains in a plastic state.

For this study, the liquid limit was determined using Casa grade's method. This method employs a firm rubber base with a British Standard [37] hardness ranging from 21 to 25. A brass cup, which descends from a specified height onto the rubber base, is operated via a handle-controlled cam mechanism. Adjustable screws allow for precise modification of the cup's drop height, initially set at 1 cm to commence the test. The plastic limit is defined as the lowest moisture content at which soil can undergo plastic deformation. In standardized testing, it signifies the minimum water content at which the soil begins to fragment when rolled into slender threads, typically around 3 mm in diameter. This parameter indicates the point at which the soil achieves minimal stiffness or strength. Understanding these limits is essential for evaluating the potential use of phosphogypsum as a binder in sediment remediation efforts.

2.4.3. Compaction According to Proctor's Test

The Proctor Compaction Test is used to determine the maximum dry unit weight that a specific soil type can achieve when compacted under controlled conditions at optimal moisture content. In the laboratory, soil samples are compacted in a mold with standardized dimensions of height and diameter. The compaction is performed in layers, with each layer receiving a specified number of blows from a standard weighted hammer. This process is repeated for four different moisture contents, and the dry densities of the compacted samples are measured. The results are plotted to create a compaction curve, with the peak of the curve indicating the maximum dry density and corresponding optimal moisture content. According to the standard [38], a compaction energy of 600 kNm/m^3 should be used to create uniaxial compressive strength. However, due to the equipment available, it was not possible to determine the force on the press, so it was decided to have a compaction force of 2750 kNm/m^3. A compaction energy of 2750 kNm/m^3 was used to make the samples that were tested for the California bearing ratio.

2.5. Mechanical Analysis

The resistant and deformable properties of the sediment with or without phosphogypsum were determined on samples—test bodies—following the test program. Tests were performed with procedures (standards) used in the European Community and National standard. Table 2 shows the types of tests, the scope of tested samples (test bodies), and the applied standards.

Table 2. Type of mechanical analysis test, scope of test, and applied standards.

Seq. Num.	Type of Testing	Number of Samples	Applied Standards
1.	Compressive strength—uniaxial strength	12	SRPS EN ISO 13286-41:2022 [38]
2.	California bearing ratio (CBR)	3	SRPS EN ISO 13286-47:2022 [39]

2.5.1. Compressive Strength—Uniaxial Strength

The Uniaxial Compressive Strength (UCS) is a critical geomechanical property that measures the maximum axial load a rock sample can withstand under unconfined conditions, without lateral stress. UCS is sometimes referred to as "unlimited compressive strength". In contrast, hardness is a basic quantitative property of the rock. Assessing the strength and deformability of rock masses is essential for numerical analyses in rock mechanics. For accurate testing, the cylindrical surfaces of the rock sample must be ground to a smooth finish, and the ends should be leveled with a tolerance of 0.02 mm. The vertical axis of the sample must also be aligned within 0.06 degrees. The load is applied gradually, and failure should occur within 5 to 10 min of loading, with the load increasing at a rate of 0.5 to 1 MPa.

For a general overview of the characteristics of sediment and posphogypsum as a building material and for calculating stability and load-bearing capacity, the parameters obtained by determining the strength in uniaxial compression and free lateral expansion are used. The diameter of the sample that was made was 250 mm, and the height was 200 mm. The sample was compacted in five layers of 25 blows to obtain the best representative sample for testing. The prepared bodies were stored in a plastic bag at a temperature of 20 °C. The test was performed after 7 and 28 days of age, and three samples were made for each mixture.

2.5.2. California Bearing Ratio (CBR)

The California Bearing Ratio (CBR) test is a penetration test used to evaluate the strength of materials such as subgrade, subbase, and base courses, including recycled materials. The CBR test is essential for designing roadways and airfield pavements and was originally developed by the California State Highway Department. It measures the pressure required to penetrate a soil sample with a standard-area plunger. As the surface hardness of the soil increases, so does the CBR value. The test is typically performed on soils with a maximum particle size of 20 mm. For soils with larger particles, a plate-bearing test is used instead.

3. Results

3.1. Physicochemical and Thermal Characterization of Sediment Samples Treated with Phosphogypsum

3.1.1. Pseudo-Total Metal Content

When determining the pseudo-total metal concentrations presented in Table 3, it is observed that zinc is present in the highest concentration in the initial sediment, while arsenic is found in the lowest concentration. The concentrations of metal were first adjusted to standard sediment levels and then classified according to national regulations [25]. The sediment quality was assessed based on the parameters that fell into the worst category as predicted by the model.

Table 3. Pseudo-total metal content in sediment sample.

Analysed Metals	Cr (mg/kg)	Ni (mg/kg)	Cu (mg/kg)	Zn (mg/kg)	As (mg/kg)	Cd (mg/kg)	Pb (mg/kg)
Sediment of Begej	304.9	58.42	345.1	1415	18.28	18.65	177.9
Corrected value	287.02	53.63	307.4	1272	16.60	16.35	163.7
Target value	100	35	36	140	29	0,8	85
Remedial value	380	210	190	720	55	12	530
Classification	1	3	4	4	0	4	1
Final classification: 4							
Class 0—natural sediment background; class 1—slightly polluted sediment; class 2—moderately polluted sediment; class 3—heavily polluted sediment; class 4 (4+)—extremely polluted sediment							

From the results in Table 3, it can be seen that cadmium, copper, and zinc are classified as belonging to the fourth class of sediment—extremely polluted—based on the concentrations of these specific metals. In contrast, the sediment is classified as third class—heavily polluted—regarding nickel concentrations. According to the "Official Gazette of RS", no. 50/12 [25], sediments categorized as fourth and third class are considered polluted, necessitating treatment before their disposal in the environment. Meanwhile, chromium, lead, and arsenic fall into the first and zero classes—slightly polluted and natural background sediments, respectively.

3.1.2. Content of Organic Matter and Moisture

The analysis of sediment samples treated with phosphogypsum reveals certain differences in dry matter, moisture content, and organic matter between mixtures F-3 and F-5. Sample F-5 (containing 5% phosphogypsum) has a higher dry matter content (95.8%) compared to F-3 (containing 3% phosphogypsum) at 92.3%, indicating that more phosphogypsum reduces moisture content. Sample F-3 has a higher moisture content (7.7%) than F-5 (4.2%), showing an inverse relationship between dry matter and moisture. The organic matter content, measured by annealing at 550 °C to determine mass loss on annealing, was consistent between the two samples.

For sample F-5, it is 15.25%, and for F-3, it is 15.14%, which suggests that phosphogypsum has a minimal effect on organic matter. From these results, it can be concluded that increasing the content of phosphogypsum in the sediment reduces moisture and increases dry matter, while the content of organic matter remains stable. Figure 2 shows the percentage content of dry and organic matter as well as the moisture content in mixtures F3 and F5.

3.1.3. pH and Conductivity

The conductivity and pH of sediment samples treated with phosphogypsum are shown in Table 4. The conductivity was 2430 μS/cm for sample F-5 and 2990 μS/cm for sample F-3. This suggests that the lower phosphogypsum content of F-3 may increase ion mobility, possibly due to the higher presence of dissolved salts or ions. The pH values are similar: for sample F-5, it was 6.38, and for F-3, it was 6.50, within the neutral to slightly acidic range. This indicates that the addition of phosphogypsum does not significantly affect the pH of the sediment. While conductivity varies between samples, indicating differences in ion content, pH remains stable, suggesting that phosphogypsum has minimal effect on sediment acidity or alkalinity, which is important for geochemical stability [1,40].

The first weight loss that occurs below 100° or nearly 100° in all samples corresponding to an endothermic reaction (Figure 3). This first mass loss (between 25 and 200 °C) is primarily attributed to the dehydration of the samples. Also, the significant peak of DTA curves at 135–150 °C probably corresponding to the dehydration of gypsum is observed for samples with phosphogypsum (PG) but also in sediment without PG with reduced intensity. This is emphasized in the case of both samples with PG, especially in the case of the sample with 5% PG. As can be seen, a slightly larger amount of lost mass in this interval is observed at samples with PG compared to a sediment sample, but the difference is not significant (Table 5).

In the second interval, 200–400 °C, a broad exothermic peak associated with the thermal degradation of organic matter was observed in the sediment sample (Figure 3). Keeping in mind that this broad peak was not observed in the samples with PG (3 or 5%), it can be assumed that organic matter was reduced or protected in this way.

3.1.4. Thermal Analysis

The results of the TGA/DTA measurement are shown in Figure 3 The mass loss and thermal stability of the material were monitored over the increase in temperature. Four ranges were found in the degradation process of materials (25–200 °C, 200–400 °C, 400–700 °C, and 700–1000 °C) along with several endothermic and exothermic phenomena. The mass losses of tested samples at different temperature intervals are given in Table 5.

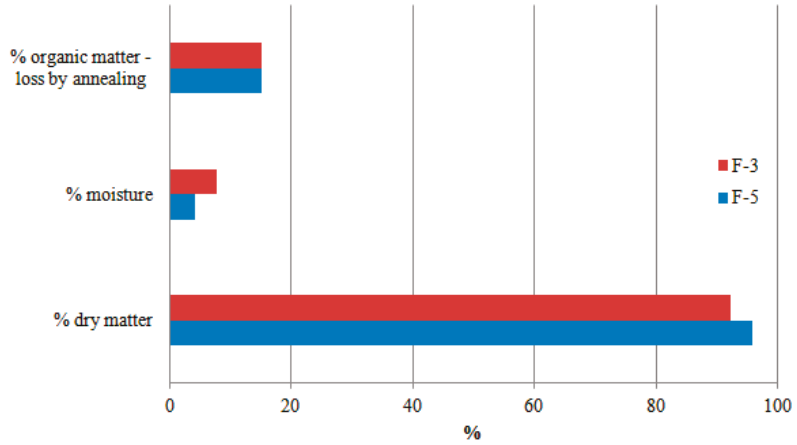

Figure 2. Percentage content of moisture, organic matter and dry matter in mixtures F-3 and F-5.

Table 4. Results of electrical conductivity and pH samples.

Sample	Conductivity (µS/cm)	pH
F-5	2430	6.38
F-3	2990	6.50

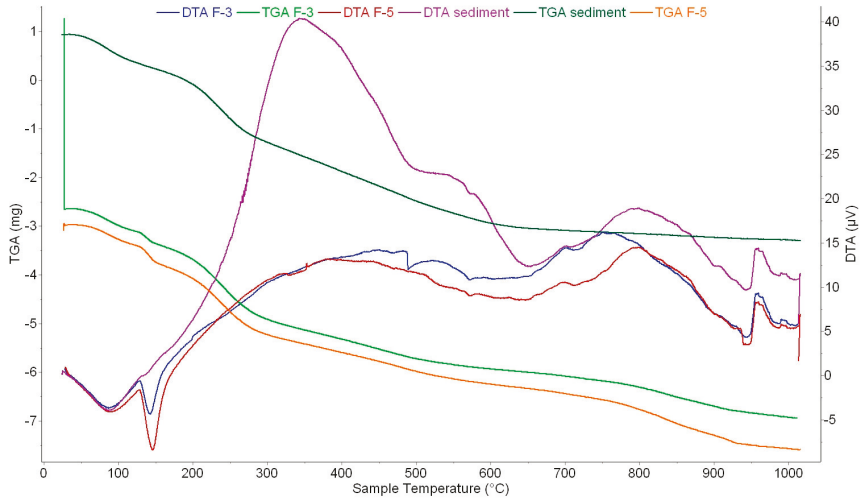

Figure 3. TGA/DTA results of sediment and sediment with PG.

Table 5. The mass losses (%) of samples at different temperature intervals.

Temperature [T]		25–200	200–400	400–700	700–1000	Total
Mass loss [%]	Sediment	3.3	5.7	3.8	0.6	13.4
	F-3	3.5	5.3	2.5	2.8	14.1
	F-5	3.6	4.8	2.6	3.5	14.5

The peak of DTA curves around 570 °C (third range of 400–700 °C, Figure 3) could be attributed to the dehydroxylation of clay minerals, especially kaolin [41]. In some cases,

this can be connected to the conversion of one form quartz to another 43]. The sediment sample had the highest mass loss values compared to the other two samples (Table 5).

The weight loss in the last range at 700–1000 °C is mainly caused by the carbonate decomposition [41]. Mass loss is significant in this interval when it comes to samples with PG. The highest mass loss is observed for sample with 5% PG, followed by the sample with 3%PG, and finally the sediment sample with minor weight loss. The biggest differences between included samples are observed in this interval. An exothermic peak around 950 °C (Figure 3) indicates the crystallization of the high-temperature phases (maybe mullite) [42].

3.1.5. XRF Analysis

The chemical compositions of the sediment and both mixtures are primarily comprised of SiO_2 and Al_2O_3, which indicates that clay minerals are significantly present (Table 6). Apart from these dominant oxides, there are also MgO, K_2O and CaO, while SO_3 is present in a higher percentage in the F-3 and F-5 mixtures, which is understandable. Oxides Na_2O and P_2O_5 are presented in trace amounts. The assumption is that "other" includes a significant part of the organic substance. The mineral composition of phosphogypsum, which includes gypsum ($CaSO_4 \cdot 2H_2O$) and other impurities, may provide reactive sites for heavy metal ions. This interaction can lead to the formation of less soluble complexes, thereby sequestering heavy metals and minimizing their concentration in the bulk sediment.

The concentration of seven heavy metals (Cr, Ni, Cu, Zn, As, Cd and Pb) in sediment and mixtures is also determined by XRF and is shown in Table 6. As can be seen, the amount of all heavy metals is lower in the mixture with sediment and phosphogypsum compared to just sediment. The structural properties of phosphogypsum may also enhance the physical encapsulation of heavy metals within the sediment matrix, limiting their mobility and reducing leaching potential, as explained in the next section.

3.1.6. ANS 16.1 Test

Figure 4 shows cumulative leaching percentages of heavy metals (Cr, Ni, Cu, Zn, As, Cd, and Pb) from S/S mixtures F-3 and F-5 over 90 days using deionized water as the leaching solution. Using phosphogypsum as a binding agent is to immobilize these metals and reduce their environmental mobility. However, the results show that the degree of effectiveness varies with the type of metal.

Table 6. Chemical compositions of samples.

Sample	Chemical Composition [%]								
	Na_2O	**MgO**	**Al_2O_3**	**SiO_2**	**P_2O_5**	**SO_3**	**K_2O**	**CaO**	**Other**
Sediment	0.36	1.85	13.11	43.89	0.41	0.53	1.82	1.17	36.92
F-3	0.28	1.50	11.51	40.40	0.34	1.78	1.67	1.80	40.72
F-5	0.31	1.65	12.56	41.06	0.37	2.39	1.76	2.51	37.39
	Heavy metals [μg/g]								
	Cr	Ni		Cu	Zn	As	Cd		Pb
Sediment	348.6	53.2		322.4	1209	9.6	17.1		124.7
F-3	310.9	46.3		290.9	1139	8.0	15.5		118.6
F-5	319.3	47.0		293.7	1173	8.8	16.5		118.2

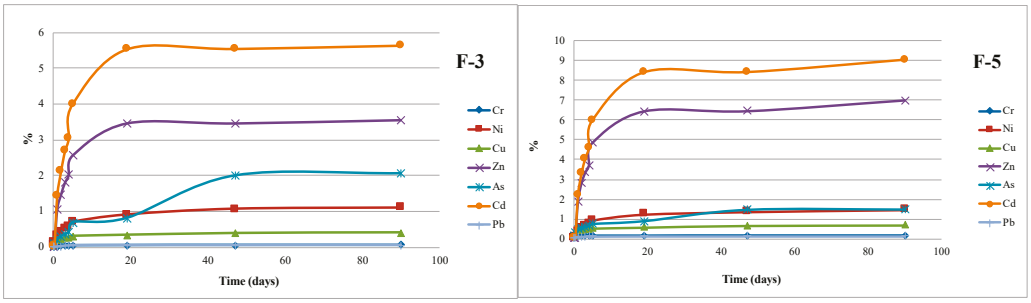

Figure 4. Cumulative leached metal fractions from S/S mixtures F-3 and F-5.

Cadmium showed the highest cumulative leaching percentage, particularly in the 5% phosphogypsum mixture (F-5), with up to 9.01% leaching after 90 days. This indicates that cadmium remains relatively mobile even after treatment. Studies by Ruangcharus et al. (2020) [43] support these findings, suggesting that phosphate amendments can sometimes increase cadmium leachability due to the formation of soluble cadmium-phosphate complexes, influenced by specific pH and redox conditions. On the other hand, lead elution was very low, up to 0.13% in the F-5 mixture, indicating effective immobilization, although the concertation was not high. This can be attributed to the formation of highly stable lead–phosphate compounds. Pontoni et al. (2020) [44] demonstrated that lead forms insoluble complexes with phosphates, significantly reducing its leaching potential under various environmental conditions. Zinc showed significant leaching, particularly in the F-5 mixture, reaching 6.99% after 90 days, suggesting that zinc remains somewhat mobile even with higher phosphogypsum content. Zinc can form soluble complexes or remain adsorbed on the surface of particles, making it susceptible to leaching, especially under mildly acidic conditions [45].

Arsenic exhibited moderate leaching levels, with 2.07% for F-3 and 1.49% for F-5 after 90 days. The reduction in arsenic mobility is likely due to adsorption processes or the formation of arsenic–phosphate compounds. Nickel and chromium showed moderate leaching percentages, suggesting some stabilization but not complete immobilization. Li et al. (2022) [46] found that these metals can form relatively stable complexes within S/S matrices, although environmental conditions can still influence their mobility. Copper displayed moderate leaching levels, with a maximum of 0.69% for the F-5 mixture. While copper can form stable complexes with phosphates, some leaching is still observed. The mobility of copper in S/S systems can vary depending on the binding agent and environmental factors such as pH [47].

The ANS 16.1 leaching model utilizes Fick's diffusion theory to evaluate the diffusion rate, providing a basis for assessing the effectiveness of solidification/stabilization (S/S) treatments [26,48]. This assessment is primarily achieved through the determination of diffusion coefficients (De) and the calculation of the leaching index (LX). The average values of diffusion coefficients (De) and LX values are presented in Table 7 and Figure 5. In this context, the average diffusion coefficients (De) for the F-5 mixture demonstrated a range of values: from 1.22×10^{-8} cm^2s^{-1} for cadmium, indicating moderate mobility, to 9.45×10^{-12} cm^2s^{-1} for lead, suggesting limited mobility. According to Nathwani and Phillips (1980) [31], the diffusion coefficients of metals from S/S mixtures can span a wide range, from values indicative of very mobile metals (approximately 1×10^{-5} cm^2s^{-1}) to those that represent practically immobilized metals (around 1×10^{-15} cm^2s^{-1}). The diffusion coefficients observed for the F-3 and F-5 mixtures, which lie between 10^{-8} and 10^{-12} cm^2s^{-1}, suggest that the metals within these mixtures exhibit moderate mobility.

Table 7. Mean diffusion coefficients De (cm^2s^{-1}) in S/S mixtures F-3 and F-5.

Mixtures	$\overline{De}$ (cm^2/s)						
	Cr	**Ni**	**Cu**	**Zn**	**As**	**Cd**	**Pb**
F-3	1.98×10^{-12}	2.06×10^{-10}	4.93×10^{-11}	2.43×10^{-9}	1.59×10^{-10}	5.62×10^{-9}	1.24×10^{-12}
F-5	1.73×10^{-11}	3.13×10^{-10}	1.56×10^{-10}	8.10×10^{-9}	2.70×10^{-10}	1.22×10^{-8}	9.45×10^{-12}

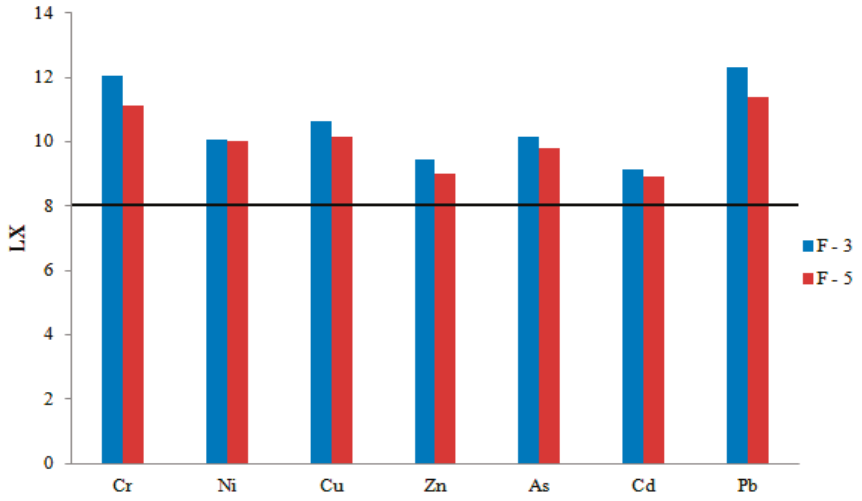

Figure 5. Average leaching indices (LX) in S/S mixtures F-3 and F-5.

These findings have significant implications for the environmental performance of S/S treatments. Metals with diffusion coefficients in the range of 10^{-8} to 10^{-12} cm^2s^{-1} are not as readily leachable as highly mobile species, yet they are not fully immobilized. The moderate mobility of these metals implies that, over time, there may be a gradual release of contaminants into the surrounding environment. This controlled release may be beneficial in certain scenarios, as it can mitigate acute toxicity risks by preventing the sudden leaching of high concentrations of metals. However, it also necessitates continuous monitoring and potential long-term management to ensure that the release rates do not exceed acceptable environmental thresholds.

According to the Canadian Environmental Protection Agency [32], the leaching index (LX) values serve as a crucial criterion for assessing the suitability of solidification/stabilization (S/S)-treated waste for various use and disposal scenarios. An LX value above 9 signifies effective treatment, making the S/S-treated waste suitable for "controlled use" applications, such as quarry rehabilitation, lagoon closure, or use as a road base. LX values ranging from 8 to 9 indicate that the treated waste is appropriate for disposal in sanitary landfills. Conversely, LX values below 8 denote that the S/S treated waste is unsuitable for disposal, indicating a higher potential for leaching and environmental contamination [32,48,49].

Figure 5 illustrates the average leaching index (LX values) for the tested mixtures, demonstrating that the S/S treatment effectively immobilizes the metals. Both S/S mixtures exhibit LX values greater than 9 for the majority of metals, suggesting high immobilization efficiency. The F-3 mixture shows LX values above 9 across all metals, confirming its suitability for "controlled use" applications. This high level of immobilization indicates that the metals are securely bound within the matrix, reducing the likelihood of their release into the environment under standard conditions of use. For the F-5 mixture, while most metals also show LX values above 9, cadmium is an exception, with its LX value ranging between 8 and 9. This range indicates that the S/S treated waste containing cadmium is

less immobilized compared to other metals but is still within the threshold that allows for safe disposal in sanitary landfills.

The use of phosphogypsum as an immobilization agent in the S/S process has proven effective in reducing the leachability of the investigated metals. Phosphogypsum's role in forming stable complexes with metal ions likely contributes to the observed high LX values, as it enhances the structural integrity of the S/S matrix and its resistance to leaching. The effectiveness of phosphogypsum in immobilizing heavy metals suggests that it can be a viable agent in S/S treatment formulations, especially for applications requiring strict leachate control. The ability to achieve high LX values not only demonstrates the feasibility of using such materials in environmentally sensitive applications but also provides a framework for the development of guidelines and regulations governing the use of S/S treated waste.

When comparing the slope values from the graph showing the relationship between the cumulative fraction of leached metal (mg m^{-2}) and time (Figure 6), it is noted that surface wash-off appeared to be the main controlling leaching mechanism for chromium, copper and lead for both mixtures, since the values are below 0.4. This suggests that these metals are predominantly released from the surface of the S/S material, rather than diffusing through the matrix or dissolving, implying that the surface of the S/S matrix retains some solubility or that physical processes at the surface facilitate metal release. The relatively low slope values for these metals highlight the effectiveness of the S/S process in limiting their mobility and subsequent environmental impact. In the F-5 mixture, arsenic also displays slope values below 0.4, similarly suggesting surface wash-off as the controlling mechanism.

Conversely, for both S/S mixtures, nickel shows slope values ranging between 0.4 and 0.6, indicating that diffusion is the dominant leaching mechanism for this metal. In this range, the leaching process is characterized by the gradual migration of nickel ions from the interior of the matrix to the surface. Similarly, arsenic in the F-3 mixture falls into this category, suggesting that diffusion plays a more significant role in its leaching compared to the F-5 mixture.

For zinc and cadmium in both mixtures, slope values exceeding 0.6 indicate that dissolution is the primary leaching mechanism, suggesting these metals have higher solubility within the S/S matrix. This could result in increased mobility and potential for environmental release. While these findings highlight some limitations of the current S/S treatment for zinc and cadmium, the gradual release of these metals may still be manageable with proper monitoring to ensure it remains within regulatory limits.

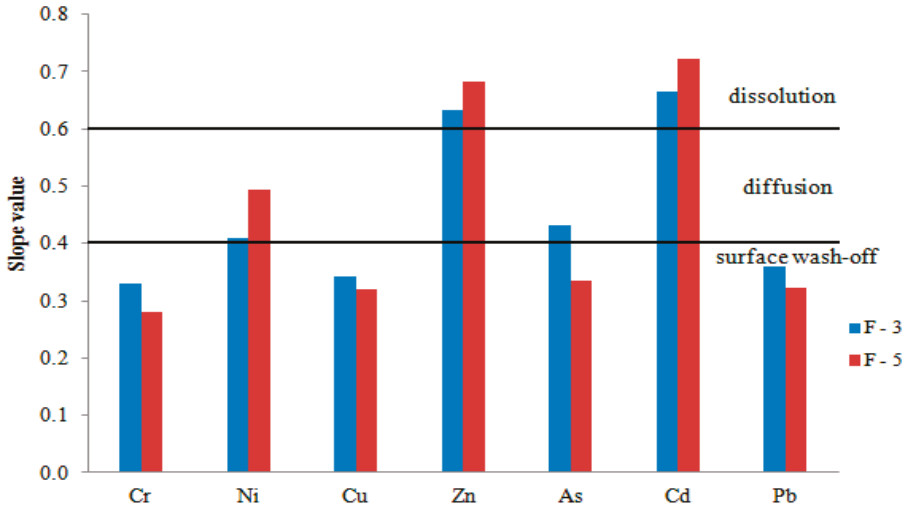

Figure 6. Leaching mechanism determined based on slope values from graphs of cumulative leached fraction of metals versus time for S/S mixtures.

3.2. Physical-Mechanical Characterization

The mechanical characteristics of the material were performed for two mixtures, where phosphogypsum was used as a binder, and the percentages were 3% and 5%. Atterberg's consistency, Proctor's test, uniaxial compressive strength, and California bearing index were performed for this type of samples. For clean sediment, the following were determined and performed: granulometric composition, consistency limits, Proctor's test, and the California Bearing Ratio.

3.2.1. Granulometric Composition Analysis

Figure 7 illustrates the granulometric composition of the aggregate, revealing a complex interplay of particle sizes within the mixture. The analysis indicates that over 20% of the particles are clay, while approximately 45% consist of fine dust-like materials. The sandy component constitutes around 30%, with gravel particles measuring less than 3.5%, as determined by a 4 mm sieve. This particle size distribution suggests that the material is predominantly plastic and clayey–dusty in nature. The higher proportion of finer particles, particularly in the 0.063–0.02 mm and 0.02–0.006 mm ranges, enhances the mixture's cohesiveness and may significantly improve its mechanical properties, such as compressive strength [50,51].

Furthermore, the increased clay content (particles < 0.002 mm) is likely to contribute to enhanced plasticity, improved water retention, and stronger binding properties. These characteristics may render the material more stable and suitable for various applications, particularly in construction and environmental remediation contexts. The findings underscore the importance of understanding granulometric composition in predicting the performance and applicability of sediment mixtures in engineering projects.

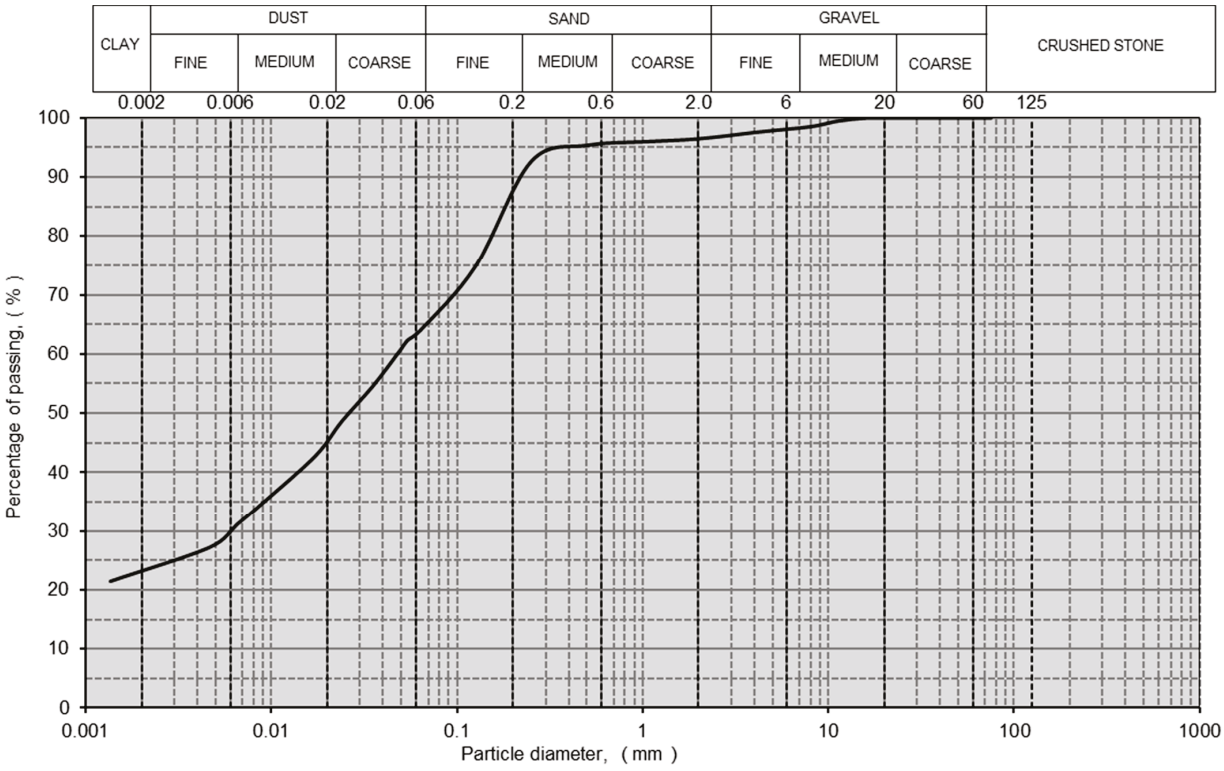

Figure 7. Granulometric composition of the sediment.

3.2.2. Consistency Limits

Atterberg's consistency limits were determined for three characteristic mixtures: clean sediment, sediment samples with 3% phosphogypsum added, and those with 5% phosphogypsum added. The test results include the Liquid Limit (Wl), Plastic Limit (Wp), and Plastic Index (Ip) of the material and binder. Figure 8 displays the tested samples, with the x-axis representing the proportion of the binder and the y-axis showing the percentage values of the individual tests (Wl, Wp, and Ip). As the percentage of phosphogypsum increases, both the Liquid Limit and Plastic Index of the material also increase, while there is a slight decrease in the Plastic Limit. This indicates that phosphogypsum serves as an effective sediment stabilization binder, exhibiting similar effects to those observed with some commercial hydraulic binder-based materials. The authors performed soil stabilization of different types of soil materials with the addition of cement binder, and based on this, they obtained values of the Liquid Limit in the range of 33.32 to 51.59%, the Plasticity Limit in the range of 24.24 to 30.18, and the Plastic Index was 9.05 to 22.49% [52].

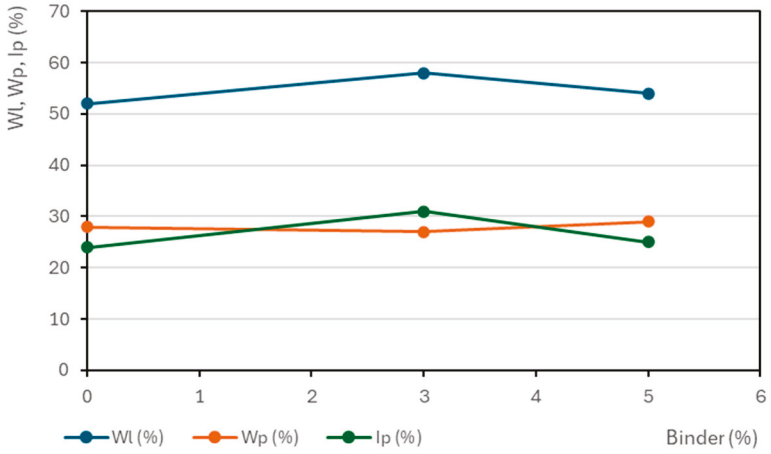

Figure 8. Atterberg's consistency limits.

3.2.3. Uniaxial Compressive Strength (UCS)

The uniaxial compressive strength (UCS) values are presented in Figure 9. The test results are shown after 7 days (left side of Figure 10) and after 28 days (right side of Figure 10). The x-axis displays the phosphogypsum content, while the y-axis indicates the strength values in N/mm^2. It was observed that the UCS values increase with the addition of more binder. This improvement is attributed to the accelerated reaction resulting in the formation of expanding ettringite crystals from the Ca^{2+} and SO_4^{2-} ions in phosphogypsum. As these ettringite crystals filled the sample pores and interconnected through their needle-like structure, the overall compactness of the material increased, leading to enhanced strength. Based on these findings, it is crucial to continue increasing the binder content and monitoring the UCS values to fully understand its impact on the material's strength [53].

Three test samples were used during the assessment, and the mean value of these samples was calculated for further analysis. Recommendations regarding the suitability of the material for use as stabilization in the road embankment must meet specific criteria. For coherent materials, the uniaxial compressive strength (UCS) after seven days must be at least 0.5 N/mm^2. For incoherent materials, the requirement is 2.0 N/mm^2 [54].

The mean value of the tested mixture after seven days with 3% phosphogypsum was 0.30 N/mm^2, while the mixture with 5% phosphogypsum yielded a mean value of 0.36 N/mm^2. Based on the regulations set forth by the Roads of Serbia, neither the 3% nor the 5% binder content can be utilized as road material in embankments. However,

it is important to explore increasing the binder content to determine the percentage of phosphogypsum required to achieve a UCS of 0.5 N/mm^2.

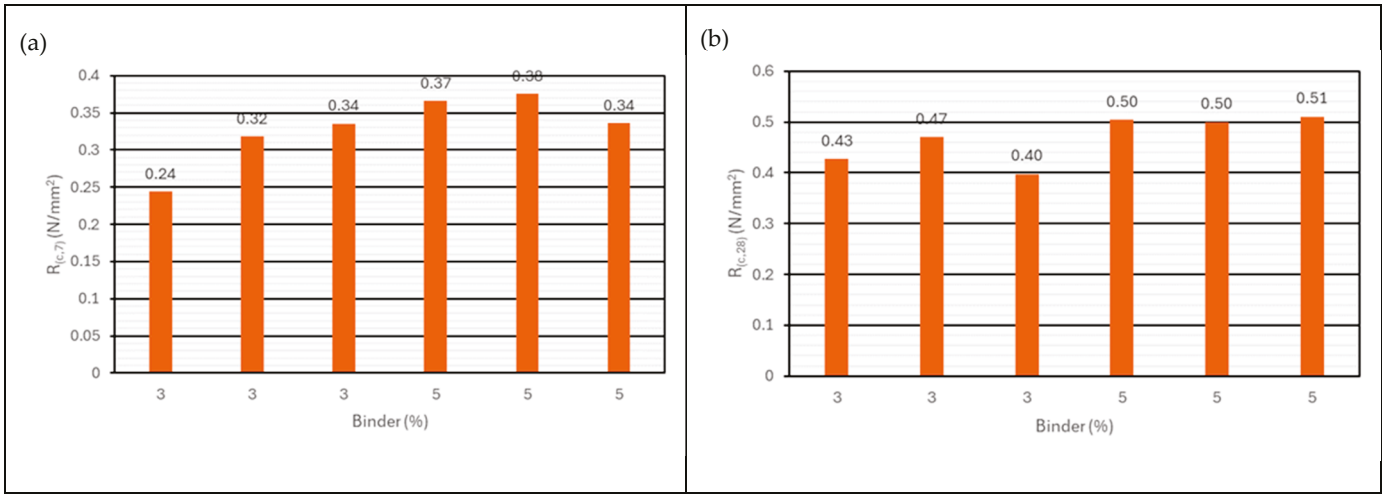

Figure 9. (**a**) Compressive strength—uniaxial strength after 7 and (**b**) compressive strength—uniaxial strength after 28 days (right image).

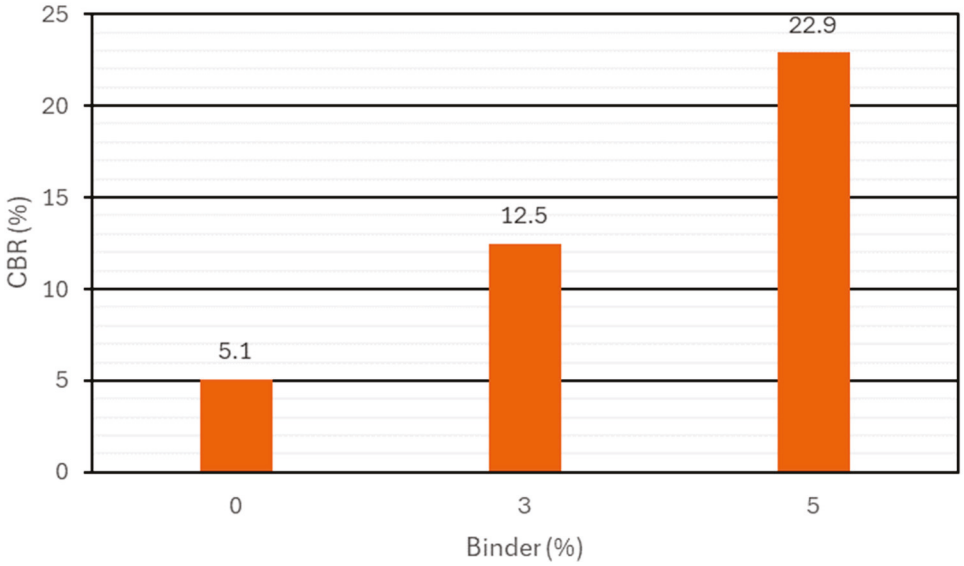

Figure 10. California bearing ratio.

3.2.4. California Bearing Ratio (CBR)

The California Bearing Ratio (CBR) measures the resistance of a piston as it is pressed into a soil sample. In this study, three samples were tested: one made of pure sediment (0% phosphogypsum), one with 3% phosphogypsum added, and one with 5% phosphogypsum added. When preparing samples for CBR, the following optimal material humidity was used (Table 8).

Table 8. Maximum volumetric mass and optimum humidity.

Samples	Sediment (0%)	3%	5%
Optimum humidity	12.7	13.1	13.9
Maximum volumetric mass	1.60	1.65	1.67

The test results for these prepared samples are displayed in Figure 10. As shown in Figure 10, increasing the amount of binder correlates with a rise in the California Bearing Index values. The mixtures of phosphogypsum and sediment demonstrated promising results, with a CBR value of 12.5% for the 3% phosphogypsum mixture and 22.9% for the 5% phosphogypsum mixture. In contrast, clean sediment alone exhibited a CBR value of 5.1%. According to the technical specifications set forth by the Roads of Serbia, the minimum CBR value required for the construction of road embankments is 5%. Based on this criterion, all three mixtures can be utilized in road embankment construction. Moreover, while some local studies report lower CBR values (typically ranging from 4% to 8%) for phosphogypsum-stabilized soils with higher binder contents (10–30%), the values obtained in this study suggest that even at relatively low binder contents (3% and 5%), phosphogypsum can significantly enhance the material's performance, making it a promising option for soil stabilization in road construction [55].

This increase in CBR values is directly correlated with the effectiveness of phosphogypsum as a binder in stabilizing the sediment. Phosphogypsum works by facilitating the formation of ettringite crystals, which bind the particles together, filling voids, and improving the overall compaction and load-bearing capacity of the material.

The increased UCS values observed with higher phosphogypsum content (from 0.30 N/mm^2 at 3% binder to 0.36 N/mm^2 at 5% binder after 7 days) suggest that the material becomes progressively more compact and stronger, a trend consistent with the CBR findings. The improvements in UCS and CBR values indicate that the material becomes more resistant to deformation under load, which is critical for its use in road embankments.

4. Conclusions

This study offers a thorough assessment of the potential of phosphogypsum as a stabilizing agent in sediment mixtures, focusing on its effectiveness in immobilizing heavy metals and enhancing mechanical properties as subgrade material. The analysis of pseudo-total metal content indicates that the initial sediment is highly contaminated, particularly with cadmium, copper, and zinc, which classify it as extremely polluted. This underscores the need for effective treatment of contaminated sediments to mitigate environmental risks.

The sediment's granulometric composition, dominated by fine particles, enhances its cohesiveness and mechanical properties, making it suitable for construction applications. Thermal analysis via TGA/DTA demonstrates the thermal stability of the sediment mixtures, revealing distinct mass loss phases that correlate with specific thermal reactions. XRF analysis further confirms the predominant presence of clay minerals and highlights the effectiveness of phosphogypsum in reducing the concentrations of heavy metals in treated mixtures. The leaching index (LX) values for the treated sediments, particularly those incorporating phosphogypsum, indicate that they meet the criteria for "controlled use" applications, making them suitable for specific environmental remediation efforts. The analysis of leaching mechanisms reveals that surface wash-off is predominant for several metals, while diffusion and dissolution contribute to the release of others, necessitating continued monitoring to mitigate risks. Mechanical testing results indicate that while the uniaxial compressive strength (UCS) of the mixtures with phosphogypsum does not yet meet the minimum requirements for road construction, the California Bearing Ratio (CBR) values demonstrate potential suitability for subgrade material in road embankments. According to the Roads of Serbia's specifications, all tested mixtures can be considered for subgrade material in road embankment construction. This suggests that further optimization of phosphogypsum content is necessary to achieve desired strength characteristics.

In summary, this study highlights the dual benefits of using phosphogypsum in sediment treatment: it not only aids in the stabilization of heavy metals, thereby reducing environmental risks, but also enhances the physical properties of the sediment for potential engineering applications. Future work should focus on exploring long-term environmental impacts of using these treated sediments in construction and remediation projects.

Author Contributions: Conceptualization, N.S., D.R.V. and V.B.; Formal analysis, N.S., D.R.V., M.Š. and V.B.; Investigation, M.Š.; Methodology, N.S., D.R.V. and V.B.; Project administration, D.T.P.; Supervision, N.D.; Validation, N.D.; Visualization, M.Š.; Writing—original draft, D.T.P.; Writing—review and editing, D.T.P. All authors helped revise the draft of the manuscript. All authors have read and agreed to the published version of the manuscript.

Funding: This research was supported by the Science Fund of the Republic of Serbia, #7753609, BEuSED.

Institutional Review Board Statement: Not applicable.

Informed Consent Statement: Not applicable.

Data Availability Statement: The datasets during and/or analyzed during the current study are available from the corresponding author upon reasonable request.

Conflicts of Interest: All authors are aware the given information regarding this manuscript is correct. All authors have agreed that there are no conflicts of interest in this manuscript. All authors have declared that they have no known competing financial interests or personal relationships that could have appeared to influence the work reported in this paper.

References

1. Akfas, F.; Elghali, A.; Aboulaich, A.; Munoz, M. Exploring the potential reuse of phosphogypsum: A waste or a resource? *Sci. Total Environ.* **2024**, *908*, 168196. [CrossRef] [PubMed]
2. Zan, C.; Shi, L.; Zu Song, Y.; Shan Zhu, M. Evaluation method for thermal processing of phosphoric acid with waste heat recovery. *Energy* **2006**, *31*, 2791–2804. [CrossRef]
3. Cánovas, C.R.; Macías, F.; Pérez-López, R.; Basallote, M.D.; Millán-Becerro, R. Valorization of wastes from the fertilizer industry: Current status and future trends. *J. Clean. Prod.* **2018**, *174*, 678–690. [CrossRef]
4. Carbonell-Barrachina, A.; DeLaune, R.D.; Jugsujinda, A. Phosphogypsum chemistry under highly anoxic conditions. *Waste Manag.* **2002**, *22*, 657–665. [CrossRef]
5. Guerrero-Márquez, J.L.; Peña, F.M.; Mantero, J.; Manjón, G.; García-Tenorio, R.; Bolívar, J.P. Occupational, public and environmental radiological impact caused by the phosphoric acid industry: The case of Huelva (Spain). In *Phosphoric Acid Industry-Problems and Solutions*; IntechOpen: London, UK, 2017.
6. Santos, A.J.G.; Mazzilli, B.P.; Fávaro, D.I.T.; Silva, P.S.C. Partitioning of radionuclides and trace elements in phosphogypsum and its source materials based on sequential extraction methods. *J. Environ. Radioact.* **2006**, *87*, 52–61. [CrossRef]
7. Fernandes, C.; Fontaínhas-Fernandes, A.; Cabral, D.; Salgado, M.A. Heavy metals in water, sediment and tissues of Liza saliens from Esmoriz-Paramos lagoon, Portugal. *Environ. Monit. Assess.* **2008**, *136*, 267–275. [CrossRef]
8. Birch, C.; Harper-Simmonds, L.; Lindeque, P.; Middleton, A. Benefits of bush control in Namibia: A national economic study for Namibia and a case for the Otjozondjupa Region. In *Report for the Economics of Land Degradation Initiative*; ELD Initiative: Bonn, Germany, 2017; pp. 4–45.
9. Suthar, S.; Bishnoi, P.; Singh, S.; Mutiyar, P.K.; Nema, A.K.; Patil, N.S. Nitrate contamination in groundwater of some rural areas of Rajasthan, India. *J. Hazard. Mater.* **2009**, *171*, 189–199. [CrossRef]
10. Guédron, S.; Tisserand, D.; Garambois, S.; Spadini, L.; Molton, F.; Bounvilay, B.; Charlet, L.; Polya, D.A. Baseline investigation of (methyl)mercury in waters, soils, sediments and key foodstuffs in the lower Mekong Basin: The rapidly developing city of Vientiane (Lao PDR). *J. Geo. Explor.* **2014**, *143*, 96–102. [CrossRef]
11. Valdés, J.; Guiñez, M.; Castillo, A.; Vega, S.E. Cu, Pb, and Zn content in sediments and benthic organisms from San Jorge Bay (northern Chile): Accumulation and biotransference in subtidal coastal systems. *Cien. Mar.* **2014**, *40*, 45–58. [CrossRef]
12. Tashakor, M.; Yaacob, W.Z.W.; Mohamad, H.; Ghani, A.A.; Saadati, N. Assessment of selected sequential extraction and the toxicity characteristic leaching test as indices of metal mobility in serpentinite soils. *Chem. Speciat. Bioavailab.* **2014**, *26*, 139–147. [CrossRef]

13. Won, E.J.; Kim, K.T.; Choi, J.Y.; Kim, E.S.; Ra, K. Target organs of the Manila clam Ruditapes philippinarum for studying metal accumulation and biomarkers in pollution monitoring: Laboratory and in-situ transplantation experiments. *Environ. Monit. Assess.* **2016**, *188*, 478. [CrossRef] [PubMed]
14. Saravanan, P.; Pradhap, D.; Krishnakumar, S.; Silva, D.J.; Vidyasakar, A.; Sackaria, M.; Godson, S.P.; Arumugam, K.; Magesh, S.N. A baseline study on trace element based sediment pollution and potential ecological risk of reef sediments of Musal, Manoli and Manoli putti Islands, Gulf of Mannar, India. *Mar. Pollut. Bull.* **2018**, *133*, 117–123. [CrossRef] [PubMed]
15. Libralato, G.; Minetto, D.; Lofrano, G.; Guida, M.; Carotenuto, M.; Aliberti, F.; Conte, B.; Notarnicola, M. Toxicity assessment within the application of in situ contaminated sediment remediation technologies: A review. *Sci. Total Environ.* **2018**, *621*, 85–94. [CrossRef]
16. Zhang, C.; Yu, Z.G.; Zeng, G.M.; Jiang, M.; Yang, Z.Z.; Cui, F.; Zhu, M.Y.; Shen, L.Q.; Hu, L. Effects of sediment geochemical properties on heavy metal bioavailability. *Environ. Int.* **2014**, *73*, 270–281. [CrossRef]
17. Dubovina, M.; Krčmar, D.; Grba, N.; Watson, M.; Rađenović, D.; Tomašević-Pilipović, D.; Dalmacija, B. Distribution and ecological risk assessment of organic and inor- ganic pollutants in the sediments of the transnational Begej canal (Serbia- Romania). *Environ. Pollut.* **2018**, *236*, 773–784. [CrossRef]
18. Wang, L.; Yu, K.; Li, J.S.; Tsang, D.C.W.; Poon, C.S.; Yoo, J.C.; Baek, K.; Ding, S.; Hou, D.; Dai, J.G. Low-carbon and low-alkalinity stabilization/solidification of high-Pb contaminated soil. *Chem. Eng. J.* **2018**, *351*, 418–427. [CrossRef]
19. Wang, L.; Chen, L.; Cho, D.W.; Tsang, D.C.W.; Yang, J.; Hou, D.; Baek, K.; Kua, H.W.; Poon, C.S. Novel synergy of Si-rich minerals and reactive MgO for stabilisation/solidification of contaminated sediment. *J. Hazard. Mat.* **2019**, *365*, 695–706. [CrossRef]
20. Layr, K. Market Analysis for Urban Mining of Phosphogypsum. Master's Thesis, University of Leoben, Leoben, Austria, 2020.
21. Haneklaus, N.; Barbossa, S.; Basallote, M.D.; Bertau, M.; Bilal, E.; Chajduk, E.; Chernysh, Y.; Chubur, V.; Cruz, J.; Dziarczykowski, K.; et al. Closing the upcoming EU gypsum gap with phosphogypsum. *Resour. Conserv. Recycl.* **2022**, *182*, 106328. [CrossRef]
22. Dalmacija, B.; Prica, M.; Ivančev-Tumbas, I.; Van der Koolj, A.; Rončević, S.; Krčmar, D.; Bikit, I.; Teodorović, I. Pollution of the Begej Canal sediment-metals, radioactivity and toxicity assessment. *Environ. Int.* **2006**, *32*, 606–615. [CrossRef]
23. *Method 3051A*; Microwave Assisted Acid Digestion of Sediments, Sludges, Soils, and Oils. U.S. Environmental Protection Agency (USEPA): Washington, DC, USA, 2007.
24. *Method 7010*; Graphite Furnace Atomic Absorption Spectrophotometry. U.S. Environmental Protection Agency (USEPA): Washington, DC, USA, 2007.
25. *No. 50/2012*; Regulation on Limit Values of Pollutants in Surface and Ground Waters and Sediments and Deadlines for Their Achievement. Official Gazette of the Republic of Serbia: Belgrade, Serbia, 2012.
26. *ANSI/ANS 16.1*; American National Standard for the Measurement of the Leachability of Solidified Low Level Radioactive Wastes by Shortterm Tests Procedures. American National Standards Institute (ANSI): New York, NY, USA, 1986.
27. *SRPS EN ISO 17892-4:2017*; Geotechnical Investigation and Testing—Laboratory Testing of Soil—Part 4: Determination of Particle Size Distribution. Institute for Standardization of Serbia (ISS): Belgrade, Serbia, 2017.
28. *NEN 5754:1994*; Determination of Organic Matter Content in Soil as Loss-On-Ignition. The Netherlands Normalisation Institute (NEN): Delft, The Netherlands, 1994.
29. *SRPS ISO 10390:2007*; Soil Quality—Determination of pH. Institute for Standardization of Serbia (ISS): Belgrade, Serbia, 2007.
30. *SRPS ISO 11265:2007*; Soil Quality—Determination of the Specific Electrical Conductivity. Institute for Standardization of Serbia (ISS): Belgrade, Serbia, 2007.
31. Nathwani, J.S.; Phillips, C.R. Leachability of Ra-226 from uranium mill tailings consolidated with naturally occurring materials and/or cement: Analysis based on mass transport equation. *Water Air Soil. Pollut.* **1980**, *14*, 389–402. [CrossRef]
32. Environment Canada. *Proposed Evaluation Protocol for Cement-Based Solidified Wastes, Environmental Protection Series, Report No. EPS 3/HA/9*; Environment and Climate Change Canada: Toronto, ON, Canada, 1991.
33. De Groot, G.J.; van der Sloot, H.A. Determination of leaching characteristics of waste materials leading to environmental product certification. In *Stabilization and Solidification of Hazardous, Radioactive, and Mixed Wastes*; ASTMSTP: West Conshohocken, PA, USA, 1992; Volume 2, 514p.
34. *SRPS EN ISO 17892-12:2018*; Geotechnical Investigation and Testing—Laboratory Testing of Soil—Part 12: Determination of Liquid and Plastic Limits. Institute for Standardization of Serbia (ISS): Belgrade, Serbia, 2018.
35. *SRPS EN 13286-2:2022*; Unbound and Hydraulically Bound Mixtures—Part 1: Test Methods for Laboratory Reference Density and Water Content—Introduction, General Requirements and Sampling. Institute for Standardization of Serbia (ISS): Belgrade, Serbia, 2022.
36. *SRPS EN 13286-50:2012*; Unbound and Hydraulically Bound Mixtures—Part 50: Method for the Manufacture of Test Specimens of Hydraulically Bound Mixtures Using Proctor Equipment or Vibrating Table Compaction. Institute for Standardization of Serbia (ISS): Belgrade, Serbia, 2012.

37. *BS 1377-2:2022*; Methods of Test for Soils for Civil Engineering Purposes—Classification Tests and Determination of Geotechnical Properties. BSI: London, UK, 2022.
38. *SRPS EN ISO 13286-41:2022*; Unbound and Hydraulically Bound Mixtures—Part 41: Test Method for the Determination of the Compressive Strength of Hydraulically Bound Mixtures. Institute for Standardization of Serbia (ISS): Belgrade, Serbia, 2022.
39. *SRPS EN ISO 13286-47:2022*; Unbound and Hydraulically Bound Mixtures—Part 47: Test Method for the Determination of California Bearing Ratio, Immediate Bearing Index and Linear Swelling. Institute for Standardization of Serbia (ISS): Belgrade, Serbia, 2022.
40. Kumar, S.S.; Kumar, A.; Singh, S.; Malyan, S.K.; Baram, S.; Sharma, J.; Singh, R.; Pugazhendhi, A. Industrial wastes: Fly ash, steel slag and phosphogypsum-potential candidates to mitigate greenhouse gas emissions from paddy fields. *Chemosphere* **2020**, *241*, 124824. [CrossRef] [PubMed]
41. Zhang, O.; Lu, Z.; Wang, S.; Yu, X.; Chen, W. Utilisation of biomass ash after high-temperature treatment for strengthening purple soil under various curing conditions. *Constr. Build. Mater.* **2024**, *435*, 136806. [CrossRef]
42. Mimboe, A.G.; Grace, A.; Abo, M.T.; Djobo, J.N.Y.; Tome, S.; Kaze, R.C.; Deutou, J.G.N. Lateritic soil based-compressed earth bricks stabilized with phosphate binder. *J. Build. Eng.* **2020**, *31*, 101465. [CrossRef]
43. Ruangcharus, C.; Kim, S.U.; Hong, C.O. Mechanism of cadmium immobilization in phosphate-amended arable soils. *Appl. Biol. Chem.* **2020**, *63*, 36. [CrossRef]
44. Pontoni, D.; Melo, V.F.; Borgo, J.; Stipp, R.; Bonfleur, E.J. Integrated assessment of the liquid and solid phases of lead-contaminated soils remediated with phosphate. *Geoderma* **2020**, *360*, 113993. [CrossRef]
45. Wisawapipat, W.; Janlaksana, Y.; Christl, I. Zinc solubility in tropical paddy soils: A multichemical extraction technique study. *Geoderma* **2017**, *301*, 1–10. [CrossRef]
46. Li, Q.; Wang, Y.; Li, Y.; Li, L.; Tang, M.; Hu, W.; Chen, L.; Ai, S. Speciation of heavy metals in soils and their immobilization at micro-scale interfaces among diverse soil components. *Sci. Total Environ.* **2022**, *825*, 153862. [CrossRef]
47. Król, A.; Mizerna, K.; Bożym, M. An assessment of pH-dependent release and mobility of heavy metals from metallurgical slag. *J. Hazard. Mater.* **2020**, *384*, 121502. [CrossRef]
48. Kundu, S.; Gupta, A.K. Immobilization and leaching characteristics of arsenic from cement and/or lime solidified/stabilized spent adsorbent containing arsenic. *J. Hazard. Mater.* **2008**, *153*, 434–443. [CrossRef]
49. Moon, D.H.; Dermatas, D. Arsenic and lead release from fly ash stabilized/solidified soils under modified semi-dynamic leaching conditions. *J. Hazard. Mater.* **2007**, *141*, 388–394. [CrossRef]
50. Abbey, S.J.; Eyo, E.U.; Ngámbi, S. Swell and microstructural characteristics of high-plasticity clay blended with cement. *Bull. Eng. Geol. Environ.* **2020**, *79*, 2119–2130. [CrossRef]
51. Utkarsh, P.; Kumar, J. Enhancing the properties of swelling soils with lime, fly ash, and expanded polystyrene—A review. *Heliyon* **2024**, *10*, e32908. [CrossRef] [PubMed]
52. Fawzia, K.; Šešlija, M.; Milović, T.; Starčev-Ćurčin, A.; Bulatović, V.; Radović, N. Stabilization of Different Soil Types Using a Hydraulic Binder. *Buildings* **2023**, *13*, 2040. [CrossRef]
53. Wang, H.; Shi, M.; Tian, X.; Yu, C.; Du, X. Experimental Study on Phosphogypsum-Amended Red Mud as Road Base Material. *Sustainability* **2023**, *15*, 1. [CrossRef]
54. PC Roads of Serbia. *Technical Conditions for Road Construction in the Republic of Serbia, 2. Special Technical Conditions, 2.2. Road Works*; PC Roads of Serbia: Belgrade, Serbia, 2012.
55. Malkawi, D.; Rababáh, S.; AlSyouf, M.; Aldeeky, H. Utilizing expansive soil treated with phosphogypsum and lime in pavement construction. *Results Eng.* **2023**, *19*, 101256. [CrossRef]

Disclaimer/Publisher's Note: The statements, opinions and data contained in all publications are solely those of the individual author(s) and contributor(s) and not of MDPI and/or the editor(s). MDPI and/or the editor(s) disclaim responsibility for any injury to people or property resulting from any ideas, methods, instructions or products referred to in the content.

applied sciences

MDPI

Article

Development of a Novel Beam-Based Finite-Element Approach for the Computationally Efficient Prediction of Residual Stresses and Displacements in Large 3D-Printed Polymer Parts

Irja B. Hepler and William G. Davids *

Department of Civil and Environmental Engineering, University of Maine, Orono, ME 04469, USA; irja.hepler@maine.edu

* Correspondence: william.davids@maine.edu; Tel.: +1-207-581-2116

Abstract: Recently, 3D printing of large, structural polymer parts has received increasing interest, especially for the creation of recyclable structural parts and tooling. However, the complexity of large-scale 3D polymeric printing often dictates resource-intensive trial and error processes to achieve acceptable parts. Existing computational models used to assess the impact of fabrication conditions typically treat the 3D-printed part as a continuum, incorporate oversimplified boundary conditions and take hours to days to run, making design space exploration infeasible. The purpose of this study is to create a structural model that is computationally efficient compared with traditional continuum models yet retains sufficient accuracy to enable exploration of the design space and prediction of part residual stresses and deformations. To this end, a beam-based finite element methodology was created where beads are represented as beams, vertical springs represent inter-bead transverse force transfer and multi-point, linear constraints enforce strain compatibility between adjacent beads. To test this framework, the fabrication of a large Polyethylene terephthalate glycol (PETG) wall was simulated. The PETG was modeled as linearly elastic with an experimentally derived temperature-dependent coefficient of thermal expansion and elastic modulus using temperature history imported from an ABAQUS thermal model. The results of the simulation were compared to those from a continuum model with an identical material definition, showing reasonable agreement of stresses and displacements. Further, the beam-based model required an order of magnitude less run time. Subsequently, the beam-based model was extended to allow separation of the part from the printing bed and the inclusion of part self-weight during fabrication to assess the significance of these effects that pose challenges for existing continuum models.

Keywords: additive manufacturing; finite element; modeling; polymer

1. Introduction

With recent advances in technology, 3D printing for structural applications has become increasingly popular. One type of 3D printing is material extrusion, or fused deposition modelling (FDM). A computer model of the desired part is created, and a program called a slicer converts the geometry into instructions for the printer, called G-code. The printer uses the G-code to construct the part layer by layer, where molten polymer is pushed out of a moving nozzle and deposited in a bead or raster. Depending on the part geometry, a single layer can consist of several beads. After the layer cools for a predetermined amount of time, the next layer is printed on top in the same fashion. FDM allows for creation of complex parts with relative ease and low labor requirements [1]. Originally, FDM printers were quite small, with build volumes allowing part sizes on the scale of inches [2]. Within the last decade, researchers have begun working with large-scale printers with print volumes on the order of meters. Furthermore, these printers can use short-fiber reinforcing material which can increase strength and stiffness [3], enabling the applicability of FDM in construction. Large-scale 3D printers have been used to produce concrete form work [4,5],

a culvert diffuser [6], a mold for a vacuum-infused prototype FRP bridge girder [7] and even a small house [8]. These examples show the potential of large-scale 3D printing.

However, because of the manufacturing process which induces repeated heating and cooling of the polymer, there are some unique pitfalls to navigate when 3D printing. If the part cools too much between the placement of layers, this can cause warping and poor inter-layer adhesion. However, printing another layer on an excessively hot part can cause collapse [9]. Furthermore, due to the directional nature of the printing process, the strength of these parts is highly anisotropic. Both the strength and unwanted distortions are dependent on the printing parameters, e.g., print speed, layer height, raster direction, bed temperature and chamber temperature to name a few [10]. It is not usually clear a priori which combination of settings produces a successful print, and this can cause an inefficient trial and error manufacturing process that wastes time and materials [11]. In order to remedy this, some researchers have turned to computational models to help predict the behavior of 3D-printed parts.

Many different computational models of the FDM printing process have been created. Laminate analysis, typically used for fiber reinforced composites, has been applied to 3D-printed specimens. Each layer of the part is assumed to be a linear elastic orthotropic lamina with a direction of reinforcement, in this case the printing direction. Layers are typically assumed to be perfectly bonded together. Researchers have looked at Acrylonitrile Butadiene Styrene (ABS) [12–17] or Polylactic Acid (PLA) [14,15,18,19], either neat [12,14–16] or reinforced with short carbon fiber [13,17,18], long carbon fiber [20] or wood flour [19], obtaining their material properties from either their own uniaxial coupon testing [12–14,16,18–20] or from existing published literature [15]. Many have focused on using classical lamination theory (CLT) [12–14,17–20], first-order shear deformation theory [15] and/or homogenization [15–17] to predict the stiffness of uniaxial coupons or multi-layered plates and some have predicted failure using the Azzi–Tsai [16], Hill [13], Tsai–Hill [12,19] or Tsai–Wu [20] failure criterion. Comparisons of predicted to experimental stiffness and yield strength are typically within 10%. Though laminate analysis shows promise for simple parts made of unidirectional layers, many FDM parts have complex geometry and infill, which cannot be modeled using this method. As a result, some researchers have used beam [21–23] or shell [24] elements to model the infill of small-scale FDM parts. Other researchers have used various continuum models employing 2D or 3D solid elements to predict 3D-printed specimen behavior. They have focused on creating material models of various reinforced and unreinforced plastics, including isotropic [25–28], orthotropic [29,30], viscoelastic [31–35], elastic–plastic [31,33,35–38], damage [35,37,38] and hyperelastic [31,39]. Some have used modelling strategies including multiscale or representative volume element (RVE) simulation [28–30,32,33,37], cohesive elements [37], XFEM [33], embedded elements [26], or the explicit inclusion of voids [27,31]. Though continuum models have been successfully applied to the behavior of FDM parts, such models do not accurately capture the parts' structure, which is not homogenous but consists of voids, beads, and inter-bead bonds. While multiscale modeling can incorporate this heterogeneity, none of the papers above took into account the thermal loading on their modeled parts during printing, which can induce significant residual stresses. Also, while one of the strengths of FDM is the ability to fabricated complex structures, the vast majority of the papers above looked at simple geometries, either coupons or plates.

Sequentially coupled thermal mechanical analysis (SC-TMA) is one way to simulate the effects of the printing process and printing-induced stresses. This method was first applied to the FDM of polymers by Wang [40] and Zhang and Chou [41]. As interest in 3D modelling increased, commercial finite element programs incorporated built-in tools for using this method to simulate FDM, which explicitly model the deposition and thermal behavior of material during printing. Some typical characteristics of these commercial codes are small strains, no self-weight, rectangular bead cross-sections, perfect bond between beads, part fixity to the bed, and treatment of the part as a continuum. Some authors used these tools with material properties provided by the software to model tensile coupons or cubes [42–46]. While SC-TMA can more closely simulate the stress state of a part, it has

been shown that 3D printing also affects the strength of parts compared to neat polymer or traditional manufacturing methods and so using general material properties is most likely inaccurate. Cattenone et al. [47] manufactured and modeled the printing of two complex geometries of ABS (termed planar spring and bridge) employing SC-TMA in ABAQUS v.2017 using 3D solid brick elements. An elastic–plastic material model was used, with temperature-dependent material properties taken from the literature [47]. During printing, the part was fixed to the bed, but once cooled, a portion of the part was released based upon experimental observations [47]. Vertical displacements from the model were compared to those measured after actual printing and agreed relatively well [47]. Similar to Cattenone et al., Trofimov et al. [48], Syrlybayev et al. [49] and Corvi et al. [50] all modeled various geometries (plate and bridge, tensile coupon, and plate, respectively) with an elastic–plastic model with thermally dependent properties using commercial software. All three groups compared measured versus simulated distortions at the edge of the part and errors ranged from 10% to well over 100% [48–50]. Other groups have also applied SC-TMA to the printing of FDM parts. Akbar et al. [51] used SC-TMA in ABAQUS to model the printing and behavior of rectangular prisms of polyurethane-based amorphous thermoplastic using experimentally derived material properties in a linearized thermo-elastic model. Their comparisons between experimental and simulated warpage had a maximum difference of 12% [51]. Jiang et al. [52] modeled short carbon fiber PLA square and circular pipes using Digimat AM. Their material model was thermoelastic with parameters determined through experimental testing and included the effects of crystallization [52]. The model predicted warpage better for the square pipes than the circular with a maximum percent difference overall of 25% [52]. Samy et al. [53–57] examined the effects of various printing parameters using a SC-TMA model built in COMSOL that included gravity effects. Short rectangular prisms made of polypropelene were represented using a thermo-viscoelastic material model that included crystallization [53–57]. While Samy et al. [53–57] state that contact between the bed and part was modeled using a spring foundation, no details of the implementation are provided and their cited source has a fixed then released boundary condition [58]. The warpage at one or two points per specimen is compared to experiments and agrees very well with measured values [53–57].

FEA-based SC-TMA is not the only method being used to model FDM. Wang and Papadopoulos [59] presented a fully coupled thermo-mechanical model of a two-dimensional wall. Unlike in a sequentially coupled analysis where the thermal problem is independent and can be solved before the structural problem, in a fully coupled analysis, both responses are dependent on the other and the two problems must be solved simultaneously [59]. They compared their results to those from a SC-TMA and found very small differences in final displacement [59]. Sreejith et al. [60] devised a framework to model deposition from the nozzle and liquid, transition and solid phases of the polymer during FDM. They used the Arbitrary Lagrangian–Eulerian method to solve their coupled governing equations [60]. They applied the method to a hypothetical polystyrene wall one bead thick and four beads tall in plane strain conditions [60]. Xia et al. [61] applied the one fluid formulation to fully modelling FDM which is a finite volume, front tracking method with two meshes, one stationary and one moving. They used the method to examine the effects of overhang using an inverted cone, spacing between two adjacent filaments using a two-bead-wide by two-bead-high wall and bridging by printing a single filament connecting two spaced out single bead walls four beads high [61]. Though these methods have the potential to more accurately capture the physics of FDM, their complexity and computational demand are quite high. None of these methods were compared against experimental data and the one that was compared to a SC-TMA found only small differences in displacements. Furthermore, these models consist of novel code that would be difficult to implement for wider classes of simulations and for the reduction in trial and error during large-format FDM.

While the discussion above shows there has been much work on simulating small-scale 3D printing, the simulation of large-scale 3D printing poses other challenges. Radiative heat transfer is a significant mode of heat transfer, unlike in small-scale printing [62]. Also, be-

cause of the reduced surface area to volume ratio, large-scale parts cool much more slowly and can therefore be more prone to sagging [62]. While most findings from small-scale SC-TMA are most likely applicable to large-scale SC-TMA in a general sense, it is still very important to have models specifically designed for use at large scale. Talagani et al. [63] created a structural simulation including element activation of the printing of a car made of short carbon ABS. Material properties were determined using a multi-scale homogenization approach that included damage, and stresses in each layer were calculated using CLT [63]. Measured temperatures were input into the structural model [63]. Locations of high stress in the model qualitatively matched where the printed structure cracked [63]. Kim et al. [64] performed a SC-TMA on the printing of a 122 cm long by 38.1 cm tall single bead wall made of carbon fiber ABS. The wall was printed on an aluminum bar that allowed for deflection measurements and the material properties of the wall were temperature dependent and determined through experiments and multiscale modeling [64]. Measured and simulated deflections of the end of the bar throughout printing were qualitatively similar [64]. Friedrich and Choo [65] modeled a pyramid of ABS using a SC-TMA. The ABS was modeled as thermoviscoelastic with properties from the literature [65]. The size of the model was reduced by using quarter symmetry [65]. Simulated versus measured final displacements along one line of the structure were within roughly 10% [65]. Brenken et al. [11] created a simulation tool in ABAQUS AM that includes the effects of thermoviscoelasticity and crystallization. The tool was tested by simulating the printing of plates and rings made of short carbon-reinforced polyphenylene sulfide [11]. Material properties were determined using experimentation and micromechanical modeling. Comparisons between experiment and simulation of the curvature of the plate and deformation of the ring were within 7% [11]. Though this model is accurate, it is also very computationally expensive, with a simulation of an autoclave mold taking around 11 h with two computers, each with 10 cores and 128 GB of RAM [11].

To accurately simulate the printing of a large 3D-printed part, the height of an element must be at most the bead height, which is typically on the order of millimeters or perhaps centimeters. This limits the size of traditional solid elements resulting in meshes with many elements. Further, because of complex geometries and/or printing paths, models can rarely take advantage of symmetry. Model runs on the order of hours or more makes a comprehensive exploration of a part design space impractical using available FEA-based SC-TMA strategies and tools, motivating the development of more computationally efficient models. There has been some work on speeding up thermal simulations of small [66,67] or large [67,68] parts, using, for example, mesh merging [66], modified beam elements [67] or a one-dimensional model [68]. Bhandari and Lopez Anido [69] developed a discrete event simulation thermal model and modeled the printing of a "miniature... ashtray model" made of PLA or ABS. The authors then used the model as part of a SC-TMA of a large-scale culvert outlet diffuser printed with PLA reinforced with wood flour, simulated using a visco-elastic–plastic material model [9]. Viscous plastic deformations due to self-weight (no thermal shrinkage) were calculated using a finite element model, which were then used to predict whether the print will fail or not [9]. Bhandari and Lopez Anido also developed a different model to simulate the printing of a 0.5 m $\times$ 0.5 m $\times$ 0.5 m open top box made of carbon fiber-reinforced ABS [70]. The material is assumed to be orthotropic and its properties are not dependent on temperature [70]. A SC-TMA is written in MATLAB, using a fourth-order Runge–Kutta finite difference approximation with mesh merging for the thermal simulation and finite element analysis using CLT with solid hexahedral elements for the structural simulation [70]. Thermal stresses begin to develop once an element cools to below its glass transition temperature and self-weight is ignored [70].

Though there has been some work performed on computationally efficient SC-TMA of large scale FDM, the vast majority of prior work has focused on advancing thermal simulations. Available continuum structural models rely on brick elements that do not accurately capture bead geometry and make it challenging, if not impossible, to simulate imperfect bond at interfaces between beads. Such models also require a large number of

elements to discretize each bead, resulting in models that quickly become computationally intractable. Further, the simulation of part-bed separation and other complex boundary conditions is challenging with solid models. In the big picture, the ongoing aim of this work is to develop a beam-element-based, computationally efficient structural model of large 3D-printed parts to determine residual stresses and deformations developed during printing. The use of beam elements allows for the more realistic simulation of bead cross-sections, decreases the difficulty of simulating imperfect inter-bead bonds and simplifies the implementation of boundary conditions such as part-bed separation. Because maximum element lengths are no longer constrained by bead height, models can employ far fewer degrees of freedom than brick element-based continuum models, greatly increasing simulation speed. The model provides a convenient framework for addressing the shortcomings of existing solid models while allowing designers to determine optimal printing parameters before a print and reduce costly trial and error iterations. Toward those ends, the purpose of this paper is to establish the model methodology and evaluate its predictions and performance relative to an existing continuum model to assess its potential moving forward. More details of the model, its application to a wall print and comparison to an ABAQUS model can be found in Section 2. Section 3 discusses the results, Section 4 their implications and Section 5 provides ideas on future work and concludes the paper.

2. Development of Beam Element-Based Simulation

2.1. Model Description

A two-dimensional, beam-based, small-strain and deformation finite element model is presented here. As discussed in the introduction, an FDM part consists of layers made up of one or more beads, which all bond to their neighbors. As shown in Figure 1, the beads are represented in the model with beam elements and the inter-bead bond is simulated using multipoint constraints and vertical axial-only elements (termed vertical springs for the rest of this paper). The model is structural only and requires temperatures versus location and time as input.

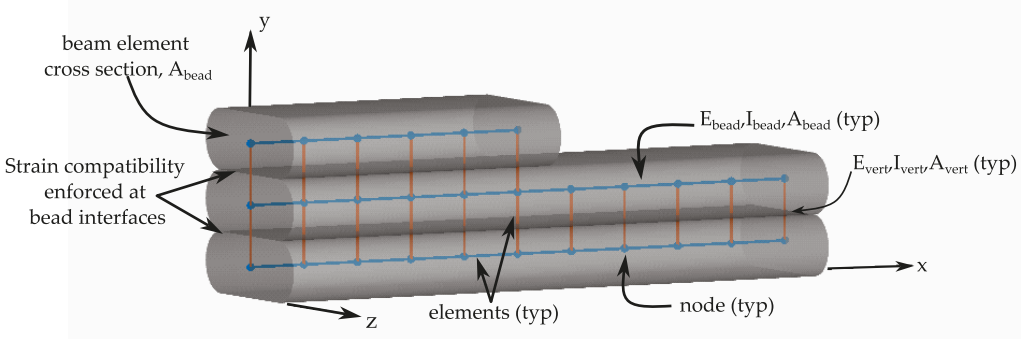

Figure 1. Element discretization.

Examining the FDM process, the print head continuously deposits molten material (which forms a bead) at a given temperature, moving at a certain speed and extrusion rate, pauses to allow the bead to cool if directed by the G-code and then repeats the process for the next bead. This continuous process is approximated using discrete time steps in the model and in each time step only introducing elements whose centroids have already been printed. The settings defining this process determine the cross-section of the bead in addition to the area of the inter-bead bond, and the aspects relevant to the model are captured via the elemental cross-sectional areas (A_{bead} or A_{vert}) and moment of inertia (I_{bead} or I_{vert}). As the bead's temperature fluctuates due to cooling and rewarming due to the placement of adjacent beads, the stiffness of the bead increases and decreases, respectively. This phenomenon is incorporated into the model by defining the elastic modulus (E_{bead} or E_{vert}) as a function of temperature. Changes in bead temperature also induce thermal strains, which are included in the model as element pre-strains. It is assumed that thermal strains

accumulate only once the bead temperature falls below the glass transition temperature of the polymer (T_g). The stiffness of the inter-bead bond is dependent on printing parameters and is accounted for in the vertical direction in the model by allowing $E_{vert} \neq E_{bead}$, where both moduli of elasticity can be calibrated to the specific printer and parameters through material testing. Linear, multipoint constraints are employed to enforce inter-bead shear transfer and assume full composite action (i.e., no interlayer slip). Flowcharts for both the process and the model's representation of that process are shown in Figure 2. The grey dotted lines denote correspondence between process and model steps. All aspects of the model are elaborated on in the following sections.

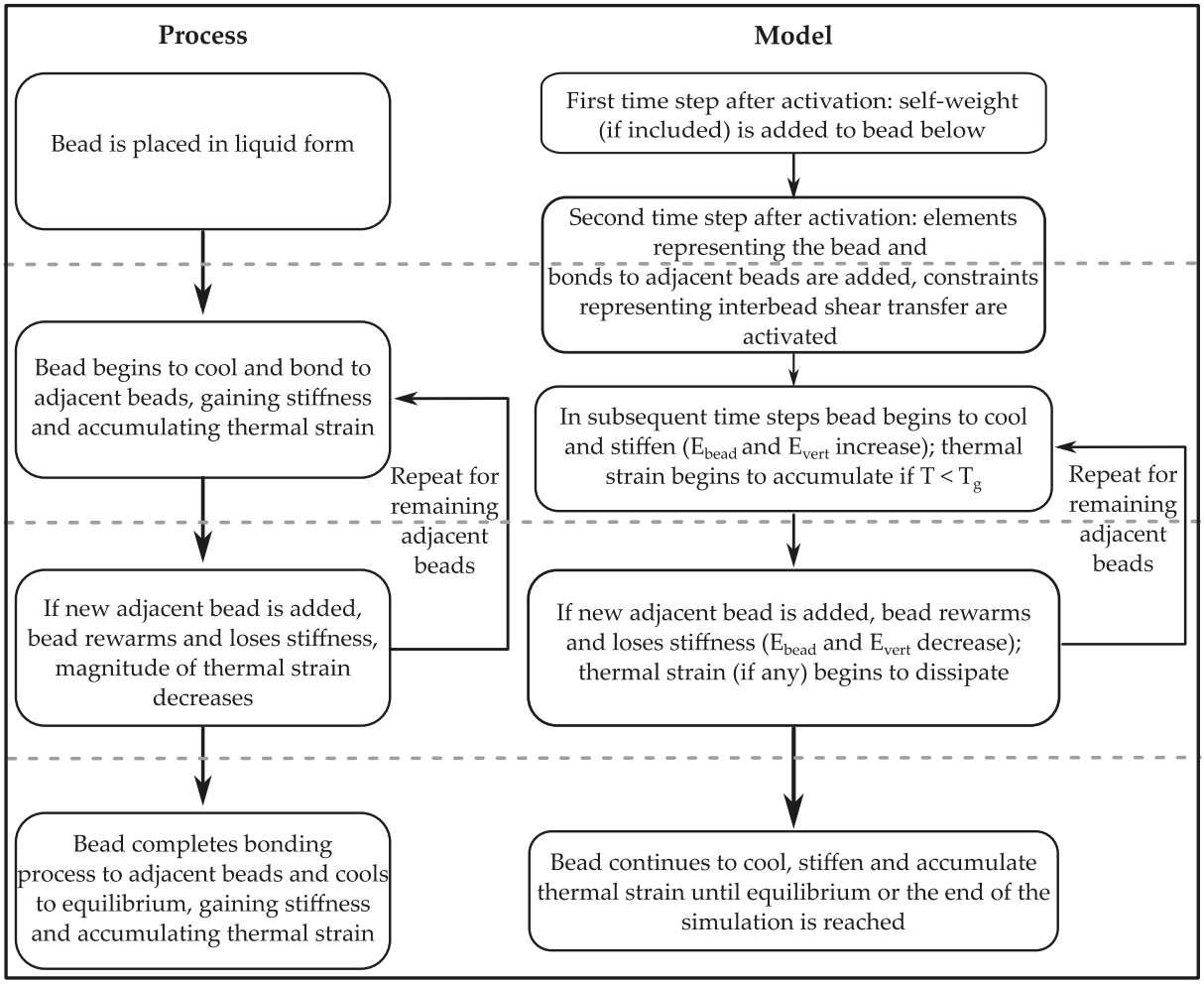

Figure 2. Process-model flowchart.

Employing the principle of virtual work for the current model produces Equation (1),

$$\delta W_{int_b} + \delta W_{int_{ax}} + \delta W_{int_f} - \delta W_{ext} = 0 \tag{1}$$

where sub-subscript b denotes bending, ax denotes axial and f denotes a spring foundation supporting the base of the printed part, which is discussed later. Substituting the well-established expressions for each virtual work term produces the weak form of the governing differential equation for a beam element in the model, shown in Equation (2),

$$\int_0^l EIv''\delta v''dx + \int_0^l A\sigma\delta\epsilon dx + \int_0^l kv\delta v dx - \int_0^l q\delta v dx = 0 \tag{2}$$

where E is modulus of elasticity; I is the second area moment of inertia; a prime denotes differentiation with respect to x, the position along the element; v is the transverse displacement along the element; δ denotes the variation of a displacement, strain or curvature; A is the cross-sectional area of the element; σ is the axial stress; ϵ is the axial strain; k is the stiffness of the foundation; q represents the applied vertical loads due to self-weight; u is the axial displacement and U^{el} is a vector of element nodal displacements. Thermal pre-strains are incorporated in the axial stress–strain relationship. To obtain Equation (3), the standard shape functions for an Euler–Bernoulli beam denoted by N_{ax} and N_b for axial and bending, respectively, are substituted into Equation (2) for the corresponding displacements, virtual displacements and their derivatives. Further, applying $\sigma = E(\epsilon - \epsilon_T)$ where ϵ_T is a thermally induced strain and letting $\epsilon = u\prime$ from standard small strain kinematics produces

$$\int_0^l EIN_b'' U^{el} N_b'' \delta U^{el} dx + \int_0^l AEN_{ax}' U^{el} N_{ax}\prime \delta U^{el} dx + \int_0^l kN_b U^{el} N_b \delta U^{el} dx - \int_0^l qN_b \delta U^{el} dx - \int_0^l AE\epsilon_T N_{ax}\prime \delta U^{el} dx = 0 \tag{3}$$

Simplifying and combining like terms produces Equation (4),

$$\delta U^{el\,T} \left(\left(\int_0^l EIN_b''^{\,T} N_b'' dx + \int_0^l AEN_{ax}'^{\,T} N_{ax}\prime dx + \int_0^l kN_b^T N_b dx \right) U^{el} - \int_0^l qN_b^{\,T} dx - \int_0^l AE\epsilon_T N_{ax}\prime^T dx \right) = 0 \tag{4}$$

Because the virtual displacements are arbitrary, Equation (5) must hold.

$$\left(\int_0^l EIN_b''^{\,T} N_b'' dx + \int_0^l AEN_{ax}'^{\,T} N_{ax}\prime dx + \int_0^l kN_b^T N_b dx \right) U^{el} = \int_0^l qN_b dx + \int_0^l AE\epsilon_T N_{ax}\prime^T dx \tag{5}$$

Equation (5) is the discretized version of the weak form for a single element which, in conjunction with the multi-point constraints detailed later, drives the model. The terms multiplying the nodal displacements are the bending, axial and foundation contributions to the element stiffness matrix. The axial and bending stiffness matrices are the standard ones for an Euler–Bernoulli beam. The foundation contribution is non-zero only for the bottom layer of elements, and the treatment of this is detailed in Section 2.1.3.

2.1.1. Element Activation

Elements are activated as they are printed through a two-step process. It is assumed that just-printed elements contribute self-weight but not stiffness to the structure as shown in Figure 3. Element activation times, corresponding to when the centroid of an element is printed and easily derived from G-code, are input to the model. During the first time step after activation, the self-weight of the new elements is applied. In the next time step, new nodes corresponding to the new elements are activated with an initial vertical position based on the deformed position of the nodes below. Then the new elements are added to the model and their self-weight is applied to the centerline of these new elements. New elements are assigned an initial displacement based on the current position of their nodes, which does not cause stress or strain in the element.

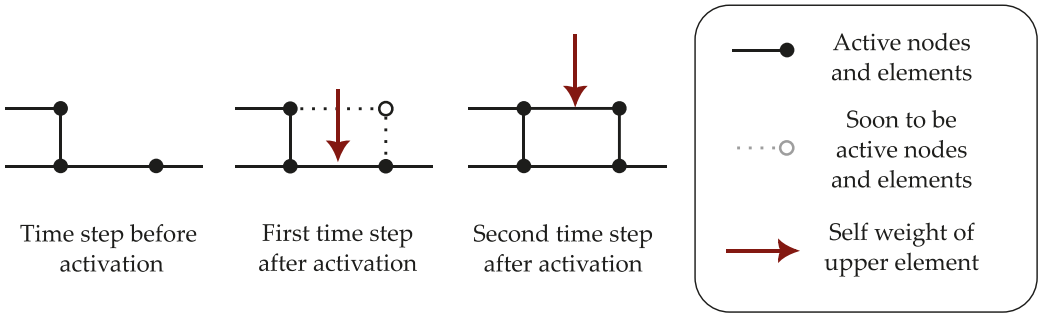

Figure 3. Element activation.

2.1.2. Multipoint Constraints

Because the beads are modeled using beams, which are one-dimensional elements, additional strategies must be employed to transfer forces between the beads. Vertical forces are transferred via vertical springs connecting a beam's end nodes to those of the beams immediately above and below it. Interface shear force transfer between beads is tackled with multipoint constraints (MPCs). For example, MPCs have been used for shear transfer in a composite beam [71], shear transfer between a bridge deck and girder [72] and during the simulation of warping of a composite beam's cross-section [73]. In the current model, multipoint constraints are employed to ensure strain compatibility at every bead–bead interface. A pair of constrained elements, with notation used throughout this paper, is shown in Figure 4.

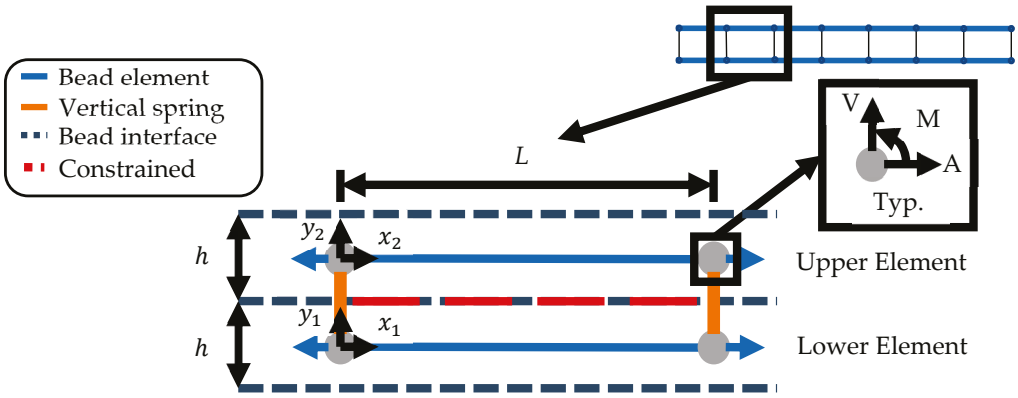

Figure 4. Constrained elements.

Full composite action is assumed between layers, meaning beads do not slip relative to each other. This implies that from the time of activation of the upper element, the change in longitudinal strain at the top of the layer below (the lower element in Figure 4) is equal to the change in longitudinal strain at the bottom of the layer above (the upper element in Figure 4). The total longitudinal strain at any point within a beam element $\epsilon(x, y)$ is given in Equation (6),

$$\epsilon(x, y) = \epsilon_a - v''(x)y, \tag{6}$$

where ϵ_a is the axial strain, v'' is the element bending curvature and y is the signed distance from the neutral axis of the beam (centerline of the bead). Using the conventional Euler–Bernoulli beam element, axial strain is constant along the length of the beam and is given by Equation (7),

$$\epsilon_a = \frac{u_j - u_i}{L}, \tag{7}$$

where u_i and u_j are the axial displacements of element starting and ending nodes i and j, respectively, and L is the element length. The curvature of a beam element is given in Equation (8),

$$v''(x) = N_b''(x)U^{el}, \tag{8}$$

where N_b'' as defined previously is the second derivative of the element bending shape functions with respect to x and $U^{el} = \begin{bmatrix} u_i & v_i & \theta_i & u_j & v_j & \theta_j \end{bmatrix}^T$ is the element displacement vector of x-direction nodal displacements u, y-direction nodal displacements v and rotations θ at nodes i and j of an Euler beam element. Since axial strain is a function of x-direction nodal displacements, the corresponding coefficients can be added to yN_b'' in the correct locations to obtain B, the matrix that relates strains to U^{el}. Total longitudinal strain at any point in a beam element can then be expressed as shown in Equation (9),

$$\epsilon(x, y) = B(x, y)U^{el}. \tag{9}$$

To enforce strain compatibility between two beads in the model at a location x at any time t after the activation of the upper element at t_u^{act}, the strain at the bottom of the upper element ϵ_u must equal the strain accumulated in the top of the lower element ϵ_l following activation of the upper element. Equation (10) offers the full constraint expression at any point x within a pair of upper and lower elements that must be enforced to ensure inter-bead shear transfer and $\epsilon_u = \epsilon_l$.

$$\epsilon_u\left(x, -\frac{h}{2}, t\right) - \left(\epsilon_l\left(x, \frac{h}{2}, t\right) - \epsilon_l\left(x, \frac{h}{2}, t_u^{act}\right)\right) = 0 \tag{10}$$

Substituting Equation (9) into Equation (10) offers the required strain compatibility Equation (11) at the bead interface in terms of element displacements in a form suitable for inclusion in a displacement-based finite element analysis,

$$B_u\left(x, -\frac{h}{2}\right)U_u^{el}(t) - B_l\left(x, \frac{h}{2}\right)U_l^{el}(t) + B_l\left(x, \frac{h}{2}\right)U_l^{el}\left(t_u^{act}\right) = 0. \tag{11}$$

For the structure as a whole, the multipoint constraints required to ensure strain compatibility at the interfaces of all beads are expressed in the form given in Equation (12),

$$G^T U = C, \tag{12}$$

where G^T is a matrix of constraint coefficients, U is a vector of global nodal displacements and rotations, and C is a vector of constraint constants. Equation (11), which applies within a single element, is a function of local element displacements that are easily transformed to global nodal displacements using standard techniques. As discussed in Section 2.1.1., elements have an initial displacement U^0, which does not cause strain, that is defined when the element is activated and must be subtracted from the total nodal displacements as shown in Equation (13) to obtain the strain producing displacement U^{el},

$$U^{el} = U - U^0. \tag{13}$$

Because the total longitudinal strain due to both bending and axial force within a single element vary linearly along the length of the element at any depth, the strain compatibility must be enforced at two locations within each pair of bonded elements to ensure strain compatibility along the full length in contact. For simplicity, the end nodes of the elements are chosen. Once activated, a constraint is present in every subsequent time step. Substituting Equation (13) into Equation (11), recognizing that the constants in G^T are terms in B_u and B_l at the element ends, and isolating the unknowns offers the final constraint equations for a single element pair, shown in Equations (14) and (15),

$$G_u(0)U_u(t) - G_l(0)U_l(t) = G_u(0)U_u\left(t_u^{act}\right) - G_l(0)U_l\left(t_u^{act}\right) \tag{14}$$

$$G_u(L)U_u(t) - G_l(L)U_l(t) = G_u(L)U_u\left(t_u^{act}\right) - G_l(L)U_l\left(t_u^{act}\right), \tag{15}$$

where vectors G_l and G_u are given below in Equations (16)–(19).

$$G_l(0) = \left[-\frac{1}{L} - \frac{3h}{L^2} - \frac{2h}{L} \; \frac{1}{L} \; \frac{3h}{L^2} - \frac{h}{L}\right], \tag{16}$$

$$G_u(0) = \left[-\frac{1}{L} \; \frac{3h}{L^2} \; \frac{2h}{L} \; \frac{1}{L} - \frac{3h}{L^2} \; \frac{h}{L}\right], \tag{17}$$

$$G_l(L) = \left[-\frac{1}{L} \; \frac{3h}{L^2} \; \frac{h}{L} \; \frac{1}{L} - \frac{3h}{L^2} \; \frac{2h}{L}\right], \tag{18}$$

$$G_u(L) = \left[-\frac{1}{L} - \frac{3h}{L^2} - \frac{h}{L}\frac{1}{L}\frac{3h}{L^2} - \frac{2h}{L} \right]. \tag{19}$$

2.1.3. Boundary Conditions

In the model, the contact between the bed and print can be modeled in two ways. The bottom layer of the print can be fixed to the bed, simulating a perfect bond between the first layer of the part and the bed. To fix vertical displacement, vertical springs are added extending from the centroid of the lowest bead to the height of the bed. The bottom ends of these elements are fixed. To lock horizontal displacements, constraints of the form of Equations (14) and (15) are added, where the first bead is the upper layer and the constraint constants and values for the lower bead are all zero.

The second option for boundary conditions in the model simulates no adhesion of the part to the bed, which means the part should be able to slide horizontally and freely lift off from the print bed but not penetrate into it. The simulation of this condition has significant practical importance, as it is not unusual to sandwich a bond breaker between a part and the print bed. To ensure numerical stability, very soft horizontal springs are attached to the lowest bead. To allow only positive vertical displacement, bilinear beam on elastic foundation (BBOEF) elements were used for the lowest bead that have distributed vertical springs with a very large compressive stiffness and very small tensile stiffness relative to other elements in the model. The derivation of the contribution of the springs to the element stiffness matrix is as follows. From the discretized weak form given in Equation (5), the contribution of the springs to element stiffness is given in Equation (20),

$$K_{se} = \int_0^l k N_b^T N_b dx. \tag{20}$$

Because k is not constant over the length of the element, the integral must be split as shown in Equation (21),

$$K_{se} = \int_{L_c} k_c N^T N dx + \int_{L_t} k_t N^T N dx, \tag{21}$$

where L_c and L_t are the portions of the element where the springs are in compression and tension, respectively. The compressive stiffness k_c is large to prevent inter-penetration of the bed, and k_t is set to a very small value to allow free separation of the part from the bed if it is unbonded. Because L_c and L_t are not known a priori, the use of these elements introduces nonlinearity, requiring an iterative solution strategy as discussed in Section 2.1.4.

The formulation of the BBOEF element was verified through comparison of the model prediction using 100 elements with the analytical solution of Zhang and Murphy [74] for the displacement of a free–free beam on a tensionless foundation with a point load at the center. The authors normalize all values by β, given in Equation (22),

$$\beta = \left(\frac{k_c}{4EI} \right)^{\frac{1}{4}}, \tag{22}$$

where E is the Young's modulus of the beam material and I is the second moment of area of the beam cross-section. Important values are normalized as shown in Equation (23),

$$\begin{aligned} l &= \beta L \\ F &= \frac{P}{4\beta^2 EI} \\ \zeta &= \beta x \\ w &= \beta v \end{aligned} \tag{23}$$

where L is physical beam length, P is the magnitude of the applied point load and v is transverse displacement. Zhang and Murphy [74] chose to show the results of a beam with normalized length of four and two cases of normalized applied load of 0.1 and 0.2. For the BBOEF beam, EI was chosen to be 4300 kN-m^2 and k_c was 1.76 $\times$ 10^6 kN/m^2. From this, β, L and P were calculated and the simulation was run. The two solutions are compared in Figure 5, which indicates excellent agreement.

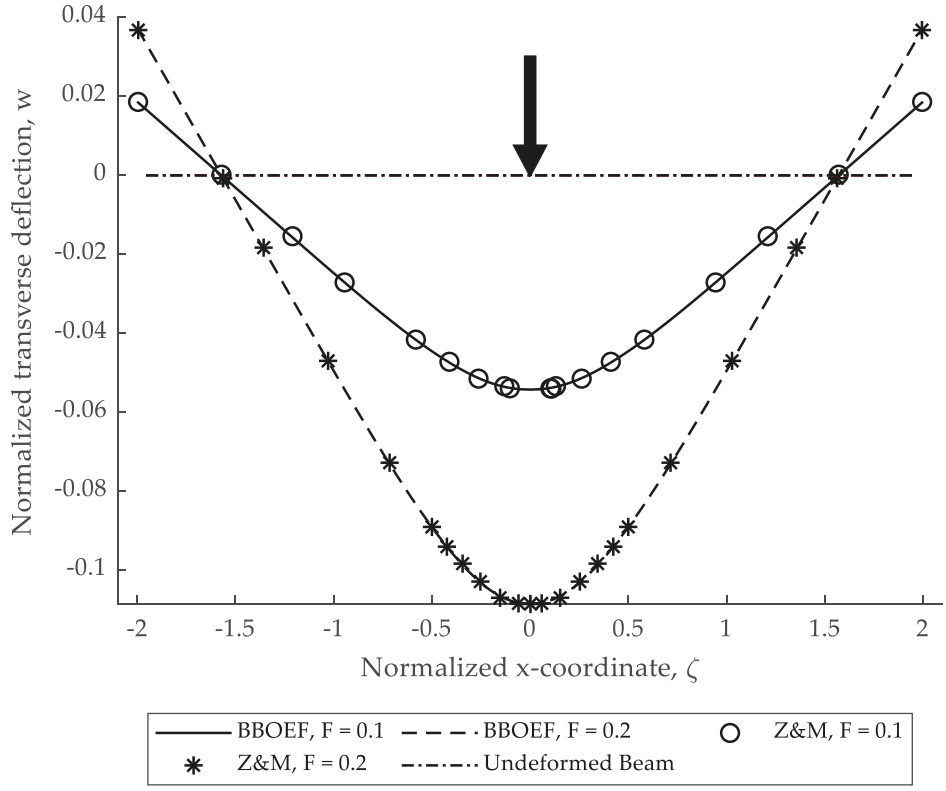

Figure 5. Comparison of BBOEF to Zhang and Murphy [74].

2.1.4. Solution Strategy

The general problem to be solved is given in Equation (24),

$$F_{int} = F_{ext}, \tag{24}$$

subject to some boundary conditions discussed later, where F_{int} are internal forces and F_{ext} are external forces, both in the global coordinate system. There are two types of external forces in the model: the self-weight of each element and thermal forces. Thermal forces develop in an element as it cools, as given by the inputted thermal profile. While element temperatures generally change between time steps, within one time step it is assumed that the temperature is constant for the whole element. The thermal force in one element, f_{th}, is given in Equation (25),

$$f_{th} = EA\alpha\Delta T, \tag{25}$$

where E is the modulus of elasticity for the material at the current temperature, A is the cross-sectional area of the element, α is the coefficient of thermal expansion at the current temperature and ΔT is the change in temperature from deposition to the current time. Thermal forces in the longitudinal and height directions are carried by the beams and vertical springs, respectively, and there can be a different coefficient of thermal expansion for each direction. Since the thickness of the wall is much smaller than the height or length, thermal expansion through the thickness of the wall is ignored.

There are two kinds of internal forces in the model, constraint and member forces. From Section 2.1.2., the system of equations of all constraints is given by Equation (12). The constraints are enforced using the penalty method, where violations are penalized by correcting forces applied by very stiff springs. These forces, F_c, given in Equation (26),

$$F_c = G\kappa\left(G^T U - G_0\right), \tag{26}$$

are calculated by pre-multiplying the error in the constraints by $G\kappa$, where κ is a diagonal matrix of spring stiffnesses corresponding to each constraint equation. The other type of internal forces in the model are member forces, shown in Equation (27) for a single element,

$$f_{el} = k_{el} u_{el}, \tag{27}$$

where k_{el} and u_{el} are the element stiffness matrix and element displacement vector, both in local coordinates. Since strain-producing element displacements are equal to nodal displacements minus initial element displacements, distributing the element stiffness matrix and assembling the two parts separately (into KU and the correction for non-strain causing displacements, F_{el_0}, respectively) produces the global internal force vector, F_{el}, shown in Equation (28),

$$F_{el} = KU - F_{el_0}, \tag{28}$$

where K and U are the global stiffness and nodal displacement vectors. Assembling the local element thermal and self-weight forces into the global external force vector, F_{ext}, and isolating terms with the unknowns, which are the global vector of nodal displacements, produces Equation (29),

$$\left(K_{bc} + G\kappa G^T\right) U = F_{ext} + G\kappa C + F_{el_0}, \tag{29}$$

where K_{bc} is the global system stiffness matrix after applying relevant boundary conditions.

Because the bilinear boundary springs make the problem nonlinear, Equation (29) is solved iteratively using Newton's method. The contribution of the BBOEF elements to system stiffness is recalculated at every time increment, and initial member forces due to the BBOEF elements must also be recalculated. To increase computational efficiency, F_{el_0} is split into two parts: F_{m_0}, the initial member force correction calculated once per increment, and F_{s_0}, the initial force correction due to the BBOEF elements, calculated every iteration. The entire solution algorithm is below.

For each time step t_i,

1. Set $U_i = U_{i-1}$;
2. Determine T_i, the current temperature, and compute $\Delta T_i = T_i - T_0$ for all elements;
3. Update K by updating elastic moduli and adding new elements, if any;
4. Compute and assemble $F_{th} = EA\alpha\Delta T_i$ for each element and update F_w if there are new elements;
5. Update G if there are new elements;
6. Compute $K\prime = \left(K_{bc} + \kappa G G^T\right)$ and $F' = F_{th} + F_w + \kappa G C + F_{el_0}$;
7. Calculate $R = F' - K'U_i$;
8. While $R > tol$,
    a. Solve $K'\Delta U = R$;
    b. $U_i = U_i + \Delta U$;
    c. $K_{bc} = K$;
    d. For each BBOEF element,
        i. Calculate $v(x) = NU_e$;
        ii. Find $v(x) = 0$, in the interval $(0, L)$;
        iii. Break into subintervals using the roots determined in ii and find state of springs in each;

iv. Calculate K_{se};
v. Add K_{se} to K_{bc};

e. $K' = \left(K_{bc} + \kappa G G^T\right)$;
f. Recalculate F_{s_0};
g. $F' = F_{th} + F_w + \kappa G C + F_{el_0}$;
h. $R = F' - K' U_i$.

3. Wall Print

To test the model, it was applied and compared to the print and continuum model created by Robles-Poblete et al. [75]. The authors describe the printing of a 1 m tall by $\frac{3}{4}$ m long single bead wide wall made of polyethylene terephthalate glycol (PETG) reinforced with short carbon fiber. The first layer of the wall was a brim slightly larger than the wall with a length of 0.87 m and a width of 0.135 m. Thermocouples were placed in the wall throughout printing. Each layer was printed left to right, making the problem unsymmetric. A SC-TMA was created in ABAQUS, which utilized a combination of experimentally derived properties and properties chosen such that error between measured and simulated temperatures was minimized. Temperature-dependent specific heat, coefficient of thermal expansion and elastic modulus in two directions were all determined experimentally, as was thermal conductivity, but only at room temperature. Room temperature shear moduli and Poisson's ratios were taken from the literature and the multifactor approach was used to estimate the temperature dependence of the stiffnesses. It was assumed that the material was transversely isotropic and that above the glass transition temperature, elastic properties were constant, and no thermal strains were induced. To minimize error between simulated and measured temperatures at relevant locations, a bed-part conductance value of 10 W/m^{2}K and a convection coefficient varying from 3 to 15 W/m^{2}K with increasing wall height were chosen. Perfect bonding between the bottom of the part and the bed was assumed and self-weight was ignored. The mesh consisted of cube-shaped hexahedral elements where side length was equal to the height of a bead which resulted in 148 elements along the wall width and 3 elements through the thickness. Full details are given in [75].

The thermal results of Robles-Poblete's model, and the event series controlling element activation were all input into the beam-based model and a copy of the ABAQUS 3D structural continuum model discussed in [75] for comparison. In the two-dimensional beam-based model, applied temperatures were averages though the thickness of the wall. The material properties for both models were from Robles-Poblete with slight modifications. In particular, elastic properties (shown in Figure 6) were at a finer resolution with the room temperature definition updated and the coefficient of thermal expansion values (depicted in Figure 7) were shifted such that the location of zero strain corresponded to the material deposition temperature of 200 degrees Celsius.

To match the continuum model, the part was fixed to the bed and self-weight was ignored in the beam-based model. Though the actual brim was several beads wide, in the beam-based model it was simulated as one large bead with the same area and moment of inertia because the model is two-dimensional. To choose mesh density of the beam-based model, a convergence study was run. The beads were meshed with increasing numbers of equal length elements varying from 15 to 240 elements per layer and constant time steps of 100 s to 2 s were also examined. The beam-based model was then extended to include self-weight and the BBOEF elements.

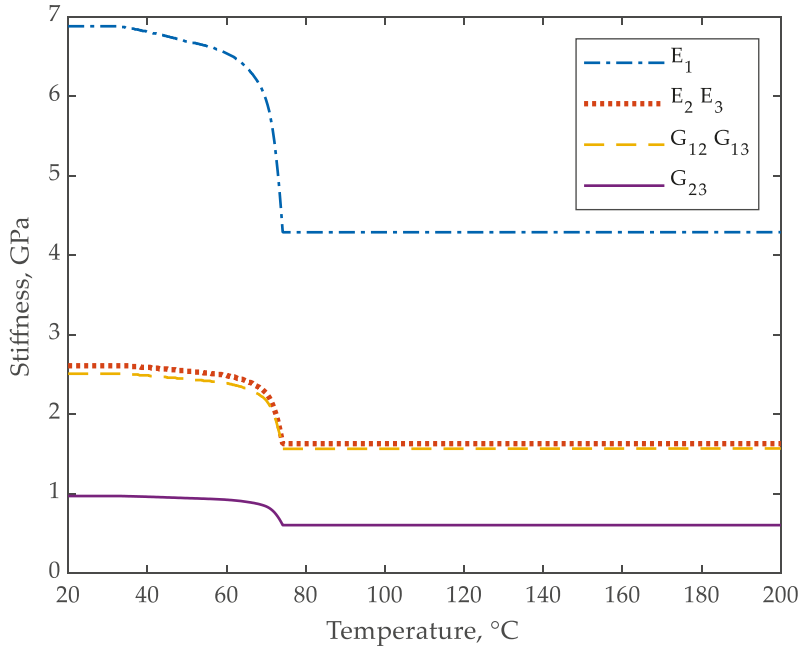

Figure 6. Elastic and shear moduli.

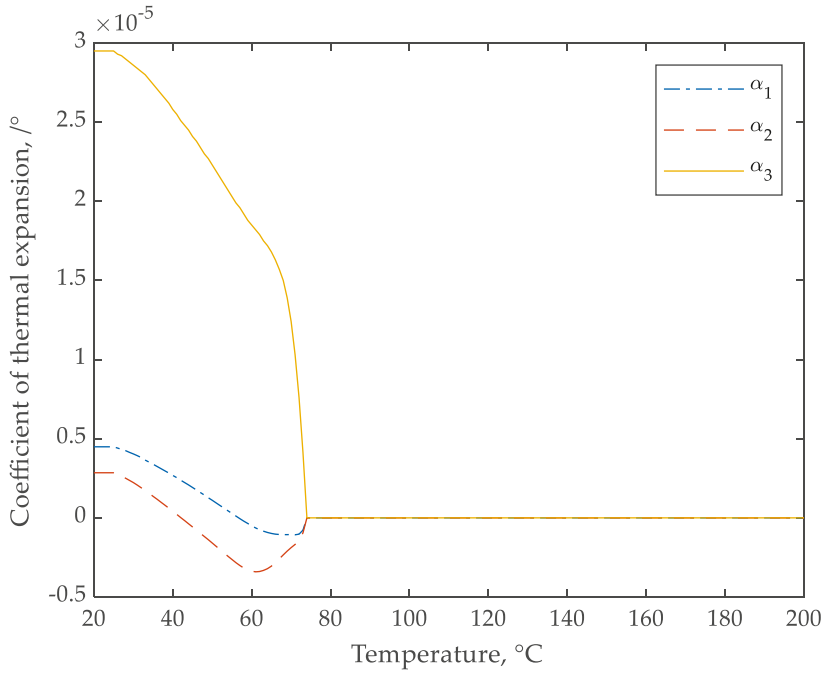

Figure 7. Thermal variation of coefficients of thermal expansion.

4. Results and Discussion

4.1. Convergence of Beam-Based Model

To check convergence of the model, the effect of time step and mesh density on both stresses and displacements must be examined. For vertical stresses, one area of interest was the corner where the lowest layer of the wall intersects the brim, because this is where the maximum stresses are located. These results and their location are depicted in Figure 8.

As Figure 8 shows, the vertical corner stress is converging to a value between 5.2 and 5.3 MPa as the number of elements per layer is increased, while time step has virtually no effect on results. Based on this, 60 elements per layer, which exhibited a 4% difference in peak stress compared to the finest mesh, is a reasonable level of mesh refinement.

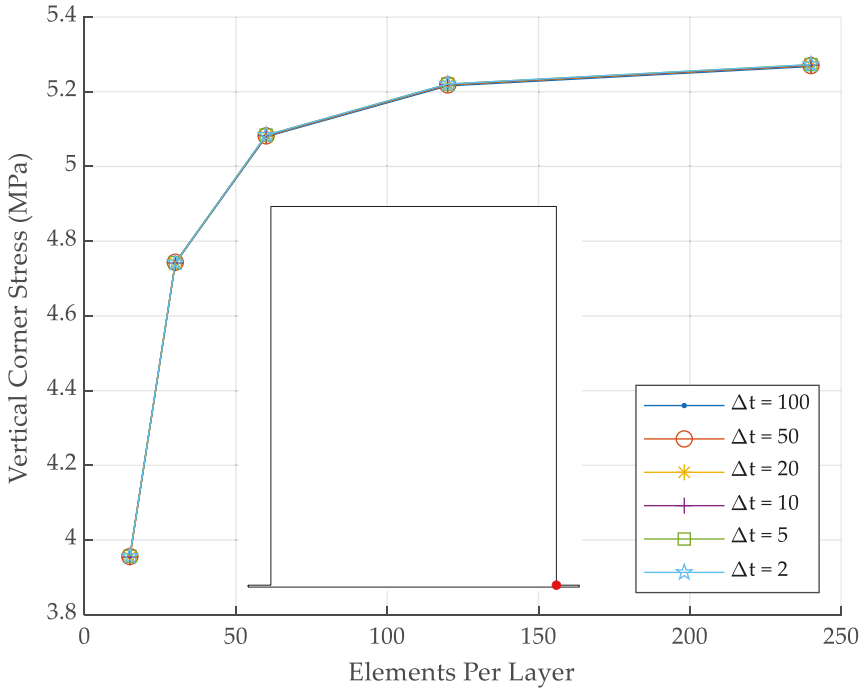

Figure 8. Final vertical stress at corner of wall versus time step and mesh density.

In the case of displacements, no obvious point of interest was visible and maximum magnitude only varied 3% from the coarsest time step and mesh density to the finest. Therefore, convergence of change in average nodal displacement for the entire wall was examined and is shown in Figure 9, which indicates that average vertical displacements are converging with decreasing time step and increasing mesh density. Mesh density has a modest effect on convergence, mainly at larger element sizes. Time step has a much larger effect on the convergence of displacements. A time step of 20 s was chosen for subsequent simulations.

Figure 10 shows the impact of time step and mesh density on model run time. As expected, simulation times grow significantly with decreasing time step and mesh density, with run times in Figure 10 varying by four orders of magnitude. For reference, the run times for the ABAQUS structural model are also given in Figure 10. The ABAQUS run times are significantly slower than all beam element model runs for the same time step, highlighting the gains in computational efficiency achievable with the beam element model. For example, the chosen configuration for the beam-based model of 60 elements per layer with a 20 s time step, shown with a red circle in Figure 10, ran in roughly six minutes, compared to 34 min and 3 h for the ABAQUS model runs with time steps of 100 and 10 s, respectively. This is due to the much larger mesh resulting from the 3D formulation with brick elements. It should be noted, however, that the ABAQUS mesh was chosen for simplicity and it is quite possible that fewer elements could be used while retaining acceptable accuracy, which could significantly reduce ABAQUS computation time. However, this is countered by the fact that the beam element model is implemented entirely in MATLAB, which is inherently slow due to the interpreted nature of the code; significant speedup would be achieved were the beam element model written in a compiled language such as FORTRAN or C. Further, while not explored here, we note that meshes with varying beam element lengths could be used to ensure convergence of peak stresses (e.g., vertical corner stress discussed above) while reducing computation costs. Overall, the time comparison indicates the promise of the beam element model for reducing run time for simulating residual stresses in large, 3D-printed polymeric parts.

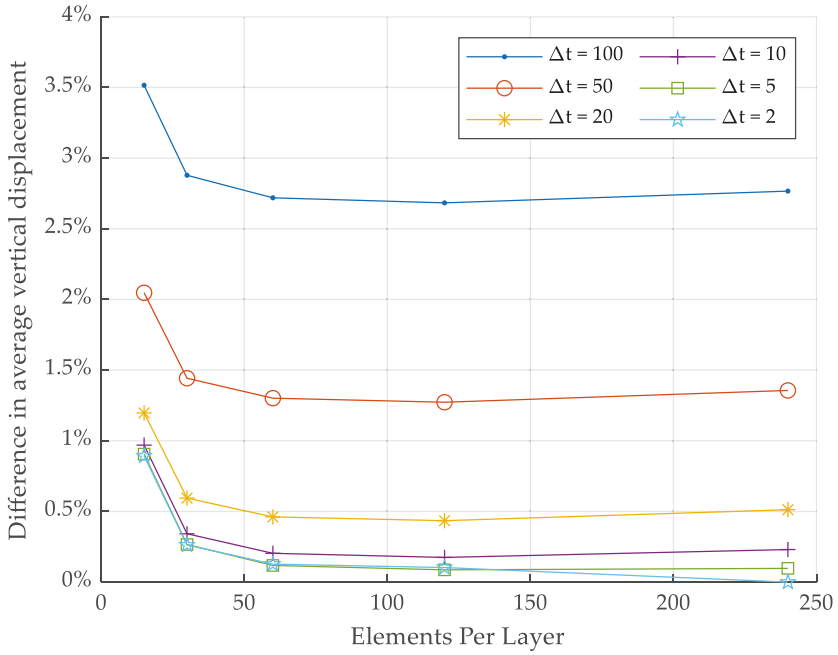

Figure 9. Difference in average vertical displacement versus time step and mesh density.

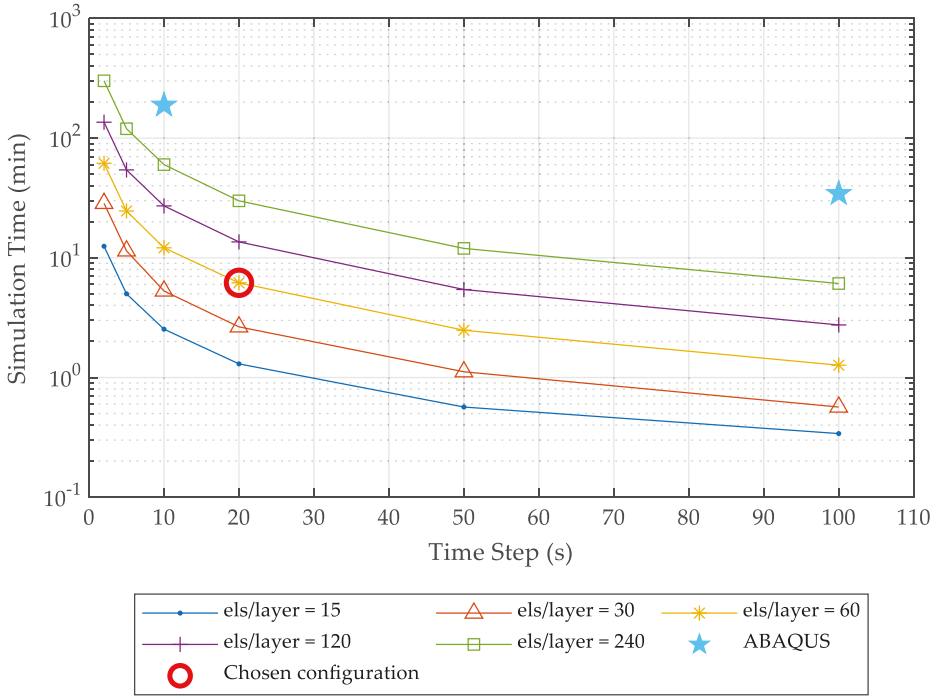

Figure 10. Simulation time versus time step and mesh density.

4.2. Comparison between Beam-Based Model and ABAQUS Structural Model

To verify the model formulation and predictions, the results of the beam-based model were compared to those of the ABAQUS continuum model. It is important to note here that at present, neither model has been validated with experimental data and so this comparison is not a validation of model accuracy. However, the previous review of the literature shows that many researchers have used continuum models incorporating ABAQUS AM Modeler, which makes it a reasonable benchmark against which to assess the beam-based model predictions. Because the two modeling approaches differ significantly (element type, dimensionality, etc.), some variation between the two sets of results is expected. The

continuum results displayed are the average through the wall thickness. Table 1 offers a summary of the results of the comparison of the final state of the part between the two models, where "Beam" denotes the beam-based model and "Cont" the continuum model. A more detailed full-field comparison of quantities follows.

Table 1. Summary of comparison of modeling approaches.

Type	Max-BB	Max-Cont	Min-BB	Min-Cont	Max Diff	Min Diff
X-displacement (mm)	0.174	0.173	−0.171	−0.172	0.803%	−0.583%
Y-displacement (mm)	1.03×10^{-5}	0	−0.355	−0.361	100%	−1.89%
Axial Stress (Mpa)	2.60	1.99	−1.12	−1.21	23.4%	−7.57%
Vertical Stress (Mpa)	5.09	3.97	−1.80	−1.25	22.0%	30.6%

Shown in Figure 11 are the full field displacements in the horizontal and vertical directions for both models at the end of simulation, after the part has cooled to ambient room temperature.

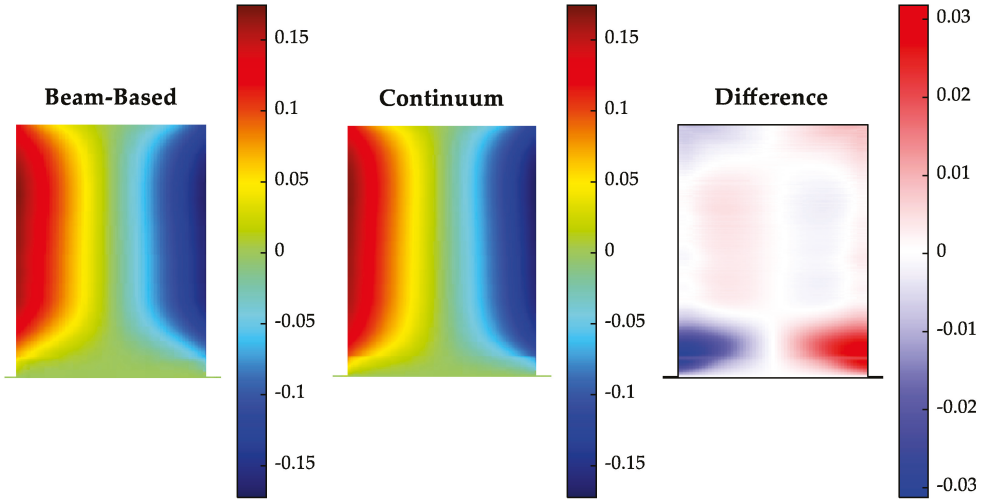

a. *x*-Displacement (mm)

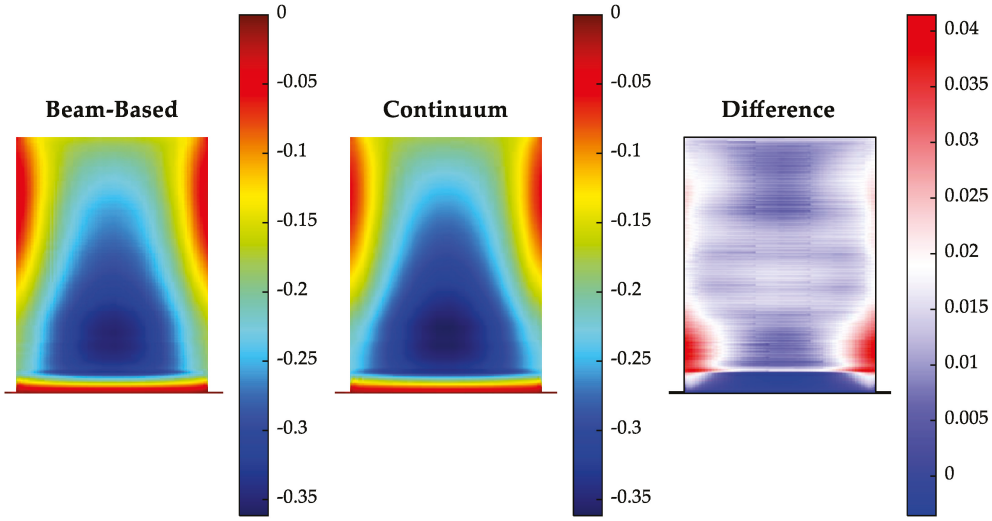

b. *y*-Displacement (mm)

Figure 11. Comparison of final displacements (mm) between beam-based and continuum models.

The spatial variation of the displacements in both directions is very similar between the two models, with the beam-based model having less displacement overall. In the case of the x-displacements (Figure 11a), the maximum difference was roughly 0.03 mm, about 20% of the maximum displacement. The largest differences are in the first third of the layers, which suggests the simplified, single-element width brim at the base of the beam-based model may be playing a significant role in the discrepancies. Examining the y-displacements (Figure 11b), there is a maximum difference of 11% of the maximum displacement or 0.04 mm. The small differences between the models in the lowest part of the wall suggests that the simplified brim discretization used in the beam-based model might not impact vertical y-displacements as significantly. Finally, the pattern of results is nearly symmetric about the wall centerline in both models, showing that the effect of the un-symmetric printing pattern is small.

Figure 12 shows x-displacements of the right edge of the wall at six points in time: four during printing, at the end of printing and at the end of cool down. At a given time step, Figure 12 shows that the shape of the curves of the two models are very similar. Though the displacements are different in the bottom of the wall between the two models, they converge at a height of roughly 300 mm and stay close after this for all but the first time step where the wall height is less than 300 mm. Figure 13 shows the vertical displacement throughout time at one point, located where the magnitude of displacement after cooling is maximum, indicating that both the trend and magnitude of y-displacements at the location shown match very well for both models.

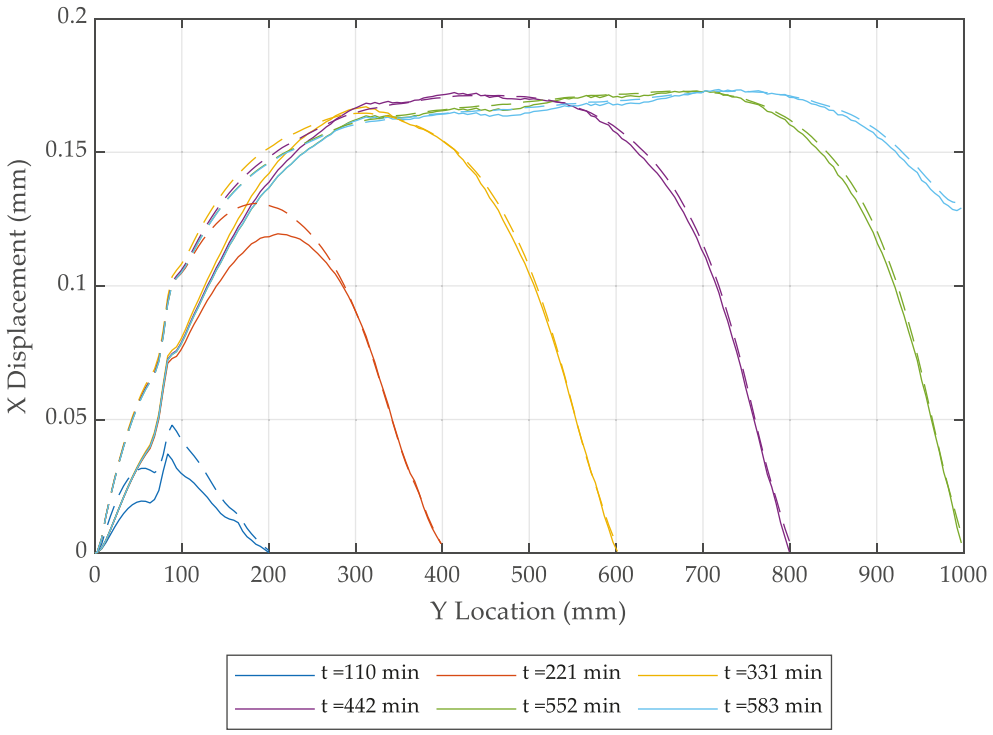

Figure 12. Comparison of x-displacement of right edge of wall throughout print (beam-based solution denoted by solid lines, continuum solution denoted by dashed lines).

Overall, displacements in both directions for both models match well, but stresses still must be examined. Figure 14 shows axial and vertical stress over the entire wall after cooldown and indicates that the largest discrepancies in stress between the two models are concentrated in the lowest third of the wall. Though the spatial variations are very similar, the magnitudes of the beam-based model are significantly higher, with the largest difference in the axial direction of 0.9 MPa being around 32% of maximum stress. In the case of vertical stresses, the largest difference of roughly 1.7 MPa coincides with the maximum

stress in the beam-based model of 5.1 MPa, corresponding to a 33% difference. These discrepancies could be caused by the use of the simplified brim in the beam-based model. Larger magnitudes of stresses in the beam based versus continuum models are consistent with the smaller magnitudes of displacements observed previously.

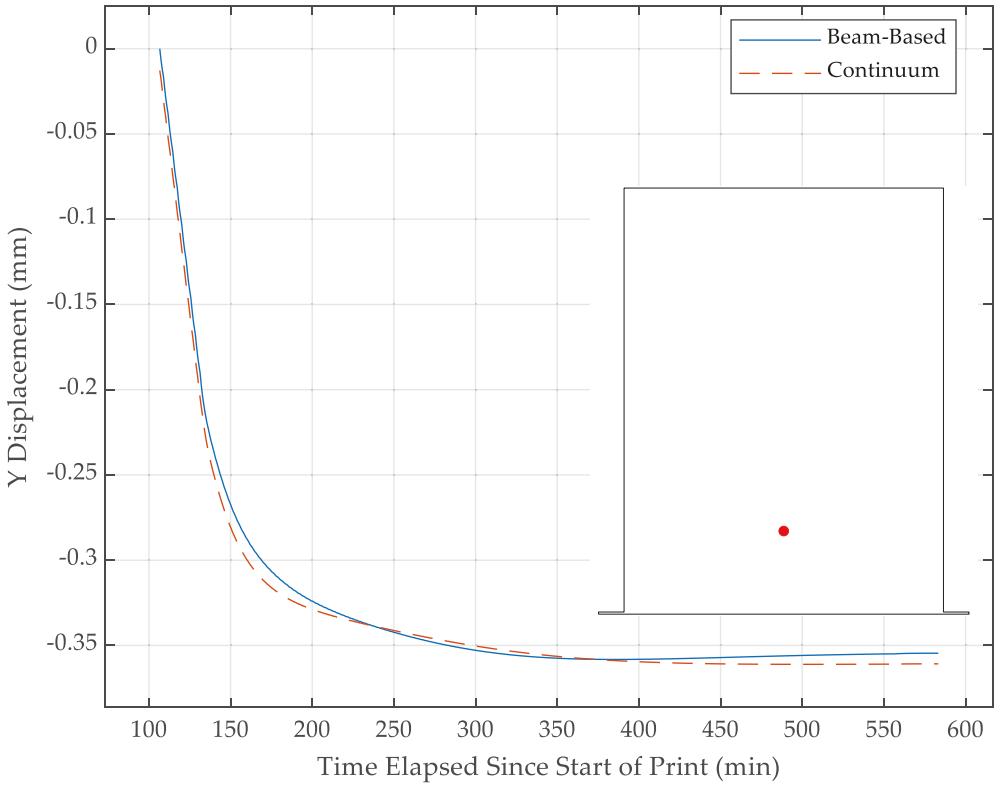

Figure 13. Comparison of y-displacement throughout print at location of final maximum.

Figure 15 shows axial (x-direction) stress at the vertical centerline of the wall as a function of height for multiple discrete times. Comparison of axial stresses shows a similar trend as x-displacements where the shapes of the curves are very similar between the models and the magnitudes match very well for portions of the wall higher than 300 mm for all time shown. The worse agreement for heights below 300 mm could be due to the beam element model's simplified discretization of the brim.

The post-cooldown maximum vertical stress in the beam-based model occurs at the interface between the brim and the second layer. Stress versus time at this location is shown in Figure 16 for both the beam-based and continuum model. Examination of Figure 16 shows that though the shapes of the two curves are very similar, at almost all times the stress in the beam-based model is larger than that of the continuum model, with a final difference of roughly 33%. It is important to note that the locations of maximum final stress of the two models do not coincide: the maximum vertical stress in the continuum model is 4 MPa and is located one bead higher, between the second and third layers. Again, these discrepancies between the magnitudes and locations of maximum vertical stress may be due to the beam-based model's simplified representation of the brim. It is important to stress that because the two modeling strategies are significantly different, discrepancies between the models are not in themselves cause for concern and without experimental data the relative accuracy of the two models cannot be compared.

Overall, temporal and spatial trends for both displacement and stresses matched well between the two models. The magnitudes of peak displacements and stresses from the two models did not match as well, especially in the lower part of the wall. However, this could be due in part to the simplified discretization of brim in the beam-based model. It is also important to note that the results of the continuum thermal model showed a significant

variation in temperature through the thickness of the brim, which could not be captured in the two-dimensional beam-based model.

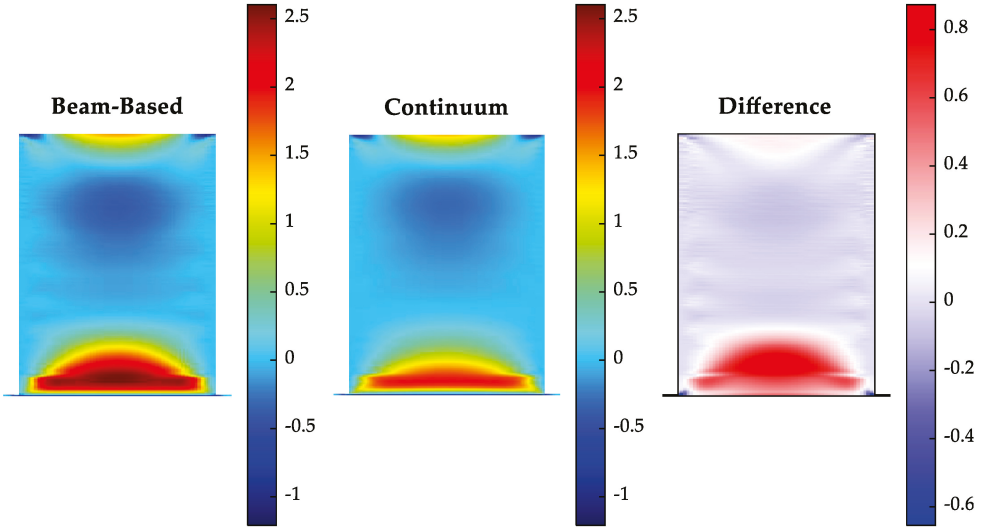

a. Axial Stress (MPa)

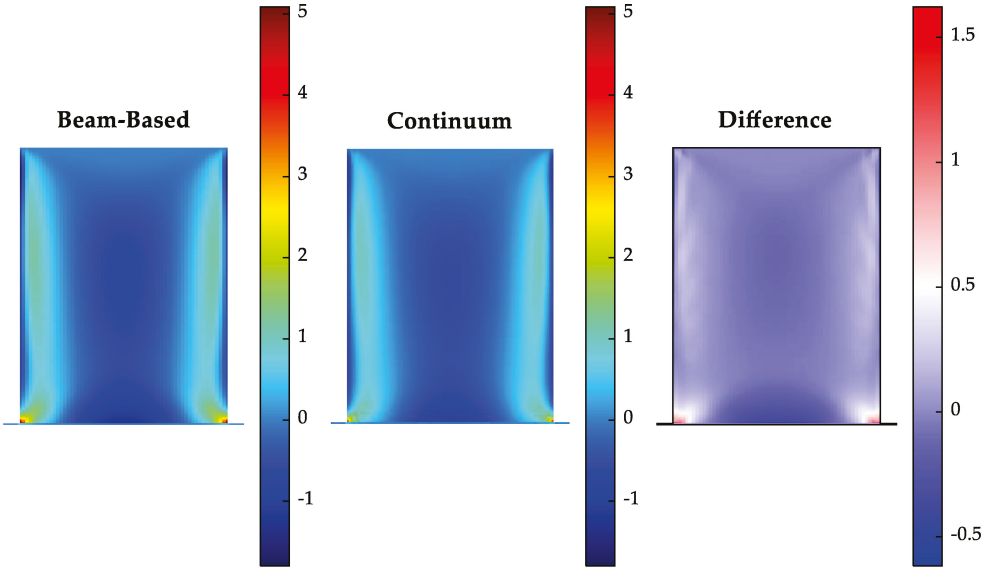

b. Vertical Stress (MPa)

Figure 14. Comparison of stress after cool down.

Comparisons were further complicated by the fact that certain algorithms in ABAQUS are not explained in documentation. For example, in the beam-based model, elements are only included in the stiffness matrix after they are activated, but inactivated elements in ABAQUS have very small non-zero stresses, suggesting they are included in the stiffness matrix before activation to some extent. This makes it impossible to determine how differences in element activation schemes impact the comparison between model results. Further, a part made using FDM is not a continuum but rather a pattern of discrete beads, which implies that a continuum FE model itself is not an ideal representation. Given these caveats, the result of the comparison between the beam-based model and ABAQUS indicate that beam-based models show significant promise for the prediction of deformations and residual stresses in large, 3D-printed polymeric parts.

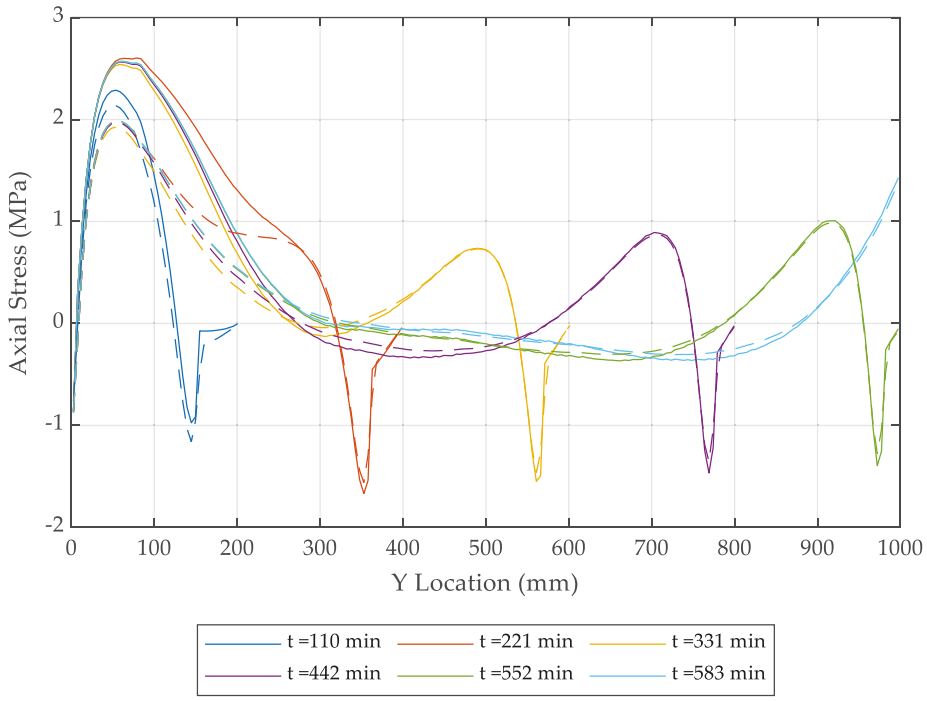

Figure 15. Comparison of axial stress throughout printing at wall centerline (beam-based solution denoted by solid lines, continuum solution denoted by dashed lines).

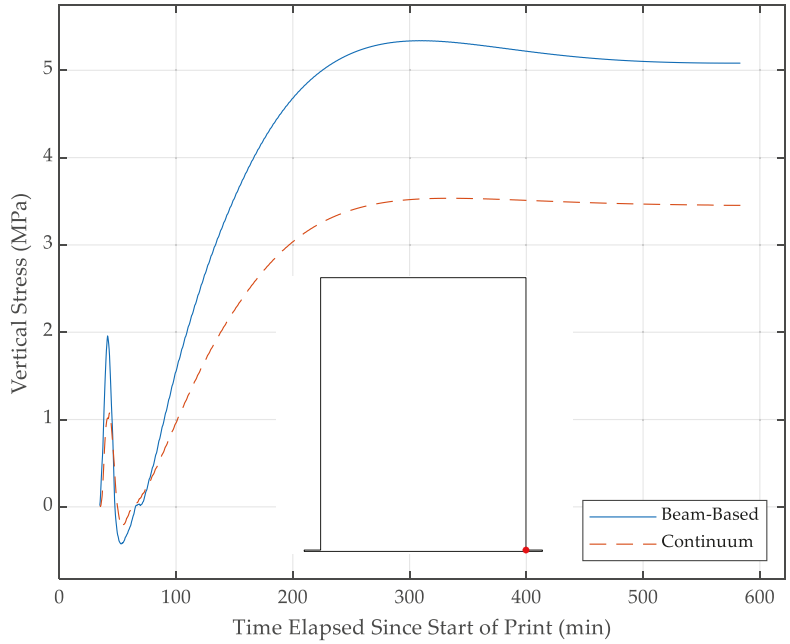

Figure 16. Comparison of vertical stress at corner between wall and brim throughout print.

4.3. Effect of Boundary Conditions on Beam-Based Model Results

An important practical detail present in many prints is de-bonding the part from the bed during the print process. To explore the significance of this, a second beam-based model was created. This model included self-weight and the elliptical cross-section of the beads with otherwise identical properties to the first beam-based model. There were two cases for boundary conditions, one which implemented a fixed boundary condition like in the first beam-based model and one which used the BBOEF elements derived previously to simulate de-bonding and part lift-off. Table 2 presents a summary of the results of the

comparison with BBOEF results termed "Spring" and the fixed results denoted "Fixed." Detailed results and a discussion are presented in the remainder of this section.

Table 2. Summary of comparison of boundary conditions of the beam-based model.

Type	Max-Spring	Max-Fixed	Min-Spring	Min-Fixed	Max Diff	Min Diff
X-displacement (mm)	0.174	0.1744	−0.171	−0.171	−0.229%	−0.467%
Y-displacement (mm)	0.232	1.03×10^{-5}	−0.330	−0.355	2260000%	−6.91%
Axial Stress (Mpa)	1.50	2.60	−1.52	−1.12	−42.5%	35.4%
Vertical Stress (Mpa)	1.25	5.09	−1.87	−1.80	−75.4%	4.29%

A comparison between final displacements predicted by the two beam-based models is shown below in Figure 17.

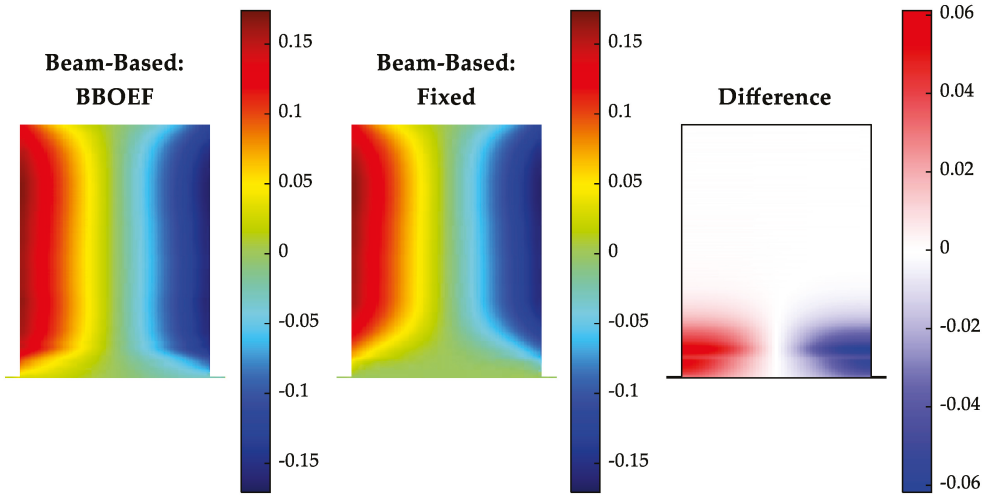

a. x-Displacement (mm)

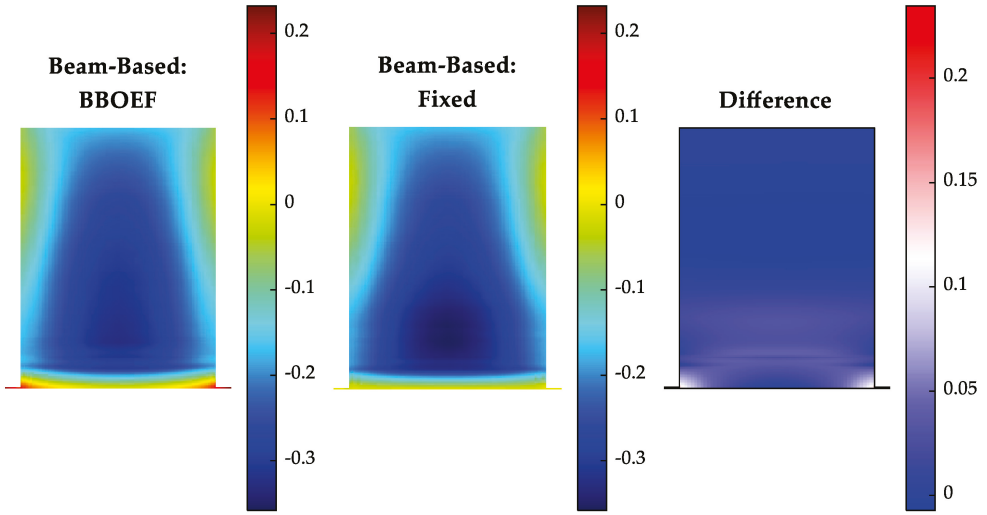

b. y-Displacement (mm)

Figure 17. Comparison of displacements between two beam-based models with different boundary conditions.

For both x- and y-direction displacements, the two models have similar patterns of variation with the BBOEF model having larger magnitudes in general. This is consistent

with the boundary conditions, where the BBOEF model is freer to move than the fixed one. It also makes sense that the largest differences are near the bottom of the wall, close to the boundary. Interestingly, though the bottom corners of the BBOEF part lift off ~0.2 mm, this deformation does not significantly affect vertical displacements in the upper half of the wall.

Figure 18 shows significant differences in magnitude and pattern of stresses between the two models. Both axial and vertical stresses are much lower for the BBOEF model, and in particular the high 5.3 MPa vertical stress near the bottom corners of the model with the fixed base is completely relieved in the BBOEF model, which predicts no stress at those locations. Such vertical stresses are a major contributor to inter-layer de-bonding during or following printing, which highlights the importance of accurately simulating boundary conditions. We also emphasize the relative ease of incorporating such boundary conditions with the beam-based modeling framework developed here.

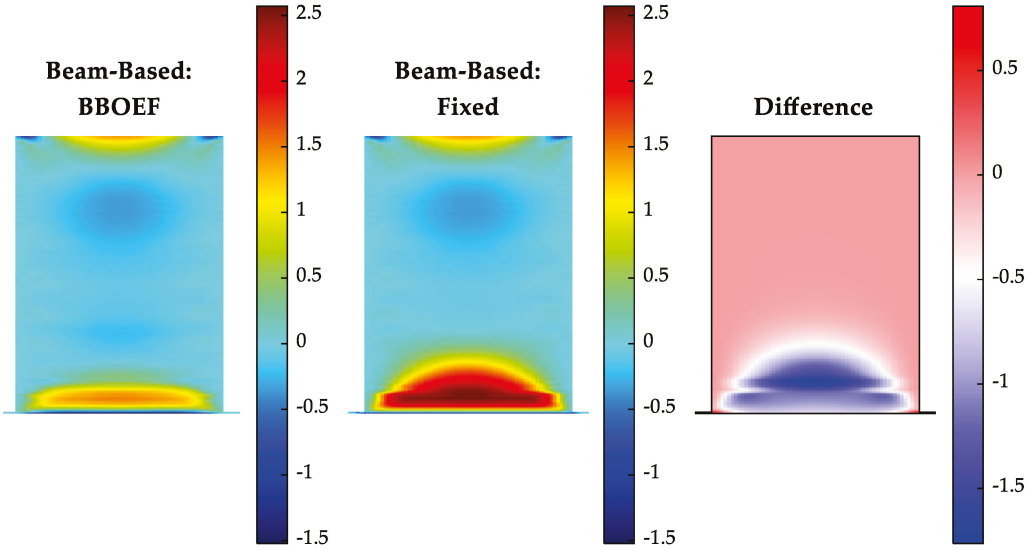

a. Axial Stress (MPa)

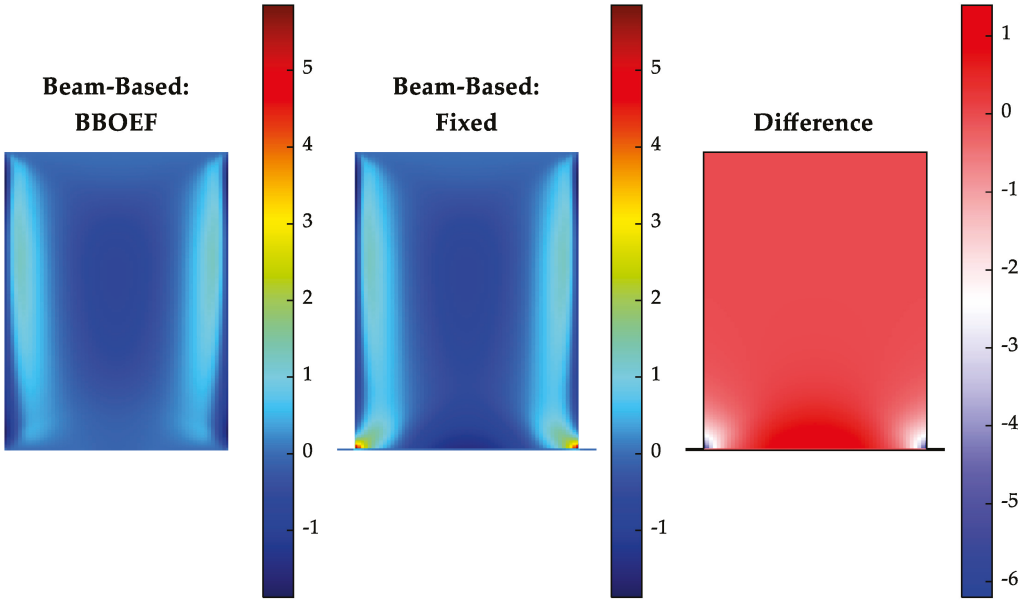

b. Vertical Stress (MPa)

Figure 18. Stresses after cooldown for both beam-based models.

5. Conclusions

A beam-based finite element framework for the simulation of the fabrication of large 3D-printed polymer parts was developed. Because the model is beam-based, it has the potential to use many fewer DOFs than existing continuum models which typically use brick elements. Not only do brick elements have more DOFs per element, but the size of the bricks is limited by layer height whereas the beam elements are not. Fewer DOFs suggests the model is faster than a comparable continuum model. Additionally, using beam elements allows for the simulation of part lift-off with relative ease. Finally, the use of beams allows for more accurate modeling of the ellipse-shaped bead cross-section, which is normally modeled as rectangular in a continuum model.

The framework is tested by comparing resulting stresses and displacements to a continuum model made with ABAQUS AM modeler. Reasonable agreement is observed, with the beam-based model also extended to allow separation of the part from the bed during printing. Specific conclusions are highlighted below.

- Spatial and temporal convergence studies showed generally smooth and adequate convergence of the beam-based model. Run times for the beam-based model were much less than for the ABAQUS AM model. Although the ABAQUS AM model was not optimized for solution efficiency, the beam-based model was developed using the MATLAB programming language, which is interpreted and relatively inefficient. Overall, convergence and run-time studies indicate that beam-based models have potential to be substantially more computationally efficient than widely available continuum modeling tools.
- The beam-based model and ABAQUS AM predicted very similar patterns of displacements and stresses. While the beam-based model tends to predict smaller displacements and somewhat larger stresses than the ABAQUS AM continuum model, these discrepancies are likely due in part to the simplified model of the brim necessitated by the two-dimensional nature of the current beam-based model.
- Simulations clearly show that simulating the practical boundary condition where part-bed separation is allowed during the print results in significantly reduced residual part stresses, indicating that accurately modeling boundary conditions is critical to accurate predictions. Part-bed separation is challenging to simulate with available continuum models, highlighting the value of this particular feature of the beam-based model developed here.

Despite its advantages, the beam-based model requires significant further development to make it a broadly useful tool for simulating the development of residual stresses and deformations in large, 3D-printed polymeric parts. Future efforts should focus on extending the beam-based model to 3D to allow the simulation of complex 3D-printed parts, obtaining experimental temperature and displacement information during the printing of large 3D polymeric parts to validate the model, and incorporating more complex phenomena like inter-layer slip, viscoelasticity and progressive fracture between printed layers.

Author Contributions: Conceptualization, W.G.D. and I.B.H.; methodology, W.G.D. and I.B.H.; software, I.B.H.; validation, I.B.H. and W.G.D.; formal analysis, I.B.H.; investigation, I.B.H. and W.G.D.; resources, W.G.D.; data curation, I.B.H.; writing—original draft preparation, I.B.H.; writing—review and editing, W.G.D.; visualization, I.B.H.; supervision, W.G.D.; project administration, W.G.D.; funding acquisition, W.G.D. All authors have read and agreed to the published version of the manuscript.

Funding: This research was funded by the US Department of Defense, grant number C5-23-1003.

Institutional Review Board Statement: Not applicable.

Informed Consent Statement: Not applicable.

Data Availability Statement: The original contributions presented in the study are included in the article, further inquiries can be directed to the corresponding author.

Acknowledgments: The authors thank Matt Ireland and Felipe Robles-Poblete for their assistance with the use of their continuum model.

Conflicts of Interest: The authors declare no conflicts of interest.

References

1. Ngo, T.D.; Kashani, A.; Imbalzano, G.; Nguyen, K.T.Q.; Hui, D. Additive Manufacturing (3D Printing): A Review of Materials, Methods, Applications and Challenges. *Compos. Part B Eng.* **2018**, *143*, 172–196. [CrossRef]
2. Love, L.J.; Duty, C.E.; Post, B.K.; Lind, R.F.; Lloyd, P.D.; Kunc, V.; Peter, W.H.; Blue, C.A. *Breaking Barriers in Polymer Additive Manufacturing*; Oak Ridge National Lab (ORNL): Oak Ridge, TN, USA; Manufacturing Demonstration Facility (MDF): Baltimore, MD, USA, 2015.
3. Love, L.J.; Kunc, V.; Rios, O.; Duty, C.E.; Elliott, A.M.; Post, B.K.; Smith, R.J.; Blue, C.A. The Importance of Carbon Fiber to Polymer Additive Manufacturing. *J. Mater. Res.* **2014**, *29*, 1893–1898. [CrossRef]
4. Roschli, A.; Post, B.K.; Chesser, P.C.; Sallas, M.; Love, L.J.; Gaul, K.T. *Precast Concrete Models Fabricated with Big Area Additive Manufacturing*; University of Texas at Austin: Austin, TX, USA, 2018.
5. Bhandari, S.; Lopez-Anido, R.A.; Rojas, F.S.; LeBihan, A. *Design and Manufacture of Precast Concrete Formworks Using Polymer Extrusion-Based Large-Scale Additive Manufacturing and Postprocessing*; ASTM International: West Conshohocken, PA, USA, 2022. [CrossRef]
6. Bhandari, S.; Lopez-Anido, R.; Anderson, J.; Mann, A. Large-Scale Extrusion-Based 3D Printing for Highway Culvert Rehabilitation. 10 May 2021. Available online: https://www.researchgate.net/publication/353130634_Large-scale_extrusion-based_3D_printing_for_highway_culvert_rehabilitation (accessed on 27 September 2024).
7. Davids, W.G.; Diba, A.; Dagher, H.J.; Guzzi, D.; Schanck, A.P. Development, Assessment and Implementation of a Novel FRP Composite Girder Bridge. *Constr. Build. Mater.* **2022**, *340*, 127818. [CrossRef]
8. Ferrini-Mundy, J.; Varahramyan, K. *2022 Research Report: R1 Global Impact-Local Relevance*; University of Maine: Orono, ME, USA, 2023.
9. Bhandari, S.; Lopez-Anido, R.A. Coupled Thermo-Mechanical Numerical Model to Minimize Risk in Large-Format Additive Manufacturing of Thermoplastic Composite Designs. *Prog. Addit. Manuf.* **2023**, *8*, 393–407. [CrossRef]
10. Dizon, J.R.C.; Espera, A.H.; Chen, Q.; Advincula, R.C. Mechanical Characterization of 3D-Printed Polymers. *Addit. Manuf.* **2018**, *20*, 44–67. [CrossRef]
11. Brenken, B.; Barocio, E.; Favaloro, A.; Kunc, V.; Pipes, R.B. Development and Validation of Extrusion Deposition Additive Manufacturing Process Simulations. *Addit. Manuf.* **2019**, *25*, 218–226. [CrossRef]
12. Alaimo, G.; Marconi, S.; Costato, L.; Auricchio, F. Influence of Meso-Structure and Chemical Composition on FDM 3D-Printed Parts. *Compos. Part B Eng.* **2017**, *113*, 371–380. [CrossRef]
13. Bhandari, S.; Lopez-Anido, R.A.; Wang, L.; Gardner, D.J. Elasto-Plastic Finite Element Modeling of Short Carbon Fiber Reinforced 3D Printed Acrylonitrile Butadiene Styrene Composites. *JOM* **2020**, *72*, 475–484. [CrossRef]
14. Casavola, C.; Cazzato, A.; Moramarco, V.; Pappalettere, C. Orthotropic Mechanical Properties of Fused Deposition Modelling Parts Described by Classical Laminate Theory. *Mater. Des.* **2016**, *90*, 453–458. [CrossRef]
15. Monaldo, E.; Marfia, S. Multiscale Technique for the Analysis of 3D-Printed Materials. *Int. J. Solids Struct.* **2021**, *232*, 111173. [CrossRef]
16. Rodrı´guez, J.F.; Thomas, J.P.; Renaud, J.E. Design of Fused-Deposition ABS Components for Stiffness and Strength. *J. Mech. Des.* **2003**, *125*, 545–551. [CrossRef]
17. Somireddy, M.; Czekanski, A. Computational Modeling of Constitutive Behaviour of 3D Printed Composite Structures. *J. Mater. Res. Technol.* **2021**, *11*, 1710–1718. [CrossRef]
18. Choi, J.Y.; Kortschot, M.T. Stiffness Prediction of 3D Printed Fiber-Reinforced Thermoplastic Composites. *Rapid Prototyp. J.* **2020**, *26*, 549–555. [CrossRef]
19. Malagutti, L.; Mazzanti, V.; Mollica, F. Tensile Properties of FDM 3D-Printed Wood Flour Filled Polymers and Mathematical Modeling through Classical Lamination Theory. *Rapid Prototyp. J.* **2022**, *28*, 1834–1842. [CrossRef]
20. van de Werken, N.; Hurley, J.; Khanbolouki, P.; Sarvestani, A.N.; Tamijani, A.Y.; Tehrani, M. Design Considerations and Modeling of Fiber Reinforced 3D Printed Parts. *Compos. Part B Eng.* **2019**, *160*, 684–692. [CrossRef]
21. Karamooz Ravari, M.R.; Kadkhodaei, M.; Badrossamay, M.; Rezaei, R. Numerical Investigation on Mechanical Properties of Cellular Lattice Structures Fabricated by Fused Deposition Modeling. *Int. J. Mech. Sci.* **2014**, *88*, 154–161. [CrossRef]
22. Damanpack, A.R.; Bodaghi, M.; Liao, W.H. Experimentally Validated Multi-Scale Modeling of 3D Printed Hyper-Elastic Lattices. *Int. J. Non-Linear Mech.* **2019**, *108*, 87–110. [CrossRef]
23. Bhandari, S.; Lopez-Anido, R. Finite Element Analysis of Thermoplastic Polymer Extrusion 3D Printed Material for Mechanical Property Prediction. *Addit. Manuf.* **2018**, *22*, 187–196. [CrossRef]
24. Scapin, M.; Peroni, L. Numerical Simulations of Components Produced by Fused Deposition 3D Printing. *Materials* **2021**, *14*, 4625. [CrossRef]
25. Abbot, D.W.; Kallon, D.V.V.; Anghel, C.; Dube, P. Finite Element Analysis of 3D Printed Model via Compression Tests. *Procedia Manuf.* **2019**, *35*, 164–173. [CrossRef]

26. Avanzini, A.; Battini, D.; Giorleo, L. Finite Element Modelling of 3D Printed Continuous Carbon Fiber Composites: Embedded Elements Technique and Experimental Validation. *Compos. Struct.* **2022**, *292*, 115631. [CrossRef]
27. Cerda-Avila, S.N.; Medellín-Castillo, H.I.; de Lange, D.F. Analysis and Numerical Simulation of the Structural Performance of Fused Deposition Modeling Samples With Variable Infill Values. *J. Eng. Mater. Technol.* **2018**, *141*, 021005. [CrossRef]
28. Özen, A.; Ganzosch, G.; Völlmecke, C.; Auhl, D. Characterization and Multiscale Modeling of the Mechanical Properties for FDM-Printed Copper-Reinforced PLA Composites. *Polymers* **2022**, *14*, 3512. [CrossRef] [PubMed]
29. Dryzek, M.; Cecot, W.; Tekieli, M. Experimental and Multiscale Computational Static and Dynamic Study of 3D Printed Elements with Mesostructure. *Finite Elem. Anal. Des.* **2023**, *215*, 103876. [CrossRef]
30. Gonabadi, H.; Chen, Y.; Yadav, A.; Bull, S. Investigation of the Effect of Raster Angle, Build Orientation, and Infill Density on the Elastic Response of 3D Printed Parts Using Finite Element Microstructural Modeling and Homogenization Techniques. *Int J. Adv. Manuf. Technol.* **2022**, *118*, 1485–1510. [CrossRef]
31. Garzon-Hernandez, S.; Arias, A.; Garcia-Gonzalez, D. A Continuum Constitutive Model for FDM 3D Printed Thermoplastics. *Compos. Part B Eng.* **2020**, *201*, 108373. [CrossRef]
32. Giri, T.R.; Mailen, R.W. Thermomechanical Behavior of Polymeric Periodic Structures. *Addit. Manuf.* **2022**, *49*, 102512. [CrossRef]
33. Hoshikawa, Y.; Shirasu, K.; Higuchi, R.; Kawagoe, Y.; Tohmyoh, H.; Okabe, T. Experimental and Numerical Investigation of the Relationship between Material Defects and Elastoplasticity Behavior of 3D-Printed Carbon-Fiber-Reinforced Thermoplastics under Compressive Loading. *Compos. Sci. Technol.* **2023**, *241*, 110116. [CrossRef]
34. Jayswal, A.; Liu, J.; Harris, G.; Mailen, R.; Adanur, S. Creep Behavior of 3D Printed Polymer Composites. *Polym. Eng. Sci.* **2023**, *63*, 3809–3819. [CrossRef]
35. Kucewicz, M.; Baranowski, P.; Małachowski, J. A Method of Failure Modeling for 3D Printed Cellular Structures. *Mater. Des.* **2019**, *174*, 107802. [CrossRef]
36. Bandinelli, F.; Peroni, L.; Morena, A. Elasto-Plastic Mechanical Modeling of Fused Deposition 3D Printing Materials. *Polymers* **2023**, *15*, 234. [CrossRef] [PubMed]
37. Corvi, A.; Collini, L. Combined RVE-Cohesive Elements Approach to the Multi-Scale Modelling of FDM 3D-Printed Components. *Theor. Appl. Fract. Mech.* **2023**, *128*, 104140. [CrossRef]
38. Vaňková, T.; Kroupa, T.; Zemčík, R.; Krystek, J.; Zemčík, H. Identification of Temperature-Dependent Parameters for an Elastic–Plastic-Damage Material Model of 3D-Printed PETG. *Polymer* **2023**, *284*, 126295. [CrossRef]
39. Afshar, R.; Jeanne, S.; Abali, B.E. Nonlinear Material Modeling for Mechanical Characterization of 3-D Printed PLA Polymer With Different Infill Densities. *Appl Compos Mater* **2023**, *30*, 987–1001. [CrossRef]
40. Wang, T.-M.; Xi, J.-T.; Jin, Y. A Model Research for Prototype Warp Deformation in the FDM Process. *Int J Adv Manuf Technol* **2007**, *33*, 1087–1096. [CrossRef]
41. Zhang, Y.; Chou, K. A Parametric Study of Part Distortions in Fused Deposition Modelling Using Three-Dimensional Finite Element Analysis. *Proc. Inst. Mech. Eng. Part B J. Eng. Manuf.* **2008**, *222*, 959–968. [CrossRef]
42. Al Rashid, A.; Koç, M. Numerical Predictions and Experimental Validation on the Effect of Material Properties in Filament Material Extrusion. *J. Manuf. Process.* **2023**, *94*, 403–412. [CrossRef]
43. Panchasara, K.M.; Ramakrishnan, A.N.; Mehle, K.; Ludtka, C.; Schwan, S. Modeling of Manufacturing Induced Residual Stress in 3D-Printed Components. *Macromol. Symp.* **2022**, *403*, 2100465. [CrossRef]
44. Alzyod, H.; Ficzere, P. Material-Dependent Effect of Common Printing Parameters on Residual Stress and Warpage Deformation in 3D Printing: A Comprehensive Finite Element Analysis Study. *Polymers* **2023**, *15*, 2893. [CrossRef]
45. Camposeco-Negrete, C.; Lavertu, P.-Y.; Lopez-de-Alda, J. Prediction and Optimization of the Yield Stress of Material Extrusion Specimens Made of ABS, Using Numerical Simulation and Experimental Tests. *Int J Adv Manuf Technol* **2022**, *118*, 3657–3671. [CrossRef]
46. El Moumen, A.; Tarfaoui, M.; Lafdi, K. Modelling of the Temperature and Residual Stress Fields during 3D Printing of Polymer Composites. *Int J Adv Manuf Technol* **2019**, *104*, 1661–1676. [CrossRef]
47. Cattenone, A.; Morganti, S.; Alaimo, G.; Auricchio, F. Finite Element Analysis of Additive Manufacturing Based on Fused Deposition Modeling (FDM): Distortion Prediction and Comparison with Experimental Data. *J. Manuf. Sci. Eng.* **2018**, *141*, 011010. [CrossRef]
48. Trofimov, A.; Le Pavic, J.; Pautard, S.; Therriault, D.; Lévesque, M. Experimentally Validated Modeling of the Temperature Distribution and the Distortion during the Fused Filament Fabrication Process. *Addit. Manuf.* **2022**, *54*, 102693. [CrossRef]
49. Syrlybayev, D.; Zharylkassyn, B.; Seisekulova, A.; Perveen, A.; Talamona, D. Optimization of the Warpage of Fused Deposition Modeling Parts Using Finite Element Method. *Polymers* **2021**, *13*, 3849. [CrossRef] [PubMed]
50. Corvi, A.; Collini, L.; Sciancalepore, C.; Lutey, A. Influence of Process Parameters on Temperature Field and Residual Strain in FFF-Printed Parts. *J Mech Sci Technol* **2023**, *37*, 5521–5527. [CrossRef]
51. Akbar, I.; El Hadrouz, M.; El Mansori, M.; Lagoudas, D. Continuum and Subcontinuum Simulation of FDM Process for 4D Printed Shape Memory Polymers. *J. Manuf. Process.* **2022**, *76*, 335–348. [CrossRef]
52. Jiang, B.; Chen, Y.; Ye, L.; Chang, L.; Dong, H. Residual Stress and Warpage of Additively Manufactured SCF/PLA Composite Parts. *Adv. Manuf. Polym. Compos. Sci.* **2023**, *9*, 2171940. [CrossRef]

53. Antony Samy, A.; Golbang, A.; Archer, E.; Mcilhagger, A. Simulation on Influence of Environmental Conditions on Part Distortion in Fused Deposition Modelling (FDM). 22 April 2021. Available online: https://www.researchgate.net/publication/351703060 (accessed on 27 September 2024).
54. Antony Samy, A.; Golbang, A.; Harkin-Jones, E.; Archer, E.; McIlhagger, A. Prediction of Part Distortion in Fused Deposition Modelling (FDM) of Semi-Crystalline Polymers via COMSOL: Effect of Printing Conditions. *CIRP J. Manuf. Sci. Technol.* **2021**, *33*, 443–453. [CrossRef]
55. Samy, A.A.; Golbang, A.; Harkin-Jones, E.; Archer, E.; Tormey, D.; McIlhagger, A. Finite Element Analysis of Residual Stress and Warpage in a 3D Printed Semi-Crystalline Polymer: Effect of Ambient Temperature and Nozzle Speed. *J. Manuf. Process.* **2021**, *70*, 389–399. [CrossRef]
56. Antony Samy, A.; Golbang, A.; Harkin-Jones, E.; Archer, E.; Dahale, M.; McIlhagger, A. Influence of Ambient Temperature on Part Distortion: A Simulation Study on Amorphous and Semi-Crystalline Polymer. *Polymers* **2022**, *14*, 879. [CrossRef]
57. Antony Samy, A.; Golbang, A.; Harkin-Jones, E.; Archer, E.; Dahale, M.; McAfee, M.; Abdi, B.; McIlhagger, A. Influence of Raster Pattern on Residual Stress and Part Distortion in FDM of Semi-Crystalline Polymers: A Simulation Study. *Polymers* **2022**, *14*, 2746. [CrossRef] [PubMed]
58. Courter, B.; Savane, V.; Bi, J.; Dev, S.; Hansen, C. Finite Element Simulation of the Fused Deposition Modelling Process. In Proceedings of the NAFEMS World Congress, Stockholm, Sweden, 13 June 2017.
59. Wang, J.; Papadopoulos, P. Coupled Thermomechanical Analysis of Fused Deposition Using the Finite Element Method. *Finite Elem. Anal. Des.* **2021**, *197*, 103607. [CrossRef]
60. Sreejith, P.; Kannan, K.; Rajagopal, K. A Thermodynamic Framework for Additive Manufacturing, Using Amorphous Polymers, Capable of Predicting Residual Stress, Warpage and Shrinkage. *Int. J. Eng. Sci.* **2021**, *159*, 103412. [CrossRef]
61. Xia, H.; Lu, J.; Tryggvason, G. Simulations of Fused Filament Fabrication Using a Front Tracking Method. *Int. J. Heat Mass Transf.* **2019**, *138*, 1310–1319. [CrossRef]
62. D'Amico, T.; Peterson, A.M. Bead Parameterization of Desktop and Room-Scale Material Extrusion Additive Manufacturing: How Print Speed and Thermal Properties Affect Heat Transfer. *Addit. Manuf.* **2020**, *34*, 101239. [CrossRef]
63. Talagani, F.; DorMohammadi, S.; Dutton, R.; Godines, C.; Baid, H.; Abdi, F.; Kunc, V.; Compton, B.; Simunovic, S.; Duty, C.; et al. Numerical Simulation of Big Area Additive Manufacturing (3D Printing) of a Full Size Car. *Sampe J.* **2015**, *51*, 27–36.
64. Kim, S.; Baid, H.; Hassen, A.A.; Kumar, A.; Lindahl, J.; Hoskins, D.; Ajinjeru, C.; Duty, C.; Yeole, P.; Vaidya, U.; et al. Analysis on Part Distortion and Residual Stress in Big Area Additive Manufacturing with Carbon Fiber-Reinforced Thermoplastic Using Dehomogenization Technique. In Proceedings of the Composites and Advanced Materials Expo (CAMX 2019), Anaheim, CA, USA, 1 January 2019.
65. Friedrich II, B.K.; Choo, K. Thermal-Stress Characteristics of a Large Area Additive Manufacturing. *Heat Transf. Eng.* **2023**, *44*, 1083–1098. [CrossRef]
66. Ramos, N.; Mittermeier, C.; Kiendl, J. Efficient Simulation of the Heat Transfer in Fused Filament Fabrication. *J. Manuf. Process.* **2023**, *94*, 550–563. [CrossRef]
67. Nagaraj, M.H.; Maiaru, M. A Novel Higher-Order Finite Element Framework for the Process Modeling of Material Extrusion Additive Manufacturing. *Addit. Manuf.* **2023**, *76*, 103759. [CrossRef]
68. Liu, L.; Jo, E.; Hoskins, D.; Vaidya, U.; Ozcan, S.; Ju, F.; Kim, S. Layer Time Optimization in Large Scale Additive Manufacturing via a Reduced Physics-Based Model. *Addit. Manuf.* **2023**, *72*, 103597. [CrossRef]
69. Bhandari, S.; Lopez-Anido, R.A. Discrete-Event Simulation Thermal Model for Extrusion-Based Additive Manufacturing of PLA and ABS. *Materials* **2020**, *13*, 4985. [CrossRef] [PubMed]
70. Bhandari, S.; Lopez-Anido, R.A. Efficient Residual Stress Modeling for Large-Format Polymer Composite Extrusion-Based Additive Manufacturing. In Proceedings of the American Society for Composites-Thirty-Eighth Technical Conference, Lowell, MA, USA, 18 September 2023.
71. Erkmen, R.E. Multiple-Point Constraint Applications for the Finite Element Analysis of Shear Deformable Composite Beams—Variational Multiscale Approach to Enforce Full Composite Action. *Comput. Struct.* **2015**, *149*, 17–30. [CrossRef]
72. Chung, W.; Sotelino, E.D. Nonlinear Finite-Element Analysis of Composite Steel Girder Bridges. *J. Struct. Eng.* **2005**, *131*, 304–313. [CrossRef]
73. Lezgy-Nazargah, M.; Vidal, P.; Polit, O. A Penalty-Based Multifiber Finite Element Model for Coupled Bending and Torsional-Warping Analysis of Composite Beams. *Eur. J. Mech. A/Solids* **2020**, *80*, 103915. [CrossRef]
74. Zhang, Y.; Murphy, K.D. Response of a Finite Beam in Contact with a Tensionless Foundation under Symmetric and Asymmetric Loading. *Int. J. Solids Struct.* **2004**, *41*, 6745–6758. [CrossRef]
75. Robles Poblete, F.; Ireland, M.; Slattery, L.; Davids, W.G.; Lopez-Anido, R.A. In Situ, Real-Time Temperature Mapping and Thermal FE Simulations of Large-Format 3D Printed PETG/CF Vertical Wall. *Materials* **2023**, *16*, 6486. [CrossRef]

Disclaimer/Publisher's Note: The statements, opinions and data contained in all publications are solely those of the individual author(s) and contributor(s) and not of MDPI and/or the editor(s). MDPI and/or the editor(s) disclaim responsibility for any injury to people or property resulting from any ideas, methods, instructions or products referred to in the content.

applied sciences

MDPI

Article

Estimation of Critical Fatigue Conditions Based on the Accelerated Fatigue Locati Method by Mean of Net Damage

Isidro A. Carrascal, Soraya Diego *, Jose A. Casado, Jose A. Sainz-Aja and Diego Ferreño

LADICIM (Laboratory of Materials Science and Engineering), University of Cantabria, Av./Los Castros 44, 39005 Santander, Spain; carrasci@unican.es (I.A.C.); casadoja@unican.es (J.A.C.); jose.sainz-aja@unican.es (J.A.S.-A.); ferrenod@unican.es (D.F.)
* Correspondence: diegos@unican.es

Abstract: The increasing utilization of short fiber-reinforced thermoplastics, due to their advantageous mechanical properties and manufacturing convenience, has led to their application in areas traditionally dominated by metals. This shift underscores the importance of understanding the fatigue behavior of these materials. This study evaluates the fatigue behavior of short fiber-reinforced thermoplastics through three characterization methods: continuous fatigue, interrupted fatigue, and the Locati method, with the latter serving as a novel approach for estimating critical fatigue conditions from a single specimen. Continuous fatigue testing provides the baseline for comparison. The effect of load interruption is explored through the interrupted fatigue method. The Locati method, characterized by incrementally increasing load steps until failure, offers a significant benefit by enabling the estimation of critical fatigue conditions efficiently. This research aims to provide a comprehensive understanding of the fatigue behavior of short fiber-reinforced thermoplastics, contributing to the optimization of their use in engineering applications.

Keywords: polyamide; fatigue; Locati; net damage

1. Introduction

In recent years, short fiber-reinforced thermoplastics (SFRTs) have gained importance, especially as they have begun to replace metal elements in certain applications, primarily due to their ease of fabrication and superior mechanical properties [1]. Polyamide 6 (PA-6) is one of the most widely used materials in this category due to the following characteristics: its ease of manufacture by injection moulding, high strength, stiffness, toughness, translucency, fatigue resistance, and abrasion resistance [2]. Enhancing PA-6 with short glass fibers improves its strength, stiffness, heat distortion temperature, and abrasion resistance, though it may introduce anisotropic properties [3]. Given the common use of this material in engineering components, understanding its fatigue behavior is crucial.

Traditionally, the fatigue limit or endurance—the stress level below which a material can withstand an infinite number of loading cycles without fatigue failure—has been determined from Wöhler curves or S-N curves [4,5]. This approach, however, requires between 16 and 20 specimens to yield reliable results. An alternative, the Staircase method, can achieve similar outcomes with only 11 to 15 specimens [6,7]. This paper proposes using the Locati methodology [8–10] to achieve results that are both rapid and cost-effective. The Locati method, an accelerated fatigue test, aims to determine the fatigue limit from a single specimen by applying incrementally increasing stress loads until failure.

Various researchers have employed the Locati method to ascertain the fatigue limits of different materials. Nonetheless, a unified criterion for defining the fatigue limit based on Locati test results has yet to be established. The fatigue effect of laser quenching on the boronized layer of Cr12MoV steel was investigated by Kong et al. [11] through the analysis of fatigue accumulation damage. Maximov et al. [12] studied the high-cycle fatigue

of 2024-T3 high-strength aluminum alloy, estimating endurance based on the Palmgren–Miner linear damage theory. Sainz-Aja et al. [13] utilized μCT analysis alongside the Locati method to determine the fatigue limit of recycled aggregate mortar, and in another study, the variation in resonance frequency to define the fatigue limit of recycled aggregate concrete [14]. Casado et al. [15] analyzed the fatigue failure behavior of short glass fiber-reinforced PA 6.6, using strain evolution to determine the critical step. The Locati method was also applied by Thomas et al. [16] to identify the fatigue limit of recycled aggregate concrete, establishing a correlation between the maximum load a specimen can withstand and its fatigue limit.

Traditionally [17,18], damage formulation is based on the concepts of stress and actual strain. Effective stress reflects the material's response to net section reduction caused by various damage mechanisms, allowing damage (D) to be defined from Equation (1).

$$D = 1 - \frac{\tilde{E}}{E} \tag{1}$$

Within this framework, E represents the material's undamaged elastic modulus, while $\tilde{E}$ denotes the apparent elastic modulus of the material once damage has occurred. The damage parameter (D) quantifies the extent of material deterioration, ranging from 0 (indicating no damage) to a critical damage level (D_c) corresponding to failure.

Fatigue-induced damage in polymeric composites manifests through the formation and propagation of discontinuities, including micro-cracks, voids, and cracks, which progressively undermine the material's strength leading to failure [19]. This damage can be conceptualized as the variation in energy relative to the initial state at each moment.

In this study, a model to predict fatigue behavior was developed, aimed at characterizing materials swiftly, economically, and with high precision. This model is anchored in the Locati method and accommodates pauses during fatigue tests and the application of cycles with varying load amplitudes. Through a comprehensive experimental campaign, the damage incurred by each test specimen was evaluated from an energetic perspective. Subsequent analyses incorporated corrections to account for the influence of breaks and fluctuating load intensities.

2. Materials and Methods

The specimens analyzed in this study comprised a composite material consisting of Polyamide 6 (PA-6) reinforced with 25 weight percent (wt.%) short glass fiber (SGFR-PA6). These specimens were fabricated using injection molding techniques and conformed to standardized dimensions and geometry Type 1B as specified in EN ISO 527-2 [20]. The specific dimensions of the specimens are illustrated in Figure 1.

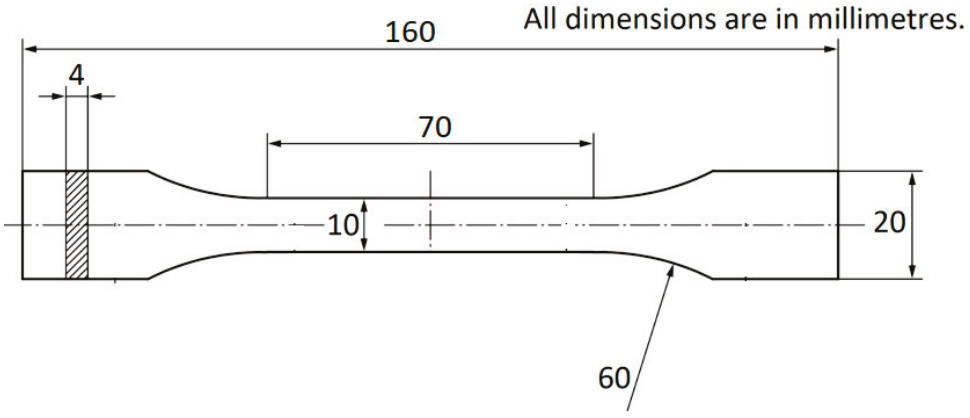

Figure 1. Test specimen dimensions used for the study.

Polyamide 6 (PA 6) is inherently hygroscopic, with moisture absorption having a notable impact on its mechanical properties, particularly its dynamic attributes. To mitigate this and standardize the condition of the specimens, they were subjected to a conditioning process to achieve a moisture content of approximately 2.4%. Under these controlled conditions, the specimens demonstrated a static tensile strength of 100 MPa and a breaking strain exceeding 5%.

2.1. Tensile Tests

Tensile testing of Polyamide 6 (PA6) specimens was conducted to determine the material's mechanical properties under controlled uniaxial deformation conditions, following the guidelines of EN ISO 527-1 [21] and EN ISO 527-2 [22] standards. These standards specify the procedure for preparing specimens, testing conditions, deformation speed, specimen geometry, and results' interpretation for plastics. Specimens are typically prepared by injection molding or machining, with a focus on maintaining proper moisture content due to PA6's hygroscopic nature. The test is performed at a standard temperature of 23 ± 2 °C and $50 \pm 5\%$ relative humidity, unless specified otherwise, with data on applied force and specimen deformation collected to calculate elasticity modulus, yield strength, maximum tensile strength, and elongation at break. This process ensures a standardized approach to evaluating PA6's mechanical performance, facilitating comparison across different conditions or formulations.

2.2. Fatigue Tests

In all fatigue tests performed for this work, a sinusoidal waveform was used, the stress ratio (R) was 0.1, and the frequency (f) was 5 Hz. The experimental campaign was divided into 3 phases: monotonous fatigue, monotonous fatigue with breaks, and Locati tests. The Locati tests were also divided into 4 stages: a reference Locati, analyzing the influence of breaks, analyzing the influence of the number of cycles per step, and analyzing the effect of the load values of each step. These tests were performed in a servo-hydraulic machine with a capacity of 5 kN and a dynamic extensometer with a measuring base of 50 mm and a displacement of 12.5 mm to measure the strain of the specimen.

In the first phase, monotonic fatigue tests were performed until the specimens broke. These tests were performed with maximum load values between 1400 and 2700 N. The load variation between tests was 100 N. These tests were performed in order to define the Wöhler curve and the fatigue limit ($\Delta\sigma e$).

In the second phase, monotone fatigue tests with breaks were performed. In these tests, every 25,000 cycles the test was stopped for one hour. This period of time was enough for the specimen temperature to reset to the room temperature value. These interruptions allow the analysis of the behaviour of materials previously damaged by fatigue.

In the third phase, Locati accelerated fatigue tests were performed. This methodology consists of applying a fixed number of cycles at a given frequency. The load values of these steps are increased step by step. Figure 2 shows a diagram of the test and Table 1 shows the variables used.

As previously mentioned, the Locati method tests were carried out in four different stages. The first of these was used as a reference, with 25,000 cycles per step, with a maximum load variation between consecutive steps of 100 N, and without making breaks. The second one was similar to the reference one except that, between steps, a 1 h stop was made. The third was similar to the reference except that the load increase between consecutive steps was reduced to 50 N. Finally, in the fourth stage, the difference from the reference test was that the number of cycles per step was doubled. See Table 2.

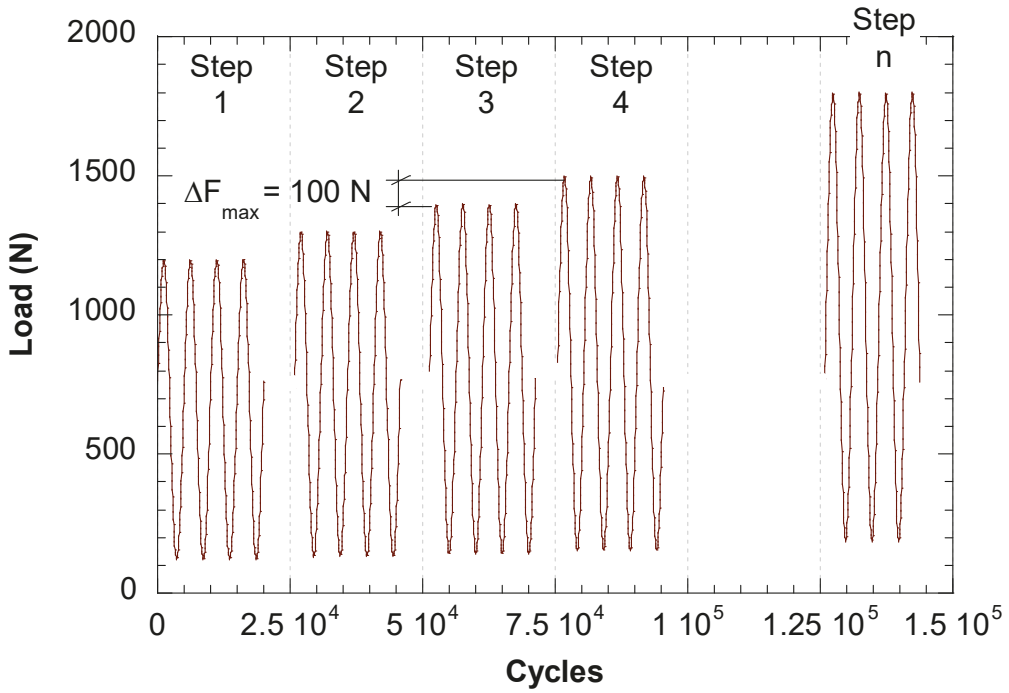

Figure 2. Descriptive loading scheme of the Locati fatigue test.

Table 1. Load values during the Locati test steps.

Step.	F_{max} (N)	F_{min} (N)	σ_{max} (MPa)	σ_{min} (MPa)	$\Delta\sigma$ (MPa)
1	1200	120	30	3	27
2	1300	130	32.5	3.25	29.25
3	1400	140	35	3.5	31.5
4	1500	150	37.5	3.75	33.75
5	1600	160	40	4	36
6	1700	170	42.5	4.25	38.25

Table 2. Locati test variants.

Stage.	Break? (Yes/No)	Cycles/Step (Cycles)	ΔF_{max} (N)
Locati 1	No	25,000	100
Locati 2	Yes	25,000	100
Locati 3	No	25,000	50
Locati 4	No	50,000	100

2.3. Energy and Damage Quantification

During the fatigue process, the energy in the volume of material consisting of a prismatic base cross-section of the specimen and height being the separation between the reference points of the extensometer, within a cycle and between two instants of time t_i and t_i+1 is obtained from Equation (2).

$$E_{t_i/t_{i+1}} = \int_{t_i}^{t_{i+1}} dE = \int_{t_i}^{t_{i+1}} F \cdot d\Delta \tag{2}$$

For a whole cycle, this total energy can be decomposed into: dissipated energy represented by the hysteresis loop (E_d) and accumulated energy (E_a), which is recovered by the element at the end of the cycle, as shown in Figure 3.

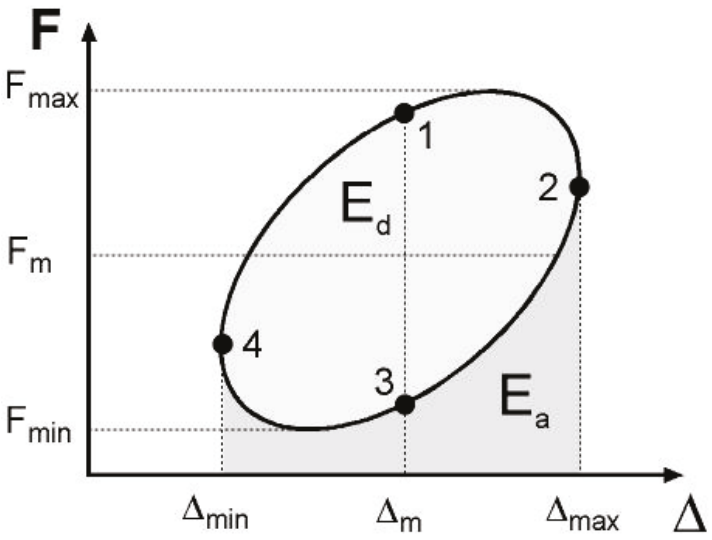

Figure 3. Descriptive diagram of the energy dissipated and accumulated during a dynamic load cycle.

Therefore, as shown in Equation (3), the total energy per cycle, E_T, is the total of the two previous ones. This E_T will be the energy used to determine the damage generated in the fatigue process.

$$E_T = E_a + E_d \tag{3}$$

A parameter called total damage, T_D, is defined to quantify the damage suffered by the material during the fatigue process. The definition of this parameter will be made from the variation in energy parameters with respect to their initial value and will be obtained from the expression:

$$T_D = \left(1 - \frac{E_{T0}}{E_{Ti}}\right) \cdot 100\ [\%] \tag{4}$$

where E_{T0} will be the total energy measured in the first of the fatigue cycles and E_{Ti} the total energy measured in cycle *i*.

Since the stress level throughout the Locati test is changing, a new parameter is defined, which will be the individual net damage (D_I) and will consider the variation in the total energy with respect to the initial one of each of the steps. See Figure 4.

$$D_{NI_j} = D_{I_j} - \left(D_{0_j} - D_{NIf_{j-1}}\right) \tag{5}$$

where D_{NIfj-1} is the individual net damage value of the previous step.

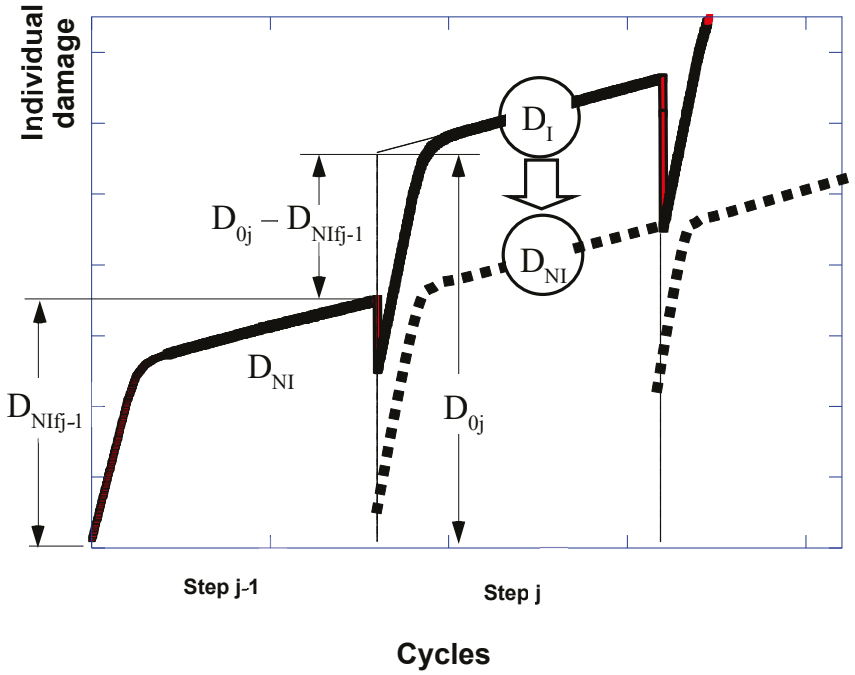

Figure 4. Explanatory scheme for the determination of individual net damage (D_{NI}).

3. Results and Discussion

The main results of the first phase tests, the monotonic fatigue tests and the specimens' breaks, are shown in Figure 5 which gives the Wöhler curve. The fatigue limit was defined as $\Delta\sigma$ = 40.5 MPa (180–1800 N) as all the analysed variables were stabilized after 2×10^6 cycles.

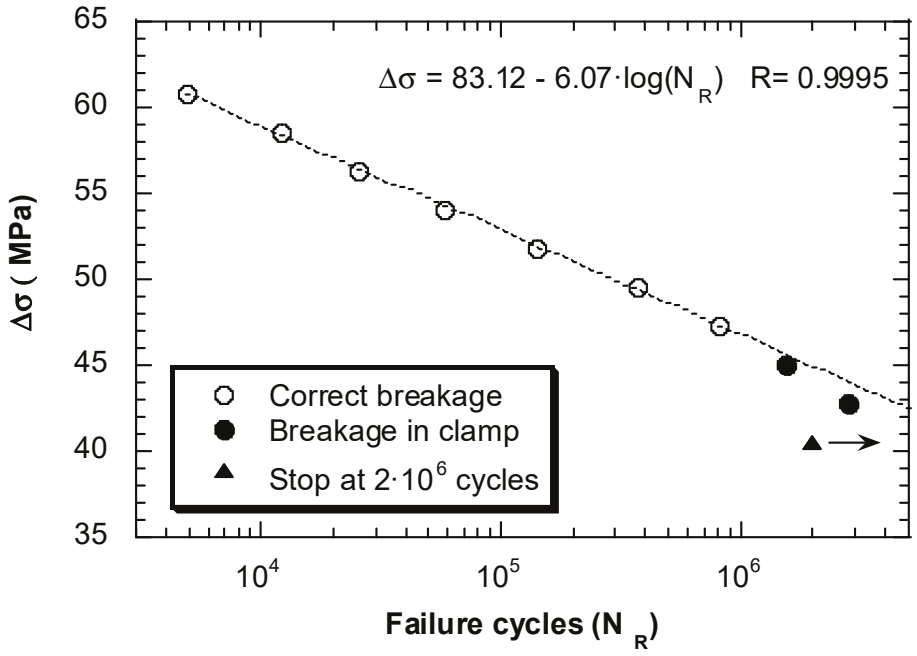

Figure 5. Wöhler curve obtained from monotonic fatigue tests.

Figure 6 shows the evolution of E_T as a function of the number of cycles for the different stress ranges.

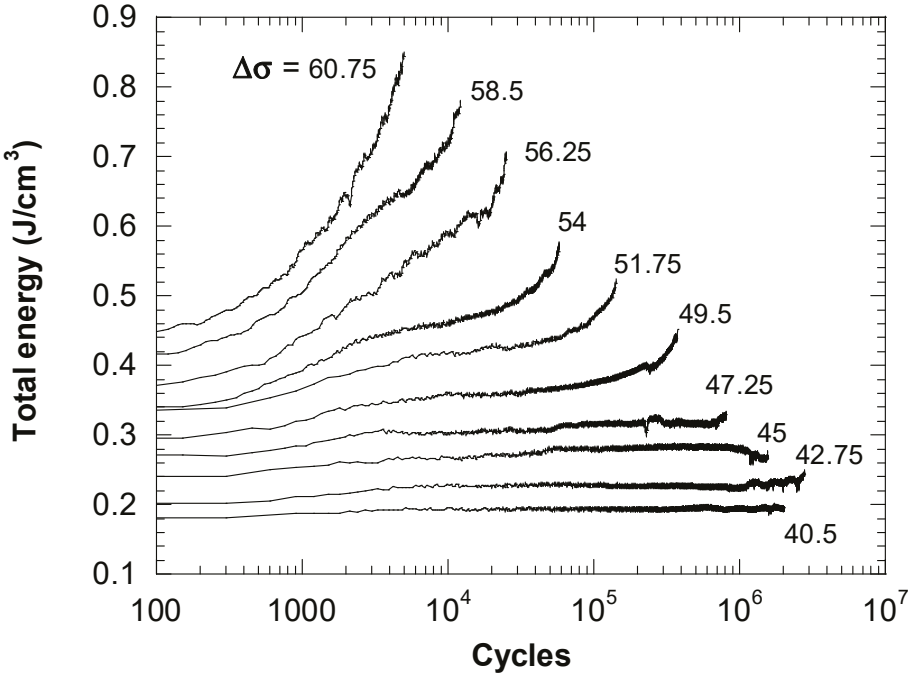

Figure 6. Total energy evolution as function of the number of cycles and the stress range or the monotonic fatigue tests.

Figure 7 shows that in the thermal fatigue processes, with higher stresses, E_T has a clear increasing trend, while in terms of mechanical fatigue, the energy parameters tend to stabilize or even decrease in some cases.

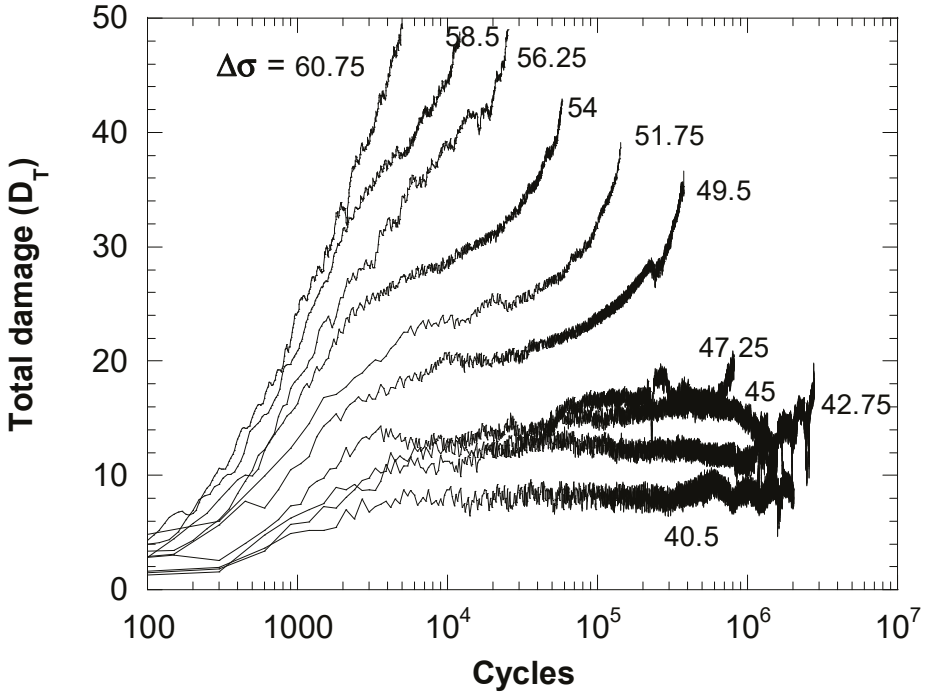

Figure 7. Evolution of total damage for the monotonic fatigue tests.

Figure 8 shows the evolution of total damage for the different stress levels.

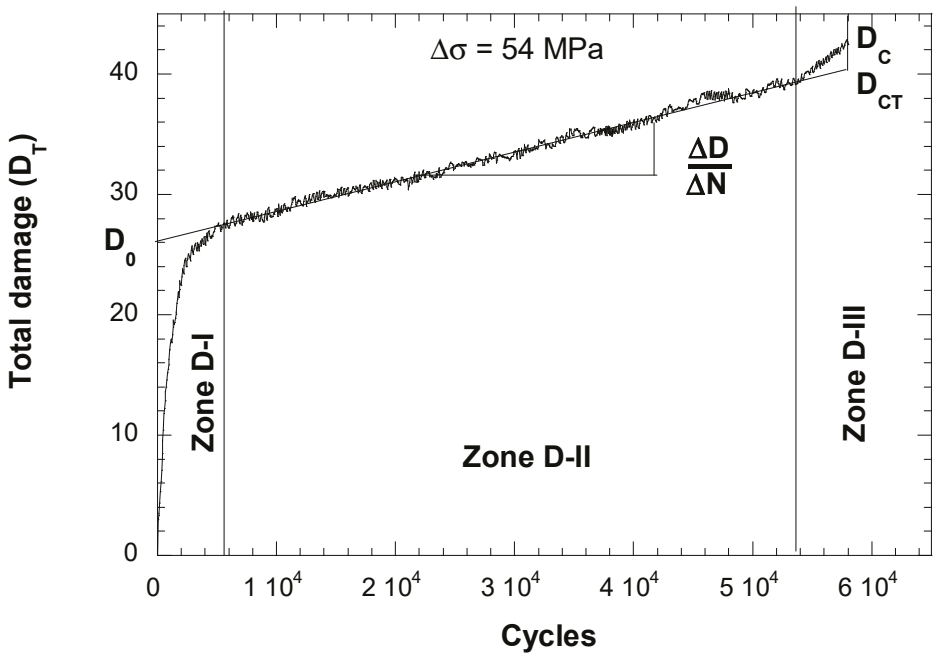

Figure 8. Evolution of total damage (Δσ = 54 MPa) for the monotonic fatigue tests.

It can be seen that for the fatigue limit, Δσ = 40.5 MPa, both E_T and T_D are fully stabilized after 2×10^6 cycles. The damage in all cases followed the same pattern, with an initial rapid growth with a decreasing slope, zone D-I, then a linear growth of the damage, zone D-II, and finally an accelerated growth until break, zone D-III, as can be seen in Figure 8. Both the growth rate, $\Delta T_D/\Delta N$, and the orderly one at the origin of the adjustment of the section D-II, D_0, and the critical damage, real and theoretical, D_C and D_{CT}, are increasing with the stress level.

The second test phase is formed by fatigue tests with breaks and monotonic load values. By analyzing the results of monotonous fatigue with interruptions, see Figure 9, it can be seen that a part of the damage caused during a load step (25,000 cycles) is recovered during the resting period, so that, when the next step is started, the initial damage is less than the damage that ended the previous step. This means that the damage would be composed of an elastic component, which recovers when the cyclic stress is released, and another plastic component, which is the one that remains after the stress and the one that actually causes the material to deteriorate.

The elastic component of the damage will be identified with the one ordered at the origin of the section D-II, D_0, or initial damage, and therefore, a plastic or net damage, D_N, can be defined from Equation (6):

$$D_N = D_T - D_0 \tag{6}$$

Figure 10 shows the evolution of net damage for all levels of monotonous fatigue without breaks. In contrast to the results obtained for total damage, where the critical damage values depended on the stress level, increasing as the stress increased, for net damage, it can be seen that in the case of thermal fatigue, the theoretical critical net damage values, D_{NCT}, are stabilised at around 15%, regardless of the stress. In the case of mechanical fatigue, the value of critical damage could not be verified because, as mentioned, the breakage took place through the clamp, thus not reaching the number of theoretical breakage cycles.

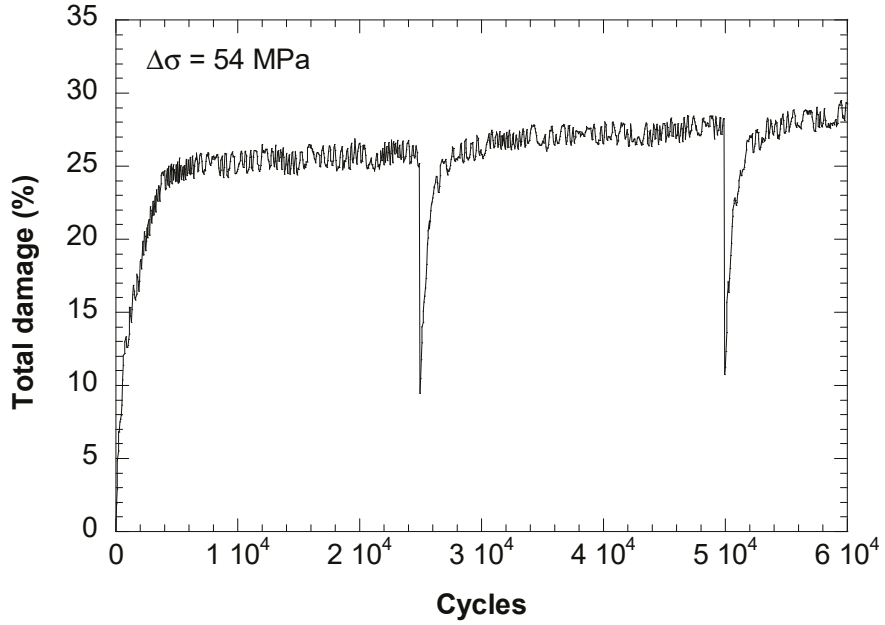

Figure 9. Evolution of total damage during monotonous fatigue with interruptions.

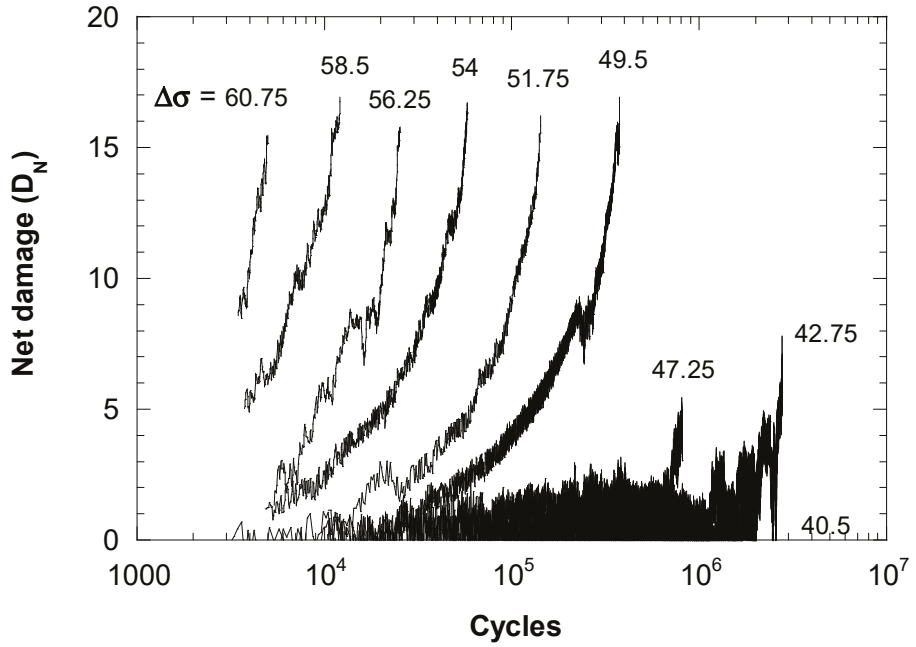

Figure 10. Net damage during the monotonic fatigue without breaks.

Figure 11 shows that in the case of fatigue breaks, the number of cycles is higher than in the monotonous one of the same levels, but the theoretical net damage also reaches values close to 15%.

The third experimental phase corresponds with the Locati tests. Analyzing the evolution of the total damage, D_T, in the Locati tests, there was no indication detected that allows it to be established as to which of the steps corresponds to the fatigue limit. Figure 12 shows, on a double-axis of abscissa to facilitate comparison between the different tests, the evolution of total damage, verifying that the results of the four tests are coincidental, reaching very similar values at break.

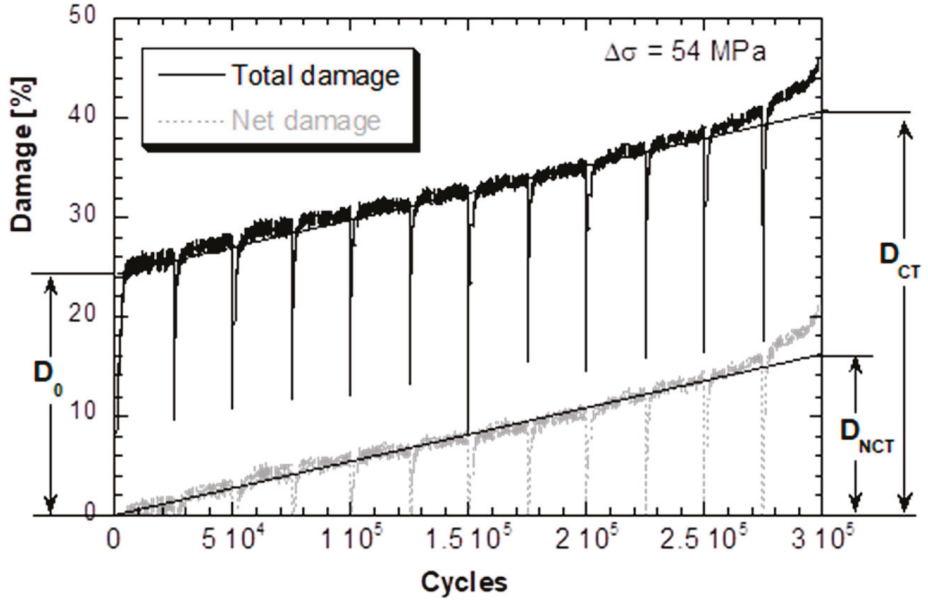

Figure 11. Evolution of net damage during the monotonic fatigue with breaks (Δσ = 54 MPa).

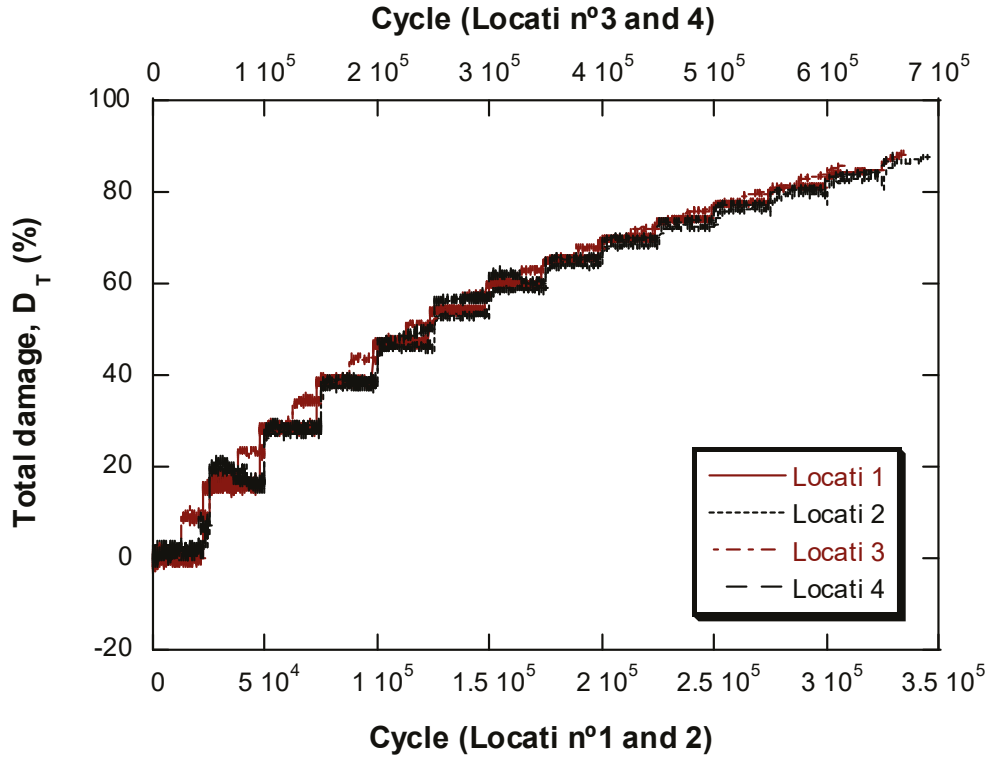

Figure 12. Total damage during the Locati tests.

Similar behaviour can also be observed when analyzing the evolution of the phase angle between the load and strain signal, see Figure 13. It can also be seen in this figure that the value of the critical phase angle is similar in all cases and close to 0.12 radians, so this value could also be a constant in breakage.

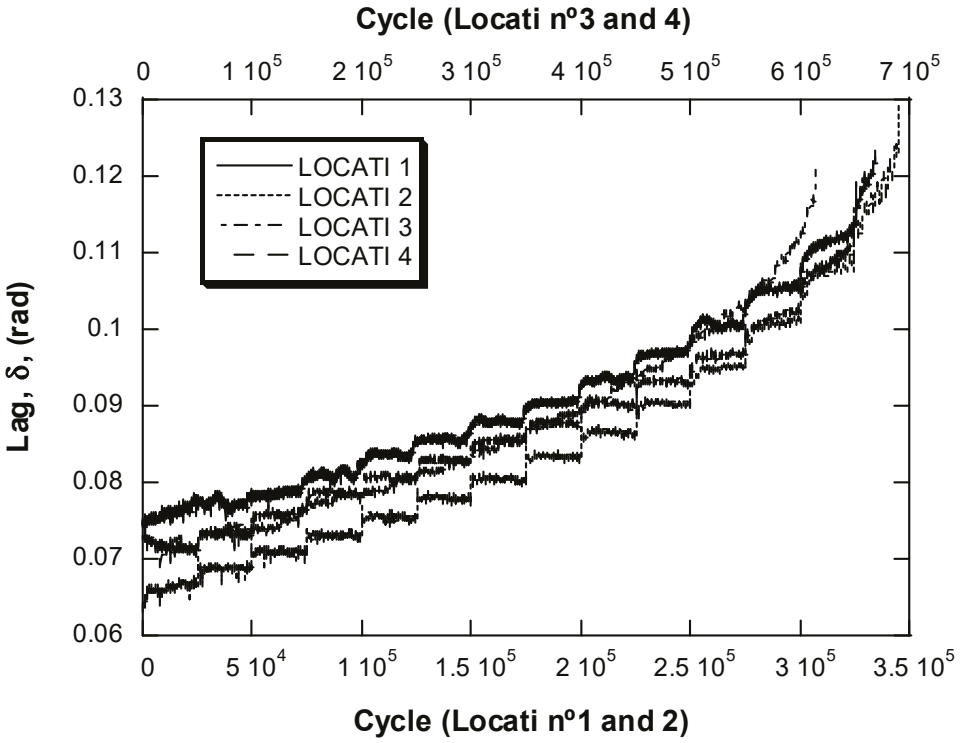

Figure 13. Phase angle between the load and strain signal during the Locati tests.

Figures 14–17 show the D_{NI} for the four Locati tests carried out. The step corresponding to the fatigue limit (Δσe) measured from the monotonic fatigue tests is indicated on the graphs. It can be seen that the D_{NI} in all cases remains constant below Δσe, and once exceeded, it begins to grow. Therefore, the fatigue limit can be defined from the individual net damage, D_{NI}, in a Locati test as that step from which the parameter begins to grow.

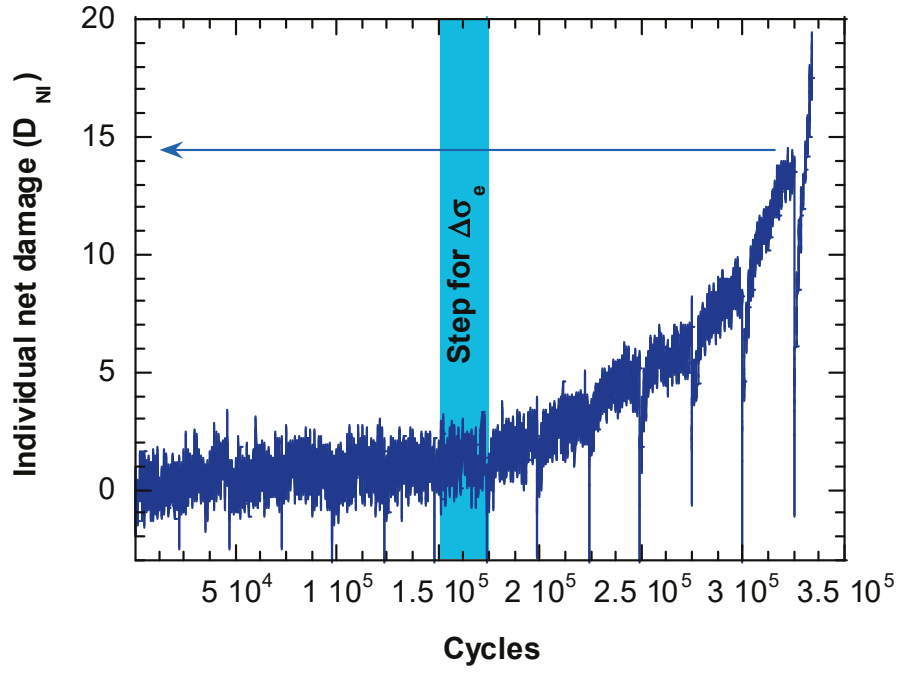

Figure 14. Individual net damage (D_{NI}) of Locati 1.

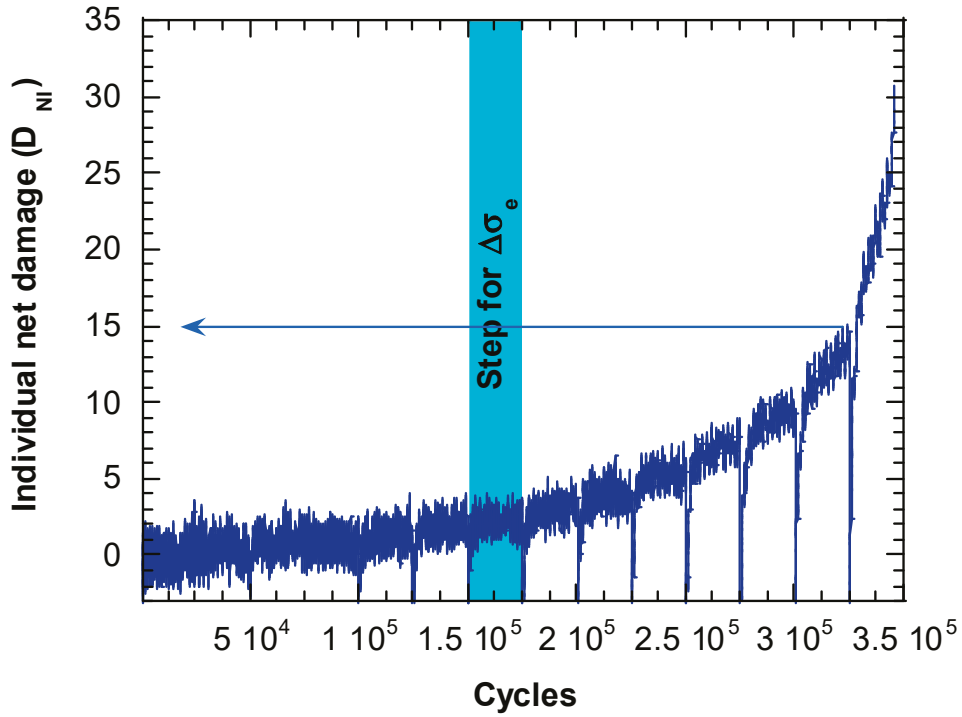

Figure 15. Individual net damage (D_{NI}) of Locati 2.

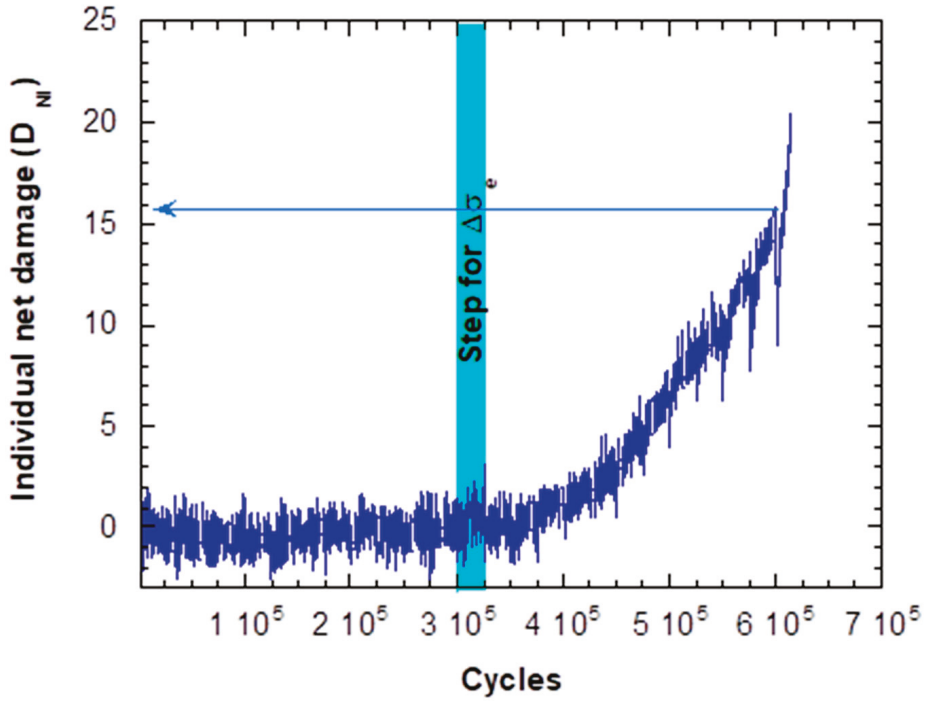

Figure 16. Individual net damage (D_{NI}) of Locati 3.

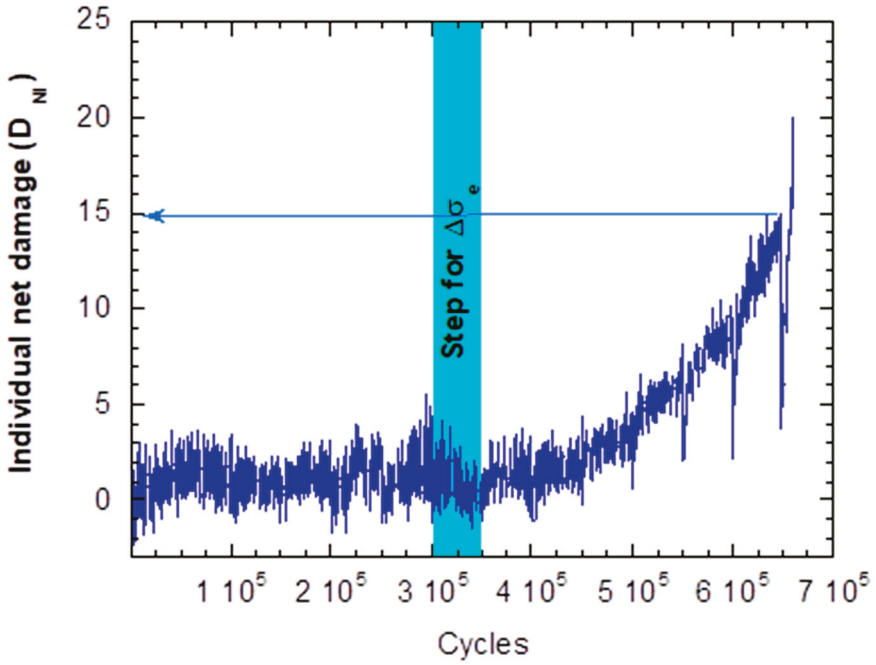

Figure 17. Individual net damage (D_{NI}) of Locati 4.

It is also observed that the theoretical critical value of individual net damage would be slightly higher than 15%, as already seen in the monotonous and interrupted fatigue tests.

4. Conclusions

This study has provided valuable insights into the fatigue behavior of short glass fiber-reinforced Polyamide 6 (SGFR-PA6), a material of increasing importance in applications traditionally served by metals. Our investigation, utilizing monotonous fatigue tests with and without breaks, alongside the Locati method, has led to several important conclusions regarding the material's performance under cyclic loading conditions.

Firstly, the differentiation between initial (or elastic) damage and plastic (or net) damage in the total damage observed from monotonous fatigue tests with breaks underscores the material's capacity for partial recovery between load applications. This phenomenon highlights the composite's inherent resilience to fatigue, with the elastic component of damage being recoverable upon the release of cyclic stress. The introduction of a model to identify net damage through variations in total energy per cycle relative to initial conditions represents a significant advancement in our understanding of fatigue processes in composite materials. This model provides a robust framework for predicting the onset of critical damage, thereby enhancing the material's application in engineering designs.

Secondly, our findings confirm that the net critical damage in thermal fatigue processes for SGFR-PA6 stabilizes at values close to 15%, irrespective of the stress level applied. This stabilization indicates a threshold beyond which further stress does not proportionally increase the rate of damage accumulation, suggesting a material property that could be exploited in designing components subjected to high cyclic loads.

Furthermore, the comparative analysis of the four Locati test variants reveals minimal influence from the number of cycles per step, the presence or absence of breaks, and the stress increase value between steps on the overall fatigue behavior of SGFR-PA6. This observation not only validates the efficiency of the Locati method in determining the fatigue limit but also suggests the potential for simplifying the test procedure without compromising the reliability of the results.

The ability to define the fatigue limit from the individual net damage (D_{NI}) in a Locati test, as demonstrated by the step from which this parameter begins to increase, offers a practical and accurate method for evaluating the fatigue strength of SGFR-PA6.

This methodology promises to reduce the time and resources required for fatigue testing, facilitating quicker material evaluation and application in design processes.

In conclusion, the research conducted provides a comprehensive assessment of the fatigue behavior of SGFR-PA6, offering critical insights into its damage recovery capabilities, the stability of its critical damage level under thermal fatigue, and the effectiveness of the Locati method for rapid fatigue limit estimation. These findings contribute significantly to the field of materials science, particularly in the optimization and efficient use of short fiber-reinforced thermoplastics in engineering applications.

Future research will focus on exploring the Locati method under various environmental conditions, such as different temperatures and humidity levels, to better understand their impact on the fatigue behavior of SGFR-PA6. Additionally, we plan to test other types of short fiber-reinforced thermoplastics to determine the generalizability of our findings. Developing more advanced predictive models that incorporate real-time monitoring data and sophisticated error analysis techniques will also be a priority. These efforts will contribute to the broader goal of optimizing the use of short fiber-reinforced thermoplastics in engineering applications.

Author Contributions: Conceptualization, I.A.C.; methodology, I.A.C.; formal analysis, I.A.C., J.A.C., and S.D.; data curation, I.A.C., S.D., and J.A.S.-A.; writing—original draft preparation, I.A.C.; writing—review and editing, J.A.C., D.F., J.A.S.-A., and S.D. All authors have read and agreed to the published version of the manuscript.

Funding: This study forms part of the ThinkInAzul programme and was supported by Ministerio de Ciencia e Innovación of Spain with funding from European Union NextGeneration EU (PRTR-C17.I1) and Comunidad de Cantabria.

Institutional Review Board Statement: Not applicable.

Informed Consent Statement: Not applicable.

Data Availability Statement: Data will be made available upon request from the corresponding author.

Conflicts of Interest: The authors declare no conflicts of interest.

References

1. Mallick, P.K. *Fiber-Reinforced Composites: Materials, Manufacturing, and Design*; CRC Press: Boca Raton, FL, USA, 2007; ISBN 1420005987.
2. Brydson, J.A. *Plastics Materials*; Elsevier: Amsterdam, The Netherlands, 1999; ISBN 0080514081.
3. Ibáñez-Gutiérrez, F.T.; Cicero, S.; Carrascal, I.A.; Procopio, I. Effect of fibre content and notch radius in the fracture behaviour of short glass fibre reinforced polyamide 6: An approach from the Theory of Critical Distances. *Compos. Part B Eng.* **2016**, *94*, 299–311. [CrossRef]
4. *EN 1992-4*; Eurocode 2—Design of Concrete Structures. Part 1-1 General Rules and Rules for Buildings. British Standards Institution: London, UK, 2015. [CrossRef]
5. Wöhler, A. Versuche über die Festigkeit der Eisenbahnwagenachsen. *Z. Für Bauwes.* **1860**, *10*, 160–161.
6. *EN 14587-1*; Railway applications-Infrastructure-Flash Butt Welding of New Rails—Part 1: R220, R260, R260Mn, R320Cr, R350HT, R350LHT, R370CrHT and R400HT Grade Rails in a Fixed Plant. CEN: Brussels, Belgium, 2018.
7. Rice, R.C. Fatigue data analysis. In *ASM Handbook*; ASM International: Materials Park, OH, USA, 1985; Volume 8, pp. 695–720.
8. Locati, L. Programmed fatigue test, variable amplitude rotat. *Metall. Ital.* **1952**, *44*, 135–144.
9. Locati, L. *La fatica dei Materiali Metallici*; Hoepli; Ulrico Hoepli: Milano, Italy, 1950.
10. Cantero, B.; Sainz-Aja, J.; Yoris, A.; Medina, C.; Thomas, C. Resonance fatigue behaviour of concretes with recycled cement and aggregate. *Appl. Sci.* **2021**, *11*, 5045. [CrossRef]
11. Kong, D.J.; Xie, C.Y. Effect of laser quenching on fatigue properties and fracture morphologies of boronized layer on Cr12MoV steel. *Int. J. Fatigue* **2015**, *80*, 391–396. [CrossRef]
12. Maximov, J.T.; Anchev, A.P.; Dunchev, V.P.; Ganev, N.; Duncheva, G.V.; Selimov, K.F. Effect of slide burnishing basic parameters on fatigue performance of 2024-T3 high-strength aluminium alloy. *Fatigue Fract. Eng. Mater. Struct.* **2017**, *40*, 1893–1904. [CrossRef]
13. Sainz-Aja, J.; Carrascal, I.; Polanco, J.A.J.A.; Thomas, C. Fatigue failure micromechanisms in recycled aggregate mortar by μCT analysis. *J. Build. Eng.* **2020**, *28*, 101027. [CrossRef]
14. Di Marzo, M.; Tomassi, A.; Placidi, L. A Methodology for Structural Damage Detection Adding Masses. *Res. Nondestruct. Eval.* **2024**, *25*, 172–196. [CrossRef]

15. Casado, J.A.; Carrascal, I.; Polanco, J.A.; Gutiérrez-Solana, F. Fatigue failure of short glass fibre reinforced PA 6.6 structural pieces for railway track fasteners. *Eng. Fail. Anal.* **2006**, *13*, 182–197. [CrossRef]
16. Thomas, C.; Sosa, I.; Setién, J.; Polanco, J.A.; Cimentada, A.I. Evaluation of the fatigue behavior of recycled aggregate concrete. *J. Clean. Prod.* **2014**, *65*, 397–405. [CrossRef]
17. Sullivan, R.W. Development of a viscoelastic continuum damage model for cyclic loading. *Mech. Time-Depend. Mater.* **2008**, *12*, 329. [CrossRef]
18. Gamstedt, E.K.; Berglund, L.A.; Peijs, T. Fatigue mechanisms in unidirectional glass-fibre-reinforced polypropylene. *Compos. Sci. Technol.* **1999**, *59*, 759–768. [CrossRef]
19. Jessen, S.M.; Plumtree, A. Continuum damage mechanics applied to cyclic behaviour of a glass fibre composite pultrusion. *Composites* **1991**, *22*, 181–190. [CrossRef]
20. *UNE-EN ISO 527-2:1997*; Plastics—Determination of Tensile Properties—Part 2: Test Conditions for Moulding and Extrusion Plastics. First Edition. AENOR: Madrid, Spain, 1997.
21. *ISO 527-1:2019*; Plastics—Determination of Tensile Properties—Part 1: General Principles. ISO: Geneva, Switzerland, 2019.
22. *ISO 527-2:2012*; Plastics—Determination of Tensile Properties—Part 2: Test Conditions for Moulding and Extrusion Plastics. Edition 2; CEN: Brussels, Belgium, 2012.

Disclaimer/Publisher's Note: The statements, opinions and data contained in all publications are solely those of the individual author(s) and contributor(s) and not of MDPI and/or the editor(s). MDPI and/or the editor(s) disclaim responsibility for any injury to people or property resulting from any ideas, methods, instructions or products referred to in the content.

applied sciences

MDPI

Article

Evaluation of Early-Age Compressive Strength in Winter Prefabrication: A Comparative Study

Bechara Haddad [1], Farjallah Alassaad [2] and Nassim Sebaibi [1,*]

[1] Builders Lab, Builders Ecole d'Ingénieurs, COMUE Normandie Université, 1 Rue Pierre et Marie Curie, 14610 Epron, France; bechara.haddad@builders-ingenieurs.fr
[2] CMEG–Coopérative Métropolitaine Entreprise Générale, Z.A. de Cardonville, Rue Compagnie D, 14740 Bretteville-L'Orgueilleuse, France; farjallah.alassaad@gmail.com
* Correspondence: nassim.sebaibi@builders-ingenieurs.fr

Abstract: In the field of prefabrication, the timely demolding of concrete elements is crucial to prevent structural failures during panel lifting. This study investigates the early-age compressive strength of different concrete mixtures by simulating various prefabrication plant scenarios. Special attention is given to winter conditions, where concrete hydration tends to be slower, potentially compromising the minimum compressive strength requirement of 10 MPa. The first scenario (reference), set at an ambient temperature of 20 °C with raw materials at room temperature, establishes the baseline for comparison. Two alternative dispositions are explored: Scenario 2, with an external temperature of 8 °C and the water for mixing at 35 °C, and Scenario 3, with the same external temperature but utilizing a heating hood to maintain the concrete at 35 °C. The experimental results shed light on the effectiveness of different strategies in achieving the desired early-age compressive strength under winter conditions. The use of warm mixing water and heating hoods are evaluated as potential measures to counteract the hydration slowdown. The findings contribute valuable insights for optimizing prefabrication processes in cold weather, ensuring the structural integrity of precast concrete elements.

Keywords: precast concrete; early-age strength; cold-weather hydration

1. Introduction

The continual evolution of the construction industry has been significantly characterized by the introduction of novel methodologies that prioritize efficiency, sustainability, and the reduction of construction timelines [1–3]. The precast concrete technique has established itself as an innovative approach, revolutionizing the traditional paradigms of structural development and execution. Based on the off-site manufacture of structural elements, this method represents an innovative alternative to conventional methods of pouring concrete on-site, underlining a shift in building methodologies [4].

At the heart of concrete prefabrication lies an innovative engineering process that facilitates the production of architectural and structural components within a controlled factory environment substantially distant from the actual site of construction. This prefabricated methodology has several advantages, ranging from unparalleled dimensional accuracy to the substantial acceleration of construction schedules. Concrete, known for its durability, is pivotal in this methodology, serving as the backbone that supports structural integrity and facilitates a wide range of architectural expressions [5–7].

The underlying efficiency of the prefabrication process is further enhanced by the standardization of components, which not only enables mass production but also makes construction requirements more cost-effective. Such a methodological transformation has not only changed the construction landscape but has also become a cornerstone in meeting the growing demand for sustainable and resilient construction practices [8].

This exposition lays the groundwork for an in-depth examination of the complexities inherent in concrete prefabrication, defining its qualities, the challenges it faces, and its transformative influence on contemporary construction methodologies [9].

Concrete prefabrication signifies a fundamental shift, redefining the traditional methodologies of constructing edifices. It encompasses the off-site manufacture of building components, marking a new era in construction characterized by superior precision, efficiency, and economic viability. Within this innovative framework, concrete is of essential importance, subjected to complex processes to ensure not just optimal strength but also lasting durability [10].

A critical aspect of prefabrication is the early demolding of concrete elements, a procedure that demands acute attention to the factors that influence compressive strength [11,12]. The industry norm suggests casting concrete on day 'd' and proceeding with demolding on day 'd + 1', or in some instances, as soon as 20 h after casting. However, this expedited process encounters notable challenges, especially under wintry conditions, where the concrete's hydration process, crucial for strength development, is impeded by low temperatures. This poses a significant risk to attaining the minimum compressive strength of 10 MPa required for the safe handling of prefabricated panels [13–17].

In addressing these challenges, a diverse array of strategies is employed, from the use of warm mixing water to the application of heating hoods, highlighting the dynamic approaches to optimizing prefabrication processes against winter-related challenges. This research focuses on the detailed examination of early-age compressive strength across concrete compositions, each designed to mirror the distinctive conditions prevalent in prefabrication factories.

This study looks at the complexities of winter-induced challenges with the aim of elucidating strategies to improve the prefabrication process. It provides new perspectives by systematically examining two industrial systems for mitigating winter-induced challenges, advancing current understanding, and offering practical solutions for improving the structural integrity of precast concrete elements. The ultimate aim is to preserve the structural integrity of precast concrete elements in adverse weather conditions. Through meticulous comparative analysis of different layouts, assessed using calorimetry to understand the internal reactions of concrete, this research seeks to provide a granular understanding and practical solutions to advance precast methodologies. As a result, this survey not only addresses the current challenges facing the sector but also seeks to pave the way for a more resilient and efficient future in prefabricated construction.

Despite extensive research into the prefabrication of concrete elements, there remains a significant gap in our understanding of how different environmental conditions, particularly winter conditions, affect the early strength development of precast concrete [13,18,19]. However, the specific challenges associated with cold weather accelerated curing processes are less explored, particularly with regard to the overall structural integrity and safety of precast concrete elements. Our study aims to fill this gap by systematically exploring the effectiveness of various industrial strategies designed to mitigate the negative effects of winter on the precasting process. Using advanced calorimetric analysis, we provide detailed information on concrete hydration kinetics, providing a nuanced understanding that can directly inform and improve cold-weather concreting practices.

2. Materials and Methods

2.1. Portland Cement

As part of this research, a comprehensive review of industrial references within the studied region revealed the predominance of three specific types of Portland cement: CEM I 52.5 N CE CP2 NF, CEM II/A-LL 52.5 N CE CP2 PM-CP2 NF and CEM II/A-LL 42.5 R CE [20–22]. It is imperative to highlight that each of these cement varieties has been subjected to meticulous conformity assessments in alignment with the standards stipulated by CE labeling. This ensures their adherence to the established quality specifications.

A comprehensive description of their chemical and physical properties is systematically presented in Tables 1 and 2, respectively.

Table 1. Chemical composition of different Portland cement types.

Chemical Characteristics [%]	CEM I 52.5 N CE CP2 NF	CEM II/A-LL 52.5 N CE CP2 PM-CP2 NF	CEM II/A-LL 42.5 R CE
PAF	2.4	-	6
CaO	64.0	63.0	64.5
SiO_2	19.3	19.0	17.9
Al_2O_3	4.8	4.6	4.4
Fe_2O_3	3.0	3.7	2.5
MgO	1.9	1.0	1.2
SO_3	3.2	2.5	2.4
K_2O	1.1	0.96	0.9
Na_2O	0.2	0.06	0.1
Na_2O equival. Actif	0.9	0.71	0.7
Cl^-	0.05	0.04	0.05

Table 2. Evolution of compressive strength in Portland cement variants.

Compressive Strength [MPa]	CEM I 52.5 N CE CP2 NF	CEM II/A-LL 52.5 N CE CP2 PM-CP2 NF	CEM II/A-LL 42.5 R CE
24 h	25	25	-
2 days	39	37	30
7 days	51	51	45
28 days	62	60	54

2.2. Limestone Filler

Due to its economic efficiency, limestone filler finds extensive application across the majority of pre-cast manufacturing factories within the local proximity. This preference is mainly influenced by financial feasibility while preserving the qualities essential for concrete production. To elucidate a thorough comprehension of the limestone filler's attributes utilized, an elaborate product characterization is systematically presented in Table 3.

Table 3. Characterization of limestone filler.

Component	$CaCO_3$	98.2%
	Cl^-	0.003%
	Sulfates	0.01%
	Total silica	0.02
	Others	≈1.77%
Particle size	Particles < 0.125 mm	98%
	Particles < 0.063 mm	90%
Density	2700 kg/m^3	

2.3. Sand

Sand constitutes an essential component within concrete formulations, significantly influencing the attributes and efficacy of the resultant concrete product. The sand incorporated in these mixtures is classified as a washed 0/4 sand. To provide a clear depiction of the material's composition, the physical characteristics of both fine and coarse particulates are delineated in Table 4.

Table 4. Characterization of mechanical and physical properties of washed 0/4 fine aggregate.

Properties	Washed 0/4 sand
Density	2630 kg/m^3
Water absorption	0.1%
Sand equivalent	81.3
Fineness modulus	2.3

2.4. Coarse Aggregate

The preparation of the concrete mix involves the use of semi-crushed, washed stones as the coarse aggregate, with a maximal aggregate dimension of 12.5 mm. Materials procured locally are selected and integrated into the mixture to conform to the agreed specifications. A comprehensive depiction of both the physical and mechanical characteristics of the fine and coarse aggregates is provided in Table 5.

Table 5. Physico-mechanical characterization of semi-crushed washed stones.

Properties	Semi-crushed washed stones
Density	2460 kg/m^3
Water absorption	2.4%
Freeze/thaw resistance	0.2
LOS Angeles	16.0

2.5. Additive

To increase the workability of self-compacting concrete, a superplasticizing additive is added. The superplasticizer used is a non-chlorinated, high water-reducing additive based on 30% solids polycarboxylate technology developed for the prefabrication industry. Furthermore, within the scope of the industrial manufacturing process, the application of an acceleration admixture is adopted to expedite the early-stage demolding process. The Set Accelerator used is a chlorine-free liquid admixture designed to accelerate concrete setting to 43% dry extract. This strategy is instrumental in enhancing the efficiency of production timelines while maintaining the structural and mechanical integrity of the concrete.

3. Experimental Methods

3.1. Mixture Proportioning and Preparation

This study meticulously designed its experimental approach for the effect due to varied environmental conditions while varying the cement types. The concrete mixes were systematically formulated on a constant basis, the main variable being the type of cement used. This variation yielded three distinct mix formulations, each subjected to a unique experimental scenario to investigate the interaction between cement composition, temperature conditions, and the resultant concrete properties.

3.1.1. First Experimental Scenario: Ambient Conditions

Storage of Materials: All the constituent materials, including the cement, were standardized by storing them at an ambient temperature of 20 °C in order to reduce the influence of temperature variability on the properties of the materials.

Mix Preparation and Sample Storage: The preparation of the concrete mix, along with the storage of the resulting samples, was consistently maintained at the ambient temperature of 20 °C. This condition aimed to replicate the standard environmental setting in which concrete is often produced and utilized.

3.1.2. Second Experimental Scenario: Controlled Cold Environment with Warm Mixing Water

Storage of Materials: In this scenario, all the components, with the exception of water, were subjected to a controlled cold environment at 8 °C in order to assess the impact of a reduced temperature on the performance of the concrete. This temperature represents mean temperature in Normandy, France. Conversely, the water was heated to 35 °C prior to mixing to emulate the conditions of warm mixing water typically employed in precast concrete manufacturing facilities, as depicted in Figure 1.

Figure 1. Regulated water temperature for concrete mixing in precast factory.

Mix Preparation and Sample Storage: Both the preparation of the concrete mix and the subsequent storage of samples were conducted within the same controlled environment at 8 °C, providing a consistent temperature setting for the duration of the experimental process.

3.1.3. Third Experimental Scenario: Simulating Post-Casting Heat Treatment

In this scenario, all components were subjected to a controlled cold environment maintained at 8 °C to simulate the application of a heating hood set at 35 °C, as illustrated in Figure 2. The preparation of the concrete mix and the storage of samples both took place within the heating hood, ensuring a uniform temperature environment throughout the experimental process.

In all scenarios, the samples were cured under highly controlled humidity conditions, maintained at 95% relative humidity, ensuring optimum moisture content for the concrete curing process. This rigorous control of the curing environment is crucial to the accurate assessment of the impact of cement under varying temperature conditions. The experimental framework, as described above, provides a comprehensive basis for understanding the behavior of the material under various conditions, reflecting real-world applications. The detailed examination of each scenario highlights the complex dynamics between cement

composition, environmental conditions, and concrete mechanical properties, contributing to the body of knowledge essential to the advancement of concrete technology.

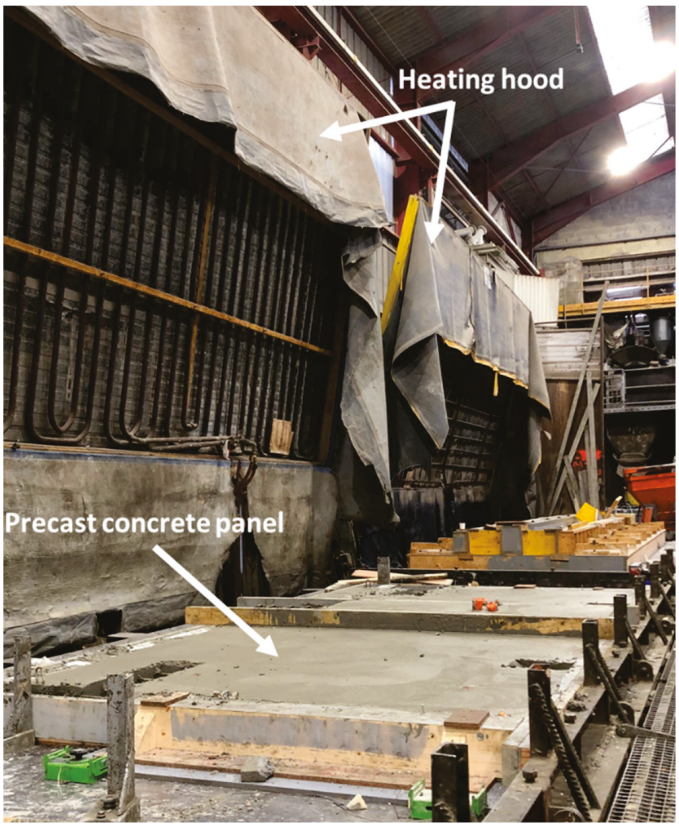

Figure 2. Heated hood system in precast factory.

Formulations and specific experimental conditions are represented in Table 6, with proprietary considerations preventing the disclosure of formulation specifics. This confidentiality is in observance of the proprietary rights of local manufacturing entities. For each experimental mix and scenario, three cylindrical specimens were prepared, along with calorimetric samples for in-depth analysis of thermal evolution, underlining the study's commitment to a systematic and rigorous examination of concrete performance characteristics.

Table 6. Overview of experimental scenarios and formulations for concrete mixes in diverse environmental.

	Scenario 1 T = 20 °C			**Scenario 2 Raw Material 8 °C Water Heated 35 °C Storage 8 °C**			**Scenario 3 Raw Material 8 °C Heat 35 °C**		
	Fi-1	**Fii-1**	**Fiii-1**	**Fi-2**	**Fii-2**	**Fiii-2**	**Fi-3**	**Fii3**	**Fiii-3**
CEM I 52.2N [kg/m^3]	370	-	-	370	-	-	370	-	-
CEM II/A 52.5N [kg/m^3]	-	370	-	-	370	-	-	370	-
CEM II/A-S 42.5R [kg/m^3]	-		370	-	-	370	-	-	370
Limestone filler [kg/m^3]	160	160	160	160	160	160	160	160	160
0/4 sand + 4/12.5 Coarse aggregate [kg/m^3]	1590	1590	1590	1590	1590	1590	1590	1590	1590
Superplasticizer + Accelerator [kg/m^3]	6.6	6.6	6.6	6.6	6.6	6.6	6.6	6.6	6.6
Efficient Water [kg/m^3]	170	170	170	170	170	170	170	170	170

The mixing process utilized a 100-L rotary paddle mixer, adhering to the following steps to ensure consistency and optimal material properties:

Pre-Wetting: Prior to adding the materials, the mixer was pre-wetted to minimize additional water absorption from the mixer walls, which could otherwise affect the water-to-cement ratio and, consequently, the concrete's performance.

Adding Materials: Solid constituents were introduced in a specific order—first gravel, followed by sand, and finally cement. This sequence helps in achieving a more uniform distribution of the fine particles around the coarser aggregates before the cement coats and binds them.

Dry Mixing: The dry components were mixed for 30 s to ensure thorough blending of the aggregates with the cement, which is crucial for the homogeneity of the mix.

Water and additive: Water and additive were then added, and the mixture was blended for 60 s. This initial short mixing period with water allows for the beginning of the hydration process.

Final Mixing: Following the addition of water, the mixture was further mixed for an additional 60 s. This extended mixing time ensures a well-blended mixture, promoting consistency in hydration and performance across all samples.

3.2. Slump Test

In precast concrete applications, the slump test is a key procedure to ensure the concrete's workability matches the requirements for producing high-quality precast elements. The test is conducted by filling a slump cone with fresh concrete in three layers and then lifting the cone to allow the concrete to slump. The degree of slump, measured immediately after cone removal, indicates the concrete's workability. For precast purposes, measurements ranging from 660 to 750 mm classify the concrete as SF2 slump class, signifying a desirable fluidity and ease of mold filling. This classification, aligning with standards such as EN 12350-2, confirms the concrete's suitability for precast applications, ensuring optimal workability for mold filling and structural compactness.

3.3. Compressive Strength Test

Firstly, compressive strengths for Scenario 1 at 20 °C were evaluated to understand different formulations and cement effects in strict adherence to the guidelines specified in the NF EN 12390-3 standard. Subsequently, for the other two scenarios, the assessment of concrete compressive strength was conducted at a concrete age of 24 h. The decision to test at this specific time point was motivated by the need to evaluate early demolding characteristics in unfavorable conditions. In prefabrication factories, the challenge often lies in achieving early-age strength to facilitate rapid demolding, as opposed to the final strength, which typically presents fewer concerns.

The evaluation process involved the use of cylindrical samples measuring 11 $\times$ 22 cm, a dimension specified by the standard for assessing compressive strength. To ensure robust and representative results, three cylindrical samples were tested for each concrete mixture, and the average compressive strength was calculated.

3.4. Calorimetry Test

The study utilizes the calorimetry technique, specifically the calorimetry method conforming to the Langavant method and specifications of the NF EN 196-9 standard, to quantitatively assess the hydration heat evolution of cement across various experimental scenarios during the initial hydration stages. This methodological approach is critical for elucidating the thermal dynamics of cement hydration, an essential factor in understanding the setting and hardening processes of concrete.

3.4.1. Analytical Procedure and Experimental Setup

The calorimetry test is meticulously designed to capture the temperature evolution attributable to the exothermic reaction of cement hydration. By accurately measuring the

heat released during this process, the test provides invaluable insights into the kinetics of cement hydration, offering a detailed understanding of the material's behavior under specific environmental conditions. The hydration heat of foamed concrete is measured during the first few hours using a calorimeter as per the NF EN 196-9 standard. This setup allows the determination of the amount of heat released by the cement from the temperature evolution.

3.4.2. Equipment and Calculations

Experiments are conducted using a calorimeter, which measures the temperature evolution and, thereby, the heat released by the cement during hydration. At a given time, the total heat of cement hydration, Q, is calculated as the sum of the heat accumulated $Qacc$ in the calorimeter and the heat dissipated to the outside $Qdis$, according to $Q = Qacc + Qdis$. Heat accumulated, $Qacc$, is determined using $\frac{c}{mc} \times \Delta T$, where c represents the total heat capacity of the calorimeter, mc is the mass of the cement in the test sample, and ΔT is the temperature difference between the test and reference calorimeters at time t. The heat dissipated, $Qdis$, is calculated from $\frac{1}{mc}\int_0^t \alpha \cdot \Delta T.dt$, where α is the total heat loss coefficient of the calorimeter.

3.4.3. Adaptation to Variable Experimental Conditions

To ensure the relevance and applicability of the calorimetric data to real-world scenarios, both the calorimeter setup and the raw materials are carefully adjusted to replicate the temperature and environmental conditions unique to each experimental scenario. This adaptation is essential for simulating the real conditions under which concrete products could be used, which enhances the validity of the results.

3.4.4. Significance and Implications of Findings

Through the calorimetry analysis, the study aims to derive a comprehensive profile of the thermal characteristics of cement hydration under varied conditions. The data acquired not only reveal the state of the material's heat output at an early age, but also enable concrete mixes and curing processes to be optimized. By understanding the factors influencing the rate and magnitude of heat release during cement hydration, concrete technologists can tailor mix formulations and curing environments to achieve desired performance characteristics, such as setting time and early strength development.

4. Results and Discussion

4.1. Slump Test

Self-compacting concrete is adopted for its ease of implementation. Results in Table 7 show a spread ranging from 660 to 750 mm, categorizing the concrete into the SF2 slump class [23,24]. This exposure class is commonly used for standard horizontal applications. These measurements on fresh concrete were taken before the concrete was placed in storage or subjected to any heating processes.

Table 7. Workability measurements of precast concrete using slump test.

	Scenario 1			**Scenario 2**			**Scenario 3**		
	Fi-1	**Fii-1**	**Fiii-1**	**Fi-2**	**Fii-2**	**Fiii-2**	**Fi-3**	**Fii-3**	**Fiii-3**
Slump flow [mm]	740	725	750	740	730	745	730	725	745

4.2. Compressive Strength Test

In the initial phase of the study, a comprehensive and quantitative evaluation was carried out on the cement formulations under standard test conditions of 20 °C, assessing compressive strength at 24 h, 7 days, and 28 days after mixing. Table 8 represents the outcomes, revealing a compressive strength progression that aligns with the anticipated classes of cement strength. Specifically, the CEM II 42.5 displayed a 28-day compressive

strength of 56.1 MPa, which is lower than the 62.9 MPa and 65.8 MPa observed for CEM I 52.5 and CEM II 52.5, respectively. These results confirm the proportional relationship between early-age strength parameters and subsequent strength achievement, underlining the key industry standard of exceeding the 10 MPa threshold essential for demolding. (Table 8).

Table 8. Early-age and long-term compressive strength of cement formulations under standard conditions (20 °C) in scenario 1.

Compressive Strength [MPa]	Scenario 1 T = 20 °C		
	Fi-1	**Fii-1**	**Fiii-1**
24 h	32.3	31.8	24.3
7 days	55.9	54.3	46.9
28 days	62.9	65.8	56.1

Turning to the analysis of thermal effects on early compressive strength, Table 9 presents data from two divergent scenarios. Scenario 2 recorded a rapid decrease in compressive strength over 24 h, with values of 7.7 MPa, 9.3 MPa, and 3.2 MPa for Fi-2, Fii-2, and Fiii-2, respectively, falling below the demolding criterion despite increasing the initial mix temperature using hot water.

Table 9. Comparative analysis of compressive strength across different formulations and conditions.

	Scenario 1 T = 20 °C			Scenario 2 Material 8 °C Water Heated 35 °C Storage 8 °C			Scenario 3 Material 8 °C Heat 35 °C		
	Fi-1	**Fii-1**	**Fiii-1**	**Fi-2**	**Fii-2**	**Fiii-2**	**Fi-3**	**Fii-3**	**Fiii-3**
Compressive strength [MPa] 24 h	32.3 ± 1	31.8 ± 0.5	24.3 ± 0.7	7.7 ± 0.2	9.3 ± 0.5	3.2 ± 0.2	38.3 ± 1	39.8 ± 1.5	30.9 ± 0.7

This reduction in resistance led to major operational obstacles due to unexpected drops in temperature during the storage phase. In stark contrast, Scenario 3 implemented a sustained heating approach with a hood set to 35 °C. This intervention resulted in a significant improvement in the compressive strength of the early-age concrete, whose initial temperature, with recorded strengths of 38.3 MPa, 39.8 MPa, and 30.9 MPa for Fi-3, Fii-3, and Fiii-3, surpassing the Scenario 1 reference values. The initial material temperatures in this scenario denote a pronounced and beneficial response to the applied heating strategy [25,26]. The findings from these scenarios conclusively indicate the superiority of maintaining consistent temperature control throughout the concrete's setting phase, thus significantly bolstering the material's compressive strength and mechanical properties (Table 9).

4.3. Calorimetric Test

Merging the findings of Figures 3–5 and Table 10, we obtain a cohesive overview of the impact of environmental conditions and cement type on hydration kinetics and mechanical performance across three scenarios: standard ambient curing, cold storage with warm mixing water, and post-mixing heat treatment.

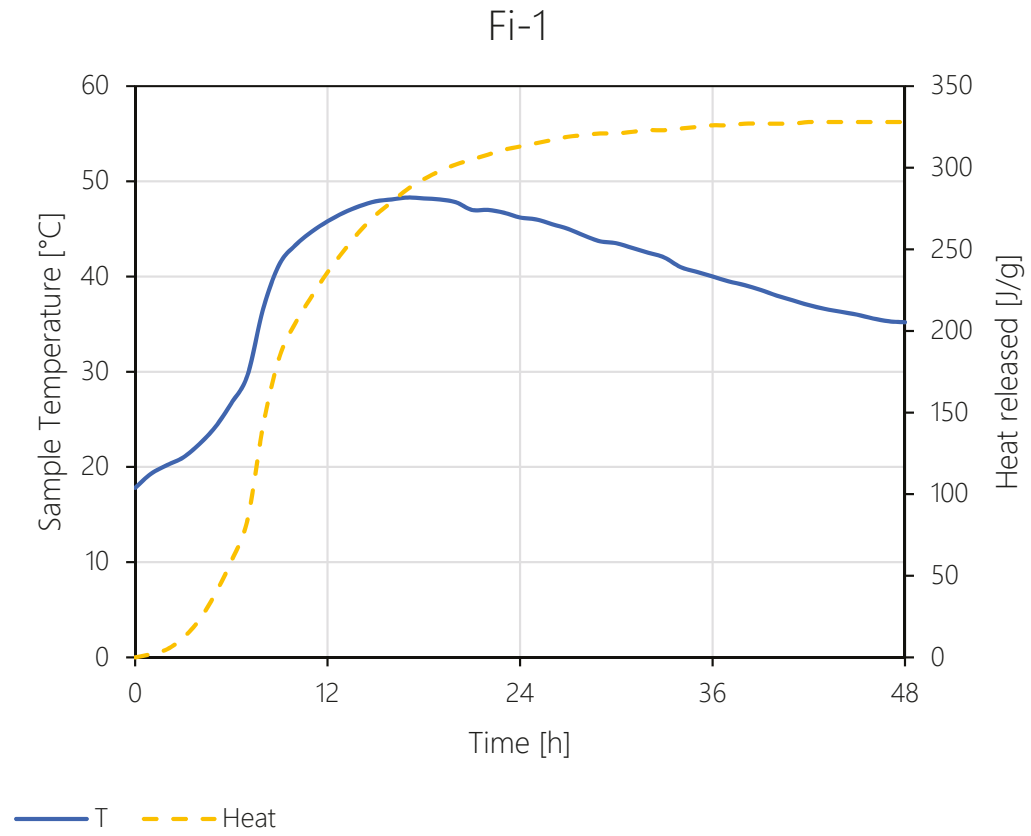

Figure 3. Calorimetric analysis of hydration in fi-1 cement: standard curing conditions.

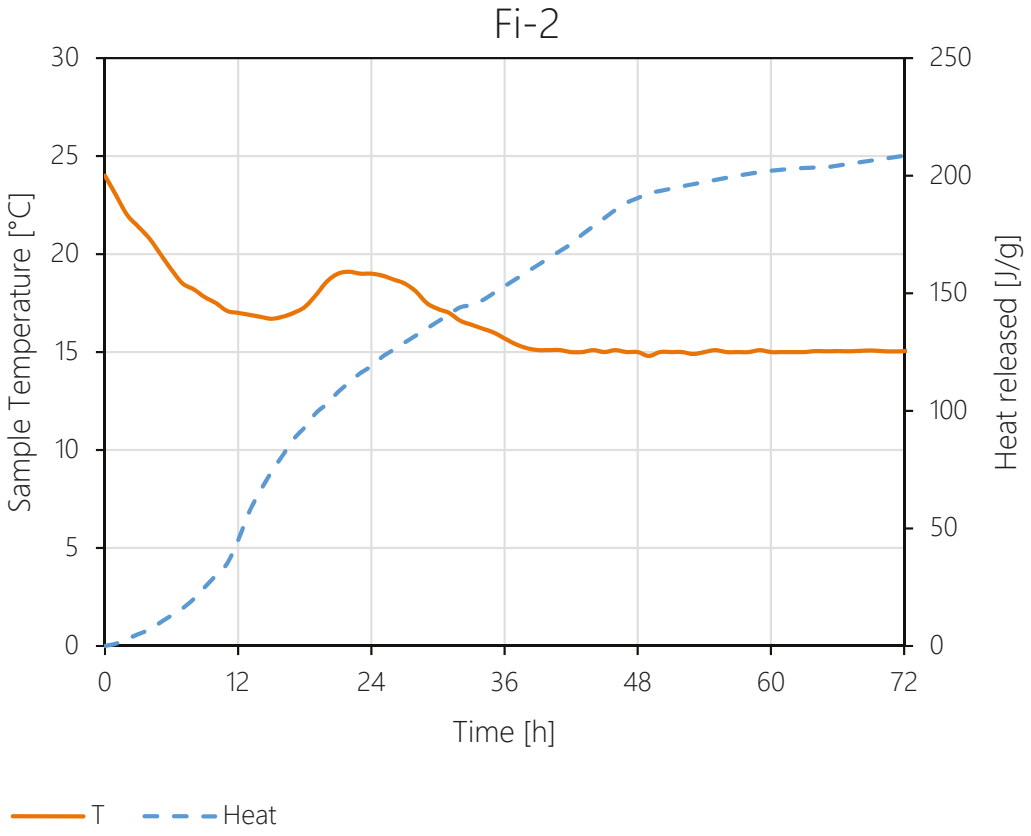

Figure 4. Calorimetric analysis of hydration in fi-2 cement: cold storage conditions.

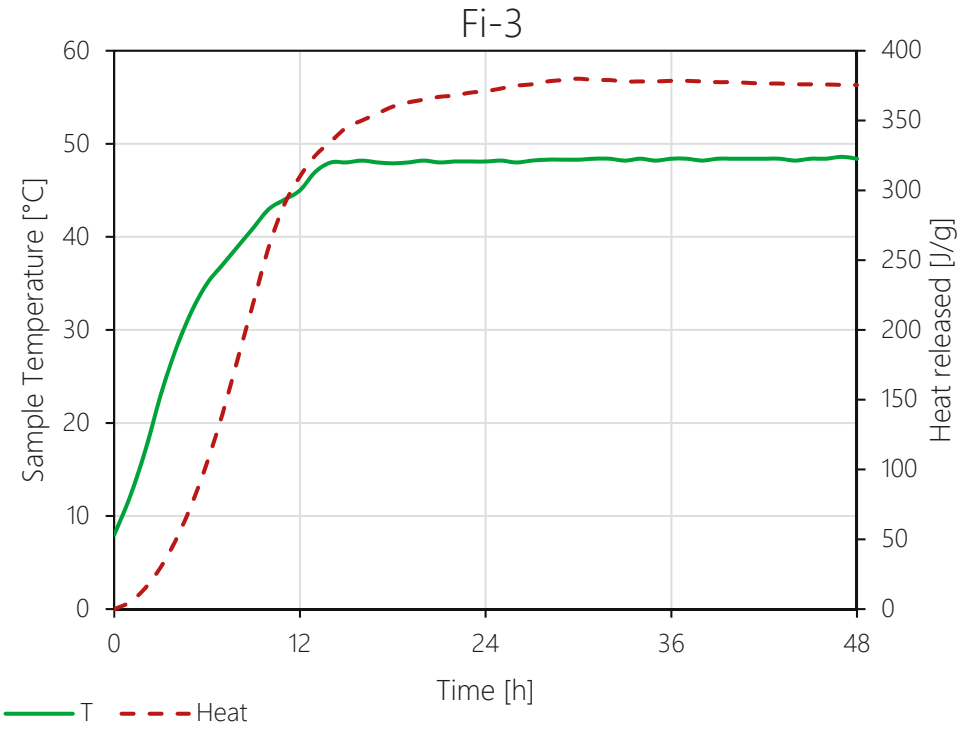

Figure 5. Calorimetric analysis of hydration in fi-3 cement: post-mixing heat treatment.

Table 10. Summary of heat release measurements for cement samples across three curing scenarios.

	Scenario 1 T = 20 °C			**Scenario 2 Material 8 °C Water Heated 35 °C Storage 8 °C**			**Scenario 3 Material 8 °C Heat 35 °C**		
	Fi-1	**Fii-1**	**Fiii-1**	**Fi-2**	**Fii-2**	**Fiii-2**	**Fi-3**	**Fii-3**	**Fiii-3**
Heat realized [J/g]	328	325	241	210	215	82	380	388	310

- Scenario 1: Standard ambient curing

Fi-1: Exhibits a sharp rise in temperature and heat released, indicative of rapid hydration kinetics, primarily due to the high reactivity of CEM I 52.2N. The early peak in temperature followed by a sustained heat release suggests an aggressive exothermic reaction typical of high-grade Portland cement. The calorimetric data reveal the highest heat release at 328 J/g, corresponding with a significant early-age compressive strength of 32.3 MPa.

Fii-1 and Fiii-1: Show moderated calorimetric profiles due to the inclusion of SCMs (Supplementary Cementitious Materials), with heat releases of 325 J/g and 241 J/g, respectively. This moderation is reflected in the slightly adjusted strength values of 31.8 MPa and 24.3 MPa, indicating the SCMs' effectiveness in tailoring the hydration kinetics and strength development path.

- Scenario 2: Cold Storage with warm mixing water

Fi-2: The rise in temperature is less marked, and the increase in heat released is more gradual, with a significant reduction in the heat released at 210 J/g due to cold storage conditions. This scenario highlights a delayed and prolonged dormant phase of hydration, leading to a markedly lower compressive strength of 7.7 MPa.

Fii-2 and Fiii-2: Reflect slightly higher total heat releases (215 J/g and 82 J/g, respectively) than Fi-2, showing the mitigating effect of SCMs on cold cure conditions. The resultant compressive strengths of 9.3 MPa and 3.2 MPa provide insight into the complex interactions between cement hydration and SCM reactivity under adverse temperature conditions.

- Scenario 3: Post-Mixing heat treatment

Fi-3: The calorimetric profile indicates a rapid temperature increase followed by a sharp rise in heat release, suggesting a highly accelerated hydration process facilitated by post-mixing heat treatment. This is evidenced by a pronounced heat release of 380 J/g, directly correlating with a significant increase in compressive strength to 38.3 MPa.

Fii-3 and Fiii-3: Also exhibit substantially higher heat releases (388 J/g and 310 J/g, respectively), indicating accelerated hydration kinetics due to elevated temperature curing. The observed compressive strengths (39.8 MPa and 30.9 MPa) highlight the potential of controlled heating to enhance both the rate and extent of cement hydration, significantly impacting mechanical performance.

The comprehensive analysis intertwining calorimetric data and mechanical performance across different curing scenarios unveils profound insights into the complex nature of cement hydration and its implications for concrete technology. By meticulously examining the interaction between environmental conditions, cement chemistry, and supplementary cementing materials, we gain a polyvalent understanding of concrete comportment [27–29].

- Enhanced understanding of hydration phases

Calorimetric profiles and mechanical data give a detailed insight into the hydration process:

Initial Reaction Phase: The pronounced temperature rise and heat release in the initial reaction phase, especially evident in Fi-1, underscores the high reactivity of CEM I 52.2N. This rapid onset of hydration highlights the sensitivity of this phase to cement composition, setting the stage for early strength development.

Dormant Period: The extended dormant period observed in Fi-2, marked by lower heat release and a flat temperature profile, illustrates how environmental conditions, specifically cold, can significantly delay the hydration process. This delay has critical implications for the curing of concrete in adverse conditions, underlining the need for appropriate curing practices.

Acceleration to Steady State: The swift transition to a steady-state phase in Fi-3, facilitated by post-mixing heat treatment, demonstrates an optimized environment for continuous hydration product formation. This phase is essential for achieving high strength and durability in the early stages of aging, as it ensures a sustained reaction that contributes to the development of the microstructure [30,31].

- Correlation of heat and temperature dynamics with mechanical properties

The analysis shows a direct correlation between the calorimetric data and the mechanical properties of the concrete [32,33]:

Heat-Temperature Lag: The observed lag between temperature peaks and maximum heat release, particularly in Fi-1, could be indicative of the timing in the formation of critical hydration products like calcium silicate hydrate (C-S-H), which is instrumental in strength development. This lag not only reflects the kinetics of chemical reactions but also the evolving microstructure of the concrete [34].

Temperature Stability: The stable temperature profile in the midst of increasing heat release, as seen in Fi-3, suggests a curing environment conducive to sustained hydration. This stability is essential for the development of a dense microstructure, which is essential for the durability and strength of the product [32,33,35–39].

- Strategic curing practices

The data support the use of strategic curing practices to enhance concrete performance:

Heat Treatment: The significant role of heat treatment in enhancing early-age strength, particularly in Scenario 3, points to its potential in precast concrete operations. This finding suggests that controlled thermal environments can substantially accelerate strength development, enabling more efficient production cycles [40,41].

Environmental and Material Considerations: The impact of cold curing conditions on hydration kinetics highlights the importance of managing ambient and material tempera-

tures. Adjusting curing practices, such as employing heated mixing water or insulating forms, can mitigate the adverse effects of cold environments, highlighting the need for flexibility and adaptation in curing strategies.

5. Conclusions

This study summarizes the results of our detailed research into the impact of various environmental and thermal management strategies on the hydration kinetics and mechanical properties of cementitious formulations. It provides essential information with considerable implications for concrete technology.

In particular, under the challenging conditions that exist in cold weather precast concrete production, the research provides a convincing argument for the complex interactions between cement composition, supplementary cementitious materials (SCMs), and curing methodologies.

Quantitative assessments, including workability tests via slump measurements and compressive strength evaluations, as well as calorimetric analysis, form the experiential backbone of our discourse. These methodologies reveal a nuanced understanding of how strategic thermal management significantly influences the hydration process and, by extension, the structural and mechanical integrity of concrete.

Workability tests consistently place self-compacting concrete in slump class SF2, indicating consistently high workability in all scenarios. This quantitative evidence demonstrates the material's adaptability to standard horizontal applications, highlighting the critical nature of consistent workability to ensure efficient production and structural integrity of precast concrete elements, whatever the curing environment.

The study of compressive strength provides a remarkable illustration of the differences in performance under different curing conditions. Notably, under controlled heating conditions (Scenario 3), the concrete showed a remarkable increase in compressive strength at an early age—measurements such as 38.3 MPa, 39.8 MPa, and 30.9 MPa significantly exceeded those of standard ambient curing (Scenario 1) and interventions using warm mixing water (Scenario 2). These quantitative results not only illustrate the negative impact of cold weather on the early strength development of concrete but also support the effectiveness of sustainable heating approaches, such as fume hoods, in improving structural efficiency and durability.

In addition, calorimetric analysis provides a deeper understanding of concrete hydration kinetics, establishing a clear correlation between thermal management strategies and the hydration process. The acceleration of hydration kinetics demonstrated in the post-mix heat treatment scenario, marked by increased heat release and temperature stability, elucidates the optimization of the hydration process. This is essential to achieve a rapid gain in strength and improve the microstructural development of the concrete matrix, thus contributing to the durability and performance of the material.

In conclusion, our results argue for a strategic re-evaluation of curing practices in precast concrete production, highlighting the critical role of environmental and thermal management in mitigating the adverse effects of cold weather conditions. The superior performance of concrete under controlled heating conditions highlights the need for the construction industry to adopt innovative strategies that optimize structural and mechanical performance in a variety of climatic scenarios.

This study not only advances the field of concrete technology by providing a quantitative benchmark for future research but also highlights the imperative for actors in the construction industry to incorporate advanced hardening technologies and material innovations. This research is highly relevant to the precast concrete industry as it provides practical solutions and valuable insights to address the critical challenge of achieving adequate early-age compressive strength under adverse winter conditions, which is essential for the efficient and safe production of prefabricated concrete elements. The aim is to meet the industry's evolving challenges and lead the way in the development of resilient, durable, and high-performance concrete structures. The ideas gathered here provide the basis for new research

and development efforts aimed at refining precast concrete methodologies to achieve an optimal balance between material performance, durability, and architectural versatility.

Author Contributions: Conceptualization, B.H. and F.A.; methodology, B.H., N.S. and F.A.; formal analysis B.H., N.S. and F.A.; writing—original draft preparation, B.H. and F.A.; supervision, N.S. All authors have read and agreed to the published version of the manuscript.

Funding: This research received no external funding.

Data Availability Statement: The raw data supporting the conclusions of this article will be made available by the authors on request.

Acknowledgments: The authors would like to acknowledge the contribution of Master Builders Solution in providing raw materials and technical support.

Conflicts of Interest: Author Farjallah Alassaad was employed by the company CMEG. The remaining authors declare that the research was conducted in the absence of any commercial or financial relationships that could be construed as a potential conflict of interest.

References

1. Zhang, C.; Hu, M.; Yang, X.; Amati, A.; Tukker, A. Life cycle greenhouse gas emission and cost analysis of prefabricated concrete building façade elements. *J. Ind. Ecol.* **2020**, *24*, 1016–1030. [CrossRef]
2. Haddad, B.; Karaky, H.; Boutouil, M.; Boudart, B.; Sebaibi, N. Investigation Properties of Pervious and Water-Retaining Recycled Concrete to Mitigate Urban Heat Island Phenomena. *Sustainability* **2023**, *15*, 5384. [CrossRef]
3. Vujovic, S.; Haddad, B.; Karaky, H.; Sebaibi, N.; Boutouil, M. Urban Heat Island: Causes, Consequences, and Mitigation Measures with Emphasis on Reflective and Permeable Pavements. *CivilEng* **2021**, *2*, 459–484. [CrossRef]
4. Rocha, P.F.; Ferreira, N.O.; Pimenta, F.; Pereira, N.B. Impacts of Prefabrication in the Building Construction Industry. *Encyclopedia* **2022**, *3*, 28–45. [CrossRef]
5. Seo, W.; Choi, B.; Shin, D.; Kim, J. Development of a quality management system for precast concrete factories. *J. Civ. Eng. Manag.* **2023**, *29*, 475–486. [CrossRef]
6. Jiang, R.; Mao, C.; Hou, L.; Wu, C.; Tan, J. A SWOT analysis for promoting off-site construction under the backdrop of China's new urbanisation. *J. Clean. Prod.* **2018**, *173*, 225–234. [CrossRef]
7. Yu, T.; Man, Q.; Wang, Y.; Shen, G.Q.; Hong, J.; Zhang, J.; Zhong, J. Evaluating different stakeholder impacts on the occurrence of quality defects in offsite construction projects: A Bayesian-network-based model. *J. Clean. Prod.* **2019**, *241*, 118390. [CrossRef]
8. Blismas, N.; Wakefield, R.; Hauser, B. Concrete prefabricated housing via advances in systems technologies: Development of a technology roadmap. *Eng. Constr. Archit. Manag.* **2010**, *17*, 99–110. [CrossRef]
9. Fei, D. Research and analysis on technological innovation of prefabricated building construction. In *Advances in Urban Construction and Management Engineering*; CRC Press: Boca Raton, FL, USA, 2023.
10. Placzek, G.; Schwerdtner, P. Concrete Additive Manufacturing in Construction: Integration Based on Component-Related Fabrication Strategies. *Buildings* **2023**, *13*, 1769. [CrossRef]
11. Dushimimana, A.; Niyonsenga, A.A.; Nzamurambaho, F. A review on strength development of high performance concrete. *Constr. Build. Mater.* **2021**, *307*, 124865. [CrossRef]
12. Nunez, I.; Marani, A.; Flah, M.; Nehdi, M.L. Estimating compressive strength of modern concrete mixtures using computational intelligence: A systematic review. *Constr. Build. Mater.* **2021**, *310*, 125279. [CrossRef]
13. Fan, C.; Qian, J.; Sun, H.; Fan, Y. Development and Promotion of Concrete Strength at Initial 24 Hours. *Materials* **2023**, *16*, 4452. [CrossRef] [PubMed]
14. Zou, F.; Hu, C.; Wang, F.; Ruan, Y.; Hu, S. Enhancement of early-age strength of the high content fly ash blended cement paste by sodium sulfate and C–S–H seeds towards a greener binder. *J. Clean. Prod.* **2020**, *244*, 118566. [CrossRef]
15. Dorn, T.; Blask, O.; Stephan, D. Acceleration of cement hydration—A review of the working mechanisms, effects on setting time, and compressive strength development of accelerating admixtures. *Constr. Build. Mater.* **2022**, *323*, 126554. [CrossRef]
16. Dongxu, L.; Jinlin, S.; Lin, C.; Xuequan, W. The influence of fast-setting/early-strength agent on high phosphorous slag content cement. *Cem. Concr. Res.* **2001**, *31*, 19–24. [CrossRef]
17. Su, Y.; Wu, L.; He, X.; Zheng, Z.; Tan, H.; Yang, J.; Ma, Q.; Ding, J.; Bao, M. A novel early strength agent prepared by wet-grinding concrete waste slurry and its effect on early hydration and mechanical properties of cement based materials. *Constr. Build. Mater.* **2023**, *362*, 129673. [CrossRef]
18. Kosar, K.; Khazanovich, L.; Salles, L. Evaluation of Early Age Concrete Pavement Strength by Combined Nondestructive Tests. *Appl. Sci.* **2023**, *13*, 2240. [CrossRef]
19. Li, L.; Shi, J.; Yan, Z.; Kou, J. Triaxial tests on high ductile concrete under different environmental conditions. *Struct. Concr.* **2023**, *24*, 4015–4028. [CrossRef]
20. Bullard, J.W.; Jennings, H.M.; Livingston, R.A.; Nonat, A.; Scherer, G.W.; Schweitzer, J.S.; Scrivener, K.L.; Thomas, J.J. Mechanisms of cement hydration. *Cem. Concr. Res.* **2011**, *41*, 1208–1223. [CrossRef]

21. Portland Cement Hydration—An Overview | ScienceDirect Topics. Available online: https://www.sciencedirect.com/topics/engineering/portland-cement-hydration (accessed on 29 March 2024).
22. Scrivener, K.L.; Juilland, P.; Monteiro, P.J.M. Advances in understanding hydration of Portland cement. *Cem. Concr. Res.* **2015**, *78*, 38–56. [CrossRef]
23. Udayasree, B.; Kumar, G.S. Properties of self-compacting concrete modified with m-sand and spent foundry slag. *Int. Rev. Appl. Sci. Eng.* **2023**, *14*, 426–430. [CrossRef]
24. Shruthi, B.S. Anilkumar An Experimental Study on Self-Compacting Concrete by Using Silica Fume and Fly Ash. In *Recent Advances in Civil Engineering*; Nandagiri, L., Narasimhan, M.C., Marathe, S., Eds.; Springer Nature: Singapore, 2023; pp. 185–196.
25. Popovics, S. *Strength and Related Properties of Concrete: A Quantitative Approach*; John Wiley & Sons: Hoboken, NJ, USA, 1998.
26. Gutteridge, W.A.; Dalziel, J.A. Filler cement: The effect of the secondary component on the hydration of Portland cement: Part I. A fine non-hydraulic filler. *Cem. Concr. Res.* **1990**, *20*, 778–782. [CrossRef]
27. Delannoy, G. Durabilité d'Isolants à Base de Granulats Végétaux. Ph.D. Thesis, Université Paris-Est, Créteil, France, 2018. Available online: https://theses.hal.science/tel-02141189 (accessed on 29 March 2024).
28. Aïtcin, P.-C. Supplementary cementitious materials and blended cements. In *Science and Technology of Concrete Admixtures*; Elsevier: Amsterdam, The Netherlands, 2016; pp. 53–73. [CrossRef]
29. Page, J. Formulation et Caractérisation d'un Composite Cimentaire Biofibré pour des Procédés de Construction Préfabriquée. Ph.D. Thesis, Normandie Université, Mont-Saint-Aignan, France, 2017. Available online: https://theses.hal.science/tel-01713160 (accessed on 29 March 2024).
30. Dragomirová, J.; Palou, M.T.; Kuzielová, E.; Žemlička, M.; Novotný, R.; Gméling, K. Optimization of cementitious composite for heavyweight concrete preparation using conduction calorimetry. *J. Therm. Anal. Calorim.* **2020**, *142*, 255–266. [CrossRef]
31. Khalaf, M.A.; Ban, C.C.; Ramli, M. The constituents, properties and application of heavyweight concrete: A review. *Constr. Build. Mater.* **2019**, *215*, 73–89. [CrossRef]
32. Kearsley, E.; Mostert, D. Designing mix composition of foamed concrete with high fly ash contents. In Proceedings of the International Conference Use of Foamed Concrete in Construction, Scotland, UK, 5 July 2005; pp. 29–36.
33. Kearsley, E.P.; Wainwright, P.J. The effect of high fly ash content on the compressive strength of foamed concrete. *Cem. Concr. Res.* **2001**, *31*, 105–112. [CrossRef]
34. Berodier, E. Understanding the Filler Effect on the Nucleation and Growth of C-S-H. *J. Am. Ceram. Soc.* **2014**, *97*, 3764–3773. Available online: https://ceramics.onlinelibrary.wiley.com/doi/abs/10.1111/jace.13177 (accessed on 29 March 2024). [CrossRef]
35. De Silva, P.S.; Glasser, F.P. Phase relations in the system CaO Al_2O_3 SiO_2 H_2O relevant to metakaolin—Calcium hydroxide hydration. *Cem. Concr. Res.* **1993**, *23*, 627–639. [CrossRef]
36. Gruyaert, E.; Tittelboom, K.V.; Rahier, H.; Belie, N.D. Activation of Pozzolanic and Latent-Hydraulic Reactions by Alkalis in Order to Repair Concrete Cracks. *J. Mater. Civ. Eng.* **2015**, *27*, 04014208. [CrossRef]
37. Balčiūnas, G.; Pundienė, I.; Lekūnaitė-Lukošiūnė, L.; Vėjelis, S.; Korjakins, A. Impact of hemp shives aggregate mineralization on physical–Mechanical properties and structure of composite with cementitious binding material. *Ind. Crop. Prod.* **2015**, *77*, 724–734. [CrossRef]
38. Pore Structure and Permeation Characteristics of Foamed Concrete. Available online: https://www.jstage.jst.go.jp/article/jact/12/12/12_535/_article (accessed on 29 March 2024).
39. Huang, Y.; Liu, G.; Huang, S.; Rao, R.; Hu, C. Experimental and finite element investigations on the temperature field of a massive bridge pier caused by the hydration heat of concrete. *Constr. Build. Mater.* **2018**, *192*, 240–252. [CrossRef]
40. Taylor, H.F.W.; Famy, C.; Scrivener, K.L. Delayed ettringite formation. *Cem. Concr. Res.* **2001**, *31*, 683–693. [CrossRef]
41. Thiebaut, Y.; Multon, S.; Sellier, A.; Lacarrière, L.; Boutillon, L.; Belili, D.; Linger, L.; Cussigh, F.; Hadji, S. Effects of stress on concrete expansion due to delayed ettringite formation. *Constr. Build. Mater.* **2018**, *183*, 626–641. [CrossRef]

Disclaimer/Publisher's Note: The statements, opinions and data contained in all publications are solely those of the individual author(s) and contributor(s) and not of MDPI and/or the editor(s). MDPI and/or the editor(s) disclaim responsibility for any injury to people or property resulting from any ideas, methods, instructions or products referred to in the content.

MDPI AG
Grosspeteranlage 5
4052 Basel
Switzerland
Tel.: +41 61 683 77 34

Applied Sciences Editorial Office
E-mail: applsci@mdpi.com
www.mdpi.com/journal/applsci

Disclaimer/Publisher's Note: The title and front matter of this reprint are at the discretion of the Guest Editors. The publisher is not responsible for their content or any associated concerns. The statements, opinions and data contained in all individual articles are solely those of the individual Editors and contributors and not of MDPI. MDPI disclaims responsibility for any injury to people or property resulting from any ideas, methods, instructions or products referred to in the content.

Academic Open
Access Publishing

mdpi.com

ISBN 978-3-7258-7668-6